



Sudan University of Science and Technology
College of Graduate studies



MODELLING MECHANICAL AND THERMAL PROPERTIES OF CARBON NANOTUBES REINFORCED METAL MATRIX COMPOSITES

نمذجة الخواص الميكانيكية والحرارية للمركبات ذات الكنان المعدني
المدعمة باسطوانات الكربون النانويه

A thesis submitted in fulfillment of the requirements for the
award of the degree of Doctor of Philosophy in Mechanical
Engineering

Prepared by: GEHAD G.S. HAMDAN

Supervised by: PROF. SAAD MOHAMED AHMED SULIMAN

Co-Supervisor: ASSOC.PROF. DR. AL-KHAWAD ALI ELFAKI

2017م - 1438هـ

DECLARATION

I, the signing here-under, declare that I'm the sole author of the Ph.D. thesis entitled: **Modeling Mechanical and Thermal Properties of Carbon Nanotubes Reinforced Metal Matrix Composites**, which is an original intellectual work. Willingly, I assign the copy-right of this work to the College of Graduate Studies (CGS), Sudan University of Science and Technology (SUST). Accordingly, SUST has all the rights to publish this work for scientific purposes.

Candidate's name: Gehad G.S. Hamdan

Candidate's signature:

Date:

الأستهلالات



سورة يوسف الآية (76)

“We raise by grades (of mercy) whom We will, and over every lord of knowledge there is one more knowing. ”

Joseph; Verses76

DEDICATION

**Specially dedicated to the memory of my
Parents**

**To Adib DAJANI, words are short to depict the
proper image he deserves**

**To Rodwan, Taha, Salsabeel, and Farah who
have given my life a new light, value and
made me see unique and especial.**

ACKNOWLEDGEMENTS

I would like to express my most sincere gratitude and deep appreciation to Prof. Saad Mohamed Ahmed Suliman the chairman of my supervisory committee, for his excellent supervision, constructive comments. My thanks also goes to the members of my supervisory committee, Dr. Al-Khawad Ali Elfaki for his ennobling association, and for giving me another dimension to life and taking time off from his busy schedule to serve in the committee. My thanks also go to Dr. Mohanad Al-Herbawi, Dr. Ali Matar, Dr. Mohamed Aqel, and Dr-Abdul Hafeez Eleila for the tremendous help they offered; constant encouragement, support, their guidance and assistance were priceless, so also their fruitful suggestions, support and vision and unfailing help during my research work.

I would like to express my gratitude to all staff members of department of Mechanical engineering, Faculty of Engineering, and the College of Graduate Studies, Sudan University of Science and Technology, for their kind assistance during my studies.

It is worth to mention my friends and colleagues from whom I received direct and indirect support; I would like to thank Dr. Fares Elsagga, Mr. Medhat Hassan, Mr. Mohanad Khairy, Mr. Munther Ahmed, Mr. Musbah, and all friends whose names have not been mentioned, for their companionship support and concern.

Above all, I would like to thank my wife, brothers, and sisters for their sacrifice, patience, understanding, help and encouragement throughout the study.

Last, but definitely not least, many thanks to my family friends (Nimat Dajani) for their tremendous support and help.

There are some supporting people that I might have forgotten a big thank you to everyone who have helped me in one way or another. My humblest apologies to those are not cited here among these lines but they have earned it for themselves by being the most generous and helpful.

ABSTRACT

The research dealt with the implementation of a macro working under ANSYS to enable simulation a set of models using square representative volume element and a MATLAB code using the theories available for predicting nanocomposites properties in terms of longitudinal and transverse Young's modulus, shear modulus, major Poisson's ratio, and study the impact of different geometric and distribution of carbon nanotubes on four factors affecting the thermal conductivity of nanocomposites which are length, diameter, resistance between carbon nanotubes and metal matrix and finally the volume fraction of carbon nanotubes in the metal matrix to predict the mechanical and thermal properties of the carbon nanotubes reinforced metal matrix related to this research and then compared. The research used three metals: iron, copper and aluminum, which were reinforced by three types of carbon nanotubes to be studied according to two cases: the first case is the assumption that the carbon nanotubes as long fiber and placed throughout the square representative volume element and the second case, the carbon nanotubes will treated as short fiber. The problem of the research was the understanding of mechanical and thermal properties of carbon nanotubes reinforced metal matrix is not enough and scarce, which affect choosing the optimal design for use in the nanotechnology engineering fields because of the difficulty and cost of conducting experiments due to the small size of the components. Modeling and computer simulation therefore play an important role in predicting the properties of these composite materials. The importance of the research stems from the increasing interest in composite materials in recent years as an engineering material. These materials have proved very successful in various fields due to their unique properties. Nanotechnology has become one of the most important and exciting fields in physics, chemistry, biology, engineering and many other fields. It has given great hope to scientific revolutions that will change the way of technology and have now received great attention because of its promising applications. The concept of nanotechnology is based on the use of carbon nanotubes because of its outstanding properties which was the inspiration for many research and scientific publications in this field and become an important element for the development of a new generation of composite materials specifically in the field of

reinforcing metal matrix. The results were obtained by using the macro to simulate the geometry of the different models, which showed a good agreement with the analytical results using the MATLAB code. Consequently, the results showed that the effect of the various factors contributed to increasing the effectiveness of the mechanical and thermal conductivity properties predicted by different Theoretical models. Since theoretical models are based on different assumptions, these assumptions also affect such characteristics theoretically, experimentally through various computational methods as well as modeling work using different simulations. The research recommended the need to do more specialized research on some subjects that can be done by these models.

المستخلص

تناولت الدراسة مجال تصميم ماكرو يعمل تحت برنامج ANSYS باستخدام نماذج أحجام مربعة متماثله ليتمكن من عمل محاكاة لمجموعه من مربعات الأحجام المتماثلة وكذلك كتابة برنامج يعمل على MATLAB باستخدام النظريات المتوفرة لمثل هذه الحسابات لمركبات متناهية الصغر من حيث حساب معامل يونغ، و معامل القص ودراسة تأثير مختلف الاشكال الهندسية وتوزيع الانابيب النانوية على اربع عوامل مؤثرة على التوصيل الحراري من المركبات النانوية وهى الطول وطول القطر، ومقاومة الأنابيب النانوية و الكنان المعدني الموجودة به وأخيرا حجم أنابيب الكربون في الكنان المعدني وذلك لعمل الحسابات اللازمة للخواص الميكانيكية والحرارية للمركبات ذات الكنان المعدني والمدعمة بأنابيب الكربون النانوية المتعلقة بالدراسة ومن ثم مقارنة هيا. هذه الدراسة اعتمدت ثلاث مواد معدنية؛ وهى الحديد والنحاس والألومنيوم، حيث تم تدعيمهم بثلاثة أنواع من أنابيب الكربون النانوية لدراستها وفقا لحالتين : الحالة الاولى وهى فرضية ان يكون طول الانابيب الكربونية مساويا لطول الحجوم المربعة المتماثلة أما الحالة الثانية فستكون مع اطوال قصيرة لتدعيم ثلاثة أنواع من المعادن. تمثلت مشكلة الدراسة في أن فهم الخواص الميكانيكية للمواد المدعمة بالأنابيب النانوية الكربونية لا يزال غير كاف الأمر الذى أدى الى صعوبة ومحدودية اختيار التصميم الامثل للاستفادة منها في المجالات الهندسية لتكنولوجيا النانو وذلك لصعوبة وتكلفة اجراء التجارب العملية نظرا لصغر حجم المكونات لهذا فإن النمذجة والمحاكاة الحاسوبية تلعب دورا هاما في التنبؤ بخصائص هذه المواد المركبة . نبعت أهمية الدراسة من ازدياد الاهتمام بالمواد المركبة في السنوات الأخيرة كمادة هندسية وقد أثبتت هذه المواد نجاحا كبيرا في مختلف المجالات وذلك لخواصها الفريدة ، وحيث ان تقنية النانو أصبحت في طليعة المجالات الأكثر أهمية وإثارة في الفيزياء، الكيمياء، الأحياء والهندسة ومجالات عديدة أخرى. فقد أعطت أملاً كبيراً لثورات علمية ستغير وجه التقنية وحظيت في الوقت الحاضر بالاهتمام الكبير نظراً لما أبدته من تطبيقات واعدة وكثيرة شملت المجالات الطبية، العسكرية، الاتصالات، الالكترونية، الحاسوبية، البيتروكيميائية، الزراعية وغيرها، وأدى ذلك إلي دعم عالمي سخي واسع لأبحاث النانو في السنوات الأخيرة. يعتمد مفهوم تقنية النانو على استخدام اسطوانات الكربون النانوية نظرا لما تملكه من خصائص ومميزات كبيرة كانت الالهام للعديد من البحوث

والنشرات العلمية في هذه المجال حيث اصبحت عنصرا هاما لتطوير جيل جديد من المواد المركبة و تلقت الكثير من الاهتمام في السنوات الأخيرة وهناك بعض الأدلة على إثبات إمكانية تطبيق أنابيب الكربون في تقوية المركبات ذات الكنان المعدني.

توصلت الدراسة إلى العديد من النتائج تم الحصول عليها باستخدام الماكرو للمحاكاة الهندسية للنماذج المختلفة حيث اظهرت توافقا جيدا مع النتائج التحليلية باستخدام برمجية MATLAB وبناء على ذلك، فإن النتائج اظهرت أن تأثير العوامل المختلفة قد ساهم في زيادة فعالية خصائص المرونة و الموصلية الحرارية التي تنبأت بها مختلف النماذج النظرية. وحيث ان النماذج النظرية تستند على افتراضات مختلفة ، هذه الافتراضات تؤثر أيضا على مثل هذه الخصائص نظريا ، وتجريبيا من خلال الطرق الحسابية المختلفة وكذلك عمل النمذجة باستخدام برامج المحاكاة المختلفة. توصلت الدراسة إلى عدد من التوصيات منها ضرورة عمل المزيد من الأبحاث المتخصصة على بعض الموضوعات التي يمكن تطبيق هذه النماذج عليها.

TABLE OF CONTENT

	Page
DECLARATION	ii
الأستهلال	iii
DEDICATION	iv
ACKNOWLEDGEMENT	v
ABSTRACT	vi
المستخلص	viii
TABLE OF CONTENTS	x
LIST OF TABLES	xiii
LIST OF FIGURES	xix
LIST OF ABBREVIATIONS	xxxiii
LIST OF SYMBOLS	xxxiv
CHAPTER ONE: INTRODUCTION	
1.1 Overview	1
1.2 Significance of the Research	3
1.3 Problem Statement	4
1.4 Objectives	5
1.5 Research Limitations	5
1.6 Thesis Layout	5
CHAPTER TWO: LITERATURE REVIEW	
2.1 Overview	7
2.2 Nanocomposites Materials	7
2.3 Carbon Nanotubes	8
2.3.1 Atomic Structure	9
2.3.2 Bonding Mechanism	11
2.3.3 Synthesis of Carbon Nanotubes	14
2.3.4 Properties of Carbon Nanotubes	14
2.3.5 Carbon Nanotubes Applications and Challenges	16
2.4 Carbon Nanotubes Reinforced Composite Materials	16
2.4.1 Metal Matrix Composites with Carbon Nanotube Reinforcement	17
2.4.2 Potential and Current Challenges	17
2.5 Mechanics of Materials	22
2.5.1 Fiber Content, Density, and Void Content	23
2.5.2 Fiber-Matrix Interaction	25
2.5.3 Unidirectional Composite	25
2.6 Mechanical Behavior of Composite Materials	26
2.6.1 Determination of Elastic Properties for Continuous Fiber Composites	26
2.6.2 Determination of Elastic Properties for Short	35

	Fiber Composites	
2.6.3	Characteristics of a Fiber-Reinforced Lamina	38
2.6.4	Determination of Elastic Properties for a Lamina	40
2.6.5	Compliance and Stiffness Matrices	42
2.7	Thermal Properties of Carbon Nanotubes Based Composites	48
2.7.1	Factors Affecting Thermal Conductivity Of Composite Materials	49
2.7.2	General Theory of Heat Conduction in Composite Materials	49
2.8	Modeling of Carbon Nanotubes	73
2.8.1	Correlation between Structural and Molecular Mechanics	54
2.9	Key Issues in Carbon Nanotubes-Based Composites	57
2.9.1	Carbon Nanotubes Dispersion in the Matrix	57
2.9.2	Interfacial Phenomena	57

CHAPTER THREE: METHODOLOGY

3.1	Overview	59
3.2	The Analytical Approach	59
3.2.1	Mechanical Properties of Carbon Nanotubes reinforced Nanocomposites	59
3.2.2	Thermal Conductivity in Carbon Nanotube Reinforced Composites	63
3.3	The Computational Approach	65
3.3.1	Choice of Finite Element	66
3.3.2	Finite Element Formulation	66
3.3.3	Representative Volume Element and Material Properties	68
3.3.4	APDL code development	69
3.3.5	Materials Properties	75

CHAPTER FOUR: ANALYTICAL APPROACH RESULTS AND DISCUSSIONS

4.1	Overview	76
4.2	Prediction of the Nanocomposite Density	76
4.3	Prediction of the Elastic Properties for Long Fiber	77
4.3.1	Prediction of the Young's Modulus	77
4.3.2	Prediction of the Transverse Young's Modulus	78
4.3.3	Prediction of the Shear Modulus	79
4.3.4	Prediction of the Major Poisson's Ratio	79
4.4	Prediction of the Elastic Properties for Short Fiber	81
4.4.1	Prediction of the Young's Modulus	81
4.4.2	Prediction of the Transverse Young's Modulus	91
4.4.3	Prediction of the Shear Modulus	96
4.5	Prediction of the Thermal conductivity	97
4.5.1	Prediction of the Thermal conductivity of Carbon Nanotubes Reinforced Metal Matrix Nanocomposite	98
4.5.2	Evaluation of Factors Affecting the Effective Conductivity	99

CHAPTER FIVE: COMPUTATIONAL APPROACH RESULTS AND

DISCUSSIONS		
5.1	Overview	143
5.2	Prediction of the Elastic Properties for Long Fiber	143
	5.2.1 Prediction of Longitudinal Young's Modulus	143
	5.2.2 Prediction of Transverse Young's Modulus	144
	5.2.3 Prediction of the Shear Modulus	146
	5.2.4 Prediction of the Major Poisson's Ratio	147
5.3	Prediction of the Elastic Properties for Short Fiber	149
	5.3.1 Prediction of Longitudinal Young's Modulus	149
	5.3.2 Prediction of Transverse Young's Modulus	160
	5.3.3 Prediction of the Shear Modulus	167
5.4	Effective Thermal Conductivity Prediction	174
	5.4.1 Model Development	174
	5.4.2 Meshing and Boundary Conditions	175
	5.4.3 Estimating the Effective Thermal Conductivity Based on Finite Element Results	176
	5.4.4 Long Fiber Case	184
	5.4.5 Short Fiber Case	193
	5.4.6 Effect of Thermal Contact Conductance on the Effective Thermal Conductivity of the Nanocomposite	207
CHAPTER SIX: VALIDATION OF THE RESULTS		
6.1	Overview	229
6.2	Validation of Elastic Properties of Carbon Nanotubes Reinforced Metal Matrix Nanocomposite	229
	6.2.1 Long Fiber Case	229
	6.2.2 Short Fiber Case	236
6.3	Validation of Thermal Conductivity of Carbon Nanotubes Reinforced Metal Matrix Nanocomposite	245
	6.3.1 Validation with Existing Theoretical Models	246
	6.3.2 Validation of Thermal Conductivity of Carbon Nanotubes Reinforced Metal Matrix Nanocomposite	247
CHAPTER SEVEN: CONCLUSIONS AND PROPOSED FUTURE WORK		
7.1	Conclusions	277
7.2	Recommendations	279
REFERENCES		280
BIODATA OF THE AUTHOR		287
LIST OF PUBLICATIONS		288

LIST OF TABLES

Table No		Page
2.1	Parameters of carbon nanotubes	12
2.2	Overview on the most common carbon nanotubes synthesis techniques and their advantages and disadvantages	14
2.3	Properties of carbon Nanotubes	15
2.4	Comparison of the mechanical and physical properties of carbon nanotubes compared with common materials	15
2.5	Thermal properties of carbon nanotubes	15
2.6	Summary of processing, microstructure features and properties of various metal-CNT composites	19
2.7	Energy form in molecular mechanics and structural mechanics systems	56
3.1	Model dimensions for long carbon nanotubes case	69
3.2	Model dimensions for short carbon nanotubes case: (a) at $V_f=3\%$, (b) at $V_f=7\%$, and (c) at $V_f=11\%$	69
3.3	The mechanical and thermal properties of the materials used in the research	75
4.1	Effect of armchair carbon nanotube diameter on Young's modulus for reinforced: (a) iron, (b) copper, and (c) aluminum matrix	86
4.2	Effect of zigzag carbon nanotube diameter on Young's modulus for reinforced: (a) iron, (b) copper, and (c) aluminum matrix	86
4.3	Effect of chiral carbon nanotube diameter on Young's modulus for reinforced: (a) iron, (b) copper, and (c) aluminum matrix	87
4.4	Effect of chiral index on the Young's modulus of iron matrix ($V_f=3\%$)	88
4.5	Effect of chiral index on the Young's modulus of copper matrix ($V_f=3\%$)	90
4.6	Effect of chiral index on the Young's modulus of aluminum matrix ($V_f=3\%$)	91
4.7	Transverse modulus prediction for (a) armchair, (b) zigzag, and (c) chiral carbon nanotubes reinforced iron metal matrix	93
4.8	Transverse modulus prediction for (a) armchair, (b) zigzag, and (c) chiral carbon nanotubes reinforced copper metal matrix	93
4.9	Transverse modulus prediction for for (a) armchair, (b) zigzag, and (c) chiral carbon nanotubes reinforced aluminum metal matrix	94
4.10	The input for calculating the thermal conductivity for carbon nanotube reinforced aluminum matrix	98
4.11	Thermal conductivity results for (5, 5) carbon nanotubes reinforced metal matrix nanocomposite at 3% volume fraction	99
4.12	Effect of carbon nanotube chiral index on the thermal conductivity for reinforcing aluminum metal matrix ($V_f=3\%$)	100

Table No		Page
4.13	Comparison between different carbon nanotube chiral index on the thermal conductivity for aluminum reinforced metal matrix (Vf=3%)	101
4.14	Effect of carbon nanotube chiral index on the thermal conductivity for reinforcing copper metal matrix (Vf=3%)	103
4.15	Comparison between different carbon nanotube chiral index on the thermal conductivity for aluminum reinforced metal matrix (Vf=3%)	103
4.16	Effect of carbon nanotube chiral index on the thermal conductivity for reinforcing iron metal matrix (Vf=3%)	105
4.17	Comparison between different carbon nanotube chiral index on the thermal conductivity for iron reinforced metal matrix (Vf=3%)	105
4.18	Effect of armchair carbon nanotube diameter on the thermal conductivity for reinforcing iron matrix (Vf=3%)	112
4.19	Effect of zigzag carbon nanotube diameter on the thermal conductivity for reinforcing iron matrix (Vf=3%)	113
4.20	Effect of chiral carbon nanotube diameter on the thermal conductivity for reinforcing iron matrix (Vf=3%)	114
4.21	Effect of armchair carbon nanotube diameter on the thermal conductivity for reinforcing copper matrix (Vf=3%)	115
4.22	Effect of zigzag carbon nanotube diameter on the thermal conductivity for reinforcing copper matrix (Vf=3%)	116
4.23	Effect of chiral carbon nanotube diameter on the thermal conductivity for reinforcing copper matrix (Vf=3%)	116
4.24	Effect of armchair carbon nanotube diameter on the thermal conductivity for reinforcing aluminum matrix (Vf=3%)	118
4.25	Effect of zigzag carbon nanotube diameter on the thermal conductivity for reinforcing aluminum matrix (Vf=3%)	118
4.26	Effect of chiral carbon nanotube diameter on the thermal conductivity for reinforcing aluminum matrix (Vf=3%)	119
4.27	Effect of carbon nanotube chirality index reinforced (a) iron, (b) copper, and (c) aluminum matrix on the thermal conductivity (Vf=3%)	120
4.28	Effect of thermal contact conductance on thermal conductivity for armchair carbon nanotube reinforced iron matrix at different length: (a) at $l_c = 3$ nm, (b) at $l_c = 5$ nm, and (c) at $l_c = 8$ nm	121
4.29	Effect of thermal contact conductance on thermal conductivity for zigzag carbon nanotube reinforced iron matrix at different length: (a) at $l_c = 3$ nm, (b) at $l_c = 5$ nm, and (c) at $l_c = 8$ nm	123
4.30	Effect of thermal contact conductance on thermal conductivity for chiral carbon nanotube reinforced iron matrix at different length: (a) at $l_c = 3$ nm, (b) at $l_c = 5$ nm, and (c) at $l_c = 8$ nm	125
4.31	Effect of thermal contact conductance on thermal conductivity for different chiral index of reinforced iron matrix at different lengths (Vf=3%)	126
4.32	Effect of thermal contact conductance on thermal conductivity for armchair carbon nanotube reinforced copper matrix at different length: (a) at $l_c = 3$ nm, (b) at $l_c = 5$ nm, and (c) at $l_c = 8$ nm	128

Table No		Page
4.33	Effect of thermal contact conductance on thermal conductivity for zigzag carbon nanotube reinforced copper matrix at different length: (a) at $l_c = 3$ nm, (b) at $l_c = 5$ nm, and (c) at $l_c = 8$ nm	130
4.34	Effect of thermal contact conductance on thermal conductivity for chiral carbon nanotube reinforced copper matrix at different length: (a) at $l_c = 3$ nm, (b) at $l_c = 5$ nm, and (c) at $l_c = 8$ nm	132
4.35	Effect of thermal contact conductance on thermal conductivity for different chiral index of reinforced copper matrix at different lengths	134
4.36	Effect of thermal contact conductance on thermal conductivity for armchair carbon nanotube reinforced aluminum matrix at different length: (a) at $l_c = 3$ nm, (b) at $l_c = 5$ nm, and (c) at $l_c = 8$ nm	135
4.37	Effect of thermal contact conductance on thermal conductivity for zigzag carbon nanotube reinforced aluminum matrix at different length: (a) at $l_c = 3$ nm, (b) at $l_c = 5$ nm, and (c) at $l_c = 8$ nm	137
4.38	Effect of thermal contact conductance on thermal conductivity for chiral carbon nanotube reinforced aluminum matrix at different length: (a) at $l_c = 3$ nm, (b) at $l_c = 5$ nm, and (c) at $l_c = 8$ nm	139
4.39	Effect of thermal contact conductance on thermal conductivity for different chiral index of reinforced aluminum matrix at different lengths	141
5.1	Longitudinal Young's modulus FEA results for (a) iron, (b) copper, and (c) aluminum matrices	144
5.2	Transverse modulus FEA results for (a) iron, (b) copper, and (c) aluminum matrices	145
5.3	Shear modulus FEA results for (a) iron, (b) copper, and (c) aluminum matrices	146
5.4	Major Poisson's ratio FEA results for (a) iron, (b) copper, and (c) aluminum matrices	148
5.5	Effect of armchair carbon nanotube diameter reinforced (a) iron, (b) copper, and (c) aluminum matrices ($V_f=3\%$)	153
5.6	Effect of zigzag carbon nanotube diameter reinforced (a) iron, (b) copper, and (c) aluminum matrices ($V_f=3\%$)	154
5.7	Effect of chiral carbon nanotube diameter reinforced (a) iron, (b) copper, and (c) aluminum matrices ($V_f=3\%$)	155
5.8	Effect of chiral index on the Young's modulus of iron matrix ($V_f=3\%$)	156
5.9	Effect of chiral index on the Young's modulus of copper matrix	157
5.10	Effect of chiral index on the Young's modulus of aluminum matrix ($V_f=3\%$)	159
5.11	Effect of armchair carbon nanotube diameter reinforced: (a) iron, (b) copper, and (c) aluminum matrix on transverse modulus ($V_f=3\%$)	165
5.12	Effect of zigzag carbon nanotube diameter reinforced: (a) iron, (b) copper, and (c) aluminum matrix on transverse modulus ($V_f=3\%$)	166
5.13	Effect of chiral carbon nanotube diameter reinforced: (a) iron, (b) copper, and (c) aluminum matrix on transverse modulus ($V_f=3\%$)	167

Table No		Page
5.14	Effect of armchair carbon nanotube diameter reinforced: (a) iron, (b) copper, and (c) aluminum matrix on transverse modulus ($V_f=3\%$)	172
5.15	Effect of zigzag carbon nanotube diameter reinforced: (a) iron, (b) copper, and (c) aluminum matrix on transverse modulus ($V_f=3\%$)	173
5.16	Effect of chiral carbon nanotube diameter reinforced: (a) iron, (b) copper, and (c) aluminum matrix on transverse modulus ($V_f=3\%$)	173
5.17	Effect of chiral index of carbon nanotube reinforced iron matrix on the thermal conductivity for different models ($V_f=3\%$)	185
5.18	Effect of chiral index of carbon nanotube reinforced copper matrix on the thermal conductivity for different models ($V_f=3\%$)	185
5.19	Effect of chiral index of carbon nanotube reinforced aluminum matrix on the thermal conductivity for different models ($V_f=3\%$)	188
5.20	Effect of chiral index diameter of carbon nanotube on the thermal conductivity for reinforcing iron matrix "Model (A)" ($V_f=3\%$)	193
5.21	Effect of chiral index diameter of carbon nanotube on the thermal conductivity for reinforcing iron matrix "Model (B)" ($V_f=3\%$)	193
5.22	Effect of chiral index diameter of carbon nanotube on the thermal conductivity for reinforcing copper matrix "Model (A)" ($V_f=3\%$)	196
5.23	Effect of chiral index diameter of carbon nanotube on the thermal conductivity for reinforcing copper matrix "Model (B)" ($V_f=3\%$)	197
5.24	Effect of chiral index diameter of carbon nanotube on the thermal conductivity for reinforcing Aluminum matrix "Model (A)" ($V_f=3\%$)	200
5.25	Effect of chiral index diameter of carbon nanotube on the thermal conductivity for reinforcing aluminum matrix "Model (B)" ($V_f=3\%$)	200
5.26	Effect of chiral index diameter of carbon nanotube on the thermal conductivity for reinforcing iron matrix: (a) Model (A), and (b) Model (B)	204
5.27	Effect of chiral index diameter of carbon nanotube on the thermal conductivity for reinforcing copper matrix (a) Model (A), and (b) Model (B)	205
5.28	Effect of chiral index diameter of carbon nanotube on the thermal conductivity for reinforcing Aluminum matrix: (a) Model (A), and (b) Model (B)	206
5.29	Effect of thermal contact conductance on thermal conductivity for armchair carbon nanotube reinforced iron matrix at different length: (a) Model (A), and (b) Model (B)	208
5.30	Effect of thermal contact conductance on thermal conductivity for zigzag carbon nanotube reinforced iron matrix at different length: (a) Model (A), and (b) Model (B)	210
5.31	Effect of thermal contact conductance on thermal conductivity for chiral carbon nanotube reinforced iron matrix at different length: (a) Model (A), and (b) Model (B)	212
5.32	Effect of thermal contact conductance on thermal conductivity for armchair carbon nanotube reinforced copper matrix at different length: (a) Model (A), and (b) Model (B)	215

Table No		Page
5.33	Effect of thermal contact conductance on thermal conductivity for zigzag carbon nanotube reinforced copper matrix at different length: (a) Model (A), and (b) Model (B)	217
5.34	Effect of thermal contact conductance on thermal conductivity for chiral carbon nanotube reinforced copper matrix at different length: (a) Model (A), and (b) Model (B)	219
5.35	Effect of thermal contact conductance on thermal conductivity for armchair carbon nanotube reinforced aluminum matrix at different length: (a) Model (A), and (b) Model (B)	222
5.36	Effect of thermal contact conductance on thermal conductivity for zigzag carbon nanotube reinforced aluminum matrix at different length: (a) Model (A), and (b) Model (B)	224
5.37	Effect of thermal contact conductance on thermal conductivity for chiral carbon nanotube reinforced aluminum matrix at different length: (a) Model (A), and (b) Model (B)	226
6.1	Validation of elastic properties for carbon nanotube reinforced iron metal matrix	230
6.2	Validation of elastic properties for carbon nanotube reinforced copper metal matrix	232
6.3	Validation of elastic properties for carbon nanotube reinforced aluminum metal matrix	234
6.4	Validation of longitudinal Young's Modulus for carbon nanotube (a) armchair, (b) zigzag, and (c) chiral treated as short fiber reinforced iron metal matrix	236
6.5	Validation of longitudinal Young's modulus carbon nanotube (a) armchair, (b) zigzag, and (c) chiral treated as short fiber reinforced copper metal matrix	238
6.6	Validation of longitudinal Young's modulus for carbon nanotube (a) armchair, (b) zigzag, and (c) chiral treated as short fiber reinforced aluminum metal matrix	240
6.7	Validation of Transverse modulus for armchair carbon nanotube reinforced (a)iron, (b) copper, and (c) aluminum metal matrix (lc=3)	242
6.8	Validation of shear modulus for armchair carbon nanotube reinforced (a)iron, (b) copper, and (c) aluminum metal matrix (lc=3nm)	244
6.9	Validation of thermal conductivity for (a) armchair (b) zigzag, and (c) chiral carbon nanotube treated as long fiber reinforced iron, metal matrix	247
6.10	Validation of thermal conductivity for (a) armchair (b) zigzag, and (c) chiral carbon nanotube treated as long fiber reinforced copper metal matrix	249
6.11	Validation of thermal conductivity for (a) armchair (b) zigzag, and (c) chiral carbon nanotube treated as long fiber reinforced aluminum metal matrix	251
6.12	Validation of thermal conductivity for (a) armchair (b) zigzag, and (c) chiral carbon nanotube reinforced iron metal matrix at lc=3nm	253

Table No		Page
6.13	Validation of thermal conductivity for (a) armchair (b) zigzag, and (c) chiral carbon nanotube reinforced copper metal matrix at $l_c=3\text{nm}$	255
6.14	Validation of thermal conductivity for (a) armchair (b) zigzag, and (c) chiral carbon nanotube reinforced aluminum metal matrix at $l_c=3\text{nm}$	256
6.15	Validation of thermal conductivity for (a) armchair (b) zigzag, and (c) chiral carbon nanotube reinforced iron metal matrix at different lengths	258
6.16	Validation of thermal conductivity for (a) armchair (b) zigzag, and (c) chiral carbon nanotube reinforced copper metal matrix at different lengths	260
6.17	Validation of thermal conductivity for a) armchair (b) zigzag, and (c) chiral carbon nanotube reinforced aluminum metal matrix at different lengths	262
6.18	Validation of thermal conductivity for carbon nanotube reinforced iron metal matrix at different diameters and (a) at $l_c=3\text{ nm}$, (b) at $l_c=5\text{ nm}$, (c) at $l_c=8\text{ nm}$,	264
6.19	Validation of thermal conductivity for armchair carbon nanotube reinforced copper metal matrix at different diameters (a) at $l_c=3\text{ nm}$, (b) at $l_c=5\text{ nm}$, (c) at $l_c=8\text{ nm}$,	266
6.20	Validation of thermal conductivity for armchair carbon nanotube reinforced aluminum metal matrix at different diameters and (a) at $l_c=3\text{ nm}$, (b) at $l_c=5\text{ nm}$, (c) at $l_c=8\text{ nm}$,	268
6.21	Validation of thermal contact conductance for (a) armchair (5, 5), (b) zigzag (5, 0), (c) chiral (5, 10) carbon nanotube reinforced iron metal matrix	270
6.22	Validation of thermal contact conductance for (a) armchair (5, 5), (b) zigzag (5, 0), (c) chiral (5, 10) carbon nanotube reinforced copper metal	272
6.23	validation of thermal contact conductance for (a) armchair (5, 5), (b) zigzag (5, 0), (c) chiral (5, 10) carbon nanotube reinforced aluminum metal matrix	275

LIST OF FIGURES

Figure No		Page
2.1	The allotropic forms of carbon known to mankind	9
2.2	Rolling up a graphene sheet to form a nanotube	9
2.3	(a) Schematic showing the formation of an SWNT by rolling along different chiral vectors Ch and the resulting SWNTs, and (b), (c), and (d) high resolution TEM images showing a single, double, and seven-walled nanotube, respectively	12
2.4	Electron micrographs of various possible morphologies of carbon nanotubes, (a) SWNT (b) DWNT (c) MWNT (d) bamboo structured CNT (e) Y-junction CNT] (f) coiled CNTs	13
2.5	Bond inversion of carbon atom in a graphene sheet	13
2.6	Basic hexagonal bonding structure for one graphite layer (the <i>graphene sheet</i>); carbon nuclei shown as filled circles, out-of-plane π -bonds represented as <i>delocalized</i> ~dotted line!, and σ -bonds connect the C nuclei in-plane	13
2.7	The various processes for synthesis of CNT-reinforced composite	18
2.8	Potential Applications of Nanocomposite Materials	22
2.9	Models for describing elastic behavior of composites at different length scales	23
2.10	Ultimate fiber arrays for (a): square, (b) hexagonal, and (c) layer-wise fiber distributions	24
2.11	Schematic representation of unidirectional composite	26
2.12	Response of various types of materials under uniaxial normal and pure shear loading	27
2.13	Representative Volume Element Loaded along the fiber direction	29
2.14	Representative volume element loaded perpendicular to fiber	31
2.15	Shear loading and deformation of a Representative Volume Element	33
2.16	Shear deformation of a Representative Volume Element	34
2.17	Longitudinal tensile loading of a unidirectional discontinuous fiber lamina.	36
2.18	Definition of principal material axes and loading axes for a lamina	38
2.19	Differences in the deformations of isotropic, specially orthotropic and anisotropic materials subjected to uniaxial tension ((a) Isotropic, (b) Special orthotropic and (c) General orthotropic and anisotropic) and pure shear stresses	39
2.20	Applications of (a) longitudinal tensile stress, (b) transverse tensile stress, and (c) in-plane shear stress on a unidirectional continuous fiber 0° lamina	40
2.21	The six components to describe the state of stress at a point.	42
2.22	Stresses in a general orthotropic lamina under a plane stress condition	44
2.23	Positive Rotation of Principal Material Axis from XY Axis	46
2.24	Development of a continuum model for a SWNT. a) Schematic diagram of a carbon nanotube; b) Equivalent continuum model; c)	50

Effective solid fiber; and d) a prolate spheroidal inclusion. [89]

Figure No		Page
2.25	Different material modeling techniques	53
2.26	Equivalence of molecular mechanics and structural mechanics for covalent and non-covalent interactions between carbon atoms: (a) Molecular mechanics model and (b) structural mechanics mode	55
3.1	Research Methodology	60
3.2	Flowchart for programming by MATLAB	62
3.3	Carbon nanotube through the length of the RVE	62
3.4	Carbon nanotube inside the RVE	63
3.5	Flow chart describes the MATLAB program used for calculation of thermal conductivity	64
3.6	Steps involved for finite element method	67
3.7	Two possible RVEs for the analysis of CNT-based Nanocomposite (a) Square RVE with long fiber; (b) Square RVE with short fiber	68
3.8	RVE divided into many regular volumes	70
3.9	The Full model built by APDL ANSYS	70
3.10	PLANE182 geometry	71
3.11	SOLID185 homogeneous structural solid geometry	71
3.12	FE mesh for the RVE	72
3.13	The mesh of full model	72
3.14	Periodic boundary condition	73
3.15	The periodic condition in x direction	73
4.1	Density for carbon nanotube reinforced copper metal matrix	102
4.2	Density for carbon nanotube reinforced iron metal matrix	102
4.3	Density for carbon nanotube reinforced aluminum metal matrix	103
4.4	Effect of volume fraction on longitudinal Young's modulus for carbon nanotube reinforced copper matrix	104
4.5	Effect of volume fraction on longitudinal Young's modulus for carbon nanotube reinforced iron matrix	105
4.6	Effect of volume fraction on longitudinal Young's modulus for carbon nanotube reinforced aluminum matrix	105
4.7	Effect of volume fraction on Transverse Young's modulus for carbon nanotube reinforced copper matrix	106
4.8	Effect of volume fraction on Transverse Young's modulus for carbon nanotube reinforced iron matrix	107
4.9	Effect of volume fraction on Transverse Young's modulus for carbon nanotube reinforced aluminum matrix	107
4.10	Effect of volume fraction on shear modulus for carbon nanotube reinforced copper matrix	108
4.11	Effect of volume fraction on shear modulus for carbon nanotube reinforced iron matrix	109
4.12	Effect of volume fraction on shear modulus for carbon nanotube reinforced aluminum matrix	109
4.13	Effect of volume fraction on Major Poisson's Ratio for carbon nanotube reinforced copper matrix	110
4.14	Effect of volume fraction on Major Poisson's Ratio for carbon nanotube reinforced aluminum matrix	111
4.15	Effect of volume fraction on Major Poisson's Ratio for carbon nanotube reinforced iron matrix	111

Figure No		Page
4.16	Longitudinal Young's modulus for zigzag carbon nanotube (different length) reinforced iron metal matrix	113
4.17	Longitudinal Young's modulus for armchair carbon nanotube (different length) reinforced iron metal matrix	113
4.18	Longitudinal Young's modulus for chiral carbon nanotube (different length) reinforced iron metal matrix	114
4.19	Longitudinal Young's modulus for zigzag carbon nanotube (different length) reinforced copper metal matrix	115
4.20	Longitudinal Young's modulus for armchair carbon nanotube (different length) reinforced copper metal matrix	115
4.21	Longitudinal Young's modulus for chiral carbon nanotube (different length) reinforced copper metal matrix	116
4.22	Longitudinal Young's modulus for zigzag carbon nanotube (different length) reinforced aluminum metal matrix	117
4.23	Longitudinal Young's modulus for armchair carbon nanotube (different length) reinforced aluminum metal matrix	117
4.24	Longitudinal Young's modulus for chiral carbon nanotube (different length) reinforced aluminum metal matrix	118
4.25	Longitudinal Young's modulus for different chiral index carbon nanotube (at length $l_c=3$ nm) reinforced iron metal matrix	122
4.26	Longitudinal Young's modulus for different chiral index carbon nanotube (at length $l_c=5$ nm) reinforced iron metal matrix	122
4.27	Longitudinal Young's modulus for different chiral index carbon nanotube (at length $l_c=8$ nm) reinforced iron metal matrix	123
4.28	Longitudinal Young's modulus for different chiral index carbon nanotube (at length $l_c=3$ nm) reinforced copper metal matrix	124
4.29	Longitudinal Young's modulus for different chiral index carbon nanotube (at length $l_c=5$ nm) reinforced copper metal matrix	124
4.30	Longitudinal Young's modulus for different chiral index carbon nanotube (at length $l_c=8$ nm) reinforced copper metal matrix	125
4.31	Longitudinal Young's modulus for different chiral index carbon nanotube (length $l_c=3$ nm) reinforced aluminum metal matrix	126
4.32	Longitudinal Young's modulus for different chiral index carbon nanotube (length $l_c=5$ nm) reinforced aluminum metal matrix	126
4.33	Longitudinal Young's modulus for different chiral index carbon nanotube (length $l_c=8$ nm) reinforced aluminum metal matrix	127
4.34	Transverse Young's modulus for carbon nanotube as short fiber reinforced iron metal matrix	130
4.35	Transverse Young's modulus for carbon nanotube as short fiber reinforced copper metal matrix	130
4.36	Transverse Young's modulus for carbon nanotube as short fiber reinforced aluminum metal matrix	131
4.37	Shear modulus for carbon nanotube (as short fiber) reinforced iron matrix	132
4.38	Shear modulus for carbon nanotube (as short fiber) reinforced copper matrix	132
4.39	Shear modulus for carbon nanotube (as short fiber) reinforced aluminum matrix	133
4.40	Effect of volume fraction on thermal conductivity for armchair carbon nanotube reinforced aluminum metal matrix	138

Figure No		Page
4.41	Effect of volume fraction on thermal conductivity for zigzag carbon nanotube reinforced aluminum metal matrix	138
4.42	Effect of volume fraction on thermal conductivity for chiral carbon reinforced aluminum metal matrix	139
4.43	Effect of volume fraction on thermal conductivity for different chiral index carbon nanotube reinforced aluminum metal matrix	139
4.44	Effect of volume fraction on thermal conductivity for armchair carbon nanotube reinforced copper metal matrix	141
4.45	Effect of volume fraction on thermal conductivity for zigzag carbon nanotube reinforced copper metal matrix	141
4.46	Effect of volume fraction on thermal conductivity for chiral carbon nanotube reinforced copper metal matrix	142
4.47	Effect of volume fraction on thermal conductivity for different chiral index carbon nanotube reinforced copper metal matrix	142
4.48	Effect of volume fraction on thermal conductivity for armchair carbon nanotube reinforced iron metal matrix	143
4.49	Effect of volume fraction on thermal conductivity for zigzag carbon nanotube reinforced iron metal matrix	144
4.50	Effect of volume fraction on thermal conductivity for chiral carbon nanotube reinforced iron metal matrix	144
4.51	Effect of volume fraction on thermal conductivity for different chiral index carbon nanotube reinforced iron metal matrix	145
4.52	Effect of length on thermal conductivity for armchair carbon nanotube reinforced aluminum metal matrix	146
4.53	Effect of length on thermal conductivity for zigzag carbon nanotube reinforced aluminum metal matrix	147
4.54	Effect of length on thermal conductivity for chiral carbon nanotube reinforced aluminum metal matrix	147
4.55	Effect of length on thermal conductivity for chiral carbon nanotube reinforced aluminum metal matrix	148
4.56	Effect of length on thermal conductivity for armchair carbon nanotube reinforced copper metal matrix	149
4.57	Effect of length on thermal conductivity for zigzag carbon nanotube reinforced copper metal matrix	149
4.58	Effect of length on thermal conductivity for chiral carbon nanotube reinforced copper metal matrix	150
4.59	Effect of length on thermal conductivity for different chiral index carbon nanotube reinforced copper metal matrix	150
4.60	Effect of length on thermal conductivity for armchair carbon reinforced iron metal matrix	151
4.61	Effect of length on thermal conductivity for zigzag carbon reinforced iron metal matrix	152
4.62	Effect of length on thermal conductivity for chiral carbon reinforced iron metal matrix	152
4.63	Effect of length on thermal conductivity for different chiral index carbon nanotube reinforced iron metal matrix	153
4.64	Effect of diameter on thermal conductivity for armchair carbon nanotube reinforced iron metal matrix	154
4.65	Effect of diameter on thermal conductivity for zigzag carbon nanotube reinforced iron metal matrix	155

Figure No		Page
4.66	Effect of diameter on thermal conductivity for chiral carbon nanotube reinforced iron metal matrix	156
4.67	Effect of diameter on thermal conductivity for armchair carbon nanotube reinforced copper metal matrix	157
4.68	Effect of diameter on thermal conductivity for zigzag carbon nanotube reinforced copper metal matrix	158
4.69	Effect of diameter on thermal conductivity for chiral carbon nanotube (as short fiber) reinforced copper metal matrix	159
4.70	effect of diameter on thermal conductivity for armchair carbon nanotube reinforced aluminum metal matrix	160
4.71	Effect of diameter on thermal conductivity for zigzag carbon nanotube reinforced aluminum metal matrix	161
4.72	Effect of diameter on thermal conductivity for chiral carbon nanotube reinforced aluminum metal matrix	162
4.73	Effect of thermal contact conductance on thermal conductivity for armchair carbon nanotube (5, 5) reinforced iron metal matrix	166
4.74	Effect of thermal contact conductance on thermal conductivity for zigzag carbon nanotube (5, 0) reinforced iron metal matrix	168
4.75	Effect of thermal contact conductance on thermal conductivity for chiral carbon nanotube (5, 10) reinforced iron metal matrix	170
4.76	Effect of thermal contact conductance on thermal conductivity for different chiral index carbon nanotube reinforced iron metal matrix (at $l_c=3$ nm)	171
4.77	Effect of thermal contact conductance on thermal conductivity for different chiral index carbon nanotube reinforced iron metal matrix (at $l_c=5$ nm)	172
4.78	Effect of thermal contact conductance on thermal conductivity for different chiral index carbon nanotube reinforced iron metal matrix (at $l_c=8$ nm)	172
4.79	Effect of thermal contact conductance on thermal conductivity for armchair carbon nanotube (5, 5) reinforced copper metal matrix	174
4.80	Effect of thermal contact conductance on thermal conductivity for zigzag carbon nanotube (5, 0) reinforced copper metal matrix	176
5.1	Longitudinal Young's modulus for iron, copper, and aluminum matrix reinforced carbon nanotubes as long fiber	145
5.2	Transverse Young's modulus for iron, copper, and aluminum matrices reinforced carbon nanotubes as long fiber	146
5.3	Shear modulus for iron, copper, and aluminum matrices reinforced carbon nanotubes as long fiber	147
5.4	Major Poisson's ratio for iron, copper, and aluminum matrices reinforced carbon nanotubes as long fiber	148
5.5	Longitudinal Young's modulus for carbon nanotube (5,0) (different length) reinforced iron metal matrix	149
5.6	Longitudinal Young's modulus for carbon nanotube (5,5) (different length) reinforced iron metal matrix	150
5.7	Longitudinal Young's modulus for carbon nanotube (5, 10) (different length) reinforced iron metal matrix	150
5.8	Longitudinal Young's modulus for carbon nanotube (5,0) (different length) reinforced copper metal matrix	151

Figure No		Page
5.9	Longitudinal Young's modulus for carbon nanotube (5,5) (different length) reinforced copper metal matrix	151
5.10	Longitudinal Young's modulus for carbon nanotube (5, 10) (different length) reinforced copper metal matrix	151
5.11	Longitudinal Young's modulus for carbon nanotube (5, 0) (different length) reinforced aluminum metal matrix	152
5.12	Longitudinal Young's modulus for carbon nanotube (5, 5) (Different Length) reinforced aluminum metal matrix	152
5.13	Longitudinal Young's modulus for carbon nanotube (5, 10) (different length) reinforced aluminum metal matrix	153
5.14	Longitudinal Young's modulus for different chiral index carbon nanotube (at length $l_c=3$ nm) reinforced iron metal matrix	156
5.15	Longitudinal Young's modulus for different chiral index carbon nanotube (at length $l_c=5$ nm) reinforced iron metal matrix	156
5.16	Longitudinal Young's modulus for different chiral index carbon nanotube (at length $l_c=8$ nm) Reinforced iron metal matrix	157
5.17	Longitudinal Young's modulus for different chiral index carbon nanotube (at length $l_c=3$ nm) reinforced copper metal matrix	158
5.18	Longitudinal Young's modulus for different chiral index carbon nanotube (at length $l_c=5$ nm) reinforced copper metal matrix	158
5.19	Longitudinal Young's modulus for different chiral index carbon nanotube (at length $l_c=8$ nm) reinforced copper metal matrix	158
5.20	Longitudinal Young's modulus for different chiral index carbon nanotube (at length $l_c=3$ nm) reinforced aluminum metal matrix	159
5.21	Longitudinal Young's modulus for different chiral index carbon nanotube (at length $l_c=5$ nm) reinforced aluminum metal matrix	160
5.22	Longitudinal Young's modulus for different chiral index carbon nanotube (at length $l_c=8$ nm) reinforced aluminum metal matrix	160
5.23	Transverse modulus for zigzag carbon nanotube (5,0) (different length) reinforced iron metal matrix	161
5.24	Transverse modulus for armchair carbon nanotube (5,5) (different length) reinforced iron metal matrix	161
5.25	Transverse modulus for chiral carbon nanotube (5, 10) (different length) reinforced iron metal matrix	162
5.26	Transverse modulus for zigzag carbon nanotube as short fiber reinforced copper metal matrix at different length	162
5.27	Transverse modulus for armchair carbon nanotube as short fiber reinforced copper metal matrix at different length	163
5.28	Transverse modulus for chiral carbon nanotube as short fiber reinforced copper metal matrix at different length	163
5.29	Transverse modulus for zigzag carbon nanotube at different length reinforced aluminum metal matrix	164
5.30	Transverse modulus for armchair carbon nanotube at different length reinforced aluminum metal matrix	164
5.31	Transverse modulus for armchair carbon nanotube at different length reinforced aluminum metal matrix	165
5.32	Shear modulus for zigzag carbon nanotube treated as short fiber reinforced iron matrix	168
5.33	Shear modulus for armchair carbon nanotube treated as short fiber reinforced iron matrix	168

Figure No		Page
5.34	Shear modulus for chiral carbon nanotube treated as short fiber reinforced iron matrix	169
5.35	Shear modulus for zigzag carbon nanotube treated as short fiber reinforced copper matrix at different length	169
5.36	Shear modulus for armchair carbon nanotube treated as short fiber reinforced copper matrix at different length	170
5.37	Shear modulus for chiral carbon nanotube treated as short fiber reinforced copper matrix at different length	170
5.38	Shear modulus for zigzag carbon nanotube treated as short fiber reinforced aluminum matrix at different length	171
5.39	Shear modulus for armchair carbon nanotube (as short fiber) reinforced aluminum matrix at different length	171
5.40	Shear modulus for chiral carbon nanotube treated as short fiber reinforced aluminum matrix at different length	171
5.41	The resulting volumes of overlapping	174
5.42	The Geometrical Model: (a) Full model with Carbon nanotubes away from the center, (b) Full model with carbon nanotubes placed at the center and (c) the quarter model	175
5.43	Final RVE divided for meshing	175
5.44	The SOLID70 Geometry[138]	176
5.45	The contact and target elements generated	176
5.46	Macro temperature imposed at boundary of the RVE	177
5.47	Temperature and thermal flux distribution in the matrix and carbon nanotubes or Iron matrix	178
5.48	Temperature and thermal flux distribution in the matrix and carbon nanotubes or Copper matrix	179
5.49	Temperature and thermal flux distribution in the matrix and carbon nanotubes or Aluminum matrix	179
5.50	Temperature and thermal flux distribution in the matrix and carbon nanotubes or iron matrix (Model A)	180
5.51	Temperature and thermal flux distribution in the matrix and carbon nanotubes or Copper matrix	181
5.52	Temperature and thermal flux distribution in the matrix and carbon nanotubes or Aluminum matrix	181
5.53	Temperature and thermal flux distribution in the matrix and carbon nanotubes or Iron matrix	182
5.54	Temperature and thermal flux distribution in the matrix and carbon nanotubes or Copper matrix	183
5.55	Temperature and thermal flux distribution in the matrix and carbon nanotubes or Aluminum matrix	183
5.56	The results of SSUM command	184
5.57	Effect of thermal conductivity for zigzag carbon (as long fiber) nanotube reinforced iron metal matrix	186
5.58	Effect of thermal conductivity for armchair carbon (as long fiber) nanotube reinforced iron metal matrix	186
5.59	Effect of thermal conductivity for chiral carbon (as long fiber) nanotube reinforced iron metal matrix	186
5.60	Effect of thermal conductivity for zigzag carbon (as long fiber) nanotube reinforced copper metal matrix	187
5.61	Effect of thermal conductivity for armchair carbon (as long fiber) nanotube reinforced copper metal matrix	187

Figure No		Page
5.62	Effect of thermal conductivity for chiral carbon (as long fiber) nanotube reinforced copper metal matrix	188
5.63	Effect of thermal conductivity for zigzag carbon (as long fiber) nanotube reinforced aluminum metal matrix	189
5.64	Effect of thermal conductivity for armchair carbon (as long fiber) nanotube reinforced aluminum metal matrix	189
5.65	Effect of thermal conductivity for chiral carbon (as long fiber) nanotube reinforced aluminum metal matrix	189
5.66	Effect of volume fraction on the thermal conductivity of different carbon nanotube chiral index reinforced iron metal matrix "model (A)"	190
5.67	Effect of volume fraction on the thermal conductivity of different carbon nanotube chiral index reinforced iron metal matrix "Model (B)"	191
5.68	Effect of volume fraction on the thermal conductivity of different carbon nanotube chiral index reinforced copper metal matrix "Model (A)"	191
5.69	Effect of volume fraction on the thermal conductivity on different carbon nanotube chiral index reinforced copper metal matrix "Model (B)"	191
5.70	Effect of volume fraction on the thermal conductivity of different carbon nanotube chiral index reinforced aluminum metal matrix "Model (A)"	192
5.71	Effect of volume fraction on the thermal conductivity of different carbon nanotube chiral index reinforced aluminum metal matrix "Model (B)"	192
5.72	Effect of volume fraction on the thermal conductivity for armchair carbon nanotube reinforced iron metal matrix "Model (A)"	194
5.73	Effect of volume fraction on the thermal conductivity for zigzag carbon nanotube reinforced iron metal matrix "Model (A)"	194
5.74	Effect of volume fraction on the thermal conductivity for chiral carbon nanotube reinforced iron metal matrix "Model (A)"	195
5.75	Effect of volume fraction on the thermal conductivity for chiral carbon nanotube reinforced iron metal matrix "Model (B)"	195
5.76	Effect of volume fraction on the thermal conductivity for armchair carbon nanotube reinforced iron metal matrix "Model (B)"	195
5.77	Effect of volume fraction on the thermal conductivity for zigzag carbon nanotube reinforced iron metal matrix "Model (B)"	196
5.78	Effect of volume fraction on the thermal conductivity for armchair carbon nanotube reinforced copper metal matrix "Model (A)"	197
5.79	Effect of volume fraction on the thermal conductivity for zigzag carbon nanotube reinforced copper metal matrix "Model (A)"	198
5.80	Effect of volume fraction on the thermal conductivity for chiral carbon nanotube reinforced copper metal matrix "Model (A)"	198
5.81	Effect of volume fraction on the thermal conductivity for armchair carbon nanotube reinforced copper metal matrix "Model (B)"	199
5.82	Effect of volume fraction on the thermal conductivity for zigzag carbon nanotube reinforced copper metal matrix "Model (B)"	199
5.83	Effect of volume fraction on the thermal conductivity for chiral carbon nanotube reinforced copper metal matrix "Model (B)"	199
5.84	Effect of volume fraction on the thermal conductivity for armchair carbon nanotube reinforced aluminum metal matrix "Model (A)"	201

Figure No		Page
5.85	Effect of volume fraction on the thermal conductivity for zigzag carbon nanotube reinforced aluminum metal matrix "Model (A)"	201
5.86	Effect of volume fraction on the thermal conductivity for chiral carbon nanotube reinforced aluminum metal matrix "Model (A)"	202
5.87	Effect of volume fraction on the thermal conductivity for chiral carbon nanotube reinforced aluminum metal matrix "Model (B)"	202
5.88	Effect of volume fraction on the thermal conductivity for armchair carbon nanotube reinforced aluminum metal matrix "Model (B)"	202
5.89	Effect of volume fraction on the thermal conductivity for zigzag carbon nanotube reinforced aluminum metal matrix "Model (B)"	203
5.90	Effect of carbon nanotube diameter on the thermal conductivity for reinforcing iron metal matrix "Model (A)"	204
5.91	Effect of carbon nanotube diameter on the thermal conductivity for reinforcing iron metal matrix "Model (B)"	204
5.92	Effect of carbon nanotube diameter on the thermal conductivity for reinforcing copper metal matrix "Model (A)"	205
5.93	Effect of carbon nanotube diameter on the thermal conductivity for reinforcing copper metal matrix "Model (B)"	206
5.94	Effect of carbon nanotube diameter on the thermal conductivity for reinforcing aluminum metal matrix "Model (A)"	207
5.95	Effect of carbon nanotube diameter on the thermal conductivity for reinforcing aluminum metal matrix "Model (B)"	207
5.96	Effect of thermal contact conductance on thermal conductivity for armchair carbon nanotube (5, 5) reinforced iron metal matrix (Model "A")	209
5.97	Effect of thermal contact conductance on thermal conductivity for armchair carbon nanotube (5, 5) reinforced iron metal matrix (Model "B")	209
5.98	Effect of thermal contact conductance on thermal conductivity for zigzag carbon nanotube (5, 0) reinforced iron metal matrix (Model "A")	211
5.99	Effect of thermal contact conductance on thermal conductivity for zigzag carbon nanotube (5, 0) reinforced iron metal matrix (Model "B")	211
5.100	Effect of thermal contact conductance on thermal conductivity for chiral carbon nanotube (5,10) reinforced iron metal matrix (Model "A")	213
5.101	Effect of thermal contact conductance on thermal conductivity for chiral carbon nanotube (5, 10) reinforced iron metal matrix (Model "B")	213
5.102	Effect of thermal contact on thermal conductivity for different chiral Index carbon nanotube reinforced iron metal matrix (lc =3 nm)	214
5.103	Effect of thermal contact on thermal conductivity for different chiral index carbon nanotube reinforced iron metal matrix (lc =5 nm)	214
5.104	Effect of thermal contact on thermal conductivity for different chiral index carbon nanotube reinforced iron metal matrix (lc =8 nm)	214
5.105	Effect of thermal contact conductance on thermal conductivity for armchair carbon nanotube (5, 5) reinforced copper metal matrix (Model "A")	216

Figure No		Page
5.106	Effect of thermal contact conductance on thermal conductivity for armchair carbon nanotube (5, 5) reinforced copper metal matrix (Model "B")	216
5.107	Effect of thermal contact conductance on thermal conductivity for zigzag carbon nanotube (5, 0) reinforced copper metal matrix (Model "A")	218
5.108	Effect of thermal contact conductance on thermal conductivity for zigzag carbon nanotube (5, 0) reinforced copper metal matrix (Model "B")	218
5.109	Effect of thermal contact conductance on thermal conductivity for chiral carbon nanotube (5, 10) reinforced copper metal matrix (Model "A")	220
5.110	Effect of thermal contact conductance on thermal conductivity for chiral carbon nanotube (5, 10) reinforced copper metal matrix (Model "B")	220
5.111	Effect of thermal contact on thermal conductivity for different chiral index carbon nanotube reinforced copper metal matrix ($l_c = 3$ nm)	221
5.112	Effect of thermal contact on thermal conductivity for different chiral index carbon nanotube reinforced copper metal matrix ($l_c = 5$ nm)	221
5.113	Effect of thermal contact on thermal conductivity for different chiral index carbon nanotube reinforced copper metal matrix ($l_c = 8$ nm)	221
5.114	Effect of thermal contact conductance on thermal conductivity for armchair carbon nanotube (5, 5) reinforced aluminum metal matrix (Model "A")	223
5.115	Effect of thermal contact conductance on thermal conductivity for armchair carbon nanotube (5, 5) reinforced aluminum metal matrix (Model "B")	223
5.116	Effect of thermal contact conductance on thermal conductivity for zigzag carbon nanotube (5, 0) reinforced aluminum metal matrix (Model "A")	225
5.117	Effect of thermal contact conductance on thermal conductivity for zigzag carbon nanotube (5, 0) reinforced aluminum metal matrix (Model "B")	225
5.118	Effect of thermal contact conductance on thermal conductivity for chiral carbon nanotube (5, 10) reinforced aluminum metal matrix (Model "A")	227
5.119	Effect of thermal contact conductance on thermal conductivity for chiral carbon nanotube (5, 10) reinforced aluminum metal matrix (Model "B")	227
5.120	Effect of thermal contact on thermal conductivity for different chiral Index carbon nanotube reinforced aluminum metal matrix ($l_c = 3$ nm)	228
5.121	Effect of thermal contact on thermal conductivity for different chiral Index carbon nanotube reinforced aluminum metal matrix ($l_c = 5$ nm)	228
5.122	Effect of thermal contact on thermal conductivity for different chiral Index carbon nanotube reinforced aluminum metal matrix ($l_c = 8$ nm)	228

Figure No		Page
6.1	Longitudinal Young's modulus for carbon nanotube reinforced Iron metal matrix validation	230
6.2	Transverse Young's modulus for carbon nanotube reinforced iron metal matrix validation	230
6.3	Shear modulus for carbon nanotube reinforced iron metal matrix validation	231
6.4	Major Poisson's ratio for carbon nanotube reinforced iron metal matrix validation	231
6.5	Longitudinal Young's modulus for carbon nanotube reinforced copper metal matrix validation	232
6.6	Transverse modulus for carbon nanotube reinforced copper metal matrix validation	232
6.7	Shear modulus for carbon nanotube reinforced copper metal matrix validation	233
6.8	Major Poisson's ratio for carbon nanotube reinforced copper metal matrix validation	233
6.9	Longitudinal Young's modulus for carbon nanotube reinforced aluminum metal matrix validation	234
6.10	Transverse modulus for carbon nanotube reinforced aluminum metal matrix validation	234
6.11	Shear modulus for carbon nanotube reinforced aluminum metal matrix validation	235
6.12	Major Poisson's ratio for carbon nanotube reinforced aluminum metal matrix validation	235
6.13	Validation of longitudinal Young's modulus for armchair (5, 5) carbon nanotubes reinforced iron metal matrix (lc=3nm)	237
6.14	Validation of longitudinal Young's modulus for zigzag (5, 0) carbon nanotubes reinforced iron metal matrix (lc=3nm)	237
6.15	Validation of longitudinal Young's modulus for chiral (5, 10) carbon nanotubes reinforced iron metal matrix (lc=3nm)	237
6.16	Validation of longitudinal Young's modulus for armchair (5, 5) carbon nanotubes reinforced copper metal matrix (lc=3nm)	239
6.17	Validation of longitudinal Young's modulus for zigzag (5, 0) carbon nanotubes reinforced copper metal matrix (lc=3nm)	239
6.18	Validation of longitudinal Young's modulus for chiral (5, 10) carbon nanotubes reinforced copper metal matrix (lc=3nm)	239
6.19	Validation of longitudinal Young's modulus for armchair (5, 5) carbon nanotubes reinforced aluminum metal matrix (lc=3nm)	241
6.20	Validation of longitudinal Young's modulus for zigzag (5, 0) carbon nanotubes reinforced aluminum metal matrix (lc=3nm)	241
6.21	Validation of longitudinal Young's modulus for chiral (5, 10) carbon nanotubes reinforced aluminum metal matrix (lc=3nm)	241
6.22	Validation of transverse modulus for carbon nanotubes treated as short fiber reinforced iron metal matrix	243
6.23	Validation of transverse modulus for carbon nanotubes treated as short fiber reinforced copper metal matrix	243
6.24	Validation of transverse modulus for carbon nanotubes treated as short fiber reinforced aluminum metal matrix	243
6.25	Validation of shear modulus for carbon nanotubes treated as short fiber reinforced iron metal matrix	244

Figure No		Page
6.26	Validation of shear modulus for carbon nanotubes treated as short fiber reinforced copper metal matrix	245
6.27	Validation of shear modulus for carbon nanotubes treated as short fiber reinforced aluminum metal matrix	245
6.28	Comparison between the thermal conductivity models for carbon nanotube reinforced aluminum matrix	246
6.29	Comparison between the thermal conductivity models for carbon nanotube reinforced copper matrix	246
6.30	Comparison between the thermal conductivity models for carbon nanotube reinforced iron matrix	247
6.31	Validation of thermal conductivity of armchair carbon nanotube treated as long fiber reinforced iron metal matrix	248
6.32	Validation of thermal conductivity of zigzag carbon nanotube treated as long fiber reinforced iron metal matrix	248
6.33	Validation of thermal conductivity of chiral carbon nanotube treated as long fiber reinforced iron metal matrix	249
6.34	Validation of thermal conductivity of armchair carbon nanotube treated as long fiber reinforced copper metal matrix	250
6.35	Validation of thermal conductivity of zigzag carbon nanotube treated as long fiber reinforced copper metal matrix	250
6.36	Validation of thermal conductivity of chiral carbon nanotube treated as long fiber reinforced copper metal matrix	250
6.37	Validation of thermal conductivity of armchair carbon nanotube treated as long fiber reinforced aluminum metal matrix	252
6.38	Validation of thermal conductivity of zigzag carbon nanotube treated as long fiber reinforced aluminum metal matrix	252
6.39	Validation of thermal conductivity of chiral carbon nanotube treated as long fiber reinforced aluminum metal matrix	252
6.40	Validation of thermal conductivity for armchair (5, 5) carbon nanotubes (as short fiber "lc=3") reinforced iron metal matrix	253
6.41	Validation of thermal conductivity for zigzag (5, 0) carbon nanotubes (as short fiber "lc=3") reinforced iron metal matrix	254
6.42	Validation of thermal conductivity for chiral (5, 10) carbon nanotubes (as short fiber "lc=3") reinforced iron metal matrix	254
6.43	validation of thermal conductivity for armchair (5, 5) carbon nanotubes (as short fiber "lc=3") reinforced copper metal matrix	255
6.44	Validation of thermal conductivity for zigzag (5, 0) carbon nanotubes (as short fiber "lc=3") reinforced copper metal matrix	255
6.45	Validation of thermal conductivity for chiral (5, 10) carbon nanotubes (as short fiber "lc=3") reinforced copper metal matrix	256
6.46	Validation of thermal conductivity for armchair (5, 5) carbon nanotubes (as short fiber "lc=3") reinforced aluminum metal matrix	257
6.47	Validation of thermal conductivity for zigzag (5, 0) carbon nanotubes (as short fiber "lc=3") reinforced aluminum metal matrix	257
6.48	Validation of thermal conductivity for chiral (5, 10) carbon nanotubes (as short fiber "lc=3") reinforced aluminum metal matrix	258
6.49	Validation of thermal conductivity for armchair (5, 5) carbon nanotubes (as short fiber) reinforced iron metal matrix at different lengths	259

Figure No		Page
6.51	Validation of thermal conductivity for chiral (5, 10) carbon nanotubes (as short fiber) reinforced iron metal matrix at different lengths	260
6.52	Validation of thermal conductivity for armchair (5, 5) carbon nanotubes (as short fiber) reinforced copper metal matrix at different lengths	261
6.53	Validation of thermal conductivity for zigzag (5, 0) carbon nanotubes (as short fiber) reinforced copper metal matrix at different lengths	261
6.54	Validation of thermal conductivity for chiral (5, 10) carbon nanotubes (as short fiber) reinforced copper metal matrix at different lengths	261
6.55	Validation of thermal conductivity for armchair (5, 5) carbon nanotubes (as short fiber) reinforced aluminum metal matrix at different lengths	262
6.56	Validation of thermal conductivity for zigzag (5, 0) carbon nanotubes (as short fiber) reinforced aluminum metal matrix at different lengths	263
6.57	Validation of thermal conductivity for chiral (5, 10) carbon nanotubes (as short fiber) reinforced aluminum metal matrix at different lengths	263
6.58	Validation of thermal conductivity for carbon nanotubes (as Short Fiber) reinforced iron metal matrix at different diameters and at $l_c = 3\text{nm}$	264
6.59	Validation of thermal conductivity for carbon nanotubes (as Short Fiber) reinforced iron metal matrix at different diameters and at $l_c = 5\text{nm}$	265
6.60	Validation of thermal conductivity for carbon nanotubes (as Short Fiber) reinforced iron metal matrix at different diameters and at $l_c = 8\text{nm}$	265
6.61	Validation of thermal conductivity carbon nanotubes (as Short Fiber) reinforced Copper metal matrix at different diameters and at $l_c = 3\text{nm}$	267
6.62	Validation of thermal conductivity for carbon nanotubes (as Short Fiber) reinforced Copper metal matrix at different diameters and at $l_c = 5\text{nm}$	267
6.63	Validation of thermal conductivity for carbon nanotubes (as Short Fiber) reinforced Copper metal matrix at different diameters and at $l_c = 8\text{nm}$	267
6.64	Validation of thermal conductivity carbon nanotubes (as Short Fiber) reinforced Aluminum metal matrix at different diameters and at $l_c = 3\text{nm}$	269
6.65	Validation of thermal conductivity carbon nanotubes (as Short Fiber) reinforced Aluminum metal matrix at different diameters and at $l_c = 5\text{nm}$	269
6.66	Validation of thermal conductivity carbon nanotubes (as Short Fiber) reinforced Aluminum metal matrix at different diameters and at $l_c = 8\text{nm}$	269
6.67	Validation of thermal contact conductance for armchair (5, 5) carbon nanotubes (as Short Fiber) reinforced Iron metal matrix	271

Figure No		Page
6.68	Validation of thermal contact conductance for zigzag (5, 0) for carbon nanotubes (as Short Fiber) reinforced Iron metal matrix	271
6.69	Validation of thermal contact conductance for chiral (5, 10) carbon nanotubes (as Short Fiber) reinforced iron metal	272
6.70	Validation of thermal contact conductance for armchair (5, 5) carbon nanotubes (as Short Fiber) reinforced Copper metal matrix	273
6.71	Validation of thermal contact conductance for zigzag (5, 0) for carbon nanotubes (as short fiber) reinforced copper metal matrix	274
6.72	Validation of thermal contact conductance for chiral (5, 10) carbon nanotubes (as Short Fiber) reinforced copper metal matrix	274
6.73	Validation of thermal contact conductance for armchair (5, 5) carbon nanotubes (as short fiber) reinforced aluminum metal matrix	276
6.74	Validation of thermal contact conductance for zigzag (5, 0) carbon nanotubes (as short fiber) reinforced aluminum metal matrix	276
6.75	Validation of thermal contact conductance for chiral (5, 10) carbon nanotubes (as Short Fiber) reinforced aluminum metal matrix	276

LIST OF ABBREVIATIONS

1D	One dimension
2D	Two dimension
3D	Three dimension
ANSYS	Analysis system software
BEM	Boundary element method
CMC	Ceramic matrix composites
CNT	Carbon Nanotube
CVD	Chemical vapor deposition
DFT	density functional theory
FEA	Finite element analysis
FEM	Finite element method
GUI	Graphical user interface
HiPCO	High pressure carbon monoxide
MATLAB	Matrix Laboratory
MD	Molecular Dynamics
MMC	Metal matrix composites
MWCNT	Multi wall carbon nanotube
NR	Natural rubber
PM	Powder metallurgy
RVE	Representative volume element
SWNT	Single wall nanotube

LIST OF SYMBOLS

C_h	Chiral vector
a_1, a_2	Unit vectors
θ	Chiral Angle
E_c	Elastic modulus of the composite
E_f	Elastic modulus of the fiber
E_m	Elastic modulus of the matrix
V_c	Volume fraction of composite
V_f	Fiber volume fraction
V_m	Matrix volume fraction
W_c	Weight fraction of composite
W_f	Fiber Weight fraction
W_m	Matrix Weight fraction
w_c	Weights of composite material
w_m	Weights of matrix
w_f	Weights of fiber
v_f	Fiber volume
v_m	Matrix volume
ρ_c	Density of composite
ρ_m	Density of matrix
ρ_f	Density of fiber
$\sigma_{c(lt)}$	Composite longitudinal tensile strength
σ_{fu}	Ultimate tensile strength of the fiber
σ_f	Fiber longitudinal tensile strength
G_m	Shear Modulus of the Matrix
G_f	Shear Modulus of the Fiber
ϑ_m	Major Poisson's Ratio of the Matrix
ϑ_f	Major Poisson's Ratio of the Fiber
δ_c	Elongation of composite
δ_f	Elongation of fiber
δ_m	Elongation of matrix

t_c	Cumulative thickness of composite
t_f	Cumulative thickness of fiber
t_m	Cumulative thickness of matrix
γ_c	Composite shear strain
γ_m	Matrix shear strain
γ_f	Fiber shear strain
d_f	Fiber diameter
a	Width of the square RVE
A_c	Area of Carbon nanotube
A	Area of whole RVE
E_{Random}	Shear modulus in random conditions
E_L	Longitudinal Young's modulus (as short fiber)
E_T	Transverse Young's modulus (as short fiber)
G_{Random}	Shear modulus in random conditions
ν_{Random}	Poisson's ratio in random conditions
m_x	Influence of shear stresses on extensional strains
m_y	Influence of normal stresses on shear strain
$[C]$	Stiffness components
$[S]$	Compliance matrix
$[Q]$	Stiffness matrix
d_o	Carbon nanotube outer diameter
d_i	Carbon nanotube inner diameter
a_{c-c}	Carbon-Carbon distance
q	Heat flux per unit time per unit area
k	Thermal conductivity
$\frac{dT}{dx}$	Temperature gradient through the material
H_i	The intensity
ϕ	Temperature field
k_{ij}	thermal conductivity tensor
$\phi(S)$	Surface temperature
H_i^o	Applied far-field intensity
$k^{(2)}$	Effective thermal conductivity of the effective fiber
k_{CNT}	Thermal conductivity of carbon nanotube
k_{eff}^*	Effective thermal conductivity of the composite

ζ_0	Inverse of the eccentricity
β	Interfacial conductance
l_{CNT}	Length of the SWNT
R_{CNT}	Mean radius of the SWNT
U_r	Energy associated with bond stretch interactions
U_θ	Energy associated with bond angle bending
U_ϕ	Energy associated with torsion
U_{vdW}	Energy associated with van der Waals forces
Δr	Change in bond-length
$\Delta\theta$	Change in bond angle
$\Delta\phi$	Change in dihedral angle
k_r	The force constants associated with stretching
k_θ	The force constants associated with bending
k_ϕ	The force constants associated with torsion
$[K_e]$	Element stiffness matrix
$\{F_e\}$	Element load vector of a finite element
$\{U_e\}$	Nodal displacement vector for an element
$[B_e]$	Strain-displacement matrix
$[D_{ep}]$	Elasto-plastic constitutive matrix
$ J $	Determinate of the Jacobian matrix
u'_i, u_i	Displacement of relative opposite periodic node pairs
u_i^d	Displacement of dummy node
a_1	Semi-minor axis
a_3	Semi-major axis

CHAPTER ONE

INTRODUCTION

1.1 Overview

Nanotechnology seeks to discover and manipulate the properties of matter at the nanoscale in order to develop new applications across many fields, such as electronics, photonics, medicines, and materials [1-3]. These materials and systems can be designed to exhibit novel and significantly improved physical, chemical, and biological properties, phenomena, and processes as a result of the limited size of their constituent particles or molecules. For example, in the field of nanoscale electronics, the optimum development would be further miniaturizing the electronic circuits, which leads to faster, more sophisticated, and more portable devices.[4]

Nanotechnology includes the integration of nanoscale structures into larger material's components, systems, and architectures. However, within these larger scale systems, the control and construction remains at the nanoscale. This scale leads to dealing with a very large number of elements. Taking integrated electronic systems as an example, modern microelectronic systems contain up to 100 million devices on a single chip. Nano electronics might push this number up to 1 billion or more devices[5-7]. The primary problem is not only the large number of devices, but also the development time and the time for testing such systems. However, Nanotechnology is a very comprehensive and interdisciplinary area of research and development activity that has been growing explosively worldwide. This nanotechnology revolution promises to transform the ways, in which materials and products are created; and the wide range and nature of functionalities that can be accessed. Major technological changes can expected to be brought by the tiny atom-atom based manufacturing techniques in future[6, 8, 9].

The scientific investigations and applied research on composite materials can be dated back to 1940's[10], and these advanced materials have changed the world and it's been

introduced gradually in our daily life. Composites are also recognized as high-tech materials [11]. A Composite material is engineered material made from two or more constituent materials with significantly different physical or chemical properties which remain separate and distinct on a macroscopic level within the finished structure. The advantage is the combination of those different constituents, providing a potential for tailoring material properties to meet specific and challenging requirements. The balance of the properties can be altered by the choice of the matrix and the level of reinforcement. Composites offer the only pathway for producing such advanced “designer” materials.[11, 12]

Most composites exploited in sport, aerospace and automotive industries consist of a reinforcing phase, such as glass or carbon fibers, and a polymeric matrix[13]. Polymers are chosen for matrix materials because of their low density, low cost, and easy procedure in composite processing. However, compared with polymers, metals have other advantages, which are wanted in diverse applications, such that they combine strength and toughness, which can be maintained even at elevated temperature, do not absorb humidity, are not degraded by radiation, do not outgas in space, generally do not burn, but can conduct heat and electricity. With all of these desirable and interesting physical properties, metals were considered as matrices in composites although it would be significantly more difficult to process metal matrix composites (MMCs) than to produce polymer matrix composites. The pioneer research on metal matrix composites was taken off in the 1960’s and reached its first peak activity in the early 1980’s. By now metal matrix composites have indeed entered the engineering world as “real” industrial materials.[14]

Currently, metal matrix composites are commercially available with a variety of forms. They are utilized predominately in a wide range of applications, ranging from brake discs in trains to critical rotating parts in helicopters, from thermal substrates for advanced electronic and power modules to spikes for track shoes, and from tool materials to combustion engine components, from structural to electronic applications[15]. However, the dominant applications focus on three sectors: (i) automotive and ground transportation, (ii) aerospace and defense, (iii) thermal management for electronics. In the sector of automotive and ground transportation, metal matrix composites are used for their specific stiffness, high temperature strength and excellent wear properties.

Substantial developments have been made during the last few years in the field of Nano composites[6]. Nano-composites are a multiphase solid material where one of the

phases has one, two or three dimensions or structures having Nano-scale repeat distances between the different phases that make up the material [16]. The definition can include porous media, colloids, gels and copolymers, but is more usually taken to mean the solid combination of a bulk matrix and Nano-dimensional phase differing in properties due to dissimilarities in structure and chemistry.[16-18]

The discovery of carbon nanotubes has provided promising candidates as reinforcements for composite materials to overcome the performance limits of conventional materials [1, 19, 20], because of their attractive mechanical properties where the stiffness, strength and resilience exceed any current materials. In the past decade, numerous attempts and efforts have been made by researchers, exploiting the exceptional mechanical properties of carbon nanotubes toward the development of carbon nanotubes reinforced composite materials. The level of activity is illustrated by the number of journal articles published on Carbon nanotubes in the last decade. Studies on carbon nanotubes reinforcement of ceramic matrix are few as compared to those on polymer matrix, whereas those on carbon nanotube-reinforced MMCs are even fewer. This is quite surprising considering the fact that most of the structural materials used in today's world are metals. These articles address various aspects, such as processing, microstructure, modeling of mechanical properties and the chemical interaction of carbon nanotubes with metals[21, 22]. However, the research activity in using carbon nanotubes as reinforcements in metal matrix composites is still scarce, and metal matrix composites reinforced with carbon nanotubes have not yet been developed at a useful scale. In the limited number of reports[1, 22], the so-called metal matrix composites are in fact nanoscale composite.[21-24]

1.2 SIGNIFICANCE OF THE RESEARCH

Carbon nanotubes are nanometer sized cylinders made of carbon atoms which possess extraordinary electrical, thermal, and mechanical properties. Their potential applications include such diverse areas as conductive and high strength composites, energy storage and conversion devices, sensors, field emission displays and radiation sources, hydrogen storage media, and nanometer sized semiconductor devices, probes and interconnects. To date, carbons have contributed to welfares of human being as a "silent force behind the science". Tailoring of carbon structure, that is, controlling the physicochemical properties of carbon materials on the nanometer scale will be core technology for obtaining novel carbons with new and extraordinary functions. The function and the added value of novel carbons based on nanotechnology will provide the industry of our society with a great business opportunity. Day by day, the demand

for revitalizing the worldwide economy is growing. The only way to answer for this demand is the technological innovation. According to some economist models, new science will create a new industry and technology, and as a result, it will bring the wave of big economic activity[25, 26]. Figure 1.3 depicts the predicted world nanotube demand by market.

1.3 PROBLEM STATEMENT

Nanocomposite materials have been attracting major attention because of their promise in developing extremely strong materials and the basic opportunities they present. Although there have been many advancements in the manufacturing of Nanocomposite materials, thus far, these processes have only been moderately successful in producing isotropic properties in polymer based Nanocomposite matrices. In addition, few researchers have been exploring the development of metallic Nanocomposite materials in part because of the misconception that the nanotubes will not survive the high temperatures that are required to process these materials. However, Experimental investigation of nanoscale systems is generally difficult and expensive due to the small size of components and also time consuming. Thus a computer modeling and simulation play a significant role in predicting and designing material properties of composites. The analysis of these materials is performed by different computational methods covering different scales. The so called continuum methods, ranging from simple closed-form expressions to complex micromechanical models and numerical methods can be successfully applied in predicting the effective properties of different composites. The most frequently used experimental approaches for materials testing; among the numerical methods are the finite element method (FEM) and the boundary element method (BEM).

New composites of required properties can be fabricated by combining two or more materials. A combination of any material with carbon nanotubes, acting as a matrix and fillers, respectively, results in a new class of materials, called carbon nanotube-reinforced composite matrix. They can have an extraordinary functional and an enhanced mechanical properties, due to a unique physical and mechanical properties of carbon nanotubes. The unusual properties of carbon nanotubes, including for instance small size, low density, excellent electronic and thermal properties and extremely high stiffness and strength, can be utilized; carbon nanotubes represent a very promising material in many areas of science and industry.

1.4 OBJECTIVES

The objectives of this research are to understand the behavior of carbon nanotubes reinforced metal matrix composite based on numerical and computational modeling. The following research tasks will be conducted:

- To calculate the elastic and thermal properties of carbon nanotubes reinforced metal matrix nanocomposites by rule of mixture, and by modifying thermal conductivity model to predict these properties.
- To develop macros as a simulation preparation for the generation of the finite element models to study the elastic and thermal conductivity properties of carbon nanotubes reinforced metal matrix nanocomposites.
- To conduct simulations using ANSYS software to model the elastic and thermal properties of the carbon nanotube based metal matrix nanocomposites.
- To compare between the analytical and the simulation results for better understanding of the model and future development.

In this research, a combination of theoretical and computational frameworks has been chosen to investigate the behavior of carbon nanotubes reinforced metal matrix composite.

1.5 Research limitations

The limitation of this research is mainly in the difference between the simulation and its assumptions which cannot be achieved when it's deployed in experimental work, also the lack of results regarding metal matrix Nano-composite at different parameters such as volume fractions which affect the simulation results validation. However, the understanding of the mechanical properties of carbon nanotubes such as elastic and thermal properties when reinforcing the metal matrix is still insufficient so that the design and optimization of carbon nanotubes in Nano-engineering is limited. Another factor is the high cost regarding the materials preparation and laboratory work.

1.6 THESIS LAYOUT

The thesis organized into seven chapters. Chapter one addresses a brief introduction to nanotechnology and presents the scope, problem statement and the objectives of this research. However, it is important to have a better understanding of carbon nanotube structure and properties in order to effectively utilize them in a

composite. Different synthesis processes for carbon nanotubes and their composites with the ongoing research and challenges, detail explanation on the mechanics of composite materials, and computational approach for modeling the carbon nanotubes reinforced composites are discussed and presented in Chapter Two. In Chapter Three, the methodology in which the finite element analysis and MATLAB code explained for predicting the results of the carbon nanotube reinforced metal matrix nanocomposites are presented. The results and data interpretation for analytical and computational approaches for the new nanocomposite are described and discussed in the fourth and fifth chapters, respectively. In Chapter Six, the validation of the results is presented. Finally in chapter seven, conclusion of the present study and proposed work for future studies are included.

CHAPTER TWO

LITERATURE REVIEW

2.1 Overview

In the past few decades, the use of composite materials in structural components has been increasing rapidly and they are now gradually replacing traditional metallic materials in many applications on account of the superior physical properties they offer at only a fraction of the weight. There are many advantages that composites have as compared to traditional engineering materials. Not only do they offer very high strength to weight ratios, they provide other advantages like superior resistance to corrosion, low density, low thermal expansion and favorable fatigue life. Another great advantage that composites have is the ability to have tailored physical properties in a specific direction, thereby providing great flexibility in design. As a result their use has been rapidly increasing, especially over the last two decades.

2.2 Nanocomposite Materials

Nanocomposite materials are a new class of materials defined as those materials with at least one of Nanocomposite phases with one or more dimensions like length, width, thickness in the nanometer range, generally 1 to 100 nm. This is the range where phenomena associated with atomic and molecular interactions strongly influence the macroscopic properties of the materials[1].

Nanocomposite differs from conventional composite material due to the exceptionally high surface to volume ration of the reinforced phase or its exceptionally high aspect ratio. Large amount of reinforcement surface means that a relatively small amount of nanoscale reinforcement can have an observable effect on the nanoscale properties of the composites. For example adding carbon nanotubes improves the electrical and thermal conductivity, it also increases optical and dielectric, heat resistance, mechanical properties like stiffness, strength, resistance to wear and damage. [27]

In view of recent development, the engineering of Nanocomposite has become technically feasible. The research community has made enormous advances in the processing of Nanocomposite in terms of manipulating the size, shape, volume fraction, interface, organization, and degree of dispersion to tailor these materials [9, 28, 29]. Although the understanding of the structure – processing – property relationship of these materials is still in its infancy, exciting possibilities have already demonstrated, especially when the combined theoretical and experimental efforts have generated more information to guide further development. However, a significant gap still exists between results obtained from experiments and expectations based on theoretical predictions. [16, 30-34]

There are several different types of Nanocomposite materials from zero dimensional atom clusters to three dimensionally structured materials. Among them, carbon-based materials[35], especially nanotubes, have provided promising candidates as reinforcements for composites, because of their attractive mechanical properties where the stiffness, strength and resilience exceed any current materials.

In the past decade, numerous attempts and efforts have been made by researchers, exploiting the exceptional mechanical properties of carbon nanotubes toward the development of CNTs reinforced composite materials. Polymers, ceramics and metals have been tried out as matrices [1, 22, 36, 37]. The primary success lies in polymers reinforced with carbon nanotubes. It was found that the exceptional properties of carbon nanotubes are the consequence of their unique structure. However, before exploring the various aspects of Nanotube based composite systems, carbon nanotubes should be described first.

2.3 CARBON NANOTUBES

The Carbon is sixth element in periodic table. It is found to have three allotropes, i.e. various stable forms, namely diamond, graphite and amorphous carbon. These allotropes are illustrated in Figure 2.1 shows peerless qualities in terms of heat, electrical conductivity, transparent or absorbency, hardness or soft behaviour etc. The discovery of ‘fullerenes’ added a new dimension to the knowledge of carbon science [38]; and the subsequent discovery of ‘carbon nanotubes’ (multiwall near the year 1991 [35] and single walled near the year 1993 [39]) added a new dimension to the knowledge of technology[35].

2.3.1 Atomic Structure

Carbon nanotubes consist of honeycomb lattices representing a single atomic layer of crystalline graphite, called a graphene sheet, seamlessly rolled into a cylinder of nanometer size diameter as shown in Figure 2.2

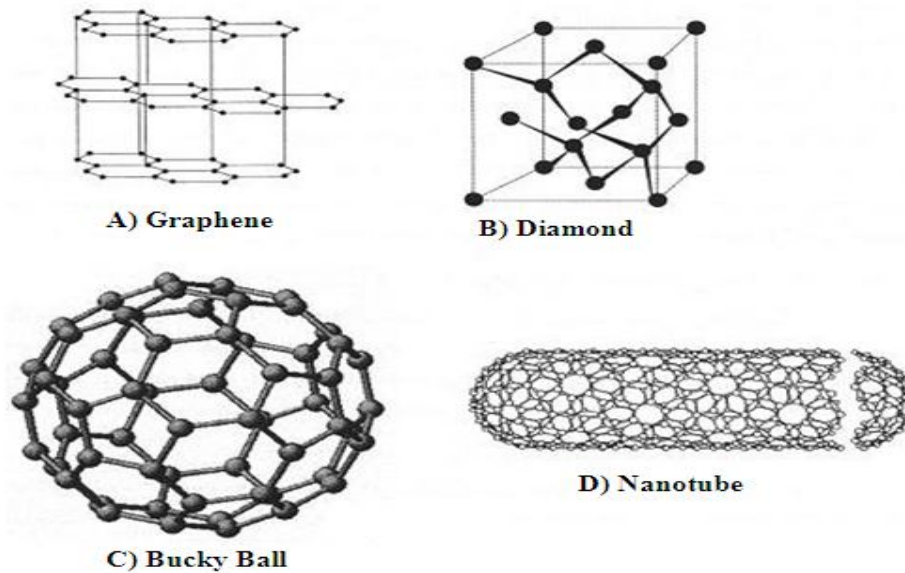


Figure 2.1: The allotropic forms of carbon known to mankind

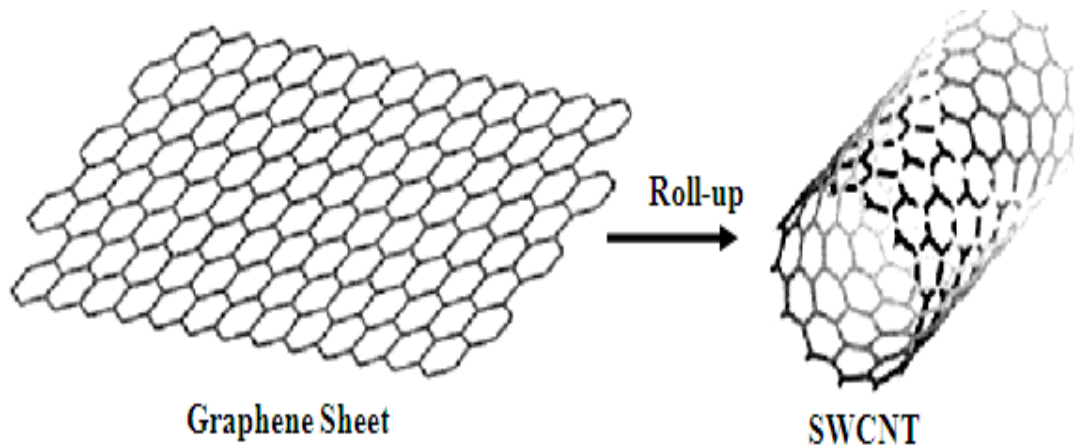


Figure 2.2: Rolling up a graphene sheet to form a nanotube

Carbon nanotubes consist of honeycomb lattices representing a single atomic layer of crystalline graphite, called a graphene sheet, seamlessly rolled into a cylinder of nanometer size diameter.

Carbon nanotubes fall under two categories, single-wall or multi-wall nanotubes, depending on the number of layers/tubes that comprise them. Multi wall carbon

nanotubes consist of multiple concentric tubes of rolled-up graphene sheets with an interlayer spacing of 0.34-0.36 nm that is close to the typical atomic spacing of graphite [40]. Their diameter is on the order of tens of nanometers and their length is usually a few microns. Single wall nanotubes on the other hand consist of a single graphene layer, as the name suggests, and are no more than a few nanometers in diameter, with similar lengths as multi-wall nanotubes. The single wall nanotubes is considered to be the ultimate fiber of molecular dimensions, since it contains all of the in-plane strength and stiffness of graphite.[5]

The direction along which the graphite sheet is rolled up to form the nanotube determines its chirality and also affects whether the nanotube is metallic or behaves like a semiconductor. This direction of roll is defined by a vector known as ‘roll-up vector’ or ‘chiral vector’(\vec{Ch}) and can be expressed as a linear combination of the unit translational vectors in the hexagonal lattice.

$$\vec{Ch} = ma_1 + na_2 \quad 2.1$$

Where m and n are integers, while a_1 and a_2 are the vectors of the hexagonal graphite lattice shown in Figure 2.3. The angle between \vec{Ch} and a_1 is known as the chiral angle, θ , and can be calculated as follows[7]

$$\theta = \sin^{-1} \left[\frac{\sqrt{3}m}{2\sqrt{n^2+m^2+nm}} \right] \quad 2.2$$

The variation of the chiral indices (m, n) results in different types of nanotubes. Table 2.1 present the Parameters of carbon nanotube[41]. The diameter of any nanotube can be calculated as follows[7]:

To calculate the Mean diameter of carbon nanotube:

$$d_{\text{mean}} = \frac{\sqrt{3} \cdot a_{c-c} \sqrt{(n^2) + (m \cdot n) + (m^2)}}{\pi} \quad 2.3$$

Where m and n is the carbon nanotube indices

$$a_{c-c} = 0.142 \text{ nanometer}$$

If $m = n$ then the carbon nanotube is called **Armchair**

If $n = 0, m \neq 0$ then the carbon nanotube is called **Zigzag**

If $m \neq n$ then the carbon nanotube is called **Chiral**

The thickness of the carbon nanotube is 0.34 nm

The inner (d_i) and outer (d_o) diameter of carbon nanotubes can be calculated as follow:

$$d_o = d_{\text{mean}} + 0.17 , \quad 2.4$$

$$d_i = d_{\text{mean}} - 0.17 , \quad 2.5$$

MWNTs are often metallic in nature, while SWNTs or DWNTs depending on their diameter and chirality can be metallic or semi conducting in nature. Depending upon the band crossing calculations, a carbon nanotube will be metallic if,

$$n - m = 3(q) \quad 2.6$$

Where q is any integer

This gives the probability that at least two third of carbon nanotubes can show semi conducting behavior and one third metallic. Also, as per this equation, the small diameter SWNTs will predominantly behave semi conducting. This is because, for such small diameter, chances that the difference between n and m will be multiple of three are low.

Apart from its atomic structure, carbon nanotubes have further different morphologies. Single, double or multi walled carbon nanotubes have already been defined before. In addition to them, coiled carbon nanotubes, Y-junction nanotubes, truncated or bended junction, bamboo structured CNTs are rigorously studied. Figure 2.4 presents different morphologies of Carbon nanotubes.

2.3.2 Bonding Mechanism

The bonding mechanism in a carbon nanotube system is similar to that of graphite, since a CNT can be thought of as a rolled-up graphene sheet. The atomic number for carbon is 6, and the atom electronic structure is $1s^2 2s^2 2p^2$ in atomic physics notation[42]. Each atom is bonded to its nearest 3 neighbors, at approximately 120 degrees in plane angles. The primary bonds between these atoms are hybridized sp^2 bonds, or σ bonds as shown in Figure 2.5. This in-plane bond is referred to as a σ -bond (*sigma*-bond). This is a very strong covalent bond that binds the atoms in the plane, and results in the high stiffness and high strength of a Carbon nanotubes.

The π -bonds are delocalized bonds and are much weaker; however they are centered, symmetrically about 0.33 Å from the central axis of the sigma bond. Thus they are primarily responsible for the out of plane properties, such as the wall bending stiffness. The bond structure of a graphene sheet is shown in Figure 2.6.

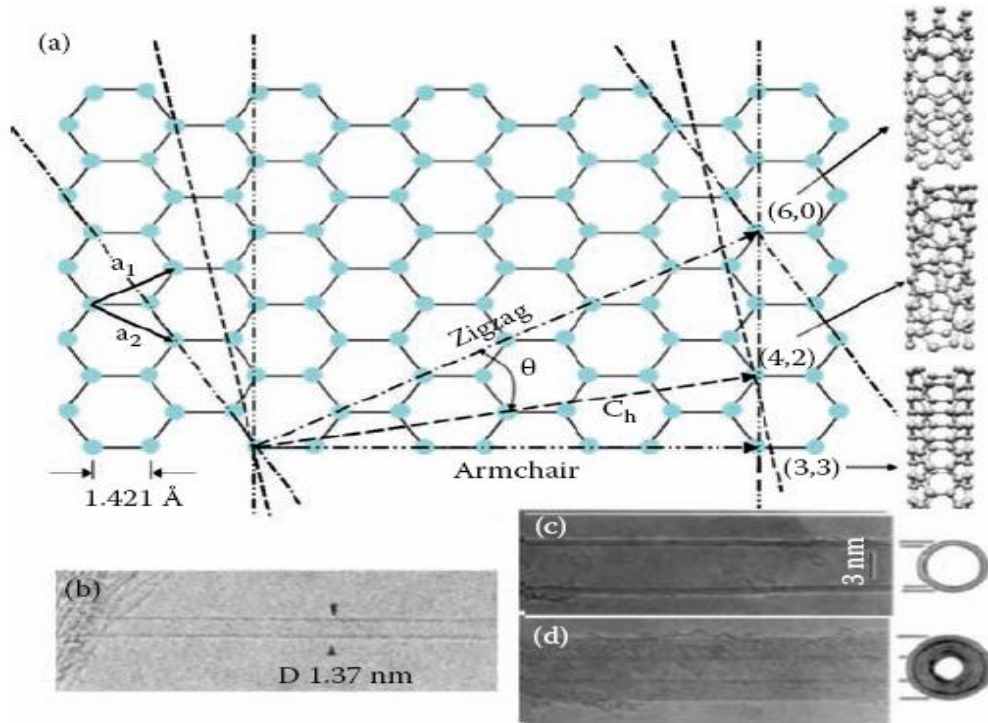


Figure 2.3: (a) Schematic showing the formation of an SWNT by rolling along different chiral vectors C_h and the resulting SWNTs, and (b), (c), and (d) high resolution TEM images showing a single, double, and seven-walled nanotube, respectively[23]

Table 2.1: Parameters of carbon nanotubes[41]

Symbol	Name	Formula	Value
a_{C-C}	Carbon-carbon distance		1.42 \AA
a	Length of unit vector	$\sqrt{3}a_{C-C}$	2.46 \AA
a_1, a_2	Unit vectors	$\left(\frac{\sqrt{3}}{2}, \frac{1}{2}\right)a, \left(\frac{\sqrt{3}}{2}, -\frac{1}{2}\right)a$	In (x, y) coordinates
C_h	Chiral vector	$C_h = na_1 + ma_2 = (n, m)$	n, m : integer
L	Circumference of Nanotube	$L = C_h = a\sqrt{n^2 + m^2 + nm}$	$0 \leq m \leq n$
d	Diameter of Nanotube	$d = \frac{L}{\pi} = \frac{\sqrt{n^2 + m^2 + nm}}{\pi}a$	
θ	Chiral Angle	$\sin \theta = \frac{\sqrt{3}m}{2\sqrt{n^2 + m^2 + nm}}$ $\cos \theta = \frac{2n + m}{2\sqrt{n^2 + m^2 + nm}}$ $\tan \theta = \frac{\sqrt{3}m}{2n + m}$	$0 \leq \theta \leq 30^\circ$

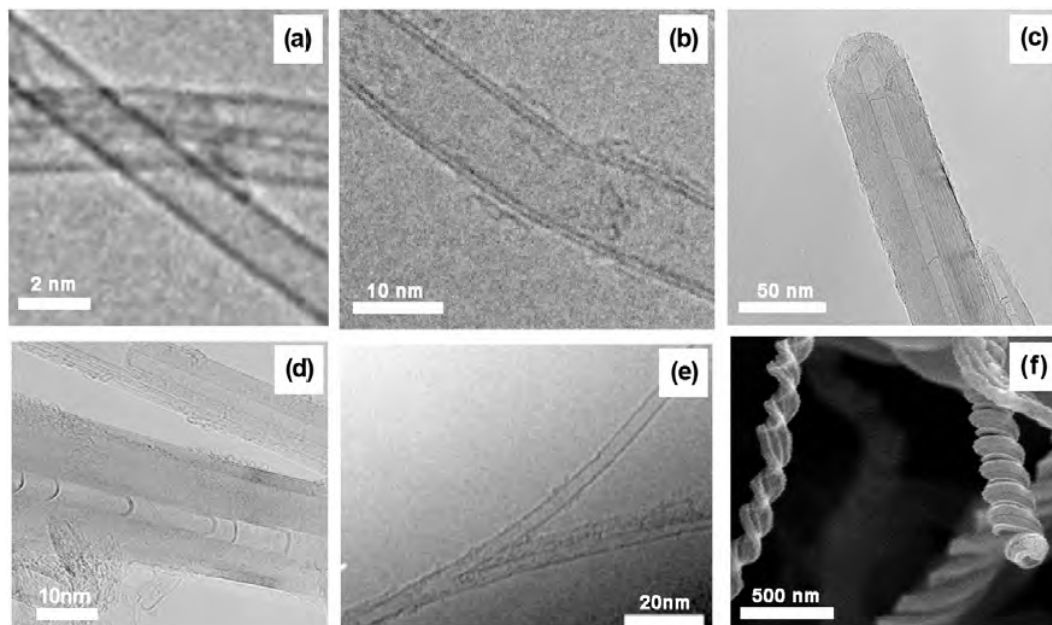


Figure 2.4: Electron micrographs of various possible morphologies of carbon nanotubes, (a) SWNT [43] (b) DWNT (c) MWNT (d) bamboo structured CNT (e) Y-junction CNT [44] (f) coiled CNTs

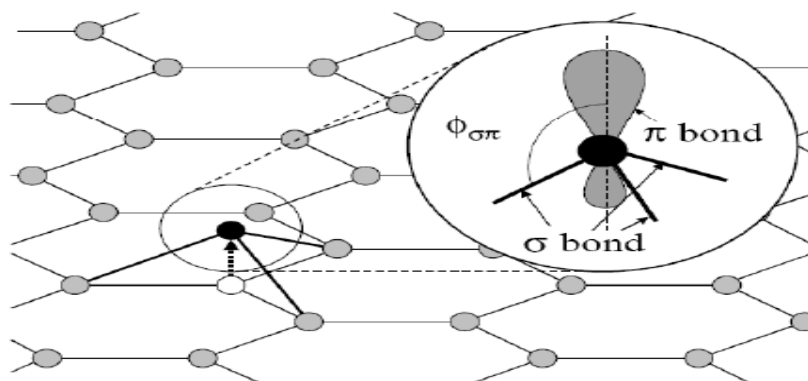


Figure 2.5: Bond inversion of carbon atom in a graphene sheet[45]

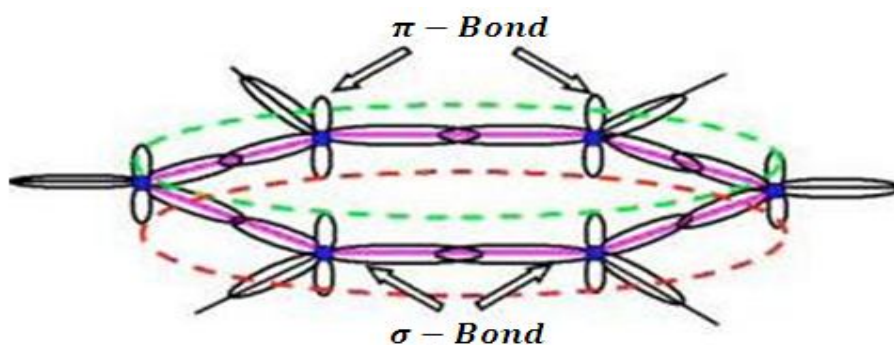


Figure 2.6: Basic hexagonal bonding structure for one graphite layer (the *graphene sheet*); carbon nuclei shown as filled circles, out-of-plane π -bonds represented as *delocalized* ~dotted line!, and σ -bonds connect the C nuclei in-plane.[42]

2.3.3 Synthesis of Carbon Nanotubes

At present carbon nanotubes are manufactured by different methods in laboratories and industry. The production of CNTs with a high order of purity, large amount, low costs, and uniformity are still one of the biggest issues in the carbon nanotube society. An overview of the most common techniques and their advantages and disadvantages are represented below in Table 2.2[46]. Nowadays, the main issue concerns the large-scale and low-cost production of nanotubes for industrial applications.

Table 2.2: Overview on the most common carbon nanotubes synthesis techniques and their advantages and disadvantages.[46]

<i>Method</i>	<i>CVD</i>	<i>Arc Discharge</i>	<i>Laser Ablation</i>	<i>HiPCO</i>
<i>Basics</i>	Decomposition of hydrocarbon gases in the presence of metal catalyst particles	Electric arc discharge generated between two graphite electrodes under an inert atmosphere (argon, helium)	Graphite target is vaporized by laser irradiation under flowing inert atmosphere and high temperature	Gas-phase growth of SWCNT with carbon monoxide as a carbon source at high temperature and pressure
<i>SWNT</i>	long, 0.6 - 4 nm diameter	short, 1.2-1.4 nm diameter	long, 1-2 nm diameter	~0.7 nm diameter, various lengths
<i>MWNT</i>	long, 10-200 nm diameter	short, 1-3 nm diameter	not applicable but possible	not applicable
<i>Yield</i>	up to 100 %	up to 90%	up to 65%	up to 70%
<i>Advantages</i>	high purity, large scale production, simple	easy, defect-free nanotubes, no catalyst	high purity, defect free SWNTs	large scale, high purity
<i>Disadvantages</i>	limited control over the structures, defects	short, tangled nanotubes, random structures	expensive, low scale production	defects

2.3.4 Properties of Carbon Nanotubes

Carbon nanotubes can have different individual structures, morphologies and properties due to their seamless cylinder structure and small diameter, Table 2.3, Table 2.4 and Table 2.5 present a comparative summary of the carbon nanotubes properties, comparison of the mechanical and physical properties of carbon nanotubes with common materials, and the thermal properties of carbon nanotubes, respectively [47, 48]. Carbon nanotubes have stiffness, strength, and electrical / thermal conductivity

which exceed most of all other known natural and synthetic materials, as well as different collective arrangements and emerging properties, all of which are determined by the method of preparation and further processing. Hence, a wide variety of synthetic methods have been developed to produce the desired materials and properties for specific scientific studies or technological applications[24]. It is now established beyond doubt that their unique properties will lead to better and newer materials.

Table 2.3: Properties of Carbon Nanotubes[46]

Property	Item		Data
Geometrical	Layers		Single/Multiple
	Aspect Ratio		10-1000
	Diameter	SWNT	~0.4nm to 3nm
		MWNT	~1.4nm to 100nm
Length		Several μm (Rope upto cm)	
Mechanical	Density		1.33 ~1.4g/ cm^3 (Al: 2.74g/ cm^3)
	Young's Modulus		~1 TPa (Steel: 0.2TPa)
	Tensile Strength		45GPa(Steel: 2GPa)
Electronic	Current Carrying Capacity		~1TA/ cm^3 (Cu: 1GA/ cm^3)
	Conductivity		Metallic/Semi-conductivity
	Field Emission		Active Phosphorus at 1~3V
Thermal	Thermal Conductivity		> 3kW/mK (Diamond: 2kW/mK)
	Resistivity		5–50 $\mu\Omega\text{cm}$

Table 2.4: Comparison of the mechanical and physical properties of carbon nanotubes compared with common materials [47, 48]

Material	Young's modulus (GPa)	Tensile Strength (GPa)	Resistivity (Ω cm)	Density (g/cm^3)
SWCNT	1054	150	Varies with chirality	1.3
MWCNT	1200	150	$\sim 10^{-4}$	2.6
Steel	208	0.4	$\sim 10^{-5}$	7.8
Diamond	1000	200	$\sim 10^{18}$	3.5
Epoxy	3.5	0.005	$\sim 10^{15}$	1.2-1.4
Wood	16	0.008	$\sim 10^7$	0.57-0.65

Table 2.5: Thermal properties of Carbon nanotubes[49]

	Thermal Conductivity (W/mK)	Electrical Conductivity (A/cm^2)	Thermal Stability ($^{\circ}\text{C}$) in air	Thermal Stability ($^{\circ}\text{C}$) in N_2	Specific Heat ($\text{m.J}/\text{g.K}$)
MWCNT	~3000	$\leq 10^9$	~680 $^{\circ}$	> 2600 $^{\circ}$	~700
SWCNT	~6000	Depends on the chirality	~680 $^{\circ}$	> 2600 $^{\circ}$	~700

2.3.5 Carbon Nanotubes Applications and Challenges

As one of the most important materials in the Nano area, carbon nanotubes have generated broad and interdisciplinary attention in the last two decades. Their outstanding properties have been studied extensively and much effort has been devoted to their applications. In particular, their high stiffness and ultimate strength and excellent resilience make them excellent candidates as reinforcements in composites. Nanotube field effect transistors are examples, which use the interesting electronic properties of CNTs. Such nanometer-sized electronic devices are promising for downsizing circuit dimensions. The field emission properties of CNTs, as a result of the extreme aspect (length-diameter) ratio, enable carbon nanotubes to be used as field emission electron sources for field emission devices such as flat panel displays and lamps. These devices have advantages over conventional tungsten and molybdenum tip arrays. Nanotubes provide stable emission, long lifetimes, and low emission threshold potentials. While the light emitting property of MWCNTs may make them good scanning probe tips in Scanning Near field Optical Microscope. CNT scanning probe tips for atomic probe microscopes are on the market. Other potential applications include energy storage and energy conversion devices, sensors and hydrogen storage media etc. [50]

Real-world applications of carbon nanotubes require either large quantities of bulk materials or device integration in a scale-up fashion. For Nanocomposite applications, the low-cost and high-yield production of high-quality CNTs at the kilogram or ton level is essential. For electronic and other devices, scale-up will unavoidably rely on the self-assembly or controlled growth in conjunction with micro fabrication processes. Although significant work has been carried out to tackle these issues, many challenges still remain in the carbon nanotube growth area. An efficient growth approach to carbon nanotubes of a controlled structure is not yet at hand even at a laboratory scale, while the growth of defect-free carbon nanotubes continuously to macroscopic lengths is still not possible.

2.4 Carbon Nanotubes Reinforced Composite Materials

The rising demand for lightweight and strong materials has prompted leading high-performance composites manufacturers to invest heavily in developing low cost and high strength new materials. Moreover, and given that the market has exploded worldwide, the need for additional capacity is sooner rather than later. Thus, there has

been enormous activity in the field of Nanocomposite to develop new materials with exceptional mechanical, electrical and thermal properties.

The discovery of carbon nanotubes provided promising candidates as reinforcements for composites. Due to the extraordinary properties, be it experimentally measured or theoretically computed, carbon nanotubes caught the attention of researchers and work on development of carbon nanotube composites started at a tremendous pace.

Polymers, ceramics and metals have been tried out as matrices [1, 24, 36, 50]. The primary success lies in polymers reinforced with carbon nanotubes. It was found that the exceptional properties of carbon nanotubes are the consequence of their unique structure. The most common techniques and methods are still under development; there are numerous variations of these techniques operating under different conditions, with different set-ups, and process parameters. Every technique provides diverse advantages and disadvantages over the quality and kinds of synthesized CNTs. An overview of these techniques are represented below in Figure 2.7[46]. In this research, the focus will be on the metal matrix reinforcement by carbon nanotubes.

2.4.1 Metal Matrix Composites with Carbon Nanotube Reinforcement

At present, a variety of metallic matrices, metals and their alloys, are employed in MMC industry. Examples include Al, Ti, Mg, Fe, Cu, Ni, W, Ag, Ni, Mo, Be, NiAl, AlCu, AlCuMg, Al-4%wtCu, Al-4%Cu-1%Mg-0.5%Ag etc. With their superior mechanical properties such as light weight, excellent strength, toughness and resistance to corrosion, which are critically important in aerospace and automotive applications, aluminum and aluminum alloys predominate as metallic matrices in the MMC industry[10, 23, 51, 52]. However, Most of the research on CNT composites is concentrated around polymer matrix composites. Research on metal-CNT Nanocomposite is very limited which could be due to possible damage of carbon nanotubes caused by high temperature processing required for metal matrices. A Summary of Processing, Microstructure Features and Properties of Various carbon nanotube-Metal Matrix Composites is provided in Table 2.6

2.4.2 Potential and Current Challenges

Carbon nanotubes based composites have attracted great interest due to an increasing technological demand for multifunctional materials with improved performance, complex shapes, and patterns manufactured in an easy way at low costs. However, several fundamental processing challenges must be overcome to enable

applicable composites with carbon nanotubes. The main problems with carbon nanotubes are connected to their production, purification, processability, manipulation and solubility. However, a significant gap still exists between results obtained from experiments and expectations based on theoretical predictions[6, 34, 69].

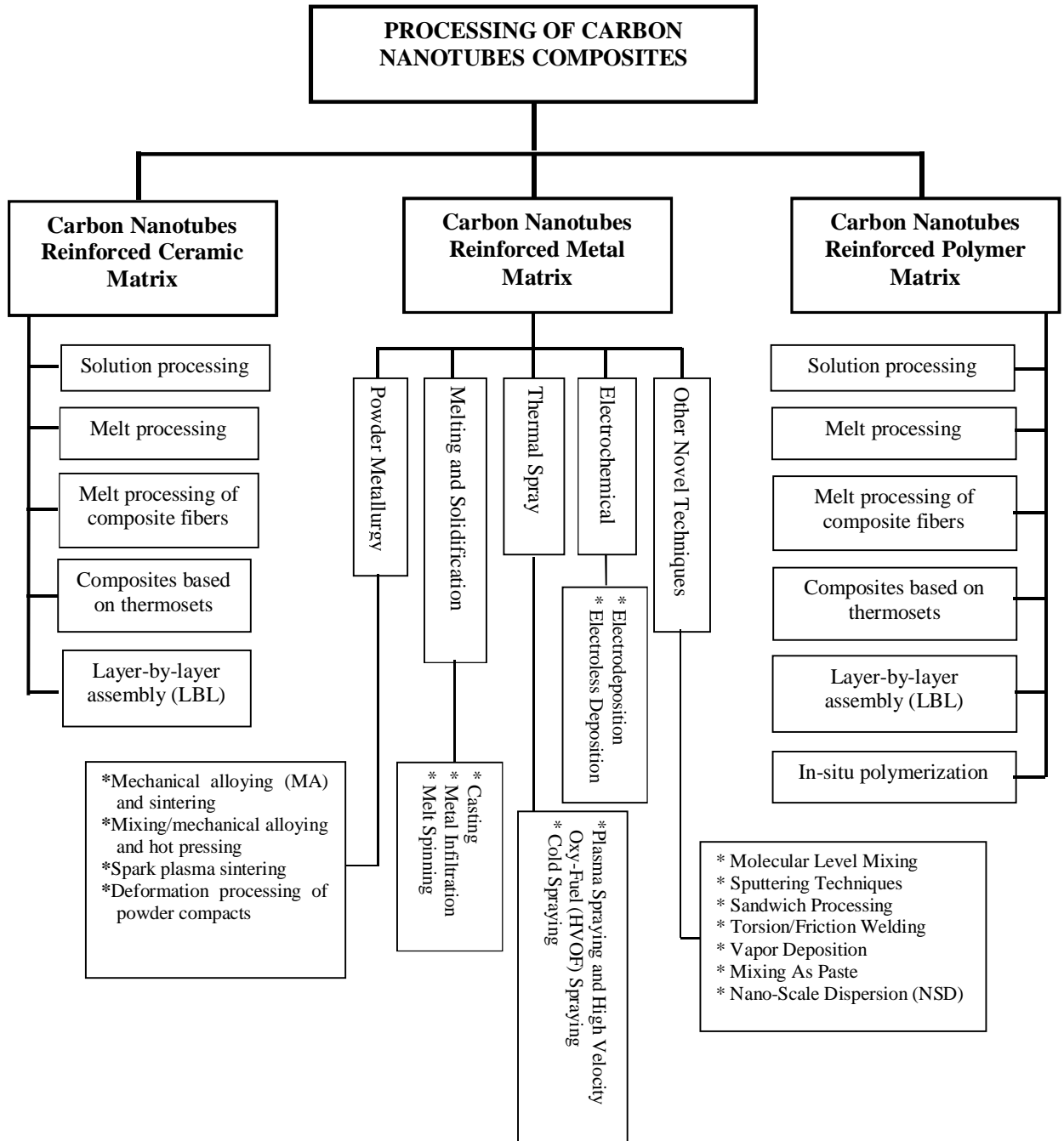


Figure 2.7: The various processes for synthesis of CNT-reinforced composite[52]

Table 2.6: Summary of Processing, Microstructure Features and Properties of Various Metal-CNT Composites

Composite	Matrix powder (Purity, size)	CNT %	Processing	Microstructure feature	Property
Al-MWCNT,[53]	99.99%, 40 μm	5-10 Wt% C powder contains 60 vol% CNT	Stir-mixing, hot pressing (64% vol reduction), extrusion (25: 1)	No carbide formation at the interface	Tensile strength Pure Al: -85 MPa With CNT: -80 MPa
Al-MWCNT,[54]	>99.5%, ~1 mm	1-10 w%	Hand grinding, hot pressing	Formation of Al-carbide phases (AlC and AlC ₂)	Resistivity Pure Al: 3.4 $\mu\Omega\text{cm}$ 4wt% CNT: 6.6 $\mu\Omega\text{cm}$
Al-SWCNT,[55]	99.85%, Nanosized	5 wt%	Ultrasonic mixing, compaction, hot pressing	Presence of physically intact CNTs	Micro hardness Pure Al: 1.62 GPa With CNT: 2.89 GPa
Al-SWCNT, MWCNT, [56]	Commercially pure, 200 mesh	SWNT: 1-2 vol%, MWNT: 0.5-2 vol%	Ball milling, compaction, sintering, hot extrusion	No formation of carbide phases. Pinning of sub grain boundaries by CNTs.	Elastic modulus 0.5 vol% SWNT: 78.1 GPa 2 vol% SWNT: 85.9 GPa 1 vol% MWNT: 70 GPa 2 vol% MWNT: 79.3 GPa
Al-MWCNT, [57]	99.7% 75 μm	0.5 and 1 wt% CNT	Powder can rolling	Better dispersion of the nanotubes	properties: tensile strength, yield strength, Young's modulus as well as lower density were achieved
Al- Si/MWCNT [58]	23 wt% Si, 2 wt% Ni, 1 wt% Cu, rest Al)	10 wt%	plasma and high velocity oxyfuel spraying	The interfacial ultrathin reaction product layer of $\beta\text{-SiC}$ (2–5 nm) between MWCNT reinforcement and Al-Si matrix remains unchanged after sintering	elastic moduli exhibited a gradual increase Overall improvement of micro hardness of the sintered composites was observed.
Cu- MWCNT, [59, 60]	Industrially Pure, 70 μm	0-25 vol%	Ball milling, isostatic pressing, sintering, rolling, annealing	Homogenous CNT distribution, pulling out and bridging of CNTs	Wear properties Low frictional coefficient, reduced weight loss Hardness Maximum at 12 vol% CNT
Cu- MWCNT, [61]	200-300 nm	0-10 vol%	High energy ball milling, pre-compaction, spark plasma sintering, cold rolling (50% vol reduction), annealing	Two phase microstructure i.e. fibrous Cu-CNT composite region and Cu matrix region	Tensile strength Pure Cu: 175 MPa 10 vol% CNT: 281 MPa Elastic modulus Pure Cu: 70 GPa 10 vol% CNT: 13.7 GPa

Continue Table 2.6:

Composite	Matrix powder (Purity, size)	CNT %	Processing	Microstructural features
Cu-MWCNT, [62, 63]	concentrated hydrochloric, nitric, Sulphoric acids	10–50µm length 15–10 nm diameter 5,15and 20 Vol% CNT/Cu	Spark plasma sintering of acid-treated and Electroless coated MWCNTs by copper.	with low CNTs vol fraction shows homogeneous distribution with segregation of the CNTs from the copper matrix. At a fine microstructure preventing grain coarsening. increasing the CNTs vol fraction to 20 vol.% there were some large pores created in the copper matrix.
Ni- MWCNT, [64, 65]	Ni-sulfate solution as electrolyte		Electroless plating on surface modified MWCNT	CNTs protruding out uniformly from the Ni deposit surface
Ni- MWCNT, [66]	Ni-sulfate solution as electrolyte	0-12 wt.%CNT with a coating of 35-40 µm thickness	Electroless plating on surface modified MWCNT, heat treatment	Amorphous matrix
Co- M WCNT, [22]	Co-sulfate solution as electrolyte		Electroless plating on surface modified MWCNT, drying, heat treatment	Heat-treated Co-plated CNTs exhibited more uniform coating with less fraction of voids and gaps
Ti- MWCNT, [67]	Ni powder	Carbon powder containing 60 vol. % CNT	Mechanical mixing, hot pressing	CNTs remained chemically stable, No formation of carbide
Mg- MWNT, [68]		2 Wt%	Dry-blending, hot pressing, hot isostatic pressing	Homogenous distribution of CNTs over Mg matrix

In addition, the scaling and manufacture of CNT Nanocomposite are difficult because of the following factors:

1. The small size of CNTs leads to strong forces (such as van der Waals forces) at the molecular scale. As a result, it is difficult to disperse carbon nanotubes within metallic, ceramic, or polymeric matrices.
2. Due to the very high aspect ratios of CNT, the addition of a small amount of CNTs to the matrix significantly increases viscosity. This fact considerably reduces manufacturability.
3. For advanced composites, a strict control of the alignment of the reinforcing agents within the matrix is crucial. Considering the size of carbon nanotubes, however, their manipulation is extremely difficult.
4. CNTs are very inert because of their atomic structure. As a result, interactions between carbon nanotubes and polymer molecules, which is an important factor in producing an effective composite, are not sufficiently strong.
5. Current manufacturing techniques of CNTs can produce only small quantities. Moreover, various purification techniques are necessary to remove impurities, resulting in longer manufacturing cycles. Mass production of carbon nanotubes is necessary for applications in bulk structures used in aerospace, sports, and automotive industries.

Due to the factors mentioned above, carbon nanotube composites are only now emerging as replacements for traditional composites. However, there may be numerous other applications where the Nanocomposite could be of significant use. At present, many research and commercial organizations are undertaking active research in discovering the potential applications of nanotube/fiber reinforced composites that would use their unique mechanical, electrical conductivity, electromagnetic, and optoelectronic properties. The core and most sought after application will be the effective utilization of this new class of Nanocomposite in technology transfer devices. All these predictions of potential applications of Nanocomposite can pose a challenging task for researchers working in the field of nanotechnology. The Potential Applications of Nanocomposite Materials are shown in Figure 2.8.

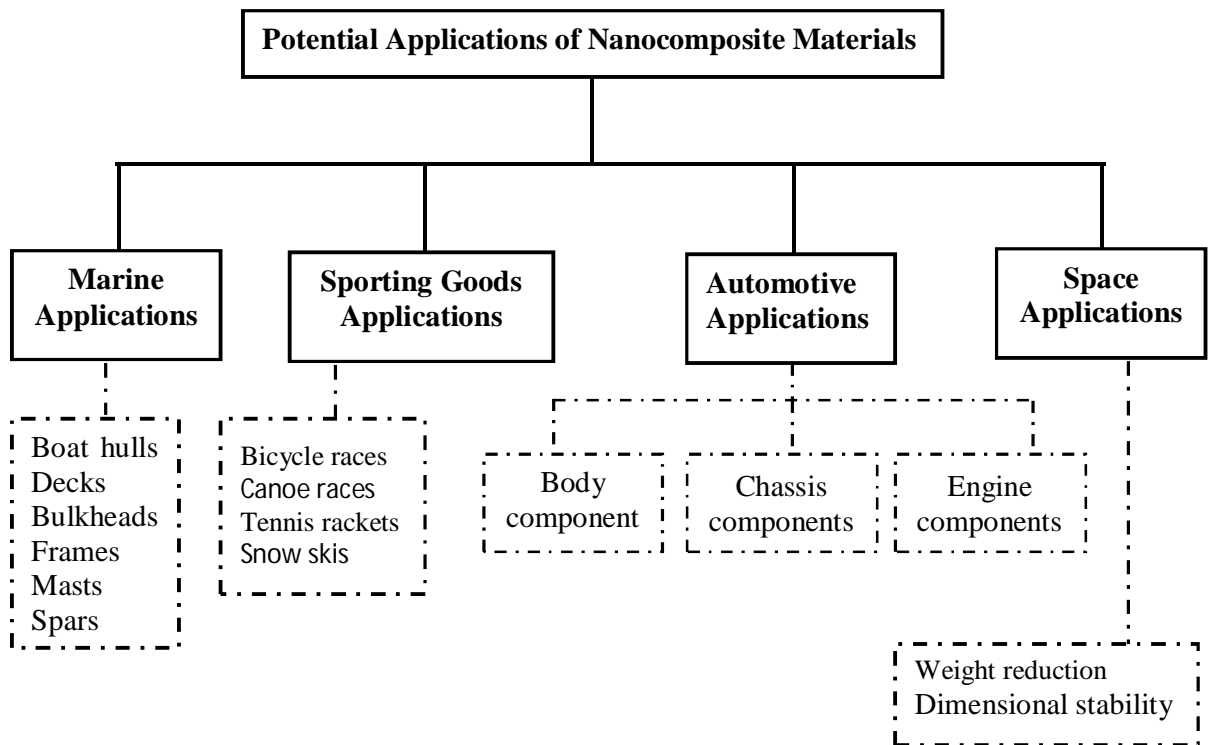


Figure 2.8: Potential Applications of Nanocomposite Materials

2.5 Mechanics of Materials

The mechanics of materials deals with stresses, strains, and deformations in engineering structures subjected to mechanical and thermal loads. A common assumption in the mechanics of conventional materials, such as steels and aluminum, is that they are homogenous and isotropic continua. For a homogenous material, properties do not depend on the location, and for an isotropic material, properties do not depend on the orientation. Unless severely cold worked, grains in metallic materials are randomly oriented so that, on a statistical basis, the assumption of isotropy can be justified. Fiber reinforced composites[70], on the other hand, are certainly one of the oldest and most widely used composite materials [71] and they are microscopically inhomogeneous and non-isotropic (orthotropic). As a result, the mechanics of fiber-reinforced composites are far more complex than that of conventional materials. Their study and development have been largely carried out due to their vast structural potential. Much information on the formulation for stiffness of conventional fiber reinforced composites can be found in many references[71-73]. Figure 2.9 illustrate Several models have been developed for the enhancement of strength and stiffness in fiber-reinforced composites.[23]

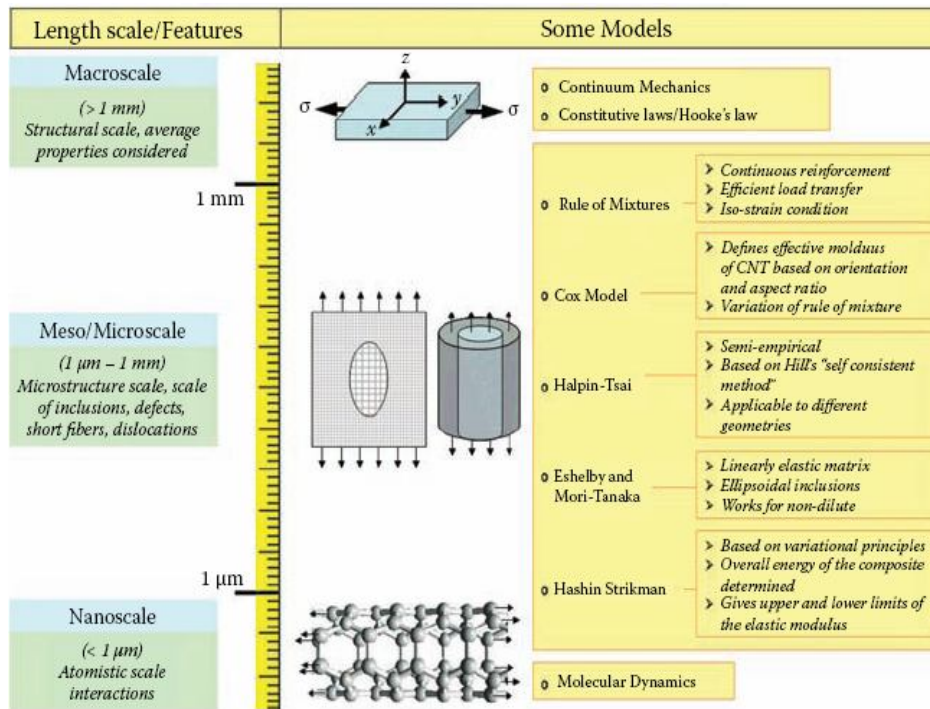


Figure 2.9: Models for describing elastic behavior of composites at different length scales [23]

2.5.1 Fiber Content, Density, and Void Content

The properties of composites are mainly determined by the relative proportions of the matrix and reinforcing materials. The relative proportions can be given as the weight fractions or the volume fractions. The weight fractions are usually obtained during fabrication or by one of the experimental methods after fabrication. However, in theoretical analysis of composite materials, the volume fractions are exclusively used. Thus expressions for conversion between the weight fractions and volume fractions are determined. These expressions are derived for a two-phase material and then generalized to a multiphase material.

Let V_c is the volume of a composite material that consists of V_f as a volume of the fibers and V_m as the volume of the matrix material. Let w_c , w_m and w_f represent weights of composite material, matrix and fibers respectively. Let the volume fraction and weight fraction be denoted by the capital letters V and W , respectively. The volume fractions and weight fractions are defined as follows:

$$V_c = V_m + V_f, \quad \text{then } V_f = \frac{V_f}{V_c}, \quad V_m = \frac{V_m}{V_c} \quad 2.7$$

$$W_c = W_m + W_f, \quad \text{then } W_f = \frac{W_f}{W_c}, \quad W_m = \frac{W_m}{W_c} \quad 2.8$$

The fiber weight fraction can be experimentally determined by either the ignition loss method (ASTM D2854-68) or the matrix digestion method (ASTM D3171-76). The ignition loss method is used for polymeric matrix composites containing fibers that do not lose weight at high temperatures, such as glass fibers. For unidirectional composites containing electrically conductive fibers (such as carbon) in a nonconductive matrix, the fiber volume fraction can be directly determined by comparing the electrical resistivity of the composite with that of fibers (ASTM D3355-74).

Since the fibers have circular cross-sections, there exists the ultimate fiber volume fraction, v_f^u which is less than unity and depends on the fiber arrangement. Ultimate arrays are presented in Figure 2.10, and the corresponding ultimate fiber volume fractions are:

$$\text{Square Array } v_f^u = \frac{1}{d^2} \left(\frac{\pi d^2}{4} \right) = \frac{\pi}{4} = 0.785 ,$$

$$\text{Hexagonal array } v_f^u = \frac{2}{d^2 \sqrt{3}} \left(\frac{\pi d^2}{4} \right) = \frac{\pi}{2\sqrt{3}} = 0.907 ,$$

$$\text{Layer-wise array } v_f^u = \frac{1}{d^2} \left(\frac{\pi d^2}{4} \right) = \frac{\pi}{4} = 0.785 ,$$

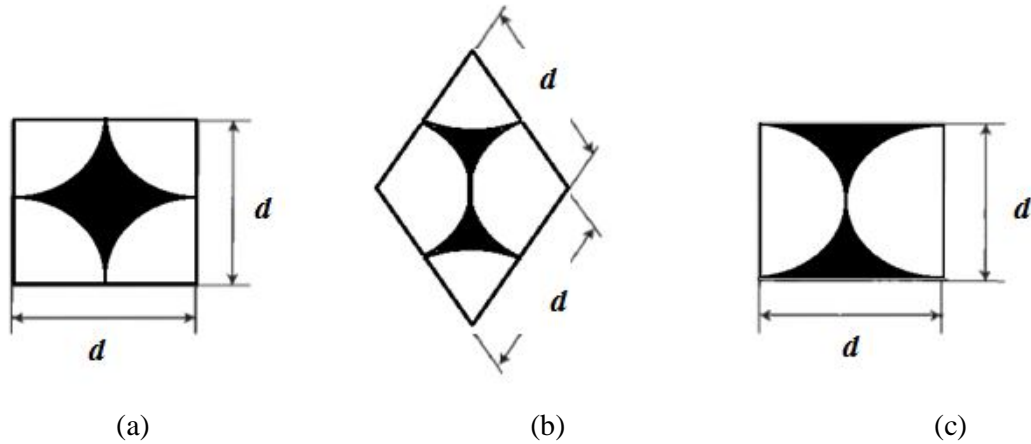


Figure 2.10: Ultimate fiber arrays for (a): square, (b) hexagonal, and (c) layer-wise fiber distributions.[74]

The density of composite material can be easily obtained in the terms of the densities of the fiber and matrix and their volume or weight.

$$\rho_c V_c = \rho_f V_f + \rho_m V_m \quad 2.9$$

By dividing both sides of the above equation with v_c and substituting the definition for the volume fraction from equation 2.7 yields

$$\rho_c = \rho_m V_m + \rho_f V_f \quad 2.10$$

The density of composite materials in terms of weight fractions can be obtained in

$$\rho_c = \frac{W_c}{W_m/\rho_m + W_f/\rho_f} \quad 2.11$$

Equations 2.10 and 2.11 have been derived for a composite material with only two constituents but can be generalized for an arbitrary number of constituents. The generalized equations are:

$$\rho_c = \sum_{i=1}^n \rho_i V_i$$
$$\rho_c = \frac{1}{\sum_{i=1}^n (W_i/\rho_i)} \quad 2.12$$

The composite density calculated theoretically from weight fractions may not always be in agreement with the experimentally determined density because of the presence of voids in the composite. The difference in densities indicates the void content.

2.5.2 Fiber-Matrix Interaction

Fiber–matrix interface determines how well the matrix transfers the load to the fibers. Chemical, mechanical, and reaction bonding may form the interface. In most cases, more than one type of bonding occurs.

Weak or cracked interfaces can cause failure in composites and reduce the properties influenced by the matrix. They also allow environmental hazards such as hot gases and moisture to attack the fibers.

Although a strong bond is a requirement in transferring loads from the matrix to the fiber, weak debonding of the fiber–matrix interface is used advantageously in ceramic matrix composites. Weak interfaces blunt matrix cracks and deflect them along the interface. This is the main source of improving toughness of such composites up to five times that of the monolithic ceramics.[75]

2.5.3 Unidirectional composite

A typical unidirectional composite is shown schematically in Fig 2.11. A unidirectional composite consists of parallel fibers embedded in a matrix. Several unidirectional layers can be stacked in a specified sequence of orientation to fabricate a laminate that will meet design strength and stiffness requirements. Each layer of a unidirectional composite may be referred to as simply a layer, ply, or lamina. The direction parallel to the fibers is generally called the longitudinal direction (axis 1). The

direction perpendicular to the fibers is called the transverse direction (any direction in the 2-3 plane). These axes are also referred to as the material axes of the ply.

Ply with short-diameter fibers have several fibers through the actually ply thickness. The fibers are randomly distributed throughout the cross section and may be in contact with each other in some locations. This type of fiber distribution in the lamina is typical of several fiber-matrix systems. Because of the structure of the composite, a unidirectional composite shows different properties in the longitudinal and transverse directions. Thus, the unidirectional composites are orthotropic with the axes 1, 2, and 3 as the axes of symmetry. A unidirectional composite has the strongest properties in the longitudinal direction. Because of the random fiber distribution in the cross section, material behavior in the other two directions (2, 3) is nearly identical. Therefore, a unidirectional composite or ply can be considered to be transversely isotropic; that is, it is isotropic in the 2-3 plane.

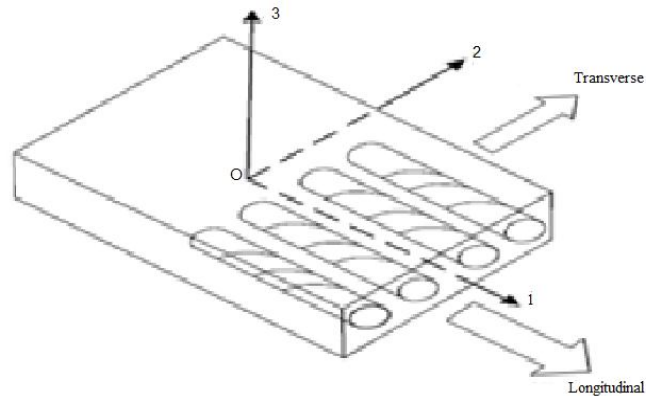


Figure 2.11: Schematic representation of unidirectional composite [74]

2.6 Mechanical Behavior of Composite Materials

Micromechanics is defined, the study of composite behavior where the interaction of constituent material is examined in detail and used to predict and define the heterogeneous composite material behavior. Some of the intrinsic characteristics of the materials are revealed in their response to simple mechanical loading, e.g., uniaxial normal stress and pure shear stress, as illustrated in Figure 2.12.[72]

2.6.1 Determination of Elastic Properties for Continuous Fiber Composites

A continuous fiber is geometrically characterized as having a very high length-to-diameter ratio. They are generally stronger and stiffer than bulk material. Fiber diameters generally range between 3-200 μm . depending upon the fiber [76].

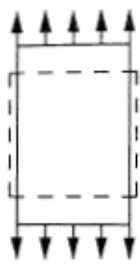
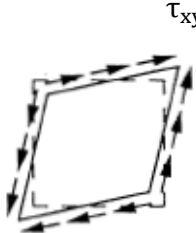
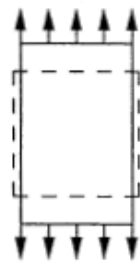
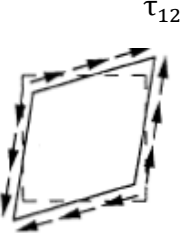
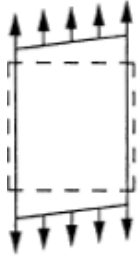

	Normal stress		Shear stress	
Isotropic	σ_x 	$\epsilon_x = \frac{\sigma_x}{E}$ $\epsilon_y = \frac{-\nu\sigma_x}{E}$	τ_{xy} 	$\gamma_{xy} = \frac{\tau_{xy}}{G}$ $\gamma_{xy} = \frac{2\tau_{xy}(1-\nu)}{E}$
Orthotropic Loaded along principal material directions	σ_1 	$\epsilon_1 = \frac{\sigma_1}{E_1}$ $\epsilon_2 = \frac{-\nu_{12}\sigma_1}{E_1}$	τ_{12} 	$\gamma_{12} = \frac{\tau_{12}}{G_{12}}$
Anisotropic or orthotropic material loaded along non principal directions	σ_x 	$\epsilon_x = \frac{\sigma_x}{E_x}$ $\epsilon_y = \frac{-\nu_{xy}\sigma_x}{E_x}$ $\gamma_{xy} = \eta_{xs} \frac{\sigma_x}{E_x}$	τ_{xy} 	$\gamma_{xy} = \frac{\tau_{xy}}{G_{xy}}$ $\epsilon_x = \eta_{sx} \frac{\tau_{xy}}{G_{xy}}$ $\epsilon_y = \eta_{sy} \frac{\tau_{xy}}{G_{xy}}$

Figure 2.12: Response of various types of materials under uniaxial normal and pure shear loading [72]

The basic assumptions dealing with fiber- matrix interactions in a unidirectional lamina are as follows:[70]

1. Fibers are uniformly distributed throughout the matrix
2. Perfect bonding exists between fibers and matrix.
3. The matrix is free of voids.
4. Applied loads are either parallel to or normal to the fiber direction.
5. The lamina is initially in a stress- free state (i.e., no residual stresses are present).
6. Both fibers and matrix behave as linearly elastic materials.

2.6.1.1 Determination of Longitudinal Modulus (E_L)

The properties of a composite material depend on the properties of its constituent materials (fiber and matrix) and their distribution, physical and chemical interactions. The properties of composites can be determined through simple and direct experimental measurements. However, experimental measurements set determine the properties of a fixed fiber-matrix system produced by a single fabrication process. Additional measurements are required when there is a change in the system variables such as the relative volumes of the constituents, constituent properties, and fabrication process. Experiments may become time consuming and cost prohibitive. Theoretical and semi empirical methods of determining composite properties can be used to predict the effects of a large number of system variables. All of these methods may not be reliable for component design purposes. They might present difficulty in selecting a representative but tractable mathematical model for some properties such as the transverse properties of unidirectional composites. However, the mathematical model for studying the longitudinal properties of a unidirectional composite is quite accurate. Properties related to loading in the fiber direction are dominated by the fibers that are usually stronger and stiffer.

Consider a unidirectional composite with uniform properties of fiber and matrix. The fibers are assumed to be parallel throughout the composite as shown in Figure 2.13. The elastic modulus or stiffness of composite material is determined in terms of the properties of fibers and matrix and in terms of the relative volumes of fiber and matrix [75]:

$$C_{ij} = C_{ij}(E_f, V_f, \nu_f, E_m, V_m, \nu_m) \quad 2.13$$

Where:

E_f and E_m : Young's modulus for fiber and matrix respectively.

V_f and V_m : Fiber and matrix volume fractions respectively.

ν_f and ν_m : Poison's ratio for fiber and matrix respectively.

It may be further assumed that a perfect bonding exists between the fibers and the matrix so that no slippage can occur at the interface. [74, 75, 77]

As a result, the strains experienced by the fiber, matrix, and the composite are equal

$$\epsilon_c = \epsilon_f = \epsilon_m \quad 2.14$$

Where ϵ_c , ϵ_f and ϵ_m are the longitudinal strains in composite, fibers, and matrix respectively.

Since both fibers and matrix are elastic, the respective longitudinal stresses can be calculated as

$$\sigma_f = E_f \varepsilon_f = E_f \varepsilon_c \quad 2.15$$

$$\sigma_m = E_m \varepsilon_m = E_m \varepsilon_c \quad 2.16$$

Comparing Equation 2.15 with Equation 2.16 and noting that $E_f > E_m$, we conclude that the fiber stress σ_f is always greater than the matrix stress σ_m . The tensile force P_c applied on the composite lamina is shared by the fibers and the matrix so that:

$$P_c = P_f + P_m \quad 2.17$$

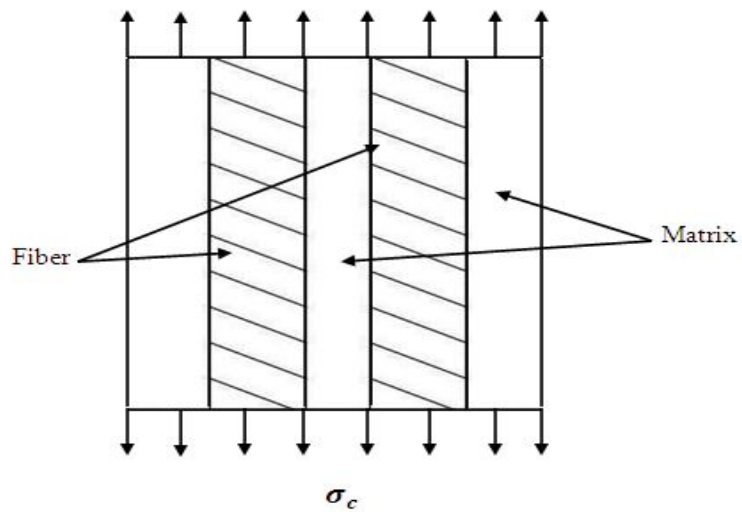


Figure 2.13: Representative Volume Element Loaded along the fiber direction

The loads P_c , P_f , and P_m carried by the composite, the fibers, and the matrix, respectively, may be written as follows in terms of stresses σ_c , σ_f , and σ_m experienced by them and their corresponding cross-sectional areas A_c , A_f , and A_m . Thus

$$\sigma_c A_c = \sigma_f A_f + \sigma_m A_m \quad 2.18$$

Or
$$\sigma_c = \sigma_f \frac{A_f}{A_c} + \sigma_m \frac{A_m}{A_c} \quad 2.19$$

Where,

σ_c = average tensile stress in the composite

A_f = net cross-sectional area for the fibers

A_m = net cross-sectional area for the matrix

$$A_c = A_f + A_m$$

But for composites with parallel fibers, the volume fractions are equal to the area fractions such that:

$$V_f = \frac{A_f}{A_c}, V_m = \frac{A_m}{A_c} \quad 2.20$$

Thus

$$\sigma_c = \sigma_f V_f + \sigma_m V_m \quad 2.21$$

The longitudinal modulus for the composite can be written as:

$$E_L = E_f V_f + E_m V_m = E_f V_f + E_m (1 - V_f) = E_m + V_f (E_f - E_m) \quad 2.22$$

Equation 2.22 [66] is called the rule of mixtures. This equation shows that the longitudinal modulus of a unidirectional continuous fiber composite is intermediate between the fiber modulus and the matrix modulus; it increases linearly with increasing fiber volume fraction; and since $E_f > E_m$, it is influenced more by the fiber modulus than the matrix modulus.[70]

Equation 2.21 can be differentiated with respect to strain, which is the same for the composite, the fibers, and the matrix. The differentiation yields

$$\frac{d\sigma_c}{d\varepsilon} = \frac{d\sigma_f}{d\varepsilon} V_f + \frac{d\sigma_m}{d\varepsilon} V_m \quad 2.23$$

Where $\frac{d\sigma}{d\varepsilon}$ represents the slope of the corresponding stress-strain diagrams at the given strain. If the stress-strain curves of the materials are linear, the slopes, $\frac{d\sigma}{d\varepsilon}$, are constants and can be replaced by the corresponding elastic modulus in Equation 2.23 to give:

$$E_L = E_f V_f + E_m V_m \quad 2.24$$

Thus equations 2.21 and 2.24 indicate that the contributions of the fibers and matrix to the average composite properties are proportional to their volume fractions. Such a relationship is called rule of mixtures. Equations 2.21 and 2.24 can be generalized as:

$$\sigma_c = \sum_{i=1}^n \sigma_i V_i \quad 2.25$$

$$E_L = \sum_{i=1}^n E_i V_i \quad 2.26$$

2.6.1.2 Determination of Transverse Modulus (E_T)

In the case of transverse normal loading, the state of stress in the matrix surrounding the fibers is complex and more affected by interaction from neighboring fibers [72]. The transverse modulus is a matrix-dominated property and it is sensitive to the local state of stress.

To determine the transverse modulus, fibers are assumed to be uniform in properties, diameter, continuous and parallel throughout the composite. The composite is stressed in the direction perpendicular to the parallel fibers that is the transverse direction. The model for predicting the transverse properties of a unidirectional composite may be considered to be made up of layers representing fibers and matrix material as shown in Figure 2.14.

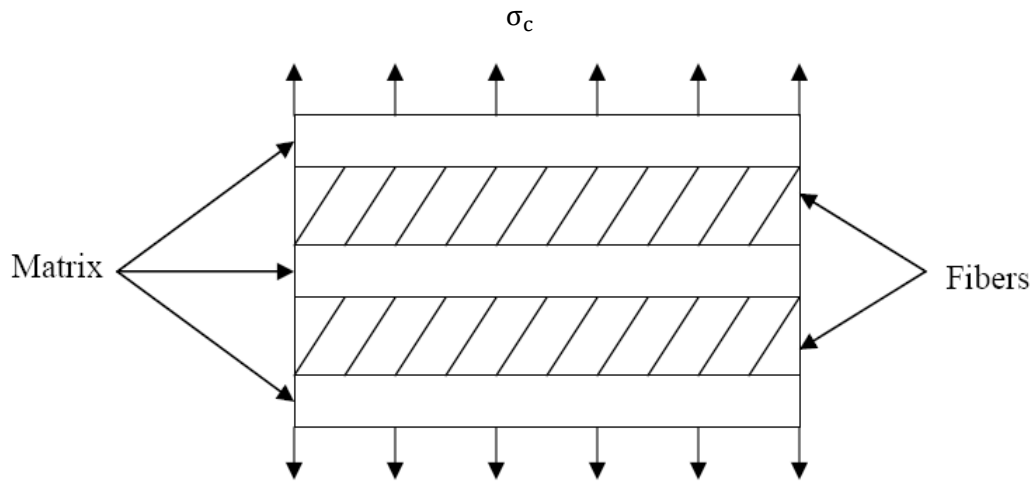


Figure 2.14: Representative volume element loaded perpendicular to fiber

Each layer of fiber and matrix is perpendicular to the direction of loading and has the same area on which the load acts. Hence each layer will carry the same load and experience equal stress, that is

$$\sigma_f = \sigma_m = \sigma_c \quad 2.27$$

The thickness of each layer is assumed to be same so that the cumulative thickness of fiber layers and matrix layers will be proportional to their respective volume fractions. In this case the sum of elongation of constituent materials that is fiber (δ_f) and matrix (δ_m) is equal to the composite elongation (δ_c) in the direction of the load,

$$\delta_c = \delta_f + \delta_m \quad 2.28$$

The elongation in the material can be written as the product of the strain and its cumulative thickness,

$$\begin{aligned}
\delta_c &= \varepsilon_c t_c \\
\delta_f &= \varepsilon_f t_f \\
\delta_m &= \varepsilon_m t_m
\end{aligned}
\tag{2.29}$$

Substituting Equation 2.29 in Equation 2.28 gives

$$\varepsilon_c t_c = \varepsilon_f t_f + \varepsilon_m t_m \tag{2.30}$$

Dividing both sides of Equation 2.30 by t_c and substituting volume fraction for thickness yields

$$\begin{aligned}
\varepsilon_c &= \varepsilon_f \frac{t_f}{t_c} + \varepsilon_m \frac{t_m}{t_c} \\
\varepsilon_c &= \varepsilon_f V_f + \varepsilon_m V_m
\end{aligned}
\tag{2.31}$$

If the fibers and the matrix are now assumed to deform elastically, the strain can be written in terms of the corresponding stress and the elastic modulus as follows:

$$\frac{\sigma_c}{E_c} = \frac{\sigma_f}{E_f} V_f + \frac{\sigma_m}{E_m} V_m \tag{2.32}$$

In view of Equation 2.28, Equation 2.32 can be simplified as:

$$\frac{1}{E_c} = \frac{V_f}{E_f} + \frac{V_m}{E_m} \tag{2.33}$$

The transverse modulus of a composite with n number of materials may be obtained by generalizing Equation 2.33

$$E_T = \frac{1}{\sum_{i=1}^n (V_i/E_i)} \tag{2.34}$$

In a real composite, the parallel fibers are dispersed randomly in the matrix material. Generally both the fibers and matrix are present at any section perpendicular to the load, especially at higher fiber volume fractions. Thus the load is shared between the fibers and the matrix, and the assumption that the stresses in the fiber and matrix are equal is inaccurate. The assumption of equal stresses also results in a mismatch of strains in the loading direction at the fiber-matrix interface. Another inaccuracy arises due to the mismatch of Poisson ratios of the fibers and the matrix, which induces stresses in the fibers and matrix perpendicular to the load with no net resultant force on the composite in that direction. For design purposes, it is often desirable to have simple and computationally fast procedures for estimating the properties of composite even though the estimates are only approximate.[77-79]

2.6.1.3 Determination of Shear Modulus (G)

The behavior of unidirectional composites under in-plane (longitudinal) shear loading is also dominated by the matrix properties and the local stress distributions [70]. As shown in Figure 2.17 a unidirectional composite is subjected to shear loading. Assuming that the shearing stresses on the fiber and matrix are the same, it can be estimated that :{[70]

$$\tau_c = \tau_m = \tau_f \quad 2.35$$

$$\gamma_m = \frac{\tau}{G_m} , \gamma_f = \frac{\tau}{G_f} \quad 2.36$$

Where, γ_m and γ_f are the shear strain in the matrix and fiber respectively

The nonlinear shear stress-strain behavior typical of fiber-reinforced composite is ignored (i.e. the behavior is regarded as linear). On a macroscopic scale, the deformations are shown in Figure 2.15. The total shearing deformation is defined in Equation 2.28

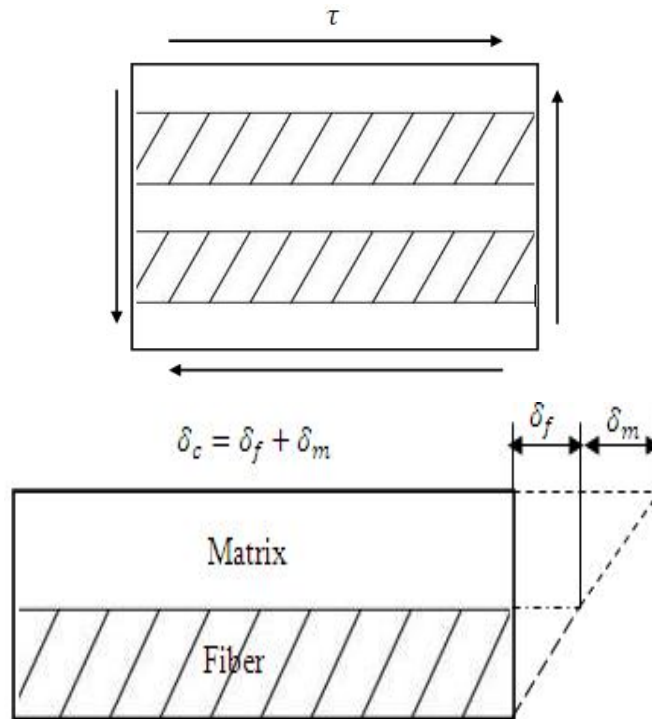


Figure 2.15: Shear loading and deformation of a Representative Volume Element

Recognizing that the shear deformation in each material can be written as the product of corresponding shear strain (γ) and the cumulative thickness of the material:[70]

$$\delta_c = \gamma_c t_c$$

$$\delta_f = \gamma_f t_f \quad 2.37$$

$$\delta_m = \gamma_m t_m$$

$$\gamma_c = \gamma_f V_f + \gamma_m V_m \quad 2.38$$

Recognizing that for the linear behavior of shear stress-shear strain of fibers and matrix, the shear strains in Equation 2.38 can be replaced by the ratios of shear stress and appropriate shear modulus yields: [70]

$$\frac{\tau_c}{G} = \frac{\tau_f}{G_f} V_f + \frac{\tau_m}{G_m} V_m \quad 2.39$$

Where, G is the in-plane shear modulus of the composite, G_f and G_m are the shear modulus of the fibers and matrix, respectively.

In view of Equation 2.35, Equation 2.39 can be simplified as: [70]

$$\frac{1}{G} = \frac{V_f}{G_f} + \frac{V_m}{G_m} \quad 2.40$$

$$G = \frac{G_f G_m}{G_m V_f + G_f V_m} \quad 2.41$$

2.6.1.4 Determination of Major Poisson's Ratio ϑ

A Poisson's ratio can be defined as the ratio of the lateral (transverse) strain to the longitudinal (axial) strain. When a unidirectional composite is loaded longitudinally, two Poisson ratios are defined, major Poisson ratio and minor Poisson ratio. Major Poisson ratio (ϑ_L) relates longitudinal stress to the transverse strain and minor Poisson ratio (ϑ_T) relates the transverse stress to the longitudinal strain.

The major Poisson ratio can be predicted using transverse modulus, (E_T), by applying a load parallel to the fibers, that is, parallel to the layers in the model. Figure 2.16 shows the deformation pattern for cumulative thickness of layers.

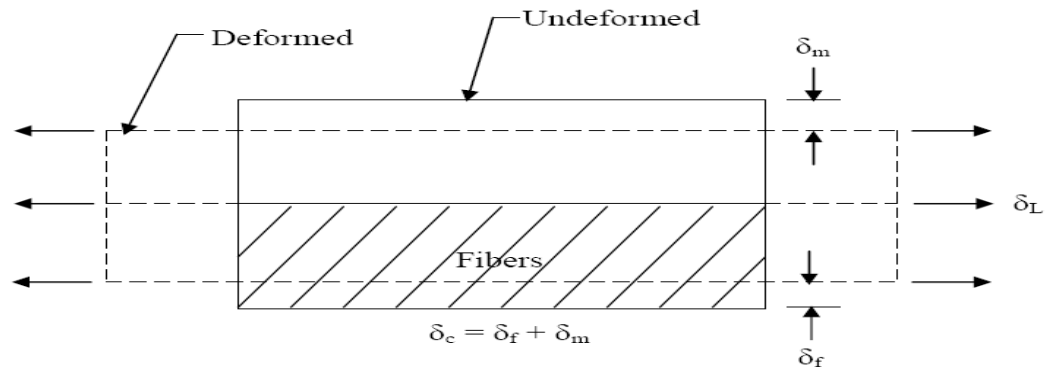


Figure 2.16: Shear deformation of a Representative Volume Element

Transverse deformations can be written as product of strain and cumulative thickness:

$$\begin{aligned}\delta_c &= t_c(\varepsilon_T)_c \\ \delta_f &= t_f(\varepsilon_T)_f \\ \delta_m &= t_m(\varepsilon_T)_m\end{aligned}\tag{2.42}$$

Substituting in Equation 2.42 transverse strains in the fibers, matrix and composite as the product of longitudinal strains and Poisson ratios yields: [70]

$$\begin{aligned}\delta_c &= -t_c\vartheta_c(\varepsilon_L)_c \\ \delta_f &= -t_f\vartheta_f(\varepsilon_L)_f \\ \delta_m &= -t_m\vartheta_m(\varepsilon_L)_m\end{aligned}\tag{2.43}$$

Where ϑ_c , ϑ_f and ϑ_m are the Poisson's ratios of the composite, fiber and matrix respectively.

The deformation of the composite is the sum of the deformations of the fibers and the matrix as defined in Equation 2.28. Therefore, from Equation 2.43 and 2.28: [70]

$$-t_c\vartheta_c(\varepsilon_L)_c = -t_f\vartheta_f(\varepsilon_L)_f - t_m\vartheta_m(\varepsilon_L)_m\tag{2.44}$$

Since the longitudinal strains due to longitudinal stress in fiber, matrix and composite are equal, Equation 2.44 becomes

$$t_c\vartheta_c = t_f\vartheta_f + t_m\vartheta_m\tag{2.45}$$

Dividing both sides of Equation 2.45 by t_c and substituting volume fraction for thickness yields

$$\vartheta_c = V_f\vartheta_f + V_m\vartheta_m\tag{2.46}$$

Equation 2.46 represents Major Poisson ratio of a unidirectional composite.

Minor Poisson ratio is obtained from the following relation

$$\frac{\vartheta_L}{E_L} = \frac{\vartheta_T}{E_T}\tag{2.47}$$

2.6.2 Determination of Elastic Properties for Short Fiber Composites

Tensile load applied to a discontinuous fiber lamina is transferred to the fibers by a shearing mechanism between fibers and matrix. Since the matrix has a lower modulus, the longitudinal strain in the matrix is higher than that in adjacent fibers. If a

perfect bond is assumed between the two constituents, the difference in longitudinal strains creates a shear stress distribution across the fiber–matrix interface. Ignoring the stress transfer at the fiber end cross sections and the interaction between the neighboring fibers, we can calculate the normal stress distribution in a discontinuous fiber by a simple force equilibrium analysis as shown in Figure 2.17

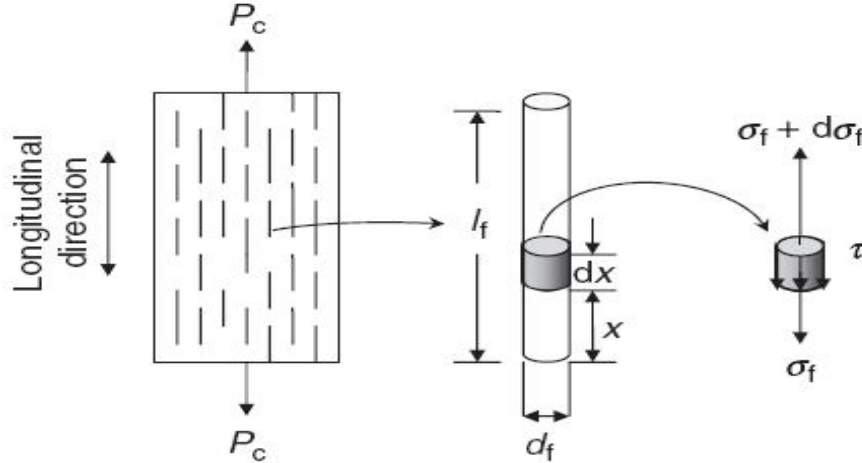


Figure 2.17: Longitudinal tensile loading of a unidirectional discontinuous fiber lamina.

From Figure 2.17, the force equilibrium equation for this length is: [70]

$$\left(\frac{\pi}{4}d_f^2\right)(\sigma_f + d\sigma_f) - \left(\frac{\pi}{4}d_f^2\right)\sigma_f - (\pi d_f dx)\tau = 0, \quad 2.48$$

This gives,

$$\frac{d\sigma_f}{dx} = \frac{4\tau}{d_f} \quad 2.49$$

Where,

σ_f = longitudinal stress in the fiber at a distance x from one of its ends

τ = shear stress at the fiber–matrix interface

d_f = fiber diameter

2.6.2.1 Moduli of Short-Fiber Composites

The modulus of short fiber composites can be predicted using the stress distribution obtained through finite-element methods[80, 81]. The results are in the form of curves for specific properties of constituent materials. Whenever the properties change, a new set of results have to be obtained. Thus the results have limited adaptability to design procedures. For design purposes, it is usually desirable to have

simple and rapid computational procedures for estimating composite properties even though the predictions are only approximate.

Halpin-Tsai [23] has developed simple and generalized semi-empirical equations to approximate the longitudinal and transverse moduli of aligned short-fiber composites. The Halpin-Tsai equations for longitudinal and transverse moduli can be written as:[80]

$$E_L = \frac{1+2\eta_L V_f}{1-\eta_L V_f} E_m \quad 2.50$$

And

$$E_T = \frac{1+2\eta_T V_f}{1-\eta_T V_f} E_m \quad 2.51$$

Halpin-Tsai [23] relationship for shear modulus is:

$$G_{12} = \frac{1+\eta_G V_f}{1+\eta_G V_m} * G_m \quad 2.52$$

Where,

$$\eta_L = \frac{(E_f/E_m)-1}{(E_f/E_m)+2(l/d)} \quad 2.53$$

$$\eta_T = \frac{(E_f/E_m)-1}{(E_f/E_m)+2} \quad , \quad 2.54$$

and

$$\eta_G = \frac{(G_f/G_m)-1}{(G_f/G_m)+1} \quad 2.55$$

It may be noted here that Halpin-Tsai empirical relations for predicting transverse modulus of unidirectional composites and longitudinal and transverse modulus of short fiber composites are all particular cases of a general equation. [70]

Randomly oriented short-fiber composites are produced to obtain composites that are essentially isotropic in a plane. The following empirical equations are often used to predict the elastic modulus and shear modulus of composites containing fibers that are randomly oriented [70] in a plane:

$$E_{\text{Random}} = \frac{3}{8} E_L + \frac{5}{8} E_T \quad 2.56$$

$$G_{\text{Random}} = \frac{1}{8} E_L + \frac{1}{4} E_T \quad 2.57$$

where E_L and E_T are respectively the longitudinal and transverse moduli of an aligned short fiber composite having the same fiber aspect ratio and volume fraction as the composite under consideration. Moduli E_L and E_T can be determined using Equations 2.51 and 2.52. [70]

2.6.3 Characteristics of a Fiber-Reinforced Lamina

One layer of a laminated composite material is generally referred to as a ply or lamina. It consists of single layer of reinforcement, unidirectional or multidirectional. It is too thin to be used for engineering applications. Several laminae are bonded together to form a structure called laminate. The properties and orientation of the lamina in a laminate are chosen to meet the laminate design requirements.

2.6.3.1 Coordinate Axes

Consider a thin lamina in which fibers are positioned parallel to each other in a matrix, as shown in Figure 2.18. To describe its elastic properties, the two right-handed coordinate systems are defined firstly, namely, the $1 - 2 - z$ system and the $x - y - z$ system. Both $1 - 2$ and $x - y$ axes are in the plane of the lamina, and the z axis is normal to this plane. In the $1 - 2 - z$ system, axis 1 is along the fiber length and represents the longitudinal direction of the lamina, and axis 2 is normal to the fiber length and represents the transverse direction of the lamina. Together they constitute the principal material directions in the plane of the lamina. In the xyz system, x and y axes represent the loading directions. [70, 71]

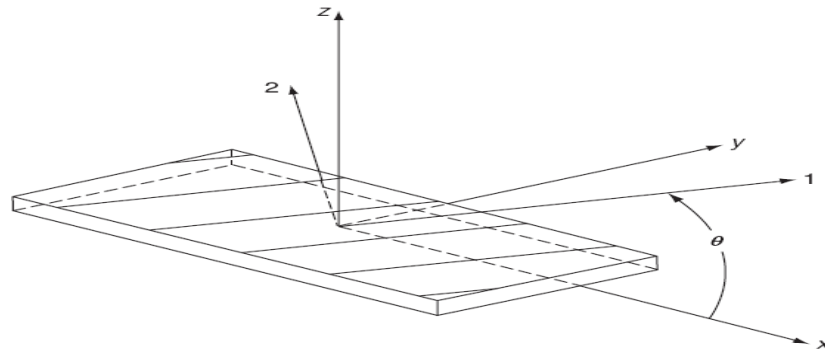


Figure 2.18: Definition of principal material axes and loading axes for a lamina

The angle between the positive x axis and the 1 -axis is called the fiber orientation angle and is represented by θ . The sign of this angle depends on the right-handed coordinate system selected.

2.6.3.2 Isotropic, Anisotropic, and Orthotropic Materials

The material properties of isotropic are the same in all directions. Thus, the material contains an infinite number of planes of material property symmetry passing through a point. In an anisotropic material, properties are different in all directions so that the material contains no planes of material property symmetry. Fiber-reinforced

composites, in general, contain three orthogonal planes of material property symmetry, namely, the 1–2, 2–3, and 1–3 plane, and are classified as orthotropic materials. The intersections of these three planes of symmetry, namely, axes 1, 2, and 3, are called the principal material directions[70]. The difference in material properties in isotropic, orthotropic, and anisotropic materials are also reflected in the mechanics and design of these types of materials, these differences are demonstrated schematically in Figure 2.19.

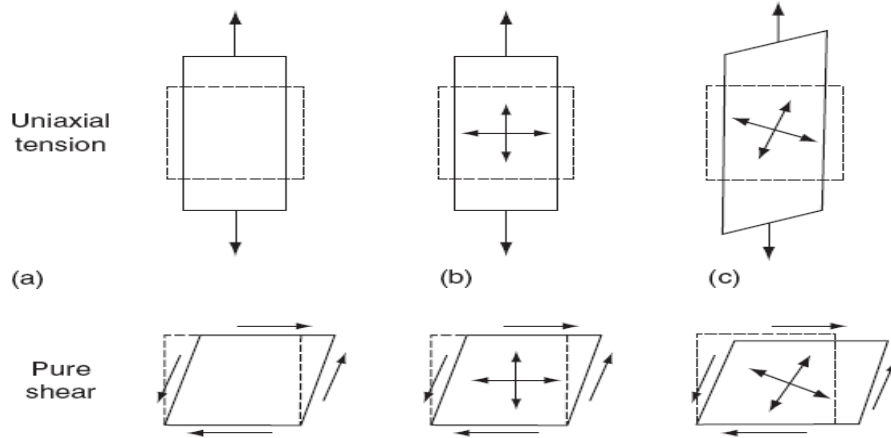


Figure 2.19: Differences in the deformations of isotropic, specially orthotropic and anisotropic materials subjected to uniaxial tension ((a) Isotropic, (b) Special orthotropic and (c) General orthotropic and anisotropic) and pure shear stresses

2.6.3.3 Stress and Strain Transformations in a Thin Lamina under Plane Stress

In stress analysis of a thin lamina with fiber orientation angle θ , it is often desirable to transform stresses in the xy directions to stresses in the 1-2 directions. The stress transformation equations are [70]:

$$\begin{cases} \sigma_{11} = \sigma_{xx}\cos^2\theta + \sigma_{yy}\sin^2\theta + 2\tau_{xy}\cos\theta\sin\theta \\ \sigma_{22} = \sigma_{xx}\sin^2\theta + \sigma_{yy}\cos^2\theta + 2\tau_{xy}\cos\theta\sin\theta \\ \tau_{12} = (-\sigma_{xx} + \sigma_{yy})\sin\theta\cos\theta + \tau_{xy}(\cos^2\theta - \sin^2\theta) \end{cases} \quad 2.58$$

where σ_{xx} , σ_{yy} , and τ_{xy} are applied stresses in the xy directions and σ_{11} , σ_{22} , and τ_{12} are transformed stresses in the 1 – 2 directions. Similar equations can also be written for strain transformation by replacing each σ with ϵ and each τ with $\gamma/2$ in Equation 2.58 [70]. Thus, the strain transformation equations [70] are:

$$\begin{cases} \epsilon_{11} = \epsilon_{xx}\cos^2\theta + \epsilon_{yy}\sin^2\theta + \gamma_{xy}\cos\theta\sin\theta \\ \epsilon_{22} = \epsilon_{xx}\sin^2\theta + \epsilon_{yy}\cos^2\theta + \gamma_{xy}\cos\theta\sin\theta \\ \gamma_{12} = 2(-\epsilon_{xx} + \epsilon_{yy})\sin\theta\cos\theta + \gamma_{xy}(\cos^2\theta - \sin^2\theta) \end{cases} \quad 2.59$$

2.6.4 Determination of Elastic Properties for a Lamina

2.6.4.1 Unidirectional Continuous Fiber 0° Lamina

Elastic properties of a unidirectional continuous fiber 0° lamina, are calculated from the following equations:

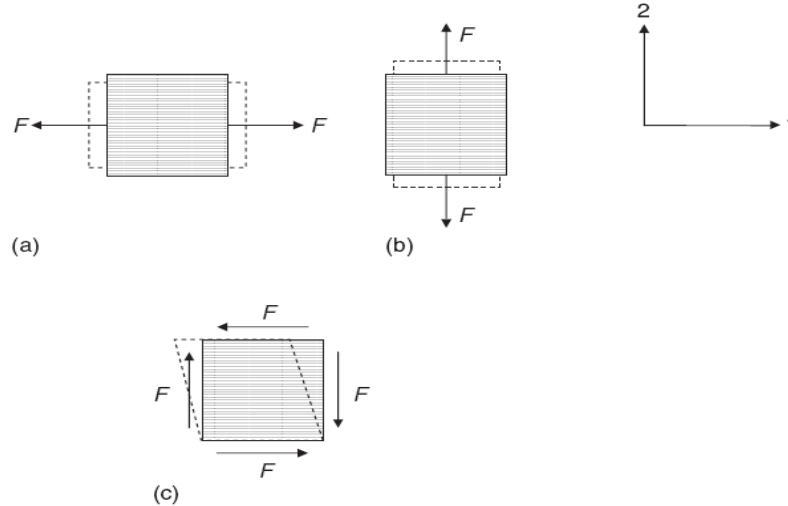


Figure 2.20: Applications of (a) longitudinal tensile stress, (b) transverse tensile stress, and (c) in-plane shear stress on a unidirectional continuous fiber 0° lamina [70]

1. Referring to Figure 2.20a in which the tensile stress is applied in the 1-direction,

Longitudinal modulus [70]:

$$E_{11} = E_f V_f + E_m V_m \quad 2.60$$

And Major Poisson's ratio:

$$\vartheta_{12} = V_f \vartheta_f + V_m \vartheta_m \quad 2.61$$

$$\text{Where } \vartheta_{12} = - \frac{\text{Strain in the 2-direction}}{\text{Strain in the 1-direction}}$$

2. Referring to Figure 2.20b in which the tensile stress is applied in the 2-direction

Transverse modulus [70]:

$$E_{22} = \frac{E_f E_m}{E_f V_m + E_m V_f} \quad 2.62$$

And Minor Poisson's ratio:

$$\nu_{21} = \frac{E_{22}}{E_{11}} \nu_{12} \quad 2.63$$

$$\text{Where } \nu_{21} = - \frac{\text{Strain in the 1-direction}}{\text{Strain in the 2-direction}}$$

3. Referring to Figure 2.20c in which the shear stress is applied in 1-2 plane [70]

In-plane shear modulus: [70]

$$G_{12} = G_{21} = \frac{G_f G_m}{G_f \nu_m + G_m \nu_f} \quad 2.64$$

The following points should be noted from the above equations and Figure 2.20: [70]

1. The longitudinal modulus (E_{11}) is always greater than the transverse modulus (E_{22}) because the longitudinal modulus (E_{11}) is associated with loading in the fiber direction are dominated by the fibers that are usually stronger, stiffer, and have a lower ultimate strain while ,the transverse modulus (E_{22}) is a matrix-dominated property and sensitive to the local state of stress
2. The major Poisson's ratio (ν_{12}) is always greater than the minor Poisson's ratio (ν_{21}). Since these Poisson's ratios are related to Equation 2.63, only one of them can be considered independent.
3. As for E_{22} , the matrix contributes more to the development of G_{12} than the fibers because the deformation response of the element to normal stresses is clearly matrix dominated. The fiber cannot play a dominant role in the deformation process because they are not directly loaded.
4. Four independent elastic constants, namely, E_{11} , E_{22} , ν_{12} , and G_{12} , are required to describe the in-plane elastic behavior of a lamina. The ratio E_{11}/E_{22} is often considered a measure of orthotropy.

Equations 2.60 through 2.64 are derived using the simple mechanics of materials approach along with the following assumptions:[70]

1. Both fiber s and matrix are linearly elastic isotropic materials.
2. Fibers are uniformly distributed in the matrix.
3. Fibers are perfectly aligned in the 1-direction.
4. There is perfect bonding between fibers and matrix.
5. The composite lamina is free of voids.

2.6.4.2 Unidirectional Continuous Fiber Angle- Ply Lamina

The following equations [70, 75, and 78] are used to calculate the elastic properties of an angle-ply lamina in which continuous fibers are aligned at an angle θ with the positive x direction.

$$\frac{1}{E_{xx}} = \frac{\cos^4\theta}{E_{11}} + \frac{\sin^4\theta}{E_{22}} + \frac{1}{4} \left(\frac{1}{G_{12}} - \frac{2\nu_{12}}{E_{11}} \right) \sin^2 2\theta \quad 2.65$$

$$\frac{1}{E_{yy}} = \frac{\sin^4\theta}{E_{11}} + \frac{\cos^4\theta}{E_{22}} + \frac{1}{4} \left(\frac{1}{G_{12}} - \frac{2\nu_{12}}{E_{11}} \right) \sin^2 2\theta \quad 2.66$$

$$\frac{1}{G_{xy}} = \frac{1}{E_{11}} + \frac{2\nu_{12}}{E_{11}} + \frac{1}{E_{22}} - \left(\frac{1}{E_{11}} + \frac{2\nu_{12}}{E_{11}} + \frac{1}{E_{22}} - \frac{1}{G_{12}} \right) \cos^2 2\theta \quad 2.67$$

$$\vartheta_{xy} = E_{xx} \left[\frac{2\vartheta_{12}}{E_{11}} - \frac{1}{4} \left(\frac{1}{E_{11}} + \frac{2\vartheta_{12}}{E_{11}} + \frac{1}{E_{22}} - \frac{1}{G_{12}} \right) \sin^2 2\theta \right] \quad 2.68$$

$$\vartheta_{yx} = \frac{E_{yy}}{E_{xx}} \vartheta_{xy} \quad 2.69$$

Where E_{11} , E_{22} , ϑ_{12} , and G_{12} , are calculated using Equations 2.60 through 2.64.[70]

2.6.5 Compliance and Stiffness Matrices

Fiber composites are among the class of materials called orthotropic materials, whose behavior lies between that of isotropic and that of anisotropic materials.

Generally, the state of stress at a point is described by the nine components of the stress tensor, σ_{ij} , as shown in Figure 2.21. Correspondingly, there is a strain tensor, ϵ_{ij} , with nine components.[12]

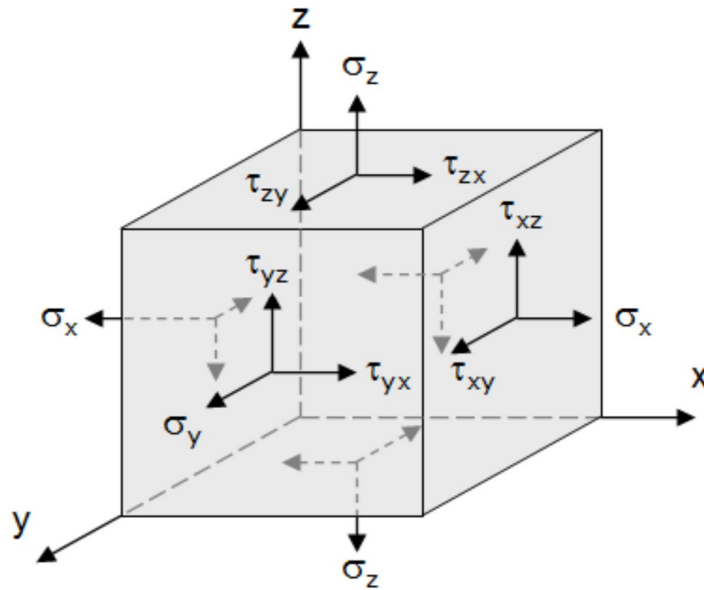


Figure 2.21: The six components to describe the state of stress at a point.

For a linear isotropic material in a three-dimensional stress state, the Hooke's law stress-strain relationships at a point in an x - y - z orthogonal system in matrix form are:

$$\begin{Bmatrix} \varepsilon_x \\ \varepsilon_y \\ \varepsilon_z \\ \gamma_{yz} \\ \gamma_{zx} \\ \gamma_{xy} \end{Bmatrix} = \begin{bmatrix} \frac{1}{E} & -\frac{\vartheta}{E} & -\frac{\vartheta}{E} & 0 & 0 & 0 \\ -\frac{\vartheta}{E} & \frac{1}{E} & -\frac{\vartheta}{E} & 0 & 0 & 0 \\ -\frac{\vartheta}{E} & -\frac{\vartheta}{E} & \frac{1}{E} & 0 & 0 & 0 \\ 0 & 0 & 0 & \frac{1}{G} & 0 & 0 \\ 0 & 0 & 0 & 0 & \frac{1}{G} & 0 \\ 0 & 0 & 0 & 0 & 0 & \frac{1}{G} \end{bmatrix} \begin{Bmatrix} \sigma_x \\ \sigma_y \\ \sigma_z \\ \tau_{yz} \\ \tau_{zx} \\ \tau_{xy} \end{Bmatrix} = [S] \begin{Bmatrix} \sigma_x \\ \sigma_y \\ \sigma_z \\ \tau_{yz} \\ \tau_{zx} \\ \tau_{xy} \end{Bmatrix} \quad 2.70$$

$$\begin{Bmatrix} \sigma_x \\ \sigma_y \\ \sigma_z \\ \tau_{yz} \\ \tau_{zx} \\ \tau_{xy} \end{Bmatrix} = \begin{bmatrix} \frac{E(1-\vartheta)}{(1-2\vartheta)(1+\vartheta)} & \frac{\vartheta E}{(1-2\vartheta)(1+\vartheta)} & \frac{\vartheta E}{(1-2\vartheta)(1+\vartheta)} & 0 & 0 & 0 \\ \frac{\vartheta E}{(1-2\vartheta)(1+\vartheta)} & \frac{E(1-\vartheta)}{(1-2\vartheta)(1+\vartheta)} & \frac{\vartheta E}{(1-2\vartheta)(1+\vartheta)} & 0 & 0 & 0 \\ \frac{\vartheta E}{(1-2\vartheta)(1+\vartheta)} & \frac{\vartheta E}{(1-2\vartheta)(1+\vartheta)} & \frac{E(1-\vartheta)}{(1-2\vartheta)(1+\vartheta)} & 0 & 0 & 0 \\ 0 & 0 & 0 & G & 0 & 0 \\ 0 & 0 & 0 & 0 & G & 0 \\ 0 & 0 & 0 & 0 & 0 & G \end{bmatrix} \begin{Bmatrix} \varepsilon_x \\ \varepsilon_y \\ \varepsilon_z \\ \gamma_{yz} \\ \gamma_{zx} \\ \gamma_{xy} \end{Bmatrix} = [Q] \begin{Bmatrix} \varepsilon_x \\ \varepsilon_y \\ \varepsilon_z \\ \gamma_{yz} \\ \gamma_{zx} \\ \gamma_{xy} \end{Bmatrix}$$

2.71

Where, ϑ is the Poisson's ratio. The shear modulus G is a function of two elastic constants, E and ϑ , as [70]

$$G = \frac{E}{2(1-\vartheta)} \quad 2.72$$

And

$$[Q] = [S^{-1}]$$

where $[S]$ represents the compliance matrix relating strains to known stresses. The inverse of the compliance matrix is called the stiffness matrix $[Q]$, which is used in relating stresses to known strains. [82, 83]

2.6.5.1 Specially Orthotropic Lamina ($\theta = 0^\circ$ or $\theta = 90^\circ$)

For a thin orthotropic lamina in plane stress ($\sigma_{zz} = \tau_{xz} = \tau_{yz} = 0$) as shown in Figure 2.22, the strain-stress relations in the elastic range are:

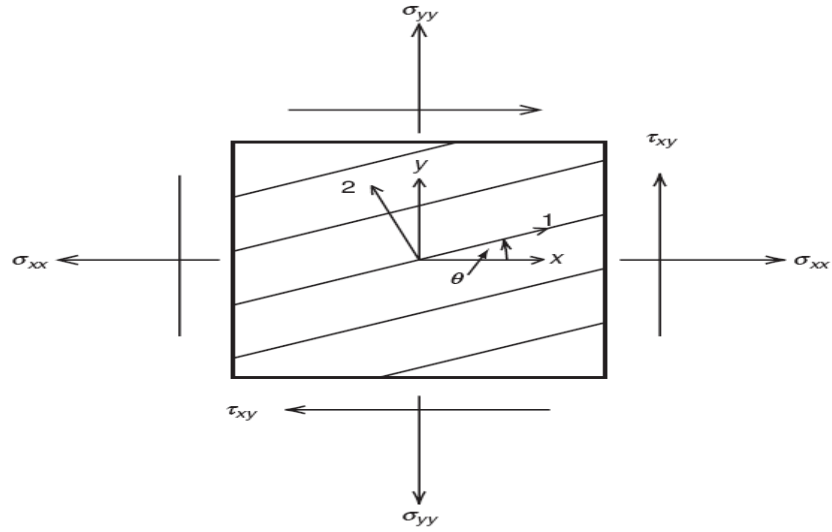


Figure 2.22: Stresses in a general orthotropic lamina under a plane stress condition

$$\begin{aligned}
 \varepsilon_{xx} &= \frac{\sigma_{xx}}{E_{xx}} - \vartheta_{yx} \frac{\sigma_{yy}}{E_{yy}} - m_x \tau_{xy}, \\
 \varepsilon_{yy} &= -\vartheta_{xy} \frac{\sigma_{xx}}{E_{xx}} + \frac{\sigma_{yy}}{E_{yy}} - m_y \tau_{xy}, \\
 \gamma_{xy} &= -m_x \sigma_{xx} - m_y \sigma_{yy} + \frac{\tau_{xy}}{G_{xy}}
 \end{aligned} \tag{2.73}$$

Where E_{xx} , E_{yy} , G_{xy} , ϑ_{xy} and ϑ_{yx} are elastic constants for the lamina obtained from Equations 2.75 through 2.79 and m_x and m_y are given by the following equations:

$$m_x = (\sin 2\theta) \left[\frac{\vartheta_{12}}{E_{11}} + \frac{1}{E_{22}} - \frac{1}{2G_{12}} - \cos^2 \theta \left(\frac{1}{E_{11}} + \frac{2\vartheta_{12}}{E_{11}} + \frac{1}{E_{22}} - \frac{1}{G_{12}} \right) \right] \tag{2.74}$$

$$m_y = (\sin 2\theta) \left[\frac{\vartheta_{12}}{E_{11}} + \frac{1}{E_{22}} - \frac{1}{2G_{12}} - \sin^2 \theta \left(\frac{1}{E_{11}} + \frac{2\vartheta_{12}}{E_{11}} + \frac{1}{E_{22}} - \frac{1}{G_{12}} \right) \right] \tag{2.75}$$

The new elastic constants m_x and m_y represent the influence of shear stresses on extensional strains and the influence of normal stresses on shear strain. These constants are called coefficients of mutual influence. [70-72, 75, and 78]

For $\theta = 0^\circ$ and 90° , both m_x and m_y are zero, and therefore, for these fiber orientations, there is no extension-shear coupling. Such a lamina, in which the principal material axes (1 and 2 axes) coincide with the loading axes (x and y axes), is called specially orthotropic. For a specially orthotropic lamina, the strain-stress relations are

$$\begin{aligned}
\varepsilon_{xx} = \varepsilon_{11} &= \frac{\sigma_{xx}}{E_{11}} - \mathfrak{g}_{21} \frac{\sigma_{yy}}{E_{22}}, \\
\varepsilon_{yy} = \varepsilon_{22} &= -\mathfrak{g}_{12} \frac{\sigma_{xx}}{E_{11}} + \frac{\sigma_{yy}}{E_{22}}, \\
\gamma_{xy} = \gamma_{yx} = \gamma_{12} = \gamma_{21} &= \frac{\tau_{xy}}{G_{12}}
\end{aligned} \tag{2.76}$$

From Hook's law, strain-stress relation for linear elastically orthotropic material, such as unidirectional fiber reinforced composite loaded parallel or perpendicular to the fiber can be written as: [70-72, 75, and 78]

$$\begin{bmatrix} \varepsilon_{xx} \\ \varepsilon_{yy} \\ \gamma_{xy} \end{bmatrix} = \begin{bmatrix} S_{11} & S_{12} & 0 \\ S_{21} & S_{22} & 0 \\ 0 & 0 & S_{66} \end{bmatrix} \begin{bmatrix} \sigma_{xx} \\ \sigma_{yy} \\ \tau_{xy} \end{bmatrix} = [S] \begin{bmatrix} \sigma_{xx} \\ \sigma_{yy} \\ \tau_{xy} \end{bmatrix} \tag{2.77}$$

where,

$$S_{11} = \frac{1}{E_{11}}, \quad S_{22} = \frac{1}{E_{22}}, \quad S_{66} = \frac{1}{G_{12}}, \quad S_{12} = S_{21} = -\frac{\mathfrak{g}_{12}}{E_{11}} = -\frac{\mathfrak{g}_{21}}{E_{22}} \tag{2.78}$$

The [S] matrix is the compliance matrix for the especially orthotropic lamina. Inverting Equation 2.87, we can write the stress-strain relations for an especially orthotropic lamina as: [70-72, 75, and 78]

$$\begin{bmatrix} \sigma_{xx} \\ \sigma_{yy} \\ \tau_{xy} \end{bmatrix} = \begin{bmatrix} Q_{11} & Q_{12} & 0 \\ Q_{21} & Q_{22} & 0 \\ 0 & 0 & Q_{66} \end{bmatrix} \begin{bmatrix} \varepsilon_{xx} \\ \varepsilon_{yy} \\ \gamma_{xy} \end{bmatrix} = [Q] \begin{bmatrix} \varepsilon_{xx} \\ \varepsilon_{yy} \\ \gamma_{xy} \end{bmatrix} \tag{2.79}$$

where [Q] represents the stiffness matrix for the specially orthotropic lamina. Various elements in the [Q] matrix are: [70-72, 75, and 78]

$$\begin{aligned}
Q_{11} &= \frac{E_{11}}{1 - \mathfrak{g}_{12}\mathfrak{g}_{21}}, & Q_{12} = Q_{21} &= \frac{\mathfrak{g}_{12}E_{22}}{1 - \mathfrak{g}_{12}\mathfrak{g}_{21}}, \\
Q_{22} &= \frac{E_{22}}{1 - \mathfrak{g}_{12}\mathfrak{g}_{21}}, & Q_{66} &= G_{12}
\end{aligned} \tag{2.80}$$

2.6.5.2 General Orthotropic Lamina ($\theta \neq 0^\circ$ or $\theta \neq 90^\circ$)

The transformation Equation for expressing strain in an (X-Y) coordinate system in terms of stress in a (1-2) coordinate systems: [70-72, 75, and 78]

$$\begin{bmatrix} \sigma_{xx} \\ \sigma_{yy} \\ \tau_{xy} \end{bmatrix} = \begin{bmatrix} \cos^2 \theta & \sin^2 \theta & -2 \sin \theta \cos \theta \\ \sin^2 \theta & \cos^2 \theta & 2 \sin \theta \cos \theta \\ 2 \sin \theta \cos \theta & -2 \sin \theta \cos \theta & \cos^2 \theta - \sin^2 \theta \end{bmatrix} \begin{bmatrix} \sigma_{11} \\ \sigma_{22} \\ \tau_{12} \end{bmatrix} \quad 2.81$$

Where, θ is the angle from the x-axis to the 1-axis as shown in Figure 2.23

Similarly, the strain transformation equations are: [70-72, 75, and 78]

$$\begin{bmatrix} \varepsilon_x \\ \varepsilon_y \\ \frac{\gamma_{xy}}{2} \end{bmatrix} = \begin{bmatrix} \cos^2 \theta & \sin^2 \theta & -2 \sin \theta \cos \theta \\ \sin^2 \theta & \cos^2 \theta & 2 \sin \theta \cos \theta \\ 2 \sin \theta \cos \theta & -2 \sin \theta \cos \theta & \cos^2 \theta - \sin^2 \theta \end{bmatrix} \begin{bmatrix} \varepsilon_1 \\ \varepsilon_2 \\ \frac{\gamma_{12}}{2} \end{bmatrix} \quad 2.82$$

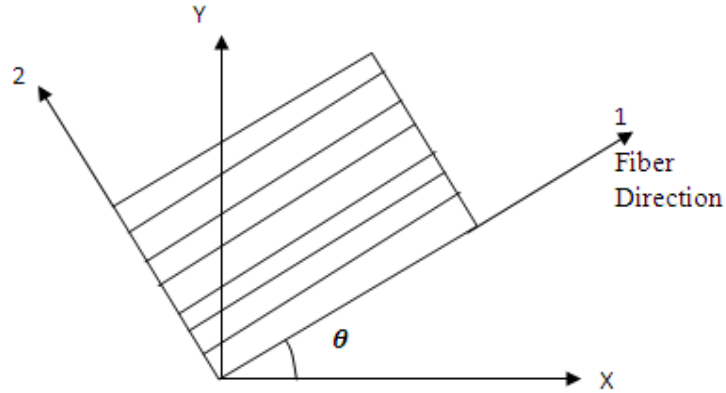


Figure 2.23: Positive Rotation of Principal Material Axis from XY Axis

The stress-strain relations for a general orthotropic lamina, Equations 2.76 can be expressed in matrix form as: [70-72, 75, and 78]

$$\begin{bmatrix} \varepsilon_{xx} \\ \varepsilon_{yy} \\ \gamma_{xy} \end{bmatrix} = \begin{bmatrix} \overline{S}_{11} & \overline{S}_{12} & \overline{S}_{16} \\ \overline{S}_{21} & \overline{S}_{22} & \overline{S}_{26} \\ \overline{S}_{16} & \overline{S}_{26} & \overline{S}_{66} \end{bmatrix} \begin{bmatrix} \sigma_{xx} \\ \sigma_{yy} \\ \tau_{xy} \end{bmatrix} = [\overline{S}] \begin{bmatrix} \sigma_{xx} \\ \sigma_{yy} \\ \tau_{xy} \end{bmatrix} \quad 2.83$$

where $[\overline{S}]$ represents the compliance matrix for the lamina. Various elements in the $[\overline{S}]$ matrix are expressed in terms of the elements in the $[S]$ matrix for a specially orthotropic lamina. These expressions are: [70-72, 75, and 78]

$$\begin{aligned}
\bar{S}_{11} &= \frac{1}{E_{xx}} = S_{11} \cos^4 \theta + 2(S_{12} + S_{66}) \sin^2 \theta \cos^2 \theta + S_{22} \sin^4 \theta \\
\bar{S}_{12} &= -\frac{g_{xy}}{E_{xx}} = S_{12} (\sin^4 \theta + \cos^4 \theta) + (S_{11} + S_{22} - S_{66}) \sin^2 \theta \cos^2 \theta \\
\bar{S}_{22} &= \frac{1}{E_{yy}} = S_{11} \sin^4 \theta + 2(S_{12} + S_{66}) \sin^2 \theta \cos^2 \theta + S_{22} \cos^4 \theta \\
\bar{S}_{16} &= -m_x = (2S_{11} + 2S_{12} - S_{66}) \sin \theta \cos^3 \theta - (2S_{22} + 2S_{12} - S_{66}) \sin^3 \theta \cos \theta \\
\bar{S}_{26} &= -m_y = (2S_{11} + 2S_{12} - S_{66}) \sin^3 \theta \cos \theta - (2S_{22} + 2S_{12} - S_{66}) \sin \theta \cos^3 \theta \\
\bar{S}_{66} &= \frac{1}{G_{12}} = 2(2S_{11} + 2S_{22} - 4S_{12} - S_{66}) \sin^2 \theta \cos^2 \theta + S_{66} (\sin^4 \theta + \cos^4 \theta)
\end{aligned} \tag{2.84}$$

Inverting Equation 2.83, the stress-strain relations for a general orthotropic lamina can be written as [75, 84, 85]

$$\begin{bmatrix} \sigma_x \\ \sigma_y \\ \tau_{xy} \end{bmatrix} = \begin{bmatrix} \bar{Q}_{11} & \bar{Q}_{12} & \bar{Q}_{16} \\ \bar{Q}_{12} & \bar{Q}_{22} & \bar{Q}_{26} \\ \bar{Q}_{16} & \bar{Q}_{26} & \bar{Q}_{66} \end{bmatrix} \begin{bmatrix} \varepsilon_x \\ \varepsilon_y \\ \gamma_{xy} \end{bmatrix} = [\bar{Q}_{ij}] \cdot \begin{bmatrix} \varepsilon_x \\ \varepsilon_y \\ \gamma_{xy} \end{bmatrix} \tag{2.85}$$

where $[\bar{Q}]$ represents the stiffness matrix for the lamina. Various elements in the $[\bar{Q}]$ matrix are expressed in terms of the elements in the $[Q]$ matrix as: [70-72, 75, 84-85]

$$\begin{aligned}
\bar{Q}_{11} &= Q_{11} m^4 + Q_{22} n^4 + (2Q_{12} + 4Q_{66}) n^2 m^2, \\
\bar{Q}_{12} &= Q_{12} (m^4 + n^4) + Q_{11} + Q_{22} - 4Q_{66} n^2 m^2, \\
\bar{Q}_{22} &= Q_{11} n^4 + Q_{22} m^4 + (2Q_{12} + 4Q_{66}) n^2 m^2, \\
\bar{Q}_{16} &= (Q_{11} - Q_{12} - 2Q_{66}) n m^3 - (Q_{22} - Q_{12} - 2Q_{66}) m n^3, \\
\bar{Q}_{26} &= (Q_{11} - Q_{12} - 2Q_{66}) n^3 m - (Q_{22} - Q_{12} - 2Q_{66}) m^3 n, \\
\bar{Q}_{66} &= (Q_{11} + Q_{22} - 2Q_{12} - 2Q_{66}) n^2 m^2 + Q_{66} (n^4 + m^4)
\end{aligned} \tag{2.86}$$

Where, $m = \cos \theta$ and $n = \sin \theta$ and θ is the angle from the x-direction to 1-direction (fiber direction) and the bar over the Q denotes that we are dealing with the transformed reduced stiffness instead of the reduced stiffness. [70-72, 75, and 78]

The reduced stiffness given in relation 2.86 are relatively complicated functions of the four primary material characteristics $E_{11}; E_{22}; \tau_{12}; G_{12}$; as well as of the angle of rotation θ . [70-72, 75, and 78]

2.7 Thermal Properties of Carbon Nanotubes Based Composites

The behavior of any material when subjected to a change in temperature (heat) is termed as the *thermal property of the material*. When heat is applied, it is absorbed and transported within the material; as a result structural changes begin, and temperature increases. Continuous heat input may even result in melting. Some thermal properties used to quantify this behavior of materials under temperature are thermal conductivity, heat capacity and thermal expansion coefficient.

The amount of heat energy required to increase the temperature of material to a certain value is different for different materials, which depends on the several factors like atomic structure, thermal vibration propagation within the material and the like. This quantity which denotes the amount of heat that needs to be supplied to increase the temperature of the material by 1°C is called the heat capacity (C) of the material.

Thermal conductivity is the ability of the material to transfer heat from a region of high temperature to a region of low temperature. This quantity is best described by the expression,

$$q = -k \frac{dT}{dx} \quad 2.87$$

where, q denotes the heat flux per unit time per unit area (taken normal to direction of heat flow) k is the thermal conductivity, and $\frac{dT}{dx}$ is the temperature gradient through the material. Equation 2.87 is the steady state (q is not a function of time) heat conduction equation. Heat conduction in solids takes place in two ways, one is lattice vibration waves (phonons) and the other is by free electrons.

The exact value of the thermal conductivity is disagreed upon but there is considerable agreement in the dependence of thermal conductivity on several factors like temperature, large phonon modes, current and vacancy concentration. the thermal conductivity found to be linearly dependent on temperature in the ranges below and above the room temperature, however with different slopes.[86]

The problem of heat transfer in composites filled with fibers has been extensively studied for decades. The main parameters affecting the thermal properties of composites are the volume fraction, aspect ratio, alignment of the fibers, and the adhesion between the fibers and the matrix, and the thermal property of the interface. Theoretical estimates show that an increase in the aspect ratio of highly conducting fibers would dramatically increase the thermal conductivity of the composite. [86]

2.7.1 Factors affecting thermal conductivity of composite materials

Thermal conductivity of composites is anisotropic in nature. Before conducting experiments to determine thermal conductivity of various composites, knowledge about effect of different parameters influencing thermal conductivity is essential. These factors are fiber which is the reinforcing face of a composite material, matrix material are formed from three types; metal, ceramic, and polymer matrixes. Another factor is the fillers. The primary advantage of using filler material in composites is to reduce the overall cost of the composite. However, Additive materials are primarily used to modify and tailor material properties of the composite. Additives help in increasing the performance or a specific property as well it increases the overall cost of the product.

2.7.2 Equivalent Continuum Model and Effective Solid Fiber

In developing a continuum model, the Nanotube geometry can be directly incorporated into the mathematical model. An individual nanotube (SWNT) can be visualized as a sheet of graphene being rolled up endlessly to form a hollow tube. A hollow cylinder having the same length and diameter as that of the nanotube is considered to represent an equivalent continuum model of the nanotube[88]. The thickness of the cylinder wall is the same as that of nanotube (0.34nm) and considered it to be made up of a homogeneous and isotropic material that has the same physical properties as that of the nanotube. The heat carrying capacity of this hollow cylinder is applied to its entire cross section and the properties of an effective solid fiber are defined [89].

Effective fiber can be defined as a solid fiber that has the same length and diameter as that of the hollow cylinder and has an identical temperature gradient across its length when the same amount of heat is flowing through it. This effective fiber thus retains the geometrical properties of the nanotube while providing us with a continuum model of the nanotube structure that is suitable for mathematical analysis[87, 89].

Figure 2.24 show the development of a continuum model for a carbon nanotube.

The expression for the conductivity of the effective solid fiber in the longitudinal direction can be derived from the following equations:

$$\left(\frac{q_1}{k_{11}}\right)_{cm} = \left(\frac{q_1}{k_{11}}\right)_{eff} \quad 2.88$$

Where, the subscripts ‘cm’ and ‘eff’ refer to the nanotube “continuum model” and “effective fiber”, respectively, and the “effective fibers” are assumed to be aligned in the x_1 direction, so that we consider the gradient in this direction.

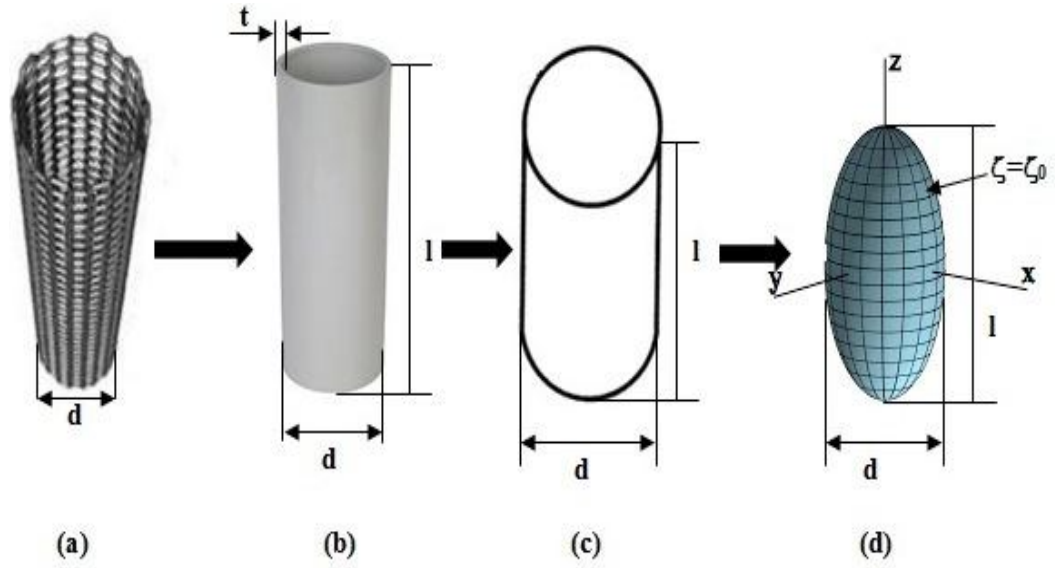


Figure 2.24: Development of a continuum model for a SWNT. a) Schematic diagram of a carbon nanotube; b) Equivalent continuum model; c) Effective solid fiber; and d) a prolate spheroidal inclusion. [89]

By using the definition of heat flux,

$$(q_1)_{cm} = \frac{Q}{A_{cm}} = \frac{Q}{\pi(d_o^2 - d_i^2)/4}, \quad 2.89$$

$$(q_1)_{eff} = \frac{Q}{A_{eff}} = \frac{Q}{\pi d^2/4} \quad 2.90$$

The effective thermal conductivity of the effective fiber will be:

$$k^{(2)} = \frac{(d_o^2 - d_i^2)}{d_o^2} k_{CNT} \quad 2.91$$

Where,

d_o is the outer diameter,

d_i is the inner diameter, and

k_{CNT} is the thermal conductivity of carbon nanotube

For simplicity, the thermal conductivity of the effective fiber assumed to be isotropic in nature. The expression for the thermal conductivity of carbon nanotube reinforced composites and has contact resistance at the interface is:

$$k_{eff}^* = k^{(1)} [1 + V_f (1 + \lambda B_1) f(\zeta_0)] \quad 2.92$$

Where V_f is the volume fraction of the carbon nanotubes phase and $f(\zeta_0)$ and λ are defined as: [87]

$$f(\zeta_0) = \left[\frac{1}{2} \zeta_0 (\zeta_0^2 - 1) \ln \left(\frac{\zeta_0 + 1}{\zeta_0 - 1} \right) - \zeta_0^2 \right]^{-1} \quad 2.93$$

Where, ζ_0 denotes the inverse of the eccentricity of the ellipsoid: [87]

$$\zeta_0 = \left(1 - \frac{a_1^2}{a_3^2} \right)^{-\frac{1}{2}} = \left(1 - \frac{d^2}{l^2} \right)^{-\frac{1}{2}} \quad 2.94$$

And,

$$\lambda = \frac{k^{(2)}}{k^{(1)}} \quad 2.95$$

The constant B_1 is obtained as a solution to the following infinite set of linear simultaneous equations: [87]

$$\delta(n) + B_{2n+1} \left[1 - (1 - \lambda)(\zeta_0^2 - 1) P_{2n+1}(\zeta_0) Q_{2n+1}(\zeta_0) \right] = \left(\frac{\lambda}{\bar{\beta}} \right) \sum_{m=0}^{\infty} B_{2m+1} X_{nm}(\zeta_0) \quad 2.96$$

Where $X_{nm}(\zeta_0)$ are defined by [87]

$$X_{nm}(\zeta_0) = \left(\frac{4n+3}{2} \right) (\zeta_0^2 - 1) \dot{Q}_{2n+1}(\zeta_0) \dot{P}_{2m+1}(\zeta_0) \int_{-1}^1 \left(\frac{\zeta_0^2 - 1}{\zeta_0^2 - \mu^2} \right)^{\frac{1}{2}} P_{2n+1}(\mu) P_{2m+1}(\mu) d\mu, \quad 2.97$$

$$\bar{\beta} = \frac{\beta c}{k^{(1)}}$$

Where, β - Interfacial conductance. [87]

$$c = (a_3^2 - a_1^2)^{\frac{1}{2}} = \left(\left(\frac{l}{2} \right)^2 - \left(\frac{d}{2} \right)^2 \right)^{\frac{1}{2}} \quad 2.98$$

P_n, Q_n Are known as Legendre polynomials of first kind and second kind respectively. and

$$P_n = \frac{1}{2^n n!} \frac{d^n}{dz^n} (z^2 - 1)^n, \quad 2.99$$

$$Q_n = \frac{1}{2} P_n(z) \ln \frac{z+1}{z-1} - W_{n-1}, \quad 2.100$$

Where,

$$W_{n-1}(z) = \frac{1}{2} P_0(z) P_{n-1}(z) + \frac{1}{n-1} P_1(z) P_{n-2}(z) + \dots + P_{n-1}(z) P_0(z), \quad 2.101$$

$\delta(n)$ is defined as [87]: $\delta(n) = \begin{cases} 0 & \text{if } n = 0 \\ 1 & \text{otherwise} \end{cases}$

2.8 Modeling of Carbon Nanotubes

Recently, modeling and characterization of Nanocomposite using computational approaches has become a challenging research topic for many researchers. They have been developing various tools to carry out this analysis. In order to estimate the outstanding effective properties of Nanocomposite at the nanoscale, molecular dynamics (MD) simulations, continuum mechanics, finite element method (FEM), constitutive modeling techniques [90] are some of the popular techniques used in the research community. The Quantum mechanical and Nano mechanical modeling tools assume the presence of a discrete molecular structure of matter. Micromechanical and Structural Mechanics assume the presence of a continuous material structure.

The word 'model' usually refers to a set of mathematical equations, but its central idea is to assemble a simplified imitation of the real world while preserving the essential features [91]. In other words, a model must 1) be simple enough to solve and 2) correctly capture the features of interest. The advents of affordable and powerful computers in the last 30 years lead to the development of an array of computational models. These models utilize computers to solve equations numerically, thus providing non-analytic solutions which could not be obtained otherwise. Increasing speed and memory of computers and the decreasing scale of interest of materials systems, simulations can now explore the behavior of realistically sized models in reasonable time. As a result, a new range of processes and phenomena are open to study. Also the paradigms of materials theory is changing due to the central role of numerical calculations in today's modeling – the requirement for a model to be simple is often replaced by the requirement for computational efficiency [92].

Figure 2.25 shows the relationship of specific modeling techniques in Computational Mechanics and Computational Chemistry. The continuum-based methods are classified as micromechanics and structural mechanics. The former is further sub-divided into analytical micromechanics which include Mori-Tanaka, Eshelby approach, Halpin-Tsai approach and computational micromechanics which include Finite Element Method (FEM), the Boundary Element Method (BEM). [93]

Numerous experimental studies and simulations have been performed to study the properties of carbon nanotube reinforced composites. It has been estimated that carbon nanotubes have Young's modulus in the range of Tera Pascal (TPa) [95], coupled with high stiffness.

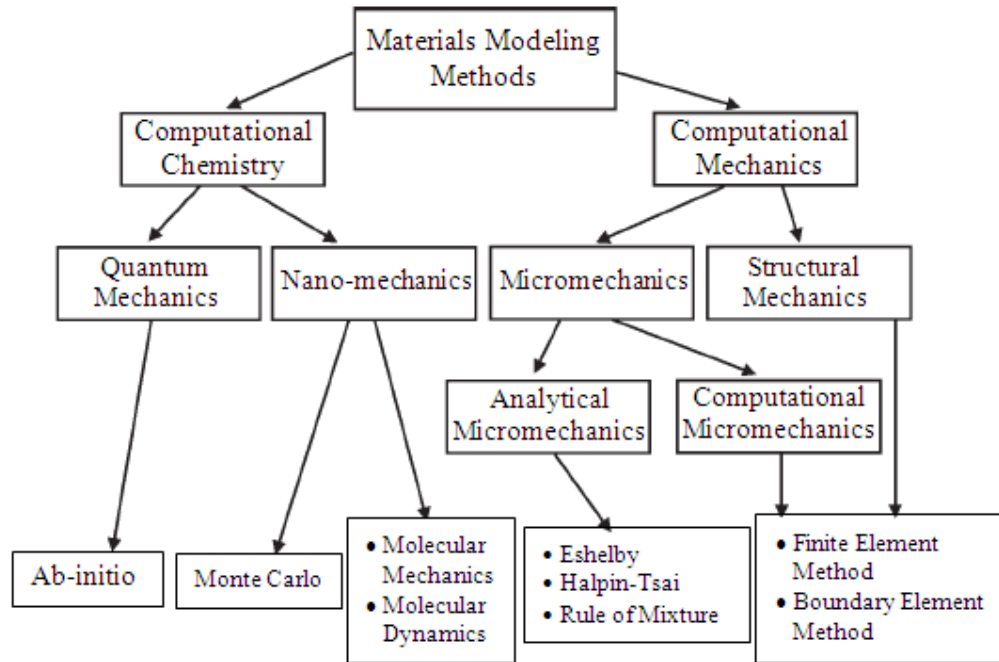


Figure 2.25: Different material modeling techniques[94]

These exceptional properties of SWNT have predicted potential applications in aerospace and biomedical fields [37, 96-98]. Empirical models have been used [99] in calculating the elastic properties of single and multilayered nanotubes and have predicted that the Young's modulus and shear modulus are comparable to that of diamond. It has been stated by some researchers that the elastic moduli is insensitive to nanotube geometry such as size, helicity and the number of layers. [37]

Qian et al. [37] characterized carbon nanotube (CNT)/polystyrene composites and have demonstrated that an addition of 1% by weight of CNTs in a matrix material resulted in an increase in the elastic stiffness of the composite between 36% and 42%, and a 25% increase in the tensile strength. Some other researchers [19] used short-fiber composite theory and have demonstrated that adding 10% by weight of the carbon fibers showed an increase in the elastic modulus, which is same as the increase in modulus by adding 1% by weight of carbon nanotubes.

Experimental characterization of Nanocomposite is a demanding and expensive task. To overcome this, computational methods have been increasingly used in the recent years in the development of nanotube materials, and in studying the influence of nanotubes on the material properties of the composites. Griebel and Hamaekers [100] examined the elastic moduli of polymer-nanotube composites by MD simulations. Stress-strain curves were derived performing MD simulations on a composite with single-walled carbon nanotube embedded in polyethylene matrix, using Parrinello-Rahman approach [101]

for the application of external stress. A new technique has been developed recently by Odegard et al [45, 102, 103] for developing constitutive models for composite materials reinforced with single walled carbon nanotube, based on an equivalent-continuum modeling technique. This method takes into account the atomistic interactions at the nanoscale, and interfacial characteristics of the nanotube and the surrounding polymer matrix using molecular dynamics simulations. Then, an equivalent continuum model was developed to determine the mechanical properties that reflect the local polymer and nanotube structure. This model exactly describes the bonded and non-bonded interactions of atoms in the molecular model. This model has been used to find the constitutive properties of the SWCNT/polymer composite for aligned and random orientations with various nanotube lengths and volume fractions. However, the validation of these models is still a challenging task.

Continuum mechanics was introduced recently in evaluating the effective material properties of CNT-based composites by Fisher, Bradshaw and Liu,[104-106]. Numerical examples based on 3-D representative volume element (RVE) using both long and short CNTs were developed using the finite element method (FEM) demonstrating significant load carrying capacities of the CNTs in a polymer matrix. These results proved to be in excellent agreement with the rule of mixtures results and are reported to be consistent with some of the experimental results in literature. But the validation of these results, using other approaches like molecular dynamics and equivalent continuum modeling remained as a question and has to be addressed.

2.8.1 Correlation between Structural and Molecular Mechanics

At the molecular level, the interaction between individual carbon atoms can be described using the force fields of the corresponding nucleus-nucleus and electron-nucleus interactions [110, 111]. If electrostatic interactions are neglected, the total steric potential energy (U_{total}), which characterizes the force field, can be obtained as the sum of energies due to valence (or bonded) and non-bonded interactions, given as:

$$U_t = U_r + U_\theta + U_\phi + U_{vdw} \quad 2.102$$

Here, U_r , U_θ , U_ϕ , and U_{vdw} correspond to energy associated with bond stretch interactions, bond angle bending, torsion (dihedral and out of plane) and van der Waals forces (non-covalent). Figure 2.31 a, illustrates the various interatomic interactions at the molecular level. Several harmonic and non-harmonic potential functions have been proposed to describe the interatomic interactions of carbon atoms.[8]

The covalent interactions between carbon atoms can be represented using simple harmonic functions, the Vibrational potential energies due to interactions between covalently bonded carbon atoms can be represented as shown in Table 2.7 which summarizes various energy forms for the two mechanical systems.[8, 112]

The terms Δr , $\Delta\theta$, $\Delta\phi$ refer to change in bond-length, bond angle and dihedral angle, respectively. The terms k_r , k_θ , k_ϕ represent the force constants associated with stretching, bending and torsion, respectively, of the chemical bond. The carbon atoms in the nanotubes are held together by covalent bonds of characteristic bond length and bond angles, and the corresponding molecular forces constrain any displacement of individual atoms.[8]

Due to the nature of the molecular force fields between two atoms, they can be treated as forces acting between two junctions (or material points) that are separated by structural beam or spring elements. Thus, the lattice of the carbon nanotubes can be considered as a three dimensional hexagonal network of beam (covalent) and spring (non-covalent) elements. Figure 2.31(b) illustrates the correlation between beam elements and the molecular forces between bonded carbon atoms.

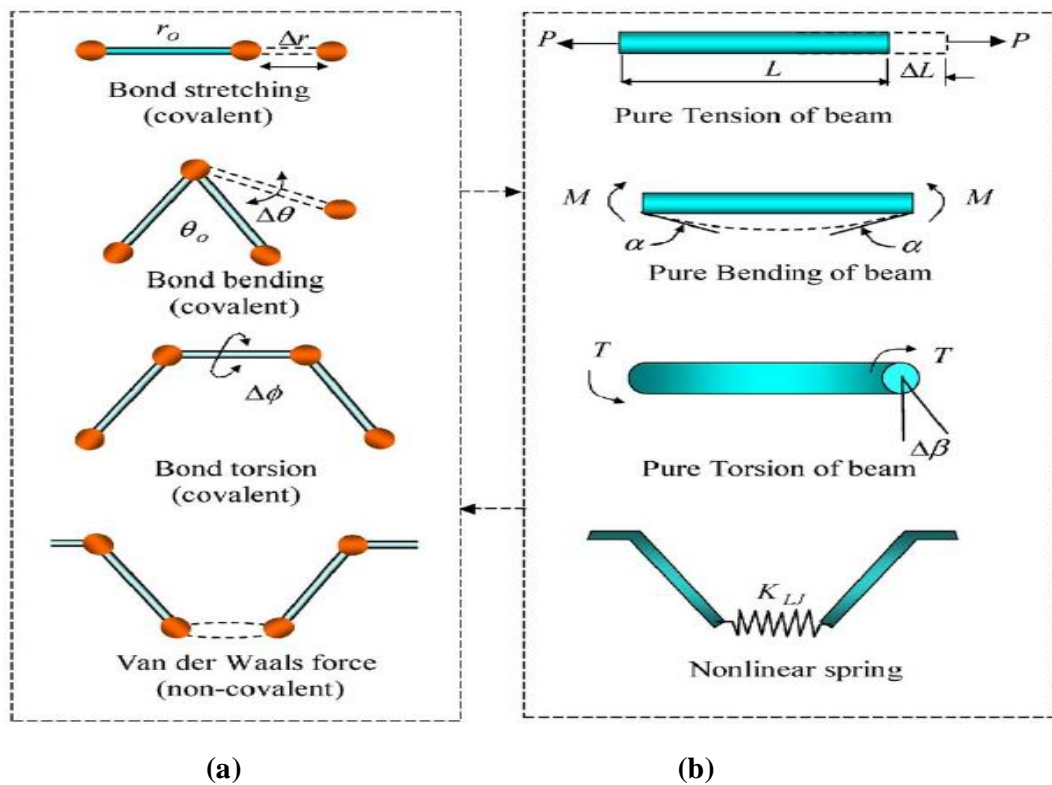


Figure 2.26: Equivalence of molecular mechanics and structural mechanics for covalent and non-covalent interactions between carbon atoms: (a) Molecular mechanics model and (b) structural mechanics model.[8, 113, 114]

Table 2.7: Energy form in molecular mechanics and structural mechanics systems[112]

Mechanics System Energy Form	Molecular mechanics	Structural mechanics	Deformation type
Stretching energy	$U_P = \frac{1}{2} \sum_i K_i (dR_i)^2$	$U_A = \frac{1}{2} \frac{EA}{L} (\Delta L)^2$	dR_i bond stretching increment ΔL axial stretching deformation
Bending energy	$U_\theta = \frac{1}{2} \sum_j C_j (d\theta_j)^2$	$U_M = \frac{1}{2} \frac{EA}{L} (2\alpha)^2$	$d\theta_j$ bond angle change 2α total relative rotation angle
Torsional energy	$U_\tau = \frac{1}{2} \sum_i A_i (d\phi_j)^2$	$U_T = \frac{1}{2} \frac{GJ}{L} (\Delta\beta)^2$	$d\phi_j$ angle of bond twisting $\Delta\beta$ relative torsion angle

To determine the force constants pertaining to the covalent interactions one could equate the potential energies of individual bonds with their corresponding beam model [113]. The beam elements representing the bond are assumed to be isotropic with length L , cross-sectional area A , and moment of inertia I [113].

The strain energy under pure axial load P , (pure tension) is given by: [113]

$$U_P = \int_0^L \frac{P^2}{2EA} dL = \frac{EA}{2L} (\Delta L)^2 \quad 2.103$$

The strain energy of beam element under pure bending moment M , is given by:

$$U_M = \int_0^L \frac{M^2}{2EI} dL = \frac{EI}{2L} (\Delta\alpha)^2 \quad 2.104$$

Similarly, the strain energy of the beam element under a pure twisting moment T , is given by:

$$U_M = \int_0^L \frac{T^2}{2GI} dL = \frac{GI}{2L} (\Delta\beta)^2 \quad 2.105$$

The terms ΔL , $\Delta\alpha$, $\Delta\beta$ are the axial deformation, bend angle and twist angle, respectively. The equations illustrated in the table 2.7 represent the same quantities in two different systems (molecular and structural) so they can be equated, thus establishing a link between the two systems. Also, assuming The terms Δr , $\Delta\theta$, $\Delta\phi$ are equivalent to their structural mechanics counterparts, that is ΔL , $\Delta\alpha$, $\Delta\beta$, $\Delta\beta$, respectively, one obtains the tensile stiffness (EA), cross-sectional bending stiffness (EI)

and torsional rigidity (GJ) of the structural model in terms of the molecular mechanics force constants k_r , k_θ , k_ϕ . These are: [113]

$$k_r = \frac{EA}{L}, \quad k_\theta = \frac{EI}{L}, \quad \text{and} \quad k_\phi = \frac{GJ}{L} \quad 2.106$$

In summary, the parameters in equation 2.106 are used to model the molecular behavior in the structural model. In case of single-walled carbon nanotubes (with only covalent bonds) the parameters in the above equations are sufficient to describe the structural model (with beam elements) [8]. In case of multi-walled carbon nanotubes, the van der Waals interactions between carbon atoms in different concentric tubes must also be considered.

2.9 Key Issues in Carbon Nanotubes-Based Composites

2.9.1 Carbon Nanotubes Dispersion in the Matrix

One of the biggest challenges in processing nanotube composites lies in achieving a ‘good’ dispersion. It is important that the individual nanotubes are distributed uniformly throughout the matrix and well-separated from each other; the presence of agglomerates is extremely undesirable, especially in ceramic matrices, as they can act as defects leading to stress-concentration, and premature failure, particularly if the matrix does not fully penetrate the agglomerate during processing. On the other hand, with a good dispersion, each nanotube is loaded individually over a maximum interfacial area, and can contribute directly to the mechanical properties and to toughening mechanisms.[33]

2.9.2 Interfacial Phenomena

Interfacial phenomena and chemical stability of the CNTs in the metal matrix are critical for several reasons. The fiber-matrix stress transfer and the interfacial strength [4] play an important role in strengthening. The applied stress is transferred to the high strength fiber through the interfacial layer, so that a strong interface would make the composite very strong but at the expense of ductility of the composite. A weak interface would lead to lower strength and inefficient utilization of fiber properties by facilitating pullout phenomena at low loads due to interface failure. Wetting of the fiber by the liquid metal is essential. Non-wetting will lead to poor interfacial bonding. Interfacial reactions leading to formation of an interfacial phase can improve wetting if

the liquid has a lower contact angle with the phase forming due to the reaction. A lot of work has been carried in reinforcing Aluminum matrix with carbon fibers. Interfacial reactions and degree of wetting of the fibers have been shown to affect the properties of the composite[52]. CNTs as integrated molecules have high chemical stability due to the covalent bond between the Carbons atom is connected with sp^2 hybrid. It has been confirmed that CNTs have much less chemical activity than carbon fiber and graphite. Authors have studied the wetting of carbon nanotubes in detail and reported that the determining factor for wetting was surface tension, with a cut-off limit between 100 and 200mN/m. This limit implied that typical pure metals, such as: aluminum (surface tension of 865 mN/m), copper (1270 mN/m), iron (1700 mN/m), would not be easily wetted on the surface of MWNTs. This means, if CNTs are used as reinforcing fibers for metal–matrix composites without any surface treatments, it will be difficult to achieve high-strength interfacial adhesion.[63]

CHAPTER THREE

METHODOLOGY

3.1 OVERVIEW

The research conducted for this thesis is divided into two parts, analytical and computational part where the finite element method was used as the solution method. In analytical part the matlab code will be constructed and used to solve the role of mixture and the thermal conductivity equations to predict different results for a new composite.

The second part is the computational modeling and simulation of the Nanocomposite can play a significant role in the development of superior Nanocomposite. Modeling and simulations will help in understanding the behavior of Nano structures under various loads and environments. A 3D model will be created by APDL code to simplify the different models generation in order to use and apply the material properties and different boundary condition to predict the results for the new composite.

Two cases will be considered for the matlab analytical part and the APDL computation part: first case will deal with long carbon nanotubes and the second case will deal with short carbon nanotubes. Finally, the results for the two methods used will be compared and validated. Figure 3.1 represents the methodology used in this research

3.2 THE ANALYTICAL APPROACH

MATLAB programming is used to predict the mechanical and thermal results of the carbon nanotubes reinforced metal matrix Nanocomposite. Detailed explanations are represented showing the results of mechanical and thermal analysis.

3.2.1 Mechanical Properties of carbon nanotubes reinforced Nanocomposite

Significant development has been made in carbon nanotubes composite materials. Their remarkable properties offer potentials for fabricating composites with

substantially enhanced physical properties including conductivity, strength, elasticity, and toughness.

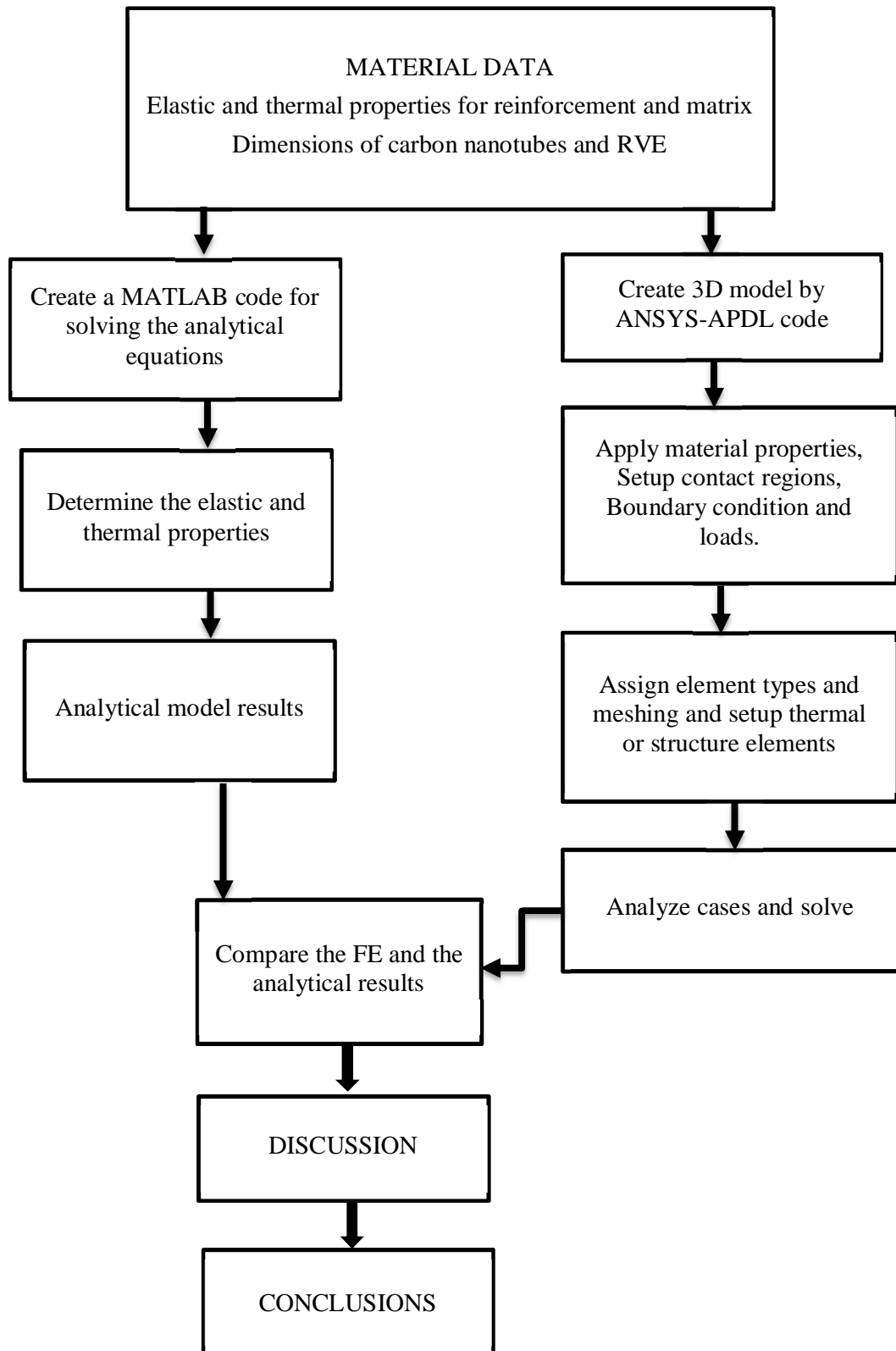


Figure 3.1: Research Methodology

The strength of materials (rule of mixtures) [115] approach for estimating the properties of fiber-reinforced composites and the extension of this method to Nanocomposite are investigated to determine the mechanical properties of the carbon nanotubes reinforced metal matrix Nano-composites [71]. However, By using the properties of carbon nanotubes and the metal matrix used in this research, the expected results of the carbon nanotube reinforced metal matrix Nano-composite to be created were calculated using the MATLAB code. Two cases were considered for these calculations: the first case deals with the continuous carbon nanotube fibers while the second case deals with short carbon nanotube fibers. The “Rule of Mixtures” equations can be used to make predictions about various properties of carbon nanotubes and the metal matrix. A flow chart of the program is presented in Figure 3.2.

3.2.1.1 Carbon nanotube through the length of the RVE (Treated as Long fiber)

Simple rules of mixtures [115] can be established based on the strength of materials theory. In this case carbon nanotube can be treated as long fiber (with large aspect ratio) and therefore a segment can be modeled using RVE [8, 71, 116, 117]. Figure 3.3 shows a simplified strength of materials model based on square RVE for estimating the effective Young’s modulus. The equations of Section 2.6.4.1 were used in the MATLAB code to predict the elastic properties of carbon nanotube treated as long fiber in reinforcing metal matrix composites.

3.2.1.2 Carbon nanotube in the RVE (Treated as short fiber)

Square RVE is divided into two segments: one segment accounting for the two ends with a total length of l_e and Young’s modulus E_m ; and another segment accounting for the center part with a length of L_c and an effective Young’s modulus E_c . Note that the two hemispherical end caps of the CNT have been ignored in this simple strength of materials model [8,71,77,105, 116]. The equations of Section 2.6.2.1 were used in the MATLAB code to predict the elastic properties of carbon nanotube treated as long fiber in reinforcing metal matrix composites. Figure 3.4 shows the Carbon nanotubes inside the RVE. The extended rule of mixtures is derived based on the strength of materials theory and compared to that given equation 2.60. Equation 3.3 can be employed to estimate the effective Young’s modulus for the case shown in Figure 3.4 when the carbon nanotube is relatively short and thus inside the square RVE.[8, 71, 77, 105, 106, 116, 118, 119]

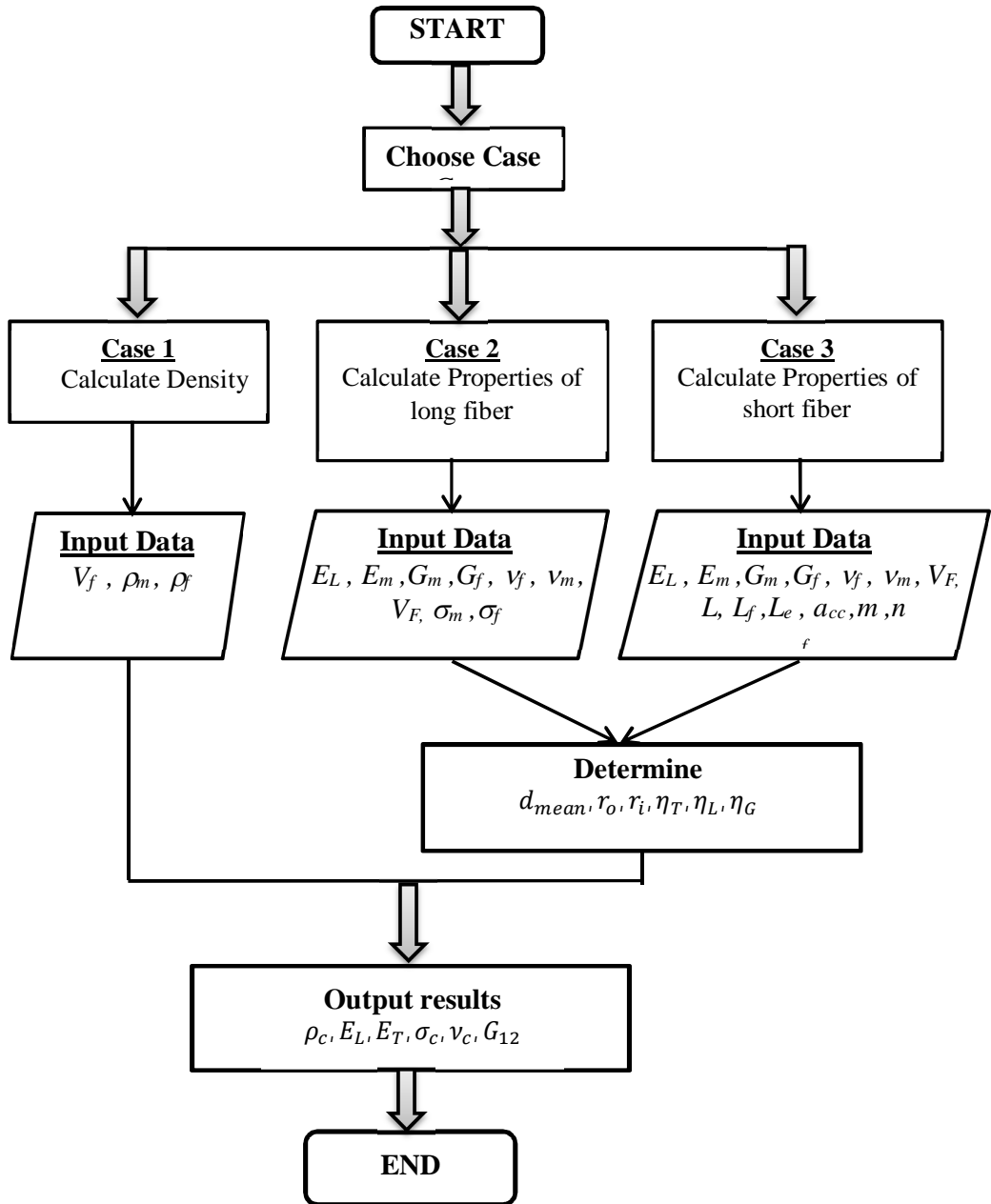


Figure 3.2: Flowchart for the MATLAB code

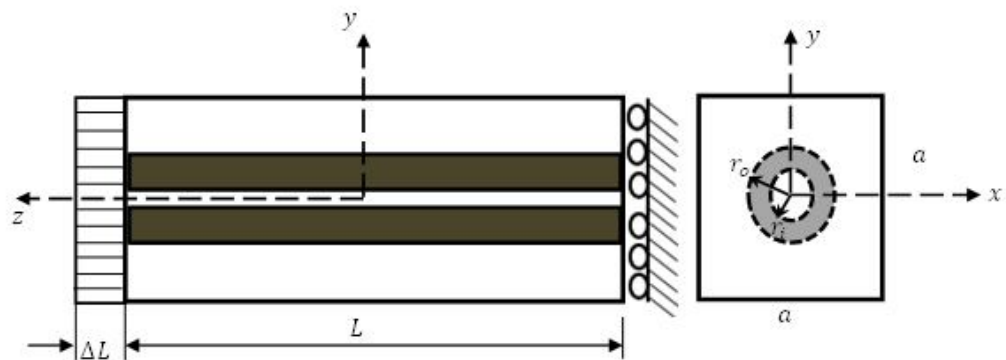


Figure 3.3: Carbon nanotubes through the length of the RVE

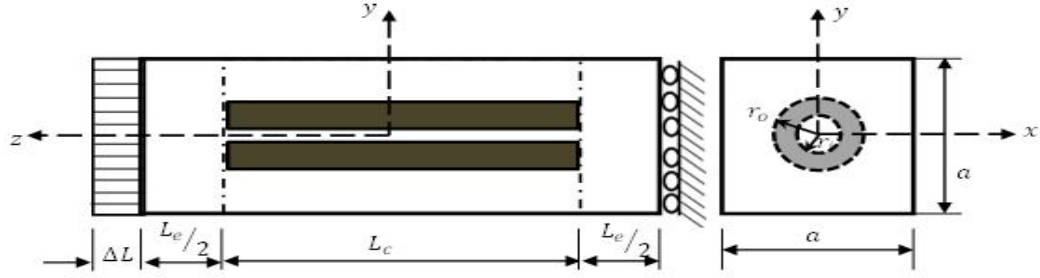


Figure 3.4: Carbon nanotubes inside the RVE

The volume fraction of the carbon nanotube is given by:

$$V_f = \frac{\pi(r_o^2 - r_i^2)}{a^2 - \pi r_i^2} \quad 3.1$$

V_f = Carbon nanotube volume fraction

a = width of the square RVE

$$a = \sqrt{\frac{\pi(r_o^2 - r_i^2)}{V_f} + \pi r_i^2} \quad 3.2$$

The effective Young's modulus E_z is found to be

$$E_z = \frac{1}{\frac{1}{E_m} \times \left(\frac{l_e}{l}\right) + \frac{1}{E_{CNT}} \times \frac{l_{CNT}}{l} \times \frac{A}{A_{CNT}}} \quad 3.3$$

Where,

$$A_{CNT} = \text{Area of Carbon nanotube} = \pi(r_o^2 - r_i^2)$$

$$A = \text{Area of whole RVE} = a^2, \text{ And } L = l_{CNT} + l_e$$

3.2.2 Thermal conductivity in carbon nanotube reinforced composites

The main parameters affecting the thermal properties of composites are the volume fraction, aspect ratio, alignment of the fibers, and the adhesion between the fibers and the matrix, and the thermal property of the interface[120]. Theoretical estimates show that an increase in the aspect ratio of highly conducting fibers would dramatically increase the thermal conductivity of the composite [87, 121-123]. A mathematical solution was developed for the effective conductivity in axial direction by using effective medium theory. A mathematical solution for calculating thermal conductivity of a carbon nanotube composite in the longitudinal direction using effective medium theory was developed by Bagachi and Nomura[87]. Thus to determine the effective thermal conductivity (k_{eff}^*), the quantities 2.137, 2.138 and 2.140 for ζ_0 , λ and $\bar{\beta}$ need to be calculated from the geometry and materials properties of the carbon nanotubes and the metal matrix considered in the finite element analysis.[87]

The MATLAB code was used to solve the linear differential equations and to calculate the various constants involved in equation 2.135 for the thermal conductivity. For numerical calculations, however, solution of an infinite set of equations is not possible and the series thus needs to be truncated at some point. The number of terms used will determine the accuracy of the solution obtained. The value of B_1 converges to a unique value after a few terms. In this research, convergence is achieved after six terms. For greater accuracy, eight terms used in the solution which gives us eight simultaneous equations to be solved.[87]. The effective thermal conductivity is calculated by varying the length of carbon nanotubes and keeping the diameter constant *i.e.* varying the aspect ratio with fixed diameter. For a fixed aspect ratio, the interface conductance is varied and the theoretical behavior is studied. Dependence of the thermal conductivity on the volume fraction is studied by keeping the aspect ratio constant and varying the volume fraction of the carbon nanotubes in the composite[124]. A flow chart describing the process of the calculation of thermal conductivity is presented in Figure 3.5

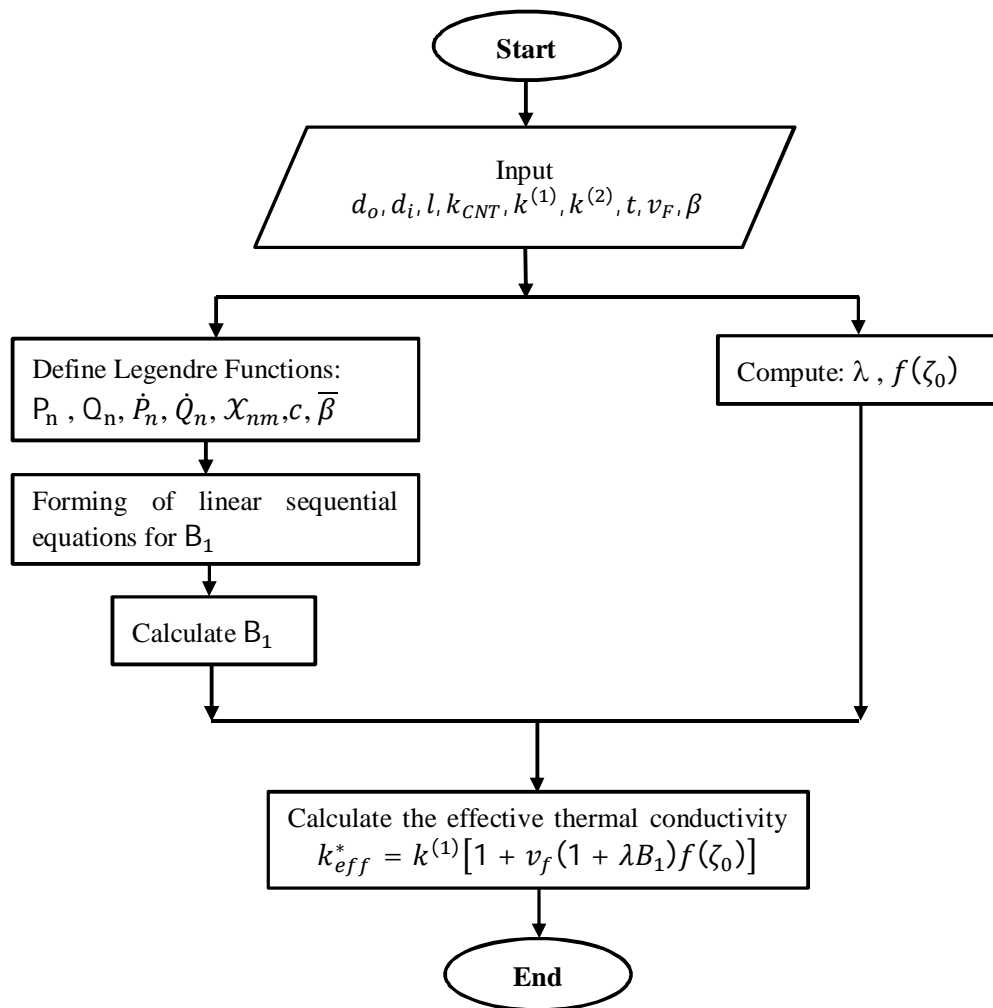


Figure 3.5: Flow chart describes the MATLAB program used for calculation of Thermal conductivity

3.3 THE COMPUTATIONAL APPROACH

Computational approach can play significant role in the development of the carbon nanotube based composites by providing simulation results to help on the understanding, analysis and design of such Nanocomposite. At the nanoscale, analytical models are difficult to establish or too complicated to solve, and tests are extremely difficult and expensive to conduct. Modeling and simulations of Nanocomposite, on the other hand, can be achieved readily and cost effectively on even a desktop computer. Characterizing the mechanical properties of carbon nanotube based composites is just one of the many important and urgent tasks that simulations can accomplish.[106]

The finite element method (FEM) has become the main method for predicting and simulating the physical behavior of complex engineering systems[80, 84]. The commercial finite element analysis (FEA) programs have gained common acceptance among engineers in industry and researchers.[125, 126]

The Finite Element Analysis (FEA) method is a powerful computational technique for approximate solutions to a variety of “real-world” engineering problems having complex domains subjected to general boundary conditions[110, 124, 127, 128]. FEA has become an essential step in the design or modeling of a physical phenomenon in various engineering disciplines [81, 129-133].

The modeling of engineering problems using FEA requires either the development of a computer program based on the FEA formulation or the use of a commercially available general-purpose FEA program such as ANSYS. The ANSYS program is a powerful, multi-purpose analysis tool that can be used in a wide variety of engineering disciplines. Figure 3.6 shows the steps involved for finite element method. In the ANSYS, there are two modes of usage, i.e., the Graphical User Interface (GUI) and Batch Mode. Every action taken by the user within the ANSYS GUI platform has an equivalent ANSYS command. Using ANSYS through the Batch Mode involves text (ASCII) files with specific ANSYS commands. These commands, along with specific rules, form a special programming language, ANSYS Parametric Design Language, or APDL, which utilizes concepts and structures very similar to common scientific programming languages. Using the APDL[134], the user can create (a) an Input File to solve a specific problem and (b) Macro File(s) that act as special functions, accepting several arguments as input. In either case, each line consists of a single command, and the lines are executed sequentially.[130, 132]

3.3.1 Choice of Finite Element

The finite element method is chosen because of its ability to analyze metal and composite structures in an accurate way, and its availability as finite element analysis packages, coupled with easy access to the required computing resources.

Generally, there are three alternate procedures of handling a structural mechanics problem. These are differential equations, energy methods and the integral equations. All the above are approximate procedures. They discretize all or part of the structure into a number of points in the sense that the behavior of a discrete point can simulate the behavior of the whole structure when loaded.

The element library in analysis system software (ANSYS) offers many element formulations or types. Many features are common to all elements in the library. Most element types use various material properties and have a degree-of-freedom set which constitutes the primary nodal unknowns to be determined by the analysis. However, element loads are surface loads, body loads, inertial loads, and ocean loads. Element loads are always associated with a particular element. ANSYS incorporates both flat and curved shell elements, which may be either triangular or quadrilateral. Both thin and thick shell elements are available, and may be more effective for Eigen-analyses since a consistent mass matrix is available[81, 126, 130].

3.3.2 Finite Element Formulation

Equilibrium equation for a finite element for eight node-isoparametric elements is given below:[81]

$$[K_e]\{U_e\} = \{F_e\} \quad 3.4$$

Where,

$[K_e]$: Element stiffness matrix

$\{F_e\}$: Element load vector of a finite element and

$\{U_e\}$: Nodal displacement vector for an element.

The force vector $\{F_e\}$ is the sum of body force vector, surface force vector and the concentrated load for an element. The stiffness matrix for a finite element is given by:

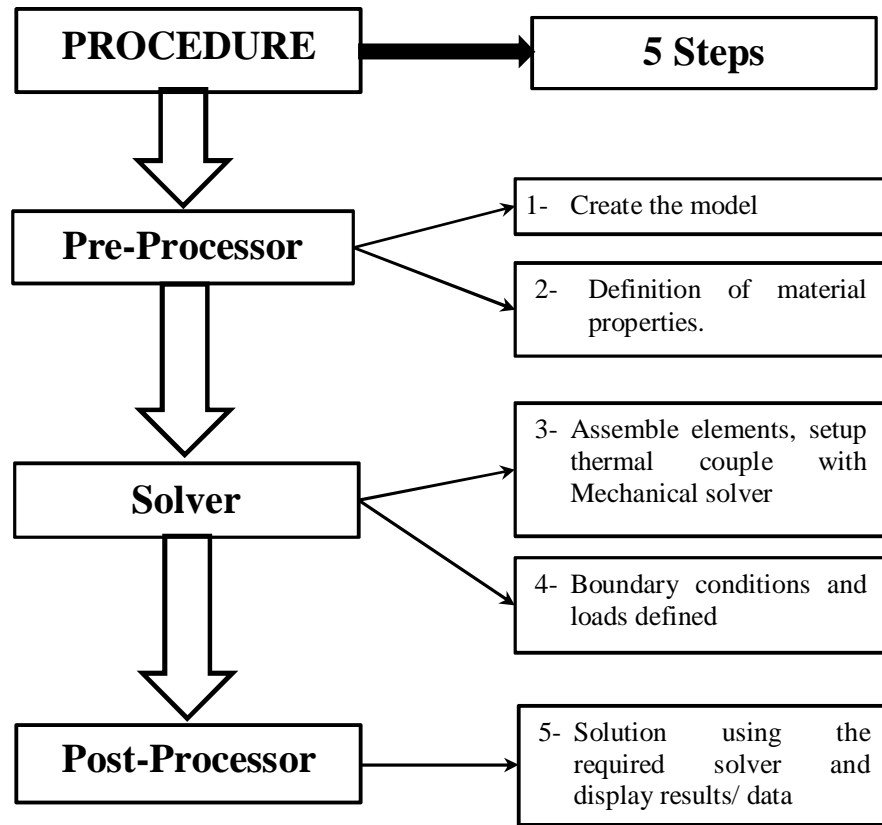


Figure 3.6: Steps involved for finite element method

$$[K_e] = \iint [B_e]^T [D_{ep}] [B_e] |J| drds \quad 3.5$$

where ,

$[B_e]$: is the strain-displacement matrix,

$[D_{ep}]$: is the elastoplastic constitutive matrix and

$|J|$: is the determinate of the Jacobian matrix.

The stiffness matrix and load vector for all the elements can be obtained using 2x2 Gauss quadrature integration scheme [135]. The stiffness matrix and load vector for all the elements were assembled to obtain the equations of equilibrium for the complete structure. The equilibrium equation for the complete structure can be expressed as: [135]

$$[K_s]\{U_s\} = \{F_s\} \quad 3.6$$

Where,

$[K_s]$: The stiffness matrix,

$\{F_s\}$: The load vector and

$\{U_s\}$: The nodal displacement vector for the complete structure

3.3.3 Representative Volume Element and Material Properties

The representative volume element (RVE) plays a central role in the mechanics and physics of random heterogeneous materials with a view to predicting their effective properties and material microstructure.[117] The RVE is very clearly defined in two situations only: (i) unit cell in a periodic microstructure, and (ii) volume containing a very large (mathematically infinite) set of micro scale elements (e.g. grains), possessing statistically homogeneous and ergodic properties. The concept of unit cells or representative volume elements (RVEs), which has been applied successfully in the studies of conventional fiber-reinforced composites at the micro scale, is extended to the study of CNT-reinforced composites at the nanoscale[136]. In this unit cell or RVE approach, a single nanotube with surrounding matrix material can be modeled, with properly applied boundary and interface conditions to account for the effects of the surrounding material[136, 137]. This RVE model was employed to study the interactions of the nanotube with the matrix, to investigate the load transfer mechanism, or to evaluate the effective elastic properties of the Nanocomposite. The study of these properties may be multidisciplinary and may involve various branches of science and engineering [103, 106, 118]. Finite element method can be applied to analyze the mechanical responses of these RVEs under different loading conditions. Square representative volume elements were proposed in this research for the evaluations of effective material properties for the CNT-based composites. Figure 3.7 represents two square RVEs consist of single wall carbon nanotube embedded in metal matrix.

The dimensions of the square representative volume element and Carbon nanotubes to generate the geometries of the models are calculated based on equation 3.1 and 3.2 and tabulated in Table 3.1 for long fiber and Table 3.2 for short fiber. The volume fractions used in this research were 3, 7, and 11%. However, the length of the square representative volume element assumed to be 10 nm.

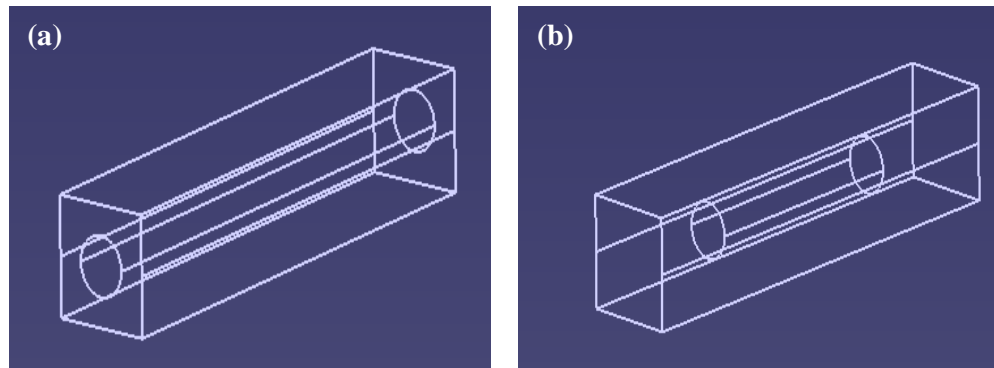


Figure 3.7: Two possible RVEs for the analysis of CNT-based Nanocomposite (a) Square RVE with long fiber; (b) Square RVE with short fiber

3.3.4 APDL code development

A parameterized ANSYS macro will be developed for predicting effective elastic modules of the materials using various RVEs. The code (script) used is APDL rather than GUI because APDL is more extensible and to ensure the flexibility and variability of the FE modeling due to many parameters can be easily changed. Therefore it is unnecessary to remake ANSYS models at each time. Firstly, RVE will be considered with one CNT, which have been conventionally used to generate a quarter models[81, 126, 130, 132]. As shown in Figure 3.8 the RVE is divided into many regular volumes for computational efficiency. Secondly, the RVE will be considered with four CNTs are placed in centers of sub-RVEs. The generated full model reflected from quarter model by two symmetry reflection, and there for the Full model is equivalent to the quarter model. Figure 3.9

Table 3.1: Model dimensions for long carbon nanotubes case

	CNT		d_o (nm)	d_i (nm)	a (width of square RVE) in (nm)		
	n	m			$V_f=3\%$	$V_f=7\%$	$V_f=11\%$
Armchair CNT	5	5	0.848	0.508	4.9041	3.8201	2.5483
	10	10	1.526	1.186	6.8898	5.3418	3.5152
	15	15	2.204	1.864	8.3765	6.4601	4.1829
Zigzag CNT	5	0	0.561	0.221	3.7329	2.9117	1.9491
	10	0	0.953	0.613	5.2650	4.0986	2.7291
	15	0	1.344	1.004	6.4238	4.9872	3.2949
Chiral CNT	5	10	1.206	0.866	6.0411	4.6947	3.1107
	10	15	1.876	1.536	7.6996	5.9536	3.8862
	15	20	2.551	2.211	9.0280	6.9428	4.4552

Table 3.2: Model dimensions for short carbon nanotubes case: (a) at $V_f=3\%$, (b) at $V_f=7\%$, and (c) at $V_f=11\%$,

(a) at $V_f=3\%$,

	CNT		d_o (nm)	d_i (nm)	a (nm)					
	n	m			Case 1		Case 2		Case 3	
					lc=3	le=7	lc=5	le=5	lc=8	le=2
Armchair CNT	5	5	0.848	0.508	3.2105		4.9041		9.8082	
	10	10	1.526	1.186	4.5104		6.8898		13.779	
	15	15	2.204	1.864	5.4837		8.3765		16.753	
Zigzag CNT	5	0	0.561	0.221	2.4438		3.7329		7.4659	
	10	0	0.953	0.613	3.4468		5.2650		10.530	
	15	0	1.344	1.004	4.2054		6.4238		12.847	
Chiral CNT	5	10	1.206	0.866	3.9548		6.0411		12.082	
	10	15	1.876	1.536	5.0406		7.6997		15.399	
	15	20	2.551	2.211	5.9102		9.0280		18.056	

(b) at $V_f=7\%$

	CNT		do (nm)	di (nm)	a (nm)					
	n	m			Case 1		Case 2		Case 3	
					lc=3	le=7	lc=5	le=5	lc=8	le=2
Armchair CNT	5	5	0.848	0.508	2.0965		3.2025		6.4049	
	10	10	1.526	1.186	2.9189		4.4588		8.9176	
	15	15	2.204	1.864	3.5122		5.3650		10.730	
Zigzag CNT	5	0	0.561	0.221	1.5997		2.4436		4.8871	
	10	0	0.953	0.613	2.2481		3.4339		6.8679	
	15	0	1.344	1.004	2.7286		4.1680		8.3361	
Chiral CNT	5	10	1.206	0.866	2.5709		3.9272		7.8545	
	10	15	1.876	1.536	3.2450		4.9568		9.9136	
	15	20	2.551	2.211	3.7642		5.7499		11.499	

(c) at $V_f=11\%$

	CNT		do (nm)	di (nm)	a (nm)					
	n	m			Case 1		Case 2		Case 3	
					lc=3	le=7	lc=5	le=5	lc=8	le=2
Armchair CNT	5	5	0.848	0.508	1.6683		2.5483		5.0966	
	10	10	1.526	1.186	2.3012		3.5152		7.0304	
	15	15	2.204	1.864	2.7384		4.1829		8.3659	
Zigzag CNT	5	0	0.561	0.221	1.2759		1.9491		3.8982	
	10	0	0.953	0.613	1.7866		2.7291		5.4582	
	15	0	1.344	1.004	2.1570		3.2949		6.5898	
Chiral CNT	5	10	1.206	0.866	2.0364		3.1107		6.2214	
	10	15	1.876	1.536	2.5441		3.8862		7.7724	
	15	20	2.551	2.211	2.9166		4.4552		8.9105	

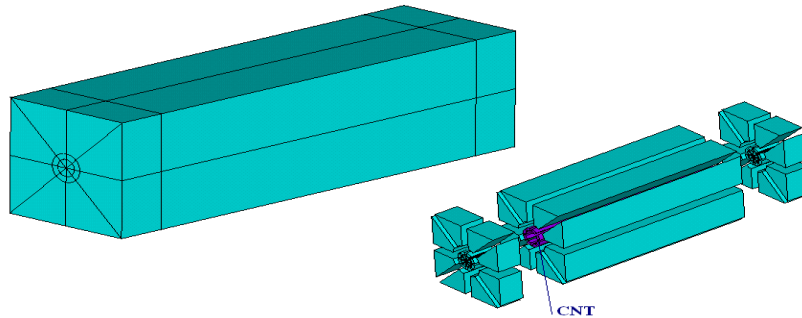


Figure 3.8: RVE divided into many regular volumes

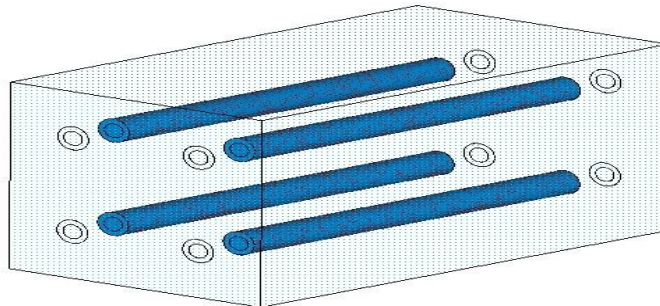


Figure 3.9: The Full model built by APDL ANSYS

3.3.4.1 Meshing

The element type PLNAE182[138] is used for 2-D modeling the solid structures. The element can be used as either a plane element (plane stress, plane strain or generalized plane strain) or an axi-symmetric element. It is defined by four nodes with two degrees of freedom for each node: translations in the nodal x and y directions. It also has mixed formulation capability for simulating deformations. Figure 3.10 represents the geometry of the PLANE 182 element.

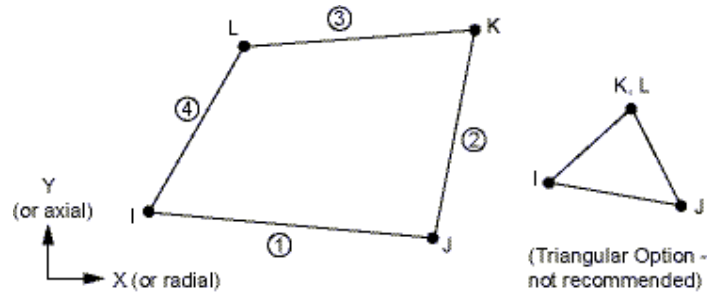


Figure 3.10: PLANE182 Geometry[138]

SOLID185 as shown in Figure 3.11 is used for 3-D modeling of solid structures. It is defined by eight nodes having three degrees of freedom at each node: translations in the nodal x, y, and z directions. It also has mixed formulation capability for simulating deformations. SOLID185[138] Structural Solid allows for prism, tetrahedral, and pyramid degenerations when used in irregular regions. Various element technologies such as B-bar, uniformly reduced integration, and enhanced strains are supported.

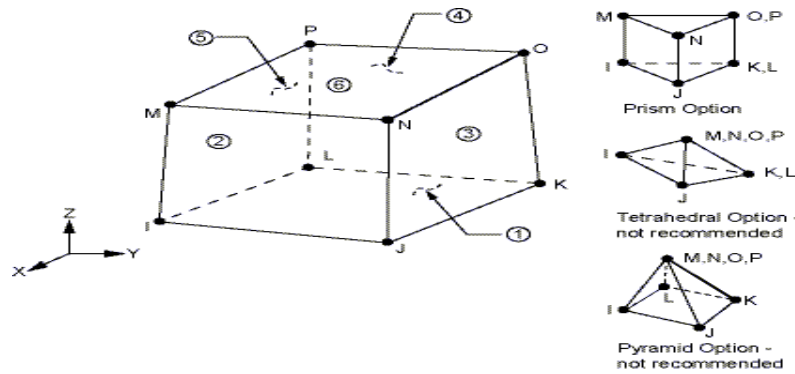


Figure 3.11: SOLID185 Homogeneous Structural Solid Geometry[138]

The interface element size in carbon nanotube is equal to a quarter of the thickness of carbon nanotube. Thus carbon nanotube is modeled by four element layers. The mapped meshing algorithm is applied through the dividing volume for long fiber case. However, in short fiber case, mapped meshing algorithm is applied to CNT and interface areas

while free meshing algorithm is applied to matrix area. The division with spacing ratio is applied to the lines of matrix area which are connected with interface area. Figure 3.12 and 3.13 show the meshing procedure for quarter and full model.

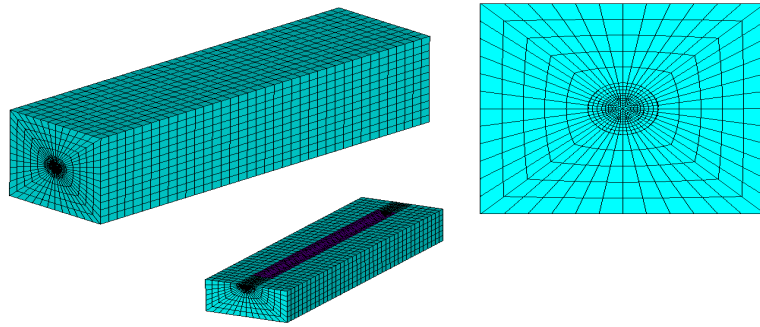


Figure 3.12: FE mesh for the RVE

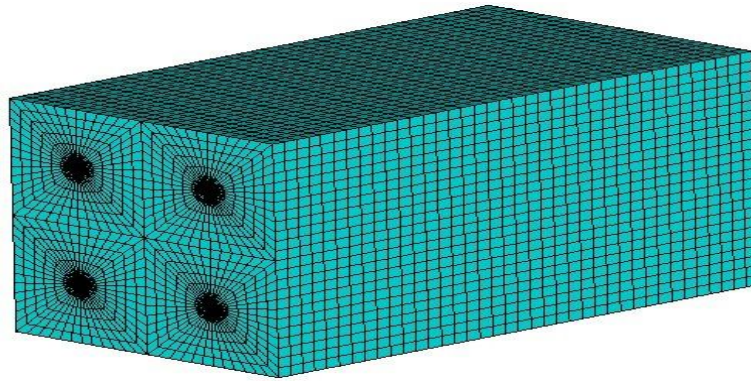


Figure 3.13: The mesh of Full model

3.3.4.2 Boundary conditions and Loads

After generating the geometric models, specific conditions have to be given in relation to the constraints at both translational and rotational degrees of freedom on the nodes at ends needed for simulation. At this step, 2D problem is considered for convenient. The correct displacement periodic boundary condition imposed as shown in Figure 3.14. The periodic constraint as follows:

$$u'_i - u_i + u_i^d = 0 \quad 3.7$$

Where

u'_i , u_i Displacement of relative opposite periodic node pairs

u_i^d : Displacement of dummy node

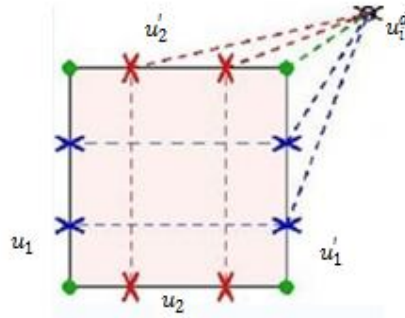


Figure 3.14: Periodic boundary condition

Continue the formulation by consider the detailed boundary condition for 3D problem.

For periodic boundary condition in x direction

$$\begin{aligned}
 u'_x - u_x + u_x^d &= 0 \\
 u'_y - u_y + u_{rotz}^d &= 0 \\
 u'_z - u_z &= 0
 \end{aligned}
 \tag{3.8}$$

For periodic boundary condition in y direction

$$\begin{aligned}
 u'_x - u_x &= 0 \\
 u'_y - u_y + u_y^d &= 0 \\
 u'_z - u_z + u_{rotx}^d &= 0
 \end{aligned}
 \tag{3.9}$$

For periodic boundary condition in z direction

$$\begin{aligned}
 u'_x - u_x + u_{roty}^d &= 0 \\
 u'_y - u_y &= 0 \\
 u'_z - u_z + u_z^d &= 0
 \end{aligned}
 \tag{3.10}$$

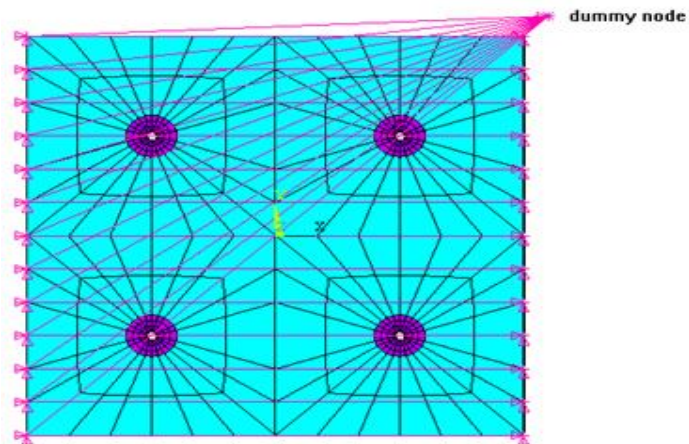


Figure 3.15: The periodic condition in x direction

For preventing rigid motion, any one node inside representative volume element is fully constrained. All displacement of the middle point of representative volume element was constrained.

3.3.4.3 Loading and Post-processing

According to the displacement of the dummy node macro strain of RVE is determined. The six independent strain modes selected

Thus,

$$\begin{pmatrix} \varepsilon_x \\ \varepsilon_y \\ \varepsilon_z \\ \gamma_{xy} \\ \gamma_{yz} \\ \gamma_{zx} \end{pmatrix} = \begin{bmatrix} 1 & 0 & 0 & 0 & 0 & 0 \\ 0 & 1 & 0 & 0 & 0 & 0 \\ 0 & 0 & 1 & 0 & 0 & 0 \\ 0 & 0 & 0 & 1 & 0 & 0 \\ 0 & 0 & 0 & 0 & 1 & 0 \\ 0 & 0 & 0 & 0 & 0 & 1 \end{bmatrix} \quad 3.11$$

Displacements of the dummy for six independent strain modes are as follows

$$\begin{pmatrix} u_x \\ u_y \\ u_z \\ rot_z \\ rot_x \\ rot_y \end{pmatrix} = \begin{bmatrix} 2a & 0 & 0 & 0 & 0 & 0 \\ 0 & 2a & 0 & 0 & 0 & 0 \\ 0 & 0 & l & 0 & 0 & 0 \\ 0 & 0 & 0 & 2a & 0 & 0 \\ 0 & 0 & 0 & 0 & l & 0 \\ 0 & 0 & 0 & 0 & 0 & l \end{bmatrix} \quad 3.12$$

In other hand, the constitutive relationship is as follows

$$\begin{pmatrix} \sigma_x \\ \sigma_y \\ \sigma_z \\ \tau_{xy} \\ \tau_{yz} \\ \tau_{zx} \end{pmatrix} = [C] \begin{pmatrix} \varepsilon_x \\ \varepsilon_y \\ \varepsilon_z \\ \gamma_{xy} \\ \gamma_{yz} \\ \gamma_{zx} \end{pmatrix} \quad 3.13$$

$$\begin{pmatrix} \varepsilon_x \\ \varepsilon_y \\ \varepsilon_z \\ \gamma_{xy} \\ \gamma_{yz} \\ \gamma_{zx} \end{pmatrix} = [C]^{-1} \begin{pmatrix} \sigma_x \\ \sigma_y \\ \sigma_z \\ \tau_{xy} \\ \tau_{yz} \\ \tau_{zx} \end{pmatrix} \quad 3.14$$

Combining equation 3.11 and 3.12, stiffness matrix $[C]$ is evaluated and inverted stiffness matrix $[C]^{-1}$ is computed.

For the transverse isotropic material,

$$[C]^{-1} = \begin{bmatrix} 1/E_x & -\nu_{yx}/E_y & -\nu_{zx}/E_z & 0 & 0 & 0 \\ -\nu_{xy}/E_x & 1/E_y & -\nu_{zy}/E_z & 0 & 0 & 0 \\ -\nu_{xz}/E_x & -\nu_{yz}/E_y & 1/E_z & 0 & 0 & 0 \\ 0 & 0 & 0 & 1/2G_{yz} & 0 & 0 \\ 0 & 0 & 0 & 0 & 1/2G_{zx} & 0 \\ 0 & 0 & 0 & 0 & 0 & 1/2G_{xy} \end{bmatrix} \quad 3.15$$

Where, $\frac{\nu_{yz}}{E_y} = \frac{\nu_{zy}}{E_z}$, $\frac{\nu_{yx}}{E_y} = \frac{\nu_{xy}}{E_x}$ and $\frac{\nu_{zx}}{E_z} = \frac{\nu_{xz}}{E_x}$

Using equation 3.14, E_x , E_z , ν_{xy} , ν_{zx} , G_{xy} and G_{xz} are determined.

In this thesis, simulations will be conducted with ANSYS software using square representative volume element models. Three metal materials are Iron, copper and aluminum, and three kinds of carbon nanotubes are considered in this thesis. It is assumed that the carbon nanotubes are treated as short and long fiber in the representative volume element. However, the parameterized ANSYS models are developed as the APDL code (script)[134], which are applicable for all cases considered in this thesis.

3.3.5 Materials Properties

There are different kinds of metal matrix used in this research, Iron, Copper and Aluminum. They differ from each other in both structural and mechanical properties. Three kinds of carbon nanotubes based on their chirality index are used as reinforcement. The mechanical and thermal properties of Iron, Copper and Aluminum are listed in tables below.[84, 88, 115]

Table 3.3: The mechanical and thermal properties of the materials used in the research

Property	Metal Matrix			Reinforcement
	Iron (Fe)	Copper (Cu)	Aluminum (Al)	Carbon Nanotube (CNT)
Density (g/cm ³)	7.85	8.96	2.712	1.3
Young's Modulus (E) GPa	210	130	70	1000
Poisson's Ratio (ν)	0.3	0.36	0.33	0.3
Shear Modulus (G) GPa	82	48	26	500
Thermal Conductivity (K) (W/m k) at 68°F	72.7	386	204	~3000

CHAPTER FOUR

ANALYTICAL APPROACH RESULTS AND DISCUSSIONS

4.1 Overview

In this chapter, the theoretical predictions, carbon nanotubes reinforced metal matrix composite having a uniform dispersion of nanotubes is considered and its effective structural and thermal properties are calculated using the theoretical hypothesis in the previous chapters. Analytical calculations will be carried out to determine the effective elastic and thermal properties of carbon nanotubes reinforced metal matrix. The nanotubes are considered to be uniformly dispersed in the metal matrix and only small nanotubes volume fractions have been considered. The expected results of the nanocomposite to be created were carried out using the MATLAB software. Two cases were considered: one case deals with continuous carbon nanotubes and the second case deals with short carbon nanotubes reinforcements at three kind of metal matrices. The obtained results are analyzed to elucidate the contribution of the various factors.

4.2 Prediction of the Nanocomposite Density:

As the volume fraction of the Carbon Nanotubes increase the density of the Carbon Nanotubes reinforced metal matrix Nanocomposite predicted to decrease linearly. Therefore, the larger the amount of Carbon Nanotubes used the lower density of the Nanocomposite is predicted to be. Figure 4.1 shows the density of the Carbon Nanotubes reinforced Copper, Iron and Aluminum matrixes Nanocomposite respectively. It is found that the reduction in the density of the new Nanocomposite varied from 1% to 40% for Copper matrix, 1% to 39% for Iron matrix, and 1% to 24% for Aluminum matrix when the volume fraction of the Carbon Nanotubes increased from 1% to 47%.

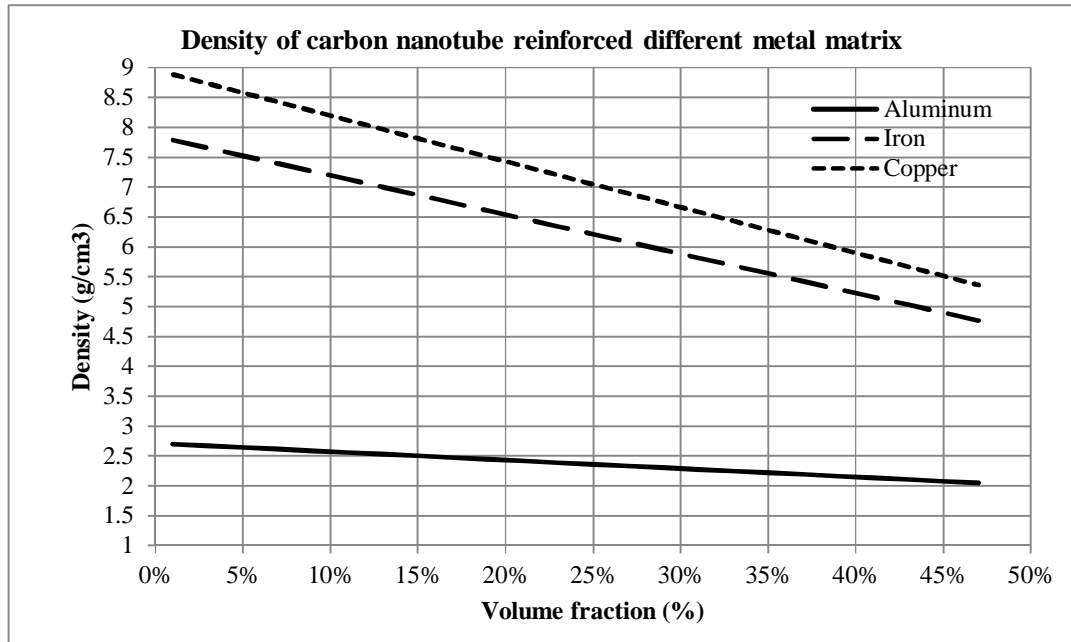


Figure 4.1: Density for carbon nanotube reinforced iron, copper and aluminum metal matrix

4.3 Prediction of the Elastic Properties for Long Fiber

Composite materials categorized into two main groups, the first group comprises composites that are known as matrix. The main feature of these materials is the existence of some basic or matrix material whose properties are improved by filling it with some particles. Usually the matrix volume fraction is more than 50% in such materials [71, 74]. The material properties being naturally modified by the fillers are governed mainly by the matrix. As a rule, filled materials can be treated as homogeneous and isotropic, i.e., traditional models of Mechanics of Materials developed for metals and other conventional materials can be used to describe their behavior. The second group of composite materials which is in the scope of this research involves composites that are called reinforced materials. The basic components of these materials are long and short fibers possessing high strength and stiffness. The fibers are bound with a matrix material whose volume fraction in a composite is usually less than 50% [71, 74].

4.3.1 Prediction of the Young's Modulus

The Young's modulus of the carbon nanotubes reinforced metal matrix Nanocomposite predicted to increase linearly as the volume fraction of the carbon nanotubes increases. Therefore, the higher the carbon nanotubes volume ratio, the better the Young's modulus of the Nanocomposite is predicted. Figure 4.2 shows the effect of

volume fraction on the Young's modulus of the carbon nanotubes reinforced copper, iron and aluminum matrixes nanocomposites, respectively. It was found that the percentage increase in the longitudinal Young's modulus of the new Nanocomposite varied from 20%, 47%, and 74% for Copper matrix, 11%, 26%, and 41% for Iron matrix, and 40%, 93%, and 146% for Aluminum matrix when the volume fraction of the carbon nanotubes increased from 3%, 7%, and 11%.

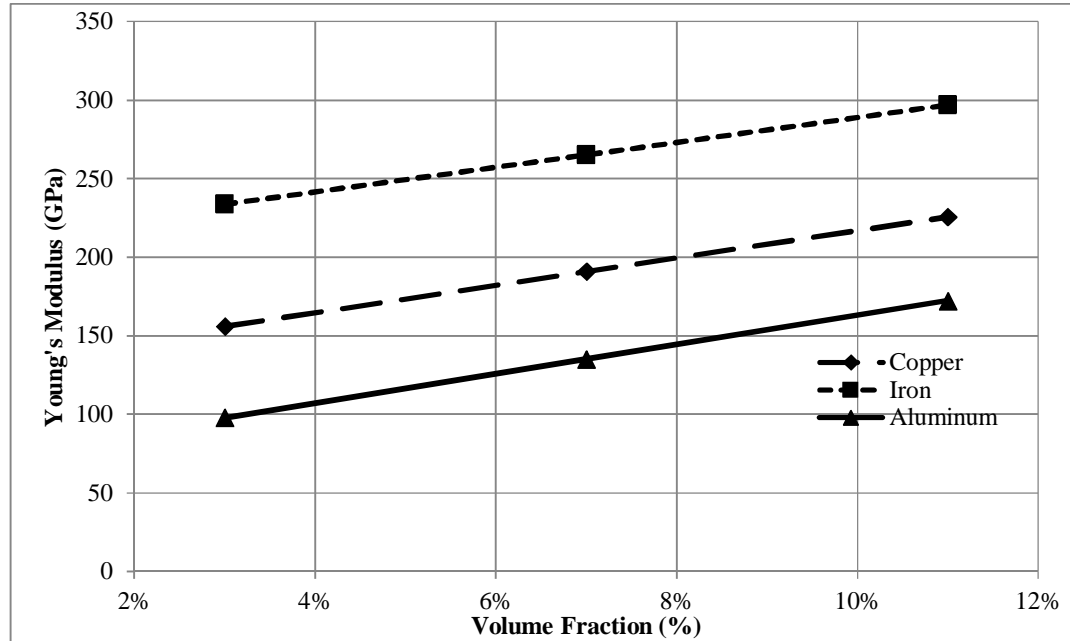


Figure 4.2: Effect of volume fraction on longitudinal Young's modulus for carbon nanotube treated as long fiber reinforced iron, copper and aluminum metal matrix

4.3.2 Prediction of the Transverse Young's Modulus

The Transverse Young's modulus of the carbon nanotubes reinforced metal matrix nanocomposite is predicted to have increasing trend as the volume fraction of the carbon nanotubes increase. Therefore, the higher the carbon nanotubes volume ratio, the higher the transverse Young's modulus of the Nanocomposite is predicted to be. Figure 4.3, shows the effect of volume fraction on the Young's modulus of the carbon nanotubes reinforced copper, iron and aluminum matrixes nanocomposite, respectively. It was found that the percentage increase in the Transverse Young's modulus of the new Nanocomposite varied from 3%, 6%, and 11% for Copper matrix, 2%, 6%, and 10% for Iron matrix, and 3%, 7%, and 11% for Aluminum matrix when the volume fraction of the carbon nanotubes increased from 3%, 7%, and 11%.

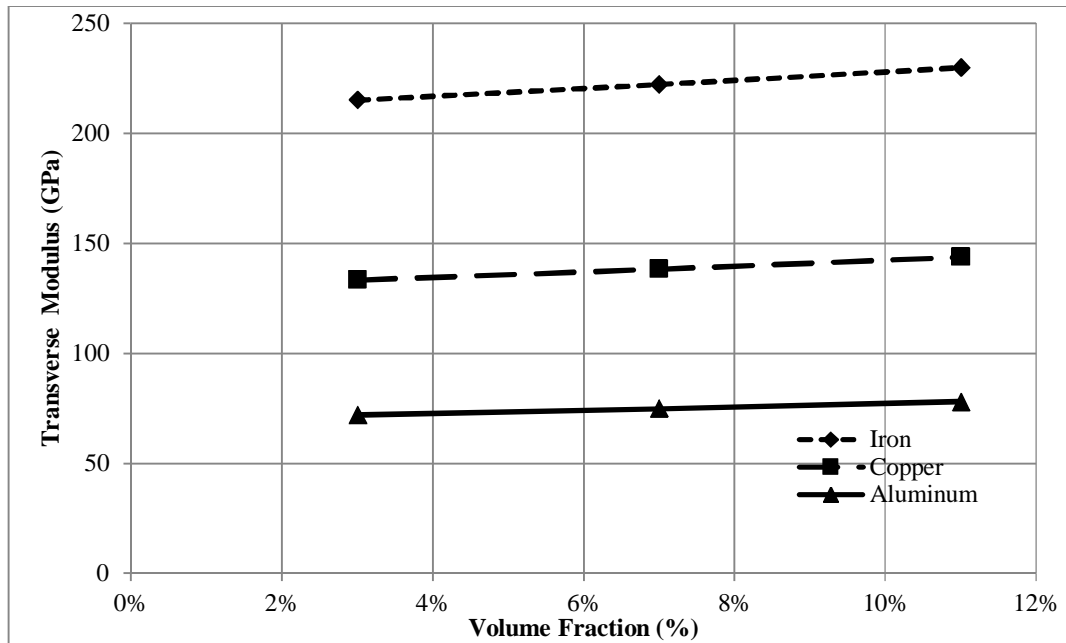


Figure 4.3: Effect of volume fraction on transverse modulus for carbon nanotube treated as long fiber reinforced iron, copper and aluminum metal matrix

4.3.3 Prediction of the Shear Modulus

The shear modulus of the carbon nanotubes reinforced metal matrix nanocomposite is predicted to have increasing trend as the volume fraction of the carbon nanotubes increase. Therefore, the higher the carbon nanotubes volume ratio, the higher the shear modulus of the Nanocomposite is predicted to be. Figure 4.4, shows the effect of volume fraction on the shear modulus of the carbon nanotubes reinforced copper, iron and aluminum matrixes nanocomposite, respectively. It was found that the percentage increase in the shear modulus of the new Nanocomposite varied from 3%, 7%, and 11% for copper matrix, 3%, 6%, and 10% for iron matrix, and 3%, 7%, and 12% for aluminum matrix when the volume fraction of the carbon nanotubes increased from 3%, 7%, and 11%, respectively.

4.3.4 Prediction of the Major Poisson's Ratio

The Major Poisson's Ratio of the Carbon Nanotubes reinforced metal matrix nanocomposite is predicted to have decreasing trend as the volume fraction of the carbon nanotubes increase. Therefore, the higher the carbon nanotubes volume ratio, the lower the major Poisson's ratio of the nanocomposite is predicted to be for Copper and Aluminum matrix.

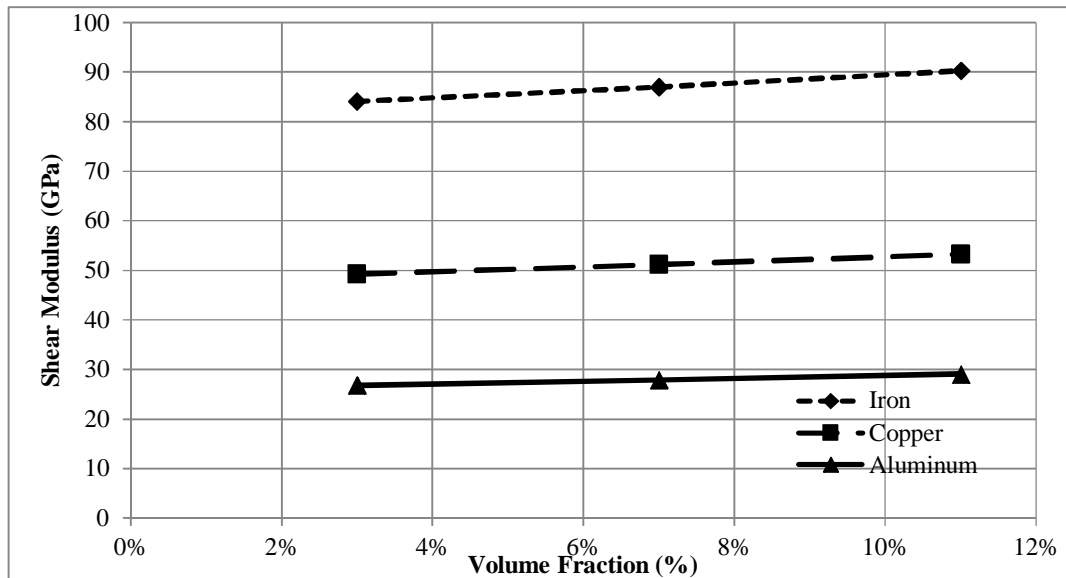


Figure 4.4: Effect of volume fraction on shear modulus for carbon nanotube treated as long fiber reinforced iron, copper and aluminum metal matrix

Figure 4.5 shows the effect of volume fraction on the major Poisson's Ratio of the carbon nanotubes reinforced Copper and Aluminum matrixes nanocomposite, respectively. It was found that the percentage decrease in the major Poisson's ratio of the new nanocomposite varied from 1%, 1%, and 2% for Copper matrix and up 1% for Aluminum matrix when volume fraction of the carbon nanotubes increased from 3%, 7%, and 11%, respectively. However, the prediction of major Poisson's ratio for iron matrix is insensitive with the increase of volume fractions because the matrix and the reinforcement have the same Poisson's ratio value.

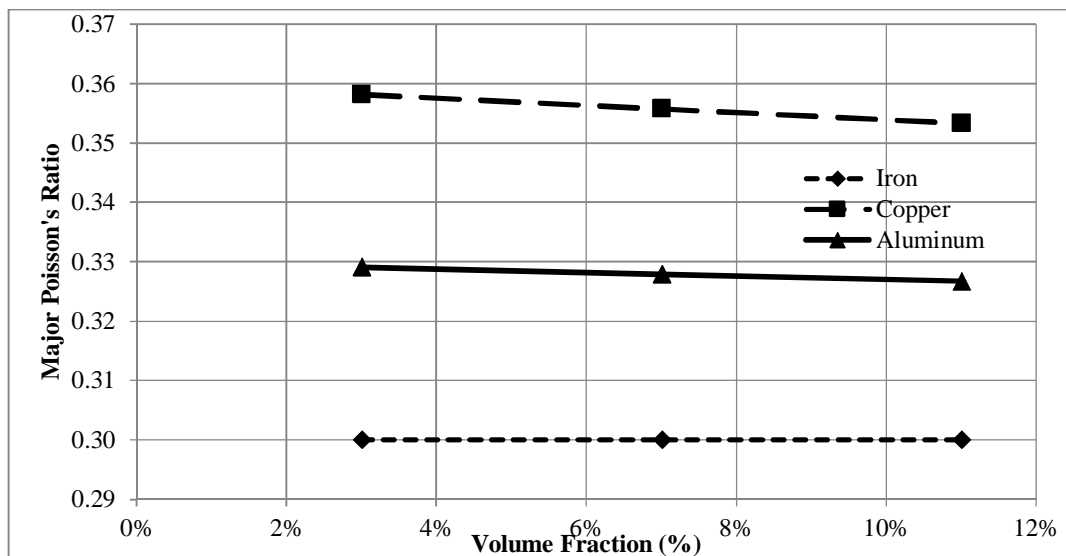


Figure 4.5: Effect of volume fraction on major Poisson's ratio for carbon nanotube treated as long fiber reinforced iron, copper and aluminum metal matrix

4.4 Prediction of the Elastic Properties for Short Fiber

Short fiber reinforced composites can offer some of the property advantages that continuous fiber reinforced composites contain, along with an economical flow processing that favors large-scale production [23]. Using MATLAB, various properties of the Carbon Nanotube reinforced metal matrix Nanocomposite can be predicted. This time discontinuous short Carbon Nanotubes were considered. The “Rule of Mixtures” equation must be modified to make predictions when short fibers are used. The results show lower properties as compared to the continuous fiber case.

4.4.1 Prediction of the Young’s Modulus

The prediction of longitudinal Young’s modulus for the short fiber carbon nanotubes reinforced iron matrix composite will be investigated according to the following factors: varying the length and fixing the diameter and fixing the length with varying the chirality index.

4.4.1.1 Effect of Length

It was observed that the increment percentage in the Young’s modulus of the iron matrix nanocomposite reinforced by 3% volume fraction of zigzag carbon nanotubes (5, 0) varied as 9.2%, 9.9% and 10.4% at carbon nanotubes length increased for 3, 5, and 8 nm, respectively. However, at 3% volume fraction for the armchair carbon nanotubes (5, 5) the increment varied as 8.2%, 9.2% and 9.8% while for chiral carbon nanotubes (5, 10) varied as 7.3%, 8.4%, and 9.2% at the same increment of length, respectively. Figures 4.6, 4.7 and 4.8 show increments of Young’s modulus for iron matrix reinforced by zigzag, armchair and chiral carbon nanotube, respectively when the volume fraction increases.

Similarly the procedure will be taken for the prediction of Young’s modulus for the copper and aluminum matrixes.

For carbon nanotube reinforced copper matrix Nanocomposite, It was observed that the increment percentage in the Young’s modulus of the copper matrix nanocomposite reinforced by 3% volume fraction of zigzag carbon nanotubes (5, 0) varied as 14.4%, 16.1% and 17.4% at carbon nanotubes length increased for 3, 5, and 8 nm, respectively.

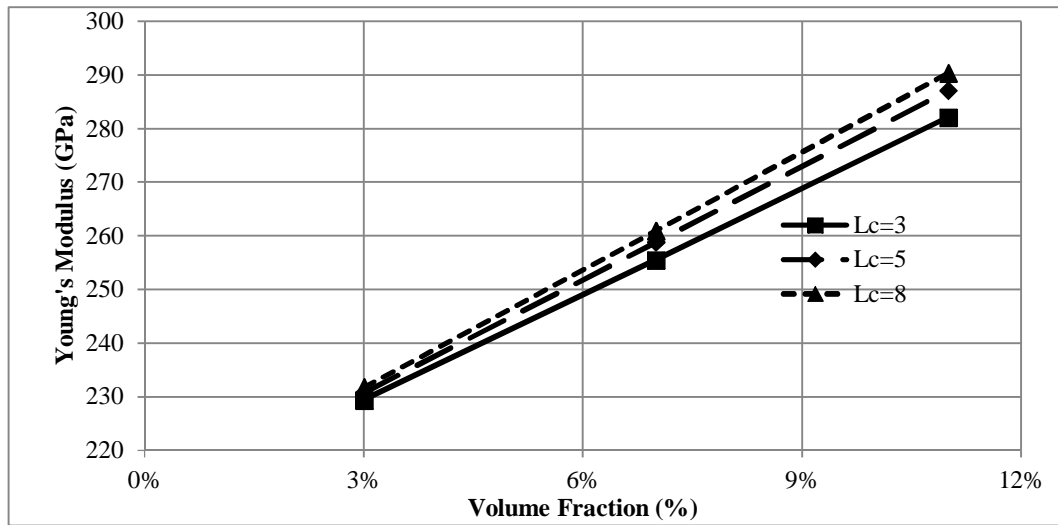


Figure 4.6: Longitudinal Young's modulus for zigzag (5,0) carbon nanotube (different length) reinforced iron metal matrix

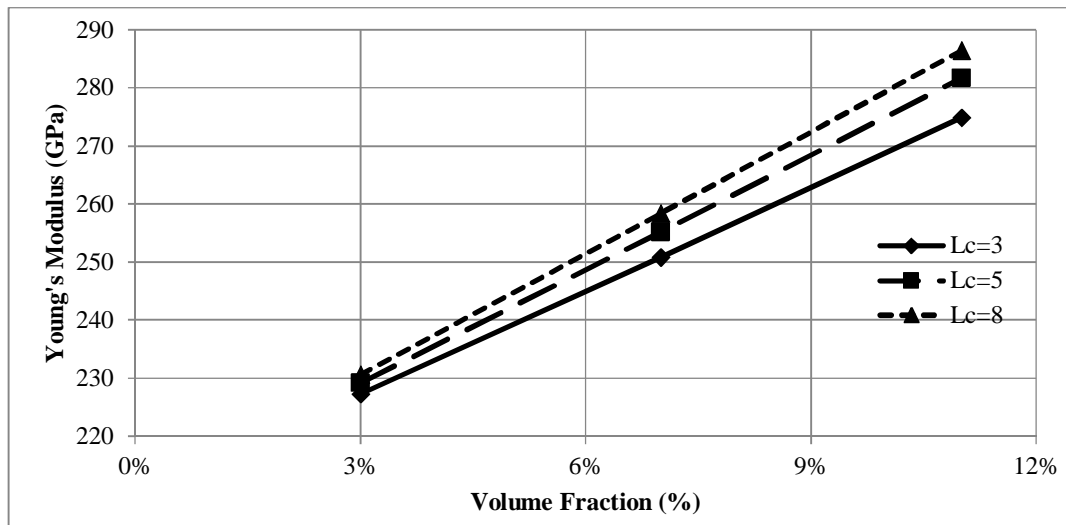


Figure 4.7: Longitudinal Young's modulus for armchair (5,5) carbon nanotube (different length) reinforced iron metal matrix

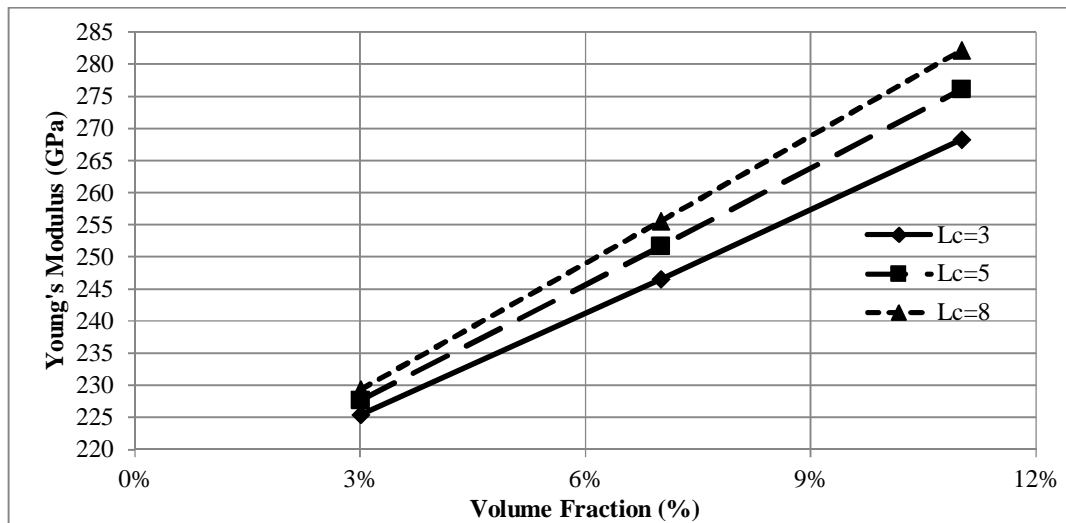


Figure 4.8: Longitudinal Young's modulus for chiral (5,10) carbon nanotube (different length) reinforced iron metal matrix

However, at 3% volume fraction for the armchair carbon nanotubes (5, 5) the increment varied as 12.1%, 14.2% and 15.9% while for chiral carbon nanotubes (5, 10) varied as 10.3%, 12.5%, and 14.4% at the same increment of length, respectively. Figure 4.9, Figure 4.10 and Figure 4.11 show increment of Young's modulus for Iron matrix reinforced by zigzag, armchair and chiral carbon nanotube, respectively when the volume fraction increases.

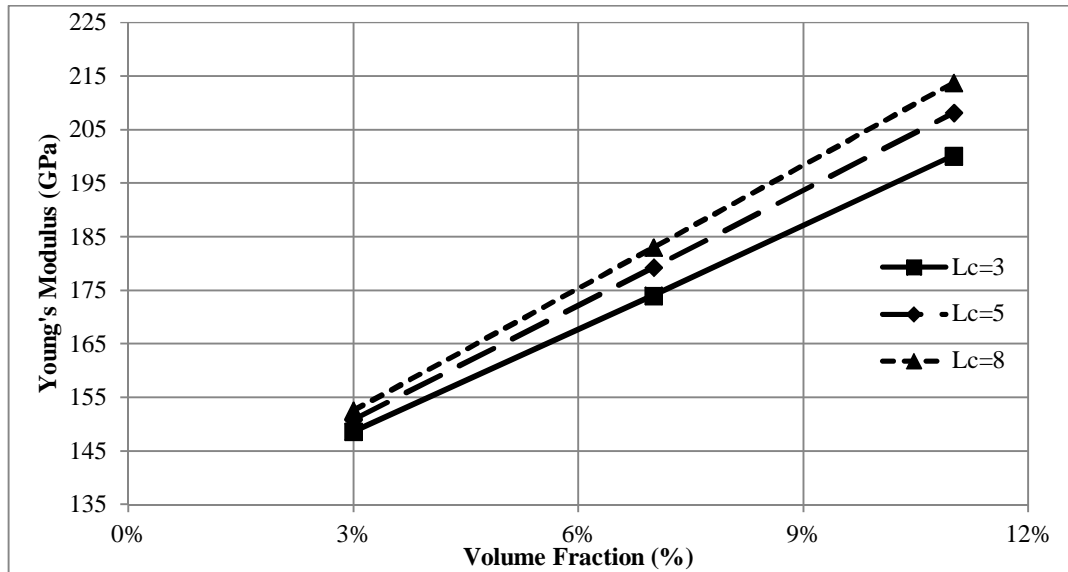


Figure 4.9: Longitudinal Young's modulus for zigzag (5,0) carbon nanotube (different length) reinforced copper metal matrix

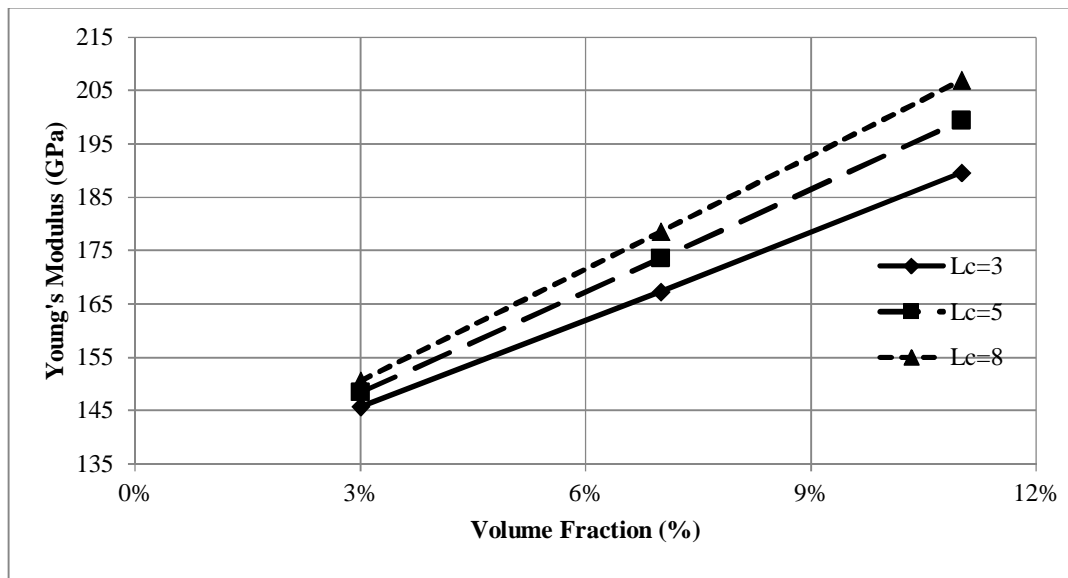


Figure 4.10: Longitudinal Young's modulus for armchair (5,5) carbon nanotube (different length) reinforced copper metal matrix

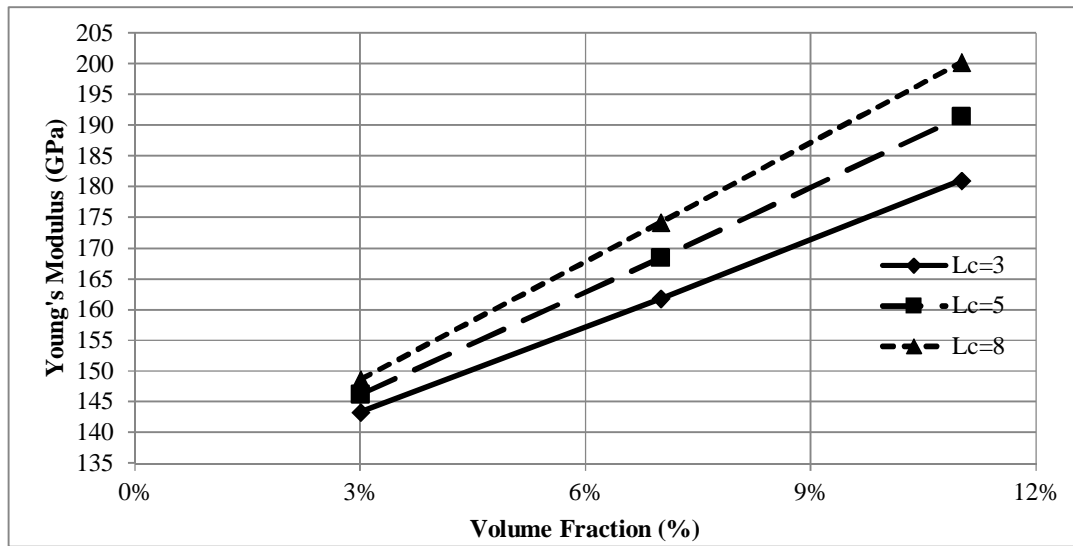


Figure 4.11: Longitudinal Young's modulus for chiral (5,10) carbon nanotube (different length) reinforced copper metal matrix

For carbon nanotube reinforced aluminum matrix Nanocomposite, It was observed that the increment percentage in the Young's modulus of the aluminum matrix nanocomposite reinforced by 3% volume fraction of zigzag carbon nanotubes (5, 0) varied as 22.3%, 26.8% and 30.5% at carbon nanotubes length increased for 3, 5, and 8 nm, respectively. However, at 3% volume fraction for the armchair carbon nanotubes (5, 5) the increment varied as 17.3%, 21.9% and 26.2% while for chiral carbon nanotubes (5, 10) varied as 13.8%, 18%, and 22.3% at the same increment of length, respectively. Figures 4.12, 4.13 and 4.14 show increment of Young's modulus for aluminum matrix reinforced by zigzag, armchair and chiral carbon nanotube, respectively when the volume fraction increases.

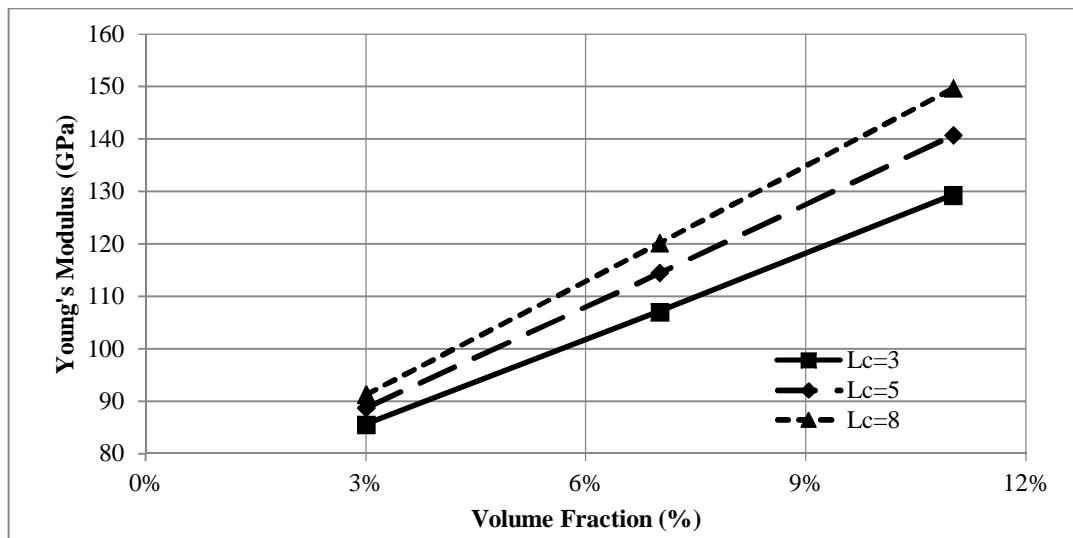


Figure 4.12: Longitudinal Young's modulus for zigzag (5,0) carbon nanotube (different length) reinforced aluminum metal matrix

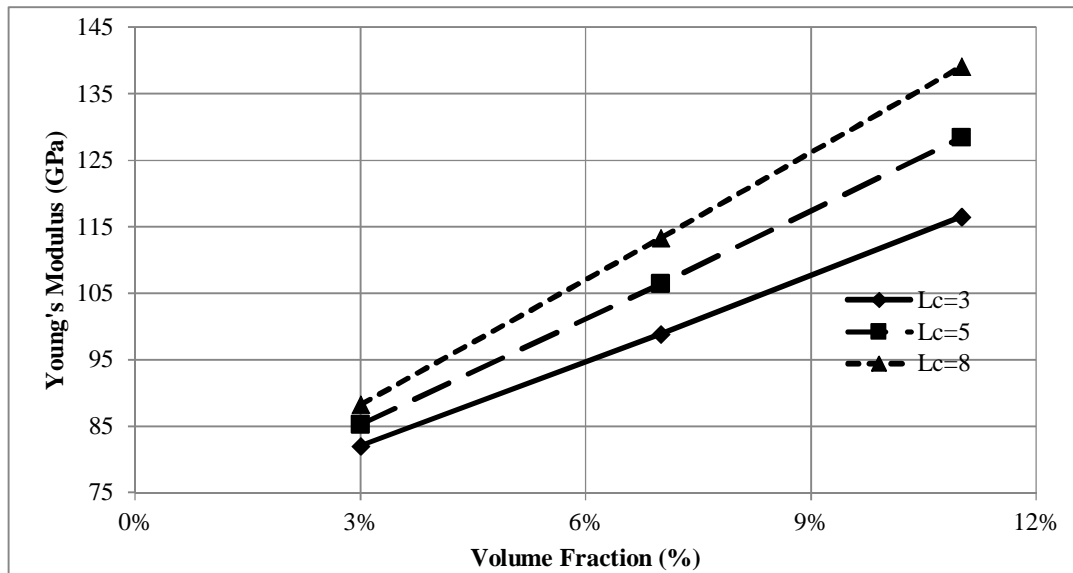


Figure 4.13: Longitudinal Young's modulus for armchair (5,5) carbon nanotube (different length) reinforced aluminum metal matrix

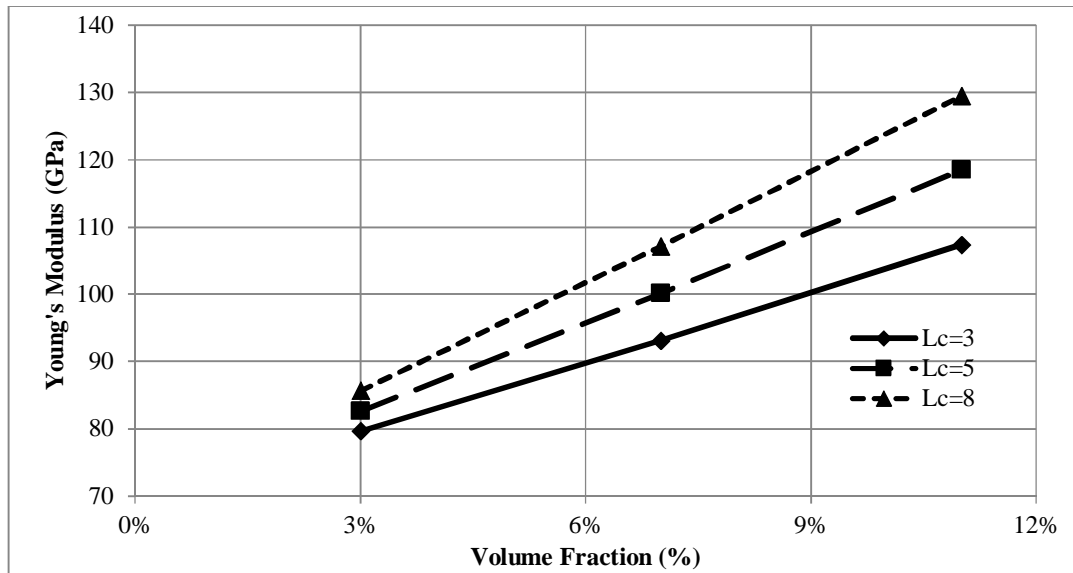


Figure 4.14: Longitudinal Young's modulus for chiral (5,10) carbon nanotube (different length) reinforced aluminum metal matrix

4.4.1.2 Effect of diameter

The analysis will be carried out for the three types of the carbon nanotubes at the same length with different diameters, which can be achieved by changing the index of carbon nanotube for the same kind. It can be observed from Table 4.1 (a) that at 3% volume fraction of carbon nanotube reinforced iron matrix, the value of Young's modulus decreases as the diameter of the armchair carbon nanotubes increases.

Table 4.1: Effect of armchair carbon nanotube diameter on Young's modulus for reinforced: (a) iron, (b) copper, and (c) aluminum matrix

(a) Iron

Carbon Nanotube index	d (nm)	l _c =3nm		l _c =5nm		l _c =8 nm	
		E (GPa)	%	E (GPa)	%	E (GPa)	%
(5,5)	0.848	227.3	8%	229.2	9%	230.6	10%
(10,10)	1.526	224.2	7%	226.5	8%	226.9	8%
(15,15)	2.204	222.3	6%	224.7	7%	226.8	8%

Similarly, the prediction of Young's modulus for the copper and aluminum matrix reinforced by armchair carbon nanotube treated as short fiber are presented in Table 4.1 (b) and (c). It can be observed that at 3% volume fraction of carbon nanotube reinforced copper and aluminum matrix, the value of Young's modulus decreases as the diameter of the armchair carbon nanotubes increases.

(b) Copper

Carbon Nanotube index	d (nm)	l _c =3nm		l _c =5nm		l _c =8 nm	
		E (GPa)	%	E (GPa)	%	E (GPa)	%
(5,5)	0.848	145.7	12%	148.5	14%	150.7	16%
(10,10)	1.526	141.9	9%	144.7	11%	145.8	12%
(15,15)	2.204	139.9	8%	142.4	10%	145.1	12%

(c) Aluminum

Carbon Nanotube index	d (nm)	l _c =3nm		l _c =5nm		l _c =8 nm	
		E (GPa)	%	E (GPa)	%	E (GPa)	%
(5,5)	0.848	82.1	17%	85.3	22%	88.3	26%
(10,10)	1.526	78.3	12%	81.0	16%	82.6	18%
(15,15)	2.204	76.5	9%	78.8	13%	81.4	16%

For zigzag carbon nanotubes reinforced iron metal matrix at same length with different diameters, Table 4.2 (a) presents the results calculated at 3% of volume fraction for Iron metal matrix reinforced by zigzag carbon nanotube type. The results show that the value of Young's modulus decreases as diameter of the zigzag carbon nanotubes increases.

Table 4.2: Effect of zigzag carbon nanotube diameter on Young's modulus for reinforced: (a) iron, (b) copper, and (c) aluminum matrix

(a) Iron

Carbon Nanotube index	d (nm)	l _c =3nm		l _c =5nm		l _c =8 nm	
		E (GPa)	%	E (GPa)	%	E (GPa)	%
(5,0)	0.561	229.4	9%	230.8	10%	231.8	10%
(10,0)	0.953	226.7	8%	228.7	9%	230.3	10%
(15,0)	1.344	224.8	7%	227.1	8%	229.0	9%

Similarly, the prediction of Young's modulus for the copper and aluminum matrix reinforced by zigzag carbon nanotube treated as short fiber are presented in Table 4.2 (b) and (c). It can be observed that at 3% volume fraction of carbon nanotube reinforced copper and aluminum matrix, the value of Young's modulus decreases as the diameter of the zigzag carbon nanotubes increases.

(b) Copper

Carbon Nanotube index	d (nm)	l _c =3nm		l _c =5nm		l _c =8 nm	
		E (GPa)	%	E (GPa)	%	E (GPa)	%
(5,0)	0.561	148.7	14%	151.0	16%	152.6	17%
(10,0)	0.953	144.9	11%	147.7	14%	150.0	15%
(15,0)	1.344	142.7	10%	145.5	12%	148.1	14%

(c) Aluminum

Carbon Nanotube index	d (nm)	l _c =3nm		l _c =5nm		l _c =8 nm	
		E (GPa)	%	E (GPa)	%	E (GPa)	%
(5,0)	0.561	85.6	22%	88.8	27%	91.3	30%
(10,0)	0.953	81.2	16%	84.4	21%	87.4	25%
(15,0)	1.344	79.0	13%	81.9	17%	84.8	21%

For chiral carbon nanotubes reinforced iron metal matrix at same length with different diameters, Table 4.3 (a) presents the results calculated at 3% of volume fraction for iron metal matrix reinforced by chiral carbon nanotube type. The results show that the value of Young's modulus decreases as the diameter of the chiral carbon nanotubes increases.

Table 4.3: Effect of chiral carbon nanotube diameter on Young's modulus for reinforced: (a) iron, (b) copper, and (c) aluminum matrix

(a) Iron

Carbon Nanotube Index	d (nm)	l _c =3nm		l _c =5nm		l _c =8 nm	
		E (GPa)	%	E (GPa)	%	E (GPa)	%
(5,10)	1.206	225.4	7%	227.7	8%	229.4	9%
(10,15)	1.876	223.1	6%	225.5	7%	227.5	8%
(15,20)	2.551	221.6	6%	223.9	7%	226.1	8%

Similarly, the prediction of Young's modulus for the copper and aluminum matrix reinforced by chiral carbon nanotube treated as short fiber are presented in Table 4.3 (b) and (c). It can be observed that at 3% volume fraction of carbon nanotube reinforced copper and aluminum matrix, the value of Young's modulus decreases as the diameter of the chiral carbon nanotubes increases.

(b) Copper

Carbon Nanotube Index	d (nm)	l _c =3nm		l _c =5nm		l _c =8 nm	
		E (GPa)	%	E (GPa)	%	E (GPa)	%
(5,10)	1.206	143.3	10%	146.2	12%	148.7	14%
(10,15)	1.876	140.7	8%	143.4	10%	146.1	12%
(15,20)	2.551	139.2	7%	141.6	9%	144.2	11%

(c) Aluminum

Carbon Nanotube Index	d (nm)	l _c =3nm		l _c =5nm		l _c =8 nm	
		E (GPa)	%	E (GPa)	%	E (GPa)	%
(5,10)	1.206	79.6	14%	82.6	18%	85.6	22%
(10,15)	1.876	77.2	10%	79.7	14%	82.4	18%
(15,20)	2.551	76.0	9%	78.0	11%	80.5	15%

4.4.1.3 Effect of chirality Index

To study the effect of chirality index, the analysis is carried out for armchair (5, 5), zigzag (5, 0) and chiral (5, 10) carbon nanotubes at the same length. It can be observed from Table 4.4 that at 3% volume fraction of carbon nanotube reinforced iron matrix, the value of Young's modulus for zigzag type is the highest, while for chiral type is the lowest because changing the chirality index will change the diameter. However, Figures 4.15, 4.16, and 4.17 shows that the Young's modulus increases as the volume fraction and the length increases and decreases when the carbon nanotube chirality index is changed from zigzag to chiral type, i.e. it decreases with the increase of diameter.

Table 4.4: Effect of chiral index on the Young's modulus of iron matrix (V_f=3%)

Carbon Nanotube index	d (nm)	l _c =3nm		l _c =5nm		l _c =8 nm	
		E (GPa)	%	E (GPa)	%	E (GPa)	%
Armchair (5,5)	0.848	227.3	8%	229.2	9%	230.6	10%
Zigzag (5,0)	0.561	229.4	9%	230.8	10%	231.8	10%
Chiral (5,10)	1.206	225.4	7%	227.7	8%	229.4	9%

Similarly the procedure will be taken for the prediction of Young's modulus for the copper and aluminum matrixes reinforced by armchair carbon nanotube type.

For carbon nanotube reinforced copper matrix Nanocomposite, it can be observed from Table 4.5 that at 3% volume fraction of carbon nanotube reinforced copper matrix, the value of Young's modulus for zigzag type is the highest, while for chiral type is the lowest because changing the chirality index will change the diameter.

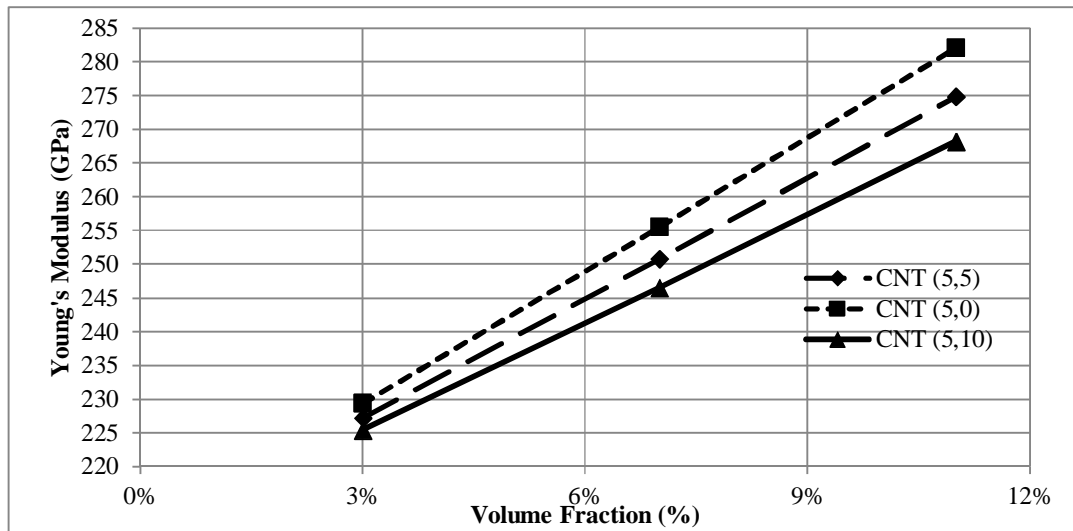


Figure 4.15: Longitudinal Young's modulus for different chiral index carbon nanotube (at length $l_c=3$ nm) reinforced iron metal matrix

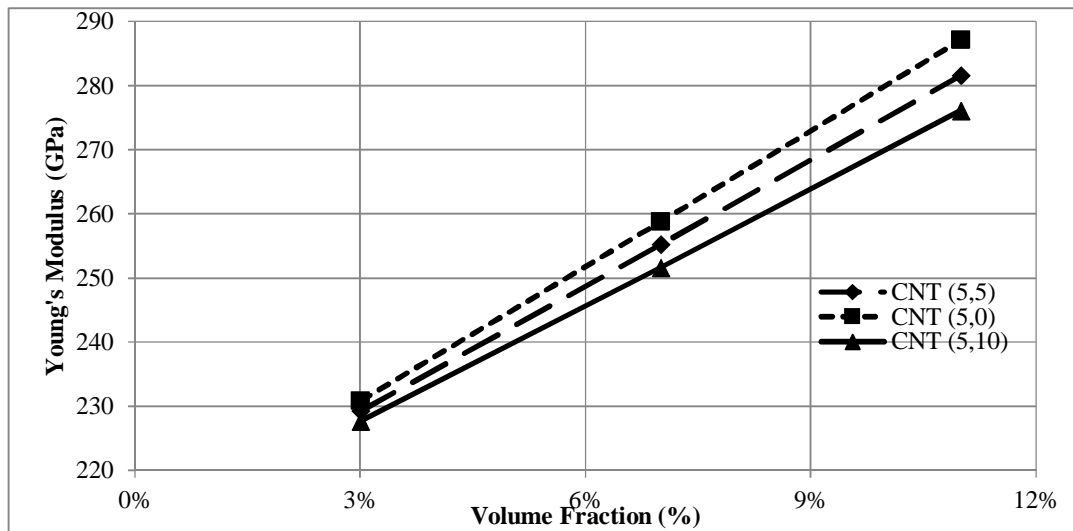


Figure 4.16: Longitudinal Young's modulus for different chiral index carbon nanotube (at length $l_c=5$ nm) reinforced iron metal matrix

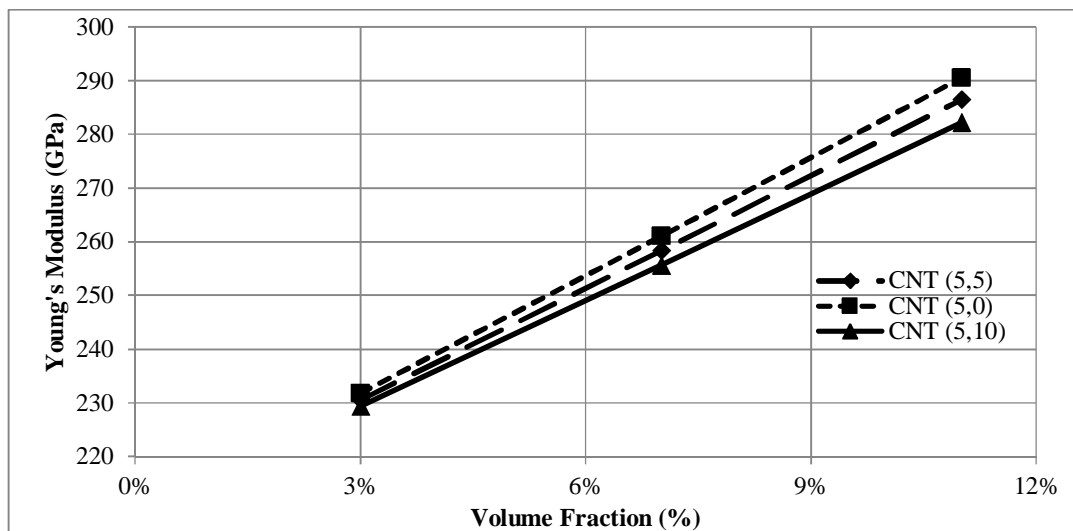


Figure 4.17: Longitudinal Young's modulus for different chiral index carbon nanotube (at length $l_c=8$ nm) reinforced iron metal matrix

However, Figures 4.18, 4.19, and 4.20 show that the Young's modulus increases as the volume fraction and the length are increased and decreases when the carbon nanotube chirality index is changed from zigzag to chiral type, i.e. it decreases with the increase of diameter.

Table 4.5: Effect of chiral index on the Young's modulus of copper matrix (Vf=3%)

Carbon Nanotube index	d (nm)	l _c =3nm		l _c =5nm		l _c =8 nm	
		E (GPa)	%	E (GPa)	%	E (GPa)	%
Armchair (5,5)	0.848	145.7	12%	148.5	14%	150.7	16%
Zigzag (5,0)	0.561	148.7	14%	151.0	16%	152.6	17%
Chiral (5,10)	1.206	143.3	10%	146.2	12%	148.7	14%

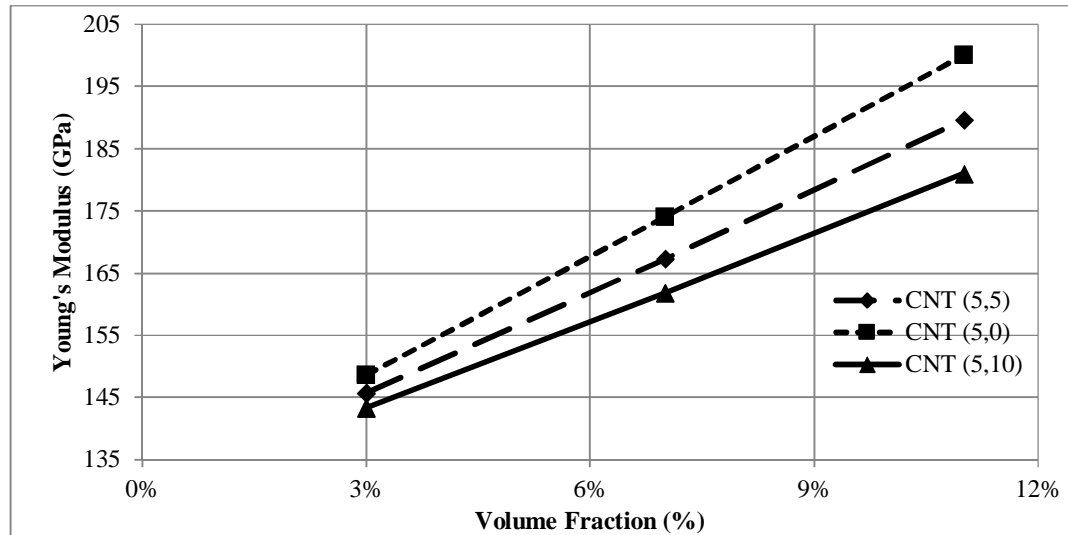


Figure 4.18: Longitudinal Young's modulus for different chiral index carbon nanotube (length l_c=3 nm) reinforced copper metal matrix

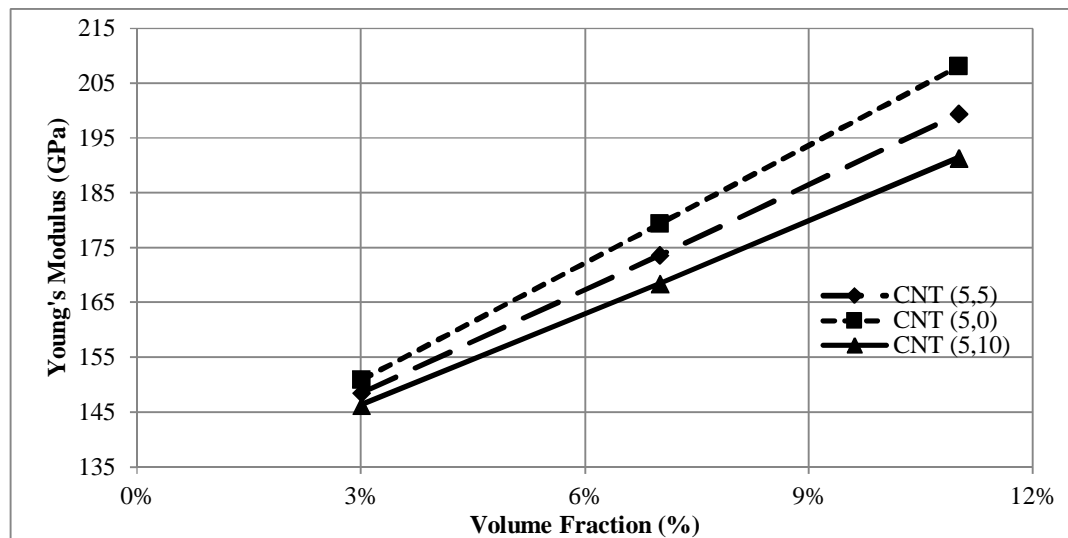


Figure 4.19: Longitudinal Young's modulus for different chiral index carbon nanotube (at length l_c=5 nm) reinforced copper metal matrix

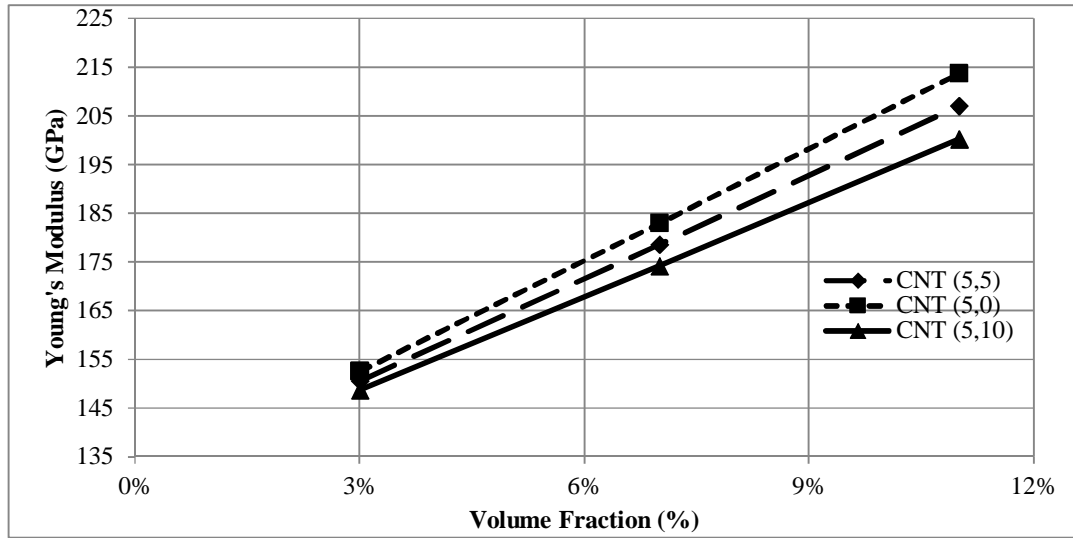


Figure 4.20: Longitudinal Young's modulus for different chiral index carbon nanotube (at length $l_c=8$ nm) reinforced copper metal matrix

Similarly, the results for carbon nanotube reinforced aluminum matrix Nanocomposite as presented in Table 4.6 show that, at 3% volume fraction of carbon nanotube reinforced aluminum matrix, the value of Young's modulus for zigzag type is the highest, while for chiral type is the lowest because changing the chirality index will change the diameter. However, Figures 4.21, 4.22, and 4.23 show that the Young's modulus increases when the volume fraction and the length are increased and decreases when the carbon nanotube chirality index is changed from zigzag to chiral type, i.e. it decreases with the increase of diameter.

Table 4.6: Effect of chiral index on the Young's modulus of aluminum matrix ($V_f=3\%$)

Carbon Nanotube index	d (nm)	$l_c = 3\text{nm}$		$l_c = 5\text{nm}$		$l_c = 8\text{ nm}$	
		E (GPa)	%	E (GPa)	%	E (GPa)	%
Armchair (5,5)	0.848	82.1	17%	85.3	22%	88.3	26%
Zigzag (5,0)	0.561	85.6	22%	88.8	27%	91.3	30%
Chiral (5,10)	1.206	79.6	14%	82.6	18%	85.6	22%

4.4.2 Prediction of the Transverse Young's Modulus

The transverse modulus of iron matrix reinforced with armchair, zigzag, and chiral carbon nanotube treated as short fiber results were presented in Table 4.7 (a), (b), and (c) respectively.

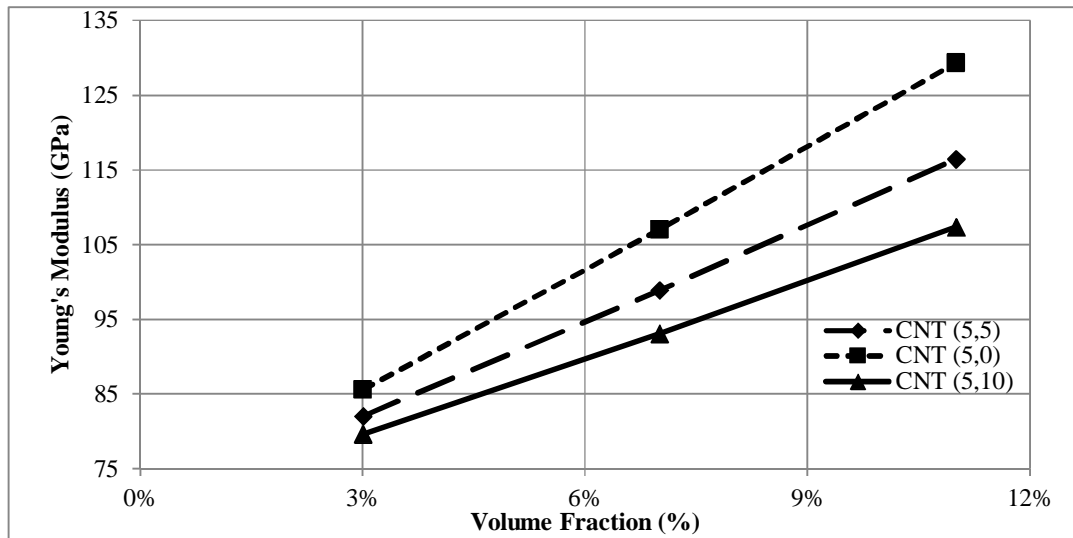


Figure 4.21: Longitudinal Young's modulus for different chiral index carbon nanotube (at length $l_c=3\text{nm}$) reinforced aluminum metal matrix

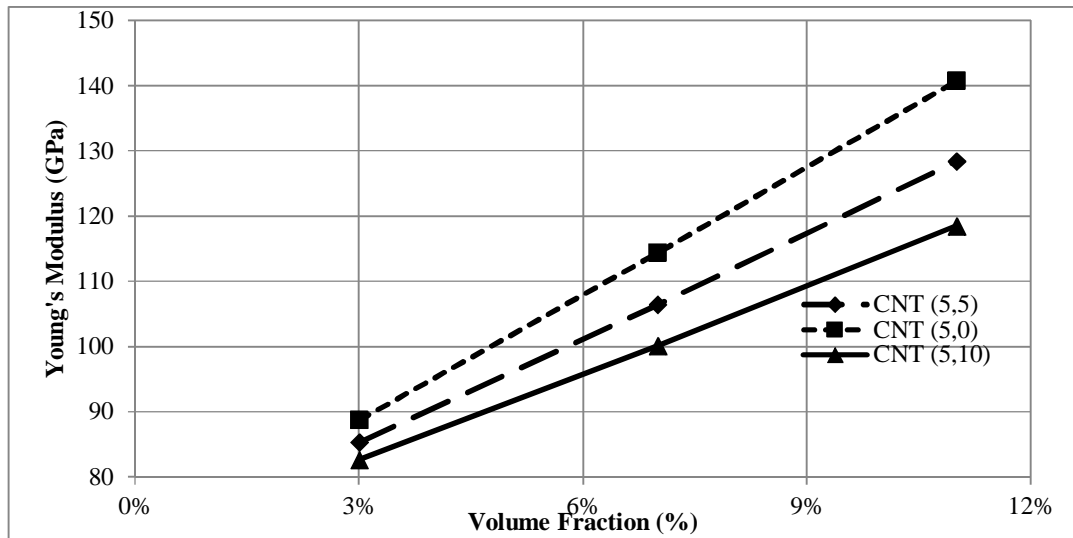


Figure 4.22: Longitudinal Young's modulus for different chiral index carbon nanotube (length $l_c=5\text{nm}$) reinforced aluminum metal matrix

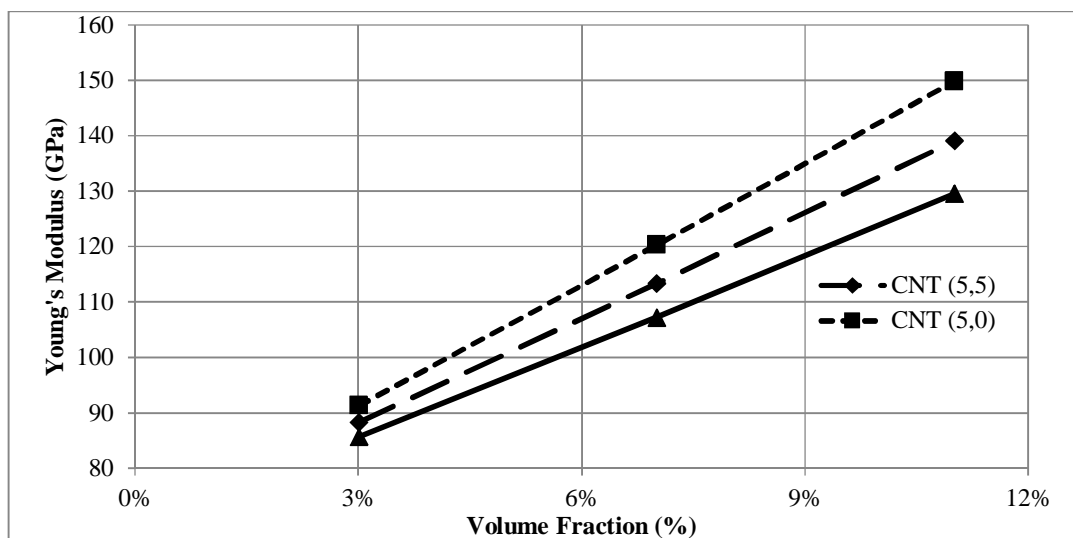


Figure 4.23: Longitudinal Young's modulus for different chiral index carbon nanotube (length $l_c=8\text{nm}$) reinforced aluminum metal matrix

However, Table 4.8 (a), (b), and (c) presented the results for copper matrix reinforced with different chiral index of carbon nanotube while Table 4.9(a), (b), and (c) presented the results for aluminum matrix reinforced with different chiral index of carbon nanotube. The results show increment with respect to the matrix transverse modulus when the carbon nanotube volume fraction and/or length increased. Figures 4.24, 4.25, and 4.26 show the prediction results of transverse modulus of carbon nanotubes reinforced iron, copper, and aluminum metal matrix nanocomposite, respectively.

Table 4.7: Transverse modulus prediction for (a) armchair, (b) zigzag, and (c) chiral carbon nanotubes reinforced iron metal matrix

(a) Armchair

V_f	$l_c = 3\text{nm}$		$l_c = 5\text{nm}$		$l_c = 8\text{ nm}$	
	E_T (GPa)	%	E_T (GPa)	%	E_T (GPa)	%
3%	214.97	2%	216.31	3%	217.26	3%
7%	217.79	4%	218.74	4%	219.85	5%
11%	220.45	5%	222.41	6%	223.80	7%

(b) Zigzag

V_f	$l_c = 3\text{nm}$		$l_c = 5\text{nm}$		$l_c = 8\text{ nm}$	
	E_T (GPa)	%	E_T (GPa)	%	E_T (GPa)	%
3%	216.31	3%	218.69	4%	219.09	4%
7%	219.02	4%	219.76	5%	220.43	5%
11%	222.70	6%	224.22	7%	225.03	7%

(c) Chiral

V_f	$l_c = 3\text{nm}$		$l_c = 5\text{nm}$		$l_c = 8\text{ nm}$	
	E_T (GPa)	%	E_T (GPa)	%	E_T (GPa)	%
3%	214.29	2%	214.29	2%	215.15	2%
7%	216.90	3%	218.20	4%	218.73	4%
11%	219.69	5%	221.08	5%	221.86	6%

Table 4.8: Transverse modulus prediction for (a) armchair, (b) zigzag, and (c) chiral carbon nanotubes reinforced copper metal matrix

(a) Armchair

V_f	$l_c = 3\text{nm}$		$l_c = 5\text{nm}$		$l_c = 8\text{ nm}$	
	E_T (GPa)	%	E_T (GPa)	%	E_T (GPa)	%
3%	136.32	3%	134.41	3%	135.16	4%
7%	138.23	4%	136.58	5%	137.32	6%
11%	141.41	6%	139.78	8%	140.67	8%

(b) Zigzag

V_f	$l_c = 3\text{nm}$		$l_c = 5\text{nm}$		$l_c = 8\text{ nm}$	
	E_T (GPa)	%	E_T (GPa)	%	E_T (GPa)	%
3%	134.79	4%	135.45	4%	136.32	5%
7%	136.24	5%	137.48	6%	138.23	6%
11%	139.73	7%	140.76	8%	141.41	9%

(c) Chiral

V_f	$l_c = 3\text{nm}$		$l_c = 5\text{nm}$		$l_c = 8\text{ nm}$	
	E_T (GPa)	%	E_T (GPa)	%	E_T (GPa)	%
3%	132.69	2%	134.00	3%	134.75	4%
7%	134.03	3%	135.51	4%	136.82	5%
11%	136.46	5%	137.38	6%	138.62	7%

Table 4.9: Transverse modulus prediction for for (a) armchair, (b) zigzag, and (c) chiral carbon nanotubes reinforced aluminum metal matrix**(a) Armchair**

V_f	$l_c = 3\text{nm}$		$l_c = 5\text{nm}$		$l_c = 8\text{ nm}$	
	E_T (GPa)	%	E_T (GPa)	%	E_T (GPa)	%
3%	74.93	5%	74.39	6%	75.02	7%
7%	75.77	7%	75.13	7%	76.06	9%
11%	76.53	9%	76.19	9%	77.19	10%

(b) Zigzag

V_f	$l_c = 3\text{nm}$		$l_c = 5\text{nm}$		$l_c = 8\text{ nm}$	
	E_T (GPa)	%	E_T (GPa)	%	E_T (GPa)	%
3%	74.00	6%	74.93	7%	75.54	8%
7%	75.49	8%	75.77	8%	76.82	10%
11%	76.30	9%	76.53	9%	77.44	11%

(c) Chiral

V_f	$l_c = 3\text{nm}$		$l_c = 5\text{nm}$		$l_c = 8\text{ nm}$	
	E_T (GPa)	%	E_T (GPa)	%	E_T (GPa)	%
3%	73.44	5%	74.07	6%	74.59	7%
7%	74.12	6%	74.76	7%	75.28	8%
11%	75.54	8%	75.84	8%	76.23	9%

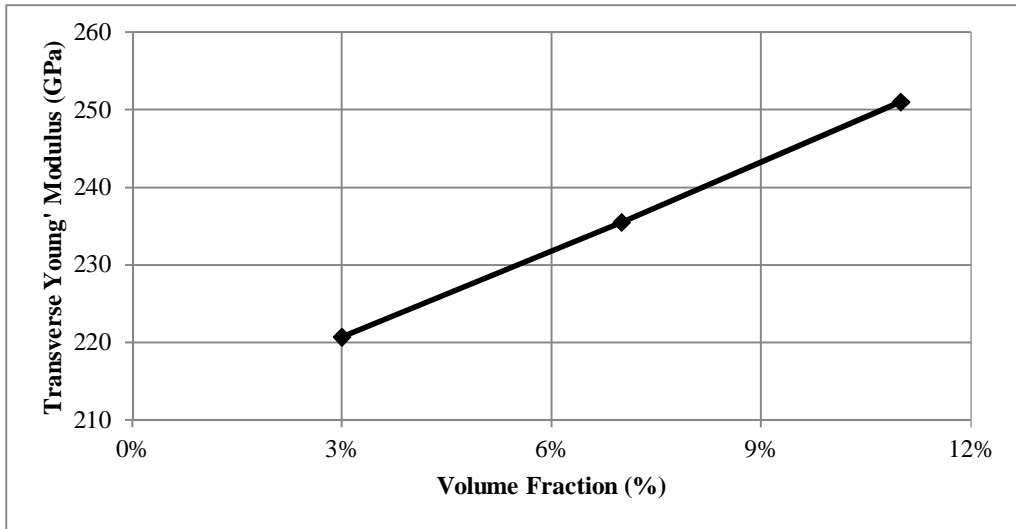


Figure 4.24: Transverse Young's modulus for carbon nanotube as short fiber reinforced iron metal matrix

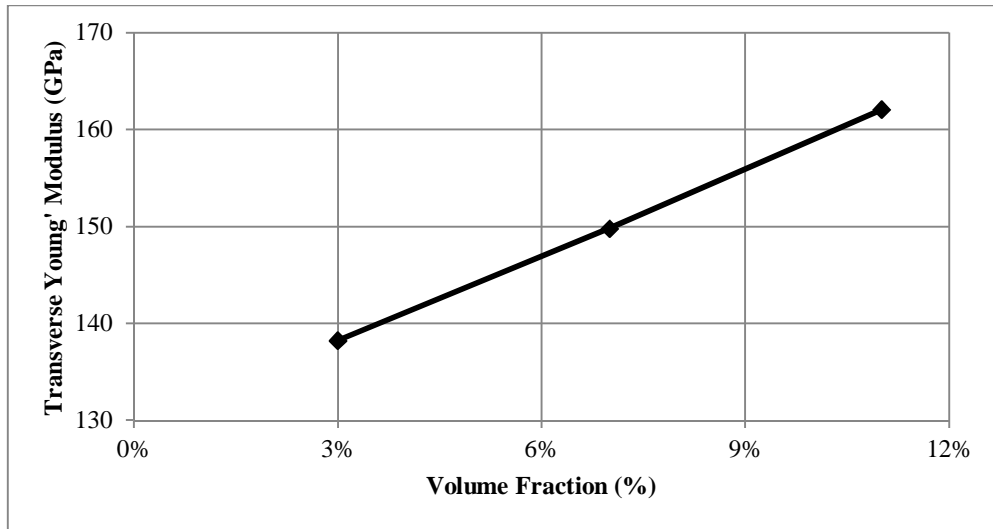


Figure 4.25: Transverse Young's modulus for carbon nanotube as short fiber reinforced copper metal matrix

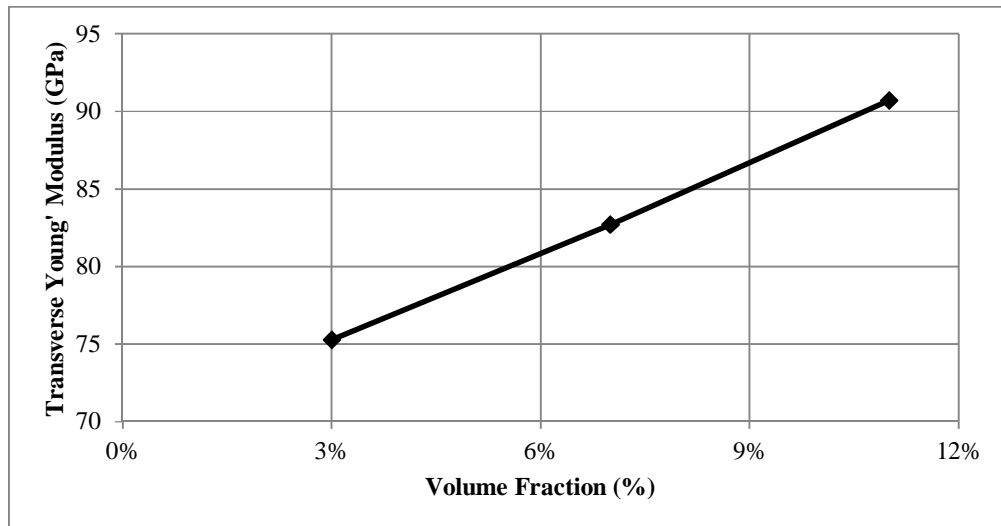


Figure 4.26: Transverse Young's modulus for carbon nanotube as short fiber reinforced aluminum metal matrix

4.4.3 Prediction of the shear modulus

The shear modulus of carbon nanotube treated as short fiber to reinforce Iron matrix results show a reduction of its value with respect to the matrix value. At 3% volume fraction of carbon nanotube, the shear modulus value was about 49 GPa which is about 40% less than the iron matrix shear modulus while for copper matrix reinforced by the same volume fraction of nanotubes, the value was 27 GPa which is about 43% less than copper matrix shear modulus. However, for aluminum matrix reinforced by the same volume of carbon nanotubes indicates 14 GPa which is about 45% less than that of Aluminum matrix as shown in Figures 4.27, 4.28, and 4.29 respectively, this reduction decreases as the volume fraction increases. The results show that the prediction of the shear modulus is insensitive to the change in length or diameter, the shear modulus depends on the ratio between the values of fiber to matrix shear modulus.

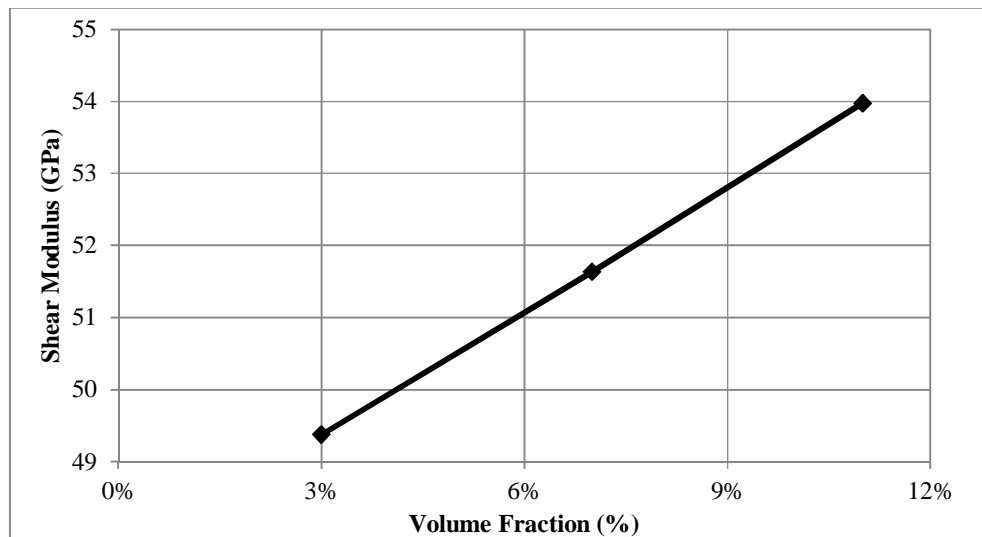


Figure 4.27: Shear modulus for carbon nanotube (as short fiber) reinforced iron matrix

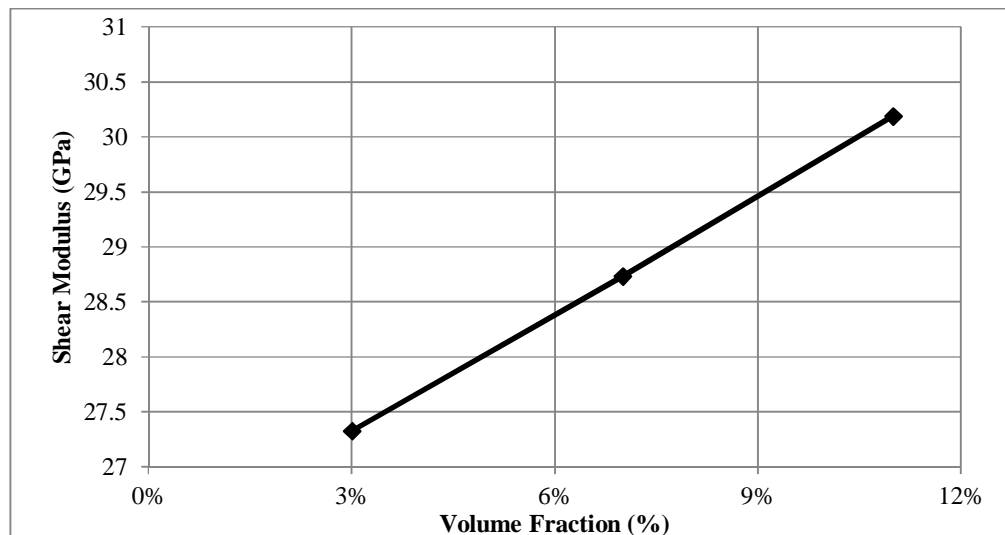


Figure 4.28: Shear modulus for carbon nanotube (as short fiber) reinforced copper matrix

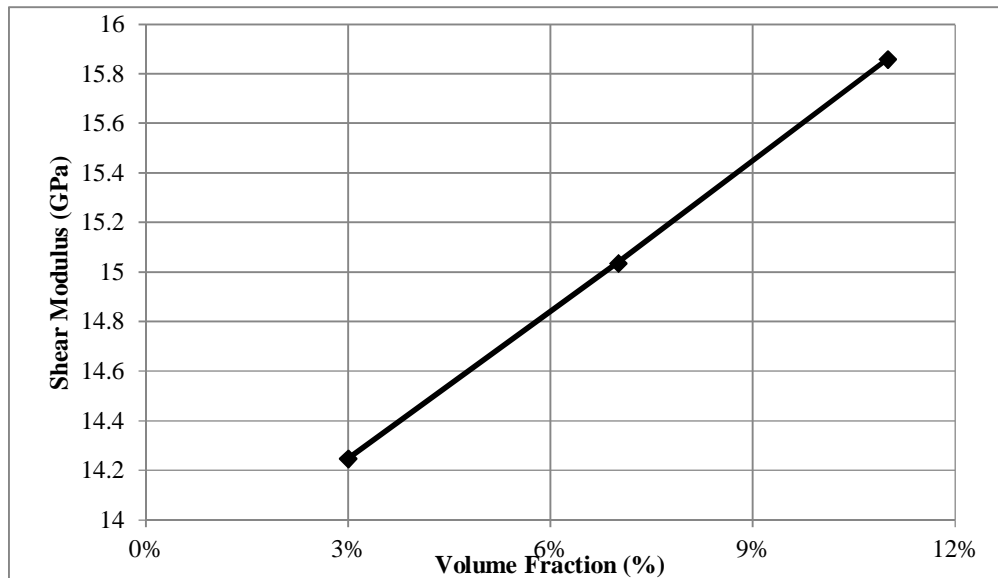


Figure 4.29: Shear modulus for carbon nanotube (as short fiber) reinforced aluminum matrix

4.5 Prediction of the Thermal conductivity

The numerical calculations will be carried out to determine the effective longitudinal conductivity of carbon nanotubes reinforced metal matrix. The nanotubes are considered to be uniformly dispersed in the metal matrix and only small nanotubes volume fractions have been considered. The necessary calculations have been carried out using the MATLAB software.

The created code has been used to solve the linear differential equations and to calculate the various constants involved in equation 2.92 for the thermal conductivity. The effective thermal conductivity is calculated by varying the length of carbon nanotubes and keeping the diameter constant, *i.e.* varying the aspect ratio with fixed diameter. For a fixed aspect ratio, the interface conductance is varied and the theoretical behavior is studied. Dependence of the thermal conductivity on the volume fraction is studied by keeping the aspect ratio constant and varying the volume fraction of the carbon nanotubes in the composite.

Thus, to determine the effective thermal conductivity, the quantities ζ_0 , λ and $\bar{\beta}$ need to be calculated from the geometry and materials properties of the carbon nanotubes and the metal matrix.

4.5.1 Prediction of the thermal conductivity of carbon nanotubes reinforced metal matrix nanocomposite

To determine the effective thermal conductivity of aluminum in the axial direction for the models used in this research, Table 4.10 shows the input parameters used to carry out the calculations. The same approach will be used to determine the values of effective thermal conductivity of reinforcing the copper and iron matrices.

Table 4.10: The input for calculating the thermal conductivity for carbon nanotube reinforced aluminum matrix

Description	Symbol	Units	Value
Average nanotubes diameter	d_{mean}	nanometer	0.678
The outer diameter	d_0	nanometer	0.848
The inner diameter	d_i	nanometer	0.508
Average nanotubes length	l	nanometer	10
Conductivity of the metal matrix	$k^{(1)}$	W/m-K	204
Conductivity of carbon nanotubes	k_{CNT}	W/m-K	3000
Interfacial Conductance	β	MW/m ² K	12
Thickness of the carbon nanotubes	t	nanometer	0.34
Conductivity of the effective fiber	$k^{(2)}$	W/m-K	Calculated

The parameters ζ_0 and c can be obtained from equation 2.94 and 2.98 by using the above data respectively, as $\zeta_0 = 1.002306$ and $c = 4.988495$ nm. Hence, the value of the function $f(\zeta_0)$ can be obtained from equation 2.93. Thus, the effective fiber Conductivity $k^{(2)}$ can be calculated from equation 2.91 and it found to be 1923.3936 W/mK, The results show that the conductivity of the effective fiber is much lower than the intrinsic conductivity of a carbon nanotubes. This is due to the fact that only the outer nanotubes layer has been assumed to be involved in the conduction of heat through the nanotubes. This assumption yields the correct value for the composite overall conductivity and hence this is a vital aspect of heat conduction in carbon nanotubes reinforced composites which needs to be considered carefully. For carbon nanotube reinforced aluminum matrix, the value of λ is obtained from equation 2.95 as $\lambda = 9.4284$. The value of β is taken to be 12 MW/m²K. This value of the interfacial conductance was determined using molecular dynamics simulations for a nanotubes suspension in an organic fluid [87]. This seems to be the only published value available

for this parameter and hence it will be used in the calculations here. Thus the value of $\bar{\beta}$ is obtained from equation 2.140 as $\bar{\beta} = 293.441$

The value of the constant B1 could be evaluated from equation 2.96, B1 is obtained as a solution to an infinite set of linear simultaneous equations. For numerical calculations; solution of an infinite set of equations is not possible and the series thus needs to be truncated at some point. The number of terms used will determine the accuracy of the solution obtained. In most cases, however, the value of B1 converges to a unique value after a few terms. On solving, the value of B1 is obtained to be -0.7283. The effective conductivity can now be directly calculated from equation 2.92. Table 4.11 shows the results of predicting the effective thermal conductivity for other carbon nanotubes reinforced metal matrix nanocomposites by using similar calculations as shown above. The results predicted show increments in the value of the effective conductivity. For reinforcing Aluminum matrix the effective thermal conductivity is 221.8 W/m K, which is about 9% increase of the matrix thermal conductivity. However, for the reinforcing Iron matrix the value is 76.5 W/m K, which is about 5% increase of the matrix thermal conductivity, while for reinforcing Copper matrix the value is 409.6 W/m K, which is about 6% increase of the matrix thermal conductivity.

Table 4.11: Thermal conductivity results for (5, 5) carbon nanotubes reinforced metal matrix nanocomposite at 3% volume fraction

Parameter	Matrix		
	Aluminum	Copper	Iron
ζ_0	1.002306	1.002306	1.002306
c	4.9885	4.9885	4.9885
$k^{(2)}$	1923.3936	1923.3936	1923.3936
λ	9.4284	4.9829	26.4566
$\bar{\beta}$	293.441	155.083	823.411
B1	-0.7283	-0.7304	-0.7156
k_{eff}^* (W/m k)	221.6	409.6	76.5
% increase of the matrix thermal conductivity	9%	6%	5%

4.5.2 Evaluation of Factors Affecting the Effective Conductivity

The results obtained will be analyzed and the contribution of the various factors affecting heat conduction in carbon nanotubes reinforced Nanocomposite will be critically evaluated. The four principal factors that have been found to greatly influence

the effective conductivity in carbon nanotubes reinforced composites are the volume fraction, fiber length, diameter, and thermal contact conductance. An evaluation of these factors will help us in better understanding the mechanism of heat conduction in carbon nanotubes reinforced composites and how it is different from heat conduction in traditional fiber reinforced composites.

4.5.2.1 Effect of volume fraction on the effective thermal conductivity of the nanocomposite

The analysis was conducted using MATABL code for the carbon nanotube reinforced metal matrix Nanocomposite with a constant CNTs diameters and length. The objective of the analysis is to study the influence of CNTs volume fraction with various carbon nanotubes categories. The calculation has shown that even at lower volume fractions the CNT inclusions are able to enhance the thermal conductivity of the matrix material. This is a very important property from the point of thermal management of electronic devices. It is possible to enhance thermal conductivity of the matrix material even with randomly dispersed nanotubes in the matrix material, though the increase may not be as high as in a composite with highly aligned nanotubes but this can help in reducing the production cost of the composite. Table 4.12 shows the results for Aluminum matrix reinforced by 3% volume fraction of different categories of carbon nanotubes. It can be noticed that the enhancement in thermal conductivity are 10% to 7%, 9% to 6%, and 8% to 5% for zigzag, armchair and chiral type, respectively, with respect to the thermal conductivity of Aluminum matrix.

Table 4.12: Effect of carbon nanotube chiral index on the thermal conductivity for reinforcing aluminum metal matrix ($V_f=3\%$)

	Armchair			Zigzag			Chiral		
	(5,5)	(10,10)	(15,15)	(5,0)	(10,0)	(15,0)	(5,10)	(10,15)	(15,20)
K (W/m k)	221.6	218.6	216.9	223.6	220.9	217.7	219.7	216.9	214.4
% change	9%	7%	6%	10%	8%	7%	8%	6%	5%

Figures 4.30, 4.31, and 4.32 show the effect of volume fraction on the thermal conductivity for aluminum reinforced by armchair, zigzag, and chiral carbon nanotube respectively. It can be observed that the thermal conductivity of the Nanocomposite varies linearly with the change in volume fractions as predicted by theoretical model. However, Table 4.13 shows that the thermal conductivity of zigzag type is the highest where the lowest is the chiral type.

Table 4.13: Comparison between different carbon nanotube chiral index on the thermal conductivity for reinforcing aluminum metal matrix ($V_f=3\%$)

Carbon Nanotube index	K (W/m K)	% change
(5,5)	221.61	9%
(5,0)	223.62	10%
(5,10)	219.72	8%

Figure 4.33 represents the effect of chiral index of carbon nanotubes on the thermal conductivity of aluminum metal matrix. It can be seen that it increases linearly with increasing volume fraction. The zigzag type has the highest slope while the chiral type has the lowest slope.

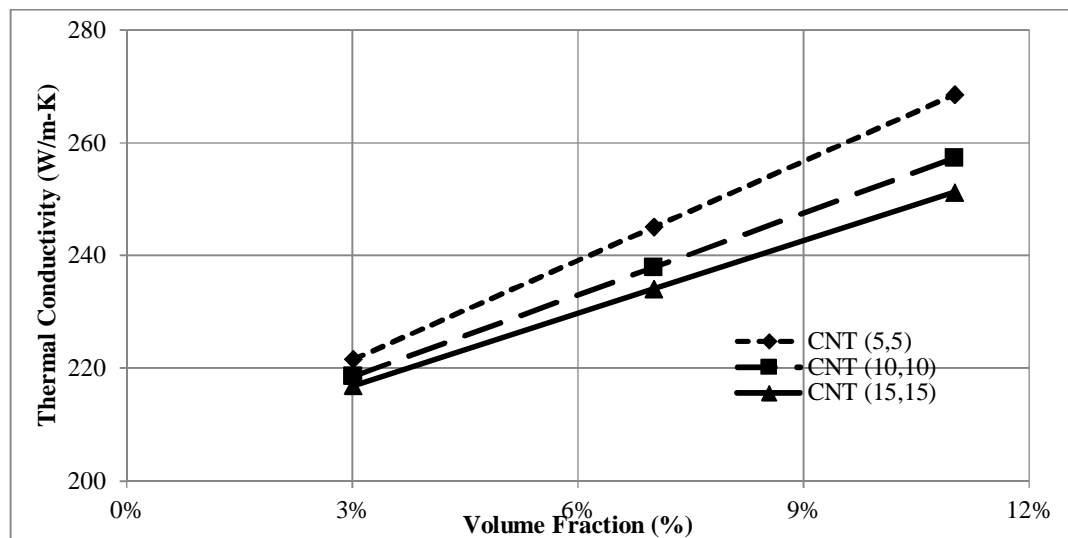


Figure 4.30: Effect of volume fraction on thermal conductivity for armchair carbon nanotube reinforced aluminum metal matrix

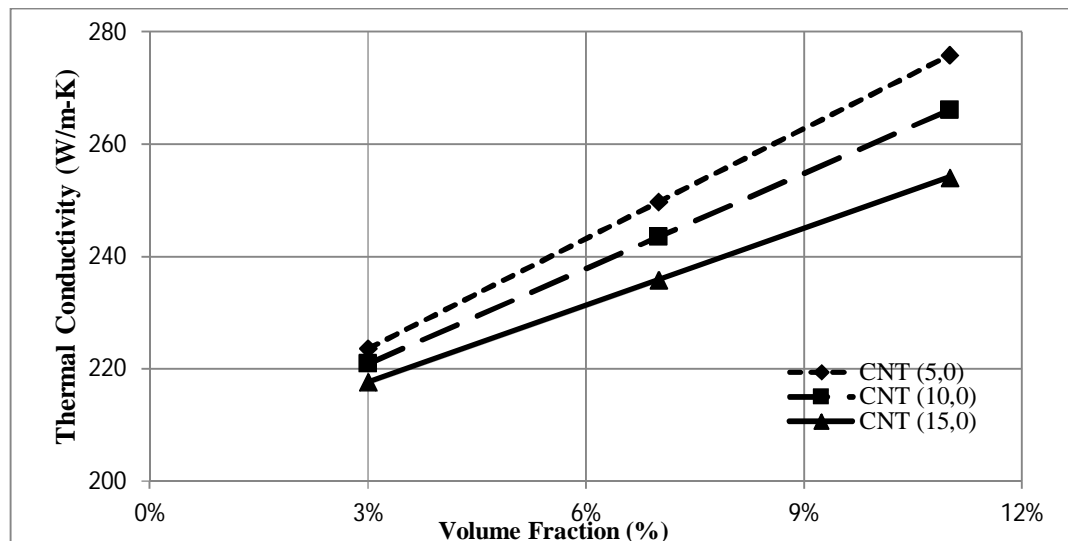


Figure 4.31: Effect of volume fraction on thermal conductivity for zigzag carbon nanotube reinforced aluminum metal matrix

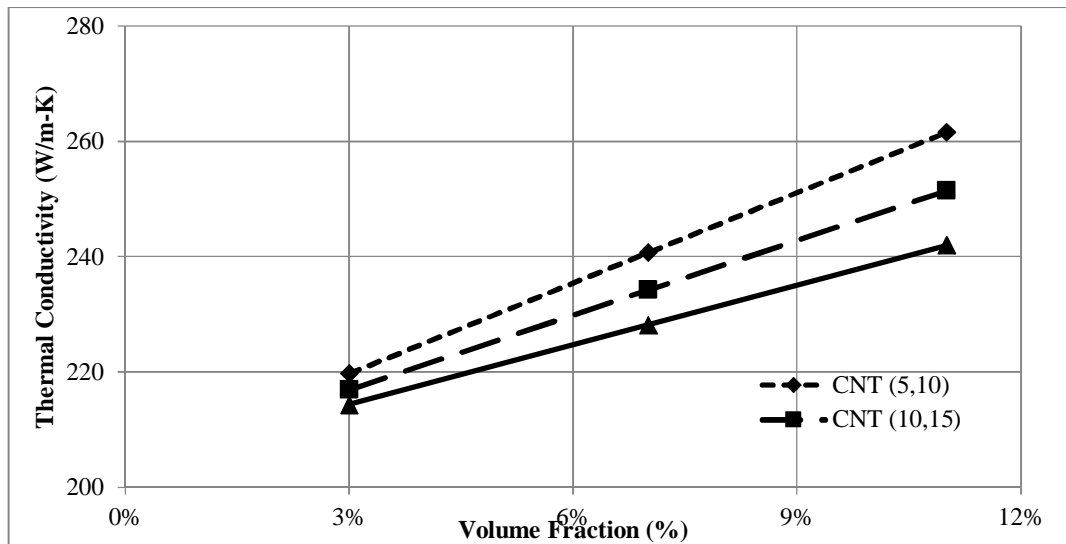


Figure 4.32: Effect of volume fraction on thermal conductivity for chiral carbon reinforced aluminum metal matrix

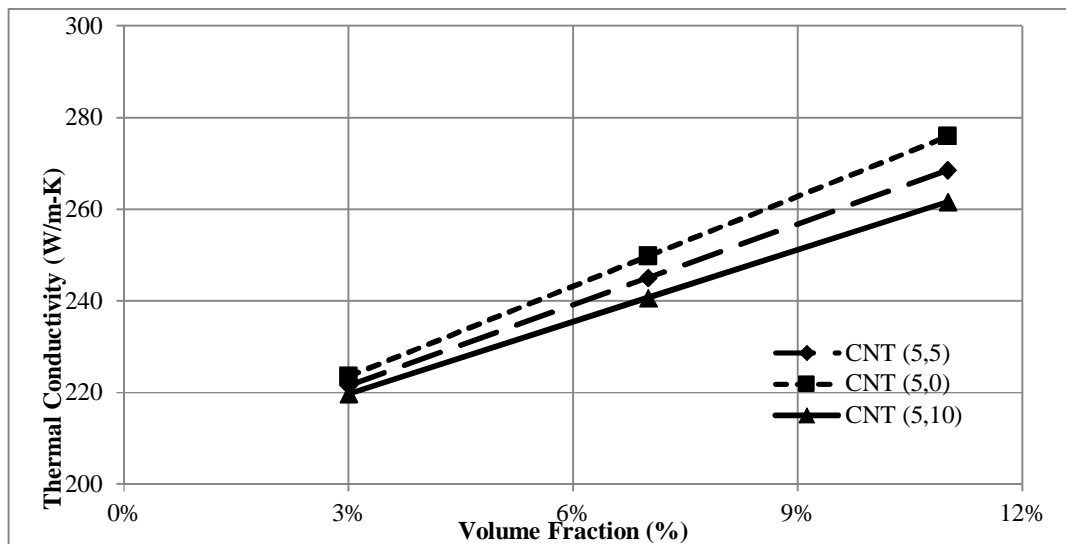


Figure 4.33: Effect of volume fraction on thermal conductivity for different chiral indices carbon nanotube reinforced aluminum metal matrix

Similarly, the same procedure will be taken for the prediction of thermal conductivity for the copper and iron matrices.

For carbon nanotube reinforced Copper matrix Nanocomposite, Table 4.14 shows the results for copper matrix reinforced by 3% volume fraction of different categories of carbon nanotubes. It can be noticed that the enhancement in thermal conductivity are 7% to 4%, 6% to 4%, and 5% to 3% for zigzag, armchair and chiral type, respectively, with respect to the thermal conductivity of copper matrix.

Table 4.14: Effect of carbon nanotube chiral index on the thermal conductivity for reinforcing copper metal matrix ($V_f=3\%$)

	Armchair			Zigzag			Chiral		
	(5,5)	(10,10)	(15,15)	(5,0)	(10,0)	(15,0)	(5,10)	(10,15)	(15,20)
K (W/m k)	409.6	406.6	401.9	414.6	409	403.3	404.7	402	398.4
% change	6%	5%	4%	7%	6%	4%	5%	4%	3%

Figure 4.34, 4.35, and 4.36 show the effect of volume fraction on the thermal conductivity for Copper reinforced by armchair, zigzag, and chiral carbon nanotube respectively. It can be observed that the thermal conductivity of the Nanocomposite varies linearly with the change in volume fractions as predicted by theoretical model. However, Table 4.15 shows that the thermal conductivity of Zigzag type is the highest where the lowest is the chiral type.

Table 4.15: Comparison between different carbon nanotube chiral index on the thermal conductivity for reinforcing copper metal matrix ($V_f=3\%$)

Carbon Nanotube index	K (W/m K)	% change
Armchair (5,5)	409.6	6%
Zigzag (5,0)	414.6	7%
Chiral (5,10)	404.7	5%

Figure 4.37 represents the effect of chiral index of carbon nanotubes on the thermal conductivity of copper metal matrix. It can be seen that it increases linearly with increasing the volume fraction. The zigzag type has the highest slope while the chiral type has the lowest slope.

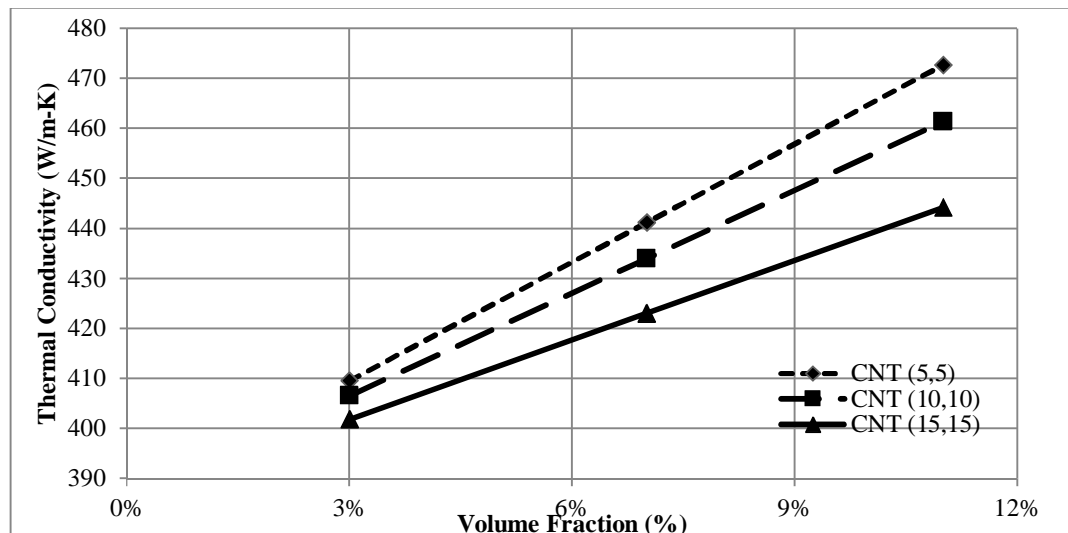


Figure 4.34: Effect of volume fraction on thermal conductivity for armchair carbon nanotube reinforced copper metal matrix

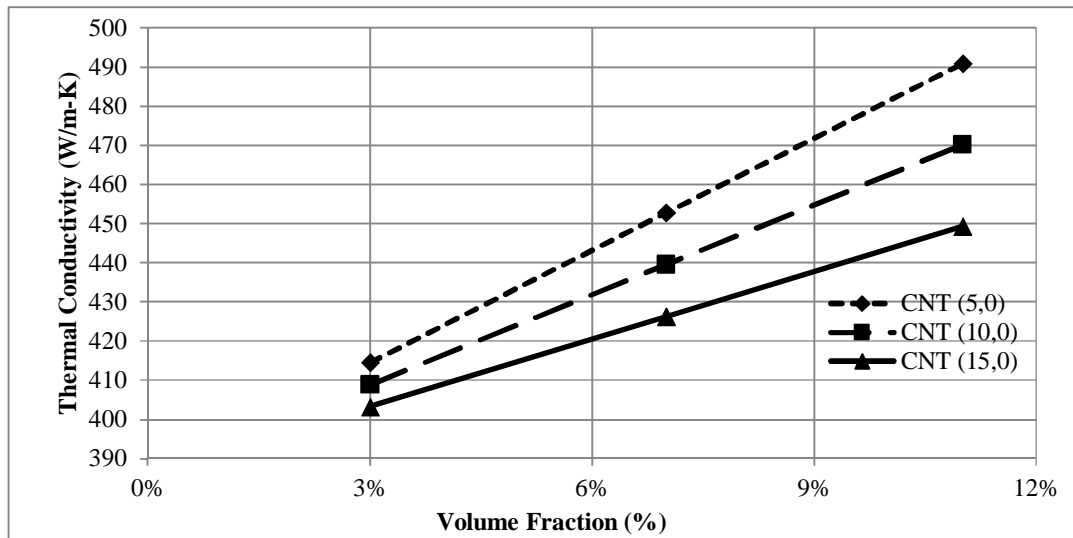


Figure 4.35: Effect of volume fraction on thermal conductivity for zigzag carbon nanotube reinforced copper metal matrix

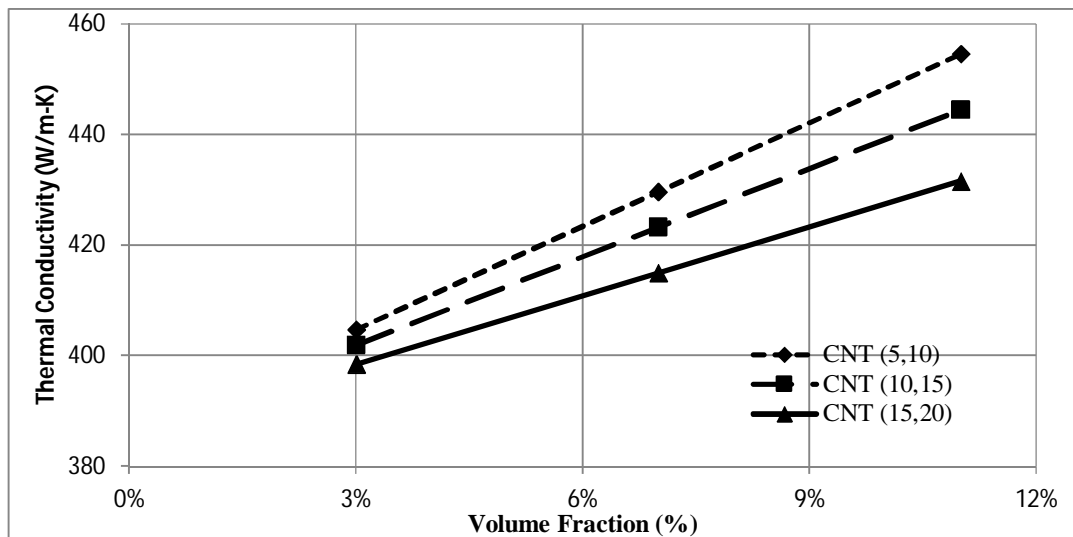


Figure 4.36: Effect of volume fraction on thermal conductivity for chiral carbon nanotube reinforced copper metal matrix

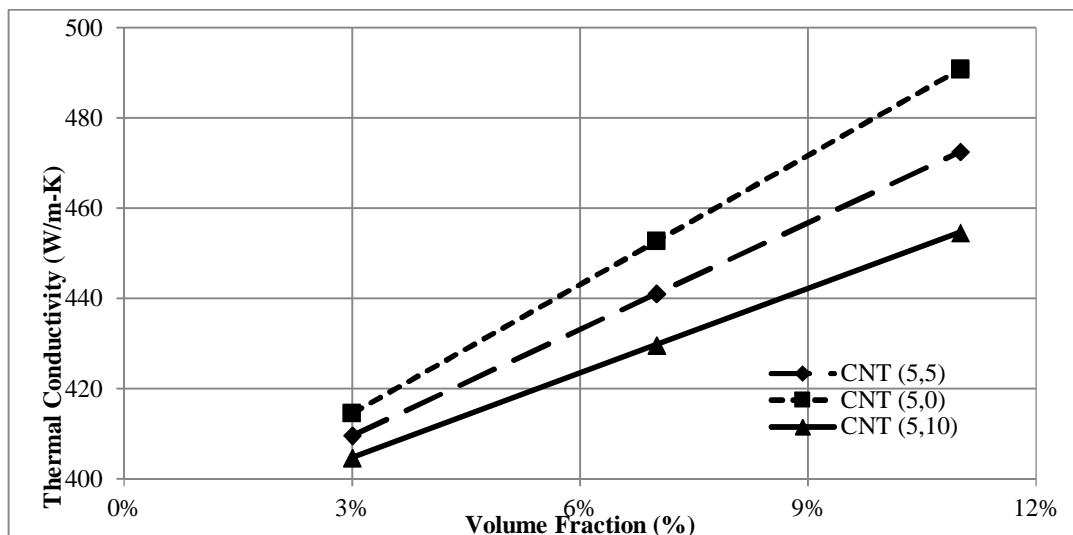


Figure 4.37: Effect of volume fraction on thermal conductivity for different chiral index carbon nanotube reinforced copper metal matrix

However, For Carbon nanotube reinforced iron matrix Nanocomposite, Table 4.16 shows the results of iron matrix reinforced by 3% volume fraction of different categories of carbon nanotubes. It can be noticed that the enhancement in thermal conductivity are 7% to 4%, 5% to 3%, and 4% to 2% for zigzag, armchair and chiral type, respectively, with respect to the thermal conductivity of iron matrix.

Table 4.16: Effect of carbon nanotube chiral index on the thermal conductivity for reinforcing iron metal matrix (Vf=3%)

	Armchair			Zigzag			Chiral		
	(5,5)	(10,10)	(15,15)	(5,0)	(10,0)	(15,0)	(5,10)	(10,15)	(15,20)
K (W/m k)	76.5	75.6	74.7	77.6	76.8	75.9	75.8	75.1	74.4
% change	5%	4%	3%	7%	6%	4%	4%	3%	2%

Figure 4.38, 4.39 and 4.40 shows the effect of volume fraction on the thermal conductivity for iron reinforced by armchair, zigzag, and chiral carbon nanotube respectively. It can be observed that the thermal conductivity of the nanocomposite varies linearly with the change in volume fractions as predicted by theoretical model.

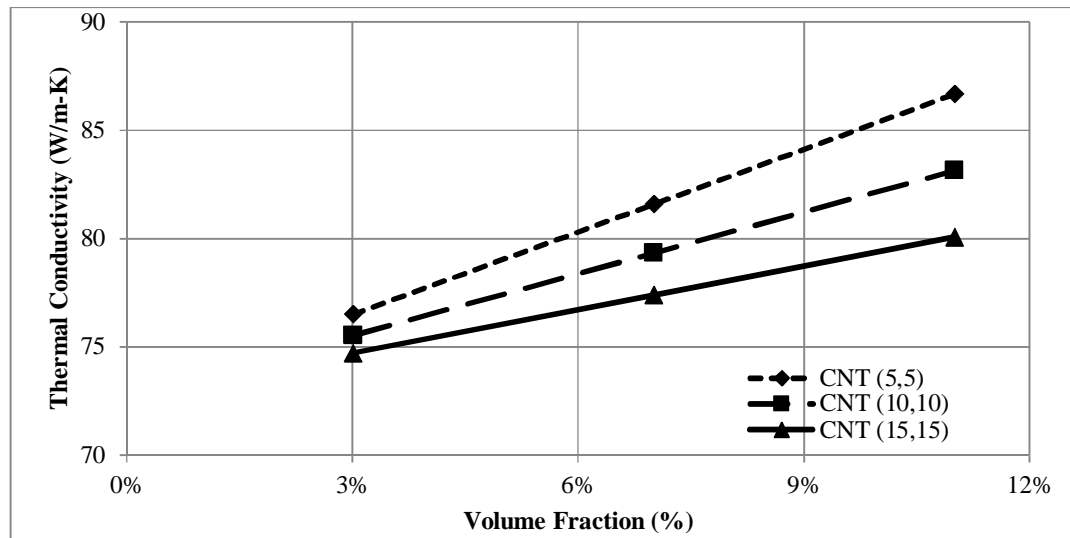


Figure 4.38: Effect of volume fraction on thermal conductivity for armchair carbon nanotube reinforced iron metal matrix

Table 4.17 shows that the thermal conductivity of zigzag type is the highest where the lowest is the chiral type

Table 4.17: Comparison between different carbon nanotube chiral index on the thermal conductivity for reinforcing iron metal matrix (Vf=3%)

Carbon Nanotube index	K (W/m K)	% change
(5,5)	76.5	5%
(5,0)	77.6	7%
(5,10)	75.8	4%

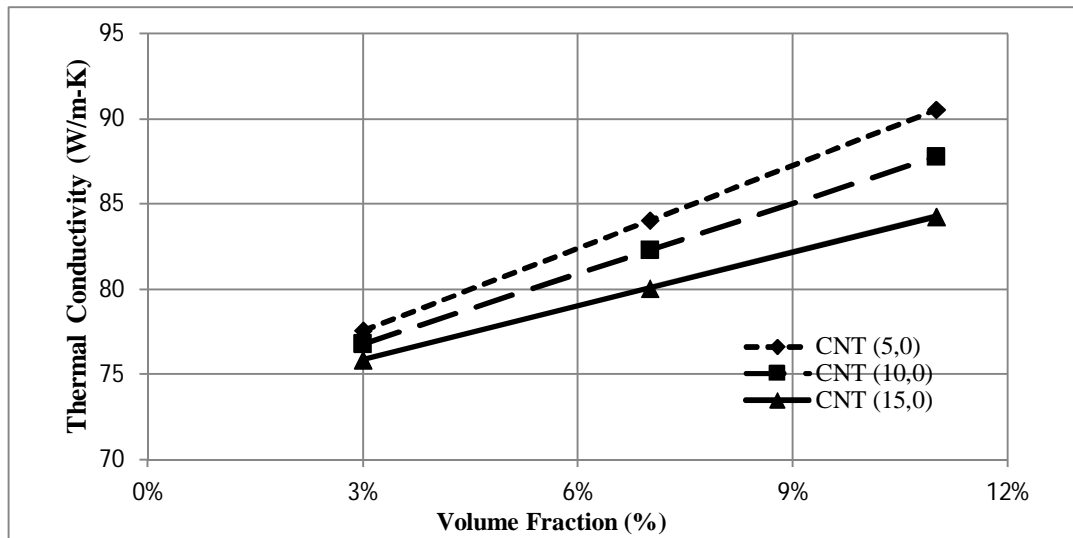


Figure 4.39: Effect of volume fraction on thermal conductivity for zigzag carbon nanotube reinforced iron metal matrix

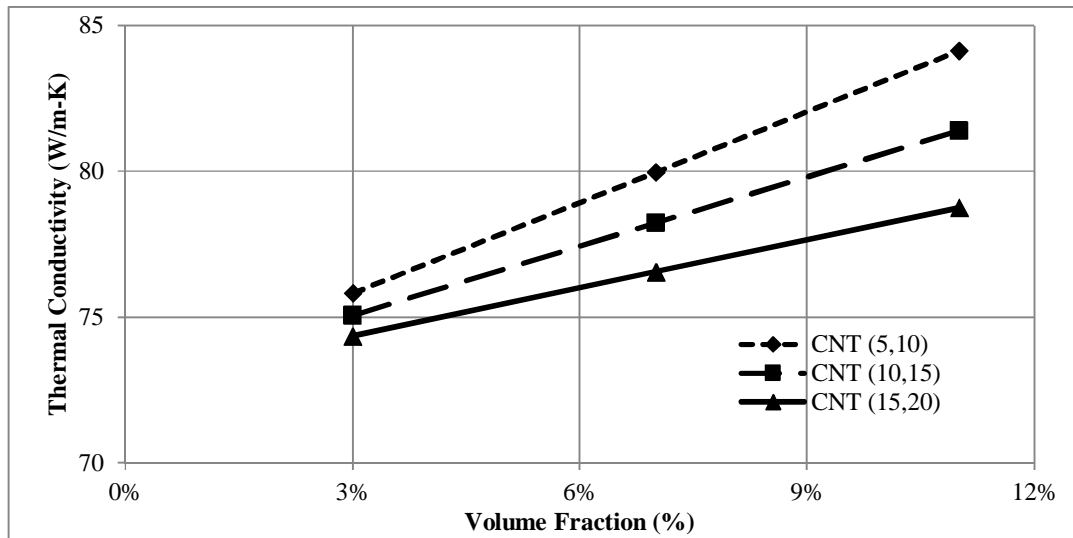


Figure 4.40: Effect of volume fraction on thermal conductivity for chiral carbon nanotube reinforced iron metal matrix

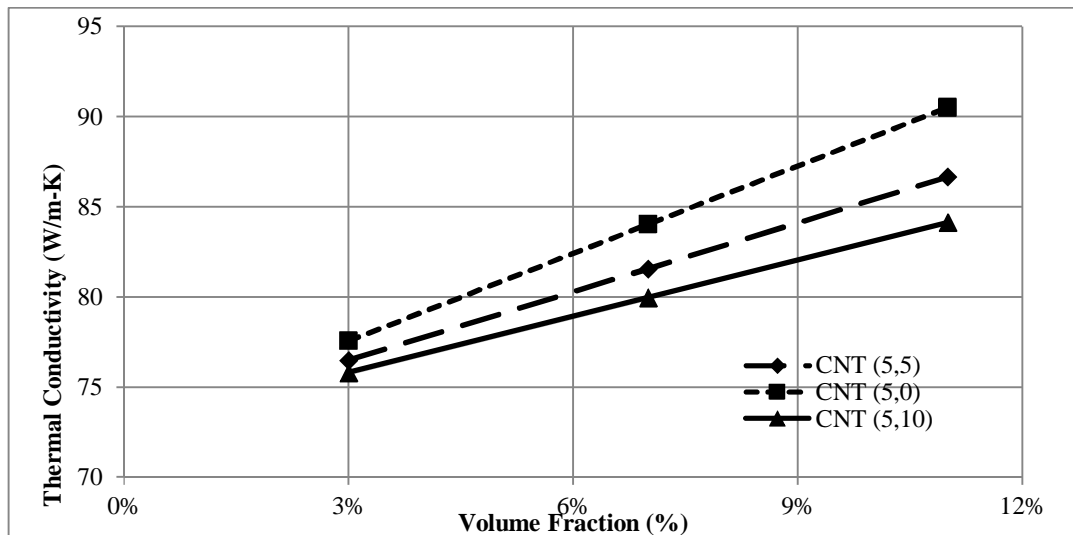


Figure 4.41: Effect of volume fraction on thermal conductivity for different chiral index carbon nanotube reinforced iron metal matrix

Figure 4.41 represents the effect of chiral index of carbon nanotubes on the thermal conductivity of iron metal matrix. It can be seen that it increases linearly with increasing volume fraction, and it has the same pattern as those of aluminum and copper matrices.

4.5.2.2 Effect of carbon nanotube length on the effective thermal conductivity

The analysis conducted using MATLAB code for the carbon nanotube reinforced metal matrix Nanocomposite with a constant carbon nanotube diameter and a fixed volume fraction of 3 %. The objective of the analysis is to study the influence of carbon nanotubes length with various aspect ratios. The calculation has shown that the thermal conductivity increases linearly with increase in length of CNT. However it can be noticed that the effective conductivity does not increase drastically when the length of the carbon nanotubes increases. In other words, there is no drastic increase in the conductivity for carbon nanotubes reinforced metal matrix Nanocomposite with high aspect ratios. The results for aluminum matrix reinforced by 3% of different types of carbon nanotubes show linear increase of thermal conductivity when the length increases from 2 to 9 nm as shown in Figures 4.42, 4.43 and 4.44. The increment percentage for the thermal conductivity are 2% to 8%, 2% to 9%, and 2% to 7% overall for armchair, zigzag, and chiral carbon nanotube, respectively. Figure 4.45 represents comparison between the three carbon nanotubes types reinforced aluminum metal matrix.

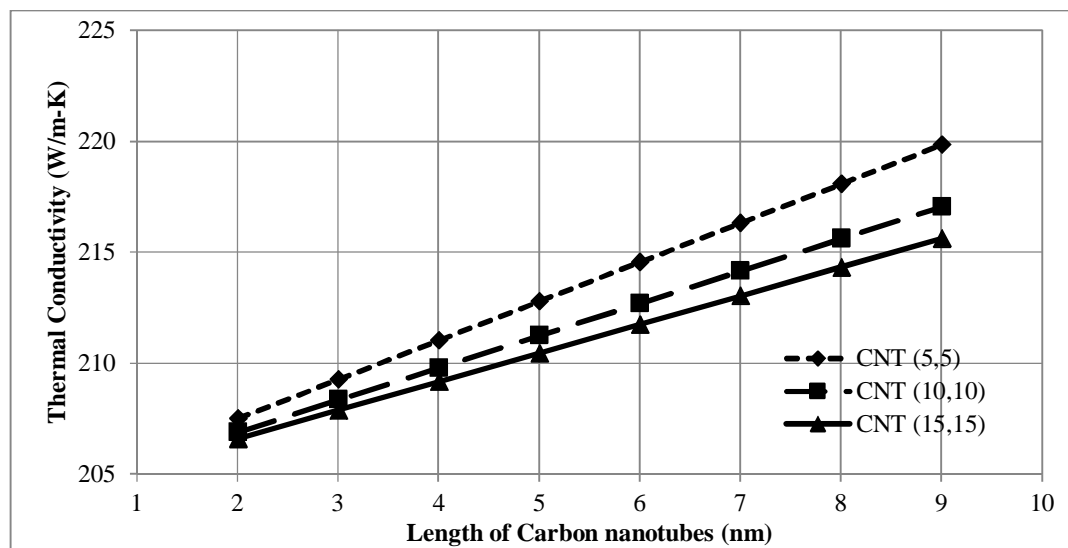


Figure 4.42: Effect of length on thermal conductivity for armchair carbon nanotube reinforced aluminum metal matrix

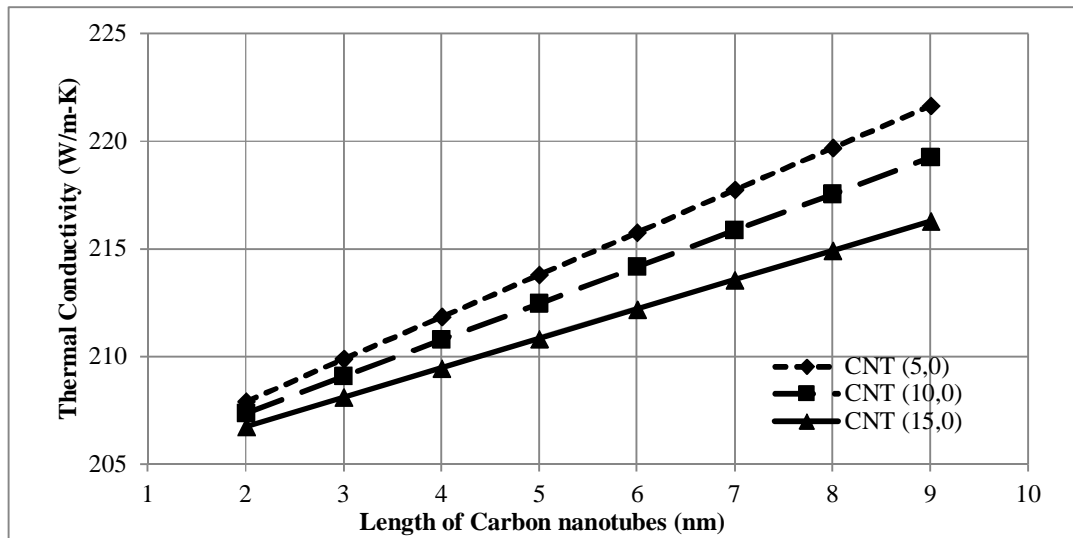


Figure 4.43: Effect of length on thermal conductivity for zigzag carbon nanotube reinforced aluminum metal matrix

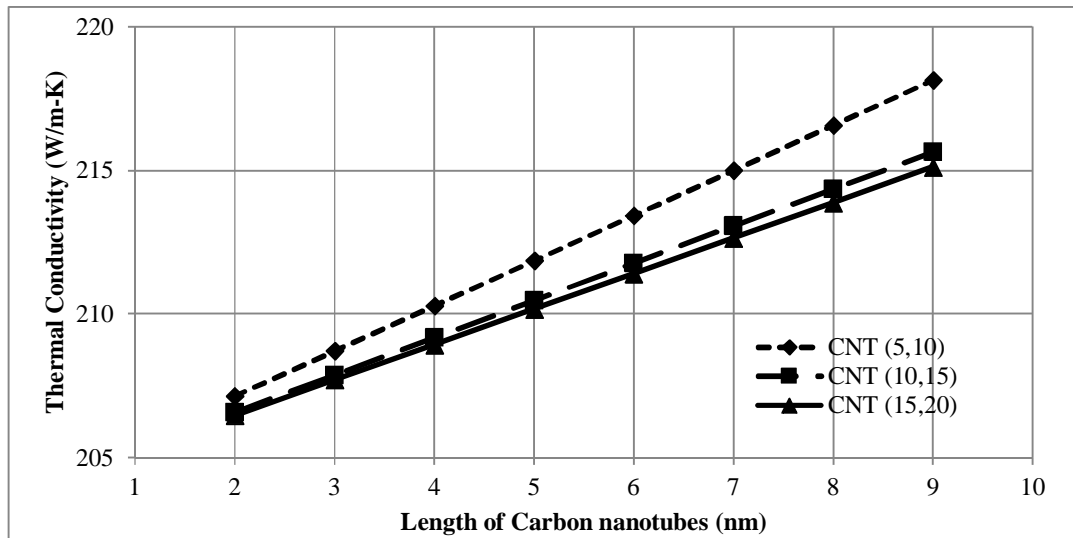


Figure 4.44: Effect of length on thermal conductivity for chiral carbon nanotube reinforced aluminum metal matrix

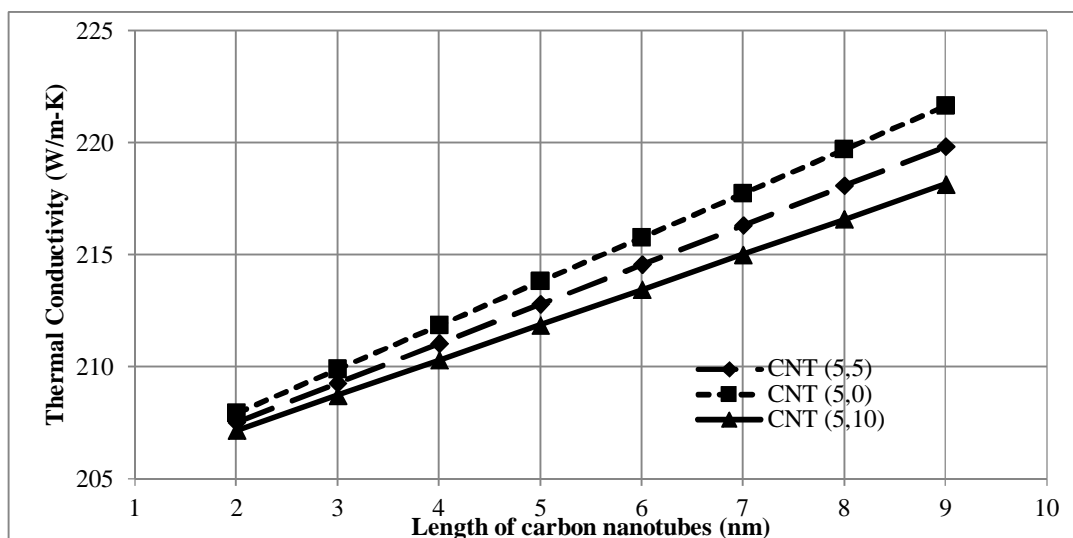


Figure 4.45: Effect of length on thermal conductivity for chiral carbon nanotube reinforced aluminum metal matrix

The same procedure is used for the prediction of the effect of carbon nanotubes length on the thermal conductivity for the copper and iron matrixes.

For carbon nanotube reinforced copper matrix Nanocomposite, the results for copper matrix reinforced by 3% of the three carbon nanotubes types show linear increase of thermal conductivity when the length increases from 2 to 9 nm as shown in Figures 4.46, 4.47 and 4.48. The increment percentage for the thermal conductivity are 1% to 6%, 1% to 7%, and 1% to 4% overall for armchair, zigzag, and chiral carbon nanotube, respectively. Figure 4.49 represents a comparison between the three types of carbon nanotubes reinforced copper metal matrix.

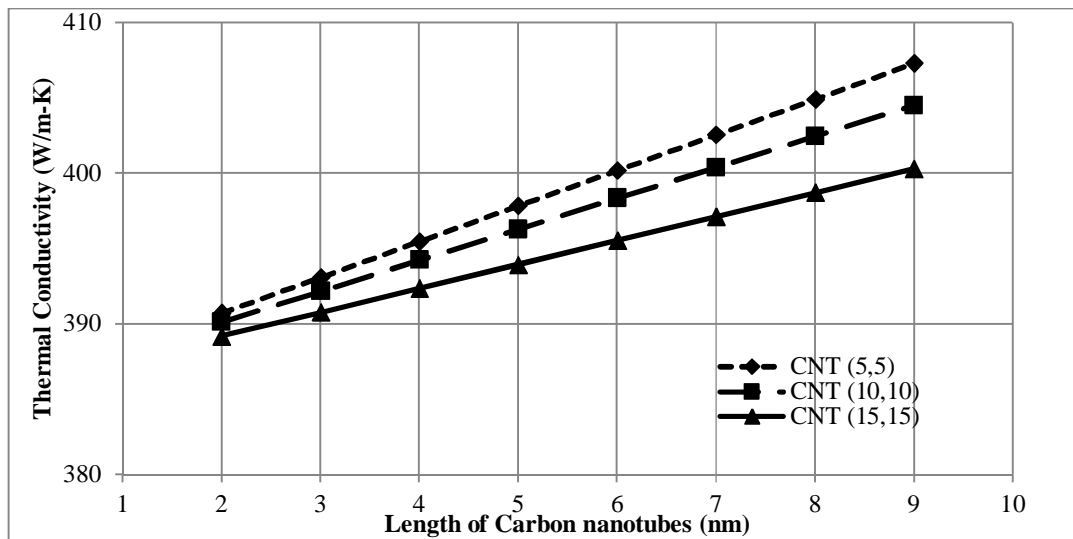


Figure 4.46: Effect of length on thermal conductivity for armchair carbon nanotube reinforced copper metal matrix

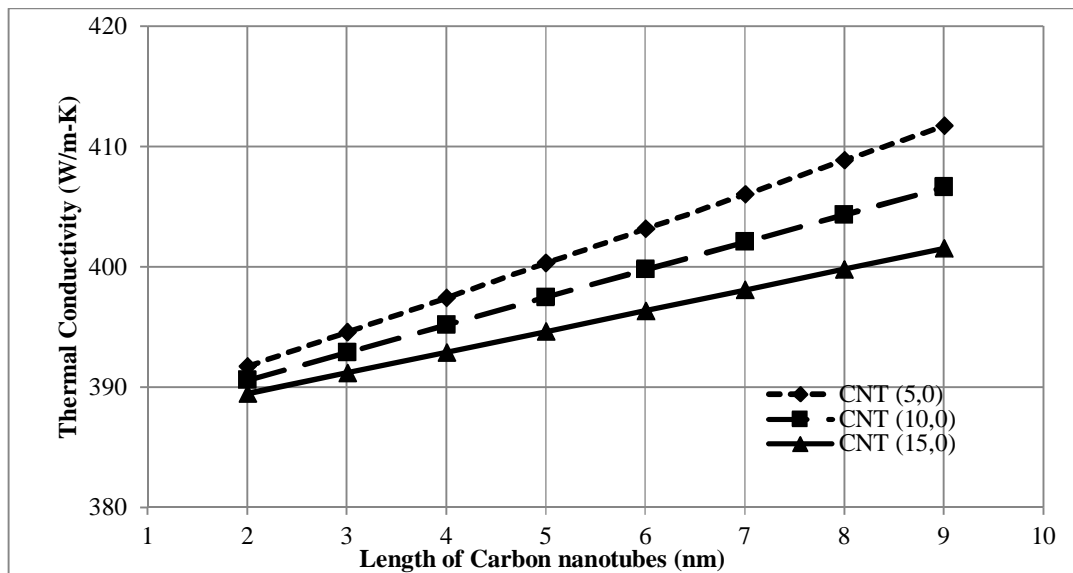


Figure 4.47: Effect of length on thermal conductivity for zigzag carbon nanotube reinforced copper metal matrix

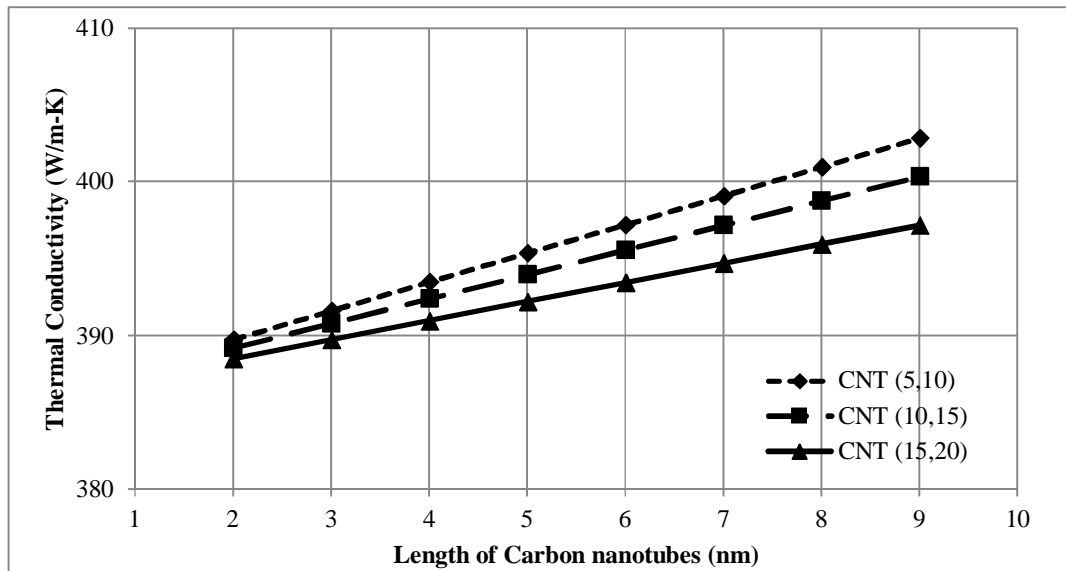


Figure 4.48: Effect of length on thermal conductivity for chiral carbon nanotube reinforced copper metal matrix

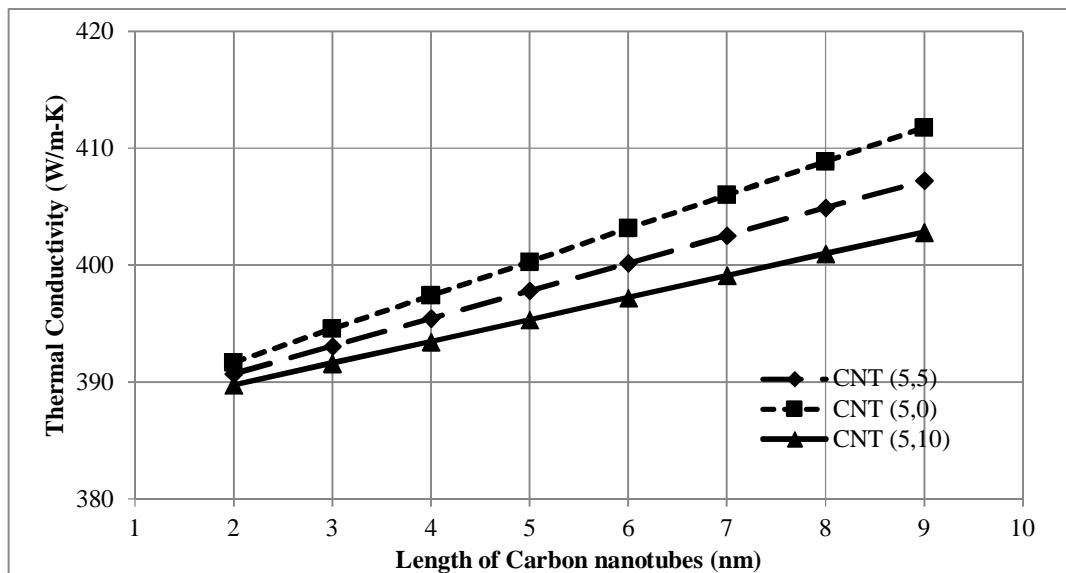


Figure 4.49: Effect of length on thermal conductivity for different chiral indices carbon nanotube reinforced copper metal matrix

However, Iron matrix reinforced by 3% of the three carbon nanotubes types results show linear increase of thermal conductivity when the length increases from 2 to 9 nm as shown in Figures 4.50, 4.51 and 4.52. The increment percentages for the thermal conductivity are 1% to 5%, 1% to 6%, and 1% to 4% for armchair, zigzag, and chiral carbon nanotube, respectively. However, Figure 4.53 represents a comparison between the three types of carbon nanotubes reinforced iron metal matrix.

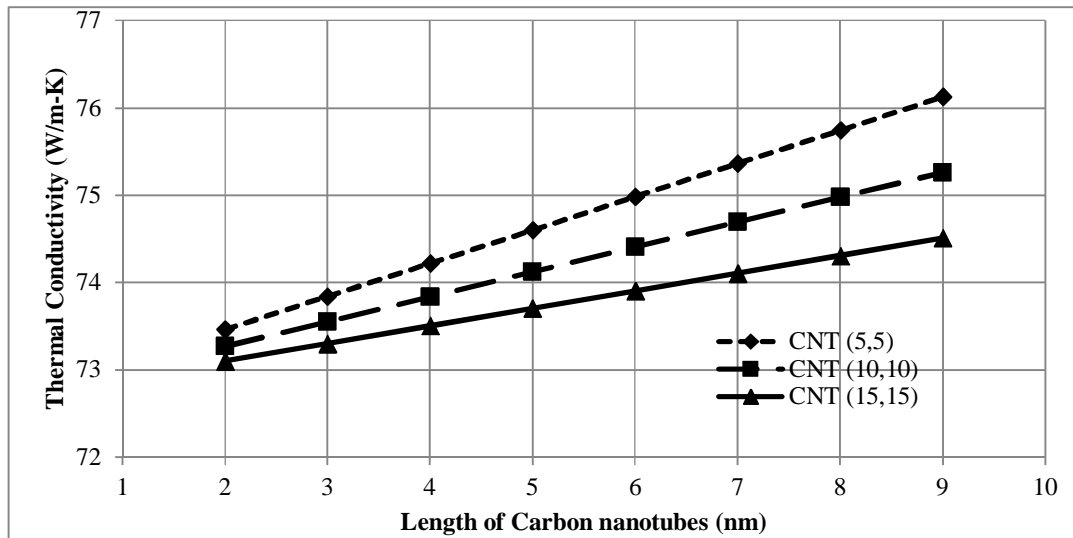


Figure 4.50: Effect of length on thermal conductivity for armchair carbon reinforced iron metal matrix

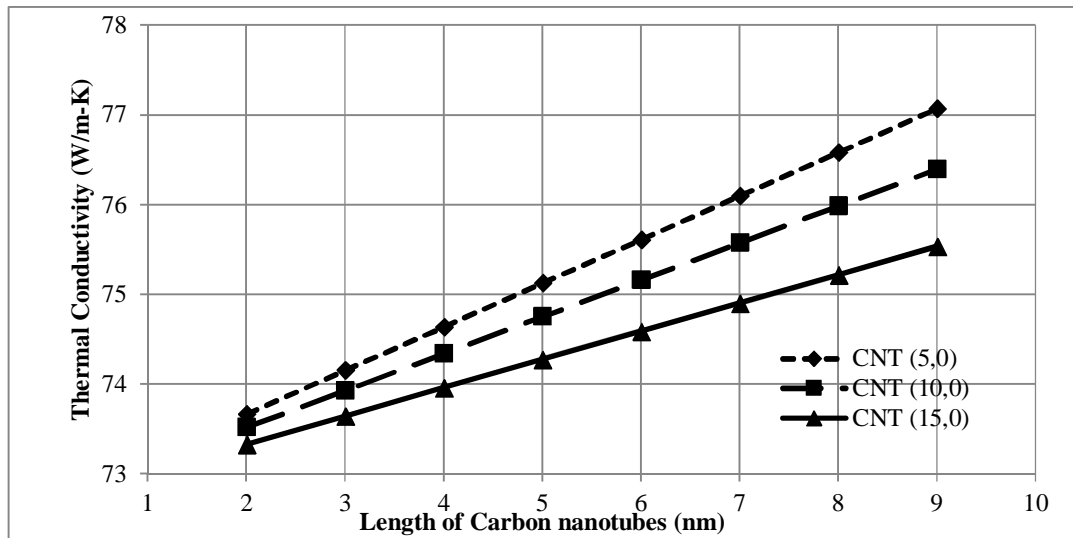


Figure 4.51: Effect of length on thermal conductivity for zigzag carbon reinforced iron metal matrix

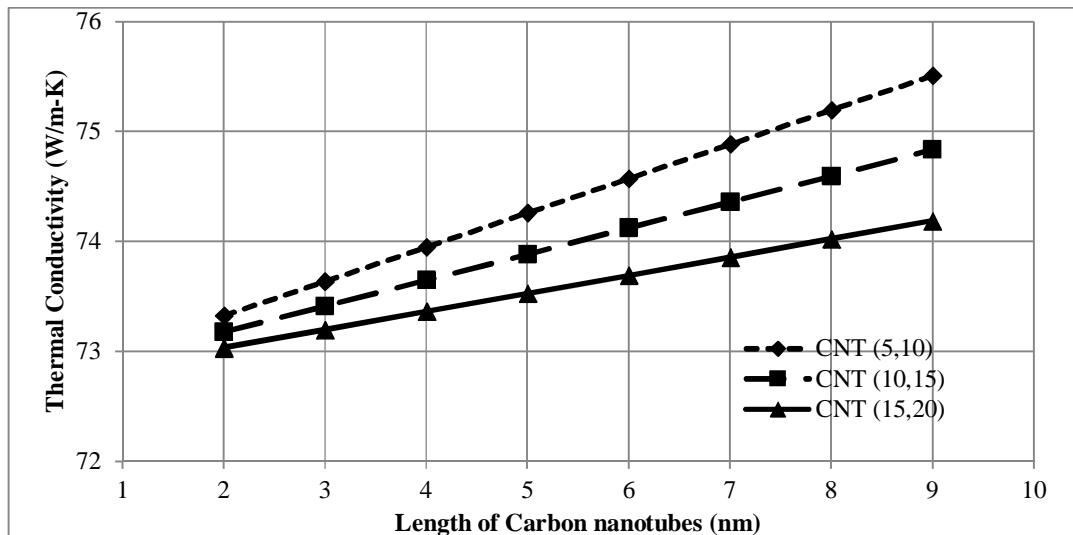


Figure 4.52: Effect of length on thermal conductivity for chiral carbon reinforced iron metal matrix

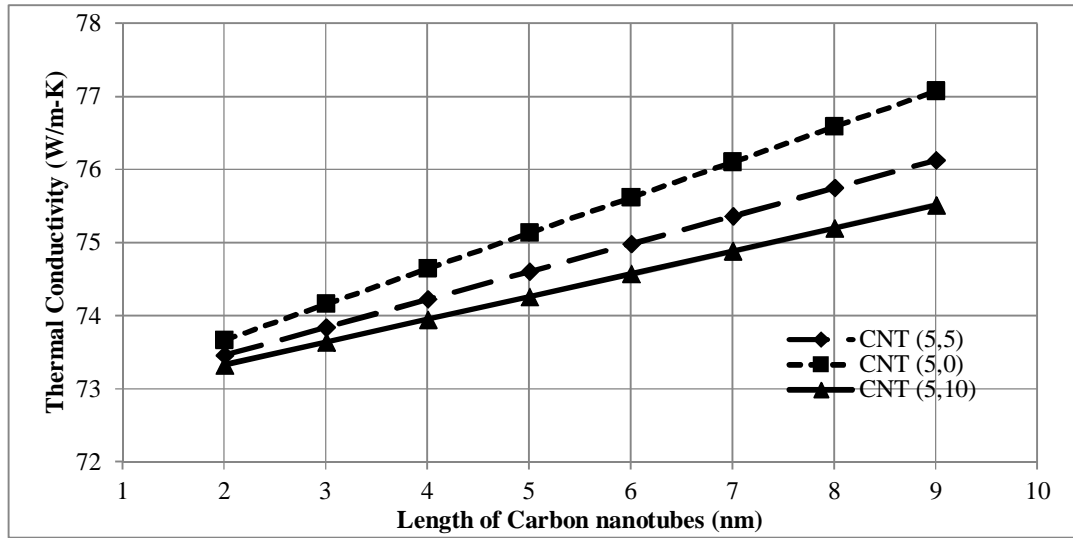


Figure 4.53: Effect of length on thermal conductivity for different chiral indices carbon nanotube reinforced iron metal matrix

4.5.2.3 Effect of the Diameter of Carbon Nanotube on the Effective Thermal Conductivity of the Nanocomposite

The analysis was conducted using MATLAB code for the carbon nanotube reinforced metal matrix Nanocomposite at fixed volume fraction of 3 % where the length of the short fiber is kept constant. The diameter is varied from 0.848 nm to 2.204 nm for armchair carbon nanotube category, from 0.561 nm to 1.344 nm for zigzag carbon nanotube category and from 1.206 nm to 2.551 nm for chiral carbon nanotube category. Table 4.18 represents the results of thermal conductivity calculated at 3% volume fraction of carbon nanotube reinforced Iron matrix and its enhancement percentage with respect to the matrix thermal conductivity. Figure 4.54 shows that the thermal conductivity has decreasing trend when the diameter of carbon nanotube increased for armchair carbon nanotubes types reinforced iron matrix Nanocomposite.

Table 4.18: Effect of armchair carbon nanotube diameter on the thermal conductivity for reinforcing iron matrix ($V_f=3\%$)

Carbon Nanotube index	d (nm)	K (W/mk)					
		$l_c=3$ nm	% change	$l_c=5$ nm	% change	$l_c=8$ nm	% change
(5,5)	0.848	73.8	2%	74.6	3%	75.7	4%
(10,10)	1.526	73.6	1%	74.1	2%	75.1	3%
(15,15)	2.204	73.3	1%	73.7	1%	74.3	2%

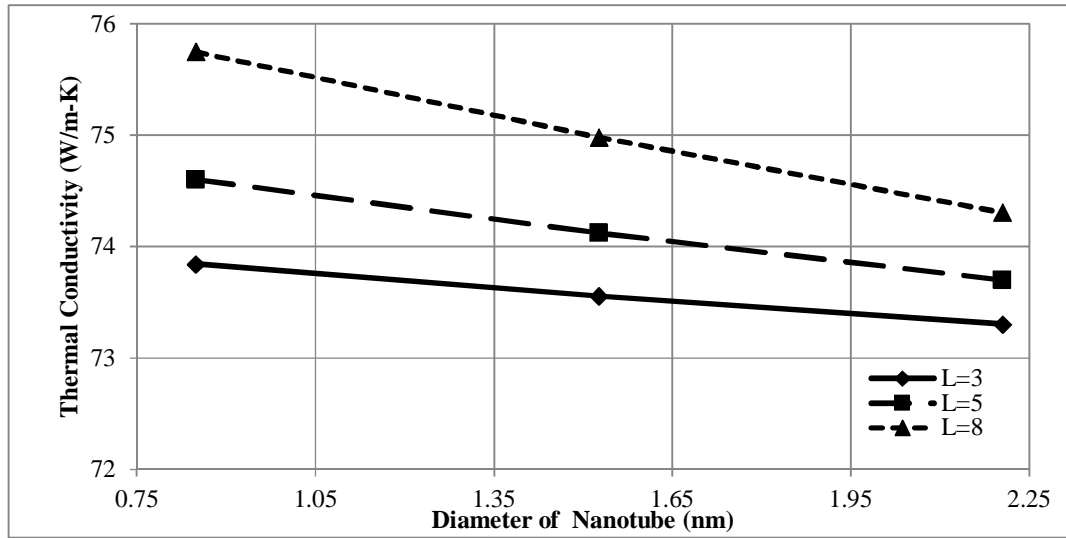


Figure 4.54: Effect of diameter on thermal conductivity for armchair carbon nanotube reinforced iron metal matrix

For zigzag carbon nanotube, Table 4.19 represents the results of thermal conductivity calculated at 3% volume fraction of zigzag carbon nanotube reinforced iron matrix and its enhancement percentage with respect to the matrix thermal conductivity. Figure 4.55 shows that the thermal conductivity has decreasing trend when the diameter of carbon nanotube increased for zigzag carbon nanotubes types reinforced iron matrix nanocomposite.

Table 4.19: Effect of zigzag carbon nanotube diameter on the thermal conductivity for reinforcing iron matrix ($V_f=3\%$)

Carbon Nanotube index	d (nm)	K (W/mk)					
		$l_c=3$ nm	% change	$l_c=5$ nm	% change	$l_c=8$ nm	% change
(5,0)	0.561	74.2	2%	75.2	3%	76.6	5%
(10,0)	0.953	73.9	2%	74.8	3%	75.9	5%
(15,0)	1.344	73.6	1%	74.3	2%	75.2	3%

However, for chiral carbon nanotube, Table 4.20 represents the results of thermal conductivity calculated at 3% volume fraction of chiral carbon nanotube reinforced iron matrix and its enhancement percentage with respect to the matrix thermal conductivity. Figure 4.56 shows that the thermal conductivity has decreasing trend when the diameter of carbon nanotube increased for chiral carbon nanotubes types reinforced iron matrix Nanocomposite.

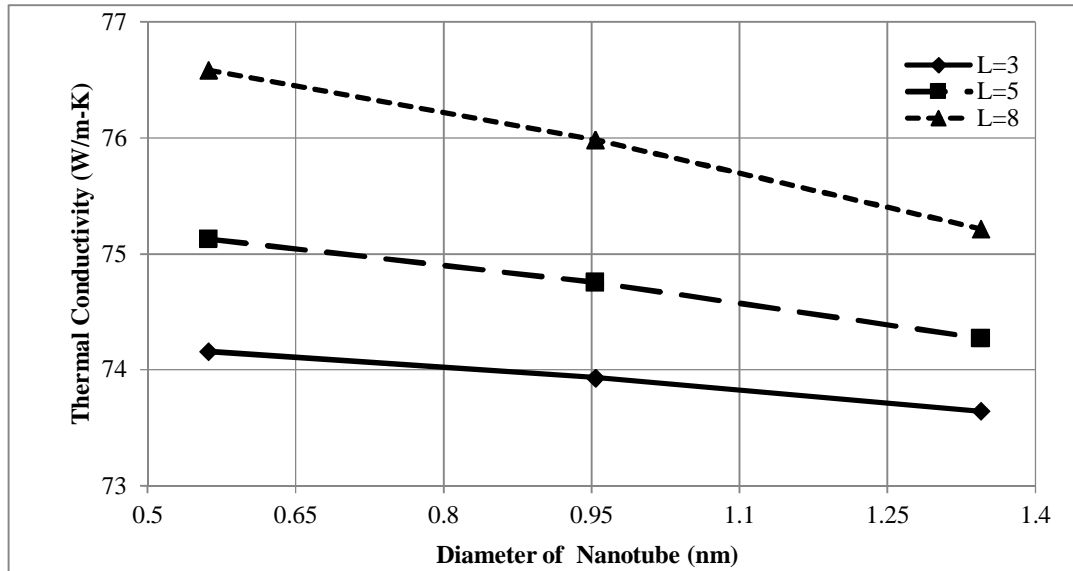


Figure 4.55: Effect of diameter on thermal conductivity for zigzag carbon nanotube reinforced iron metal matrix

Table 4.20: Effect of chiral carbon nanotube diameter on the thermal conductivity for reinforcing iron matrix ($V_f=3\%$)

Carbon Nanotube index	d (nm)	K (W/mk)					
		$l_c=3$ nm	% change	$l_c=5$ nm	% change	$l_c=8$ nm	% change
(5,10)	1.206	73.6	1%	74.3	2%	75.2	3%
(10,15)	1.876	73.4	1%	73.9	2%	74.6	3%
(15,20)	2.551	73.2	1%	73.5	1%	74.1	2%

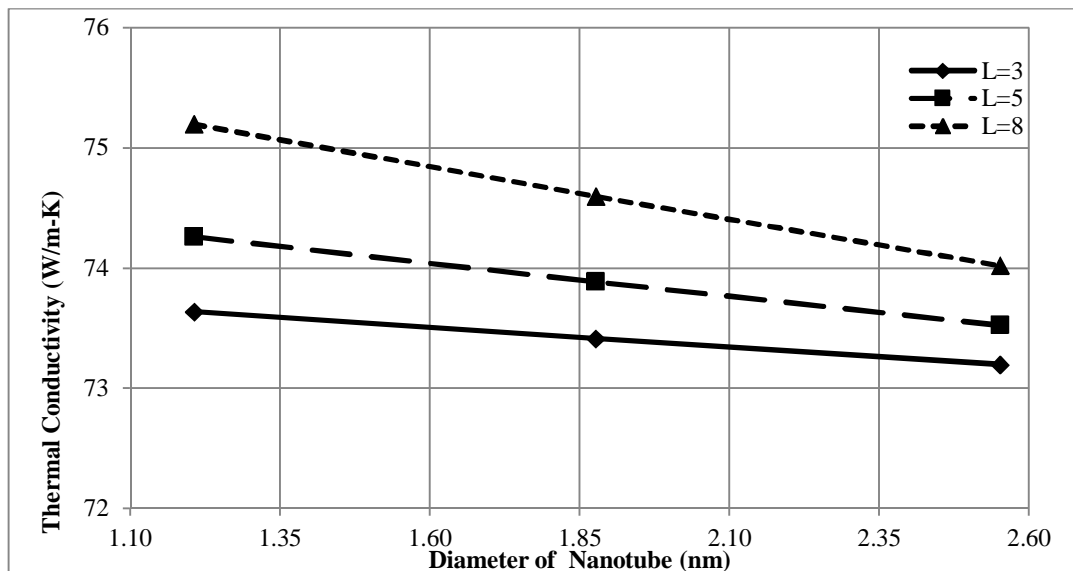


Figure 4.56: Effect of diameter on thermal conductivity for chiral carbon nanotube reinforced iron metal matrix

Similarly the procedure will be taken for the prediction of thermal conductivity for the copper and aluminum matrixes.

For carbon nanotube reinforced copper matrix Nanocomposite, Table 4.21 represents the results of thermal conductivity calculated at 3% volume fraction of carbon nanotube reinforced copper matrix and its enhancement percentage with respect to the matrix thermal conductivity. Figure 4.57 shows that the thermal conductivity has decreasing trend when the diameter of carbon nanotube increased for armchair carbon nanotubes types reinforced copper matrix nanocomposite.

Table 4.21: Effect of armchair carbon nanotube diameter on the thermal conductivity for reinforcing copper matrix ($V_f=3\%$)

Carbon Nanotube index	d (nm)	K (W/mk)					
		$l_c=3$ nm	% change	$l_c=5$ nm	% change	$l_c=8$ nm	% change
(5,5)	0.848	393.1	2%	397.8	3%	404.9	5%
(10,10)	1.526	392.2	2%	396.3	3%	402.4	4%
(15,15)	2.204	390.8	1%	393.9	2%	398.7	3%

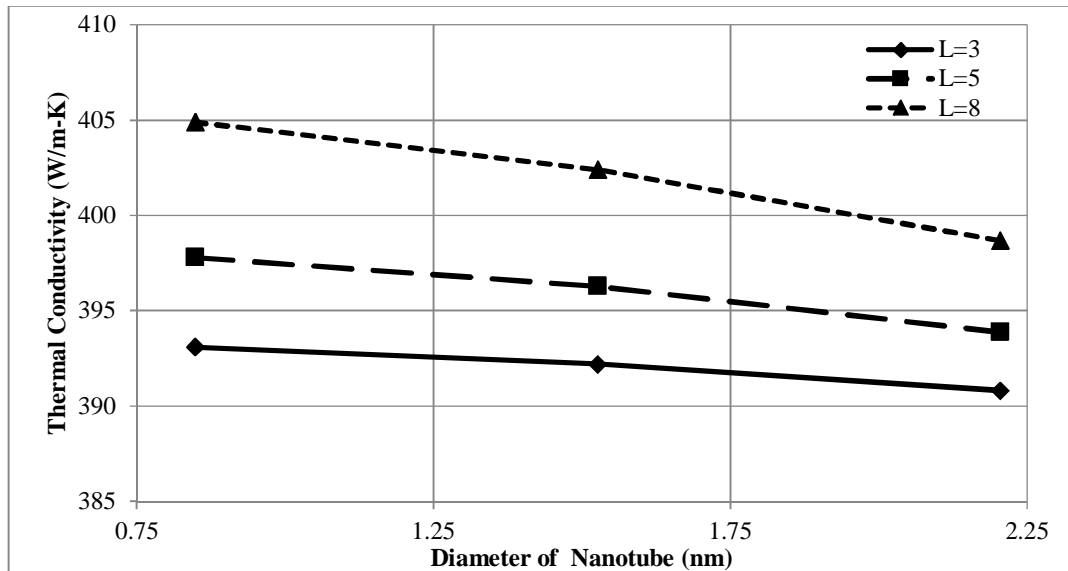


Figure 4.57: Effect of diameter on thermal conductivity for armchair carbon nanotube reinforced copper metal matrix

For zigzag carbon nanotube, Table 4.22 represents the results of thermal conductivity calculated at 3% volume fraction of zigzag carbon nanotube reinforced copper matrix and its enhancement percentage with respect to the matrix thermal conductivity. Figure 4.58 shows that the thermal conductivity has decreasing trend when the diameter of carbon nanotube increased for zigzag carbon nanotubes type reinforced copper matrix Nanocomposite.

Table 4.22: Effect of zigzag carbon nanotube diameter on the thermal conductivity for reinforcing copper matrix ($V_f=3\%$)

Carbon Nanotube index	d (nm)	K (W/mk)					
		$l_c = 3$ nm	% change	$l_c = 5$ nm	% change	$l_c = 8$ nm	% change
(5,0)	0.561	394.6	2%	400.3	4%	408.9	6%
(10,0)	0.953	392.9	2%	397.5	3%	404.4	5%
(15,0)	1.344	391.2	1%	394.6	2%	399.8	4%

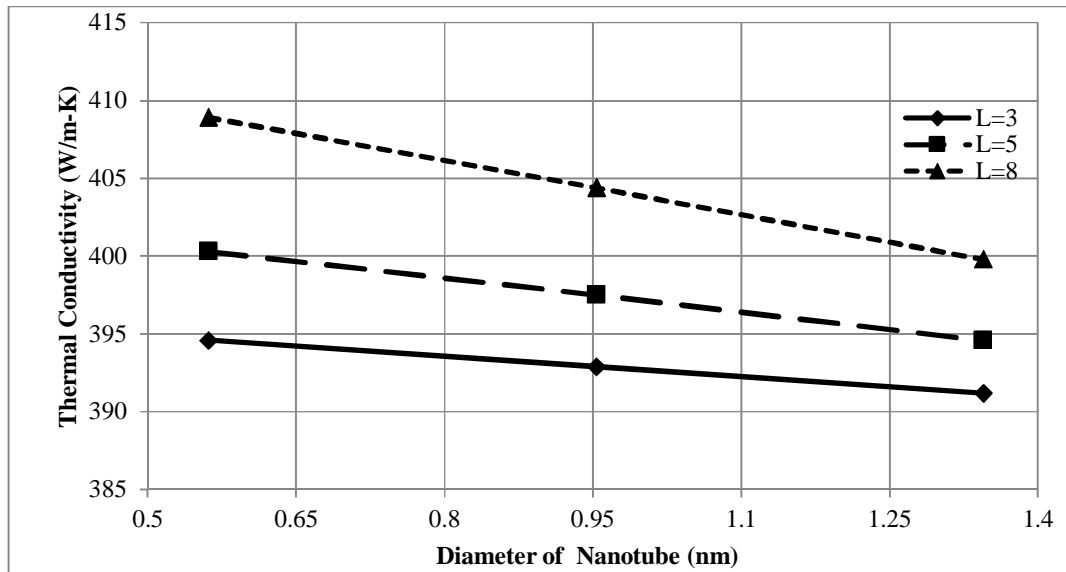


Figure 4.58: Effect of diameter on thermal conductivity for zigzag carbon nanotube reinforced copper metal matrix

However, for chiral carbon nanotube, Table 4.23 represents the results of thermal conductivity calculated at 3% volume fraction of chiral carbon nanotube reinforced copper matrix and its enhancement percentage with respect to the matrix thermal conductivity. Figure 4.59 shows that the thermal conductivity has decreasing trend when the diameter of carbon nanotube increased for chiral carbon nanotube type reinforced copper matrix Nanocomposite.

Table 4.23: Effect of chiral carbon nanotube diameter on the thermal conductivity for reinforcing copper matrix ($V_f=3\%$)

Carbon Nanotube Index	d (nm)	K (W/mk)					
		$l_c = 3$ nm	% change	$l_c = 5$ nm	% change	$l_c = 8$ nm	% change
(5,10)	1.206	391.6	1%	395.4	2%	401.1	4%
(10,15)	1.876	390.8	1%	394.1	2%	398.8	3%
(15,20)	2.551	389.7	1%	392.2	2%	395.9	3%

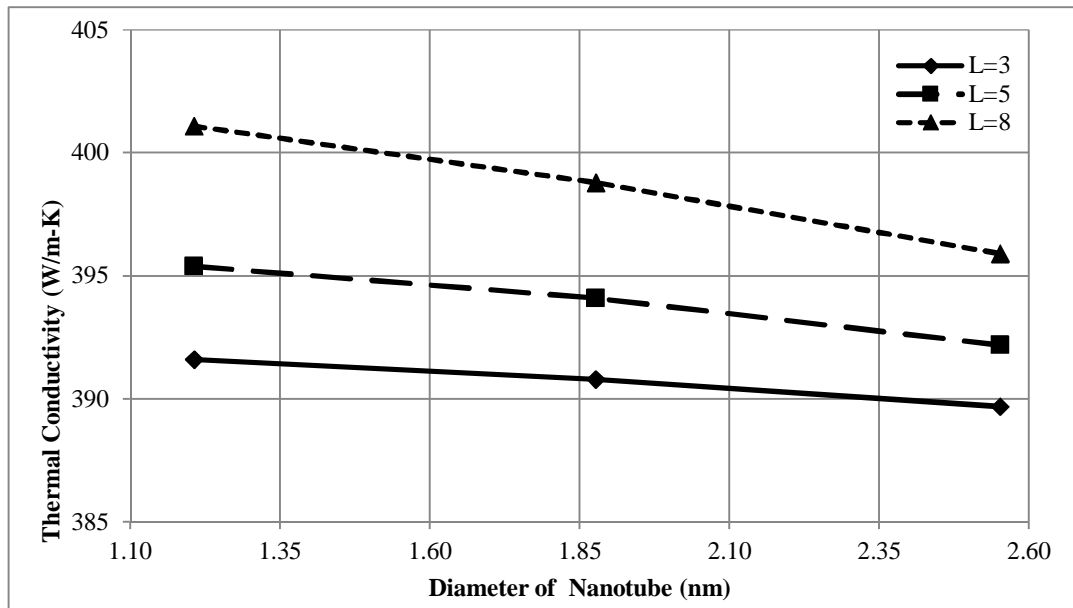


Figure 4.59: Effect of diameter on thermal conductivity for chiral carbon nanotube (as short fiber) reinforced copper metal matrix

For carbon nanotube reinforced aluminum matrix Nanocomposite, Table 4.24 represents the results of thermal conductivity calculated at 3% volume fraction of armchair carbon nanotube reinforced aluminum matrix and its enhancement percentage with respect to the matrix thermal conductivity. Figure 4.60 shows that the thermal conductivity has decreasing trend when the diameter of carbon nanotube increased for armchair carbon nanotubes types reinforced aluminum matrix Nanocomposite.

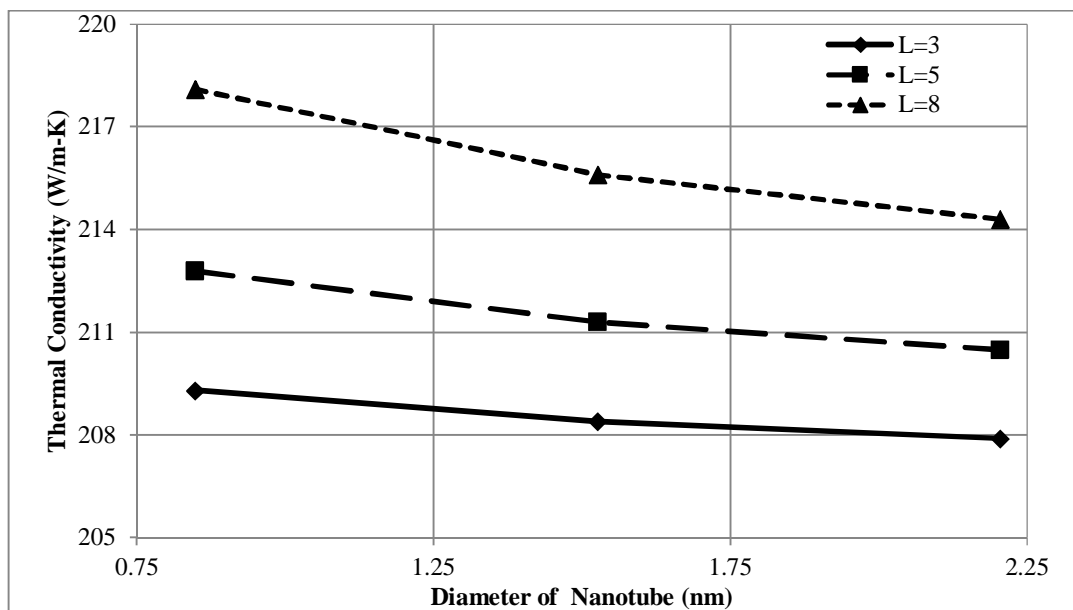


Figure 4.60: Effect of diameter on thermal conductivity for armchair carbon nanotube reinforced aluminum metal matrix

Table 4.24: Effect of armchair carbon nanotube diameter on the thermal conductivity for reinforcing aluminum matrix ($V_f=3\%$)

Carbon Nanotube index	d (nm)	K (W/mk)					
		lc=3 nm	% change	lc=5 nm	% change	lc=8 nm	% change
(5,5)	0.848	209.3	3%	212.8	4%	218.1	7%
(10,10)	1.526	208.4	2%	211.3	4%	215.6	6%
(15,15)	2.204	207.9	2%	210.5	3%	214.3	5%

For zigzag carbon nanotube, Table 4.25 represents the results of thermal conductivity calculated at 3% volume fraction of zigzag carbon nanotube reinforced aluminum matrix and its enhancement percentage with respect to the matrix thermal conductivity. Figure 4.61 shows that the thermal conductivity has decreasing trend when the diameter of carbon nanotube increased for zigzag carbon nanotubes types reinforced aluminum matrix Nanocomposite.

Table 4.25: Effect of zigzag carbon nanotube diameter on the thermal conductivity for reinforcing aluminum matrix ($V_f=3\%$)

Carbon Nanotube index	d (nm)	K (W/mk)					
		lc =3 nm	% change	lc =5 nm	% change	lc =8 nm	% change
(5,0)	0.561	209.9	3%	213.8	5%	219.7	8%
(10,0)	0.953	209.1	3%	212.5	4%	217.6	7%
(15,0)	1.344	208.1	2%	210.8	3%	214.9	5%

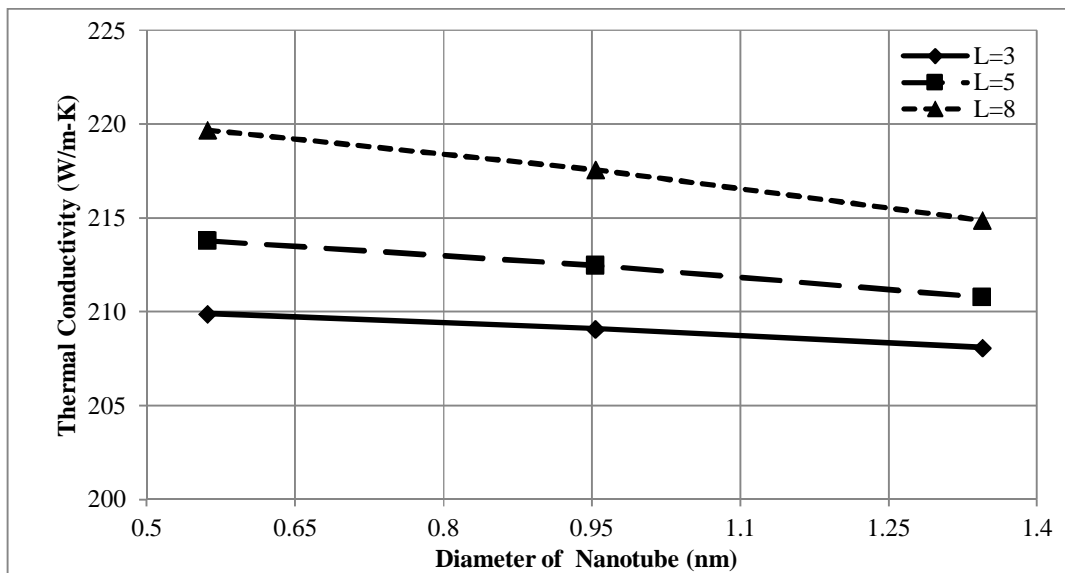


Figure 4.61: Effect of diameter on thermal conductivity for zigzag carbon nanotube reinforced aluminum metal matrix

However, for chiral carbon nanotube, Table 4.26 represents the results of thermal conductivity calculated at 3% volume fraction of chiral carbon nanotube reinforced aluminum matrix and its enhancement percentage with respect to the matrix thermal conductivity. Figure 4.62 show that the thermal conductivity has decreasing trend when the diameter of carbon nanotube increased for chiral carbon nanotubes types reinforced aluminum matrix Nanocomposite.

Table 4.26: Effect of chiral carbon nanotube diameter on the thermal conductivity for reinforcing aluminum matrix ($V_f=3\%$)

Carbon Nanotube Index	d (nm)	K (W/mk)					
		$l_c=3$ nm	% change	$l_c=5$ nm	% change	$l_c=8$ nm	% change
(5,10)	1.206	208.7	2%	211.900	4%	216.600	6%
(10,15)	1.876	207.9	2%	210.500	3%	214.400	5%
(15,20)	2.551	207.7	2%	210.200	3%	213.900	5%

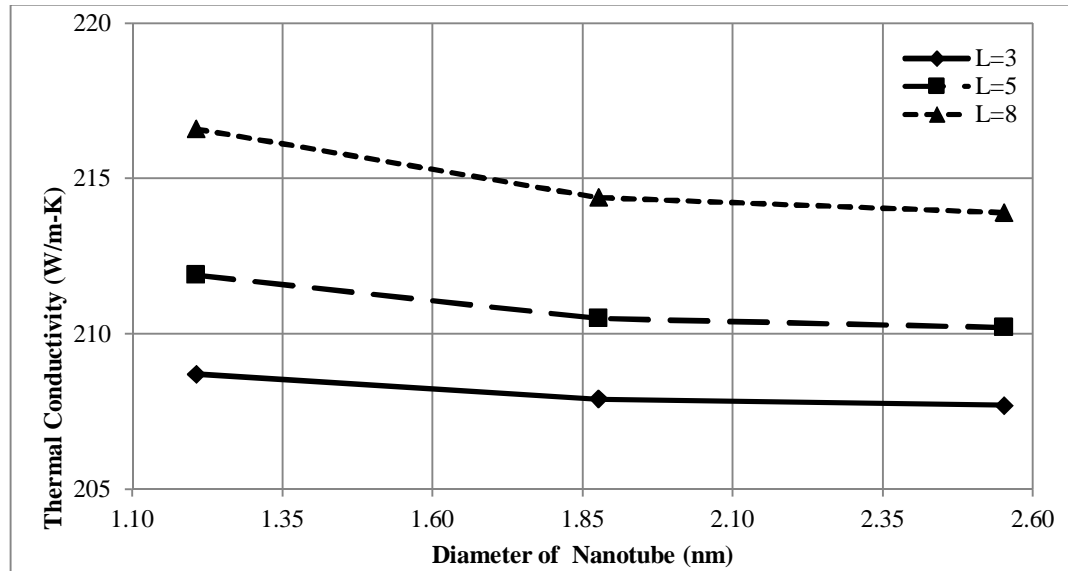


Figure 4.62: Effect of diameter on thermal conductivity for chiral carbon nanotube reinforced aluminum metal matrix

From the previous analysis, it can be observed that zigzag (5, 0) type show higher thermal conductivity than armchair (5, 5), and chiral (5, 10) shows the lowest thermal conductivity than the other carbon nanotubes types at the same length. Table 4.27 (a), (b), and (c) represent a comparison between the three types of carbon nanotube reinforced iron, copper, and aluminum matrix, respectively. It can be clearly noticed that the value of thermal conductivity decreases nonlinearly as the diameter of the carbon nanotube increases which achieved by changing the carbon nanotube chirality index. The zigzag type have the higher diameter followed by armchair, then chiral type.

Table 4.27: Effect of carbon nanotube chirality index reinforced (a) iron, (b) copper, and (c) aluminum matrix on the thermal conductivity ($V_f=3\%$)

(a) Iron

Carbon Nanotube index	d (nm)	K (W/mk)					
		$l_c = 3$ nm	% change	$l_c = 5$ nm	% change	$l_c = 8$ nm	% change
Zigzag (5,0)	0.561	74.2	2%	75.1	3%	76.6	5%
Armchair (5,5)	0.848	73.8	2%	74.6	3%	75.7	4%
Chiral (5,10)	1.206	73.6	1%	74.3	2%	75.2	3%

(b) Copper

Carbon Nanotube index	d (nm)	K (W/mk)					
		$l_c = 3$ nm	% change	$l_c = 5$ nm	% change	$l_c = 8$ nm	% change
Zigzag (5,0)	0.561	394.6	2%	400.3	4%	408.9	6%
Armchair (5,5)	0.848	393.1	2%	397.8	3%	404.9	5%
Chiral (5,10)	1.206	391.6	1%	395.4	2%	401.1	4%

(c) Aluminum

Carbon Nanotube index	d (nm)	K (W/mk)					
		$l_c = 3$ nm	% change	$l_c = 5$ nm	% change	$l_c = 8$ nm	% change
Zigzag (5,0)	0.561	209.9	3%	213.8	5%	219.7	8%
Armchair (5,5)	0.848	209.3	3%	212.8	4%	218.1	7%
Chiral (5,10)	1.206	208.7	2%	211.9	4%	216.6	6%

4.5.2.4 Effect of Thermal Contact Conductance on the Effective Thermal Conductivity of the Nanocomposite

The analysis has been carried out Using MATLAB code for a 3 % volume fraction carbon nanotubes reinforced metal matrix Nanocomposite material with a constant aspect ratio. It must be noted that the effective medium theory tends to the case of perfect interfaces for low volume fractions. However, it can be said that although the thermal contact conductance affects the overall heat conduction mechanism, it is probably not the most significant factor affecting the overall conductivity [87]. The thermal contact conductance probably has a greater influence on the heat carrying capacity of the composite rather than the effective conductivity. The variation of the

effective thermal conductivity with changes in the value of the thermal contact conductance has been presented in Table 4.28 (a), (b), and (c) for armchair (5,5) carbon nanotubes reinforced iron metal matrixes at different lengths, It can be seen from the mentioned Tables that the effective thermal conductivity is slightly increased with respect to the matrix thermal conductivity. It can be observed that at $l_c = 3$ nm and $\beta = 12$ MW/m²K, the thermal conductivity of the composite is 73.1008 W/m K which is about 0.55% increment of the matrix thermal conductivity, while at $\beta = 10000$ MW/m²K, the thermal conductivity of the new composite is 73.76 W/m K which is about 1.46% increment of the matrix thermal conductivity.

Table 4.28: Effect of thermal contact conductance on thermal conductivity for armchair carbon nanotube reinforced iron matrix at different length: (a) at $l_c = 3$ nm, (b) at $l_c = 5$ nm, and (c) at $l_c = 8$ nm

(a) At $l_c = 3$ nm

β (MW/m ² k)	K (W/m K)					
	(5,5)	% change	(10,10)	% change	(15,15)	% change
12	73.1008	0.55%	72.9008	0.28%	72.8008	0.14%
30	73.1020	0.55%	72.9020	0.28%	72.8020	0.14%
50	73.1033	0.55%	72.9033	0.28%	72.8033	0.14%
100	73.1066	0.56%	72.9066	0.28%	72.8066	0.15%
500	73.1331	0.60%	72.9331	0.32%	72.8331	0.18%
1000	73.1662	0.64%	72.9662	0.37%	72.8662	0.23%
2500	73.2655	0.78%	73.0655	0.50%	72.9655	0.37%
5000	73.4310	1.01%	73.2310	0.73%	73.1310	0.59%
10000	73.7620	1.46%	73.5620	1.19%	73.4620	1.05%

(b) At $l_c = 5$ nm

β (MW/m ² k)	K (W/m K)					
	(5,5)	% change	(10,10)	% change	(15,15)	% change
12	73.3008	0.83%	73.2008	0.69%	73.1008	0.55%
30	73.3020	0.83%	73.2020	0.69%	73.1020	0.55%
50	73.3033	0.83%	73.2033	0.69%	73.1033	0.55%
100	73.3066	0.83%	73.2066	0.70%	73.1066	0.56%
500	73.3331	0.87%	73.2331	0.73%	73.1331	0.60%
1000	73.3662	0.92%	73.2662	0.78%	73.1662	0.64%
2500	73.4655	1.05%	73.3655	0.92%	73.2655	0.78%
5000	73.6310	1.28%	73.5310	1.14%	73.4310	1.01%
10000	73.9620	1.74%	73.8620	1.60%	73.7620	1.46%

(c) At $l_c = 8 \text{ nm}$

β (MW/m ² k)	K (W/m K)					
	(5,5)	% change	(10,10)	% change	(15,15)	% change
12	73.60	1.24%	73.50	1.10%	73.40	0.96%
30	73.60	1.24%	73.50	1.10%	73.40	0.97%
50	73.60	1.24%	73.50	1.10%	73.40	0.97%
100	73.61	1.25%	73.51	1.11%	73.41	0.97%
500	73.63	1.28%	73.53	1.15%	73.43	1.01%
1000	73.67	1.33%	73.57	1.19%	73.47	1.05%
2500	73.77	1.47%	73.67	1.33%	73.57	1.19%
5000	73.93	1.69%	73.83	1.56%	73.73	1.42%
10000	74.26	2.15%	74.16	2.01%	74.06	1.87%

From the above Table, the effect of thermal contact conductance on the thermal conductivity for armchair (5, 5) carbon nanotube reinforced iron metal matrix is tabulated at different length. It can be observed that as the length of carbon nanotubes increase the thermal conductivity relatively increased. Figure 4.63 shows that the thermal conductivity is insensitive with increasing of thermal contact conductance up to $\beta = 1000 \text{ MW/m}^2\text{K}$ while increases relatively after that value because of the assumption of perfect contact between the matrix and carbon nanotubes.

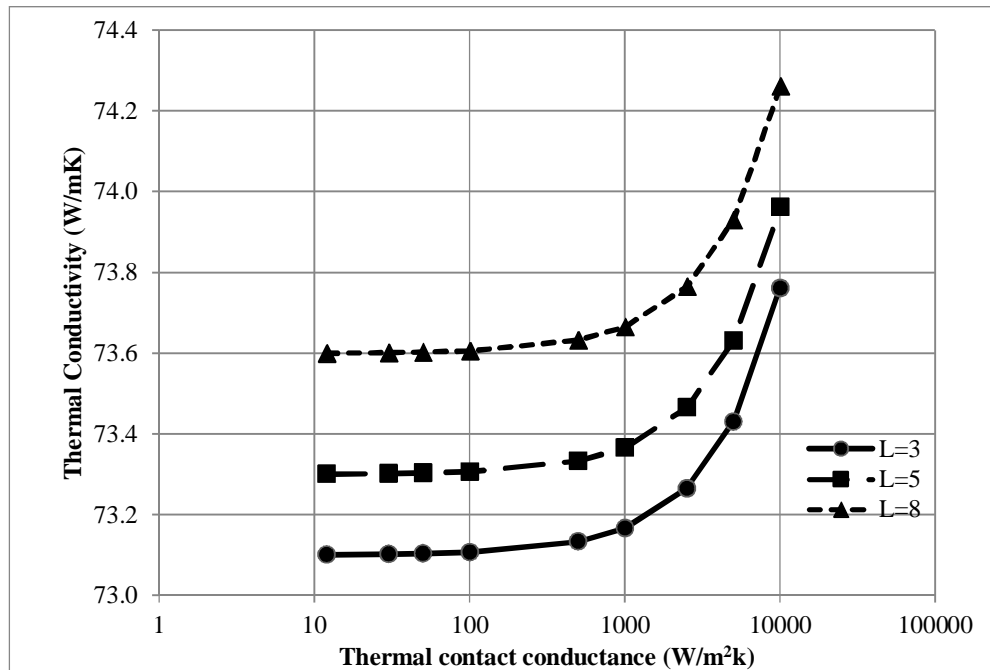


Figure 4.63: Effect of thermal contact conductance on thermal conductivity for armchair carbon nanotube (5, 5) reinforced iron metal matrix

For zigzag carbon nanotubes reinforced iron metal matrixes at different lengths, Table 4.29 (a), (b), and (C) shows the variation of the effective thermal conductivity with changes of the thermal contact conductance. It can be seen that the thermal conductivity slightly increased with respect to the matrix thermal conductivity. As an example, for zigzag (5, 0) carbon nanotube reinforced iron matrix at $l_c = 3$ nm and $\beta = 12$ MW/m²K, the thermal conductivity of the new composite is 73.301 W/m K which is about 0.83% increment of the matrix thermal conductivity while at $\beta = 10000$ MW/m²K, the thermal conductivity of the composite is 73.76 W/m K which is about 1.46% increment of the matrix thermal conductivity. From the Table 4.29 (a), (b), and (C), it can be observed that as the length of carbon nanotubes increase the thermal conductivity relatively increased. Figure 4.64 shows that the thermal conductivity is insensitive with increasing of thermal contact conductance up to $\beta = 1000$ MW/m²K while increases relatively after that value because of the assumption of perfect contact between the matrix and carbon nanotubes.

Table 4.29: Effect of thermal contact conductance on thermal conductivity for zigzag carbon nanotube reinforced iron matrix at different length: (a) at $l_c = 3$ nm, (b) at $l_c = 5$ nm, and (c) at $l_c = 8$ nm

(a) At $l_c = 3$ nm

β (MW/m ² k)	K (W/m K)					
	(5,0)	% change	(10,0)	% change	(15,0)	% change
12	73.301	0.83%	73.101	0.55%	73.001	0.41%
30	73.301	0.83%	73.101	0.55%	73.001	0.41%
50	73.302	0.83%	73.102	0.55%	73.002	0.42%
100	73.305	0.83%	73.105	0.56%	73.005	0.42%
500	73.323	0.86%	73.123	0.58%	73.023	0.44%
1000	73.346	0.89%	73.146	0.61%	73.046	0.48%
2500	73.415	0.98%	73.215	0.71%	73.115	0.57%
5000	73.530	1.14%	73.330	0.87%	73.230	0.73%
10000	73.760	1.46%	73.560	1.18%	73.460	1.05%

(b) At $l_c = 5$ nm

β (MW/m ² k)	K (W/m K)					
	(5,0)	% change	(10,0)	% change	(15,0)	% change
12	73.40	0.96%	73.30	0.83%	73.20	0.69%
30	73.40	0.96%	73.30	0.83%	73.20	0.69%
50	73.40	0.97%	73.30	0.83%	73.20	0.69%
100	73.40	0.97%	73.30	0.83%	73.20	0.69%
500	73.42	0.99%	73.32	0.86%	73.22	0.72%
1000	73.45	1.03%	73.35	0.89%	73.25	0.75%
2500	73.52	1.12%	73.42	0.98%	73.32	0.85%
5000	73.63	1.28%	73.53	1.14%	73.43	1.00%
10000	73.86	1.60%	73.76	1.46%	73.66	1.32%

(c) At $l_c = 8 \text{ nm}$

β (MW/m ² k)	K (W/m K)					
	(5,0)	% change	(10,0)	% change	(15,0)	% change
12	73.80	1.51%	73.60	1.24%	73.50	1.10%
30	73.80	1.52%	73.60	1.24%	73.50	1.10%
50	73.80	1.52%	73.60	1.24%	73.50	1.10%
100	73.81	1.52%	73.60	1.24%	73.50	1.11%
500	73.83	1.56%	73.62	1.27%	73.52	1.13%
1000	73.87	1.60%	73.65	1.30%	73.55	1.16%
2500	73.97	1.74%	73.72	1.40%	73.62	1.26%
5000	74.13	1.97%	73.83	1.55%	73.73	1.42%
10000	74.46	2.42%	74.06	1.87%	73.96	1.73%

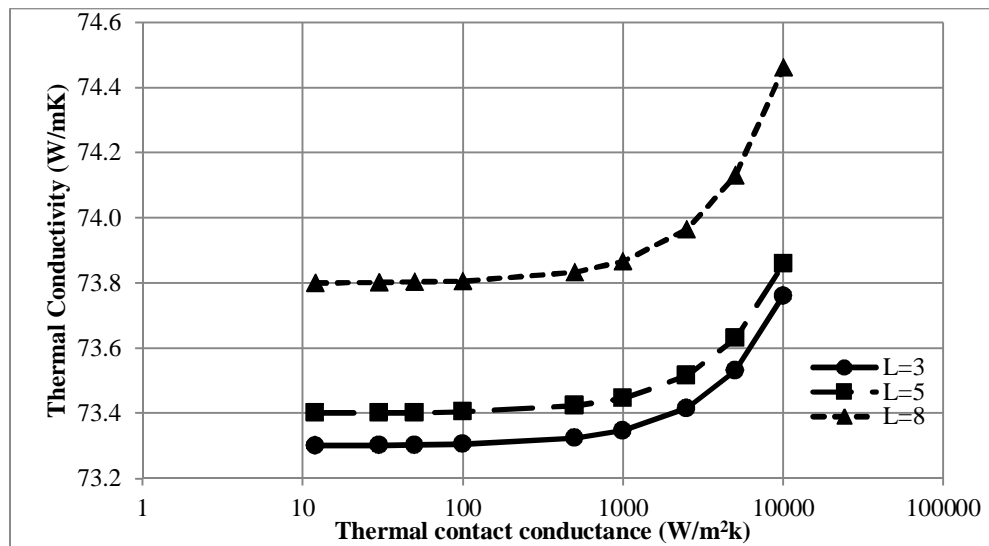


Figure 4.64: Effect of thermal contact conductance on thermal conductivity for zigzag carbon nanotube (5, 0) reinforced iron metal matrix

However, chiral carbon nanotubes reinforced iron metal matrixes at different lengths, Table 4.30 (a), (b), and (C), shows the variation of the effective thermal conductivity with changes of the thermal contact conductance. It can be seen that the thermal conductivity slightly increased with respect to the matrix thermal conductivity. As an example, for chiral (5, 10) carbon nanotube reinforced iron matrix at $l_c = 3$ and $\beta = 12 \text{ MW/m}^2\text{K}$, the thermal conductivity of the new composite is 73 W/m K which is about 0.41% increment of the matrix thermal conductivity while at $\beta = 10000 \text{ MW/m}^2\text{K}$, the thermal conductivity of the new composite is 73.331 W/m K which is about 1.32% increment of the matrix thermal conductivity. It can be observed that as the length of carbon nanotubes increase the thermal conductivity relatively increased. Figure 4.65 shows that the thermal conductivity is insensitive with increasing of thermal contact

conductance up to $\beta = 1000 \text{ MW/m}^2\text{K}$ while increases relatively after that value because of the assumption of perfect contact between the matrix and carbon nanotubes.

Table 4.30: Effect of thermal contact conductance on thermal conductivity for chiral carbon nanotube reinforced iron matrix at different length:

(a) at $l_c = 3 \text{ nm}$, (b) at $l_c = 5 \text{ nm}$, and (c) at $l_c = 8 \text{ nm}$

(a) At $l_c = 3 \text{ nm}$

β (MW/m ² k)	K (W/m K)					
	(5,10)	% change	(10,15)	% change	(15,20)	% change
12	73.000	0.41%	72.830	0.18%	72.600	-0.14%
30	73.001	0.42%	72.831	0.18%	72.601	-0.13%
50	73.002	0.42%	72.832	0.18%	72.602	-0.13%
100	73.003	0.42%	72.833	0.19%	72.603	-0.13%
500	73.007	0.46%	72.837	0.22%	72.607	-0.09%
1000	73.033	0.50%	72.863	0.27%	72.633	-0.05%
2500	73.066	0.64%	72.896	0.41%	72.666	0.09%
5000	73.166	0.87%	72.996	0.63%	72.766	0.32%
10000	73.331	1.32%	73.161	1.09%	72.931	0.77%

(b) At $l_c = 5 \text{ nm}$

β (MW/m ² k)	K (W/m K)					
	(5,10)	% change	(10,15)	% change	(15,20)	% change
12	73.100	0.55%	73.070	0.51%	72.900	0.28%
30	73.102	0.55%	73.071	0.51%	72.901	0.28%
50	73.102	0.55%	73.072	0.51%	72.902	0.28%
100	73.107	0.56%	73.073	0.52%	72.903	0.28%
500	73.107	0.60%	73.077	0.55%	72.907	0.32%
1000	73.166	0.64%	73.103	0.60%	72.933	0.37%
2500	73.166	0.78%	73.136	0.74%	72.966	0.50%
5000	73.431	1.01%	73.236	0.96%	73.066	0.73%
10000	73.431	1.46%	73.401	1.42%	73.231	1.19%

(c) At $l_c = 8 \text{ nm}$

β (MW/m ² k)	K (W/m K)					
	(5,10)	% change	(10,15)	% change	(15,20)	% change
12	73.401	0.96%	73.301	0.83%	73.201	0.69%
30	73.402	0.97%	73.072	0.83%	73.202	0.69%
50	73.403	0.97%	73.303	0.83%	73.203	0.69%
100	73.407	0.97%	73.077	0.83%	73.207	0.70%
500	73.433	1.01%	73.333	0.87%	73.233	0.73%
1000	73.466	1.05%	73.136	0.92%	73.266	0.78%
2500	73.566	1.19%	73.466	1.05%	73.366	0.92%
5000	73.731	1.42%	73.401	1.28%	73.531	1.14%
10000	73.401	0.96%	73.301	0.83%	73.201	0.69%

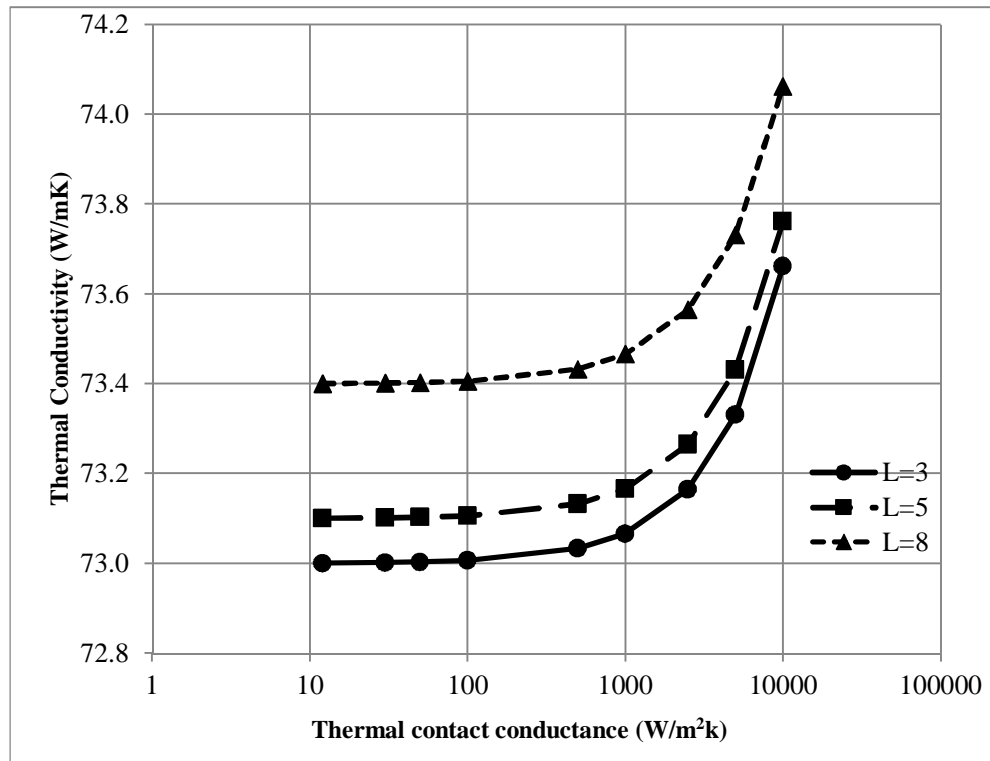


Figure 4.65: Effect of thermal contact conductance on thermal conductivity for chiral carbon nanotube (5, 10) reinforced iron metal matrix

Table 4.31 represents the effect of thermal contact conductance on thermal conductivity results for different chiral index of carbon nanotubes reinforced iron metal matrix.

Table 4.31: Effect of thermal contact conductance on thermal conductivity for different chiral index of reinforced iron matrix at different lengths ($V_f=3\%$)

β (MW/m²k)	K (W/m K) at $l_c=3$ nm			K (W/m K) at $l_c=5$ nm			K (W/m K) at $l_c=8$ nm		
	(5,0)	(5,5)	(5,10)	(5,0)	(5,5)	(5,10)	(5,0)	(5,5)	(5,10)
12	73.301	73.101	73.000	73.40	73.308	73.100	73.80	73.60	73.401
30	73.301	73.102	73.001	73.40	73.302	73.102	73.80	73.60	73.402
50	73.302	73.103	73.002	73.40	73.303	73.102	73.80	73.60	73.403
100	73.305	73.107	73.003	73.40	73.306	73.107	73.81	73.61	73.407
500	73.323	73.133	73.007	73.42	73.333	73.107	73.83	73.63	73.433
1000	73.346	73.166	73.033	73.45	73.366	73.166	73.87	73.67	73.466
2500	73.415	73.266	73.066	73.52	73.465	73.166	73.97	73.77	73.566
5000	73.530	73.431	73.166	73.63	73.631	73.431	74.13	73.93	73.731
10000	73.760	73.762	73.331	73.86	73.962	73.431	74.46	74.26	73.401

The results calculated at 3% volume fraction and length was $l_c=3$ nm show slightly increases on the thermal conductivity when the thermal contact conductance increased from 12 MW/m² K to 10000 MW/m² K. The Zigzag carbon nanotube (5, 0) shows a

higher prediction than armchair and chiral type. It can be observed from the above Table that the thermal conductivity increases by 0.83% at 12 MW/m² K and 1.46% at 10000 MW/m² K for Zigzag. However, for Armchair carbon nanotubes (5, 5) the increment varied as 0.55% to 1.46% while for chiral carbon nanotubes (5, 10) varied as 0.41% to 1.32% at the same length respectively. Figures 4.66, 4.67, and 4.68, show a comparison between different types of carbon nanotubes reinforced iron metal matrix at different lengths.

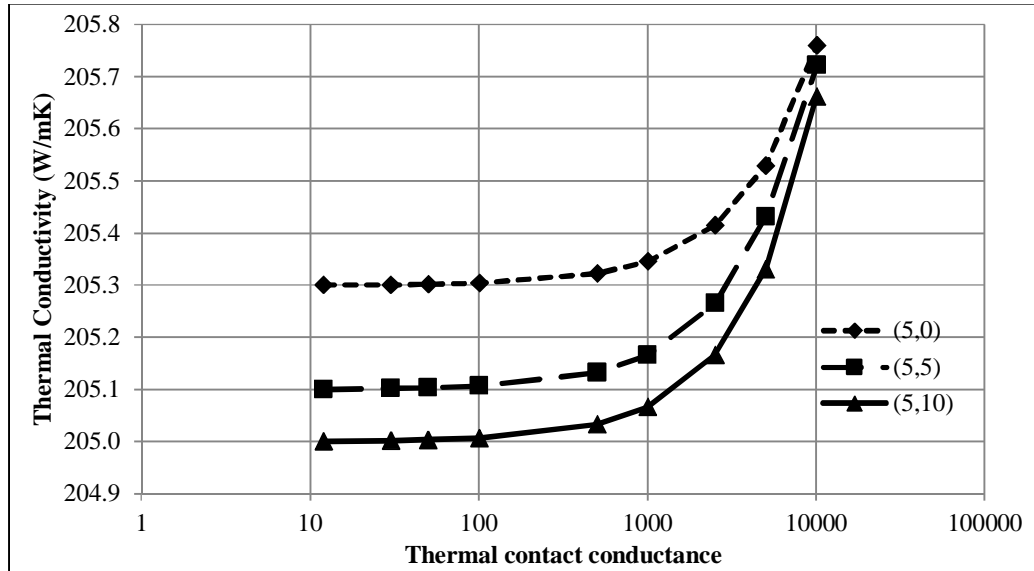


Figure 4.66: Effect of thermal contact conductance on thermal conductivity for different chiral Indices carbon nanotube reinforced iron metal matrix (at $l_c=3$ nm)

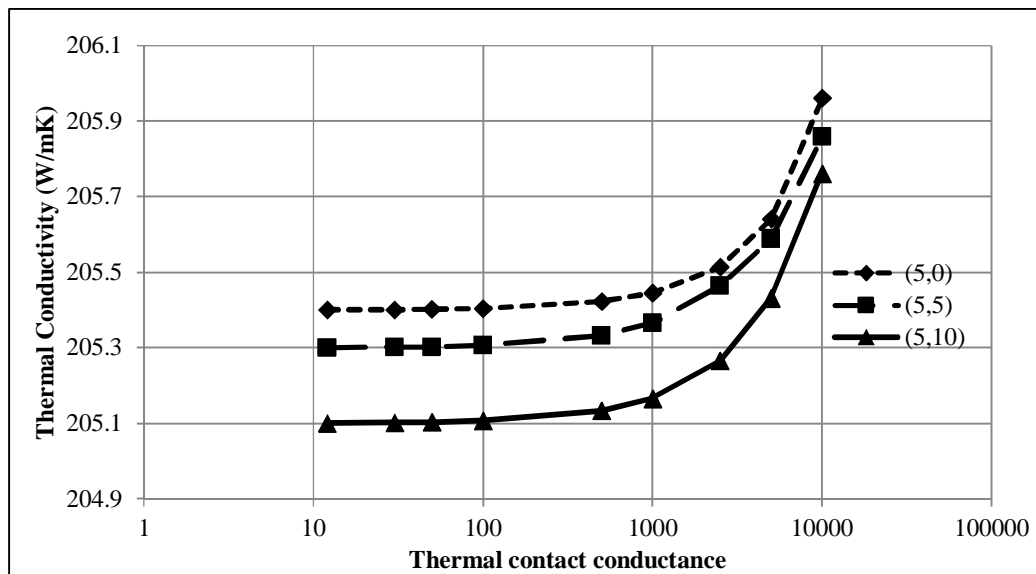


Figure 4.67: Effect of thermal contact conductance on thermal conductivity for different chiral Indices carbon nanotube reinforced iron metal matrix (at $l_c=5$ nm)

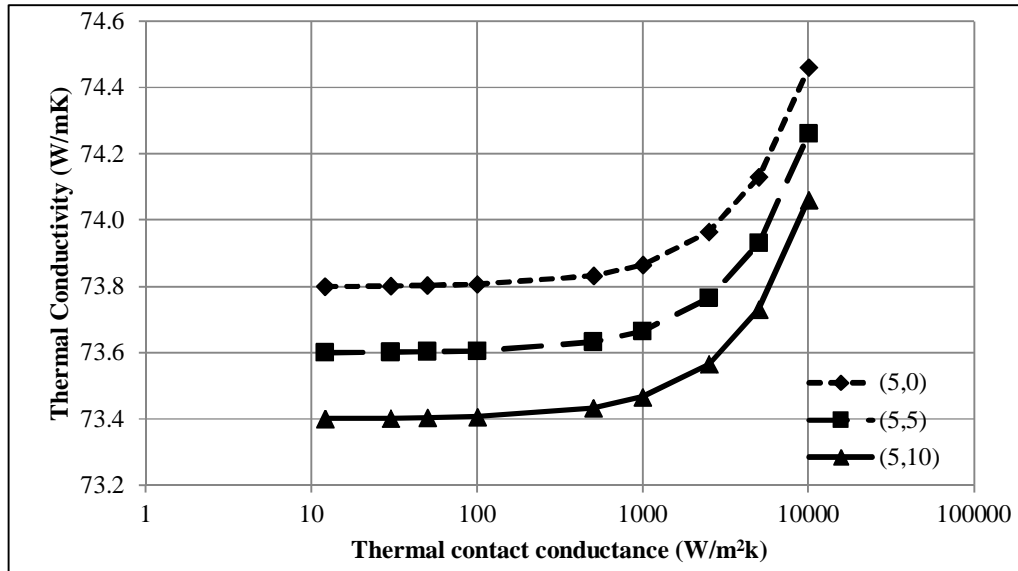


Figure 4.68: Effect of thermal contact conductance on thermal conductivity for different chiral Indices carbon nanotube reinforced iron metal matrix (at $l_c=8$ nm)

Similarly the procedure will be taken for the prediction of the effect of thermal contact conductance on the thermal conductivity for the copper and aluminum matrixes. For copper matrix, Tables 4.32 (a), (b), and (c) for armchair carbon nanotubes reinforced copper metal matrixes at different lengths, it can be seen that the effective thermal conductivity is slightly increased with respect to the matrix thermal conductivity. As an example, for armchair (5, 5) carbon nanotube reinforced copper matrix at $l_c = 3$ nm and $\beta= 12$ MW/m²K, the thermal conductivity of the new composite was 387.1010 W/m K which is about 0.29% increment of the matrix thermal conductivity while at $\beta= 10000$ MW/m²K, the thermal conductivity of the new composite was 387.762 W/m K which is about 0.46% increment of the matrix thermal conductivity.

Table 4.32: Effect of thermal contact conductance on thermal conductivity for armchair carbon nanotube reinforced copper matrix at different length: (a) at $l_c =3$ nm, (b) at $l_c =5$ nm, and (c) at $l_c =8$ nm

(a) At $l_c =3$ nm

β (MW/m ² k)	K (W/m K)					
	(5,5)	% change	(10,10)	% change	(15,15)	% change
12	387.1010	0.29%	386.902	0.23%	386.703	0.18%
30	387.1025	0.29%	386.904	0.23%	386.705	0.18%
50	387.1043	0.29%	386.906	0.23%	386.708	0.18%
100	387.1065	0.29%	386.912	0.23%	386.711	0.18%
500	387.1321	0.29%	386.934	0.24%	386.732	0.19%
1000	387.1652	0.30%	386.971	0.25%	386.774	0.20%
2500	387.2645	0.33%	387.075	0.28%	386.872	0.22%
5000	387.4310	0.37%	387.234	0.32%	387.033	0.27%
10000	387.7620	0.46%	387.562	0.40%	387.361	0.35%

(b) At $l_c = 5$ nm

β (MW/m ² k)	K (W/m K)					
	(5,5)	% change	(10,10)	% change	(15,15)	% change
12	387.311	0.34%	387.209	0.31%	387.107	0.29%
30	387.312	0.34%	387.210	0.31%	387.105	0.29%
50	387.313	0.34%	387.212	0.31%	387.111	0.29%
100	387.317	0.34%	387.216	0.31%	387.114	0.29%
500	387.333	0.35%	387.231	0.32%	387.133	0.29%
1000	387.366	0.35%	387.262	0.33%	387.165	0.30%
2500	387.466	0.38%	387.363	0.35%	387.267	0.33%
5000	387.631	0.42%	387.531	0.40%	387.433	0.37%
10000	387.962	0.51%	387.862	0.48%	387.762	0.46%

(c) At $l_c = 8$ nm

β (MW/m ² k)	K (W/m K)					
	(5,5)	% change	(10,10)	% change	(15,15)	% change
12	387.612	0.41%	387.509	0.39%	387.403	0.36%
30	387.614	0.42%	387.511	0.39%	387.406	0.36%
50	387.615	0.42%	387.513	0.39%	387.407	0.36%
100	387.618	0.42%	387.516	0.39%	387.414	0.36%
500	387.632	0.42%	387.532	0.40%	387.431	0.37%
1000	387.674	0.43%	387.576	0.41%	387.472	0.38%
2500	387.771	0.46%	387.674	0.43%	387.571	0.41%
5000	387.935	0.50%	387.832	0.47%	387.731	0.45%
10000	388.261	0.59%	388.161	0.56%	388.065	0.53%

From the above Tables, the effect of thermal contact conductance on the thermal conductivity for armchair (5, 5) carbon nanotube reinforced copper metal matrix is tabulated at different length. It can be observed that as the length of carbon nanotubes increase the thermal conductivity relatively increased. Figure 4.69 shows that the thermal conductivity is insensitive with increasing of thermal contact conductance up to $\beta = 1000$ MW/m²K while increases relatively after that value because of the assumption of perfect contact between the matrix and carbon nanotubes.

For zigzag carbon nanotubes reinforced copper metal matrixes at different lengths, Tables 4.33 (a), (b), and (c) shows the variation of the effective thermal conductivity with change of the thermal contact conductance. It can be seen that the thermal conductivity slightly increased with respect to the matrix thermal conductivity. As an example, for zigzag (5, 0) carbon nanotube reinforced copper matrix at $l_c = 3$ nm and $\beta = 12$ MW/m²K, the thermal conductivity of the new composite was 387.301 W/m K which is about 0.83% increment of the matrix thermal conductivity while at $\beta = 10000$ MW/m²K, the thermal conductivity of the new composite was 387.76 W/m K which is about 1.46% increment of the matrix thermal conductivity.

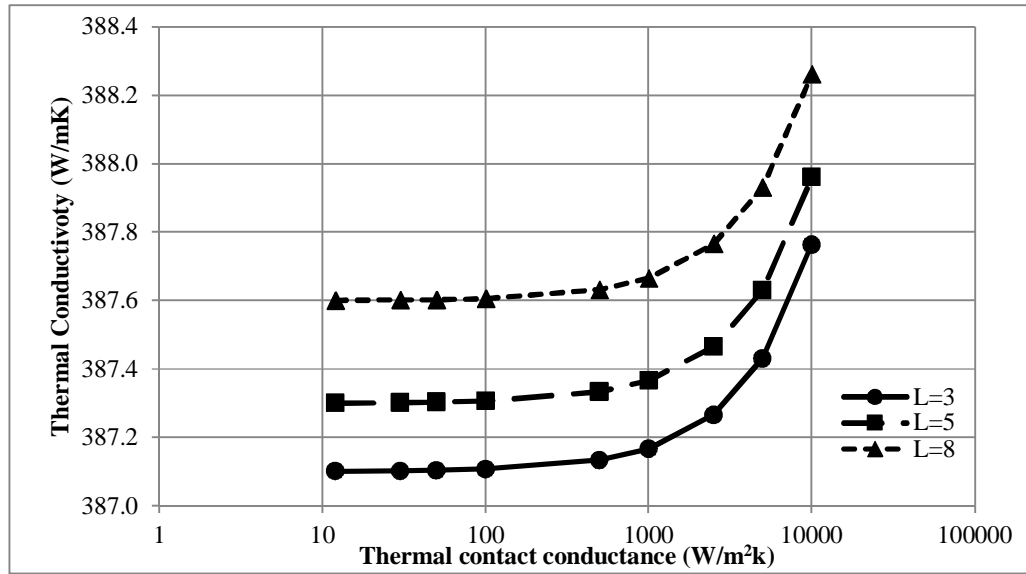


Figure 4.69: Effect of thermal contact conductance on thermal conductivity for armchair carbon nanotube (5, 5) reinforced copper metal matrix

Table 4.33: Effect of thermal contact conductance on thermal conductivity for zigzag carbon nanotube reinforced copper matrix at different length: (a) at $l_c = 3$ nm, (b) at $l_c = 5$ nm, and (c) at $l_c = 8$ nm

(a) At $l_c = 3$ nm

β (MW/m ² k)	K (W/m K)					
	(5,0)	% change	(10,0)	% change	(15,0)	% change
12	387.3015	0.34%	387.1012	0.29%	387.0012	0.26%
30	387.3016	0.34%	387.1014	0.29%	387.0013	0.26%
50	387.3021	0.34%	387.1025	0.29%	387.0021	0.26%
100	387.3052	0.34%	387.1053	0.29%	387.0053	0.26%
500	387.3232	0.34%	387.1232	0.29%	387.0234	0.27%
1000	387.3461	0.35%	387.1466	0.30%	387.0462	0.27%
2500	387.4153	0.37%	387.2151	0.31%	387.1158	0.29%
5000	387.5301	0.40%	387.3305	0.34%	387.2309	0.32%
10000	387.7603	0.46%	387.5602	0.40%	387.4606	0.38%

(b) At $l_c = 5$ nm

β (MW/m ² k)	K (W/m K)					
	(5,0)	% change	(10,0)	% change	(15,0)	% change
12	387.40	0.36%	387.30	0.34%	387.20	0.31%
30	387.40	0.36%	387.30	0.34%	387.20	0.31%
50	387.40	0.36%	387.30	0.34%	387.20	0.31%
100	387.40	0.36%	387.30	0.34%	387.20	0.31%
500	387.42	0.37%	387.32	0.34%	387.22	0.32%
1000	387.45	0.37%	387.35	0.35%	387.25	0.32%
2500	387.52	0.39%	387.42	0.37%	387.32	0.34%
5000	387.63	0.42%	387.53	0.40%	387.43	0.37%
10000	387.86	0.48%	387.76	0.46%	387.66	0.43%

(c) At $l_c = 8 \text{ nm}$

β (MW/m ² k)	K (W/m K)					
	(5,0)	% change	(10,0)	% change	(15,0)	% change
12	387.80	0.47%	387.60	0.41%	387.50	0.39%
30	387.80	0.47%	387.60	0.41%	387.50	0.39%
50	387.80	0.47%	387.60	0.42%	387.50	0.39%
100	387.81	0.47%	387.60	0.42%	387.50	0.39%
500	387.83	0.47%	387.62	0.42%	387.52	0.39%
1000	387.87	0.48%	387.65	0.43%	387.55	0.40%
2500	387.97	0.51%	387.72	0.44%	387.62	0.42%
5000	388.13	0.55%	387.83	0.47%	387.73	0.45%
10000	388.46	0.64%	388.06	0.53%	387.96	0.51%

From the Tables 4.33 (a), (b), and (c), it can be observed that as the length of carbon nanotubes increase the thermal conductivity relatively increased. Figure 4.70 shows that the thermal conductivity is insensitive with increasing of thermal contact conductance up to $\beta = 1000 \text{ MW/m}^2\text{K}$ while increases relatively after that value because of the assumption of perfect contact between the matrix and carbon nanotubes.

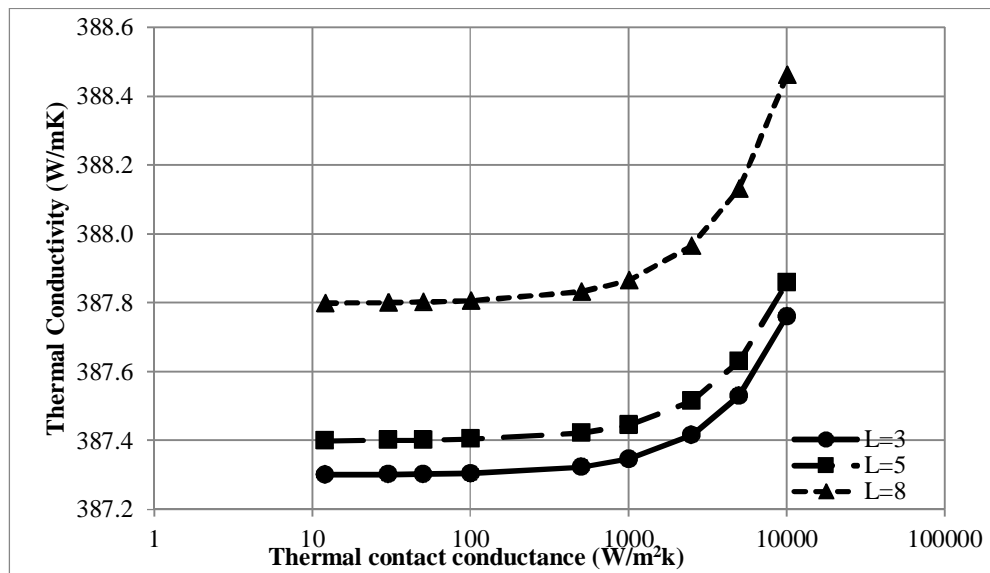


Figure 4.70: Effect of thermal contact conductance on thermal conductivity for zigzag carbon nanotube (5, 0) reinforced copper metal matrix

However, for chiral carbon nanotubes reinforced copper metal matrixes at different lengths, Tables 4.34 (a), (b), and (c), show the variation of the effective thermal conductivity with change of the thermal contact conductance. It can be seen that the thermal conductivity slightly increased with respect to the matrix thermal conductivity. As an example, for chiral (5, 10) carbon nanotube reinforced copper matrix at $l_c = 3$ and $\beta = 12 \text{ MW/m}^2\text{K}$, the thermal conductivity of the new composite was 386.910 W/m K

which is about 0.24% increment of the matrix thermal conductivity while at $\beta= 10000$ MW/m²K, the thermal conductivity of the new composite was 387.241 W/m K which is about 0.41% increment of the matrix thermal conductivity.

Table 4.34: Effect of thermal contact conductance on thermal conductivity for chiral carbon nanotube reinforced copper matrix at different length: (a) at $l_c = 3$ nm, (b) at $l_c = 5$ nm, and (c) at $l_c = 8$ nm

(a) At $l_c = 3$ nm

β (MW/m ² k)	K (W/m K)					
	(5,10)	% change	(10,15)	% change	(15,20)	% change
12	386.910	0.24%	386.830	0.22%	386.721	0.18%
30	386.911	0.24%	386.831	0.22%	386.701	0.18%
50	386.912	0.24%	386.832	0.22%	386.702	0.18%
100	386.913	0.24%	386.833	0.22%	386.703	0.18%
500	386.917	0.24%	386.837	0.22%	386.707	0.19%
1000	386.943	0.25%	386.863	0.23%	386.733	0.20%
2500	386.976	0.28%	386.896	0.26%	386.766	0.22%
5000	387.076	0.32%	386.996	0.30%	386.866	0.27%
10000	387.241	0.41%	387.161	0.39%	387.031	0.35%

(b) At $l_c = 5$ nm

β (MW/m ² k)	K (W/m K)					
	(5,10)	% change	(10,15)	% change	(15,20)	% change
12	387.101	0.29%	387.040	0.27%	386.901	0.23%
30	387.102	0.29%	387.041	0.27%	386.901	0.23%
50	387.102	0.29%	387.042	0.27%	386.902	0.23%
100	387.107	0.29%	387.043	0.27%	386.903	0.23%
500	387.108	0.29%	387.047	0.28%	386.907	0.24%
1000	387.166	0.30%	387.073	0.29%	386.933	0.25%
2500	387.168	0.33%	387.106	0.31%	386.966	0.28%
5000	387.431	0.37%	387.206	0.36%	387.066	0.32%
10000	387.431	0.46%	387.371	0.44%	387.231	0.40%

(c) At $l_c = 8$ nm

β (MW/m ² k)	K (W/m K)					
	(5,10)	% change	(10,15)	% change	(15,20)	% change
12	387.401	0.36%	387.301	0.34%	387.201	0.31%
30	387.402	0.36%	387.042	0.34%	387.202	0.31%
50	387.403	0.36%	387.303	0.34%	387.203	0.31%
100	387.407	0.36%	387.047	0.34%	387.207	0.31%
500	387.433	0.37%	387.333	0.35%	387.233	0.32%
1000	387.466	0.38%	387.106	0.35%	387.266	0.33%
2500	387.566	0.41%	387.466	0.38%	387.366	0.35%
5000	387.731	0.45%	387.371	0.42%	387.531	0.40%
10000	388.062	0.53%	387.962	0.51%	387.862	0.48%

From the Tables 4.33 (a), (b), and (c), it can be observed that as the length of carbon nanotubes increase the thermal conductivity relatively increased. Figure 4.71 shows that the thermal conductivity is insensitive with increasing of thermal contact conductance up to $\beta = 1000 \text{ MW/m}^2\text{K}$ while increases relatively after that value because of the assumption of perfect contact between the matrix and carbon nanotubes.

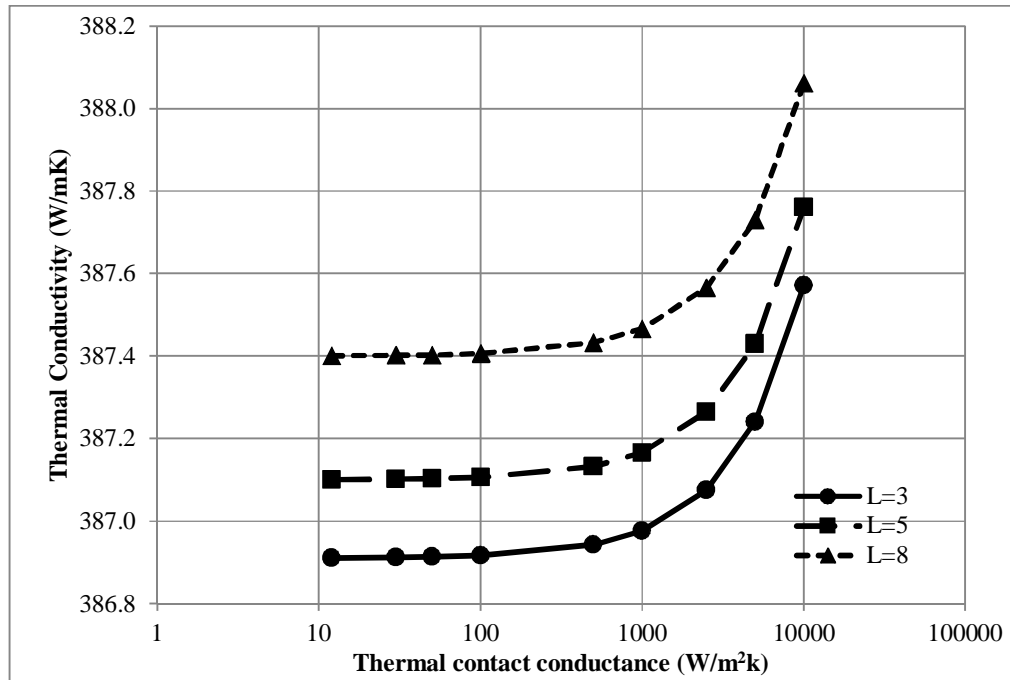


Figure 4.71: Effect of thermal contact conductance on thermal conductivity for chiral carbon nanotube (5, 10) reinforced copper metal matrix

Table 4.35 represents the effect of thermal contact conductance on thermal conductivity results for different chiral Index of carbon nanotubes reinforced copper metal matrix. The results calculated at 3% volume fraction and length was $l_c = 3 \text{ nm}$ show slightly increases on the thermal conductivity when the thermal contact conductance increased from $12 \text{ MW/m}^2 \text{ K}$ to $10000 \text{ MW/m}^2 \text{ K}$. The zigzag carbon nanotube (5, 0) shows a higher prediction than armchair and chiral type. It can be observed from the above Table that the thermal conductivity increases by 0.34% at $12 \text{ MW/m}^2 \text{ K}$ and 0.46% at $10000 \text{ MW/m}^2 \text{ K}$ for zigzag. However, for armchair carbon nanotubes (5, 5) the increment varied as 0.29% to 0.46% while for chiral carbon nanotubes (5, 10) varied as 0.24% to 0.41% at the same length ($l_c = 3 \text{ nm}$) respectively. Figures 4.72, 4.73, and 4.74, show a comparison between different types of carbon nanotubes reinforced copper metal matrix at different lengths.

Table 4.35: Effect of thermal contact conductance on thermal conductivity for different chiral index of reinforced copper matrix at different lengths

β MW/m ² k	K (W/m K) at $l_c=3$ nm			K (W/m K) at $l_c=5$ nm			K (W/m K) at $l_c=8$ nm		
	(5,0)	(5,5)	(5,10)	(5,0)	(5,5)	(5,10)	(5,0)	(5,5)	(5,10)
12	387.301	387.101	386.910	387.40	387.31	387.101	387.80	387.612	387.401
30	387.303	387.103	386.911	387.40	387.31	387.102	387.80	387.614	387.402
50	387.304	387.104	386.912	387.40	387.31	387.102	387.80	387.615	387.403
100	387.305	387.107	386.913	387.40	387.31	387.107	387.81	387.618	387.407
500	387.323	387.132	386.917	387.42	387.33	387.108	387.83	387.632	387.433
1000	387.346	387.165	386.943	387.45	387.37	387.166	387.87	387.674	387.466
2500	387.415	387.264	386.976	387.52	387.47	387.168	387.97	387.771	387.566
5000	387.530	387.431	387.076	387.63	387.63	387.431	388.13	387.935	387.731
10000	387.760	387.762	387.241	387.86	387.96	387.431	388.46	388.261	388.062

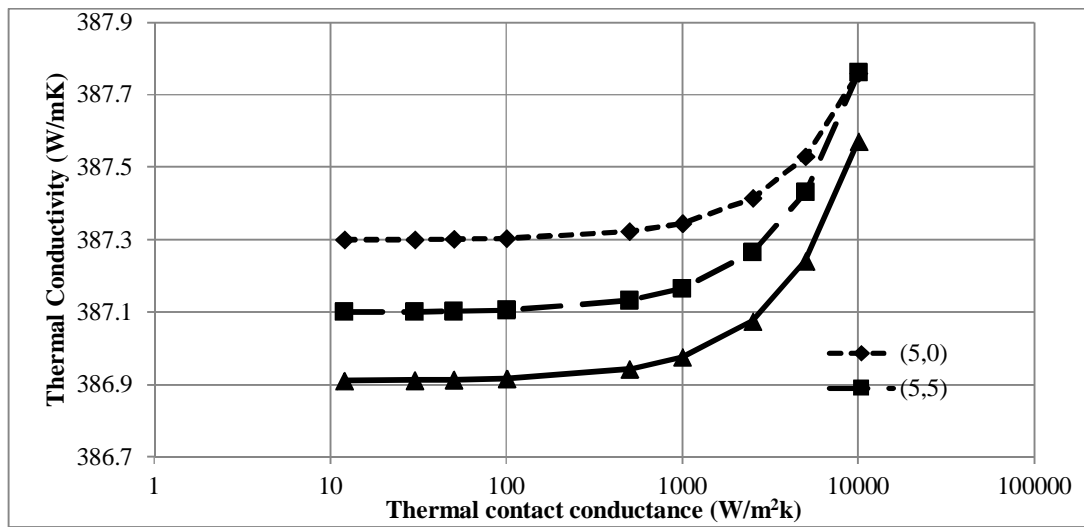


Figure 4.72: Effect of thermal contact conductance on thermal conductivity for different chiral indices carbon nanotube reinforced copper metal matrix (at $l_c=3$ nm)

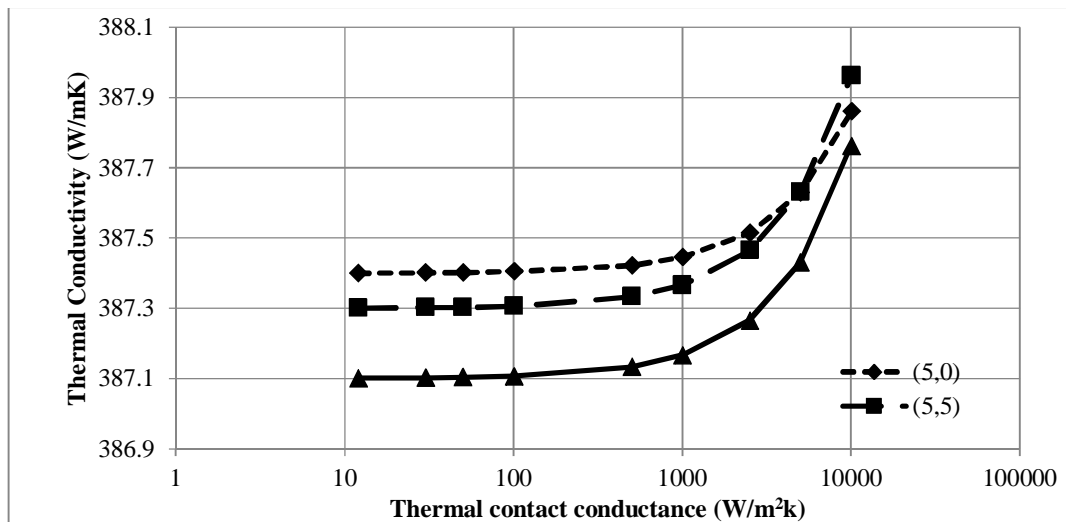


Figure 4.73: Effect of thermal contact conductance on thermal conductivity for different chiral indices carbon nanotube reinforced copper metal matrix (at $l_c=5$ nm)

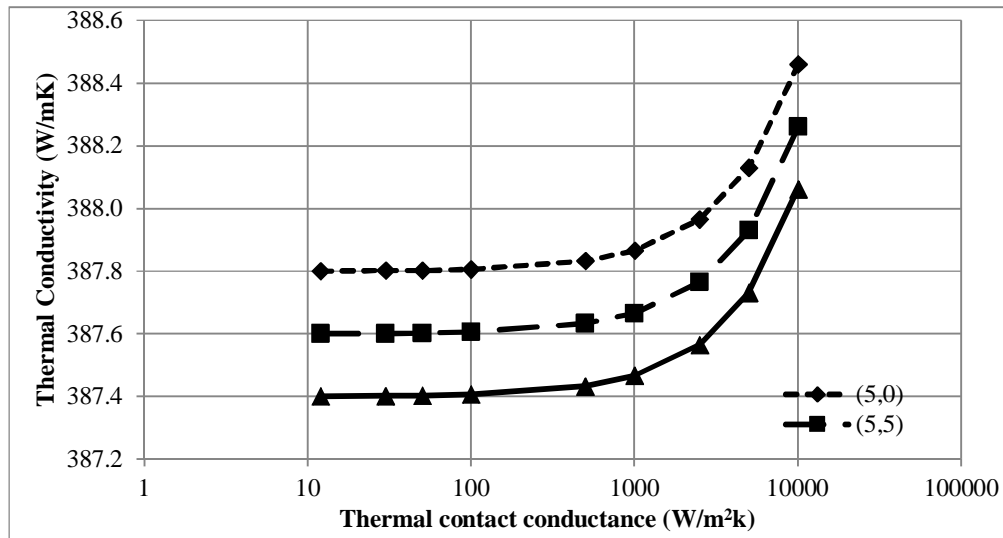


Figure 4.74: Effect of thermal contact conductance on thermal conductivity for different chiral indices carbon nanotube reinforced copper metal matrix (at $l_c=8$ nm)

However, for aluminum matrix, Tables 4.36 (a), (b), and (c), for armchair carbon nanotubes reinforced aluminum metal matrixes at different lengths, it can be seen that the effective thermal conductivity is slightly increased with respect to the matrix thermal conductivity. As an example, for armchair (5, 5) carbon nanotube reinforced aluminum matrix at $l_c=3$ nm and $\beta=12$ MW/m²K, the thermal conductivity of the new composite is 205.1008 W/m K which is about 0.54% increment of the matrix thermal conductivity while at $\beta=10000$ MW/m²K, the thermal conductivity of the new composite is 205.652 W/m K which is about 0.86% increment of the matrix thermal conductivity.

Table 4.36: Effect of thermal contact conductance on thermal conductivity for armchair carbon nanotube reinforced aluminum matrix at different length: (a) at $l_c=3$ nm, (b) at $l_c=5$ nm, and (c) at $l_c=8$ nm

(a) At $l_c=3$ nm

β (MW/m ² k)	K (W/m K)					
	(5,5)	% change	(10,10)	% change	(15,15)	% change
12	205.1008	0.54%	204.90	0.44%	204.80	0.39%
30	205.1020	0.54%	204.90	0.44%	204.80	0.39%
50	205.1033	0.54%	204.90	0.44%	204.80	0.39%
100	205.1066	0.54%	204.91	0.44%	204.81	0.40%
500	205.1331	0.56%	204.93	0.46%	204.83	0.41%
1000	205.1662	0.57%	204.97	0.47%	204.87	0.42%
2500	205.2655	0.62%	205.07	0.52%	204.97	0.47%
5000	205.4310	0.70%	205.23	0.60%	205.13	0.55%
10000	205.6520	0.86%	205.56	0.77%	205.46	0.72%

(b) At $l_c = 5$ nm

β (MW/m ² k)	K (W/m K)					
	(5,5)	% change	(10,10)	% change	(15,15)	% change
12	205.301	0.64%	205.201	0.59%	205.101	0.54%
30	205.302	0.64%	205.202	0.59%	205.102	0.54%
50	205.303	0.64%	205.203	0.59%	205.103	0.54%
100	205.307	0.64%	205.207	0.59%	205.107	0.54%
500	205.333	0.65%	205.233	0.60%	205.133	0.56%
1000	205.366	0.67%	205.266	0.62%	205.166	0.57%
2500	205.466	0.72%	205.366	0.67%	205.266	0.62%
5000	205.631	0.80%	205.531	0.75%	205.431	0.70%
10000	205.962	0.96%	205.862	0.91%	205.762	0.86%

(c) At $l_c = 8$ nm

β (MW/m ² k)	K (W/m K)					
	(5,5)	% change	(10,10)	% change	(15,15)	% change
12	205.60	0.78%	205.50	0.74%	205.40	0.69%
30	205.60	0.79%	205.50	0.74%	205.40	0.69%
50	205.60	0.79%	205.50	0.74%	205.40	0.69%
100	205.61	0.79%	205.51	0.74%	205.41	0.69%
500	205.63	0.80%	205.53	0.75%	205.43	0.70%
1000	205.67	0.82%	205.57	0.77%	205.47	0.72%
2500	205.77	0.87%	205.67	0.82%	205.57	0.77%
5000	205.93	0.95%	205.83	0.90%	205.73	0.85%
10000	206.26	1.11%	206.16	1.06%	206.06	1.01%

From the Tables 4.36 (a), (b), and (c), the effect of thermal contact conductance on the thermal conductivity for armchair (5, 5) carbon nanotube reinforced aluminum metal matrix is tabulated at different length. It can be observed that as the length of carbon nanotubes increase the thermal conductivity relatively increased. Figure 4.75 shows that the thermal conductivity is insensitive with increasing of thermal contact conductance up to $\beta = 1000$ MW/m²K while increases relatively after that value because of the assumption of perfect contact between the matrix and carbon nanotubes.

For zigzag carbon nanotubes reinforced aluminum metal matrixes at different lengths, Tables 4.37 (a), (b), and (c), show the variation of the effective thermal conductivity with change of the thermal contact conductance. It can be seen that the thermal conductivity slightly increased with respect to the matrix thermal conductivity. As an example, for zigzag (5, 0) carbon nanotube reinforced aluminum matrix at $l_c = 3$ nm and $\beta = 12$ MW/m²K, the thermal conductivity of the new composite was 205.301 W/m K which is about 0.64% increment of the matrix thermal conductivity while at $\beta = 10000$ MW/m²K, the thermal conductivity of the new composite was 205.76 W/m K which is about 0.86% increment of the matrix thermal conductivity.

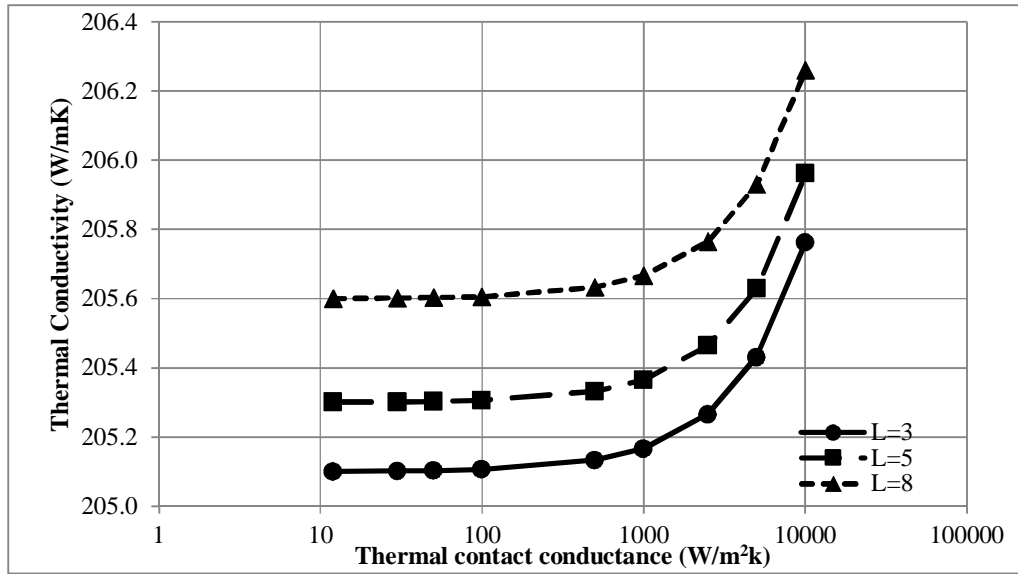


Figure 4.75: Effect of thermal contact conductance on Thermal Conductivity for armchair carbon nanotube (5, 5) (different length) reinforced aluminum metal matrix

it can be observed from the Tables 4.37 (a), (b), and (c), for zigzag (5, 0) carbon nanotube reinforced aluminum metal matrix, that as the length of carbon nanotubes increase the thermal conductivity relatively increased. Figure 4.76 shows that the thermal conductivity is insensitive with increasing of thermal contact conductance up to $\beta = 1000 \text{ MW/m}^2\text{K}$ while increases relatively after that value because of the assumption of perfect contact between the matrix and carbon nanotubes.

Table 4.37: Effect of thermal contact conductance on thermal conductivity for zigzag carbon nanotube reinforced aluminum matrix at different length: (a) at $l_c = 3 \text{ nm}$, (b) at $l_c = 5 \text{ nm}$, and (c) at $l_c = 8 \text{ nm}$

(a) At $l_c = 3 \text{ nm}$

β (MW/m ² k)	(5,0)		(10, 0)		(15,0)	
	K (W/m K)	%	K (W/m K)	%	K (W/m K)	%
12	205.301	0.64%	205.101	0.54%	205.001	0.49%
30	205.301	0.64%	205.101	0.54%	205.001	0.49%
50	205.302	0.64%	205.102	0.54%	205.002	0.49%
100	205.305	0.64%	205.105	0.54%	205.005	0.49%
500	205.323	0.65%	205.123	0.55%	205.023	0.50%
1000	205.346	0.66%	205.146	0.56%	205.046	0.51%
2500	205.415	0.69%	205.215	0.60%	205.115	0.55%
5000	205.530	0.75%	205.330	0.65%	205.230	0.60%
10000	205.760	0.86%	205.560	0.76%	205.460	0.72%

(b) At $l_c = 5 \text{ nm}$

β (MW/m ² k)	(5,0)		(10,0)		(15,0)	
	K (W/m K)	%	K (W/m K)	%	K (W/m K)	%
12	205.40	0.69%	205.30	0.64%	205.20	0.59%
30	205.40	0.69%	205.30	0.64%	205.20	0.59%
50	205.40	0.69%	205.30	0.64%	205.20	0.59%
100	205.40	0.69%	205.30	0.64%	205.20	0.59%
500	205.42	0.70%	205.32	0.65%	205.22	0.60%
1000	205.45	0.71%	205.35	0.66%	205.25	0.61%
2500	205.52	0.74%	205.42	0.69%	205.32	0.64%
5000	205.63	0.80%	205.53	0.75%	205.43	0.70%
10000	205.86	0.91%	205.76	0.86%	205.66	0.81%

(c) At $l_c = 8 \text{ nm}$

β (MW/m ² k)	(5,0)		(10,0)		(15,0)	
	K (W/m K)	%	K (W/m K)	%	K (W/m K)	%
12	205.80	0.88%	205.60	0.78%	205.50	0.74%
30	205.80	0.88%	205.60	0.78%	205.50	0.74%
50	205.80	0.88%	205.60	0.79%	205.50	0.74%
100	205.81	0.89%	205.60	0.79%	205.50	0.74%
500	205.83	0.90%	205.62	0.80%	205.52	0.75%
1000	205.87	0.91%	205.65	0.81%	205.55	0.76%
2500	205.97	0.96%	205.72	0.84%	205.62	0.79%
5000	206.13	1.04%	205.83	0.90%	205.73	0.85%
10000	206.46	1.21%	206.06	1.01%	205.96	0.96%

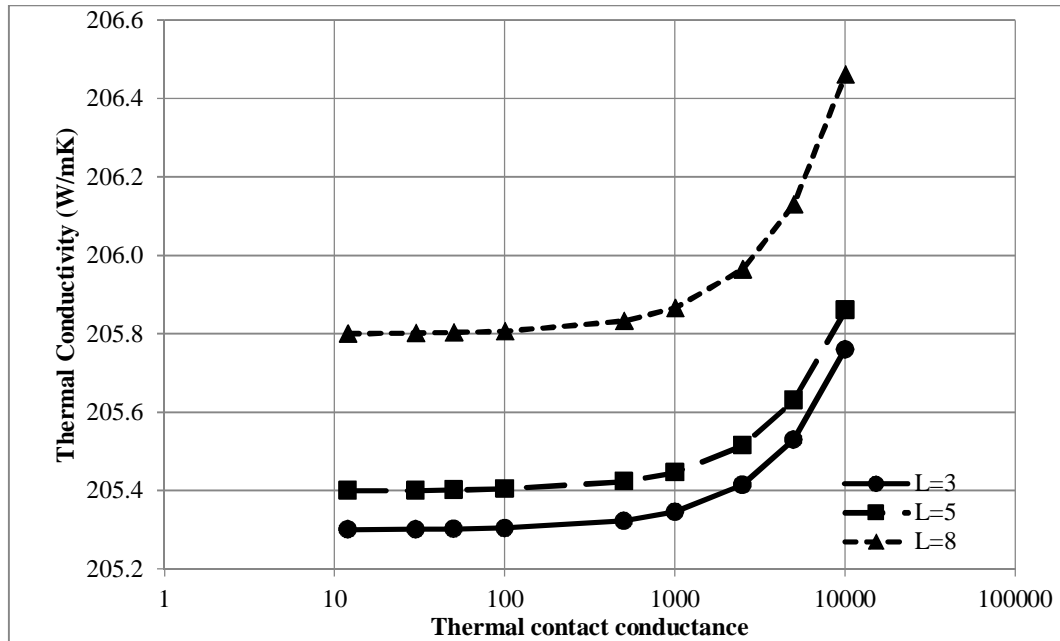


Figure 4.7b: Effect of thermal contact conductance on thermal conductivity for zigzag carbon nanotube (5, 0) (different length) reinforced aluminum metal matrix

However, for chiral carbon nanotubes reinforced aluminum metal matrixes at different lengths, Tables 4.38 (a), (b), and (c) show the variation of the effective thermal conductivity with changes of the thermal contact conductance. It can be seen that the thermal conductivity slightly increased with respect to the matrix thermal conductivity. As an example, for chiral (5, 10) carbon nanotube reinforced aluminum matrix at $l_c = 3$ and $\beta = 12$ MW/m²K, the thermal conductivity of the new composite is 205.0 W/m K which is about 0.49% increment of the matrix thermal conductivity while at $\beta = 10000$ MW/m²K, the thermal conductivity of the new composite is 205,331 W/m K which is about 0.81% increment of the matrix thermal conductivity.

Table 4.38: Effect of thermal contact conductance on thermal conductivity for chiral carbon nanotube reinforced aluminum matrix at different length: (a) at $l_c = 3$ nm, (b) at $l_c = 5$ nm, and (c) at $l_c = 8$ nm

(a) At $l_c = 3$ nm

β (MW/m ² k)	K (W/m K)					
	(5,10)	% change	(10,15)	% change	(15,20)	% change
12	205.0	0.49%	204.83	0.41%	204.6	0.29%
30	205.001	0.49%	204.831	0.41%	204.601	0.30%
50	205.002	0.49%	204.832	0.41%	204.602	0.30%
100	205.003	0.49%	204.833	0.41%	204.603	0.30%
500	205.0066	0.51%	204.8366	0.42%	204.6066	0.31%
1000	205.033	0.52%	204.863	0.44%	204.633	0.33%
2500	205.0662	0.57%	204.8962	0.49%	204.6662	0.38%
5000	205.166	0.65%	204.996	0.57%	204.766	0.46%
10000	205.331	0.81%	205.161	0.73%	204.931	0.62%

(b) At $l_c = 5$ nm)

β (MW/m ² k)	K (W/m K)					
	(5,10)	% change	(10,15)	% change	(15,20)	% change
12	205.1	0.54%	205.07	0.52%	204.9	0.44%
30	205.102	0.54%	205.071	0.53%	204.901	0.44%
50	205.102	0.54%	205.072	0.53%	204.902	0.44%
100	205.107	0.54%	205.073	0.53%	204.903	0.44%
500	205.1066	0.56%	205.0766	0.54%	204.9066	0.46%
1000	205.166	0.57%	205.103	0.56%	204.933	0.47%
2500	205.1662	0.62%	205.1362	0.61%	204.9662	0.52%
5000	205.431	0.70%	205.236	0.69%	205.066	0.60%
10000	205.431	0.86%	205.401	0.85%	205.231	0.77%

(c) At $l_c = 8$ nm

β (MW/m ² k)	K (W/m K)					
	(5,10)	% change	(10, 15)	% change	(15,20)	% change
12	205.401	0.69%	205.301	0.64%	205.201	0.59%
30	205.402	0.69%	205.072	0.64%	205.202	0.59%
50	205.403	0.69%	205.303	0.64%	205.203	0.59%
100	205.407	0.69%	205.077	0.64%	205.207	0.59%
500	205.433	0.70%	205.333	0.65%	205.233	0.60%
1000	205.466	0.72%	205.136	0.67%	205.266	0.62%
2500	205.566	0.77%	205.466	0.72%	205.366	0.67%
5000	205.731	0.85%	205.401	0.80%	205.531	0.75%
10000	206.062	1.01%	205.962	0.96%	205.862	0.91%

From the above Tables, for chiral (5, 10) carbon nanotube reinforced aluminum metal matrix, it can be observed that as the length of carbon nanotubes increase the thermal conductivity relatively increased. Figure 4.77 shows that the thermal conductivity is insensitive with increasing of thermal contact conductance up to $\beta = 1000$ MW/m²K while increases relatively after that value because of the assumption of perfect contact between the matrix and carbon nanotubes.

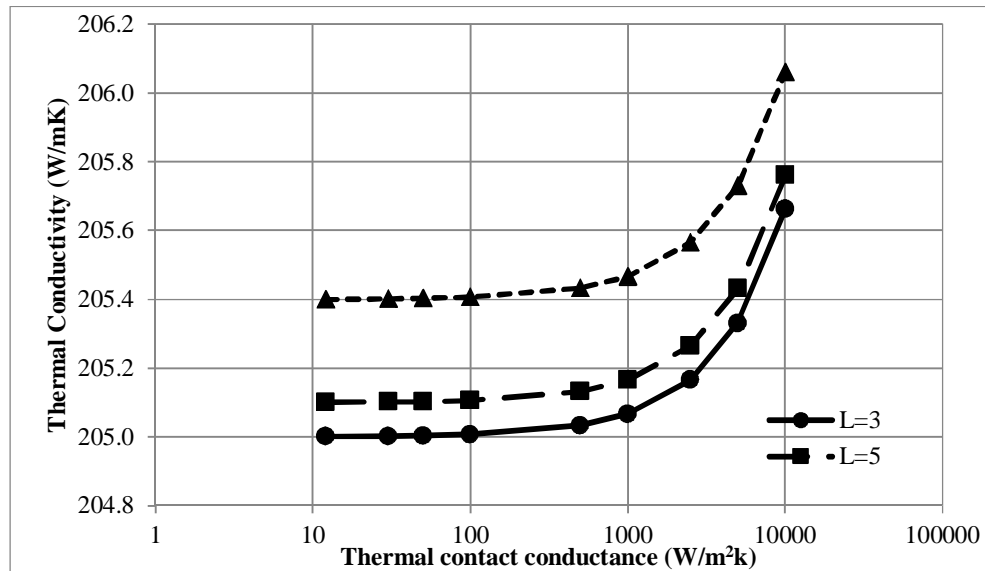


Figure 4.77: Effect of thermal contact conductance on thermal conductivity for chiral carbon nanotube (5, 10) (different length) reinforced aluminum metal matrix

Table 4.39 represents the effect of thermal contact conductance on thermal conductivity results for different chiral index of carbon nanotubes reinforced aluminum metal matrix. The results calculated at 3% volume fraction and length was $l_c = 3$ nm show slightly increases on the thermal conductivity when the thermal contact conductance

increased from 12 MW/m² K to 10000 MW/m² K. The zigzag carbon nanotube (5, 0) shows a higher prediction than armchair and chiral type. It can be observed from the above Table that the thermal conductivity increases by 0.64% at 12 MW/m² K and 0.86% at 10000 MW/m² K for zigzag. However, for armchair carbon nanotubes (5, 5) the increment varied as 0.54% to 0.86% while for chiral carbon nanotubes (5, 10) varied as 0.49% to 0.81% at the same length respectively. Figures 4.78, 4.79, and 4.80, show a comparison between different types of carbon nanotubes reinforced aluminum metal matrix at different lengths.

Table 4.39: Effect of thermal contact conductance on thermal conductivity for different chiral index of reinforced aluminum matrix at different lengths

β (MW/m ² k)	K (W/m K) at $l_c = 3$ nm			K (W/m K) at $l_c = 5$ nm			K (W/m K) at $l_c = 8$ nm		
	(5,0)	(5,5)	(5,10)	(5,0)	(5,5)	(5,10)	(5,0)	(5,5)	(5,10)
12	205.301	205.101	205	205.40	205.301	205.1	205.80	205.60	205.401
30	205.301	205.102	205.001	205.40	205.302	205.102	205.80	205.60	205.402
50	205.302	205.103	205.002	205.40	205.303	205.102	205.80	205.60	205.403
100	205.305	205.107	205.003	205.40	205.307	205.107	205.81	205.61	205.407
500	205.323	205.133	205.006	205.42	205.333	205.107	205.83	205.63	205.433
1000	205.346	205.166	205.033	205.45	205.366	205.166	205.87	205.67	205.466
2500	205.415	205.265	205.066	205.52	205.466	205.168	205.97	205.77	205.566
5000	205.530	205.431	205.166	205.63	205.631	205.431	206.13	205.93	205.731
10000	205.760	205.652	205.331	205.86	205.962	205.431	206.46	206.26	206.062

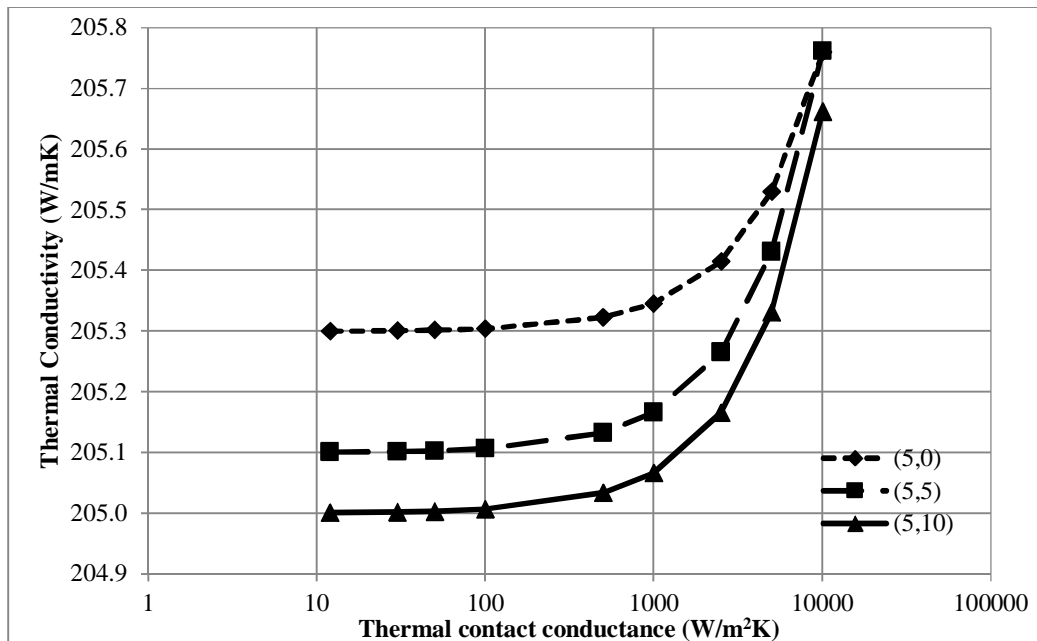


Figure 4.78: Effect of thermal contact conductance on thermal conductivity for different chiral Index carbon nanotube reinforced aluminum metal matrix (at $l_c = 3$ nm)

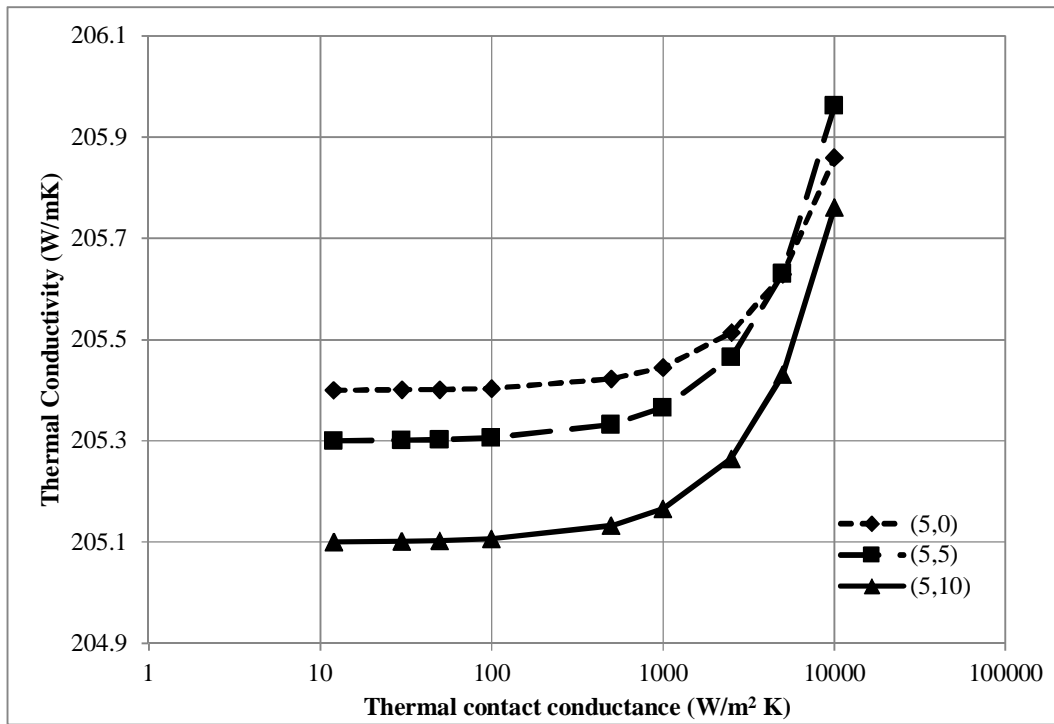


Figure 4.79: Effect of thermal contact conductance on thermal conductivity for different chiral Index carbon nanotube reinforced aluminum metal matrix (at $l_c=5$ nm)

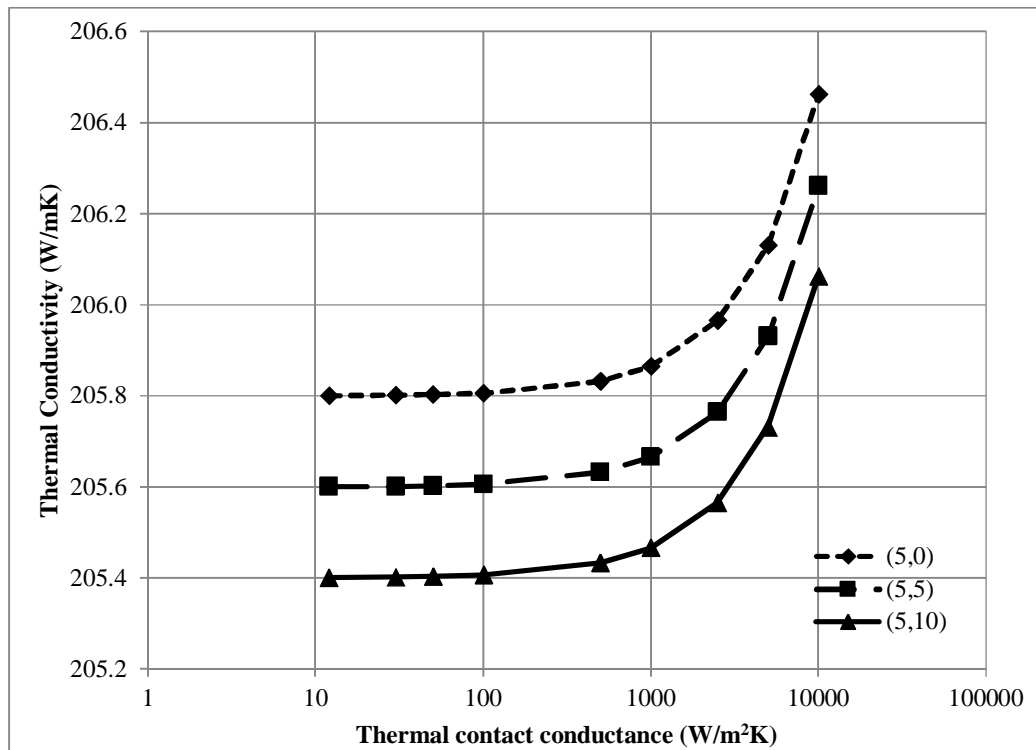


Figure 4.80: Effect of thermal contact conductance on thermal conductivity for different chiral Index carbon nanotube reinforced aluminum metal matrix (at $l_c=8$ nm)

CHAPTER FIVE

5. COMPUTATIONAL APPROACH RESULTS AND DISCUSSIONS

5.1 Overview

A finite element model is constructed using ANSYS commercial package by using the correlation technique between molecular network of a carbon nanotubes and its virtually discrete continuum structure. Two different 3D finite element models are constructed to study the elastic moduli; these models are built in by parametric APDL code (script). The code is transferred to ANSYS for computational modeling. In the first model, length of the carbon nanotubes is equal to the length of the RVE (long fiber model), while in the second one; length of the carbon nanotubes is smaller than the length of the RVE (short fiber model).

5.2 Prediction of the Elastic Properties for Long Fiber

The geometric models generated by running the APDL macro in ANSYS software used to determine the elastic properties of the carbon nanotubes treated as long fiber for reinforcing different metal matrixes Nanocomposite.

5.2.1 Prediction of Longitudinal Young's Modulus

The nanotube volume fraction V_f is probably the parameter affecting mostly the effective elastic properties of carbon nanotubes reinforced metal matrix Nanocomposite. It is obvious that large values of V_f leads to large values for the effective elastic moduli. The FEA results show that the Young's modulus of the Carbon Nanotubes reinforced metal matrix nanocomposite predicted to increase linearly when the volume fraction of carbon nanotubes increased. Therefore, the higher the carbon nanotubes volume ratio, the better the Young's modulus of the Nanocomposite is predicted to be. Table 5.1 represents the results of the longitudinal Young's modulus and its enhancement

percentage for (a) iron, (b) copper, and (c) aluminum matrices reinforced by carbon nanotube treated as long fiber. It can be observed from Table 5.1 (a) that the enhancement percentage is 12%, 28%, and 43% for iron matrix. It can be observed Table 5.1 (b) that the enhancement percentage is 21%, 48%, and 75% for Copper matrix. However, It can be observed from Table 5.1 (c) that the enhancement percentage is 36%, 64%, and 93% when the volume fraction of the Carbon Nanotubes at 3%, 7% and 11%, respectively, for iron, copper, and aluminum matrices. Figure 5.1 shows the effect of volume fraction on the Young's modulus of the carbon nanotubes reinforced iron, copper, and aluminum matrices nanocomposite, respectively. In this analysis, the effect of chiral indices did not show any effect since the analysis mainly depend on the different materials properties for carbon nanotube and metal matrix used in the research.

Table 5.1: Longitudinal Young's modulus FEA results for (a) iron, (b) copper, and (c) aluminum matrices

(a) Iron

Volume Fraction (%)	E_L (GPa)	% change
3%	234.9	12%
7%	268.1	28%
11%	301.3	43%

(b) Copper

Volume Fraction (%)	E_L (GPa)	% change
3%	156.7	21%
7%	192.2	48%
11%	227.8	75%

(c) Aluminum

Volume Fraction (%)	E_L (GPa)	% change
3%	94.96	36%
7%	114.91	64%
11%	134.86	93%

5.2.2 Prediction of Transverse Young's Modulus

The FEA results show that the transverse modulus of the Carbon Nanotubes reinforced metal matrix nanocomposite predicted to have increasing trend by increasing the volume fraction of carbon nanotubes. Table 5.2 (a) iron, (b) copper, and (c) aluminum matrices represent the results of the transverse modulus and its enhancement percentage. It can be observed from Table 5.2 (a) that the enhancement percentage is

3%, 7%, and 12% for iron matrix. It can be observed Table 5.2 (b) that the enhancement percentage is 5%, 11%, and 18% for Copper matrix. However, It can be observed from Table 5.2 (c) that the enhancement percentage is 7%, 11%, and 17% when the volume fraction of the Carbon Nanotubes at 3%, 7% and 11%, respectively, for iron, copper, and aluminum matrices.

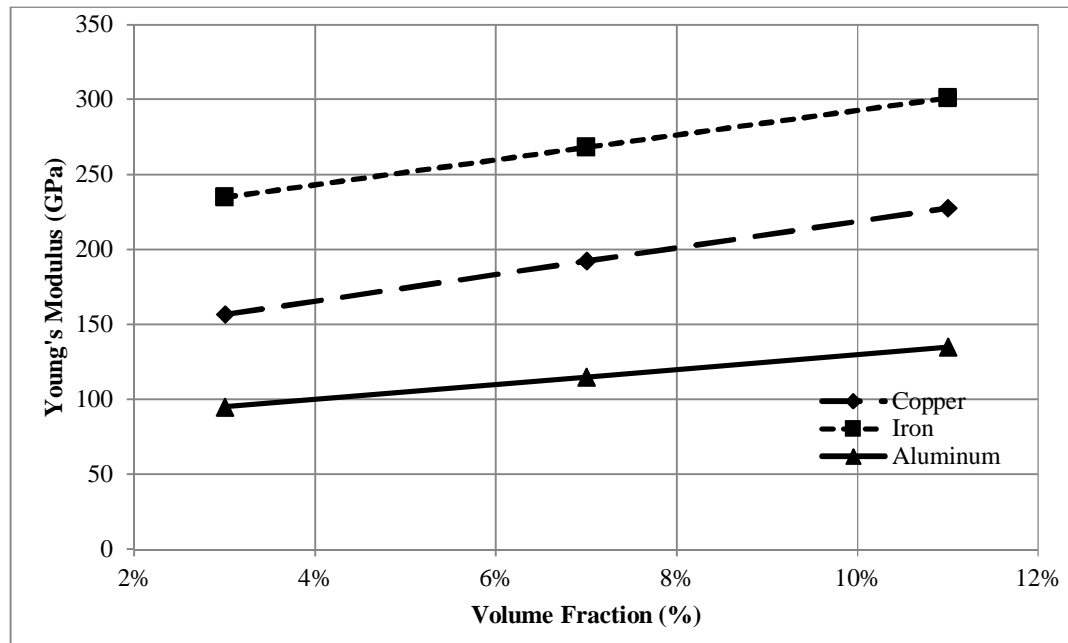


Figure 5.1: Longitudinal Young's modulus for iron, copper, and aluminum matrix reinforced carbon nanotubes as long fiber

Table 5.2: Transverse modulus FEA results for (a) iron, (b) copper, and (c) aluminum matrices

(a) Iron

Volume Fraction (%)	E_T (GPa)	% change
3%	216.63	3%
7%	225.47	7%
11%	234.31	12%

(b) Copper

Volume Fraction (%)	E_T (GPa)	% change
3%	136.24	5%
7%	144.55	11%
11%	152.87	18%

(c) Aluminum

Volume Fraction (%)	E_T (GPa)	% change
3%	74.74	7%
7%	77.54	11%
11%	81.79	17%

Figure 5.2 shows the effect of volume fraction on the transverse modulus of the carbon nanotubes reinforced iron, copper, and aluminum matrices nanocomposite, respectively. It can be observed that the results plotted have a linear trend while it's not in reality this is because the values are relatively near each other's.

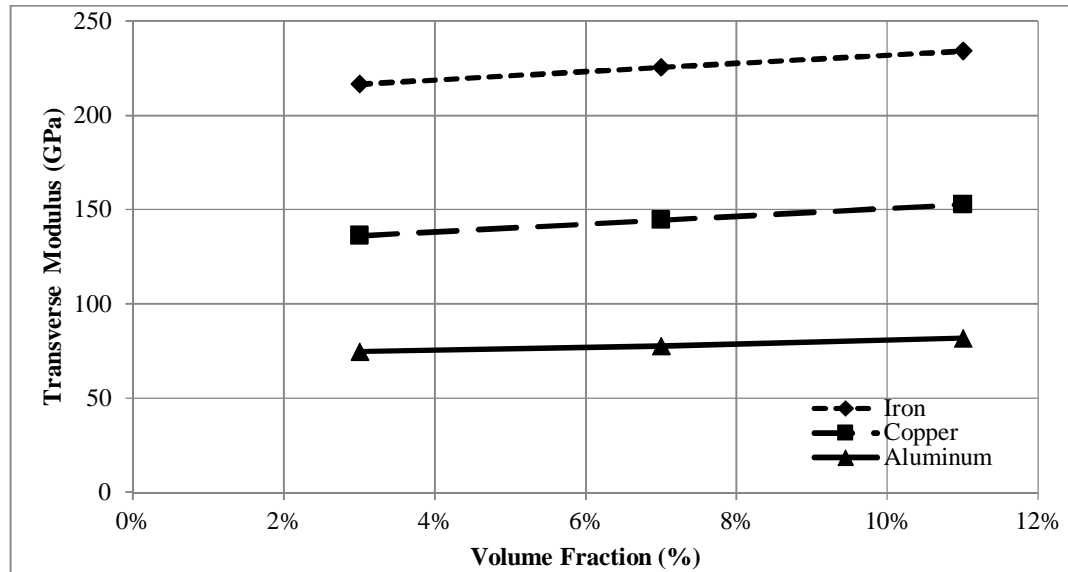


Figure 5.2: Transverse Young's modulus for iron, copper, and aluminum matrices reinforced carbon nanotubes as long fiber

5.2.3 Prediction of the Shear Modulus

Shear modulus of composite is the ratio of shear stress to the shear strain. It can be seen that the results of shear modulus for metal matrix reinforced by carbon nanotube have increasing trend when the volume fraction increases. Table 5.3 (a) iron, (b) copper, and (c) aluminum matrices represent the results of the shear modulus and its enhancement percentage. It can be observed from Table 5.3 (a) that the enhancement percentage is 3%, 7%, and 11% for iron matrix. It can be observed Table 5.3 (b) that the enhancement percentage is 5%, 9%, and 13% for Copper matrix. However, It can be observed from Table 5.3 (c) that the enhancement percentage is 4%, 9%, and 16% when the volume fraction of the Carbon Nanotubes at 3%, 7% and 11%, respectively, for iron, copper, and aluminum matrices.

Table 5.3: Shear modulus FEA results for (a) iron, (b) copper, and (c) aluminum matrices

(a) Iron

Volume Fraction (%)	G (GPa)	% change
3%	84.51	3%
7%	87.86	7%
11%	91.20	11%

(b) Copper

Volume Fraction (%)	G (GPa)	% change
3%	50.33	5%
7%	52.27	9%
11%	54.33	13%

(c) Aluminum

Volume Fraction (%)	G (GPa)	% change
3%	26.95	4%
7%	28.39	9%
11%	30.06	16%

Figure 5.3 shows the effect of volume fraction on the shear modulus of the carbon nanotubes reinforced iron, copper, and aluminum matrices nanocomposite, respectively. It can be observed that the results plotted have a linear trend while it's not in reality this is because the values are relatively near each other's.

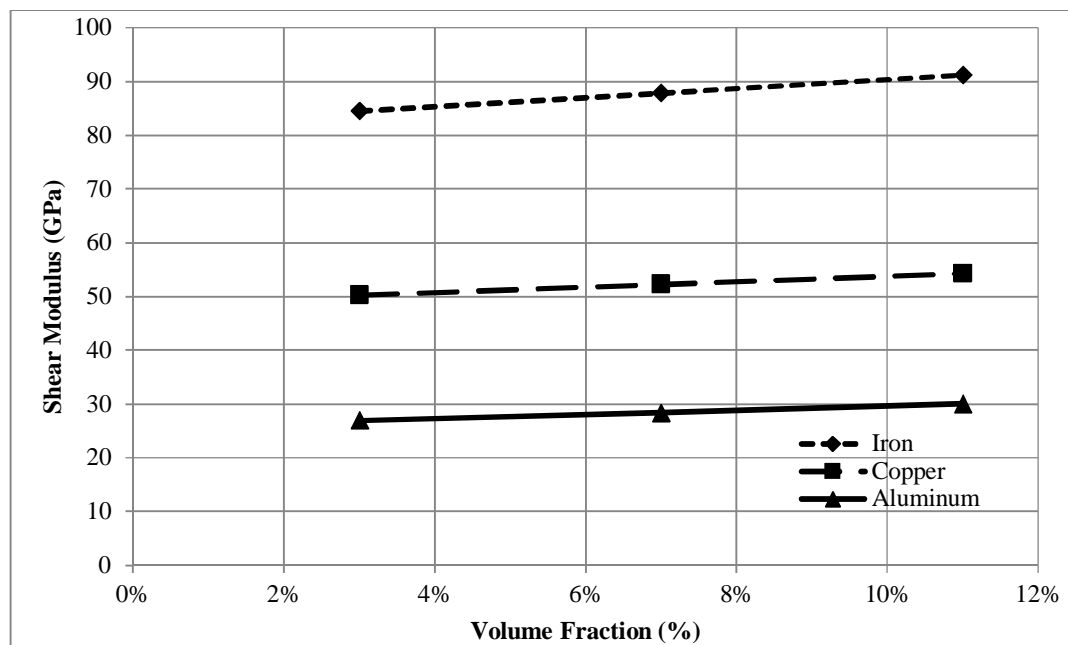


Figure 5.3: Shear modulus for iron, copper, and aluminum matrices reinforced carbon nanotubes as long fiber

5.2.4 Prediction of the Major Poisson's Ratio

Major Poisson's ratio of the carbon nanotubes reinforced metal matrix nanocomposite predicted to have decreasing trend as the volume fraction of the Carbon nanotubes increases. Table 5.4 (a) iron, (b) copper, and (c) aluminum matrices represent the results of major Poisson's ratio for iron matrix reinforced by carbon nanotubes. It can be observed from Table 5.4 (a) that the prediction of the major Poisson's ratio for

iron matrix reinforced by carbon nanotube insensitive with increasing of volume fraction because the value of both iron matrix and the carbon nanotube is the same. It can be observed Table 5.4 (b) that a decreasing value by 0.25%, 0.58%, and 0.92% with respect to the matrix Poisson's ratio. However, It can be observed from Table 5.3 (c) that a decreasing value by 0.23%, 0.53%, and 0.83% with respect to the matrix Poisson's ratio when the volume fraction of the Carbon Nanotubes at 3%, 7% and 11%, respectively, for iron, copper, and aluminum matrices.

Table 5.4: Major Poisson's ratio FEA results for (a) iron, (b) copper, and (c) aluminum matrices

(a) Iron

Volume Fraction (%)	ν	% change
3%	0.3	0%
7%	0.3	0%
11%	0.3	0%

(b) Copper

Volume Fraction (%)	ν	% change
3%	0.359	-0.25%
7%	0.358	-0.58%
11%	0.357	-0.92%

(c) Aluminum

Volume Fraction (%)	ν	% change
3%	0.32925	-0.23%
7%	0.32825	-0.53%
11%	0.32725	-0.83%

Figure 5.4 shows the effect of volume fraction on the major Poisson's ratio the carbon nanotubes reinforced iron, copper, and aluminum matrices nanocomposite, respectively.

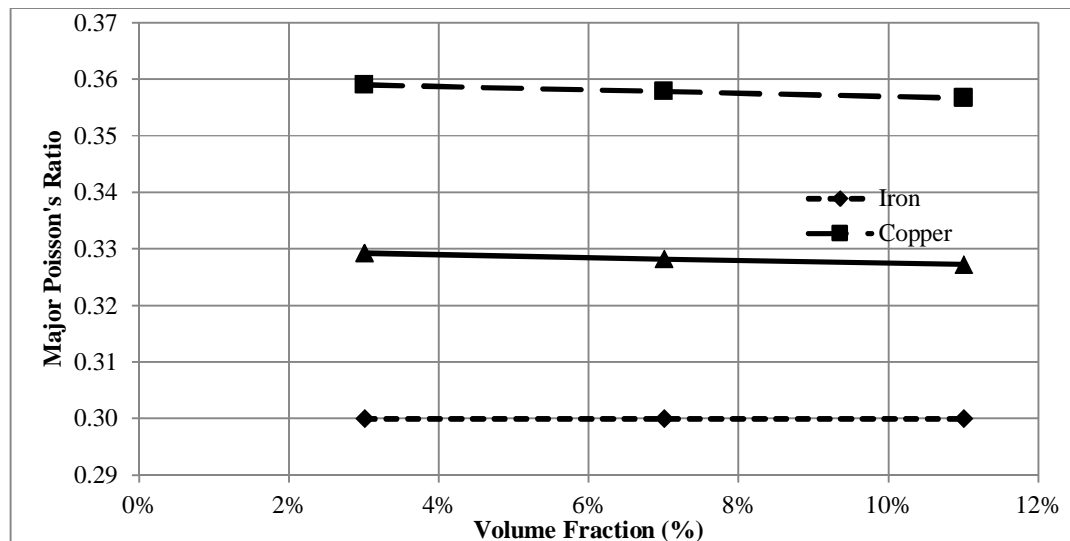


Figure 5.4: Major Poisson's ratio for iron, copper, and aluminum matrices reinforced carbon nanotubes as long fiber

5.3 Prediction of the elastic properties for short fiber

To predict the elastic properties of metal matrix reinforced by carbon nanotube treated as short fiber, the geometric models are generated in ANSYS software by running the APDL macro. The results show lower properties as compared to the continuous fiber case.

5.3.1 Prediction of Longitudinal Young's Modulus

The prediction of longitudinal Young's modulus for the carbon nanotubes reinforced metal matrix composite will be investigated according to the following factors: fixing the diameter varying the length and fixing the diameter, varying the diameter and fixing the length while varying the chirality index.

5.3.1.1 Effect of Length

The results obtained for carbon nanotubes reinforced iron metal matrix nanocomposite at same diameter with different lengths show a linear increment when the volume fraction and length increased for different carbon nanotubes. It is observed that the young's modulus of the iron matrix nanocomposite reinforced by 3% volume fraction of zigzag carbon nanotubes (5, 0) varied as 9%, 9% and 10% at carbon nanotubes lengths of 3, 5, and 8 nm, respectively. However, at 3% volume fraction for the armchair carbon nanotubes (5, 5) the increment varied as 7%, 8% and 9% while for chiral carbon nanotubes (5, 10) varied as 7%, 8%, and 8% at the same increment of length, respectively. Figure 5.5, 5.6 and 5.7 show increment of young's modulus for iron matrix reinforced by zigzag, armchair and chiral carbon nanotube, respectively, when the volume fraction increases.

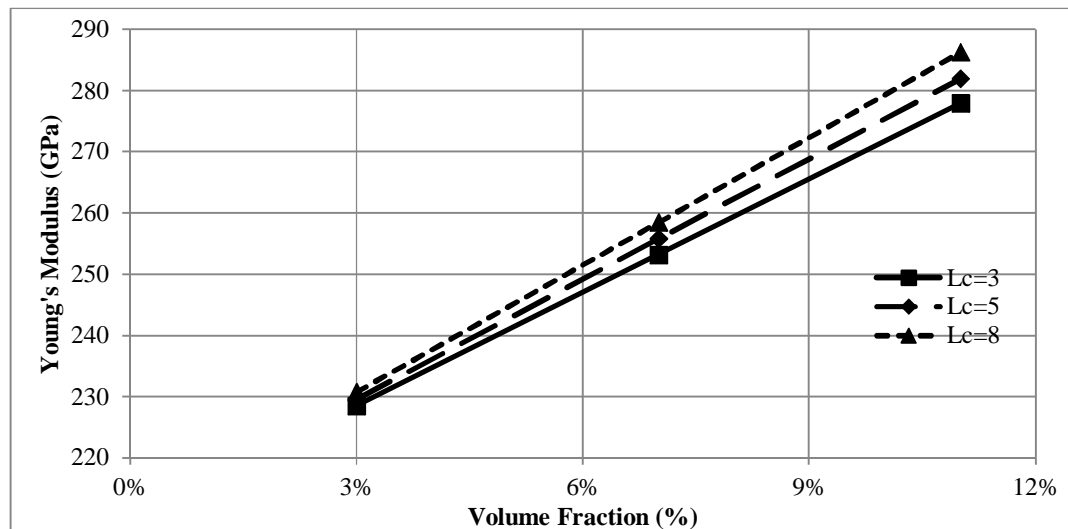


Figure 5.5: Longitudinal Young's modulus for carbon nanotube (5,0) (different length) reinforced iron metal matrix

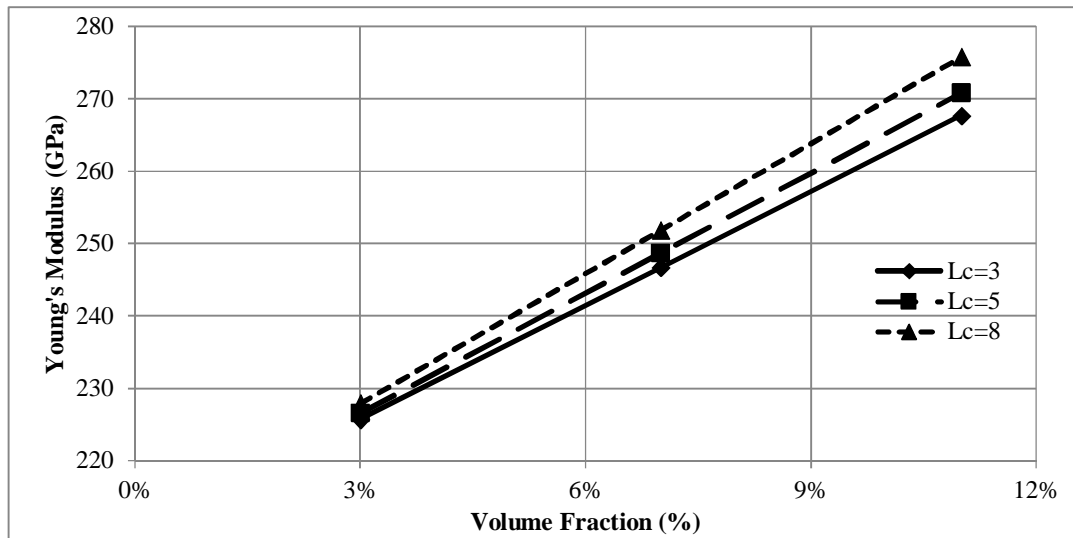


Figure 5.6: Longitudinal Young's modulus for carbon nanotube (5,5) (different length) reinforced iron metal matrix

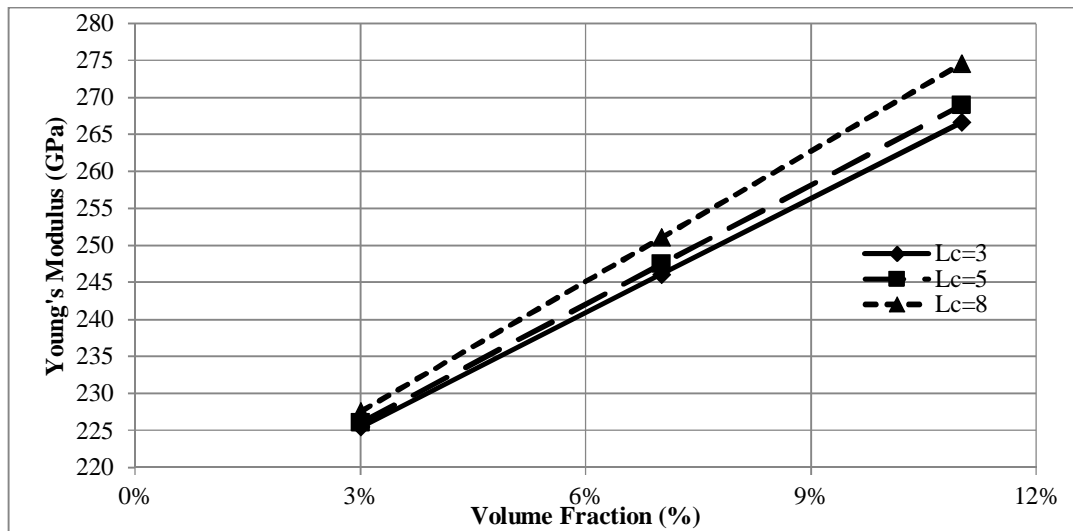


Figure 5.7: Longitudinal Young's modulus for carbon nanotube (5, 10) (different length) reinforced iron metal matrix

Similarly the procedure will be taken for the prediction of Young's modulus for the Copper and Aluminum matrixes.

For Carbon nanotube reinforced Copper matrix Nanocomposite, It is observed that the young's modulus of the copper matrix nanocomposite reinforced by 3% volume fraction of zigzag carbon nanotubes (5, 0) varied as 15%, 16% and 18% at carbon nanotubes lengths of 3, 5, and 8 nm, respectively. however, at 3% volume fraction for the armchair carbon nanotubes (5, 5) the increment varied as 13%, 15% and 16% while for chiral carbon nanotubes (5, 10) varied as 11%, 13%, and 15% at the same increment of length, respectively. Figure 5.8, 5.9, and 5.10 show increment of young's modulus for copper matrix reinforced by zigzag, armchair and chiral carbon nanotube, respectively, when the volume fraction increases.

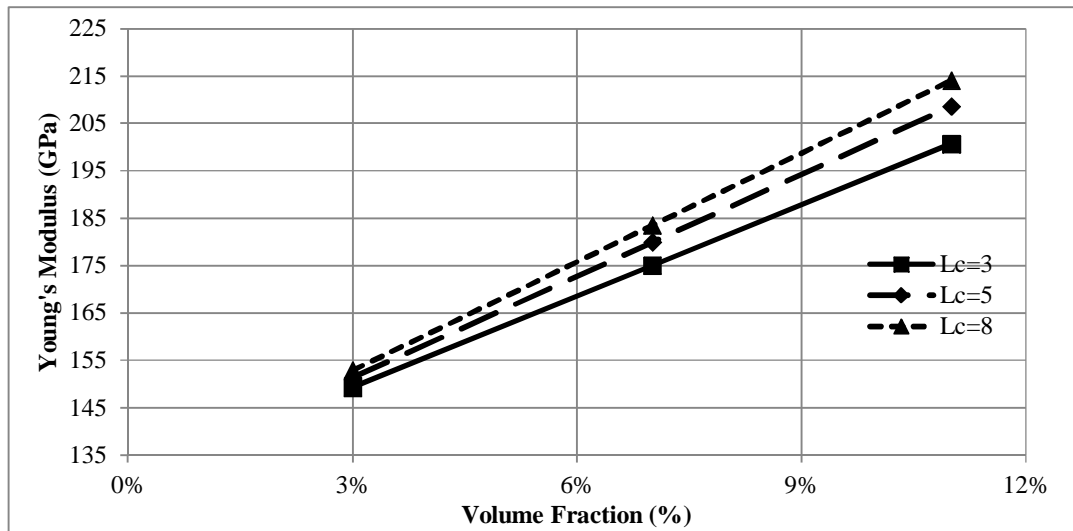


Figure 5.8: Longitudinal Young's modulus for carbon nanotube (5,0) (different length) reinforced copper metal matrix

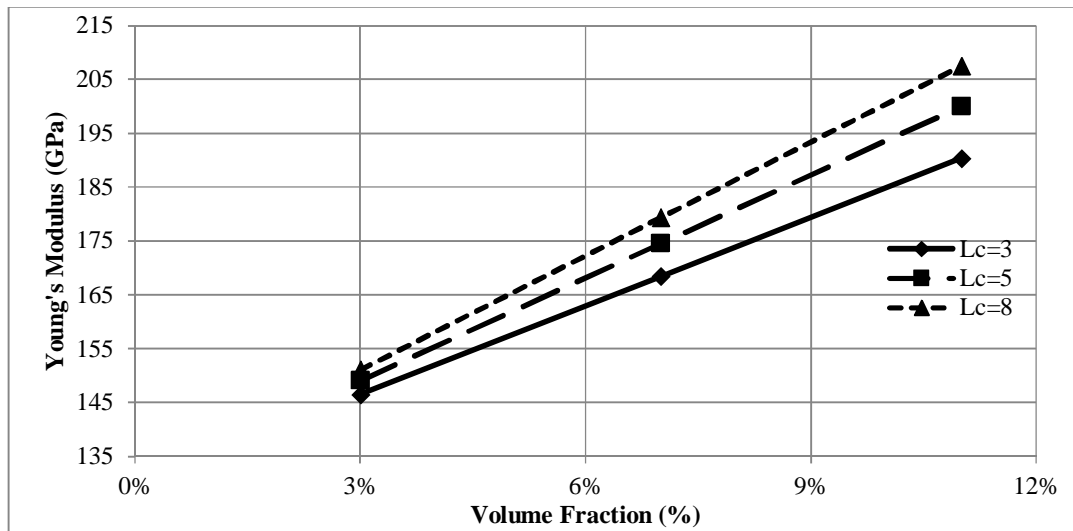


Figure 5.9: Longitudinal Young's modulus for carbon nanotube (5,5) (different length) reinforced copper metal matrix

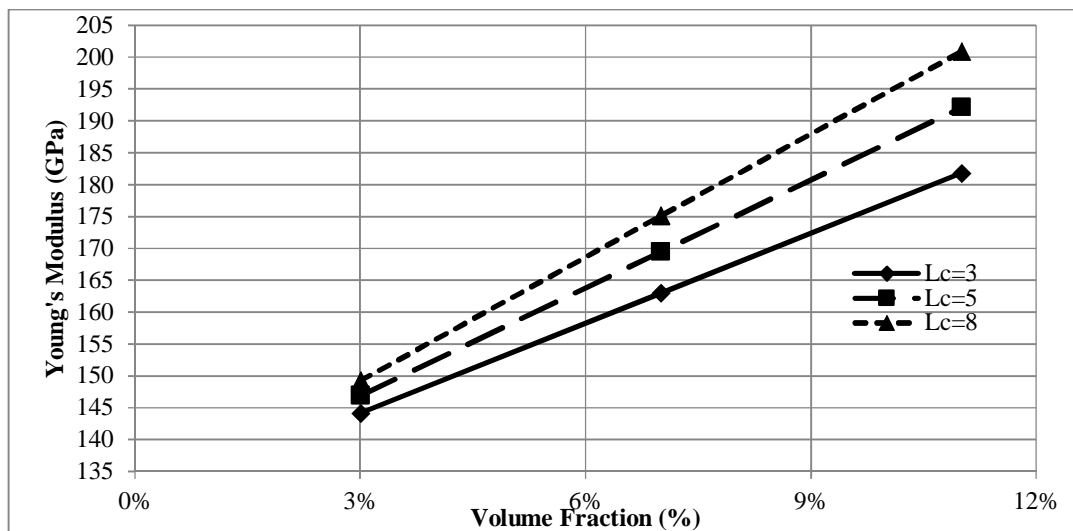


Figure 5.10: Longitudinal Young's modulus for carbon nanotube (5, 10) (different length) reinforced copper metal matrix

For Carbon nanotube reinforced Aluminum matrix Nanocomposite, it is observed that the increment percentage in the young's modulus of the new aluminum matrix nanocomposite reinforced by 3% volume fraction of zigzag carbon nanotubes (5, 0) varied as 19%, 20% and 21% at carbon nanotubes lengths 3, 5, and 8 nm, respectively. however, at 3% volume fraction for the armchair carbon nanotubes (5, 5) the increment varied as 18%, 19% and 20% while for chiral carbon nanotubes (5, 10) varied as 18%, 19%, and 19% at the same increment of length, respectively. Figure 5.11, 5.12 and 5.13 show increment of young's modulus for aluminum matrix reinforced by zigzag, armchair and chiral carbon nanotube, respectively, when the volume fraction increases.

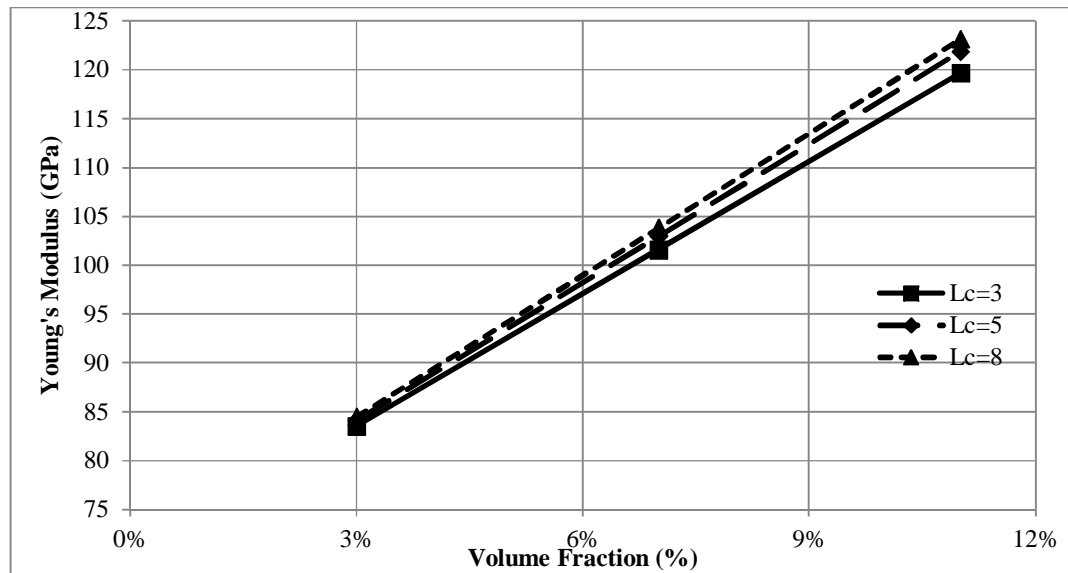


Figure 5.11: Longitudinal Young's modulus for carbon nanotube (5, 0) (different length) reinforced aluminum metal matrix

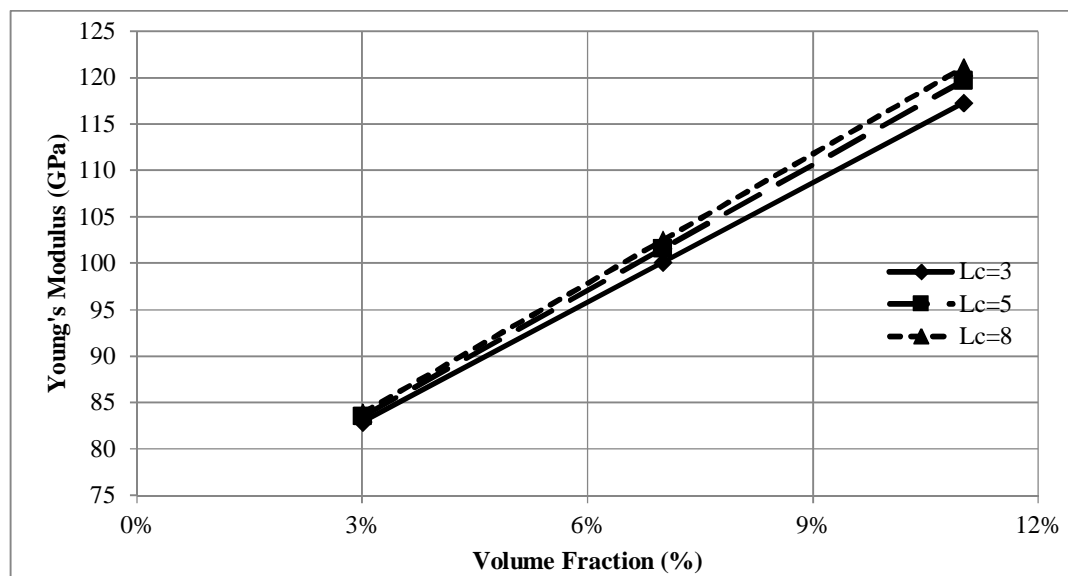


Figure 5.12: Longitudinal Young's modulus for carbon nanotube (5, 5) (Different Length) reinforced aluminum metal matrix

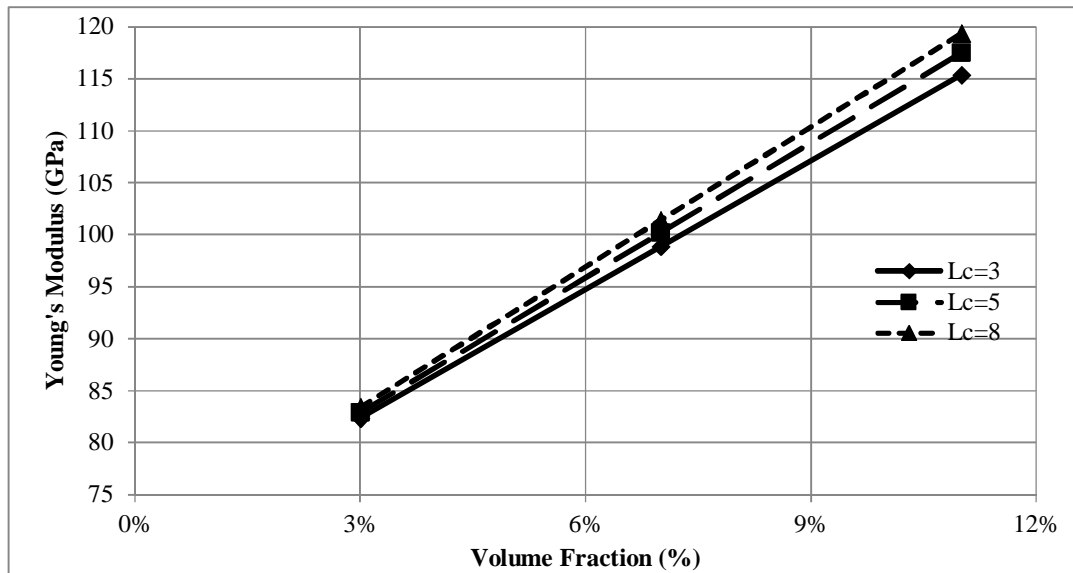


Figure 5.13: Longitudinal Young's modulus for carbon nanotube (5, 10) (different length) reinforced aluminum metal matrix

5.3.1.2 Effect of diameter

The analysis will be carried out for the three types of the carbon nanotubes at the same length with different diameters which can be achieved by changing the index of carbon nanotube for the same kind. The results of armchair Carbon nanotubes reinforced Iron metal matrix are presented in Table 5.5 (a) iron, (b) copper, and (c) aluminum matrices. It can be observed that at 3% volume fraction of armchair carbon nanotube type reinforced iron, copper, and aluminum metal matrices, the value of Young's modulus decreased as the diameter of the armchair carbon nanotubes increased.

Table 5.5: Effect of armchair carbon nanotube diameter reinforced (a) iron, (b) copper, and (c) aluminum matrices ($V_f=3\%$)

(a) Iron

Carbon Nanotube index	d (nm)	E_L (GPa)					
		lc=3 nm	% change	lc=5 nm	% change	lc=8 nm	% change
(5,5)	0.848	225.7	7%	226.6	8%	227.9	9%
(10,10)	1.526	224.8	7%	225.9	8%	227.4	8%
(15,15)	2.204	223.6	6%	225.3	7%	226.9	8%

(b) Copper

Carbon Nanotube index	d (nm)	E_L (GPa)					
		lc=3 nm	% change	lc=5 nm	% change	lc=8 nm	% change
(5,5)	0.848	146.5	13%	149.1	15%	151.1	16%
(10,10)	1.526	142.7	10%	145.5	12%	146.4	13%
(15,15)	2.204	140.6	8%	143.2	10%	145.2	12%

(c) Aluminum

Carbon Nanotube index	d (nm)	E _L (GPa)					
		lc=3 nm	% change	lc=5 nm	% change	lc=8 nm	% change
(5,5)	0.848	82.9	18%	83.5	19%	83.9	20%
(10,10)	1.526	79.9	14%	81.8	17%	82.6	18%
(15,15)	2.204	78.7	12%	79.5	14%	82.2	17%

For zigzag carbon nanotubes reinforced iron metal matrix at same length with different diameters, Table 5.6 (a) iron, (b) copper, and (c) aluminum matrices present the results calculated at 3% of volume fraction of zigzag carbon nanotube type reinforced iron, copper, and aluminum metal matrices. The results show that the value of Young's modulus decreased as the diameter of the zigzag carbon nanotubes increases.

Table 5.6: Effect of zigzag carbon nanotube diameter reinforced (a) iron, (b) copper, and (c) aluminum matrices (V_f=3%)

(a) iron

Carbon Nanotube index	d (nm)	E _L (GPa)					
		lc=3 nm	% change	lc=5 nm	% change	lc=8 nm	% change
(5,0)	0.561	228.5	9%	229.6	9%	230.8	10%
(10,0)	0.953	227.3	8%	229.2	9%	230.6	10%
(15,0)	1.344	225.5	7%	227.7	8%	229.4	9%

(b) Copper

Carbon Nanotube index	d (nm)	E _L (GPa)					
		lc=3 nm	% change	lc=5 nm	% change	lc=8 nm	% change
(5,0)	0.561	149.3	15%	151.4	16%	152.9	18%
(10,0)	0.953	145.7	12%	148.4	14%	150.6	16%
(15,0)	1.344	144.3	11%	146.3	13%	148.7	14%

(c) Aluminum

Carbon Nanotube index	d (nm)	E _L (GPa)					
		lc=3 nm	% change	lc=5 nm	% change	lc=8 nm	% change
(5,0)	0.561	83.5	19%	84.1	20%	84.5	21%
(10,0)	0.953	81.6	17%	82.4	18%	82.9	18%
(15,0)	1.344	78.8	13%	80.1	14%	82.4	18%

For chiral carbon nanotubes reinforced iron metal matrix at same length with different diameter, Table 5.7 (a) iron, (b) copper, and (c) aluminum matrices present the results calculated at 3% of volume fraction of chiral carbon nanotube type reinforced iron, copper, and aluminum metal matrices. The results show that the value of Young's modulus slightly decreased as the diameter of the chiral carbon nanotubes increases.

Table 5.7: Effect of chiral carbon nanotube diameter reinforced (a) iron, (b) copper, and (c) aluminum matrices ($V_f=3\%$)

(a) Iron

Carbon Nanotube Index	d (nm)	E_L (GPa)					
		lc=3 nm	% change	lc=5 nm	% change	lc=8 nm	% change
(5,10)	1.206	225.4	7%	226.1	8%	227.6	8%
(10,15)	1.876	223.8	7%	225.5	7%	227.0	8%
(15,20)	2.551	222.3	6%	224.6	7%	226.7	8%

(b) Copper

Carbon Nanotube Index	d (nm)	E_L (GPa)					
		lc=3 nm	% change	lc=5 nm	% change	lc=8 nm	% change
(5,10)	1.206	144.1	11%	146.9	13%	149.3	15%
(10,15)	1.876	141.5	9%	144.2	11%	148.0	14%
(15,20)	2.551	139.9	8%	142.4	10%	144.9	11%

(c) Aluminum

Carbon Nanotube Index	d (nm)	E_L (GPa)					
		lc=3 nm	% change	lc=5 nm	% change	lc=8 nm	% change
(5,10)	1.206	82.4	18%	82.95	19%	83.5	19%
(10,15)	1.876	79.5	14%	81.29	16%	82.3	18%
15,20)	2.551	78.0	11%	79.21	13%	81.7	17%

5.3.1.3 Effect of chirality Index

The analysis is carried out for armchair (5, 5), zigzag (5, 0) and chiral (5, 10) carbon nanotubes at the same length. it can be observed from table 5.8 that at 3% volume fraction of carbon nanotube reinforced iron matrix, the value of young's modulus increases as the volume fraction and/or the length increases and decreases when the chirality index is changed from zigzag to armchair to chiral type for carbon nanotube reinforced iron matrix composite. However, Figures 5.13, 5.14, and 5.15 represent the effect of Young's modulus of different carbon nanotube chiral index at different lengths and volume fractions for reinforcing iron matrix nanocomposite.

Table 5.8: Effect of chiral index on the Young's modulus of iron matrix ($V_f=3\%$)

Carbon Nanotube index	d (nm)	E_L (GPa)					
		lc=3 nm	% change	lc=5 nm	% change	lc=8 nm	% change
Armchair (5,5)	0.848	225.7	7%	226.6	8%	227.9	9%
Zigzag (5,0)	0.561	228.5	9%	229.6	9%	230.8	10%
Chiral (5,10)	1.206	225.4	7%	226.1	8%	227.6	8%

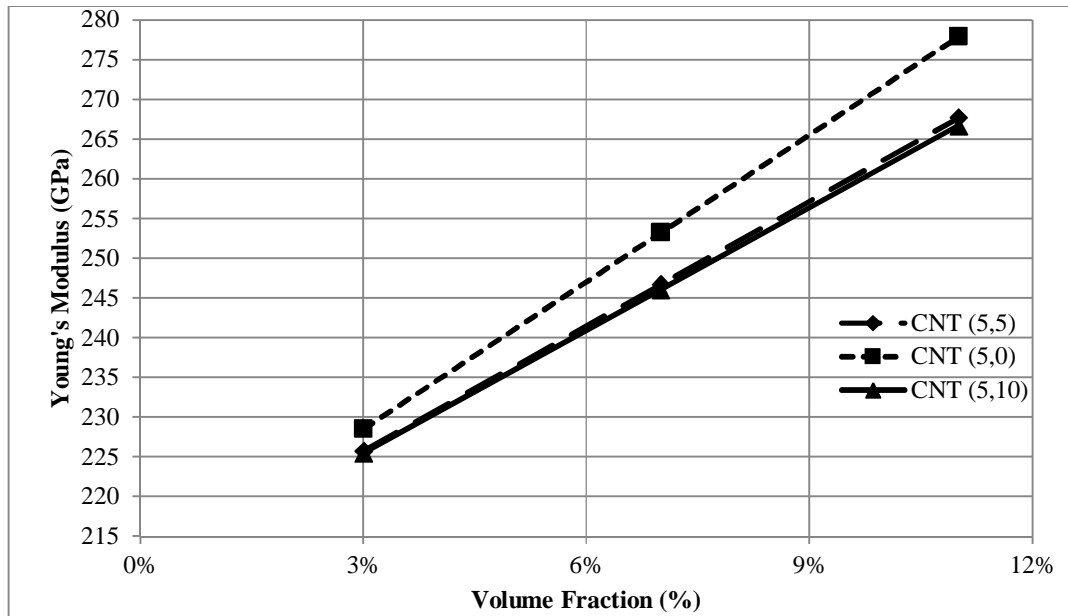


Figure 5.14: Longitudinal Young's modulus for different chiral index carbon nanotube (at length $l_c=3$ nm) reinforced iron metal matrix

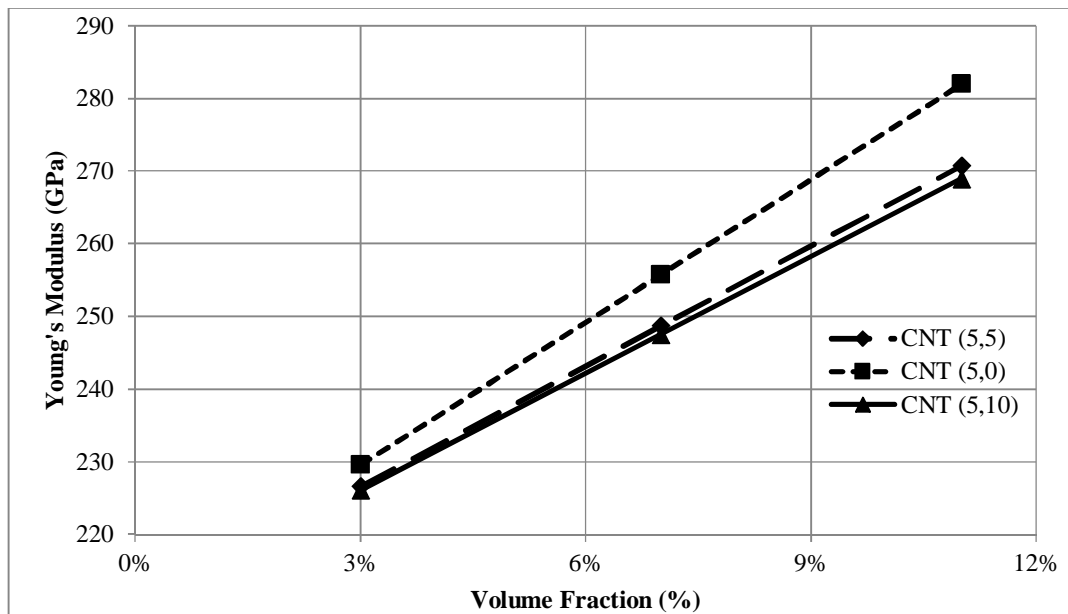


Figure 5.15: Longitudinal Young's modulus for different chiral index carbon nanotube (at length $l_c=5$ nm) reinforced iron metal matrix

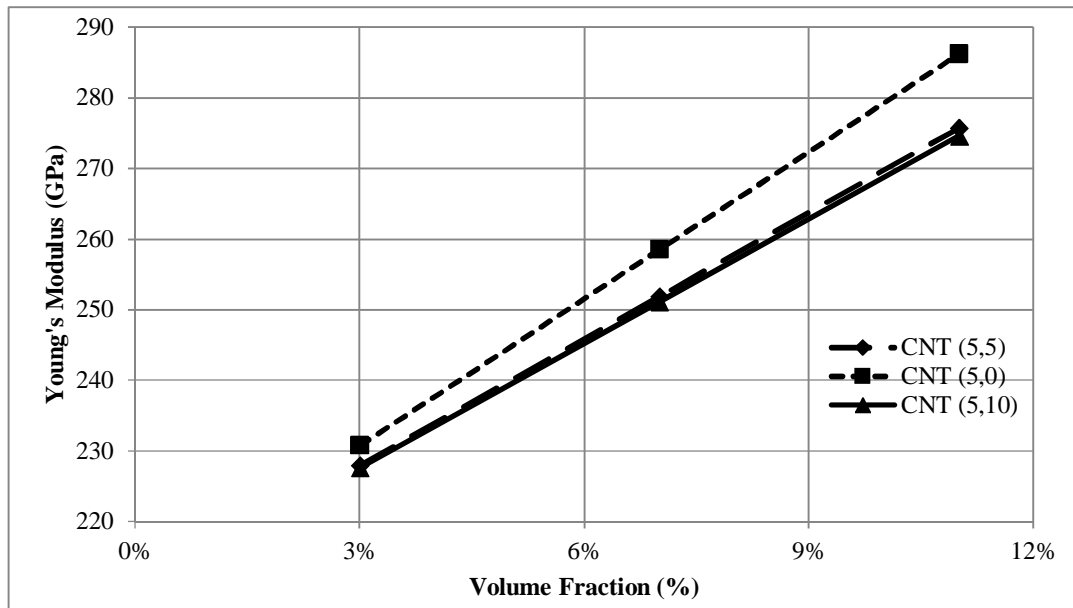


Figure 5.16: Longitudinal Young's modulus for different chiral index carbon nanotube (at length $l_c=8$ nm) Reinforced iron metal matrix

Similarly, the prediction of Young's modulus for the copper matrix reinforced by different chiral carbon nanotube index treated as short fiber presented in table 5.9. It can be observed from Table 5.9 that at 3% volume fraction of carbon nanotube reinforced copper matrix, the value of Young's modulus increases as the volume fraction and/or the length increases and decreases when the chirality index is changed from zigzag to armchair to chiral type for carbon nanotube reinforced copper matrix composite. However, it can be seen from Figures 5.17, 5.18, and 5.19 that the Young's modulus increases as the volume fractions and / or length increase, and decreases when chirality indices is changed from zigzag to armchair to chiral different carbon nanotube reinforced copper matrix nanocomposite.

Table 5.9: Effect of chiral index on the Young's modulus of copper matrix

Carbon Nanotube index	d (nm)	E_L (GPa)					
		lc=3 nm	% change	lc=5 nm	% change	lc=8 nm	% change
Armchair (5,5)	0.848	146.5	13%	149.1	15%	151.1	16%
Zigzag (5,0)	0.561	149.3	15%	151.4	16%	152.9	18%
Chiral (5,10)	1.206	144.1	11%	146.9	13%	149.3	15%

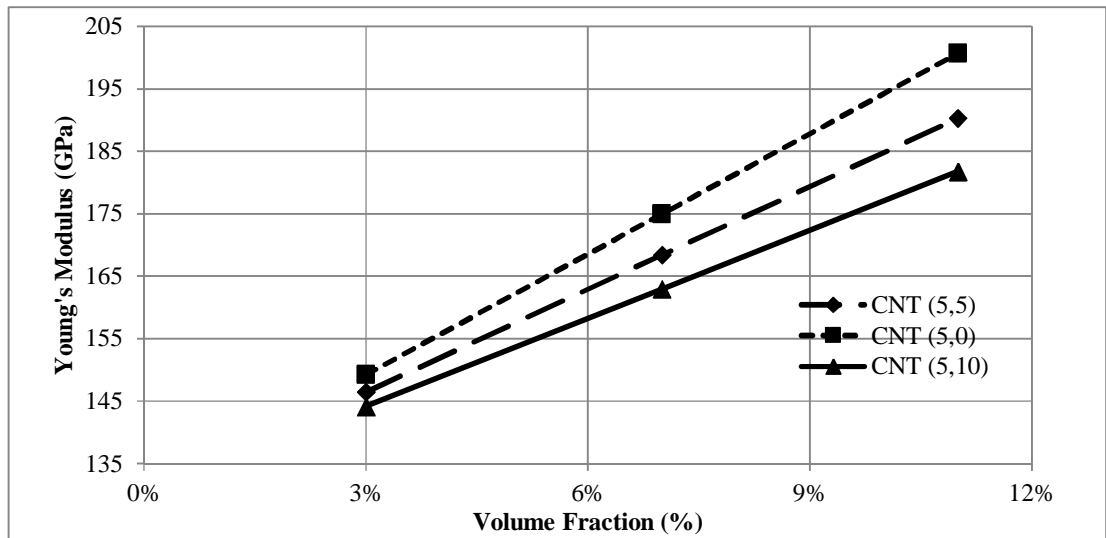


Figure 5.17: Longitudinal Young's modulus for different chiral index carbon nanotube (at length $l_c=3$ nm) reinforced copper metal matrix

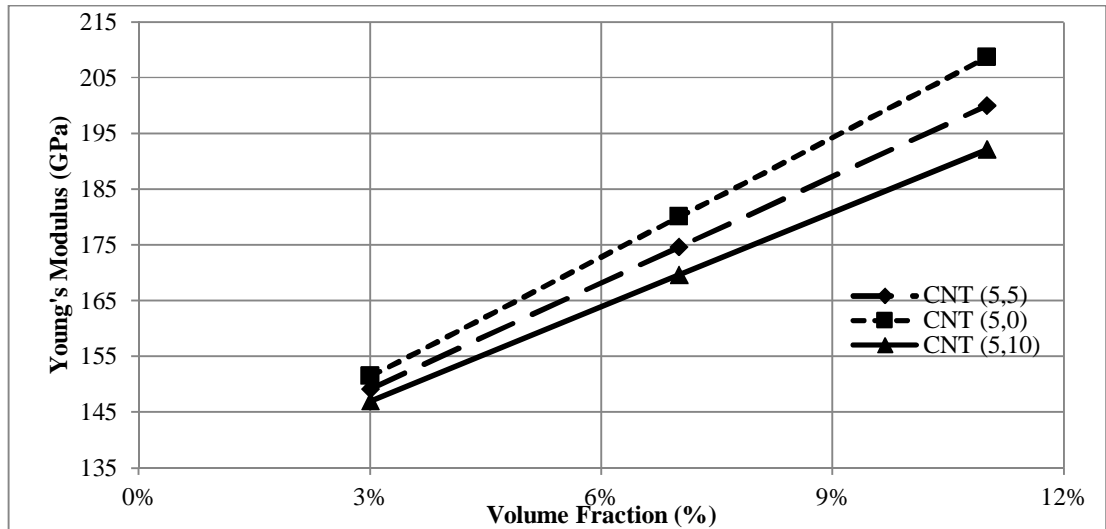


Figure 5.18: Longitudinal Young's modulus for different chiral index carbon nanotube (at length $l_c=5$ nm) reinforced copper metal matrix

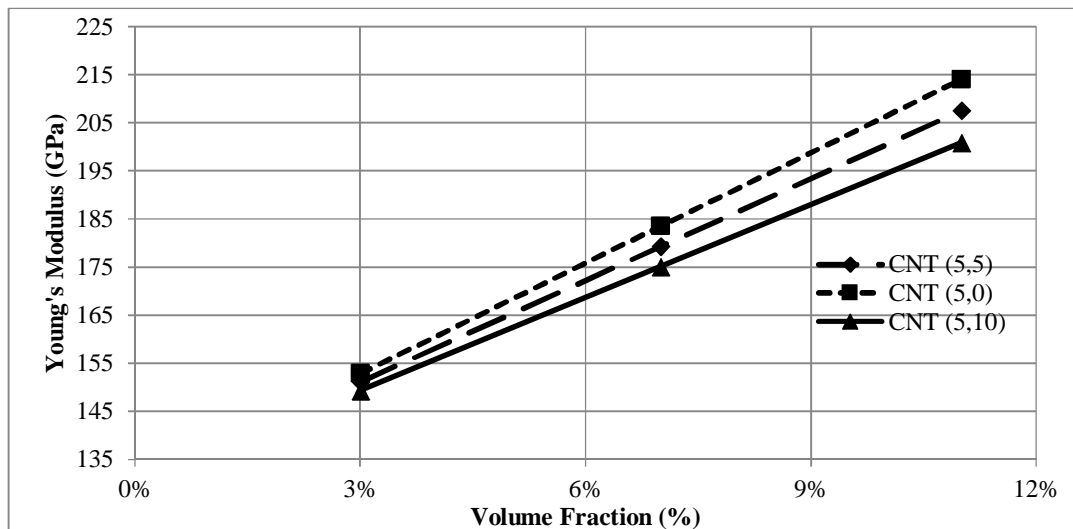


Figure 5.19: Longitudinal Young's modulus for different chiral index carbon nanotube (at length $l_c=8$ nm) reinforced copper metal matrix

However, the prediction of Young's modulus for the aluminum matrix reinforced by different chiral carbon nanotube index treated as short fiber presented in Table 5.10. It can be observed from Table 5.10 that at 3% volume fraction of carbon nanotube reinforced Aluminum matrix, the value of Young's modulus increases as the volume fraction and/or the length increases and decreases when the chirality index is changed from Zigzag to armchair to chiral type for carbon nanotube reinforced aluminum matrix composite. However, Figures 5.20, 5.21, and 5.22 represent the effect of Young's modulus or different carbon nanotube chiral index at different length and volume fractions for reinforcing aluminum matrix nanocomposite.

Table 5.10: Effect of chiral index on the Young's modulus of aluminum matrix (Vf=3%)

Carbon Nanotube index	d (nm)	E _L (GPa)					
		lc=3 nm	% change	lc=5 nm	% change	lc=8 nm	% change
Armchair (5,5)	0.848	82.9	18%	83.5	19%	83.9	20%
Zigzag (5,0)	0.561	83.5	19%	84.1	20%	84.5	21%
Chiral (5,10)	1.206	82.4	18%	83.0	19%	83.5	19%

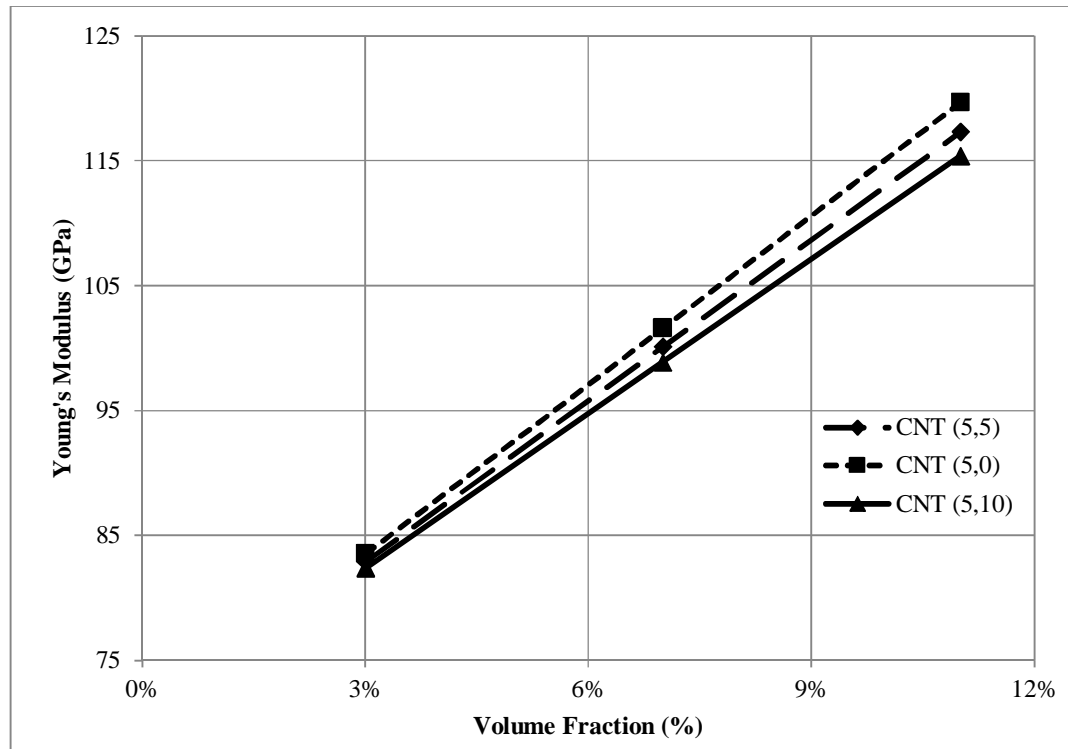


Figure 5.20: Longitudinal Young's modulus for different chiral index carbon nanotube (at length lc=3 nm) reinforced aluminum metal matrix

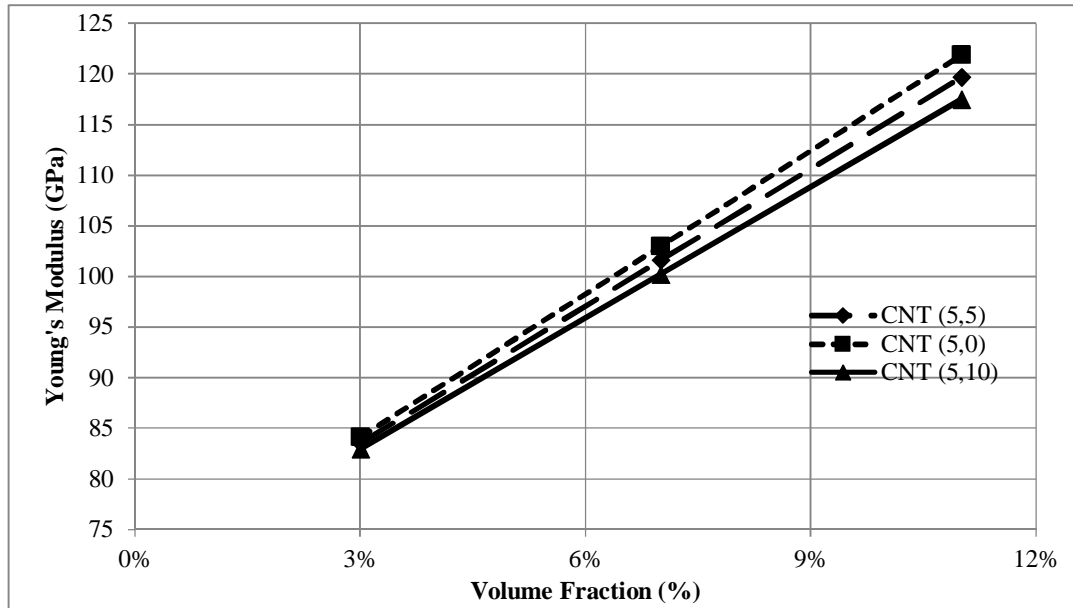


Figure 5.21: Longitudinal Young's modulus for different chiral index carbon nanotube (at length $l_c=5$ nm) reinforced aluminum metal matrix

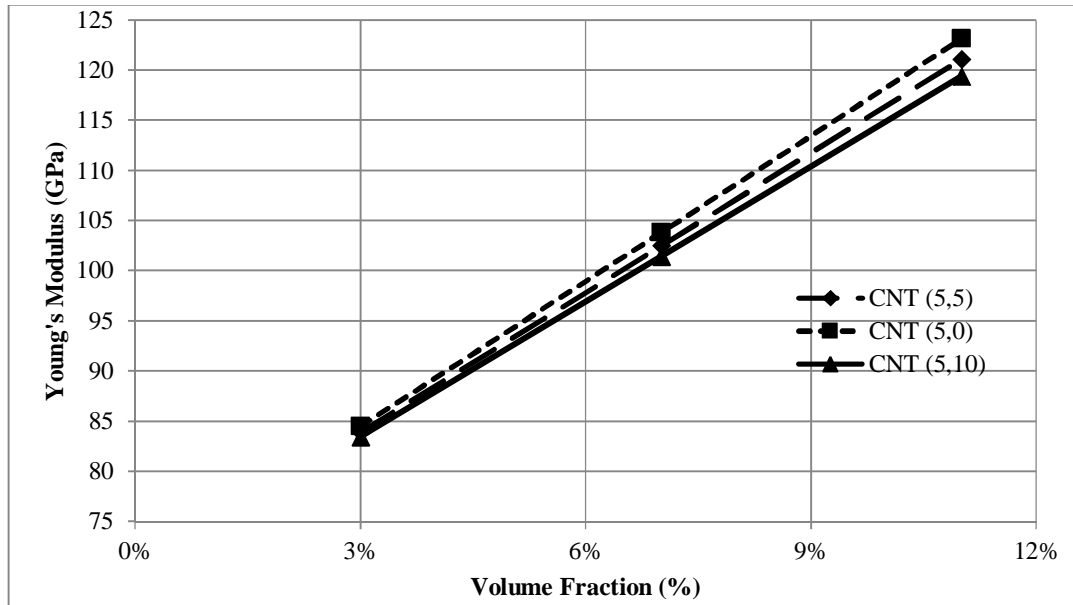


Figure 5.22: Longitudinal Young's modulus for different chiral index carbon nanotube (at length $l_c=8$ nm) reinforced aluminum metal matrix

5.3.2 Prediction of the Transverse Young's Modulus

The results of transverse Young's modulus for carbon nanotubes (treated as short fiber) reinforced iron metal matrix nanocomposite at same diameter with different length show increasing trend when the volume fraction and length increased for different carbon nanotubes. It is observed that the transverse modulus of the iron matrix nanocomposite reinforced by 3% volume fraction of zigzag carbon nanotubes (5, 0)

varied as 3%, 4% and 3% at carbon nanotubes lengths of 3, 5, and 8 nm, respectively. However, at 3% volume fraction for the armchair carbon nanotubes (5, 5) the increment varied as 2% and 3% while for chiral carbon nanotubes (5, 10) up to 2% at the same increment of length, respectively. Figure 5.23, 5.24, and 5.25 show increment of transverse modulus for iron matrix reinforced by zigzag, armchair and chiral carbon nanotube, respectively when the volume fraction increases.

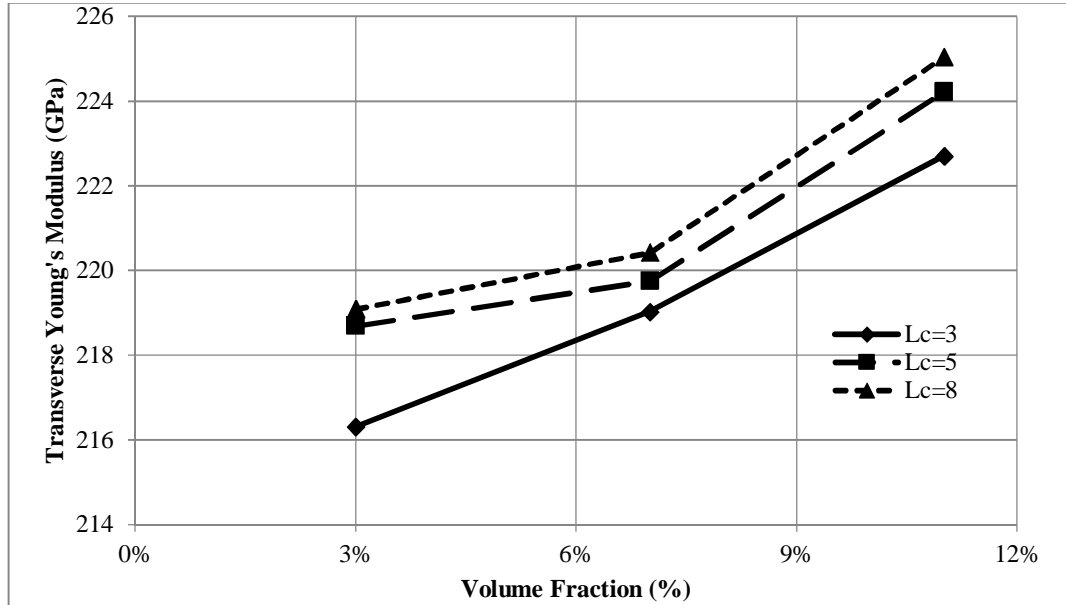


Figure 5.23: Transverse modulus for zigzag carbon nanotube (5,0) (different length) reinforced iron metal matrix

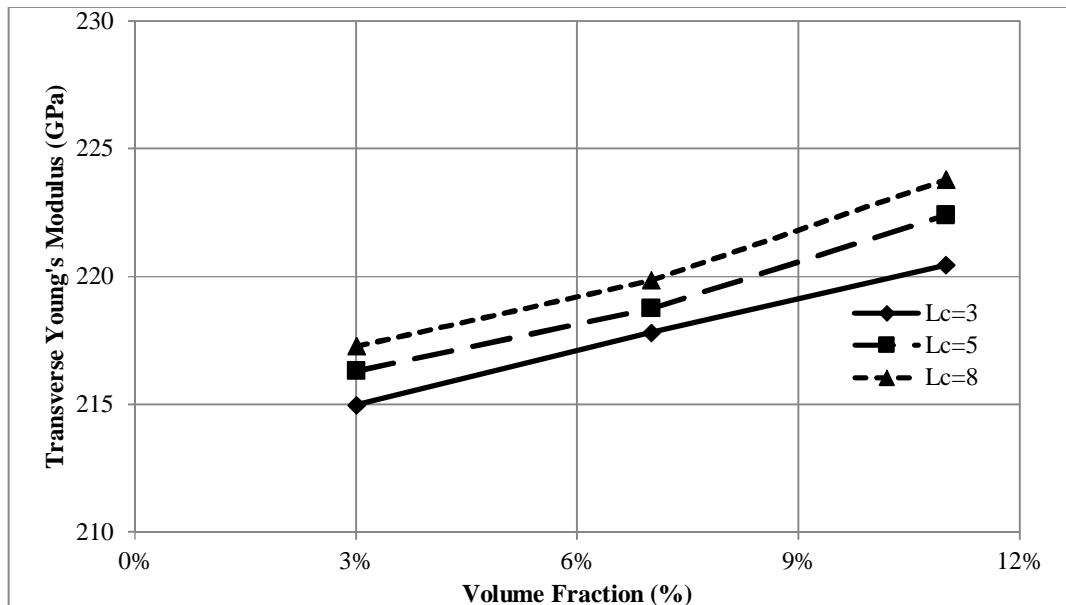


Figure 5.24: Transverse modulus for armchair carbon nanotube (5,5) (different length) reinforced iron metal matrix

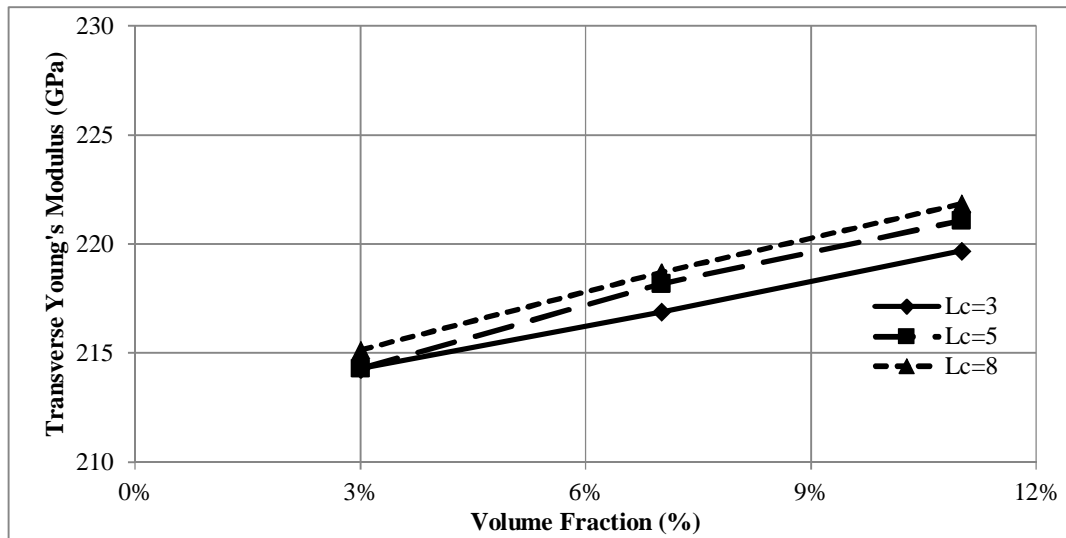


Figure 5.25: Transverse modulus for chiral carbon nanotube (5, 10) (different length) reinforced iron metal matrix

Similarly, for carbon nanotube (treated as short fiber) at same diameter with different length reinforced copper matrix nanocomposite. Transverse Young's modulus results show increasing trend when the volume fraction and length increased for different Carbon nanotubes. It is observed that the transverse modulus of the copper matrix nanocomposite reinforced by 3% volume fraction of zigzag carbon nanotubes (5, 0) varied as 4% to 5% at carbon nanotubes lengths of 3, 5, and 8 nm, respectively. However, at 3% volume fraction for the armchair carbon nanotubes (5, 5) the increment varied as 3% to 4% while for chiral carbon nanotubes (5, 10) varied as 2%, 3%, and 4% at the same increment of length, respectively. Figure 5.26, 5.27 and 5.28 show increment of transverse modulus for copper matrix reinforced by zigzag, armchair and chiral carbon nanotube respectively when the volume fraction increases.

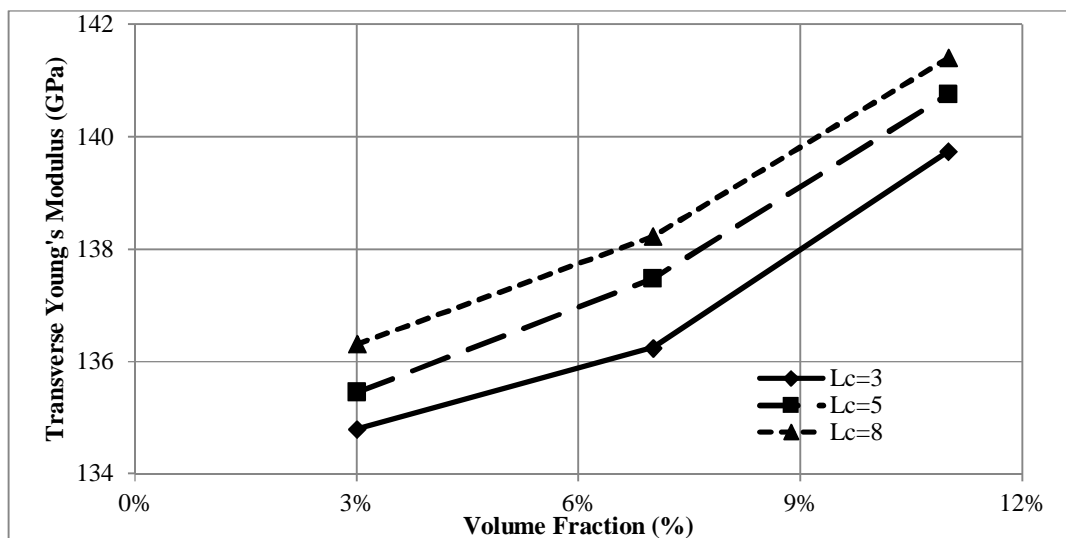


Figure 5.26: Transverse modulus for zigzag carbon nanotube as short fiber reinforced copper metal matrix at different length

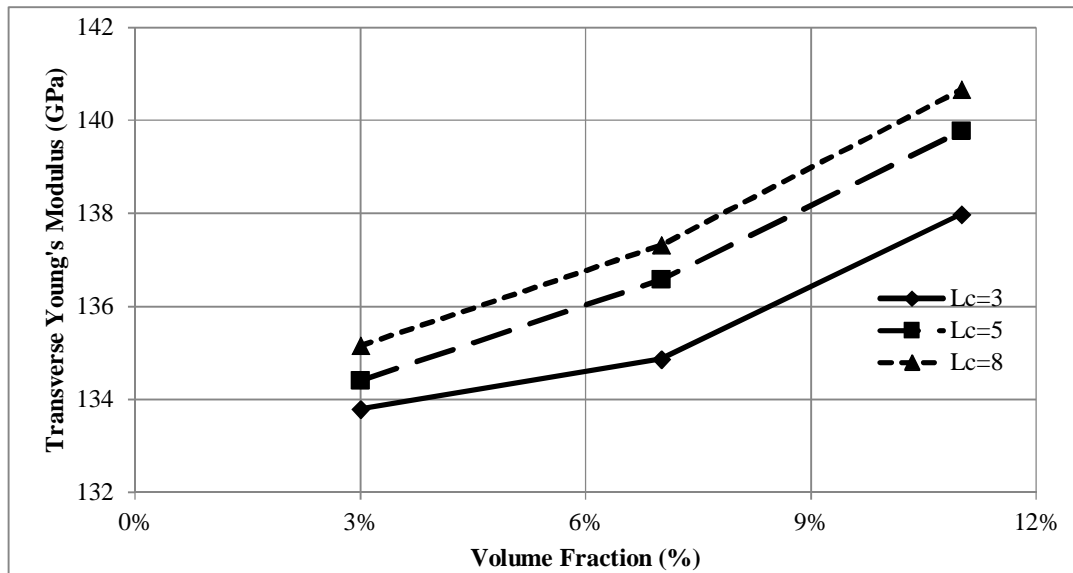


Figure 5.27: Transverse modulus for armchair carbon nanotube as short fiber reinforced copper metal matrix at different length

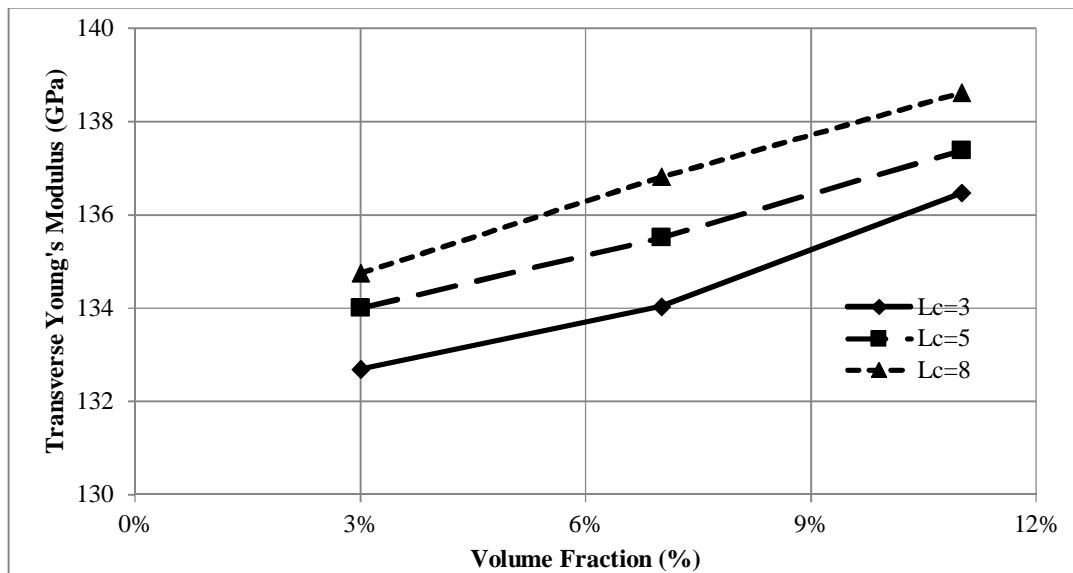


Figure 5.28: Transverse modulus for chiral carbon nanotube as short fiber reinforced copper metal matrix at different length

However, for carbon nanotube (treated as short fiber) at same diameter with different length reinforced aluminum matrix nanocomposite. Transverse Young's modulus results show increasing trend when the volume fraction and length increased for different carbon nanotubes. It is observed that the transverse modulus of the new Aluminum matrix Nanocomposite reinforced by 3% volume fraction of zigzag carbon nanotubes (5, 0) varied as 6%, 7%, and 8% at carbon nanotubes lengths of 3, 5, and 8 nm, respectively. However, at 3% volume fraction for the armchair carbon nanotubes (5, 5) the increment varied as 5%, 6%, and 7% while for chiral carbon nanotubes (5, 10)

varied as 5%, 6%, and 7% at the same increment of length, respectively. Figure 5.29, 5.30 and 5.31 show increment of Young's modulus for aluminum matrix reinforced by zigzag, armchair and chiral carbon nanotube, respectively when the volume fraction increases.

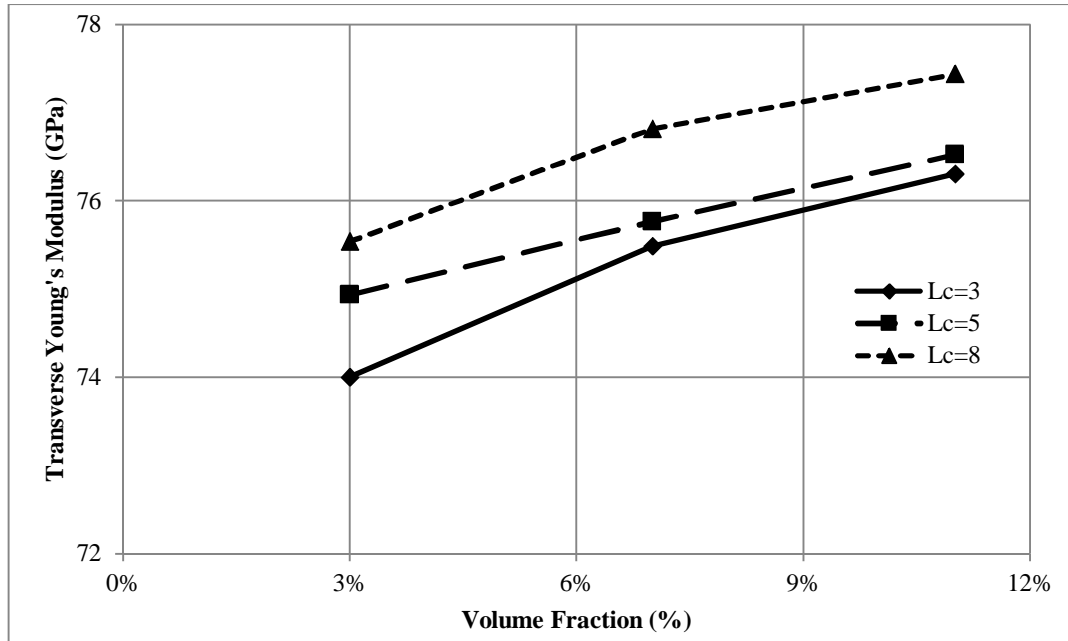


Figure 5.29: Transverse modulus for zigzag carbon nanotube at different length reinforced aluminum metal matrix

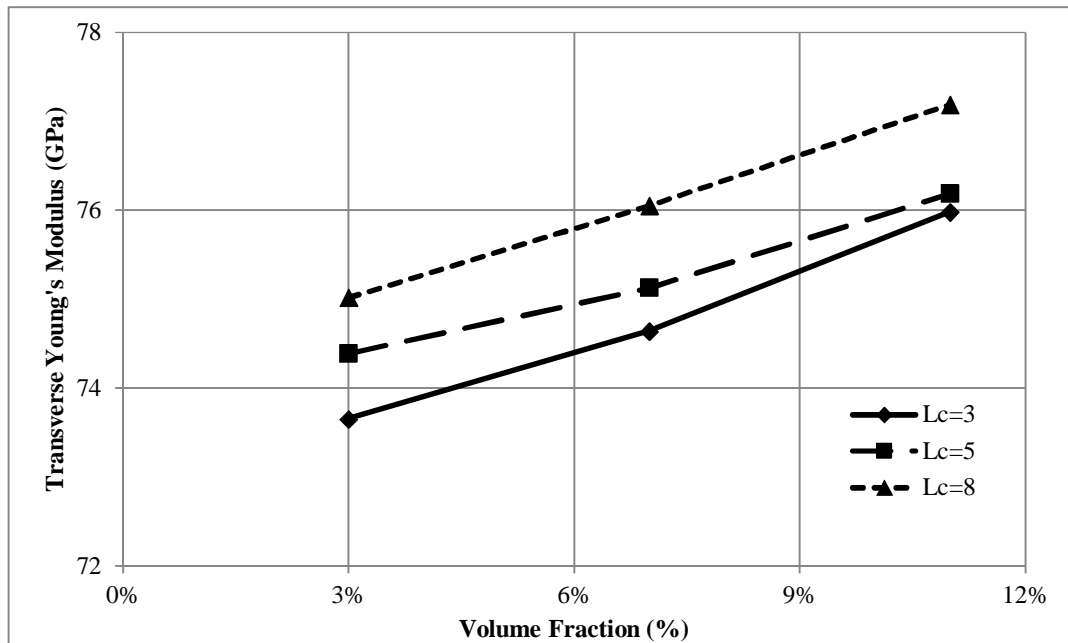


Figure 5.30: Transverse modulus for armchair carbon nanotube at different length reinforced aluminum metal matrix

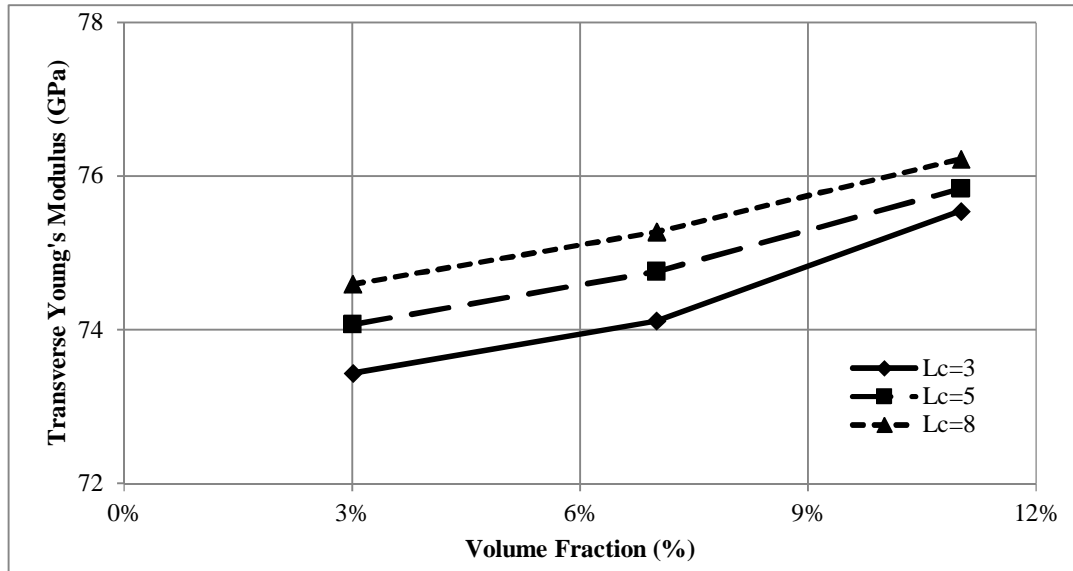


Figure 5.31: Transverse modulus for armchair carbon nanotube at different length reinforced aluminum metal matrix

The analysis is carried out for the three types of the carbon nanotubes at the same length with different diameter which can be achieved by changing the index of carbon nanotube for the same kind. The results of armchair carbon nanotubes reinforced iron, copper, and aluminum metal matrix are presented in Table 5.11 (a), (b) and (c). It can be observed that at 3% volume fraction of carbon nanotube reinforced iron matrix, the value of transverse modulus decreased as the diameter of the armchair carbon nanotubes increased.

Table 5.11: Effect of armchair carbon nanotube diameter reinforced: (a) iron, (b) copper, and (c) aluminum matrix on transverse modulus ($V_f=3\%$)

(a) Iron

Carbon Nanotube index	d (nm)	E_T (GPa)		
		lc=3nm	lc=5nm	lc=8 nm)
(5,5)	0.848	214.97	216.31	217.26
(10,10)	1.526	213.91	214.13	215.11
(15,15)	2.204	213.41	213.82	214.18

(b) Copper

Carbon Nanotube index	d (nm)	E_T (GPa)		
		lc=3nm	lc=5nm	lc=8 nm)
(5,5)	0.848	133.79	134.41	135.16
(10,10)	1.526	132.95	133.98	134.30
(15,15)	2.204	132.26	132.57	132.97

(c) Aluminum

Carbon Nanotube index	d (nm)	E _T (GPa)		
		lc=3nm	lc=5nm	lc=8 nm)
(5,5)	0.848	73.65	74.39	75.02
(10,10)	1.526	73.35	73.68	74.14
(15,15)	2.204	72.78	73.28	73.99

For zigzag carbon nanotubes reinforced metal matrix at same length with different diameter, Table 5.28(a), (b) and (c) present the results calculated at 3% of volume fraction for iron, copper, and aluminum metal matrix reinforced by zigzag carbon nanotube type. The results show that the value of transverse modulus decreased as the diameter of the zigzag carbon nanotubes increases.

Table 5.12: Effect of zigzag carbon nanotube diameter reinforced: (a) iron, (b) copper, and (c) aluminum matrix on transverse modulus ($V_f=3\%$)

(a) Iron

Carbon Nanotube index	d (nm)	E _T (GPa)		
		lc=3nm	lc=5nm	lc=8 nm)
(5,0)	0.561	216.3	218.7	219.1
(10,0)	0.953	215.8	217.2	217.5
(15,0)	1.344	214.9	216.1	216.6

(b) Copper

Carbon Nanotube index	d (nm)	E _T (GPa)		
		lc=3nm	lc=5nm	lc=8 nm)
(5,0)	0.561	134.79	135.45	136.32
(10,0)	0.953	134.12	134.44	134.90
(15,0)	1.344	132.55	133.14	133.34

(c) Aluminum

Carbon Nanotube index	d (nm)	E _T (GPa)		
		lc=3nm	lc=5nm	lc=8 nm)
(5,0)	0.561	74.0	74.9	75.5
(10,0)	0.953	73.8	74.1	74.6
(15,0)	1.344	72.8	73.8	74.1

For chiral carbon nanotubes reinforced metal matrix at same length with different diameter, Table 5.13 presents the results calculated at 3% of volume fraction of carbon nanotubes for iron, copper, and aluminum metal matrix reinforced by chiral carbon nanotube type. The results show that the value of transverse modulus decreased as the diameter of the chiral carbon nanotubes increases.

Table 5.13: Effect of chiral carbon nanotube diameter reinforced: (a) iron, (b) copper, and (c) aluminum matrix on transverse modulus ($V_f=3\%$)

(a) Iron

Carbon Nanotube index	d (nm)	E_T (GPa)		
		lc=3nm	lc=5nm	lc=8 nm)
(5,10)	1.206	214.3	214.3	215.1
(10,15)	1.876	213.2	213.9	214.4
(15,20)	2.551	212.6	213.1	213.5

(b) Copper

Carbon Nanotube index	d (nm)	E_T (GPa)		
		lc=3nm	lc=5nm	lc=8 nm)
(5,10)	1.206	132.69	134.00	134.75
(10,15)	1.876	132.45	133.30	133.78
(15,20)	2.551	131.37	132.28	132.41

(c) Aluminum

Carbon Nanotube index	d (nm)	E_T (GPa)		
		lc=3nm	lc=5nm	lc=8 nm)
(5,10)	1.206	73.4	74.1	74.6
(10,15)	1.876	72.7	73.1	74.4
(15,20)	2.551	72.3	72.9	73.4

From the above Tables, it can be observed that at 3% volume fraction of carbon nanotube reinforced metal matrix, the value of transverse modulus for zigzag type is the highest, while for chiral type is the lowest because changing the chirality index will change the diameter. However, it can be noticed that the transverse modulus increases when the volume fractions and/or the length increased and decreases when the chirality index changed of carbon nanotube reinforced iron, copper, and aluminum matrix nanocomposite.

5.3.3 Prediction of the Shear Modulus

The results of shear modulus for carbon nanotubes (treated as short fiber) reinforced iron metal matrix nanocomposite at same diameter with different length show increasing trend when the volume fraction increased and decreasing values of shear modulus at different carbon nanotubes length. It is observed that the Shear modulus at 3% volume fraction of zigzag carbon nanotubes (5, 0) varied as 3%, 2%, and 1% at carbon nanotubes length increased for 3, 5, and 8 nm, respectively. However, at 3% volume fraction for the armchair carbon nanotubes (5, 5) varied as 3%, 2%, and 1%

while for chiral carbon nanotubes (5, 10) varied as 2%, 2%, and 1% at the same increment of length, respectively. Figure 5.32, 5.33, and 5.34 show shear modulus increment for iron matrix reinforced by zigzag, armchair and chiral carbon nanotube, respectively, when the volume fraction increases.

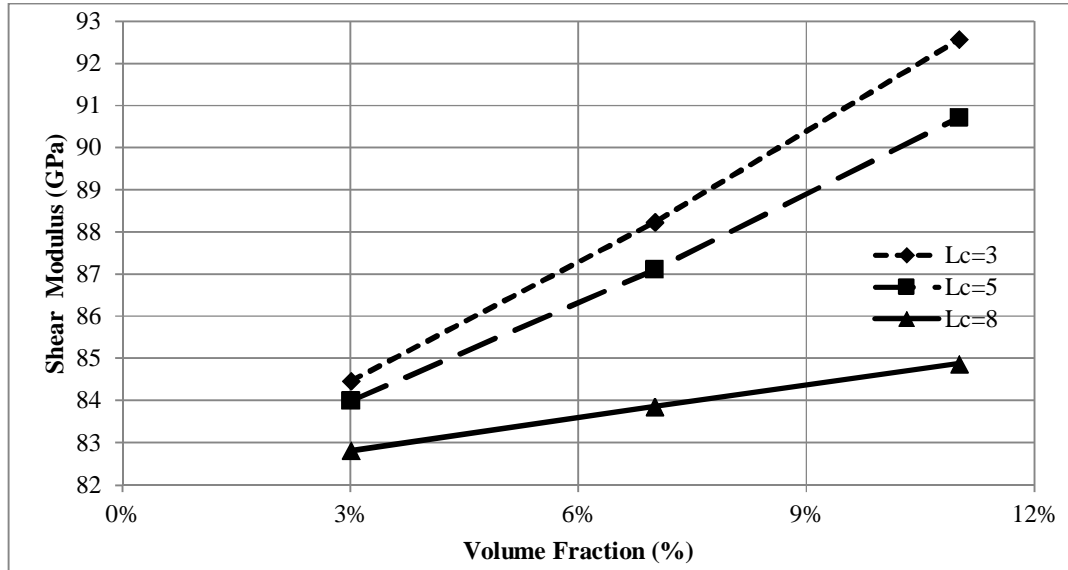


Figure 5.32: Shear modulus for zigzag carbon nanotube treated as short fiber reinforced iron matrix

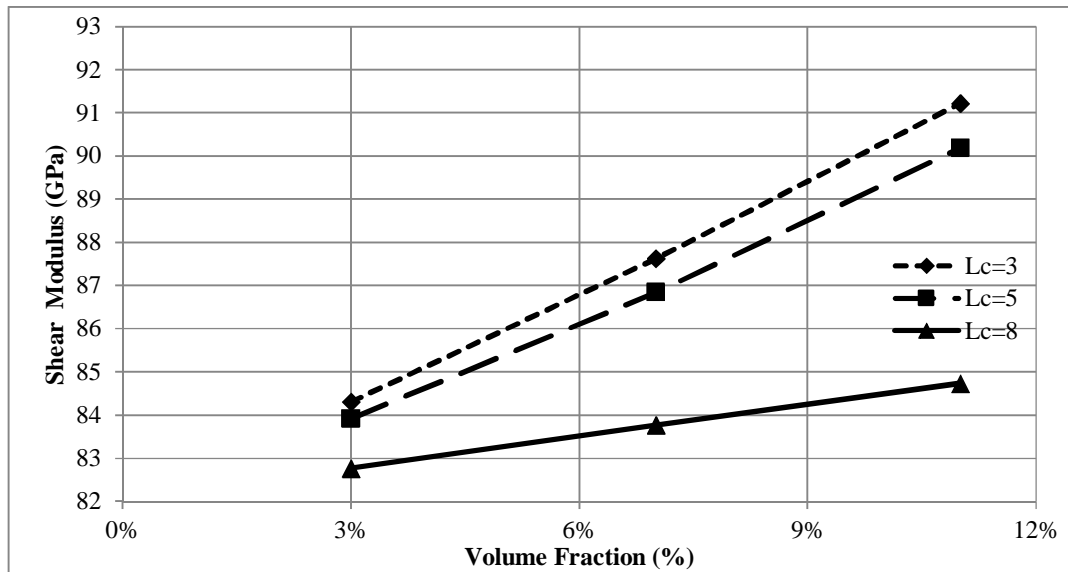


Figure 5.33: Shear modulus for armchair carbon nanotube treated as short fiber reinforced iron matrix

Similarly, the results of shear modulus for carbon nanotubes (treated as short fiber) reinforced Copper metal matrix Nanocomposite at same diameter with different length show increasing trend when the volume fraction increased and decreasing values of shear modulus at different carbon nanotubes length.

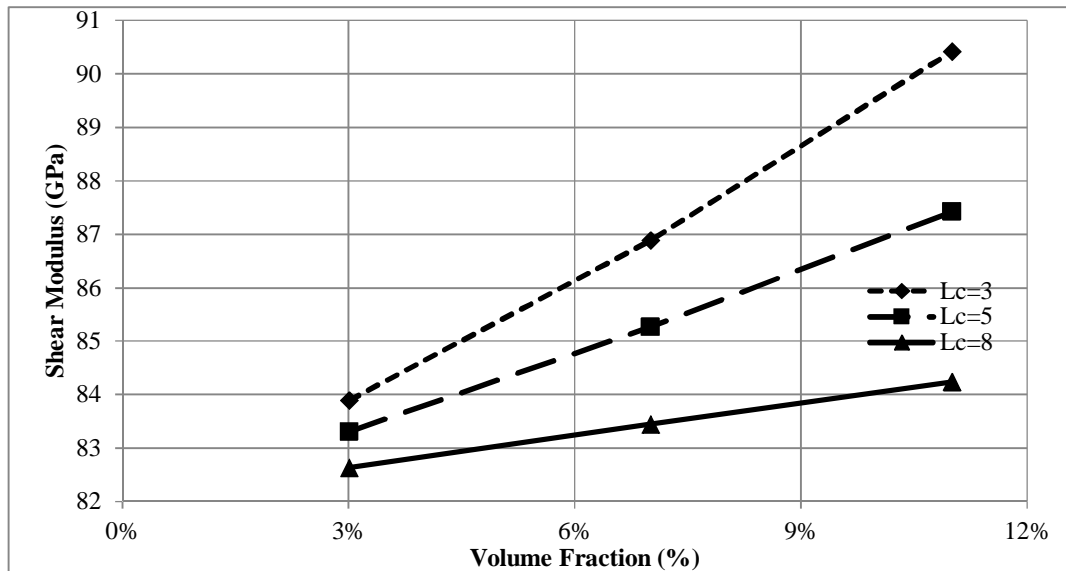


Figure 5.34: Shear modulus for chiral carbon nanotube treated as short fiber reinforced iron matrix

It is observed that the shear modulus of the copper matrix nanocomposite reinforced by 3% volume fraction of zigzag carbon nanotubes (5, 0) varied as 6%, 7%, and 8% at carbon nanotubes length of 3, 5, and 8 nm, respectively. However, at 3% volume fraction for the Armchair carbon nanotubes (5, 5) varied as 5%, 6%, and 7% while for chiral carbon nanotubes (5, 10) varied as 5%, 6%, and 7% at the same increment of length, respectively. Figure 5.35, 5.36, and 5.37 show increment of shear modulus for copper matrix reinforced by zigzag, armchair and chiral carbon nanotube, respectively, when the volume fraction increases.

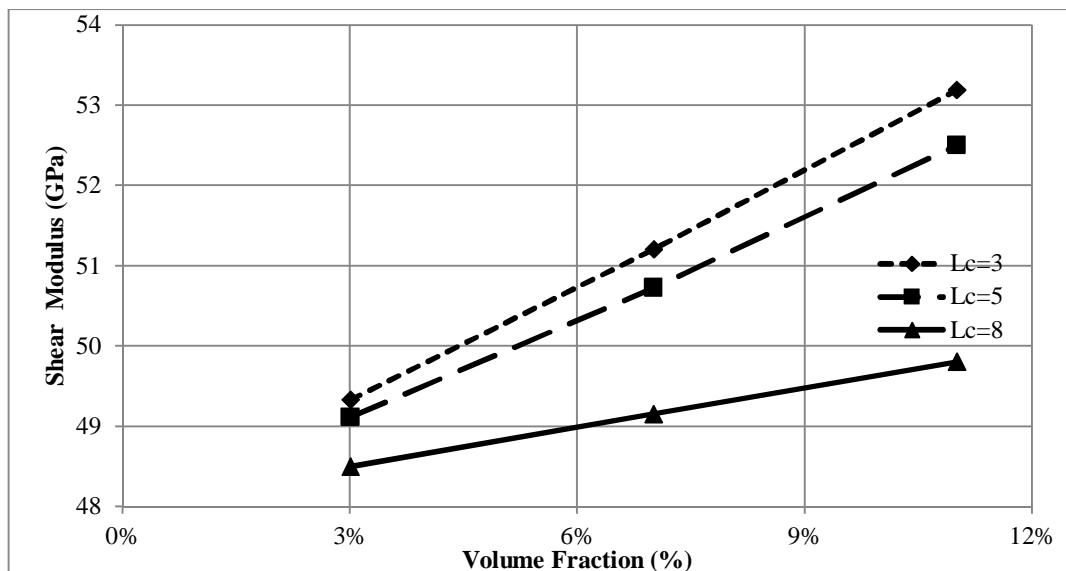


Figure 5.35: Shear modulus for zigzag carbon nanotube treated as short fiber reinforced copper matrix at different length

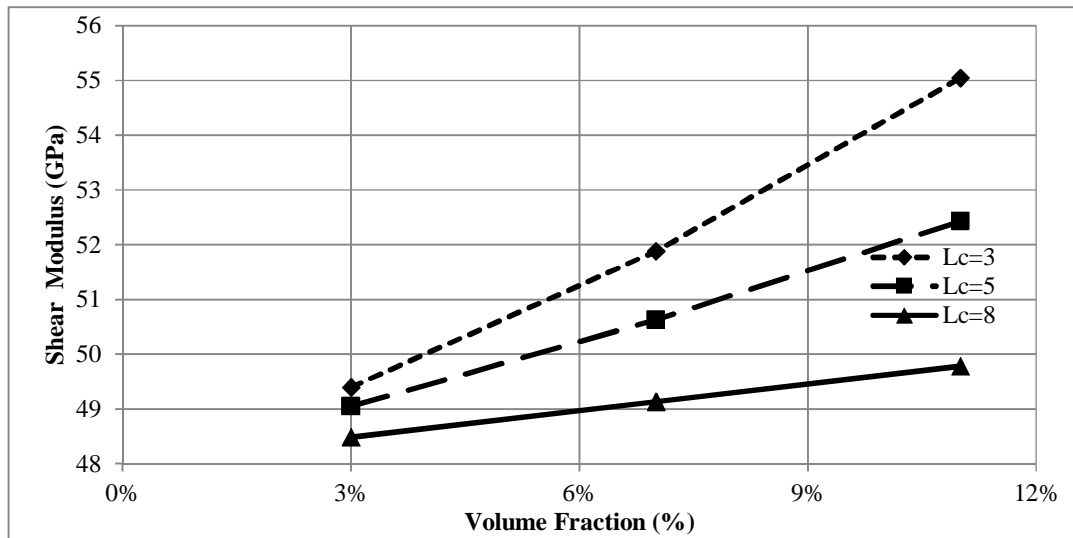


Figure 5.36: Shear modulus for armchair carbon nanotube treated as short fiber reinforced copper matrix at different length

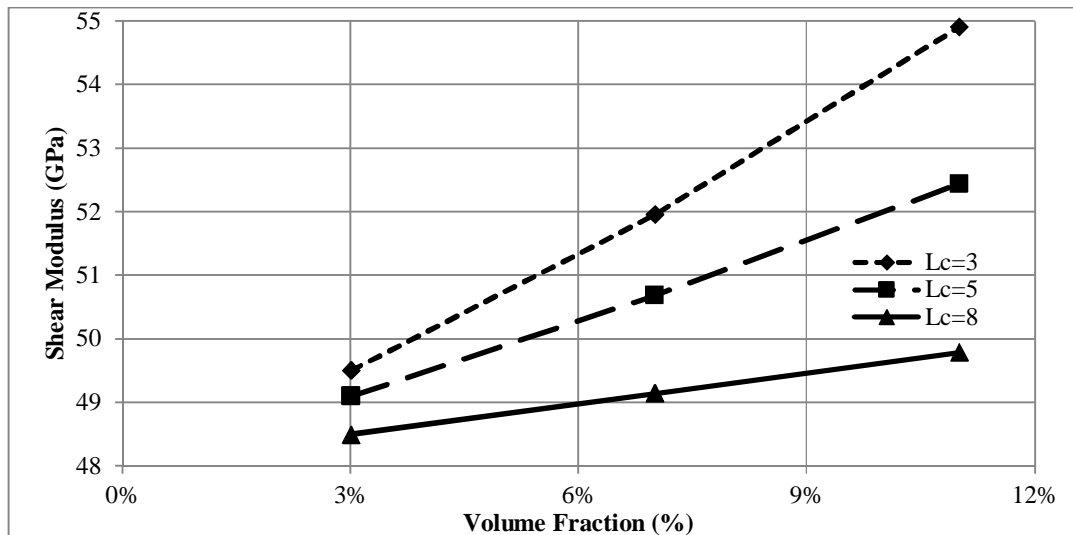


Figure 5.37: Shear modulus for chiral carbon nanotube treated as short fiber reinforced copper matrix at different length

However, the results of shear modulus for carbon nanotubes (treated as short fiber) reinforced aluminum metal matrix nanocomposite at same diameter with different length show increasing trend when the volume fraction increased and decreasing values of shear modulus at different carbon nanotubes length. It is observed that the Shear modulus at 3% volume fraction of zigzag carbon nanotubes (5, 0) varied as 3%, 2%, and 1% at carbon nanotubes length of 3, 5, and 8 nm, respectively. However, at 3% volume fraction for the armchair carbon nanotubes (5, 5) varied as 3%, 2%, and 1% while for chiral carbon nanotubes (5, 10) varied as 4%, 3%, and 1% at the same increment of length, respectively. Figures 5.38, 5.39, and 5.40 show increment of shear modulus for aluminum matrix reinforced by zigzag, armchair and chiral carbon nanotube, respectively, when the volume fraction increases.

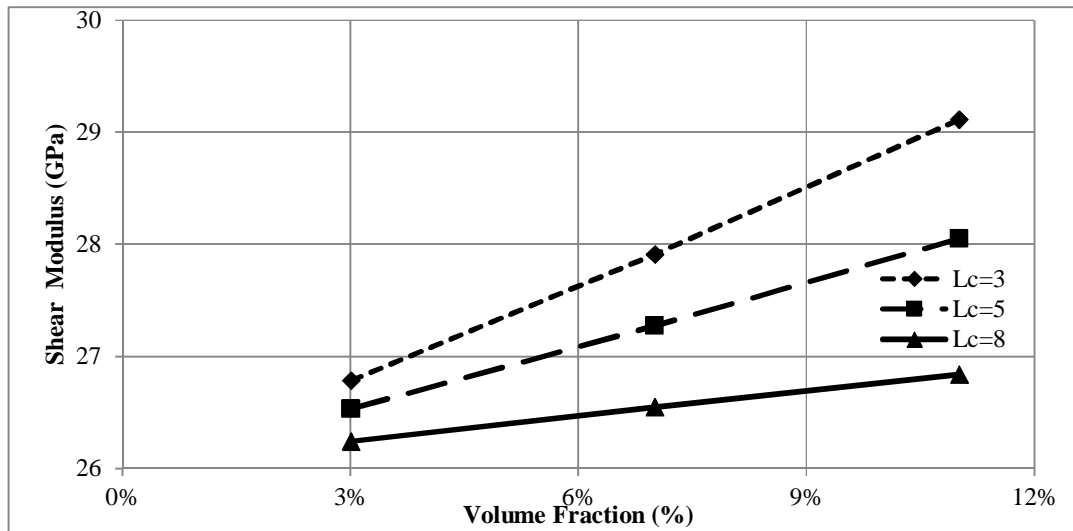


Figure 5.38: Shear modulus for zigzag carbon nanotube treated as short fiber reinforced aluminum matrix at different length

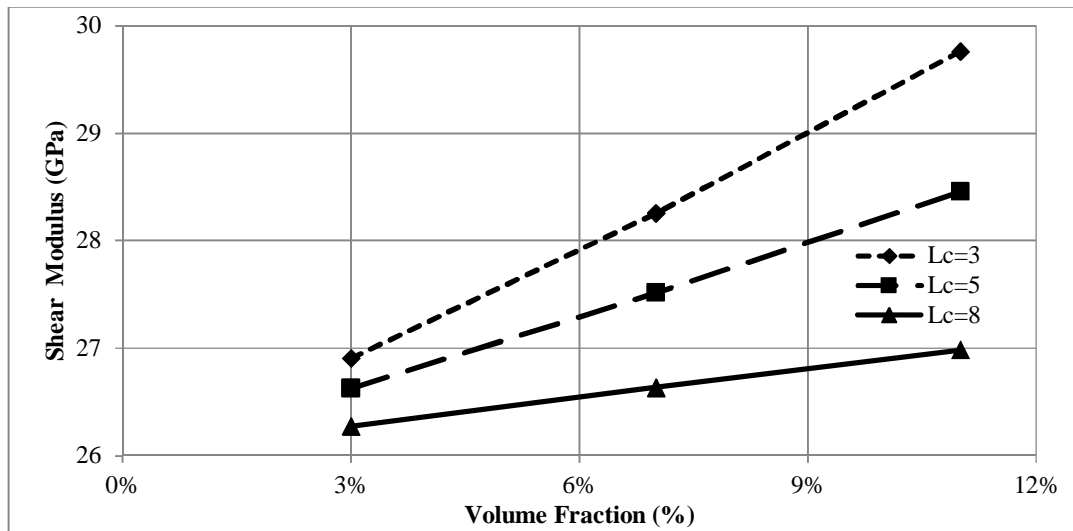


Figure 5.39: Shear modulus for armchair carbon nanotube (as short fiber) reinforced aluminum matrix at different length

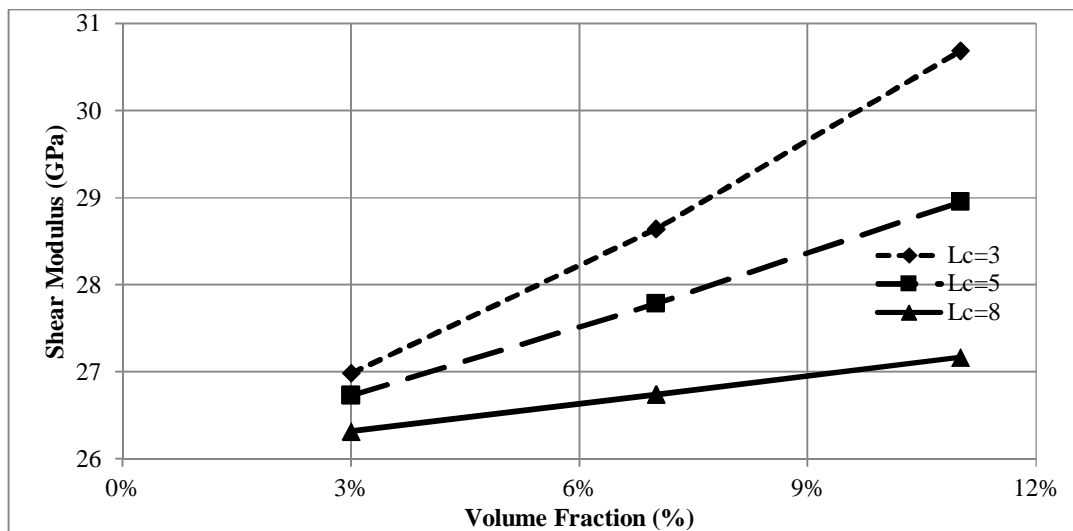


Figure 5.40: Shear modulus for chiral carbon nanotube treated as short fiber reinforced aluminum matrix at different length

The analysis will be carried out for the three types of the carbon nanotubes at the same length with different diameter which can be achieved by changing the index of carbon nanotube for the same kind. The results of armchair carbon nanotubes reinforced iron, copper, and aluminum metal matrix are presented in Table 5.14 (a), (b), and (c). It can be observed that at 3% volume fraction of carbon nanotube reinforced Iron matrix, the value of shear modulus decreased as the diameter of the armchair carbon nanotubes increased.

Table 5.14: Effect of armchair carbon nanotube diameter reinforced: (a) iron, (b) copper, and (c) aluminum matrix on transverse modulus ($V_f=3\%$)

(a) Iron

Carbon Nanotube index	d (nm)	G (GPa)		
		lc=3nm	lc=5nm	lc=8 nm)
(5,5)	0.848	84.3	83.9	82.8
(10,10)	1.526	83.7	83.3	82.6
(15,15)	2.204	83.4	83.2	82.4

(b) Copper

Carbon Nanotube index	d (nm)	G (GPa)		
		lc=3nm	lc=5nm	lc=8 nm)
(5,5)	0.848	49.4	49.05	48.5
(10,10)	1.526	49.2	49.02	48.4
(15,15)	2.204	49.1	48.96	48.1

(c) Aluminum

Carbon Nanotube index	d (nm)	G (GPa)		
		lc=3nm	lc=5nm	lc=8 nm)
(5,5)	0.848	27.1	26.8	26.3
(10,10)	1.526	27.0	26.6	26.1
(15,15)	2.204	26.9	26.4	26.1

For zigzag carbon nanotubes reinforced metal matrix at same length with different diameter, Table 5.15 (a), (b), and (c) present the results calculated at 3% of volume fraction for iron, copper, and aluminum metal matrix reinforced by zigzag carbon nanotube type. The results show that the value of Shear modulus decreased as the diameter of the zigzag carbon nanotubes increases.

Table 5.15: Effect of zigzag carbon nanotube diameter reinforced: (a) iron, (b) copper, and (c) aluminum matrix on transverse modulus ($V_f=3\%$)

(a) Iron

Carbon Nanotube index	d (nm)	G (GPa)		
		lc=3nm	lc=5nm	lc=8 nm)
(5,0)	0.561	84.5	84.0	82.8
(10,0)	0.953	84.1	83.7	82.7
(15,0)	1.344	83.9	83.4	82.4

(b) Copper

Carbon Nanotube index	d (nm)	G (GPa)		
		lc=3nm	lc=5nm	lc=8 nm)
(5,0)	0.561	49.5	49.2	48.5
(10,0)	0.953	49.4	49.1	48.4
(15,0)	1.344	49.5	48.9	48.2

(c) Aluminum

Carbon Nanotube index	d (nm)	G (GPa)		
		lc=3nm	lc=5nm	lc=8 nm)
(5,0)	0.561	27.1	26.8	26.3
(10,0)	0.953	26.9	26.7	26.2
(15,0)	1.344	26.8	26.5	26.0

For chiral carbon nanotubes reinforced metal matrix at same length with different diameter, Table 5.16 (a), (b), and (c) presents the results calculated at 3% of volume fraction for iron, copper, aluminum metal matrix reinforced by chiral carbon nanotube type. The results show that the value of shear modulus decreased as the diameter of the chiral carbon nanotubes increases.

Table 5.16: Effect of chiral carbon nanotube diameter reinforced: (a) iron, (b) copper, and (c) aluminum matrix on transverse modulus ($V_f=3\%$)

(a) Iron

Carbon Nanotube index	d (nm)	G (GPa)		
		lc=3nm	lc=5nm	lc=8 nm)
(5,10)	1.206	83.9	83.3	82.6
(10,15)	1.876	83.3	83.1	82.5
(15,20)	2.551	83.1	82.7	82.3

(b) Copper

Carbon Nanotube index	d (nm)	G (GPa)		
		lc=3nm	lc=5nm	lc=8 nm)
(5,10)	1.206	49.5	49.1	48.6
(10,15)	1.876	49.2	49.0	48.5
(15,20)	2.551	48.9	48.9	48.4

(c) Aluminum

Carbon Nanotube index	d (nm)	G (GPa)		
		lc=3nm	lc=5nm	lc=8 nm)
(5,10)	1.206	27.2	26.9	26.4
(10,15)	1.876	27.1	26.8	26.3
(15,20)	2.551	26.8	26.7	26.1

5.4 Effective Thermal Conductivity Prediction

The theoretical estimation of the effective thermal conductivity of the carbon nanotubes reinforced composite was proposed, but that is not appropriate for the complex geometrical shape and arrangement of carbon nanotubes embedded in representative volume elements. Finite element analysis may be desirable to simulate any case to predict the effective thermal properties. However, ANSYS macro was developed for the numerical estimation of effective thermal conductivity using various RVEs.

5.4.1 Model development

The model geometries was developed by using parameterized ANSYS macro for predicting effective thermal conductivity of the materials using three representative volume element models, quarter and two kinds of full model. It is assumed that the carbon nanotube fibers are full embedded with different length in RVE and there exists thermal resistance between carbon nanotubes and matrix. To generate the model geometry, a hexahedron of $A \times A \times L$ was created. Then, two cylinders are created, whose lengths is L and diameters are d_o and d_i , respectively. These cylinders and hexahedron are overlapped. Then, the part was removed in the resulting volumes of overlapping, where carbon nanotubes will be placed in matrix. Figure 5.41 shows the resulting volumes. If the volume for carbon nanotube is added, geometrical modeling is completed. It should be noted that cylinder for carbon nanotube and volumes for matrix are not bonded, but in contact. Figure 5.42 represents the geometry of the three kinds of models used.

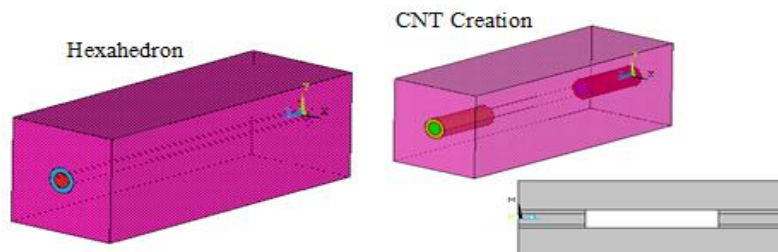


Figure 5.41: The resulting volumes of overlapping

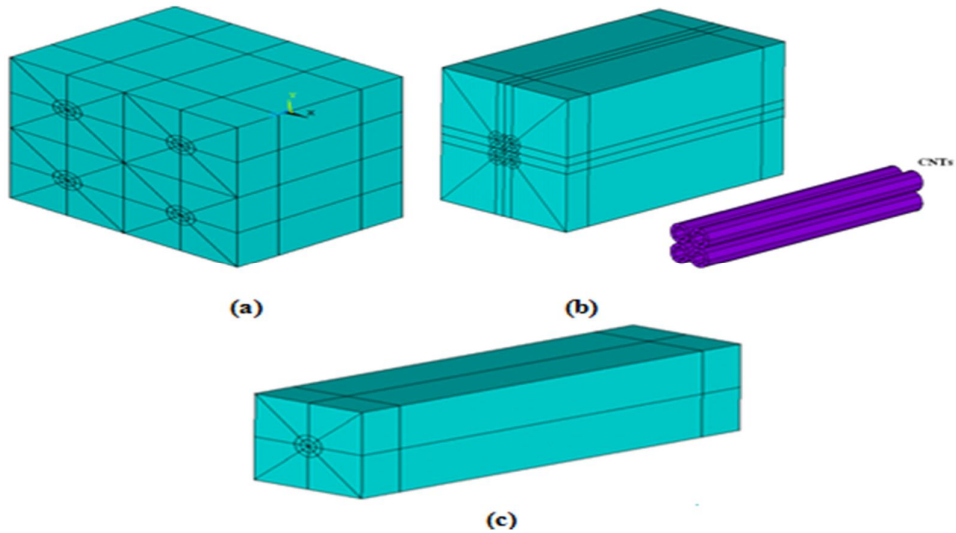


Figure 5.42: The Geometrical Model: (a) Full model with Carbon nanotubes away from the center, (b) Full model with carbon nanotubes placed at the center and (c) the quarter model

5.4.2 Meshing and Boundary Conditions

The representative volume element is divided into many regular volumes for meshing. First, all volumes of RVE are divided into equal eight parts, then, the representative volume element was divided into three parts of which the middle part corresponds to carbon nanotubes as shown in Figure 5.43.

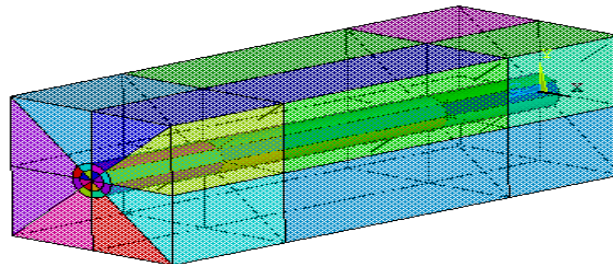


Figure 5.43: Final RVE divided for meshing

The representative volume element was meshed using hexahedron shaped element and mapped meshing algorithm. The longitudinal size is equal to the number of divisions in width is 10 and number of divisions in thickness of carbon nanotube is three. Before meshing, different materials are assigned to the volumes for matrix and carbon nanotube. Element type used was SOLID70[138] as shown in Figure 5.44. The element has eight nodes with a single degree of freedom, temperature, at each node.. The element is applicable to a 3-D, steady-state or transient thermal analysis and can compensate for mass transport heat flow.

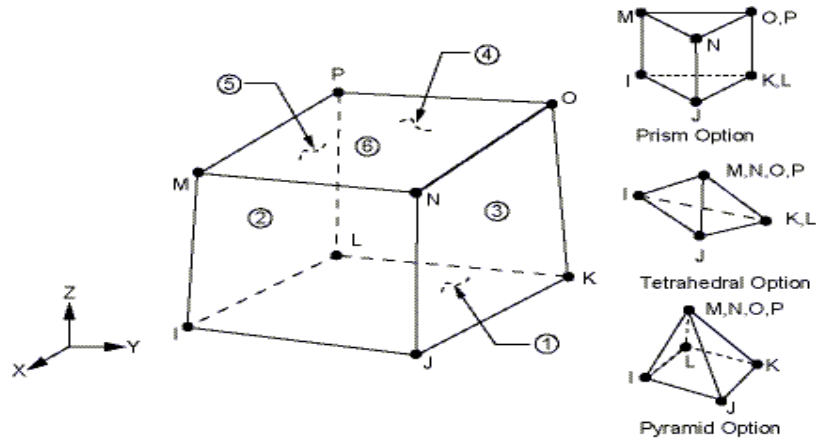


Figure 5.44: The SOLID70 Geometry[138]

The element type CONTA173 (3-D 4-Node Surface-to-Surface Contact) and TARGE170 (3-D Target Segment) used for thermal contact and loading. The interfacial conductance is reflected in the REAL constants. Contact and target elements are generated automatically using the ESURF command. Before ESURF command is issued, only contact nodes or target nodes and elements connected by those should be selected. The contacting areas of carbon nanotubes and matrix are appeared like one because they coincide geometrically. The contact and target elements generated were shown in Figure 5.45.

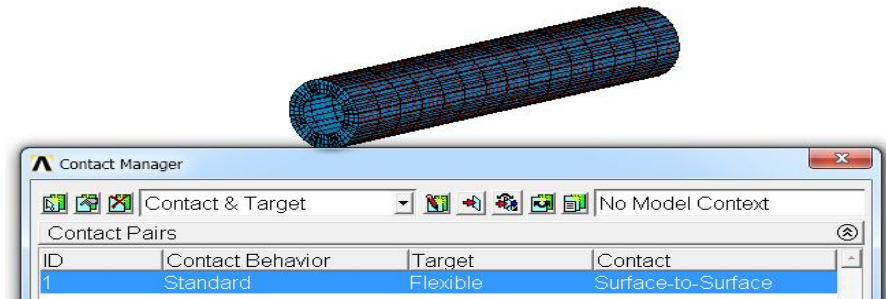


Figure 5.45: The contact and target elements generated

5.4.3 Estimating the effective thermal conductivity based on finite element results

The representative volume element was considered with volume V . The average of a field f over the RVE V is denoted by letter \bar{f} ;

$$\bar{f} = \langle f \rangle = \frac{1}{V} \int_V f(x) dx \quad 5.1$$

According to the Fourier's law, the heat flux vector q can be written as follows;

$$q = -k(x)grad(T(x)) \quad 5.2$$

Where T and k are temperature and thermal conductivity in RVE.

In macro scale, the Fourier's law is represented as follows;

$$\bar{q} = -\bar{k} grad(\bar{T}(x)) \quad 5.3$$

When \bar{q} and $grad(\bar{T}(x))$ are known, the effective thermal conductivity \bar{k} can be determined from equation 5.3. But it is unable to know both of \bar{q} and $grad(\bar{T}(x))$ at once. Applying $grad(\bar{T}(x))$ on RVE by supposing different uniform temperature on opposite sides of RVE and determine \bar{q} . The average of thermal gradient $grad(\bar{T}(x))$ is represented as follows;

$$grad(\bar{T}(x)) = \frac{\Delta T}{L} \quad 5.4$$

Where ΔT denotes difference of uniform temperature at two opposite sides. L is the length of RVE. Figure 5.46 shows the macro temperature imposed at boundary of representative volume element.

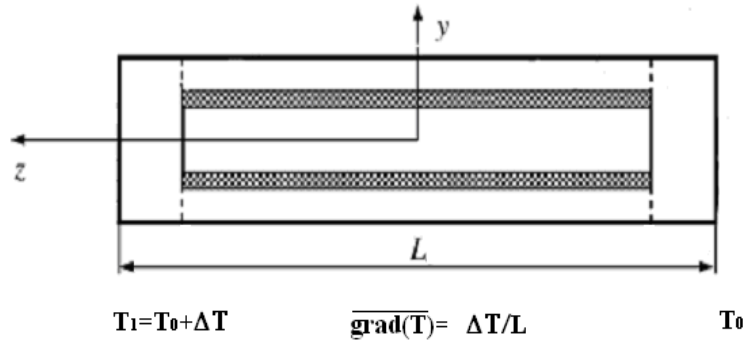


Figure 5.46: Macro temperature imposed at boundary of the RVE

As result, effective conductivity is estimated by

$$\bar{k} = -\frac{\bar{q}}{\Delta T/L} \quad 5.5$$

\bar{q} is calculated by FEA for the RVE.

In order to find the effective thermal conductivity, the average of thermal flux should be known. In context of FEA, \bar{q} can approximately be written as follows;

$$\bar{q} = \frac{\sum_{i=1}^n \bar{q}_i v_i}{V} \quad 5.6$$

Where n is the total number of elements of RVE. \bar{q}_i is the average of thermal flux over i th element and v_i is the volume of i th element. In ANSYS software, \bar{q}_i and v_i can easily be extracted from element table and \bar{q} can be calculate by multiplication and sum of the element table variables.

It is assumed that thermal Conductivity of carbon nanotube and matrix are 3000 W/m k and 204 W/m k for aluminum matrix, respectively. The interfacial conductance is $\beta = 100 MW/m^2 K, \Delta T = 300 - 299 = 1$.

Figure 5.47, 5.48, and 5.49 show temperature and thermal flux in Z-direction in the matrix and the carbon nanotubes for iron, copper and aluminum metal matrixes respectively for the quarter model.

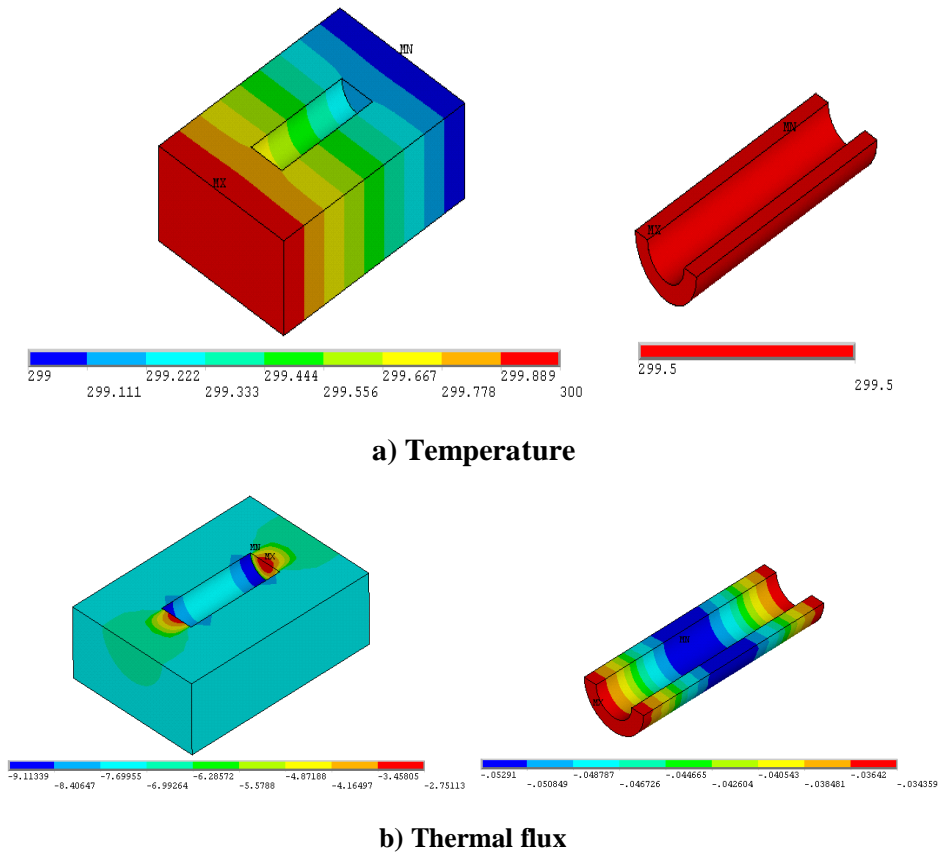
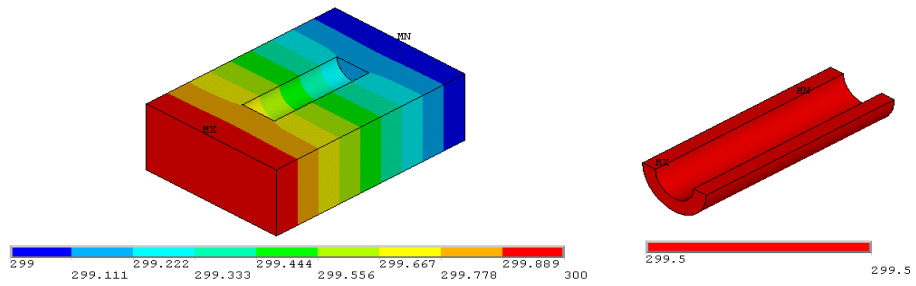
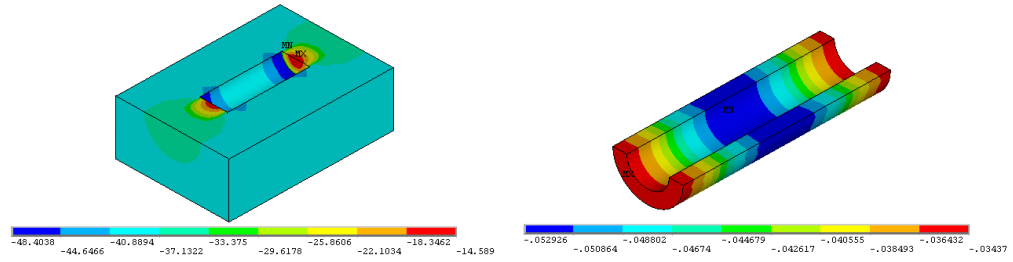


Figure 5.47: Temperature and thermal flux distribution in the matrix and carbon nanotubes or Iron matrix

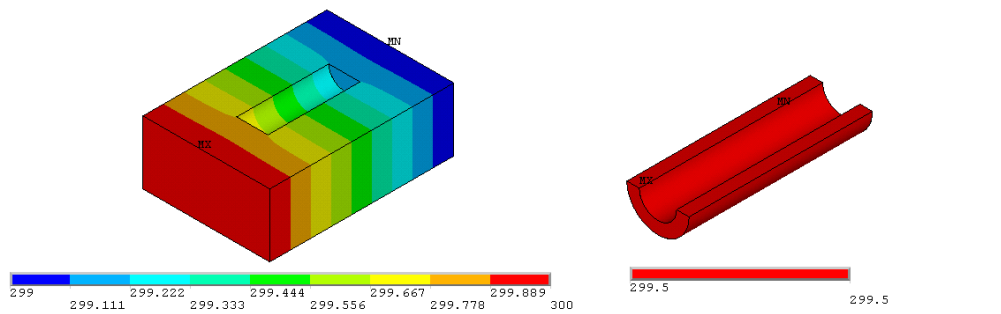


a) Temperature

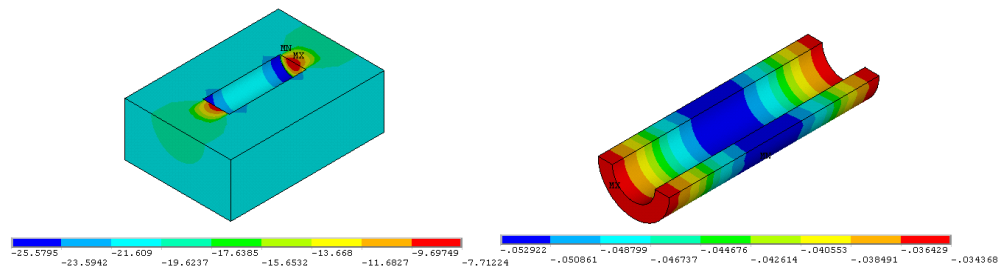


b) Thermal flux

Figure 5.48: Temperature and thermal flux distribution in the matrix and carbon nanotubes or Copper matrix



a) Temperature

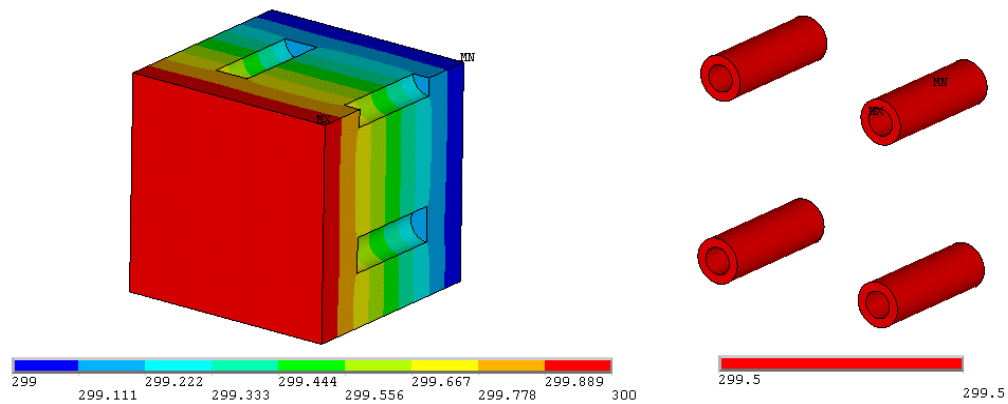


b) Thermal flux

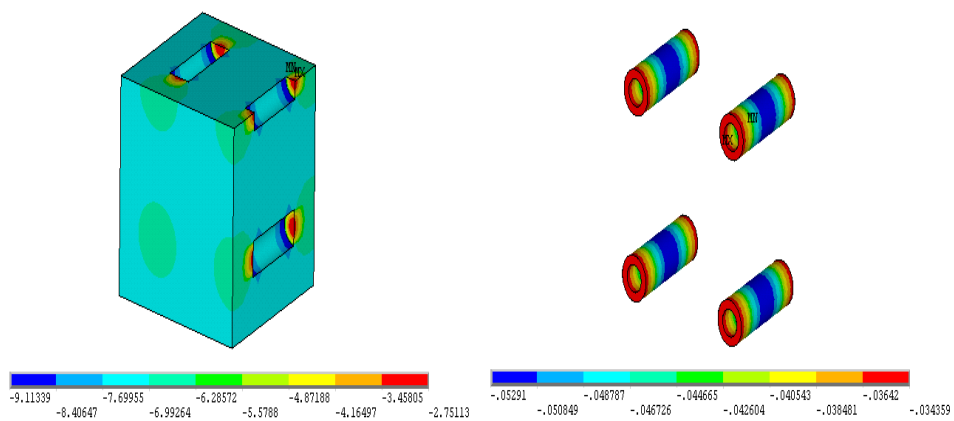
Figure 5.49: Temperature and thermal flux distribution in the matrix and carbon nanotubes or Aluminum matrix

It can be observed that temperature distribution in the entire RVE is constant irrespective of matrix material, but the magnitude of the thermal flux in z-direction depends on the matrix material.

For full model (A), Figure 5.50, 5.51 and 5.52 show the temperature and thermal flux in Z-direction in the matrix and carbon nanotubes for Iron, Copper and Aluminum metal matrixes respectively. It can be observed that the temperature distribution in the entire representative volume element is constant irrespective of matrix material, but the magnitude of the thermal flux in z-direction depends on the matrix material. In particular, distributions of the thermal fields are exactly equal the ones of the quarter models. Therefore, it can be concluded that the full model (A) is equivalent to the quarter model.

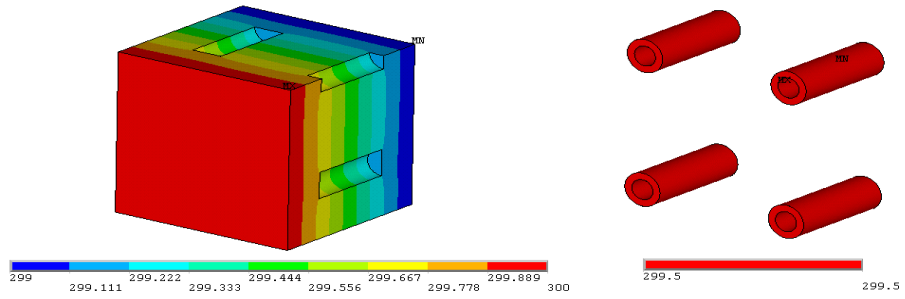


a) Temperature

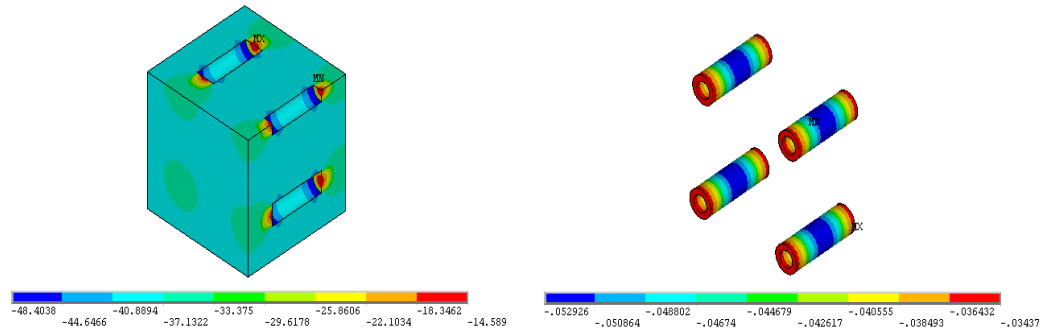


b) Thermal flux

Figure 5.50: Temperature and thermal flux distribution in the matrix and carbon nanotubes or iron matrix (Model A)

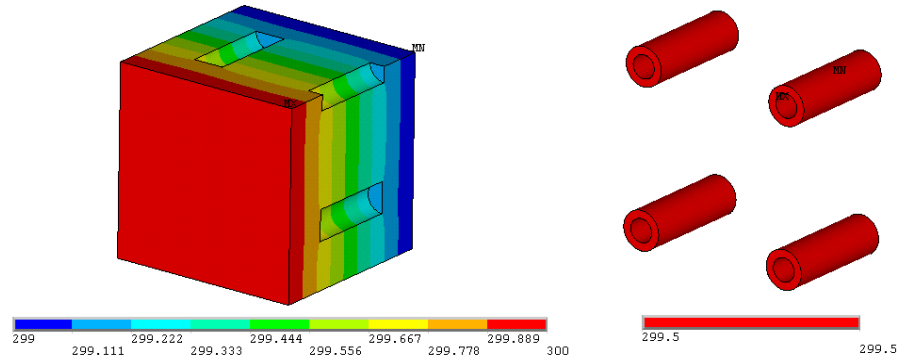


a) Temperature

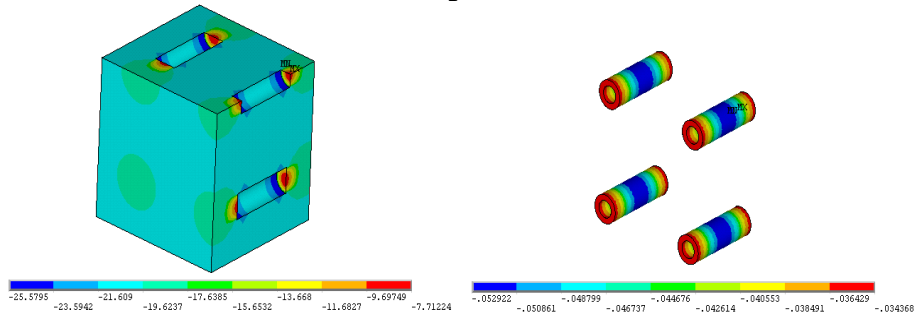


b) Thermal flux

Figure 5.51: Temperature and thermal flux distribution in the matrix and carbon nanotubes or Copper matrix



a) Temperature



b) Thermal flux

Figure 5.52: Temperature and thermal flux distribution in the matrix and carbon nanotubes or Aluminum matrix

For full model (B), Figure 5.53, 5.54 and 5.55 show the temperature and thermal flux in Z-direction in the matrix and carbon nanotubes for iron, copper and aluminum metal matrixes respectively. It can be observed that the temperature distribution in the entire RVE is complex in contrast to the quarter model or full model (B). Moreover the magnitude of the thermal flux in z-direction is very greater than ones of the quarter or full model (B). This means that the effect of the CNT on the effective thermal conductivity is so large that the effective thermal conductivity is larger than other cases as a result.

The attribution of the phase is estimated as follows

$$\bar{k}_i = -\frac{\bar{q}_i}{\Delta T/L} \quad 5.6$$

\bar{k}_i is attribution of the phase and $\bar{q}_i = \int_{V_i} q dx$

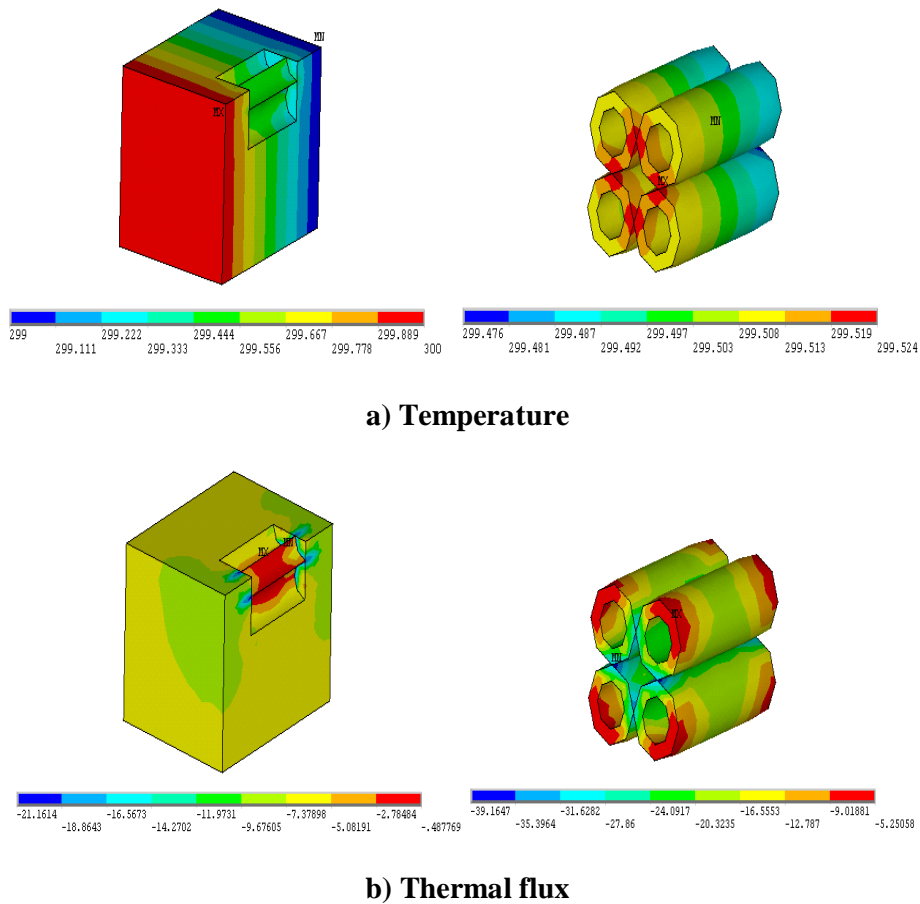
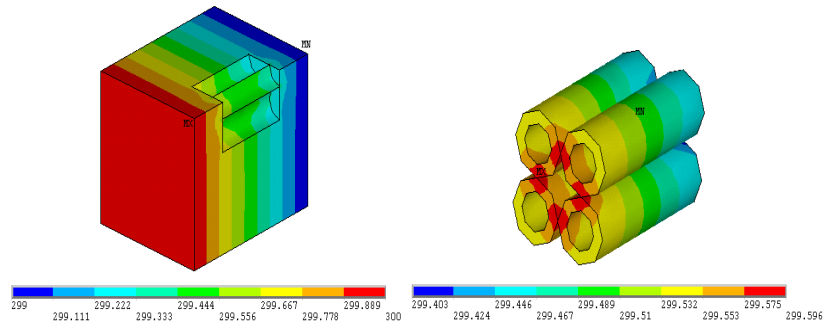
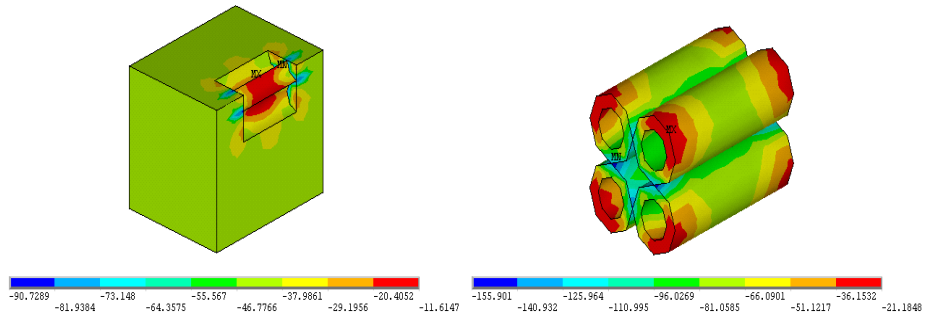


Figure 5.53: Temperature and thermal flux distribution in the matrix and carbon nanotubes or Iron matrix

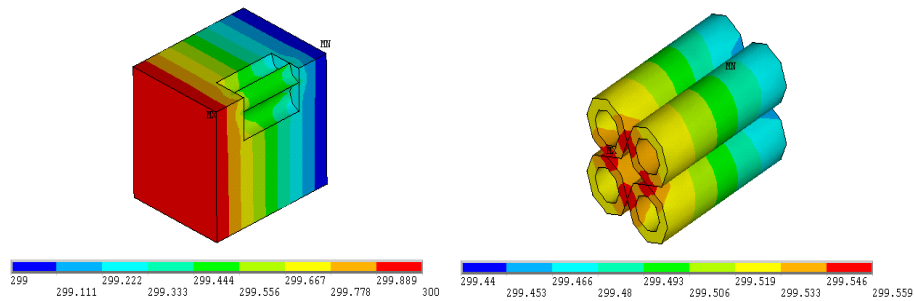


a) Temperature

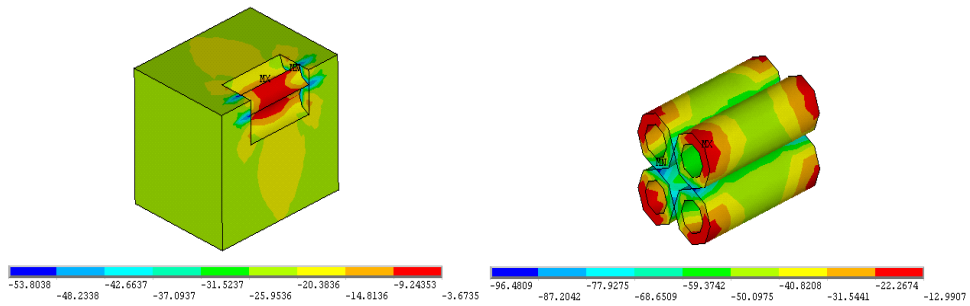


b) Thermal flux

Figure 5.54: Temperature and thermal flux distribution in the matrix and carbon nanotubes or Copper matrix



a) Temperature



b) Thermal flux

Figure 5.55: Temperature and thermal flux distribution in the matrix and carbon nanotubes or Aluminum matrix

The temperature in the CNT is constant due to superior conductivity of the CNT. The thermal flux in the end of the CNT is less than in the middle due to interfacial thermal resistance, but the magnitude of the thermal flux vector in the CNT is much less than matrix. The effective conductivity can be estimated through the equation 5.5. The thermal flux in Z-direction and volume of the elements are saved in the element table variables, then, new variable is defined by multiplying of these two variables and SSUM command is issued as shown in Figure 5.56

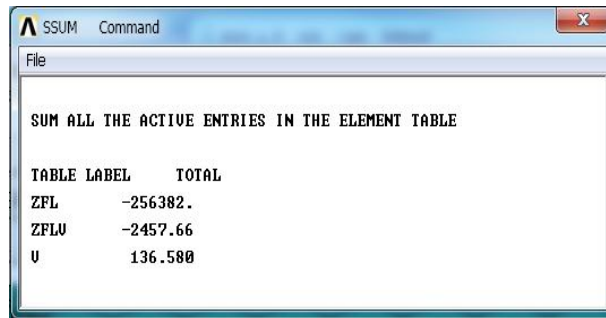


TABLE LABEL	TOTAL
ZFL	-256382.
ZFLU	-2457.66
U	136.580

Figure 5.56: The results of SSUM command

As a result, the effective conductivity is estimated as follows.

$$\bar{k} = -\frac{\bar{q}}{\Delta T/L} = -\frac{-2457.66/(3.515187^2 \times 10)}{1/10} = \frac{2457.66}{3.515187^2} = 198.89 \text{ W/Km}$$

The finite element modeling and post-processing for other dimensions and other kinds of representative volume element are very similar with above the example. In next section, the discussion on the results presented for the effective conductivity with different factors for carbon nanotubes treated as long and short fiber.

5.4.4 Long Fiber Case

5.4.4.1 Effect of Volume Fraction on the Effective Thermal Conductivity of the Nanocomposite

The analysis was conducted using ANSYS software for the carbon nanotube reinforced metal matrix nanocomposite with a constant CNTs diameters and length. The results have shown that the thermal conductivity of the nanocomposite varies linearly with the change in volume fractions from 3%. 7%, and 11% as predicted by Finite element

models and the model where the carbon nanotubes placed near the center of the representative volume element show high value of thermal conductivity than the model where the carbon nanotubes placed far from the center. Table 5.17 shows the results of thermal conductivity predicted for iron matrix reinforced by 3% volume fraction of different categories of carbon nanotubes. It can be noticed that the enhancement in thermal conductivity are varied from 7% to 8% for model “A” and from 8% to 9% for model “B” for chiral, zigzag, and armchair type respectively with respect to the thermal conductivity of iron matrix.

Table 5.17: Effect of chiral index of carbon nanotube reinforced iron matrix on the thermal conductivity for different models ($V_f=3\%$)

Carbon Nanotube index	K (W/m K)		% change	
	Model “A”	Model “B”	A	B
(5,5)	78.188	78.957	8%	9%
(5,0)	78.593	79.166	8%	9%
(5,10)	77.877	78.522	7%	8%

Figures 5.57, 5.58, and 5.59 show the effect of volume fraction on the thermal conductivity for iron matrix reinforced by armchair, zigzag, and chiral carbon nanotube respectively. It can be observed that the thermal conductivity of the Nanocomposite varies linearly with the change in volume fractions. However, it can be noticed from the above table that the thermal conductivity of zigzag type is the highest where the lowest is the chiral type

Similarly, for carbon nanotube reinforced copper matrix nanocomposite. The results for copper matrix reinforced by 3% volume fraction of different categories of carbon nanotubes are shown in Table 5.18. It can be noticed that the enhancement in thermal conductivity are varied from 6% to 7% for model “A” and from 7% to 8% for model “B” for chiral, zigzag, and armchair type, respectively, with respect to the thermal conductivity of copper matrix.

Table 5.18: Effect of chiral index of carbon nanotube reinforced copper matrix on the thermal conductivity for different models ($V_f=3\%$)

Carbon Nanotube index	K (W/m K)		% change	
	Model “A”	Model “B”	A	B
(5,5)	411.187	413.902	7%	7%
(5,0)	412.392	415.269	7%	8%
(5,10)	410.564	412.364	6%	7%

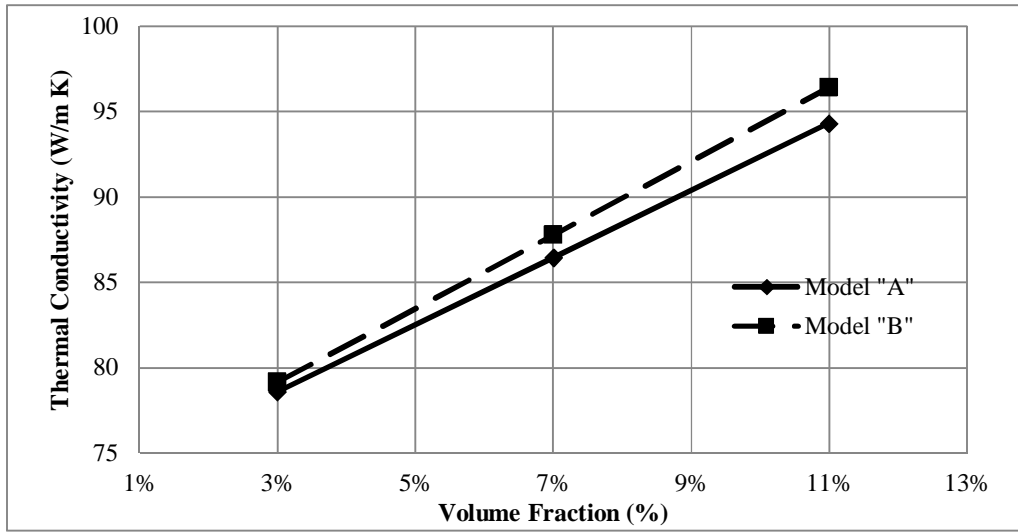


Figure 5.57: Effect of thermal conductivity for zigzag carbon (as long fiber) nanotube reinforced iron metal matrix

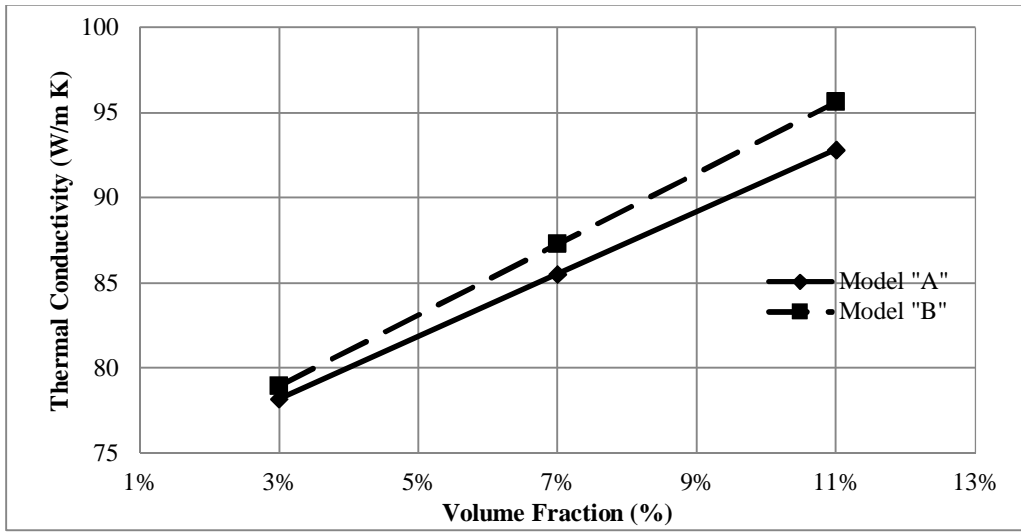


Figure 5.58: Effect of thermal conductivity for armchair carbon (as long fiber) nanotube reinforced iron metal matrix

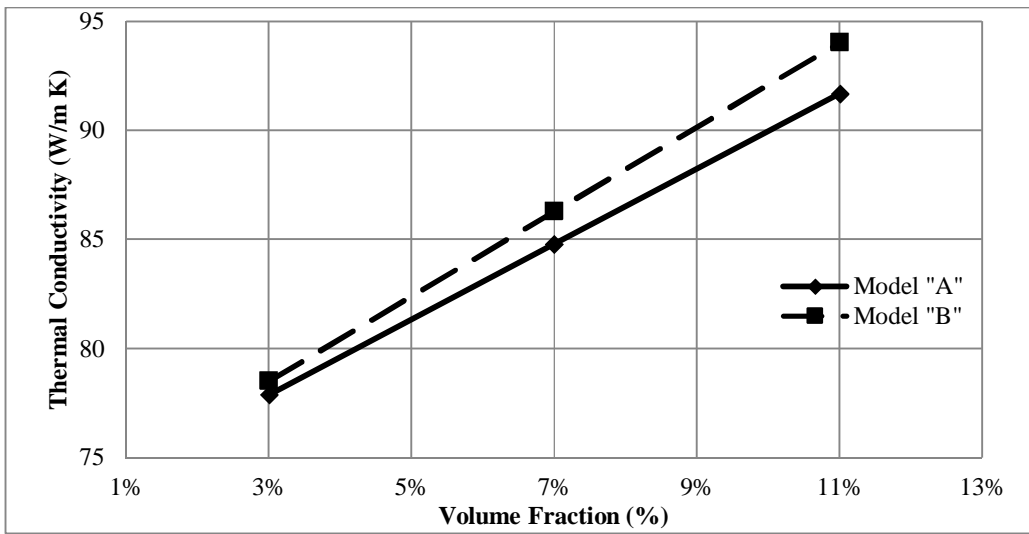


Figure 5.59: Effect of thermal conductivity for chiral carbon (as long fiber) nanotube reinforced iron metal matrix

Figure 5.60, 5.61, and 5.62 show the effect of volume fraction on the thermal conductivity for copper matrix reinforced by armchair, zigzag, and chiral carbon nanotube respectively. It can be observed that the thermal conductivity of the Nanocomposite varies linearly with the change in volume fractions. However, it can be noticed from the above table that the thermal conductivity of zigzag type is the highest where the lowest is the chiral type.

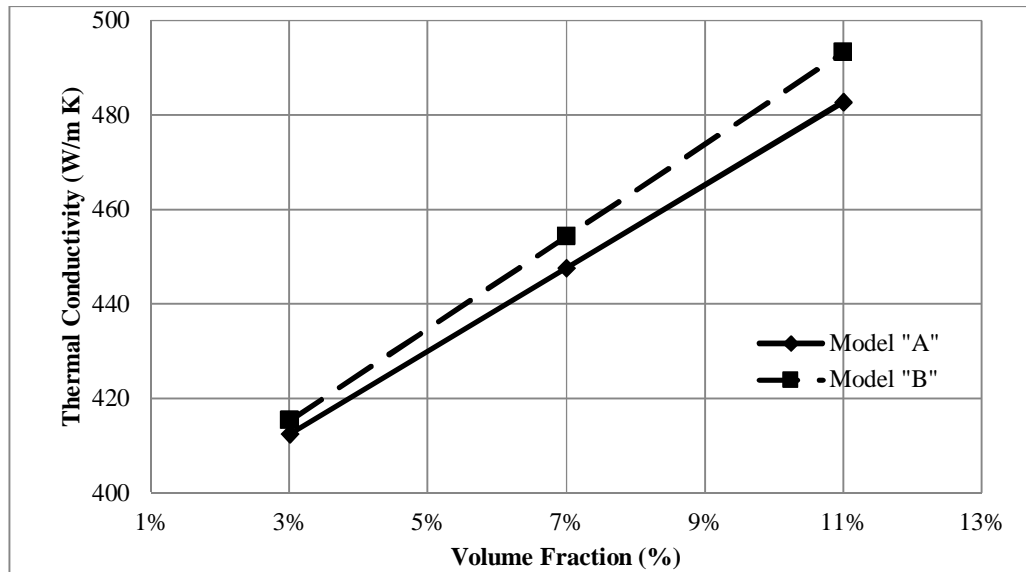


Figure 5.60: Effect of thermal conductivity for zigzag carbon (as long fiber) nanotube reinforced copper metal matrix

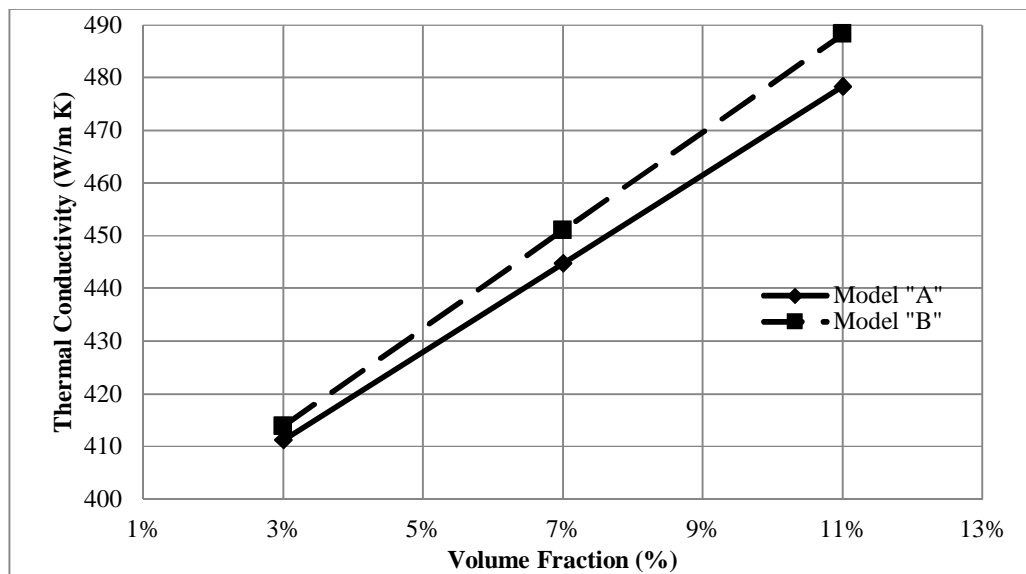


Figure 5.61: Effect of thermal conductivity for armchair carbon (as long fiber) nanotube reinforced copper metal matrix

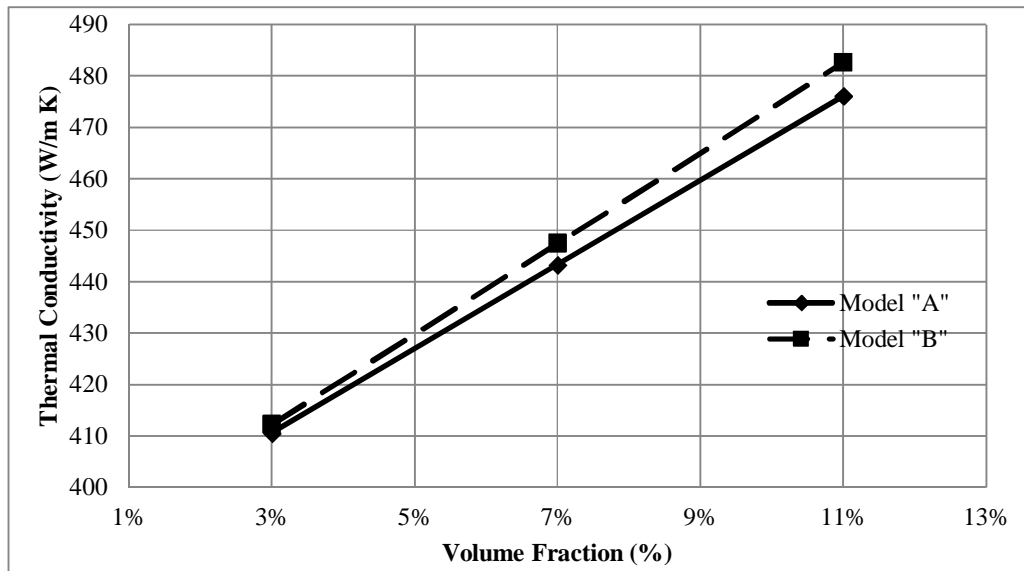


Figure 5.62: Effect of thermal conductivity for chiral carbon (as long fiber) nanotube reinforced copper metal matrix

However, for carbon nanotube reinforced aluminum matrix nanocomposite, it was observed that the increment percentage in the thermal conductivity of the new aluminum matrix Nanocomposite reinforced by 3% volume fraction of zigzag carbon nanotubes. The results for aluminum matrix reinforced by 3% volume fraction of different categories of carbon nanotubes are shown in Table 5.19. It can be noticed that the enhancement in thermal conductivity are varied from 9% to 10% for model “A” and from 10% to 11% for model “B” for chiral, zigzag, and armchair type respectively with respect to the thermal conductivity of aluminum matrix.

Table 5.19: Effect of chiral index of carbon nanotube reinforced aluminum matrix on the thermal conductivity for different models ($V_f=3\%$)

Carbon Nanotube index	K (W/m K)		% change	
	Model “A”	Model “B”	A	B
(5,5)	223.269	224.435	9%	10%
(5,0)	224.585	225.560	10%	11%
(5,10)	222.196	224.027	9%	10%

Figures 5.63, 5.64, and 5.65 show the effect of volume fraction on the thermal conductivity for Aluminum matrix reinforced by armchair, zigzag, and chiral carbon nanotube respectively. It can be observed that the thermal conductivity of the Nanocomposite varies linearly with the change in volume fraction. However, it can be noticed from the above Table that the thermal conductivity of zigzag type is the highest where the lowest is the chiral type

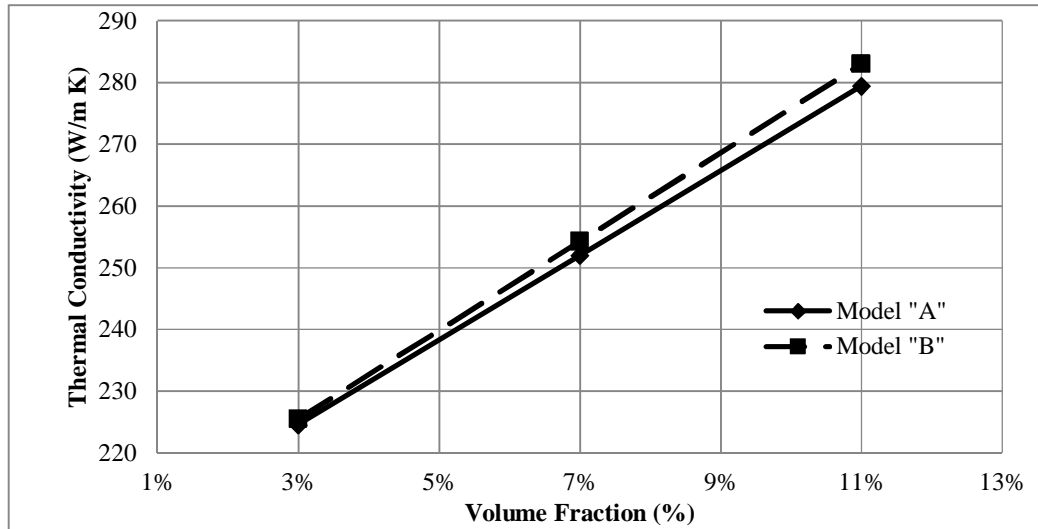


Figure 5.63: Effect of thermal conductivity for zigzag carbon (as long fiber) nanotube reinforced aluminum metal matrix

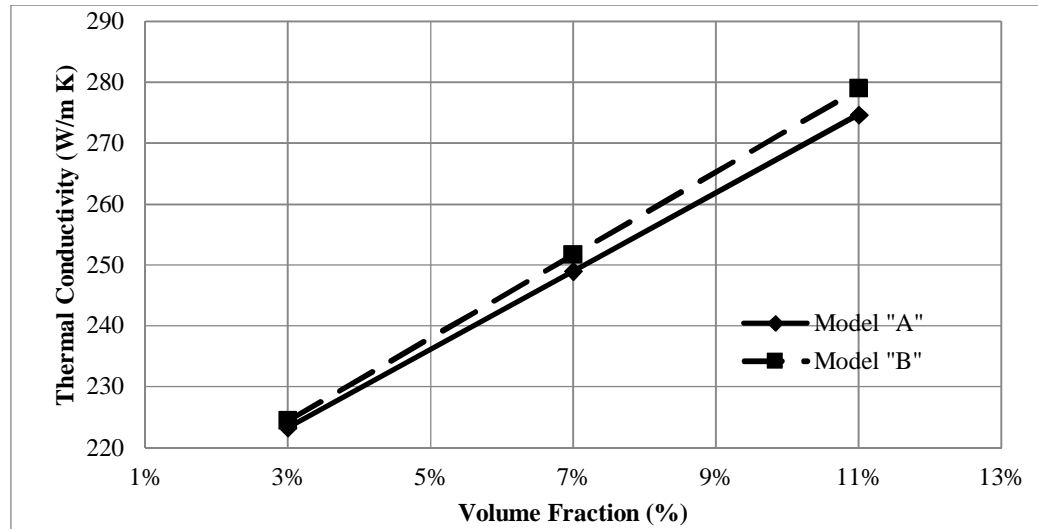


Figure 5.64: Effect of thermal conductivity for armchair carbon (as long fiber) nanotube reinforced aluminum metal matrix

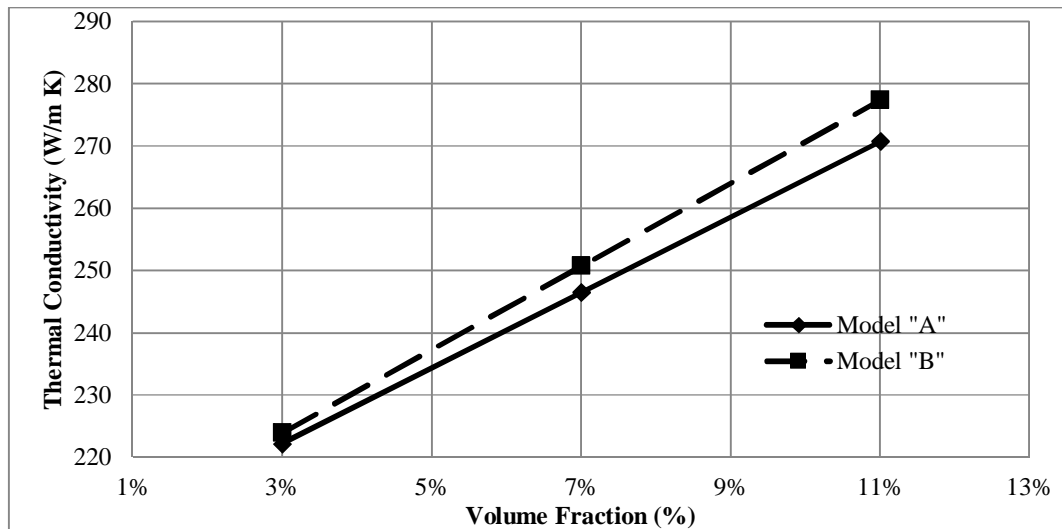


Figure 5.65: Effect of thermal conductivity for chiral carbon (as long fiber) nanotube reinforced aluminum metal matrix

5.4.4.2 Effect of chiral index on the effective thermal conductivity of the nanocomposite

The analysis was conducted using ANSYS software macro for models A and B with armchair (5, 5), zigzag (5, 0) and chiral (5, 10) carbon nanotubes reinforced metal matrix Nanocomposite at the same length. The results presented in Table 5.17 show that at 3% volume fraction of carbon nanotube reinforced iron matrix, the value of thermal conductivity for zigzag type is the highest, while for chiral type is the lowest. However, Figures 5.66, and 5.67 show that as the volume fraction increases within tested rang, the thermal conductivity increases linearly for all indices but with different slopes. The zigzag index shows the higher value of thermal conductivity while the chiral index shows the lowest. However, the thermal conductivity decreases by increasing the diameter which clearly appeared from the mentioned figures since the zigzag carbon nanotubes have the lowest diameter while the chiral carbon nanotubes have the biggest diameter.

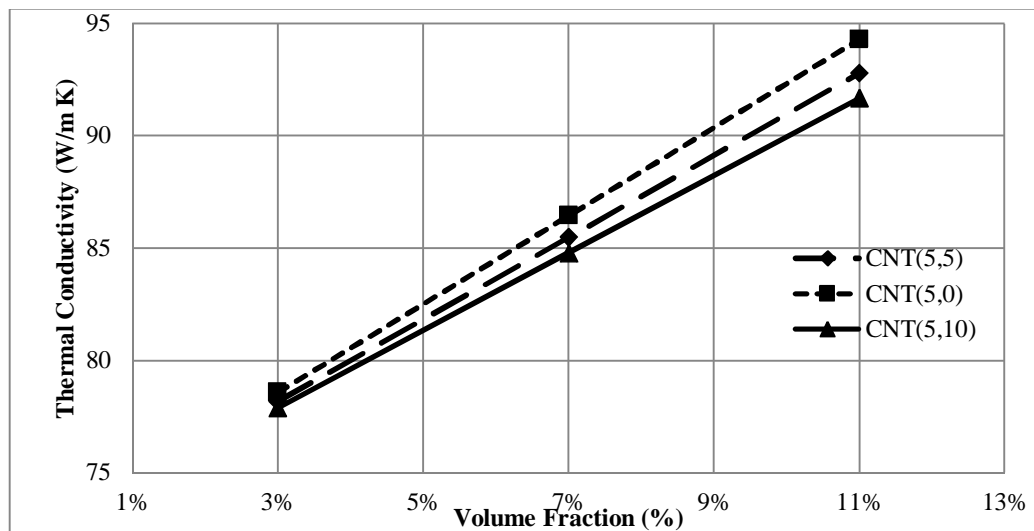


Figure 5.66: Effect of volume fraction on the thermal conductivity of different carbon nanotube chiral index reinforced iron metal matrix "model (A)"

Similarly, for carbon nanotubes reinforced copper matrix nanocomposite at the same length. The results presented in Table 5.18 show that at 3% volume fraction of carbon nanotube reinforced copper matrix, the value of thermal conductivity for zigzag type is the highest, while for chiral type is the lowest. However, Figures 5.68, and 5.69 show that as the volume fraction increases within tested range, the thermal conductivity increases linearly for all indices but with different slopes. The zigzag index shows the highest value of thermal conductivity while the chiral index shows the lowest.

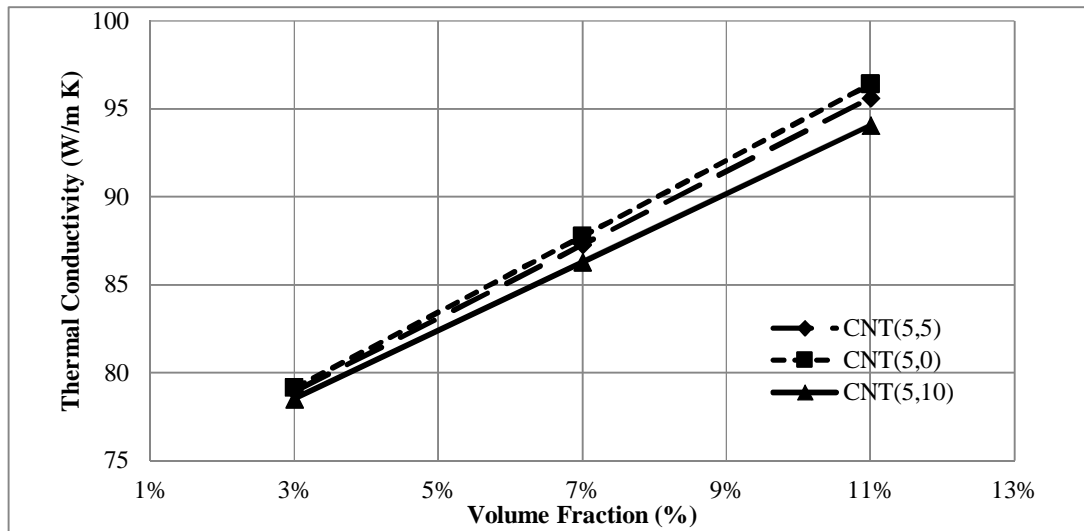


Figure 5.67: Effect of volume fraction on the thermal conductivity of different carbon nanotube chiral index reinforced iron metal matrix "Model (B)"

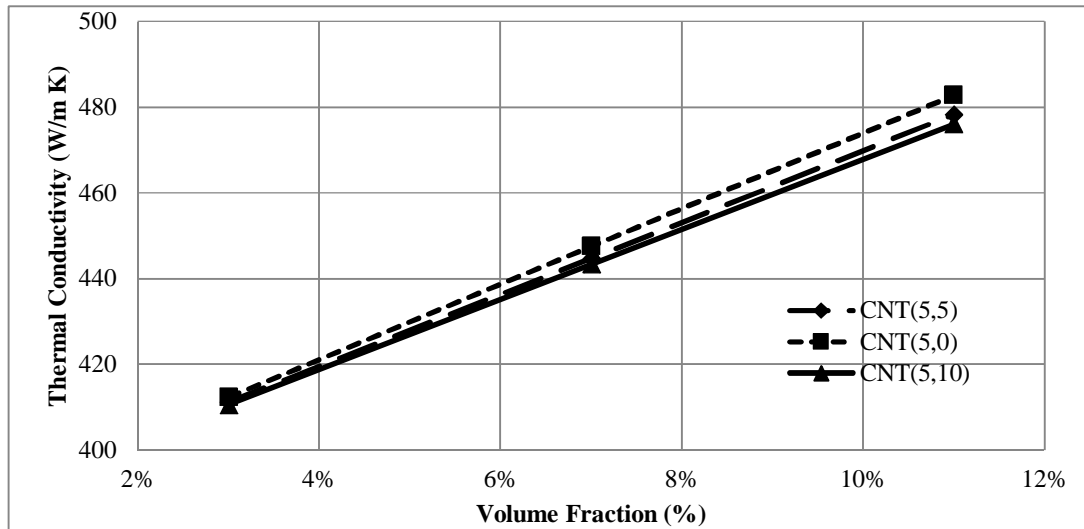


Figure 5.68: Effect of volume fraction on the thermal conductivity of different carbon nanotube chiral index reinforced copper metal matrix "Model (A)"

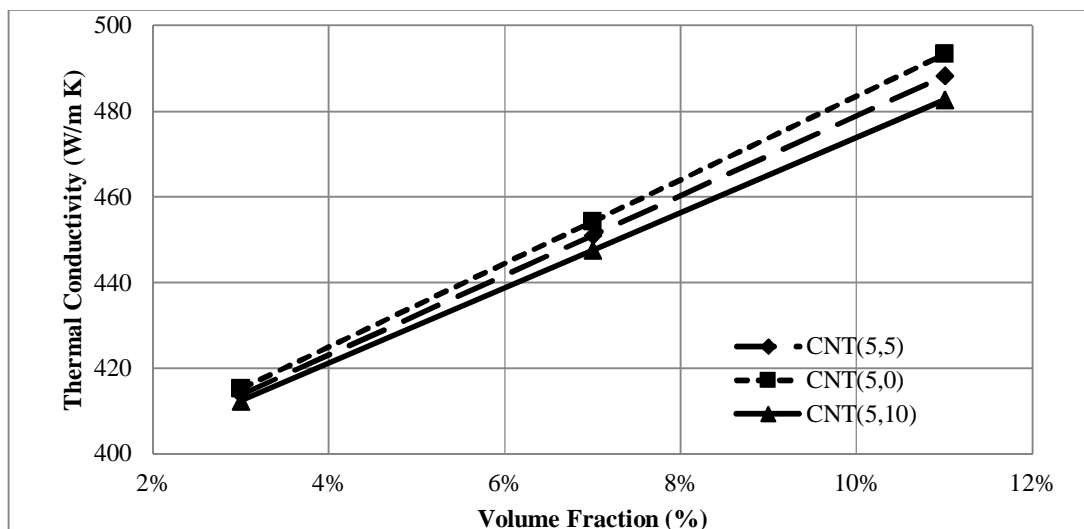


Figure 5.69: Effect of volume fraction on the thermal conductivity on different carbon nanotube chiral index reinforced copper metal matrix "Model (B)"

However, for carbon nanotubes reinforced aluminum matrix nanocomposite at the same length. The results presented in Table 5.19 show that at 3% volume fraction of carbon nanotube reinforced Aluminum matrix, the value of thermal conductivity for zigzag type is the highest, while for chiral type is the lowest. However, Figure 5.70, and 5.71 show that as the volume fraction increases within tested range, the thermal conductivity increases linearly for all indexes but with different values. The zigzag index shows the highest value of thermal conductivity while the chiral index shows the lowest.

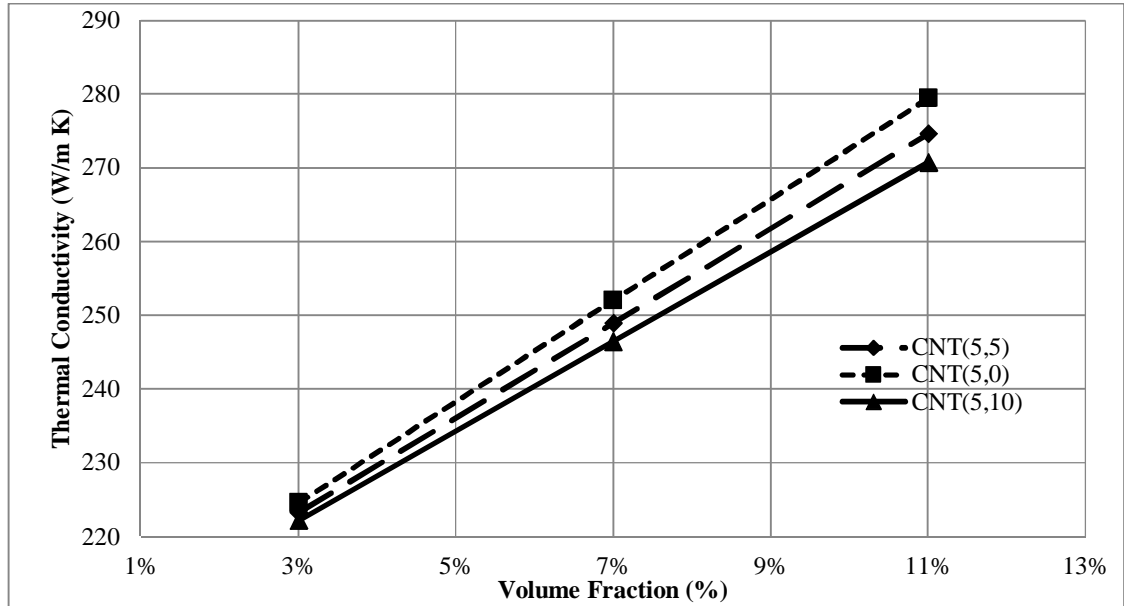


Figure 5.70: Effect of volume fraction on the thermal conductivity of different carbon nanotube chiral index reinforced aluminum metal matrix "Model (A)"

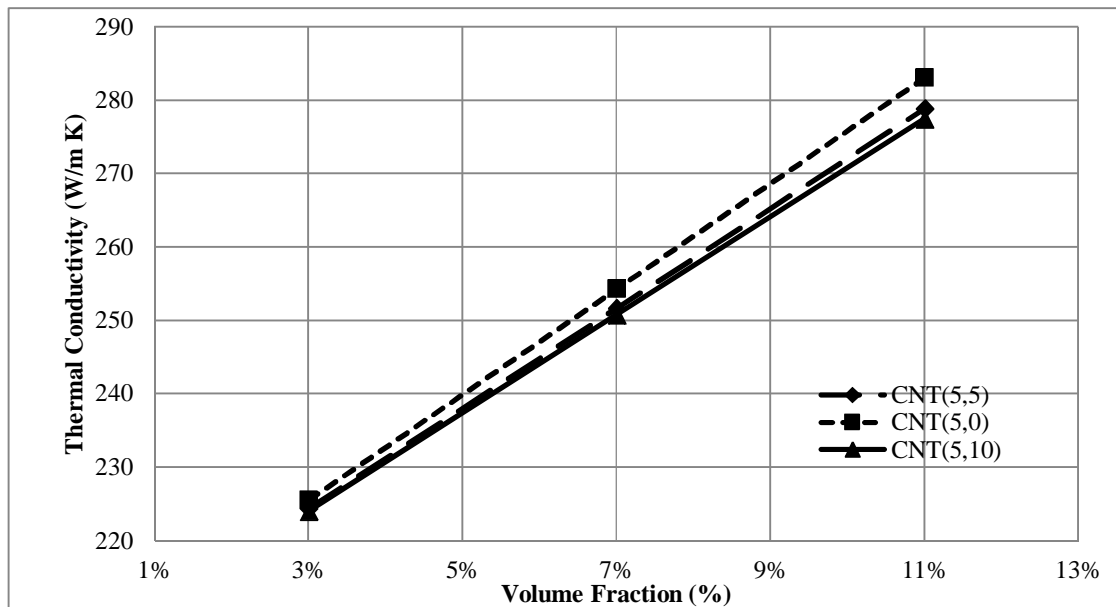


Figure 5.71: Effect of volume fraction on the thermal conductivity of different carbon nanotube chiral index reinforced aluminum metal matrix "Model (B)"

5.4.5 Short Fiber Case

5.4.5.1 Effect of Volume Fraction on the Effective Thermal Conductivity of the Nanocomposite

The analysis was conducted using ANSYS software for the carbon nanotube reinforced metal matrix Nanocomposite with a constant carbon nanotube diameters and length. The results have shown that the thermal conductivity of the Nanocomposite varies linearly with the change in volume fraction within tested range as predicted by Finite element models. Table 5.20 shows the results of thermal conductivity predicted for iron matrix reinforced by 3% volume fraction and different lengths for different categories of carbon nanotubes. It can be noticed that the enhancement in thermal conductivity for model “A” are varied from 1% to 4% for armchair (5,5), while varied from 2% to 5% and 1% to 2% for zigzag (5,0) and chiral (5,10) types, respectively, with the increase of fiber length.

Table 5.20: Effect of chiral index diameter of carbon nanotube on the thermal conductivity for reinforcing iron matrix “Model (A)” ($V_f=3\%$)

Carbon Nanotube index	d (nm)	K (W/mk)					
		lc=3 nm	% change	lc=5 nm	% change	lc=8 nm	% change
(5,5)	0.848	73.774	1%	74.485	2%	75.295	4%
(5,0)	0.5614	74.137	2%	74.929	3%	76.288	5%
(5,10)	1.206	73.639	1%	74.017	2%	74.482	2%

For model “B”, Table 5.21 shows the results of thermal conductivity predicted for iron matrix reinforced by 3% volume fraction and different lengths for different categories of carbon nanotubes. It can be noticed that the enhancement in thermal conductivity for model “B” are varied from 2% to 4% for Armchair (5, 5), while varied from 2% to 6% for and 2% to 3% for Zigzag (5, 0) and Chiral (5, 10), type, respectively, with the increase of fiber length.

Table 5.21: Effect of chiral index diameter of carbon nanotube on the thermal conductivity for reinforcing iron matrix “Model (B)” ($V_f=3\%$)

Carbon Nanotube index	d (nm)	K (W/mk)					
		lc=3 nm	% change	lc=5 nm	% change	lc=8 nm	% change
(5,5)	0.848	74.158	2%	74.656	3%	75.952	4%
(5,0)	0.5614	74.392	2%	75.184	3%	76.843	6%
(5,10)	1.206	73.978	2%	74.107	2%	75.193	3%

Figures 5.72, 5.73, and 5.74 show the effect of volume fraction on the thermal conductivity of model “A” for iron matrix reinforced by armchair, zigzag, and chiral carbon nanotube, respectively. It can be observed that the thermal conductivity of the nanocomposite varies linearly with the change in volume fractions within tested range.

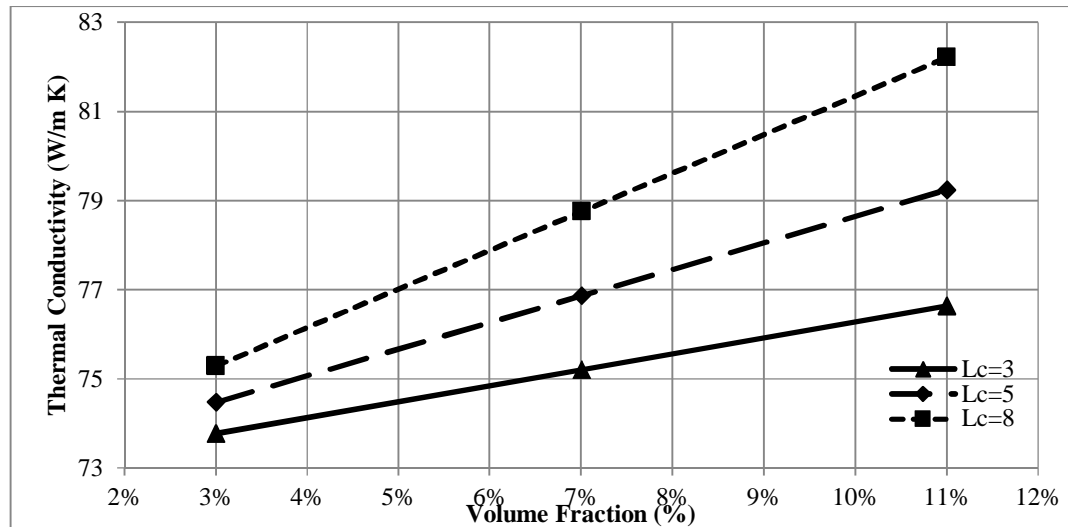


Figure 5.72: Effect of volume fraction on the thermal conductivity for armchair carbon nanotube reinforced iron metal matrix “Model (A)”

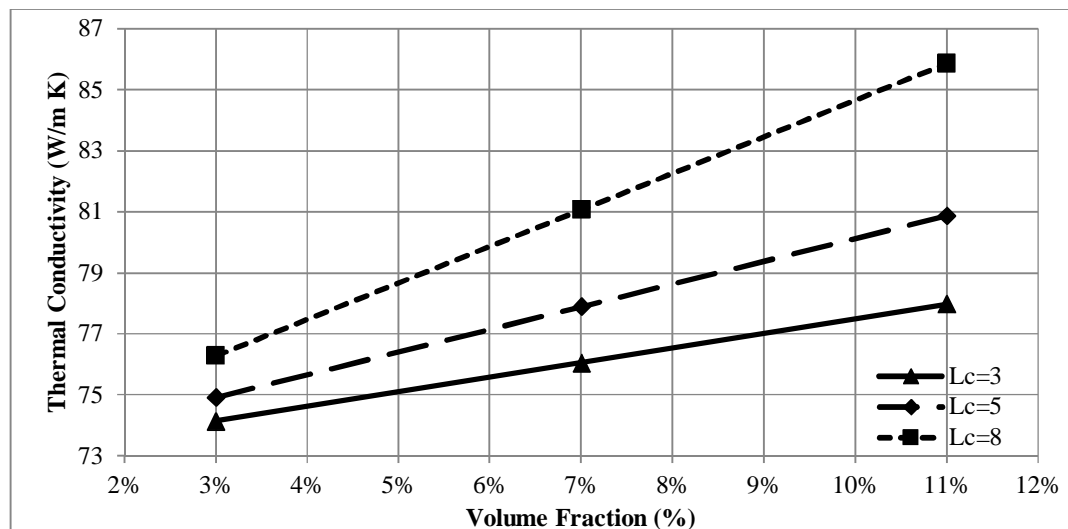


Figure 5.73: Effect of volume fraction on the thermal conductivity for zigzag carbon nanotube reinforced iron metal matrix “Model (A)”

Figures 5.75, 5.76, and 5.77 show the effect of volume fraction on the thermal conductivity of model “A” for Iron matrix reinforced by armchair, zigzag, and chiral carbon nanotube respectively. It can be observed that the thermal conductivity of the Nanocomposite varies linearly with the change in volume fraction.

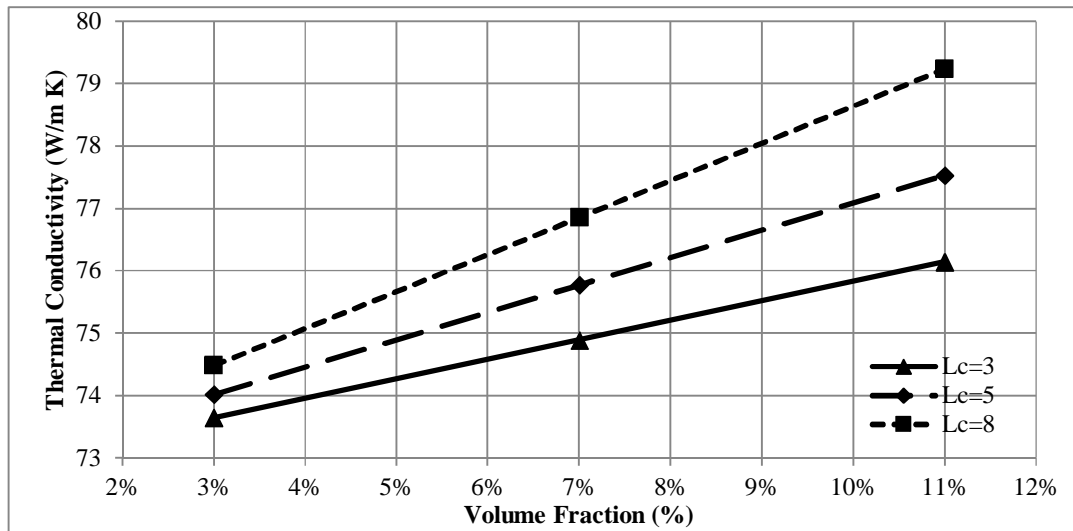


Figure 5.74: Effect of volume fraction on the thermal conductivity for chiral carbon nanotube reinforced iron metal matrix “Model (A)”

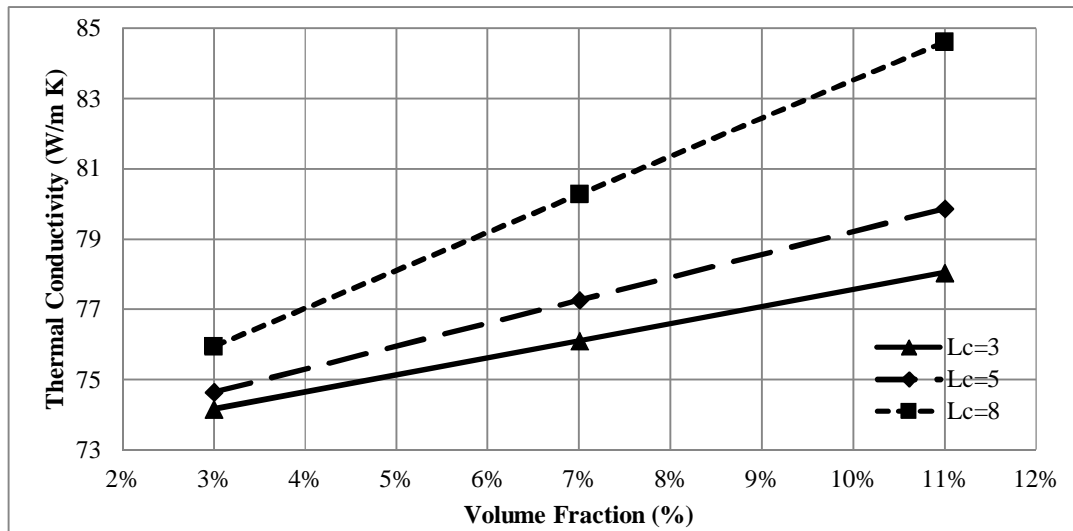


Figure 5.75: Effect of volume fraction on the thermal conductivity for chiral carbon nanotube reinforced iron metal matrix “Model (B)”

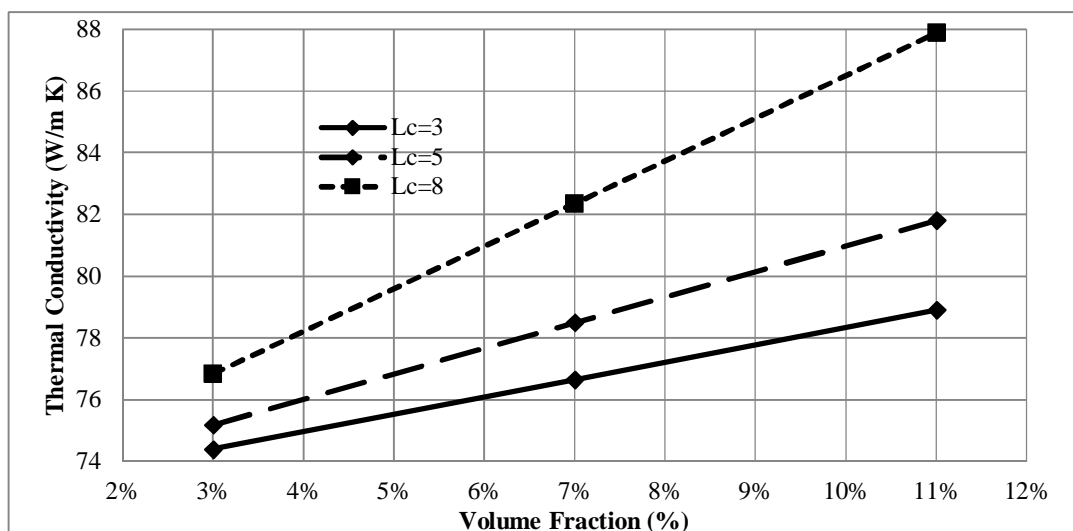


Figure 5.76: Effect of volume fraction on the thermal conductivity for armchair carbon nanotube reinforced iron metal matrix “Model (B)”

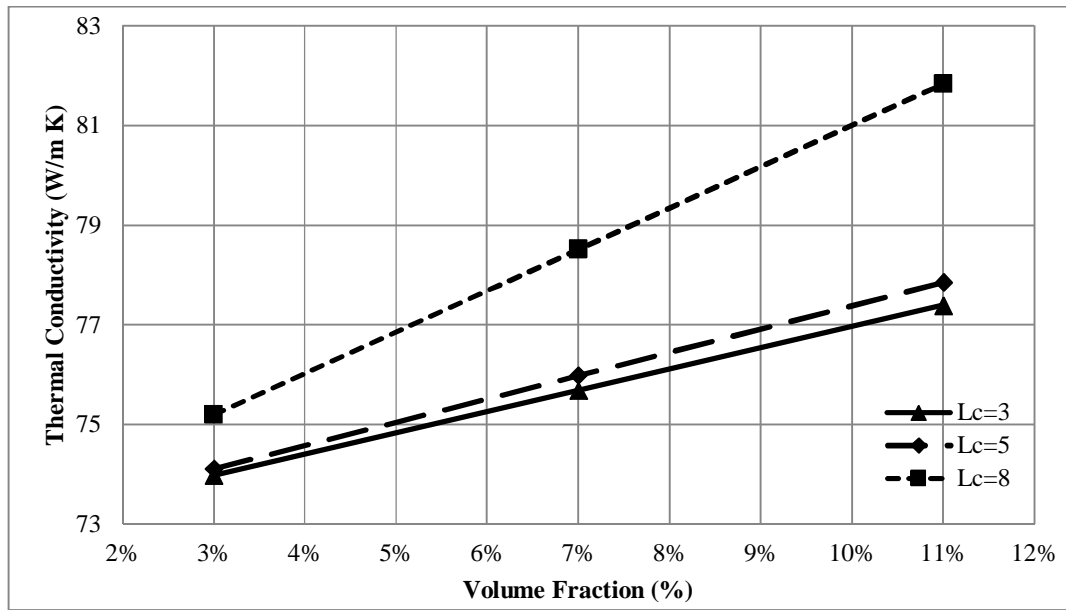


Figure 5.77: Effect of volume fraction on the thermal conductivity for zigzag carbon nanotube reinforced iron metal matrix “Model (B)”

The above mentioned results for model “A” and Model “B” show that the thermal conductivity has also increasing trend when the length of carbon nanotube increased for armchair, zigzag, and chiral Carbon nanotubes types reinforced Iron matrix Nanocomposite.

Similarly, for carbon nanotubes reinforced copper matrix Nanocomposite at different lengths Table 5.22 shows the results of thermal conductivity predicted for copper matrix reinforced by 3% volume fraction and different lengths for different categories of carbon nanotubes. It can be noticed that the enhancement in thermal conductivity for model “A” are varied from 3% to 5% for Armchair (5,5) while varied from 3% to 5% for and 2% to 3% for zigzag (5,0) and chiral (5,10), type, respectively, with the increase of fiber length.

Table 5.22: Effect of chiral index diameter of carbon nanotube on the thermal conductivity for reinforcing copper matrix “Model (A)” ($V_f=3\%$)

Carbon Nanotube index	d (nm)	K (W/mk)					
		lc=3 nm	% change	lc=5 nm	% change	lc=8 nm	% change
(5,5)	0.848	396.431	3%	399.794	4%	405.494	5%
(5,0)	0.5614	399.437	3%	400.229	4%	406.478	5%
(5,10)	1.206	395.639	2%	396.317	3%	398.882	3%

Figures 5.78, 5.79, and 5.80 show the effect of volume fraction on the thermal conductivity of model “A” for copper matrix reinforced by armchair, zigzag, and chiral carbon nanotube, respectively. It can be observed that the thermal conductivity of the Nanocomposite varies linearly with the change in volume fractions.

For model “B”, Table 5.23 shows the results of thermal conductivity predicted for Copper matrix reinforced by 3% volume fraction and different length for different categories of carbon nanotubes. It can be noticed that the enhancement in thermal conductivity for model “B” are varied from 3% to 6% for Armchair (5, 5) while varied from 4% to 6% for and 3% to 4% for zigzag (5, 0) and chiral (5, 10), type, respectively, with the increase of fiber length.

Table 5.23: Effect of chiral index diameter of carbon nanotube on the thermal conductivity for reinforcing copper matrix “Model (B)” ($V_f=3\%$)

Carbon Nanotube index	d (nm)	K (W/mk)					
		lc=3 nm	% change	lc=5 nm	% change	lc=8 nm	% change
(5,5)	0.848	398.192	3%	402.494	4%	408.032	6%
(5,0)	0.5614	400.892	4%	403.484	5%	409.643	6%
(5,10)	1.206	396.278	3%	397.607	3%	400.493	4%

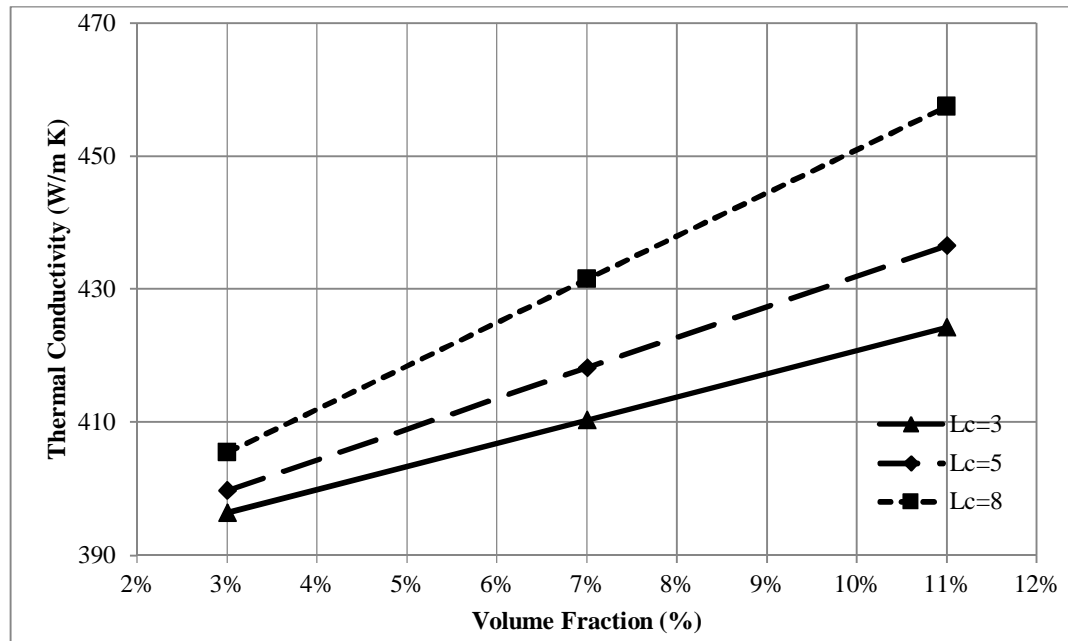


Figure 5.78: Effect of volume fraction on the thermal conductivity for armchair carbon nanotube reinforced copper metal matrix “Model (A)”

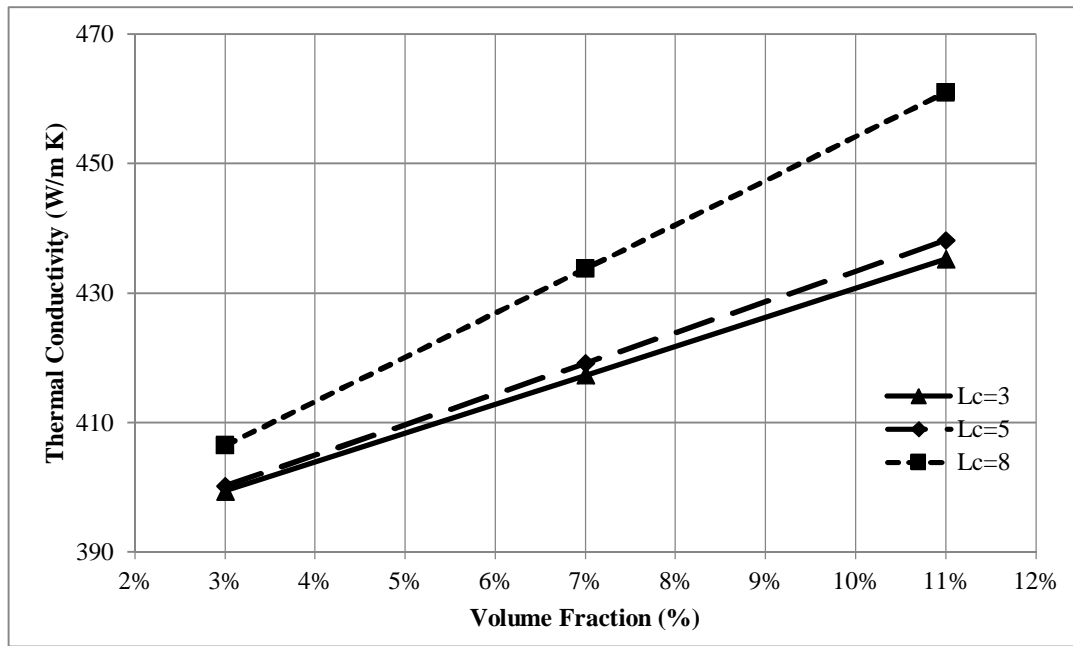


Figure 5.79: Effect of volume fraction on the thermal conductivity for zigzag carbon nanotube reinforced copper metal matrix “Model (A)”

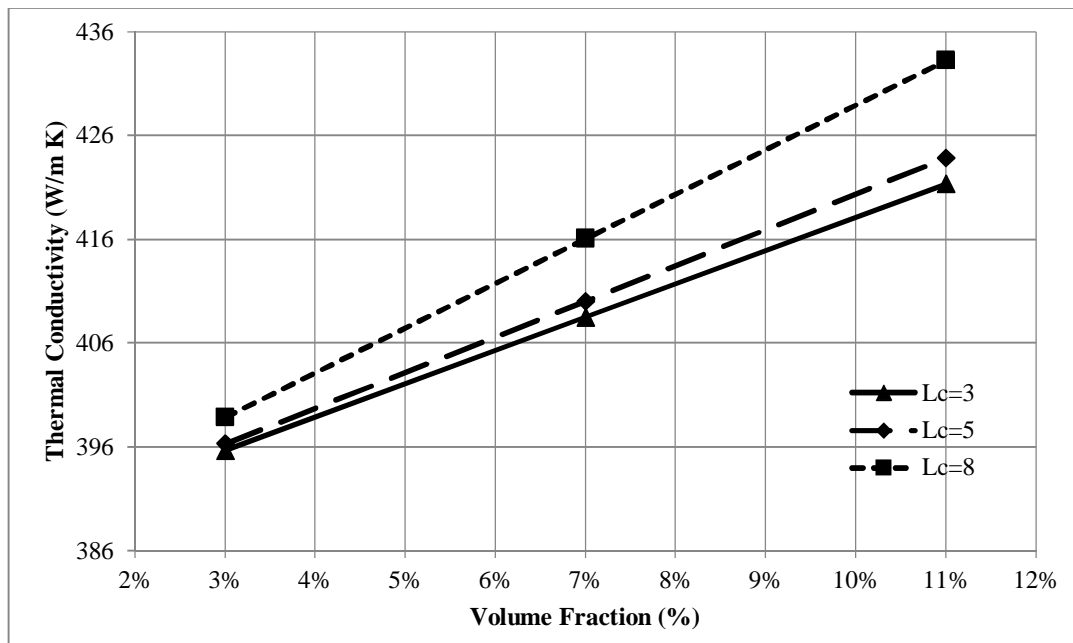


Figure 5.80: Effect of volume fraction on the thermal conductivity for chiral carbon nanotube reinforced copper metal matrix “Model (A)”

Figures 5.81, 5.82, and 5.83 show the effect of volume fraction on the thermal conductivity of model “B” for Copper matrix reinforced by armchair, zigzag, and chiral carbon nanotube respectively. It can be observed that the thermal conductivity of the Nanocomposite varies linearly with the change in volume fractions.

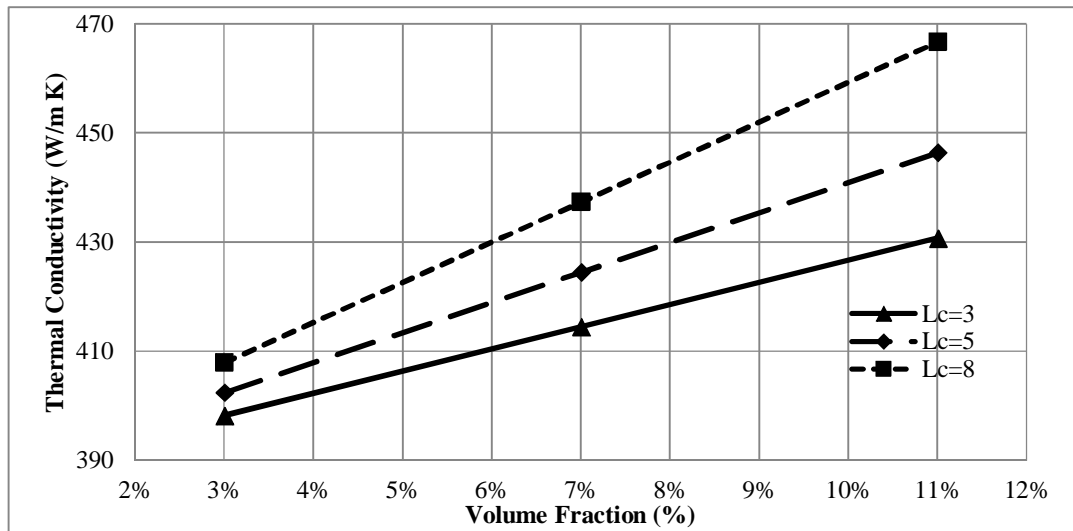


Figure 5.81: Effect of volume fraction on the thermal conductivity for armchair carbon nanotube reinforced copper metal matrix “Model (B)”

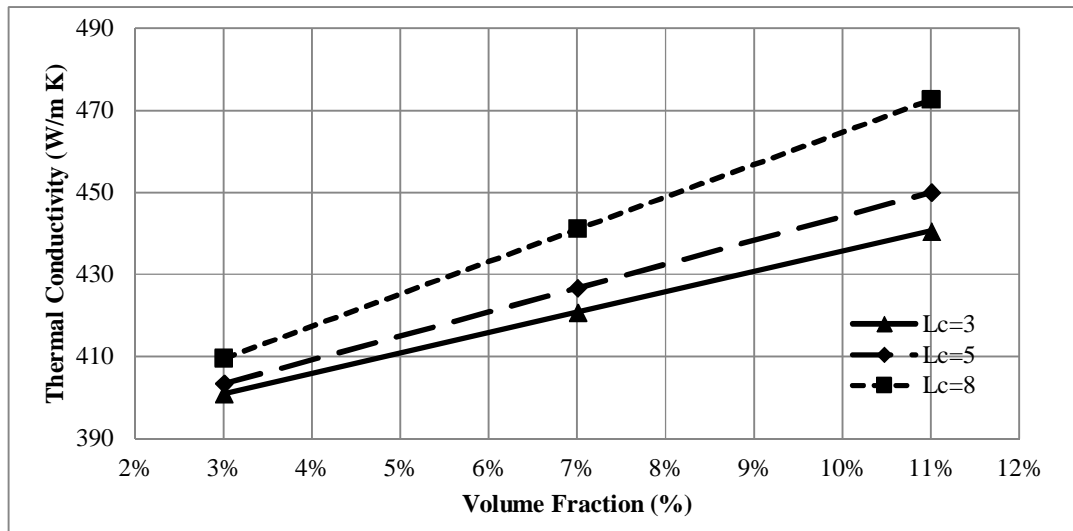


Figure 5.82: Effect of volume fraction on the thermal conductivity for zigzag carbon nanotube reinforced copper metal matrix “Model (B)”

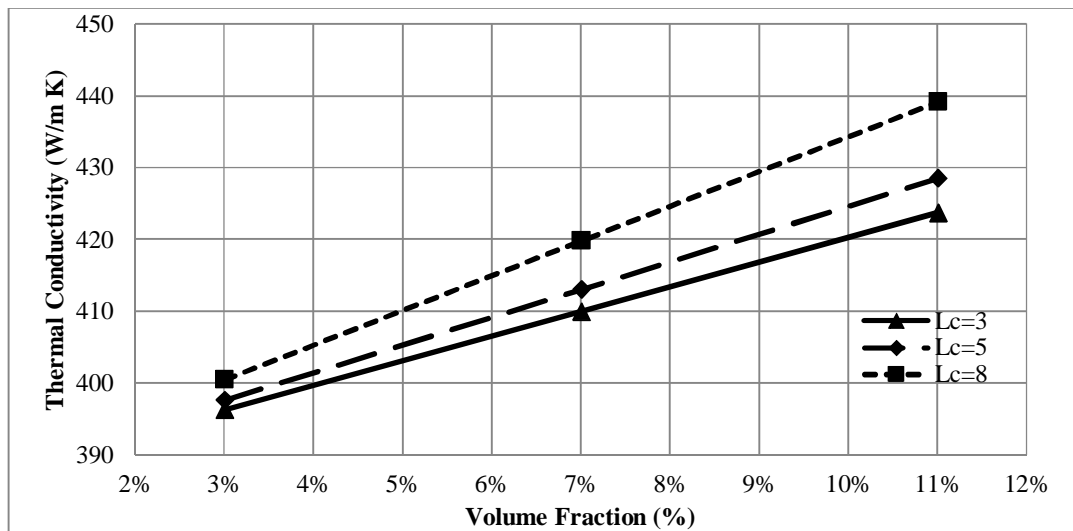


Figure 5.83: Effect of volume fraction on the thermal conductivity for chiral carbon nanotube reinforced copper metal matrix “Model (B)”

The above mentioned results for model “A” and Model “B” show that the thermal conductivity has also increasing trend when the length of carbon nanotube increased for armchair, zigzag, and chiral carbon nanotubes types reinforced copper matrix nanocomposite.

For carbon nanotubes reinforced aluminum matrix nanocomposite at different lengths Table 5.24 shows the results of thermal conductivity predicted for aluminum matrix reinforced by 3% volume fraction and different length for different categories of carbon nanotubes. It can be noticed that the enhancement in thermal conductivity for model “A” are varied from 5% to 7% for armchair (5,5) while varied from 6% to 8% for zigzag (5,0), and 3% to 6% for Chiral (5,10), type, respectively, with the increase of fiber length.

Table 5.24: Effect of chiral index diameter of carbon nanotube on the thermal conductivity for reinforcing Aluminum matrix “Model (A)” ($V_f=3\%$)

Carbon Nanotube index	d (nm)	K (W/mk)					
		lc=3 nm	% change	lc=5 nm	% change	lc=8 nm	% change
(5,5)	0.848	214.0743	5%	216.285	6%	218.895	7%
(5,0)	0.5614	215.937	6%	217.359	7%	219.588	8%
(5,10)	1.206	210.939	3%	214.317	5%	215.772	6%

For Model “B”, Table 5.25 shows the results of thermal conductivity predicted for aluminum matrix reinforced by 3% volume fraction and different length for different categories of carbon nanotubes. It can be noticed that the enhancement in thermal conductivity for model “B” are varied from 6% to 8% for armchair (5, 5) while varied from 7% to 9% for and 5% to 7% for zigzag (5, 0) and chiral (5, 10), type respectively with the increase of fiber length.

Table 5.25: Effect of chiral index diameter of carbon nanotube on the thermal conductivity for reinforcing aluminum matrix “Model (B)” ($V_f=3\%$)

Carbon Nanotube index	d (nm)	K (W/mk)					
		lc=3 nm	% change	lc=5 nm	% change	lc=8 nm	% change
(5,5)	0.848	216.558	6%	217.956	7%	221.052	8%
(5,0)	0.5614	219.192	7%	220.284	8%	221.943	9%
(5,10)	1.206	214.278	5%	215.607	6%	217.593	7%

Figures 5.84, 5.85, and 5.86 show the effect of volume fraction on the thermal conductivity of model “A” for aluminum matrix reinforced by armchair, zigzag, and chiral carbon nanotube, respectively. It can be observed that the thermal conductivity of the Nanocomposite varies linearly with the change in volume fractions.

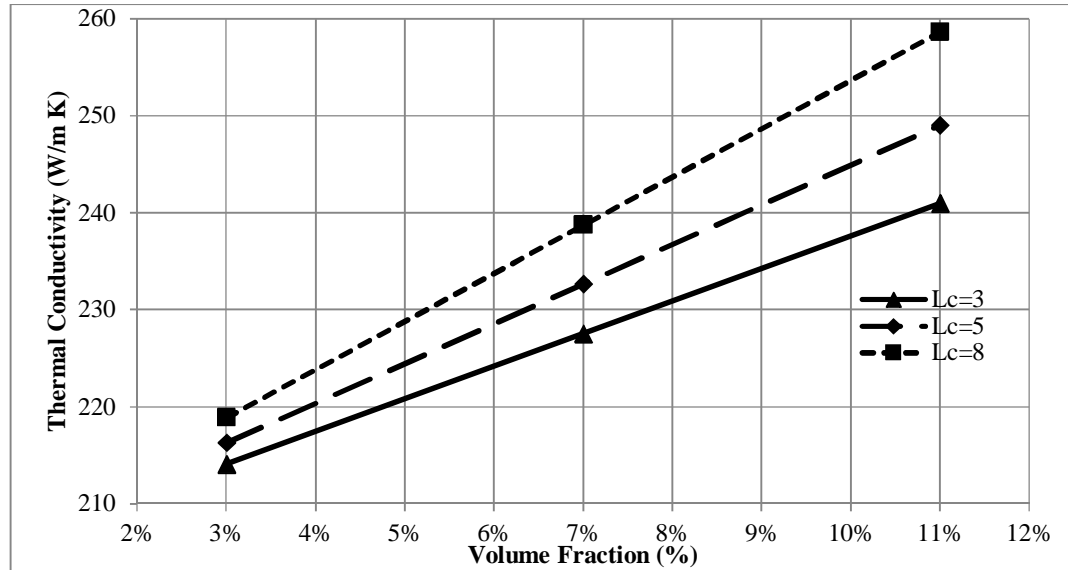


Figure 5.84: Effect of volume fraction on the thermal conductivity for armchair carbon nanotube reinforced aluminum metal matrix “Model (A)”

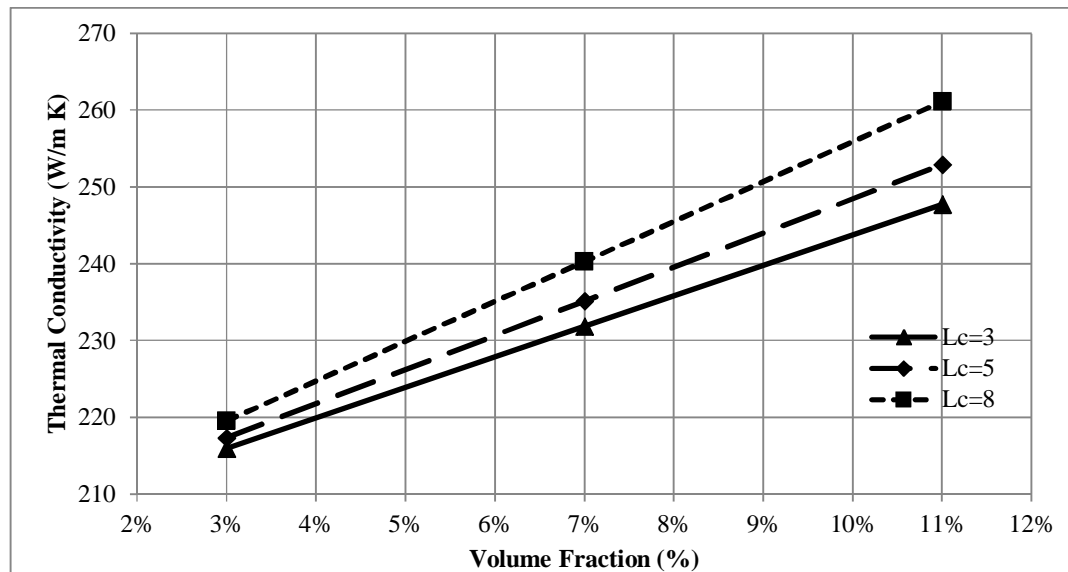


Figure 5.85: Effect of volume fraction on the thermal conductivity for zigzag carbon nanotube reinforced aluminum metal matrix “Model (A)”

Figures 5.87, 5.88, and 5.89 show the effect of volume fraction on the thermal conductivity of model “A” for aluminum matrix reinforced by armchair, zigzag, and chiral carbon nanotube, respectively. It can be observed that the thermal conductivity of the Nanocomposite varies linearly with the change in volume fractions.

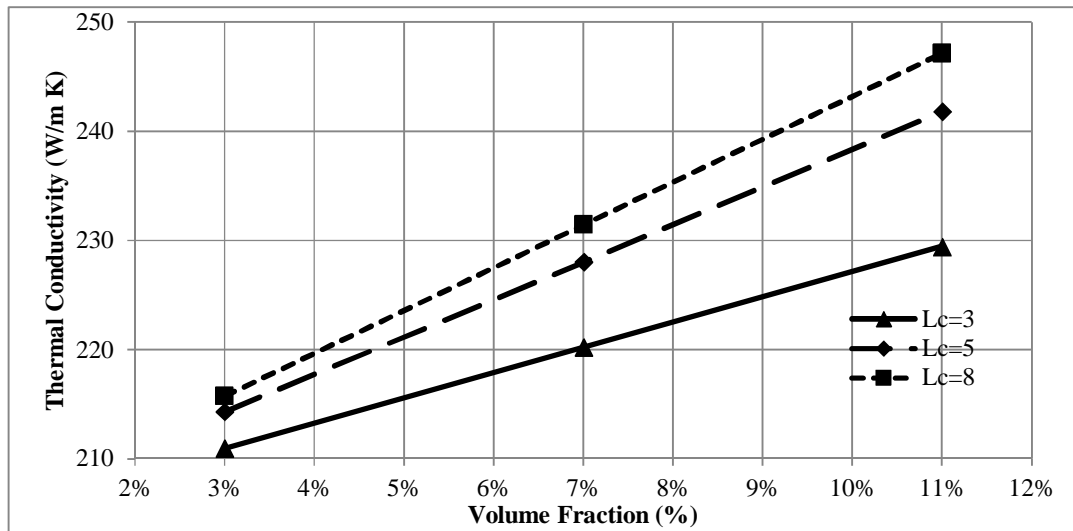


Figure 5.86: Effect of volume fraction on the thermal conductivity for chiral carbon nanotube reinforced aluminum metal matrix “Model (A)”

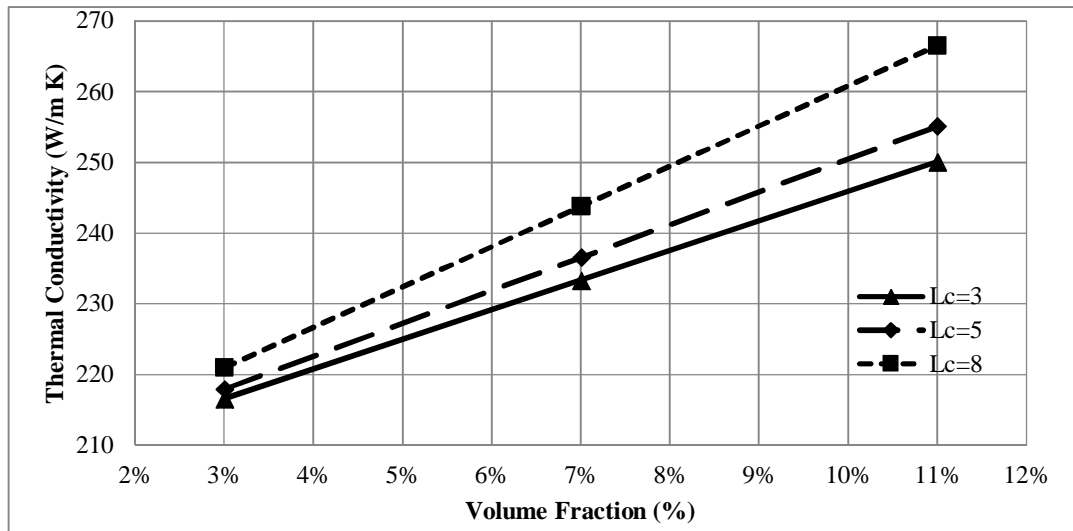


Figure 5.87: Effect of volume fraction on the thermal conductivity for chiral carbon nanotube reinforced aluminum metal matrix “Model (B)”

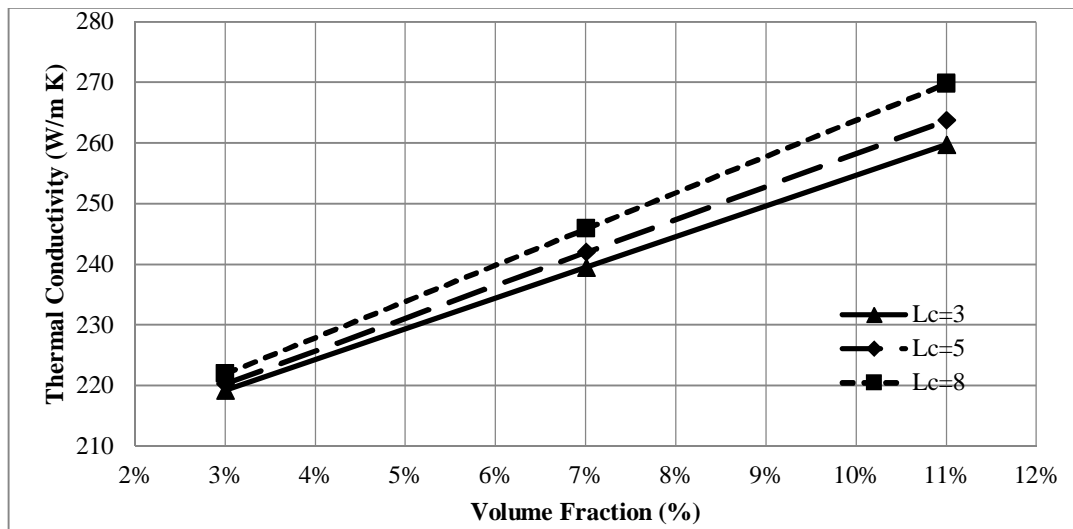


Figure 5.88: Effect of volume fraction on the thermal conductivity for armchair carbon nanotube reinforced aluminum metal matrix “Model (B)”

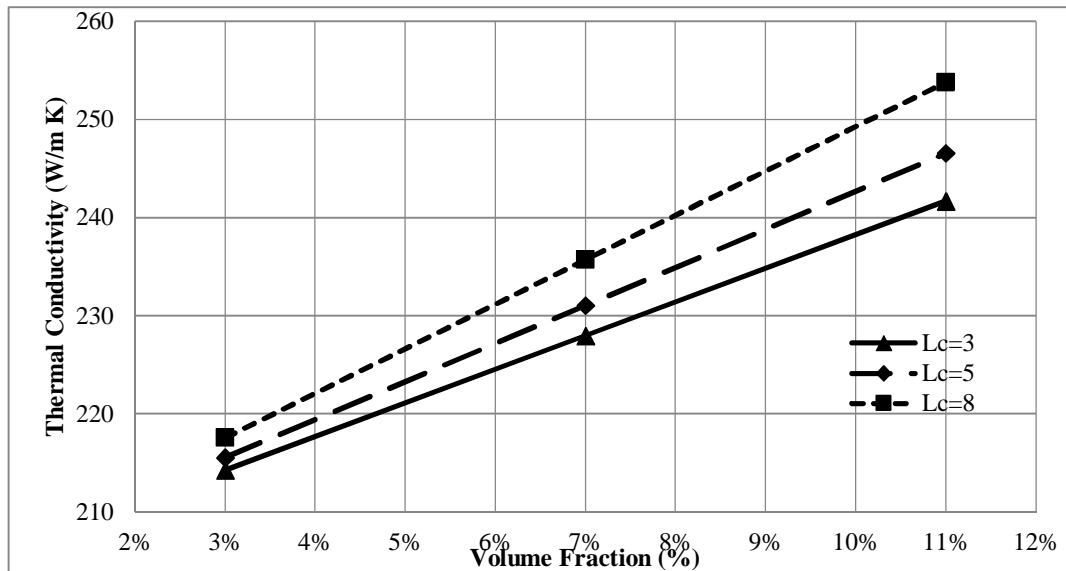


Figure 5.89: Effect of volume fraction on the thermal conductivity for zigzag carbon nanotube reinforced aluminum metal matrix “Model (B)”

The above mentioned results for model “A” and Model “B” show that the thermal conductivity has also increasing trend when the length of carbon nanotube increased for armchair, zigzag, and chiral Carbon nanotubes types reinforced aluminum matrix nanocomposite.

5.4.5.2 Effect of chiral index on the effective thermal conductivity of the Nanocomposite

The analysis was conducted using ANSYS software macro for models A and B for the carbon nanotube reinforced metal matrix nanocomposite with a different chiral indices and lengths within tested range. The results show that as the volume fraction increases the thermal conductivity increases linearly for all indices but with different slopes. The zigzag index shows the highest value of thermal conductivity, while the chiral index shows the lowest. However, the thermal conductivity decreases by increasing the diameter which clearly appeared from the mentioned figures since the zigzag carbon nanotubes have the lowest diameter while the chiral carbon nanotubes have the biggest diameter. Figure 5.90 and 5.91 show the effect of carbon nanotube diameter achieved by changing the chiral index on the thermal conductivity of model “A” and model “B” for iron matrix reinforced by carbon nanotube, respectively. It can be observed that the thermal conductivity of the nanocomposite has decreasing trend with the change in carbon nanotube diameter. Tables 5.26 (a) and (b) present the results of thermal conductivity for model “A” and model “B” respectively by changing the chiral index of carbon nanotube.

Table 5.26: Effect of chiral index diameter of carbon nanotube on the thermal conductivity for reinforcing iron matrix: (a) Model (A), and (b) Model (B)

(a) Model (A)

Chiral Index	Diameter (nm)	Volume Fraction (%)		
		3%	7%	11%
Armchair (5,5)	0.848	73.774	75.207	76.639
Zigzag 5,0)	0.5614	74.137	76.053	77.969
Chiral (5,10)	1.206	73.639	74.891	76.143

(b) Model (B)

Chiral Index	Diameter (nm)	Volume Fraction (%)		
		3%	7%	11%
Armchair (5,5)	0.848	74.158	76.102	78.046
Zigzag 5,0)	0.5614	74.392	76.648	78.904
Chiral (5,10)	1.206	73.978	75.682	77.386

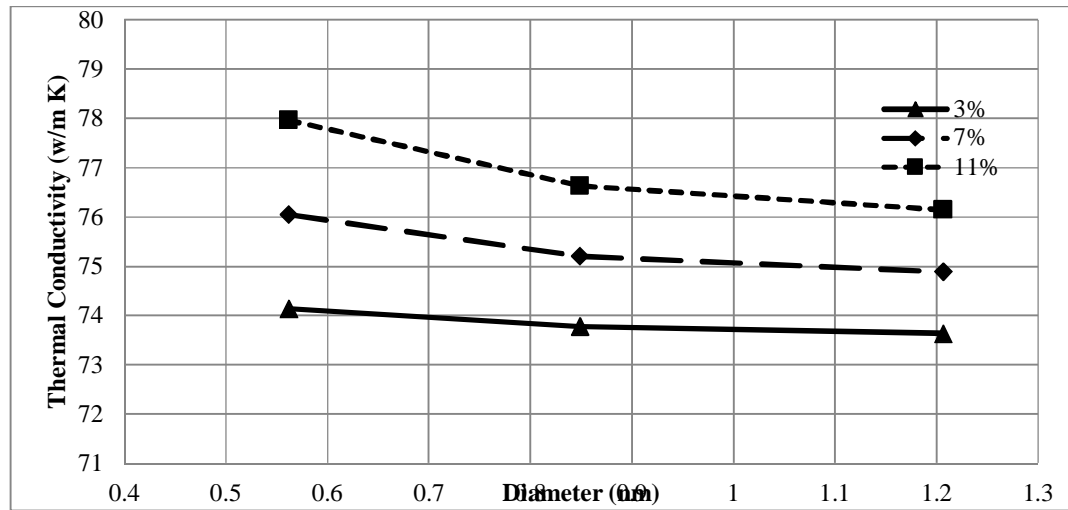


Figure 5.90: Effect of carbon nanotube diameter on the thermal conductivity for reinforcing iron metal matrix "Model (A)"

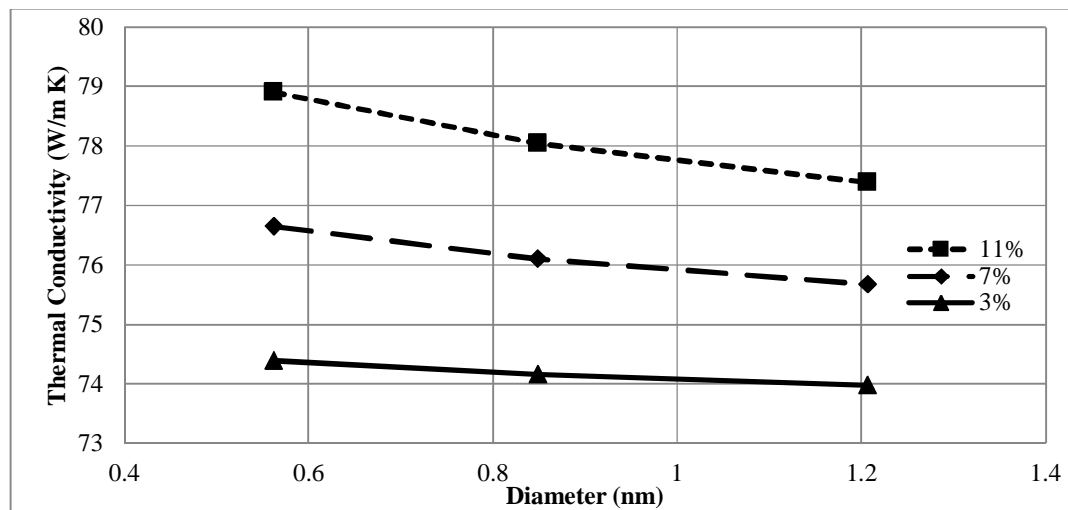


Figure 5.91: Effect of carbon nanotube diameter on the thermal conductivity for reinforcing iron metal matrix "Model (B)"

Similarly, for carbon nanotube reinforced copper matrix. Figures 5.92 and 5.93 show the effect of carbon nanotube diameter achieved by changing the chiral index on the thermal conductivity of model “A” and model “B” for copper matrix reinforced by carbon nanotube respectively. It can be observed that the thermal conductivity of the nanocomposite has a decreasing trend with the change in carbon nanotube diameter. Tables 5.27(a) and (b) represent the predicted results of thermal conductivity for model “A” and model “B”, respectively, by changing the chiral index of carbon nanotube.

Table 5.27: Effect of chiral index diameter of carbon nanotube on the thermal conductivity for reinforcing copper matrix (a) Model (A), and (b) Model (B)

(a) Model (A)

Chiral Index	Diameter (nm)	Volume Fraction (%)		
		3%	7%	11%
Armchair (5,5)	0.848	396.431	410.339	424.247
Zigzag 5,0)	0.5614	399.437	417.353	435.269
Chiral (5,10)	1.206	395.639	408.491	421.343

(b) Model (B)

Chiral Index	Diameter (nm)	Volume Fraction (%)		
		3%	7%	11%
Armchair (5,5)	0.848	398.192	414.448	430.704
Zigzag 5,0)	0.5614	400.892	420.748	440.604
Chiral (5,10)	1.206	396.278	409.982	423.686

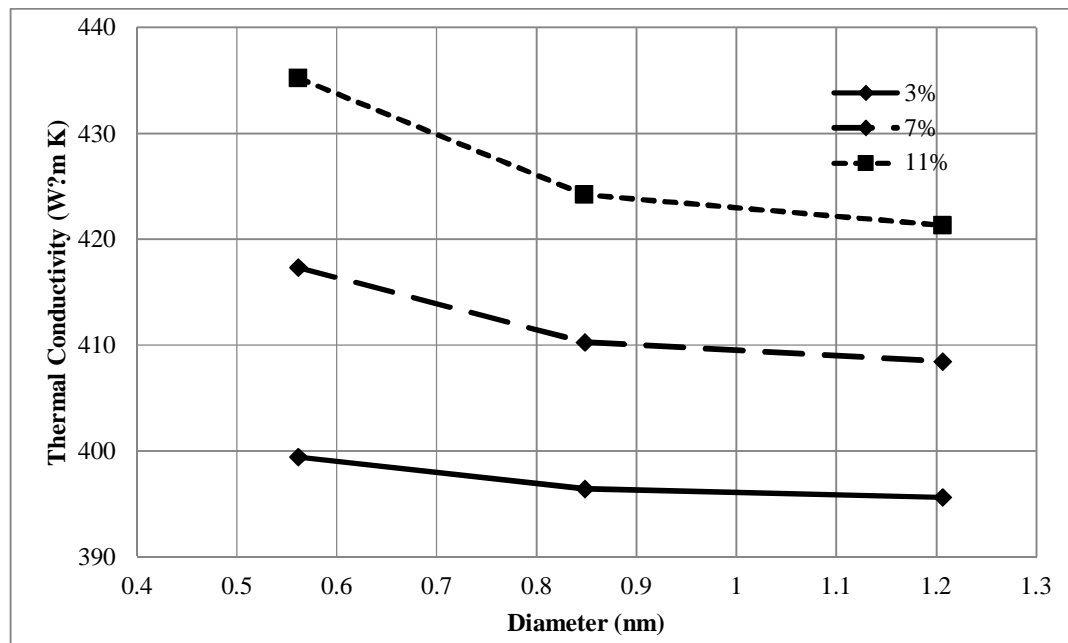


Figure 5.92: Effect of carbon nanotube diameter on the thermal conductivity for reinforcing copper metal matrix "Model (A)"

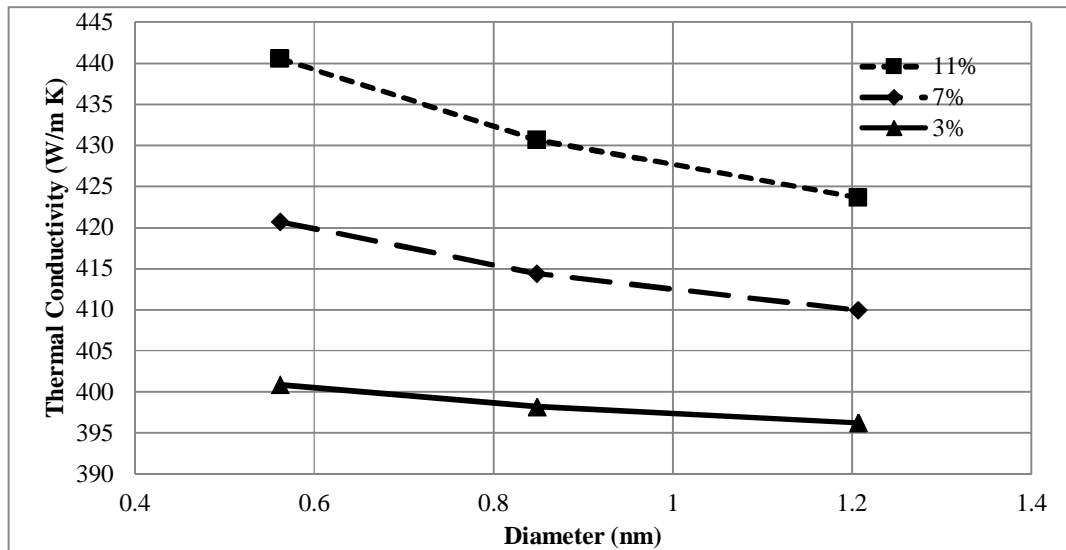


Figure 5.93: Effect of carbon nanotube diameter on the thermal conductivity for reinforcing copper metal matrix "Model (B)"

However, for carbon nanotube reinforced aluminum matrix. Figures 5.94 and 5.95 show the effect of carbon nanotube diameter achieved by changing the chiral index on the thermal conductivity of model "A" and model "B" for aluminum matrix reinforced by carbon nanotube respectively. It can be observed that the thermal conductivity of the new nanocomposite has a decreasing trend with the change in carbon nanotube diameter. Tables 5.28 (a) and (B) represent the predicted results of thermal conductivity for model "A" and model "B", respectively, by changing the chiral index of carbon nanotube

Table 5.28: Effect of chiral index diameter of carbon nanotube on the thermal conductivity for reinforcing Aluminum matrix: (a) Model (A), and (b) Model (B)

(a) Model (A)

Chiral Index	Diameter (nm)	Volume Fraction (%)		
		3%	7%	11%
Armchair (5,5)	0.848	214.074	227.507	240.939
Zigzag 5,0)	0.5614	215.937	231.853	247.769
Chiral (5,10)	1.206	210.939	220.191	229.443

(b) Model (B)"

Chiral Index	Diameter (nm)	Volume Fraction (%)		
		3%	7%	11%
Armchair (5,5)	0.848	216.558	233.302	250.046
Zigzag 5,0)	0.5614	219.192	239.448	259.704
Chiral (5,10)	1.206	214.278	227.982	241.686

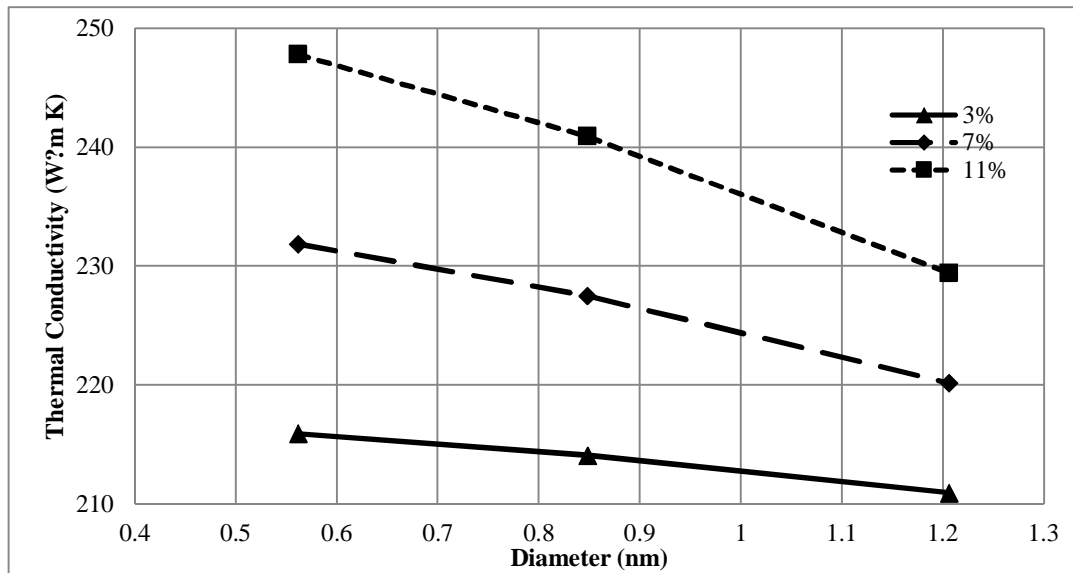


Figure 5.94: Effect of carbon nanotube diameter on the thermal conductivity for reinforcing aluminum metal matrix "Model (A)"

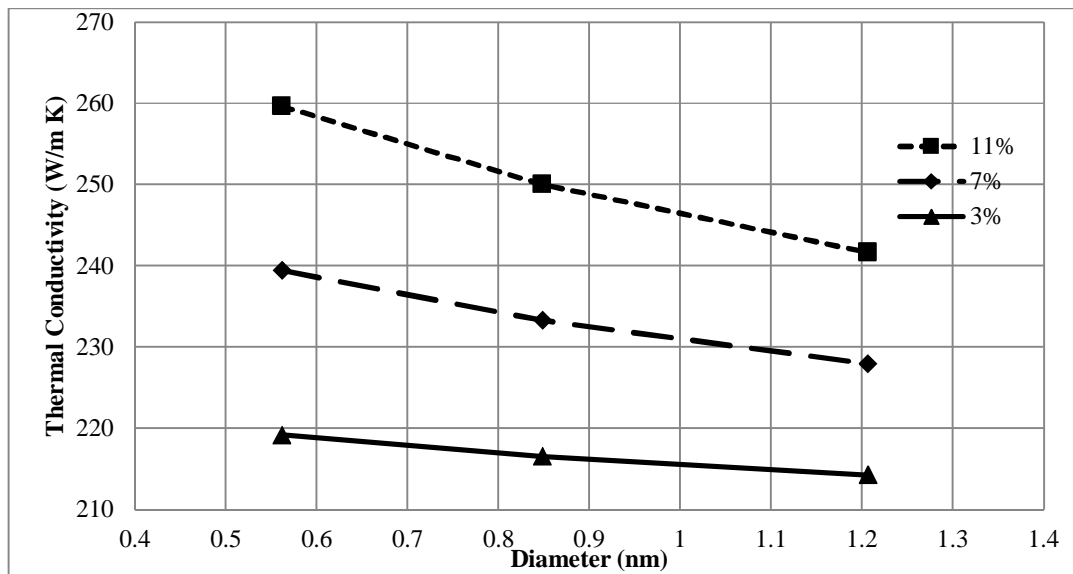


Figure 5.95: Effect of carbon nanotube diameter on the thermal conductivity for reinforcing aluminum metal matrix "Model (B)"

5.4.6 Effect of Thermal Contact Conductance on the Effective Thermal Conductivity of the Nanocomposite

The analysis has been carried out using ANSYS software for the carbon nanotube reinforced metal matrix Nanocomposite with a constant carbon nanotube diameters and length. The results have shown that the thermal conductivity of the Nanocomposite varies linearly with the changes in volume fractions as predicted by finite element models. The variation of the effective thermal conductivity with change in the value of the thermal contact conductance at 3% volume fraction is presented in

Tables 5.29 (a) and (b) for armchair (5,5) carbon nanotubes reinforced iron metal matrices at different lengths for Model “A” and Model “B”. It can be seen that the effective thermal conductivity is slightly increased with respect to the matrix thermal conductivity. For model “A”, at $l_c = 3$ nm and $\beta = 12$ MW/m²K, the thermal conductivity of the new composite was 72.0087 W/m K which is about 0.95% decrement of the matrix thermal conductivity while at $\beta = 10000$ MW/m²K, the thermal conductivity of the composite was 72.2147 W/m K which is about 0.67% decrement of the matrix thermal conductivity. Similarly for model “B”, $l_c = 3$ nm and $\beta = 12$ MW/m²K, the thermal conductivity of the new composite was 72.9597 W/m K which is about 0.36% increment of the matrix thermal conductivity while at $\beta = 10000$ MW/m²K, the thermal conductivity of the new composite was 73.2647 W/m K which is about 0.78% increment of the matrix thermal conductivity.

Table 5.29: Effect of thermal contact conductance on thermal conductivity for armchair carbon nanotube reinforced iron matrix at different length: (a) Model (A), and (b) Model (B)

(a) Model (A)

β (MW/m ² k)	K (W/m K)					
	$l_c = 3$ nm	% change	$l_c = 5$ nm	% change	$l_c = 8$ nm	% change
12	72.0087	-0.95%	72.237	-0.64%	72.523	-0.24%
30	72.0097	-0.95%	72.238	-0.64%	72.524	-0.24%
50	72.0107	-0.95%	72.239	-0.63%	72.525	-0.24%
100	72.0117	-0.95%	72.240	-0.63%	72.526	-0.24%
500	72.0127	-0.95%	72.241	-0.63%	72.527	-0.24%
1000	72.0137	-0.94%	72.242	-0.63%	72.528	-0.24%
2500	72.0147	-0.94%	72.243	-0.63%	72.529	-0.24%
5000	72.1147	-0.81%	72.343	-0.49%	72.629	-0.10%
10000	72.2147	-0.67%	72.443	-0.35%	72.729	0.04%

(b) Model (B)

β (MW/m ² k)	K (W/m K)					
	$l_c = 3$ nm	% change	$l_c = 5$ nm	% change	$l_c = 8$ nm	% change
12	72.9597	0.36%	73.324	0.86%	73.6252	1.27%
30	72.9607	0.36%	73.326	0.86%	73.6262	1.27%
50	72.9617	0.36%	73.327	0.86%	73.6272	1.28%
100	72.9627	0.36%	73.328	0.86%	73.6282	1.28%
500	72.9637	0.36%	73.329	0.86%	73.6292	1.28%
1000	72.9647	0.36%	73.330	0.87%	73.6302	1.28%
2500	73.0647	0.50%	73.331	0.87%	73.6312	1.28%
5000	73.1647	0.64%	73.431	1.00%	73.731	1.42%
10000	73.2647	0.78%	73.531	1.14%	73.831	1.56%

Figures 5.96 and Figure 5.97 show the effect of thermal contact conductance on the thermal conductivity for model “A” and Model “B”, respectively. It can be observed that as the length of carbon nanotubes increased the thermal conductivity also increased.

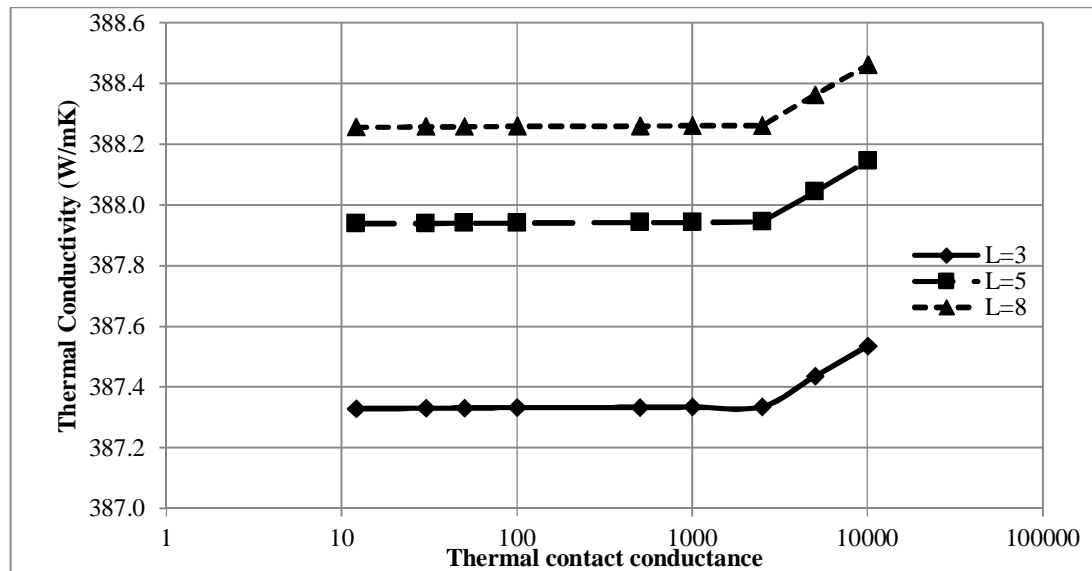


Figure 5.96: Effect of thermal contact conductance on thermal conductivity for armchair carbon nanotube (5, 5) reinforced iron metal matrix (Model “A”)

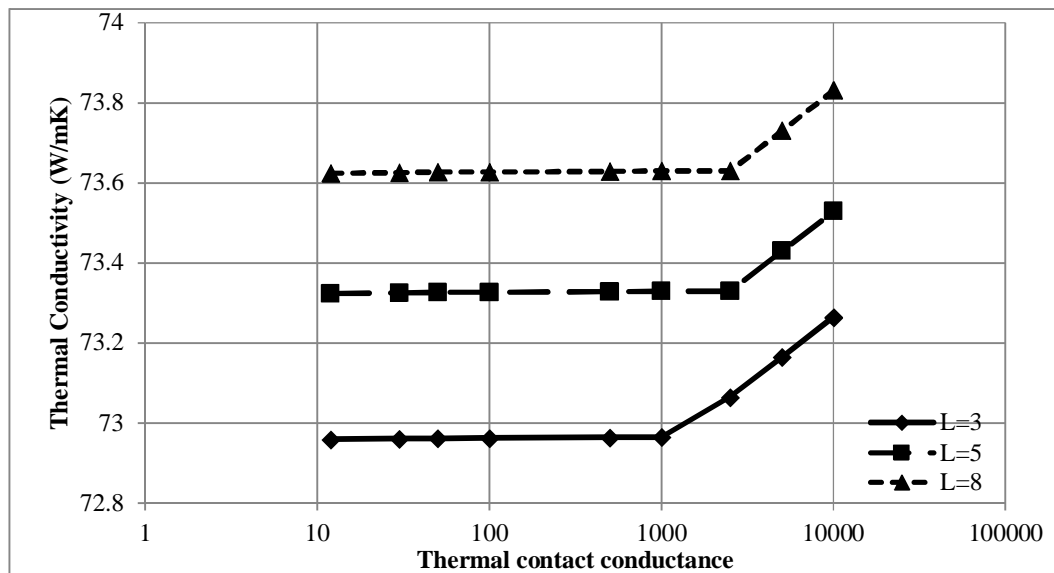


Figure 5.97: Effect of thermal contact conductance on thermal conductivity for armchair carbon nanotube (5, 5) reinforced iron metal matrix (Model “B”)

For zigzag (5, 0) carbon nanotubes reinforced iron metal matrixes at different lengths, Tables 5.30 (a) and (b) show the variation of the effective thermal conductivity with change of the thermal contact conductance for model “A” and model “B”. It can be seen that the effective thermal conductivity is slightly increased with respect to the matrix thermal conductivity. For model “A”, at $l_c = 3$ nm and $\beta = 12$ MW/m²K, the thermal

conductivity of the composite was 72.203 W/m K which is about 0.68% decrement of the matrix thermal conductivity while at $\beta= 10000$ MW/m²K, the thermal conductivity of the new composite was 72.409 W/m K which is about 0.40% decrement of the matrix thermal conductivity. Similarly for model “B”, $l_c= 3$ nm and $\beta= 12$ MW/m²K, the thermal conductivity of the composite was 73.329 W/m K which is about 0.87% increment of the matrix thermal conductivity while at $\beta= 10000$ MW/m²K, the thermal conductivity of the new composite was 73.535 W/m K which is about 1.15% increment of the matrix thermal conductivity.

Table 5.30: Effect of thermal contact conductance on thermal conductivity for zigzag carbon nanotube reinforced iron matrix at different length: (a) Model (A), and (b) Model (B)

(a) Model (A)

β (MW/m ² k)	K (W/m K)					
	$l_c=3$ nm	% change	$l_c =5$ nm	% change	$l_c =8$ nm	% change
12	72.203	-0.68%	72.46	-0.33%	72.97	0.37%
30	72.204	-0.68%	72.46	-0.33%	72.97	0.37%
50	72.205	-0.68%	72.46	-0.33%	72.97	0.37%
100	72.206	-0.68%	72.46	-0.32%	72.97	0.37%
500	72.207	-0.68%	72.47	-0.32%	72.97	0.37%
1000	72.208	-0.68%	72.47	-0.32%	72.97	0.38%
2500	72.209	-0.68%	72.47	-0.32%	72.97	0.38%
5000	72.309	-0.54%	72.57	-0.18%	73.07	0.52%
10000	72.409	-0.40%	72.67	-0.04%	73.17	0.65%

(b) Model (B)

β (MW/m ² k)	K (W/m K)					
	$l_c=3$ nm	% change	$l_c =5$ nm	% change	$l_c =8$ nm	% change
12	73.329	0.87%	73.774	1.48%	73.889	1.64%
30	73.330	0.87%	73.774	1.48%	73.890	1.64%
50	73.331	0.87%	73.774	1.48%	73.891	1.64%
100	73.332	0.87%	73.774	1.48%	73.892	1.64%
500	73.333	0.87%	73.774	1.48%	73.893	1.64%
1000	73.334	0.87%	73.774	1.48%	73.894	1.64%
2500	73.335	0.87%	73.774	1.48%	73.895	1.64%
5000	73.435	1.01%	73.874	1.62%	73.995	1.78%
10000	73.535	1.15%	73.974	1.75%	74.095	1.92%

Figures 5.98 and Figure 5.99 show the effect of thermal contact conductance on the thermal conductivity for model “A” and Model “B”, respectively. It can be observed that as the length of carbon nanotubes increased the thermal conductivity also increased.

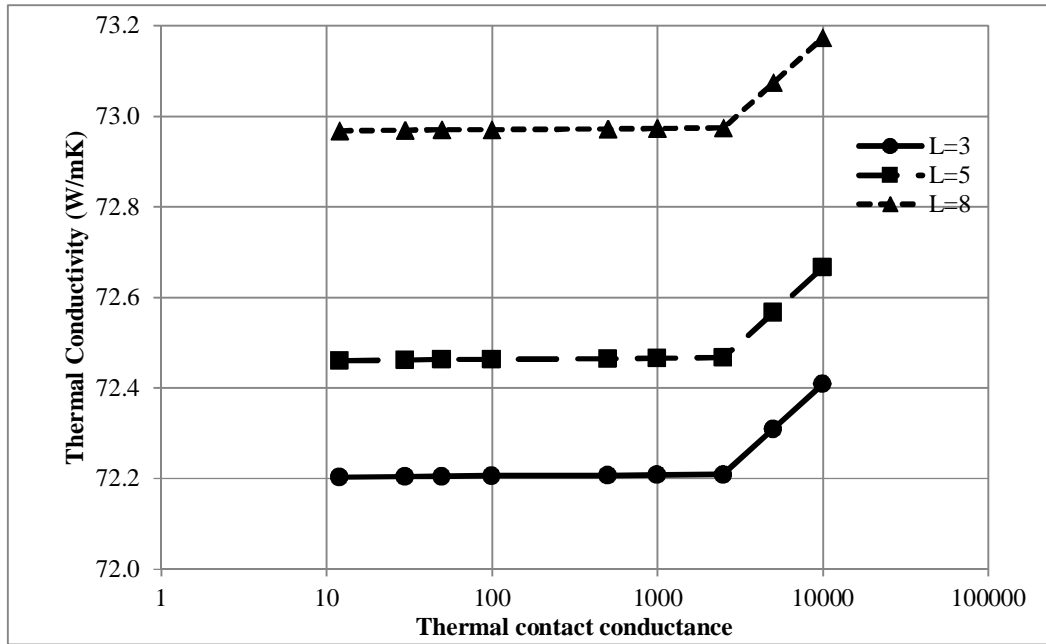


Figure 5.98: Effect of thermal contact conductance on thermal conductivity for zigzag carbon nanotube (5, 0) reinforced iron metal matrix (Model “A”)

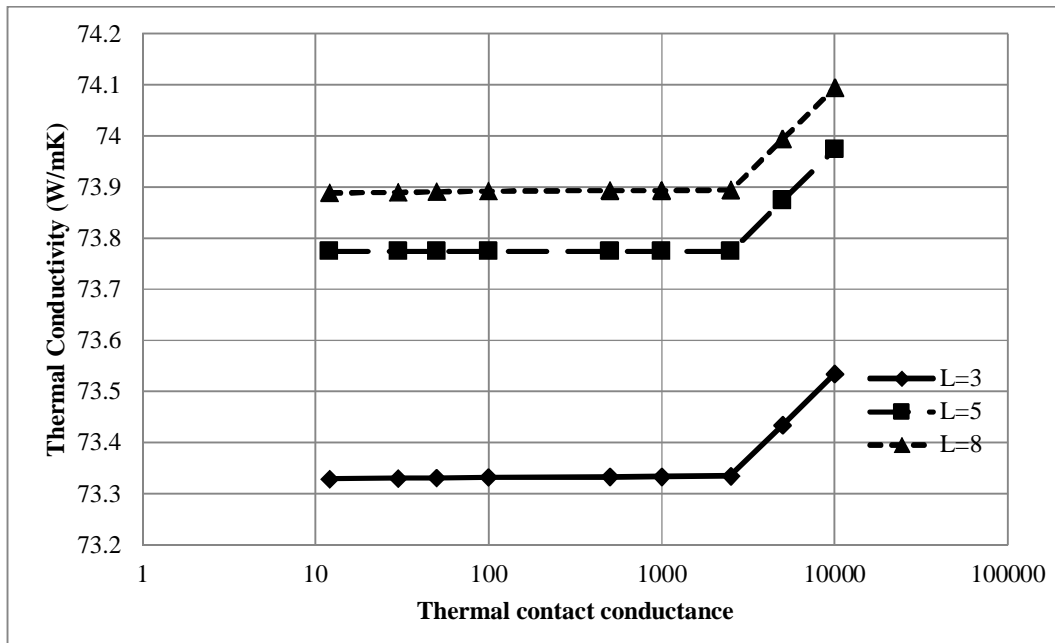


Figure 5.99: Effect of thermal contact conductance on thermal conductivity for zigzag carbon nanotube (5, 0) reinforced iron metal matrix (Model “B”)

However, For chiral (5, 10) carbon nanotubes reinforced iron metal matrixes at different lengths, Tables 5.31 (a) and (b) show the variation of the effective thermal conductivity with change of the thermal contact conductance for model “A” and model “B”. It can be seen that the effective thermal conductivity is slightly increased with respect to the matrix thermal conductivity. For model “A”, at $l_c = 3$ nm and $\beta = 12$ MW/m²K, the

thermal conductivity of the new composite was 71.718 W/m K which is about 1.35% decrement of the matrix thermal conductivity while at $\beta= 10000$ MW/m²K, the thermal conductivity of the new composite was 71.924 W/m K which is about 1.07% decrement of the matrix thermal conductivity. Similarly, for model “B”, $L= 3$ nm and $\beta= 12$ MW/m²K, the thermal conductivity of the new composite was 72.573 W/m K which is about 0.17% decrement of the matrix thermal conductivity while at $\beta= 10000$ MW/m²K, the thermal conductivity of the composite was 72.78 W/m K which is about 0.11% increment of the matrix thermal conductivity.

Table 5.31: Effect of thermal contact conductance on thermal conductivity for chiral carbon nanotube reinforced iron matrix at different length: (a) Model (A), and (b) Model (B)

(a) Model (A)

β (MW/m ² k)	K (W/m K)					
	$l_c=3$ nm	% change	$l_c =5$ nm	% change	$l_c =8$ nm	% change
12	71.718	-1.35%	72.058	-0.88%	72.457	-0.33%
30	71.719	-1.35%	72.059	-0.88%	72.458	-0.33%
50	71.720	-1.35%	72.060	-0.88%	72.459	-0.33%
100	71.721	-1.35%	72.061	-0.88%	72.460	-0.33%
500	71.722	-1.35%	72.062	-0.88%	72.461	-0.33%
1000	71.723	-1.34%	72.063	-0.88%	72.462	-0.33%
2500	71.724	-1.34%	72.064	-0.87%	72.463	-0.33%
5000	71.824	-1.21%	72.164	-0.17%	72.563	-0.19%
10000	71.924	-1.07%	72.264	-0.60%	72.663	-0.05%

(b) Model (B)

β (MW/m ² k)	K (W/m K)					
	$l_c=3$ nm	% change	$l_c =5$ nm	% change	$l_c =8$ nm	% change
12	72.573	-0.17%	72.9906	0.40%	73.052	0.48%
30	72.575	-0.17%	72.992	0.40%	73.053	0.49%
50	72.576	-0.17%	72.993	0.40%	73.054	0.49%
100	72.577	-0.17%	72.994	0.40%	73.055	0.49%
500	72.578	-0.17%	72.995	0.41%	73.056	0.49%
1000	72.579	-0.17%	72.996	0.41%	73.057	0.49%
2500	72.580	-0.17%	72.997	0.41%	73.058	0.49%
5000	72.680	-0.03%	73.097	0.55%	73.158	0.63%
10000	72.780	0.11%	73.197	0.68%	73.258	0.77%

Figures 5.100 and 5.101 show the effect of thermal contact conductance on the thermal conductivity for Model “A”, and Model “B”, respectively. It can be observed that as the length of carbon nanotubes increased the thermal conductivity also increased.

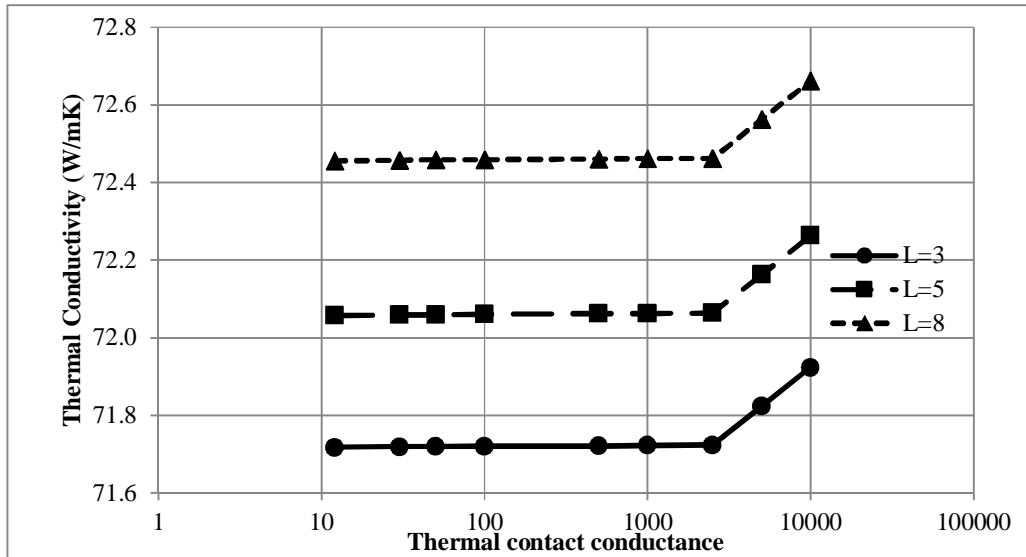


Figure 5.100: Effect of thermal contact conductance on thermal conductivity for chiral carbon nanotube (5,10) reinforced iron metal matrix (Model “A”)

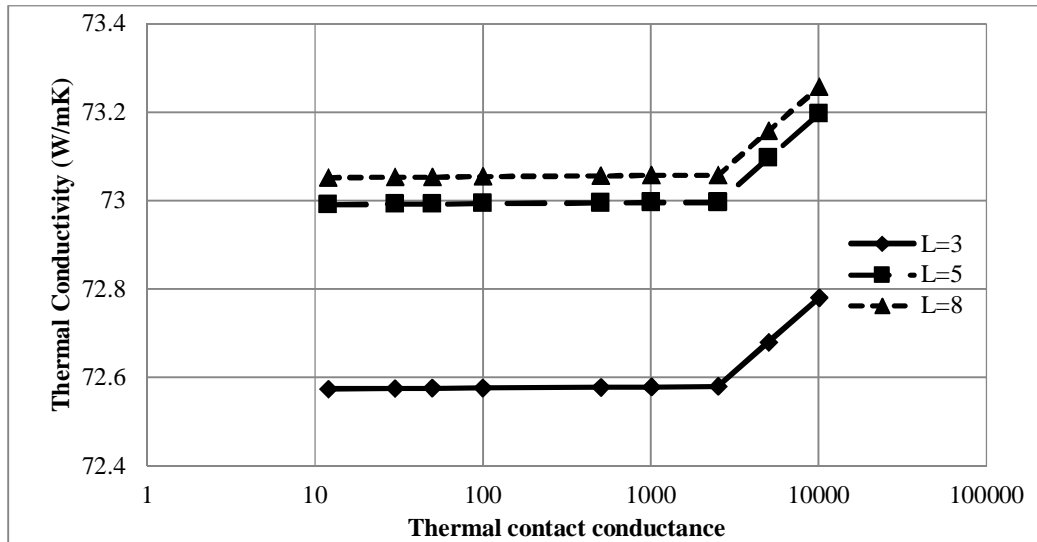


Figure 5.101: Effect of thermal contact conductance on thermal conductivity for chiral carbon nanotube (5, 10) reinforced iron metal matrix (Model “B”)

Figures 5.102, 5.103, and 5.104 present a comparison between different types of carbon nanotubes reinforced iron metal matrix at different lengths. The results calculated at 3% volume fraction show slight changing on the thermal conductivity when the thermal contact conductance increased from 12 MW/m² K to 10000 MW/m² K. The Zigzag carbon nanotube (5, 0) shows a higher prediction than armchair and chiral type. It can be observed from the previous tables that the thermal conductivity decreases by 0.68% at 12 MW/m² K and 0.4% at 10000 MW/m² K for zigzag (5, 0). However, for Armchair carbon nanotubes (5, 5) the decrement varied as 0.95% to 0.67% while for chiral carbon nanotubes (5, 10) varied as 1.35% to 1.07% at the same length of 3 nm, respectively.

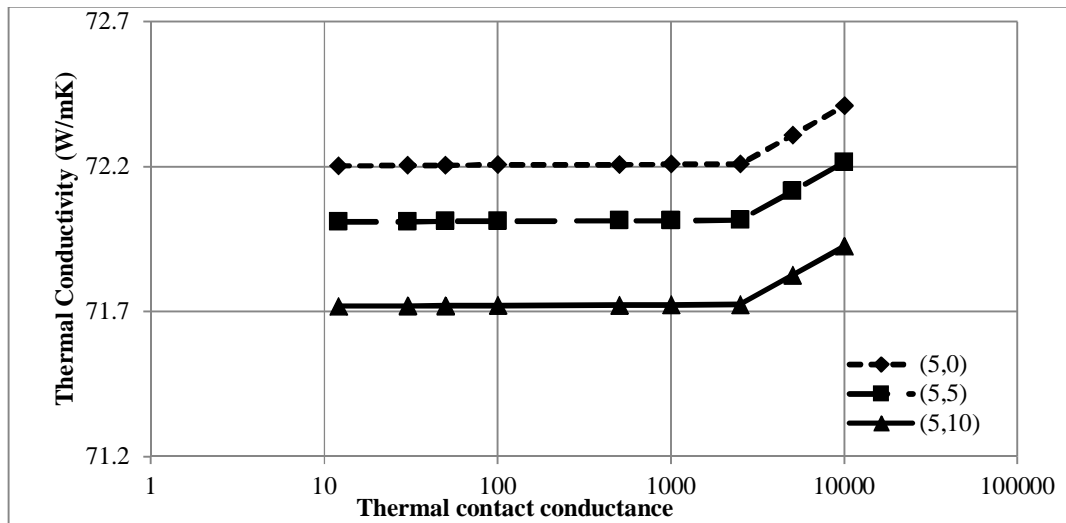


Figure 5.102: Effect of thermal contact on thermal conductivity for different chiral Index carbon nanotube reinforced iron metal matrix ($l_c = 3$ nm)

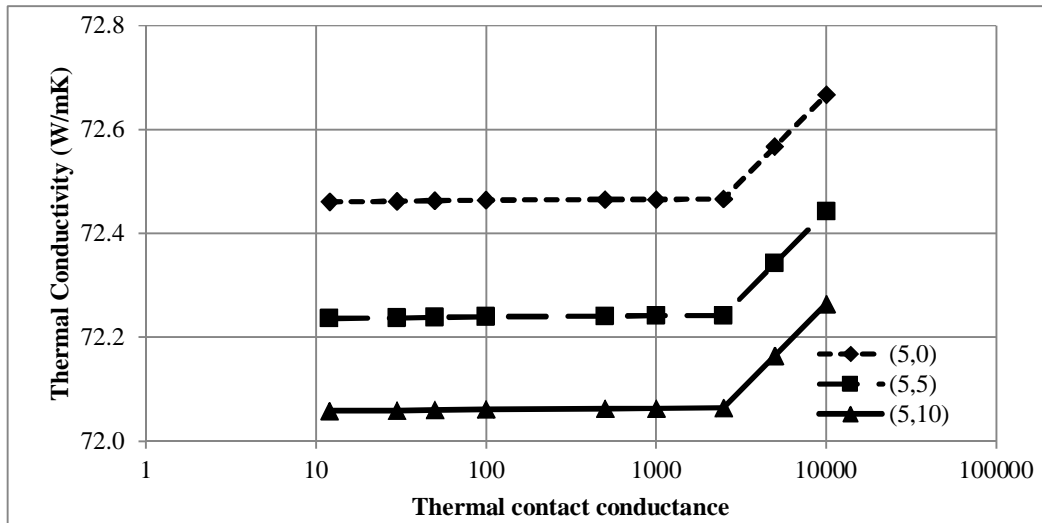


Figure 5.103: Effect of thermal contact on thermal conductivity for different chiral index carbon nanotube reinforced iron metal matrix ($l_c = 5$ nm)

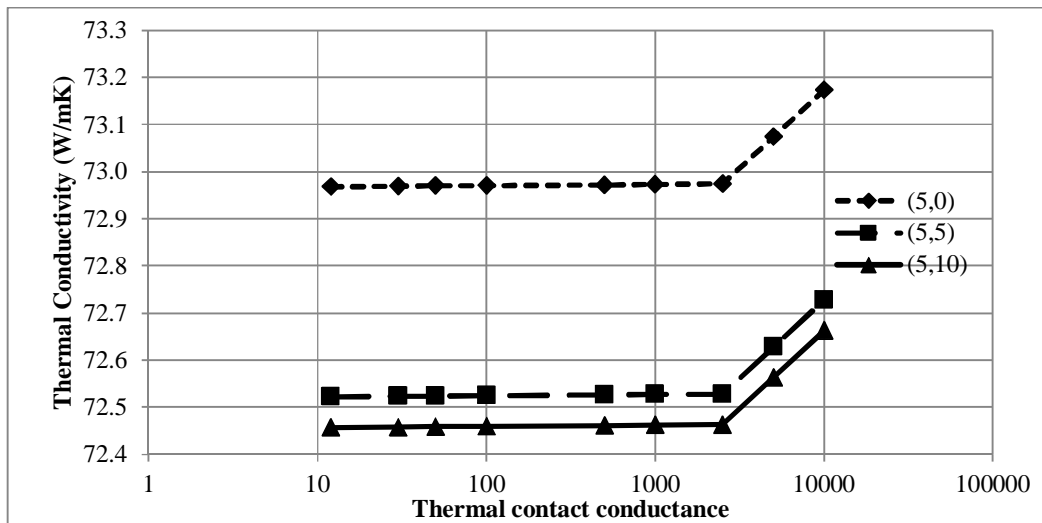


Figure 5.104: Effect of thermal contact on thermal conductivity for different chiral index carbon nanotube reinforced iron metal matrix ($l_c = 8$ nm)

Similarly, for armchair (5, 5) carbon nanotubes reinforced copper metal matrixes at different lengths, Tables 5.32 (a) and (b) show the variation of the effective thermal conductivity with change of the thermal contact conductance for model “A” and model “B”. It can be seen that the effective thermal conductivity is slightly increased with respect to the matrix thermal conductivity. For model “A”, at $l_c = 3$ nm and $\beta = 12$ MW/m²K, the thermal conductivity of the new composite was 387.329 W/m K which is about 0.34% increment of the matrix thermal conductivity while at $\beta = 10000$ MW/m²K, the thermal conductivity of the composite was 378.535 W/m K which is about 0.40% increment of the matrix thermal conductivity. Similarly for model “B”, $l_c = 3$ nm and $\beta = 12$ MW/m²K, the thermal conductivity of the new composite was 388.165 W/m K which is about 0.56% increment of the matrix thermal conductivity while at $\beta = 10000$ MW/m²K, the thermal conductivity of the new composite was 388.470W/m K which is about 0.64% increment of the matrix thermal conductivity.

Table 5.32: Effect of thermal contact conductance on thermal conductivity for armchair carbon nanotube reinforced copper matrix at different length: (a) Model (A), and (b) Model (B)

(a) Model (A)

β (MW/m ² k)	K (W/m K)					
	$l_c=3$ nm	% change	$l_c =5$ nm	% change	$l_c =8$ nm	% change
12	387.329	0.34%	387.939	0.50%	388.26	0.58%
30	387.330	0.34%	387.940	0.50%	388.26	0.58%
50	387.331	0.34%	387.941	0.50%	388.26	0.59%
100	387.332	0.35%	387.942	0.50%	388.26	0.59%
500	387.333	0.35%	387.943	0.50%	388.26	0.59%
1000	387.334	0.35%	387.944	0.50%	388.26	0.59%
2500	387.335	0.35%	387.945	0.50%	388.26	0.59%
5000	387.435	0.37%	388.045	0.53%	388.36	0.61%
10000	387.535	0.40%	388.145	0.56%	388.46	0.64%

(b) Model (B)

β (MW/m ² k)	K (W/m K)					
	$l_c=3$ nm	% change	$l_c =5$ nm	% change	$l_c =8$ nm	% change
12	388.165	0.56%	388.557	0.66%	388.903	0.75%
30	388.166	0.56%	388.558	0.66%	388.904	0.75%
50	388.167	0.56%	388.559	0.66%	388.905	0.75%
100	388.168	0.56%	388.560	0.66%	388.906	0.75%
500	388.169	0.56%	388.561	0.66%	388.907	0.75%
1000	388.170	0.56%	388.562	0.66%	388.908	0.75%
2500	388.270	0.59%	388.563	0.66%	388.909	0.75%
5000	388.370	0.61%	388.663	0.69%	389.009	0.78%
10000	388.470	0.64%	388.763	0.72%	389.109	0.81%

Figures 5.105 and 5.106 show the effect of thermal contact conductance on the thermal conductivity for Model “A” and Model “B”, respectively. It can be observed that as the length of carbon nanotubes increased the thermal conductivity also increased.

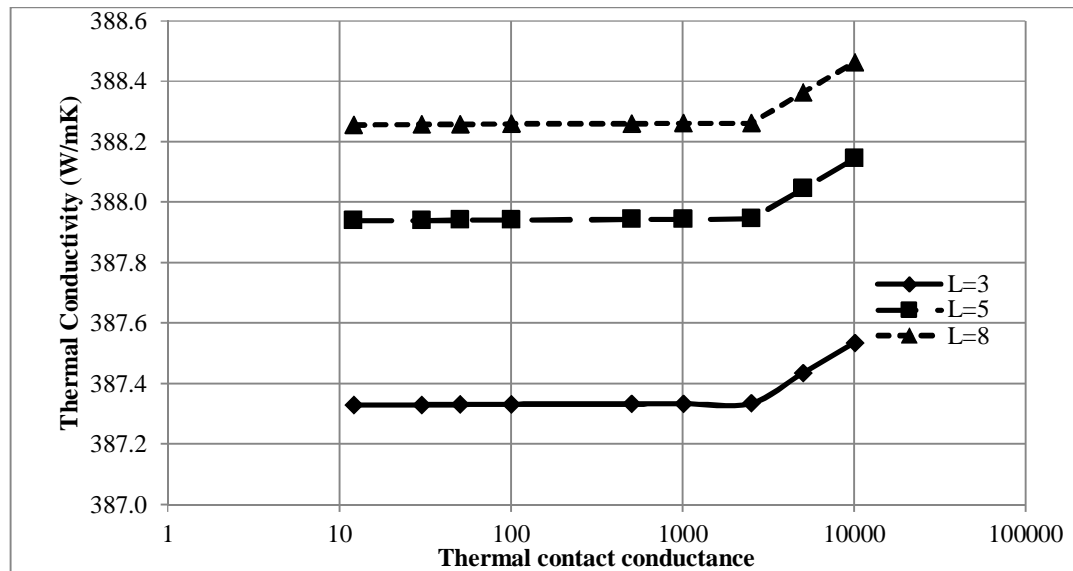


Figure 5.105: Effect of thermal contact conductance on thermal conductivity for armchair carbon nanotube (5, 5) reinforced copper metal matrix (Model “A”)

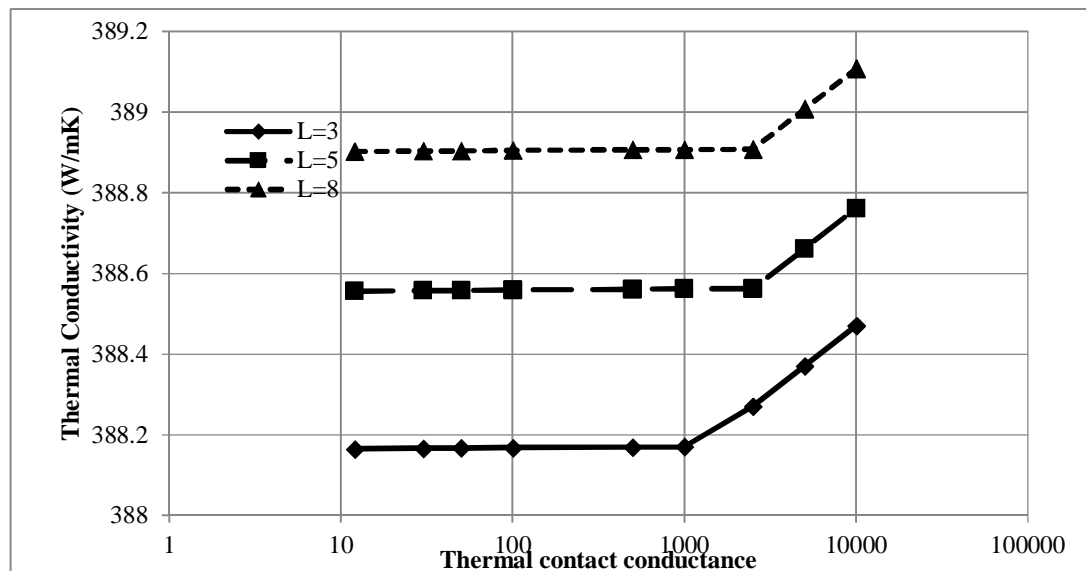


Figure 5.106: Effect of thermal contact conductance on thermal conductivity for armchair carbon nanotube (5, 5) reinforced copper metal matrix (MODEL “B”)

For zigzag (5, 0) carbon nanotubes reinforced copper metal matrixes at different lengths, Tables 5.33 (a) and (b) show the variation of the effective thermal conductivity with change of the thermal contact conductance for model “A” and model “B”. It can be seen that the effective thermal conductivity is slightly increased with respect to the

matrix thermal conductivity. For model “A”, at $l_c = 3$ nm and $\beta = 12$ MW/m²K, the thermal conductivity of the new composite was 388.2 W/m K which is about 0.57% increment of the matrix thermal conductivity while at $\beta = 10000$ MW/m²K, the thermal conductivity of the new composite was 388.41 W/m K which is about 0.62% increment of the matrix thermal conductivity. Similarly, for model “B”, $l_c = 3$ nm and $\beta = 12$ MW/m²K, the thermal conductivity of the new composite was 389.268 W/m K which is about 0.71% increment of the matrix thermal conductivity while at $\beta = 10000$ MW/m²K, the thermal conductivity of the composite was 389.468 W/m K which is about 0.76% increment of the matrix thermal conductivity.

Table 5.33: Effect of thermal contact conductance on thermal conductivity for zigzag carbon nanotube reinforced copper matrix at different length: (a) Model (A), and (b) Model (B)

(a) Model (A)

β (MW/m ² k)	K (W/m K)					
	$l_c=3$ nm	% change	$l_c =5$ nm	% change	$l_c =8$ nm	% change
12	388.200	0.57%	388.65	0.69%	388.93	0.76%
30	388.201	0.57%	388.65	0.69%	388.93	0.76%
50	388.202	0.57%	388.65	0.69%	388.93	0.76%
100	388.203	0.57%	388.65	0.69%	388.93	0.76%
500	388.204	0.57%	388.65	0.69%	388.93	0.76%
1000	388.205	0.57%	388.65	0.69%	388.94	0.76%
2500	388.206	0.57%	388.66	0.69%	388.94	0.76%
5000	388.306	0.60%	388.76	0.71%	389.04	0.79%
10000	388.406	0.62%	388.86	0.74%	389.14	0.81%

(b) Model (B)

β (MW/m ² k)	K (W/m K)					
	$l_c=3$ nm	% change	$l_c =5$ nm	% change	$l_c =8$ nm	% change
12	389.268	0.71%	389.27	0.85%	389.69	0.96%
30	389.268	0.71%	389.27	0.85%	389.69	0.96%
50	389.268	0.71%	389.27	0.85%	389.69	0.96%
100	389.268	0.71%	389.27	0.85%	389.69	0.96%
500	389.268	0.71%	389.27	0.85%	389.69	0.96%
1000	389.268	0.71%	389.27	0.85%	389.69	0.96%
2500	389.268	0.71%	389.27	0.85%	389.69	0.96%
5000	389.368	0.73%	389.37	0.87%	389.79	0.98%
10000	389.468	0.76%	389.47	0.90%	389.89	1.01%

Figures 5.107 and 5.108 show the effect of thermal contact conductance on the thermal conductivity for Model “A” and Model “B”, respectively. It can be observed that as the length of carbon nanotubes increased the thermal conductivity also increased.

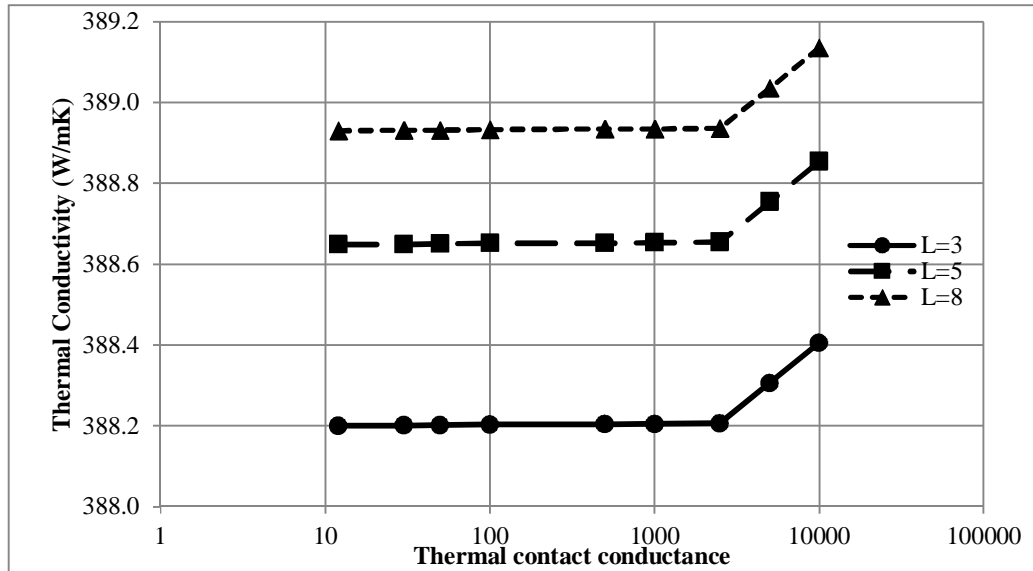


Figure 5.107: Effect of thermal contact conductance on thermal conductivity for zigzag carbon nanotube (5, 0) reinforced copper metal matrix (Model “A”)

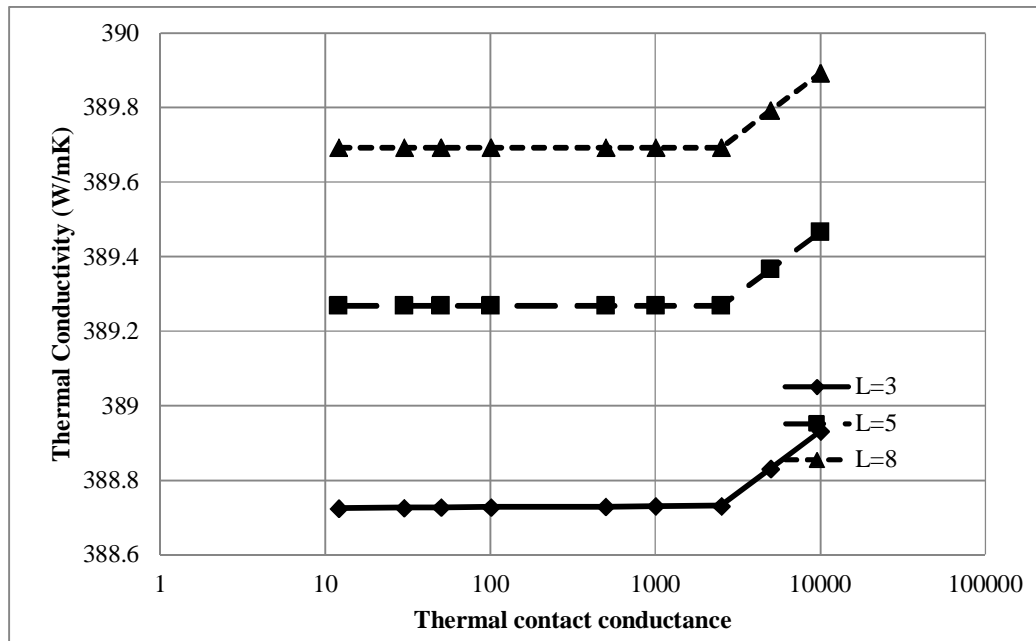


Figure 5.108: Effect of thermal contact conductance on thermal conductivity for zigzag carbon nanotube (5, 0) reinforced copper metal matrix (Model “B”)

However, For chiral (5, 10) carbon nanotubes reinforced Copper metal matrixes at different lengths, Tables 5.34 (a) and (b) show the variation of the effective thermal conductivity with change of the thermal contact conductance for model “A” and “B”. It can be seen that the effective thermal conductivity is slightly increased with respect to the matrix thermal conductivity. For model “A”, at $l_c = 3$ nm and $\beta = 12$ MW/m²K, the thermal conductivity of the new composite was 386.284 W/m K which is about 0.07%

increment of the matrix thermal conductivity while at $\beta= 10000$ MW/m²K, the thermal conductivity of the new composite was 386.49 W/m K which is about 0.13% increment of the matrix thermal conductivity. Similarly for model “B”, $l_c= 3$ nm and $\beta= 12$ MW/m²K, the thermal conductivity of the new composite was 387.1909 W/m K which is about 0.31% decrement of the matrix thermal conductivity while at $\beta= 10000$ MW/m²K, the thermal conductivity of the composite was 387.3969 W/m K which is about 0.36% increment of the matrix thermal conductivity.

Table 5.34: Effect of thermal contact conductance on thermal conductivity for chiral carbon nanotube reinforced copper matrix at different length: (a) Model (A), and (b) Model (B)

(a) Model (A)

β (MW/m ² k)	K (W/m K)					
	$l_c=3$ nm	% change	$l_c =5$ nm	% change	$l_c =8$ nm	% change
12	386.284	0.07%	386.695	0.18%	387.165	0.30%
30	386.285	0.07%	386.696	0.18%	387.166	0.30%
50	386.286	0.07%	386.697	0.18%	387.167	0.30%
100	386.287	0.07%	386.698	0.18%	387.168	0.30%
500	386.288	0.07%	386.699	0.18%	387.169	0.30%
1000	386.289	0.07%	386.700	0.18%	387.170	0.30%
2500	386.290	0.08%	386.701	0.18%	387.171	0.30%
5000	386.390	0.10%	386.801	0.31%	387.271	0.33%
10000	386.490	0.13%	386.901	0.23%	387.371	0.36%

(b) Model (B)

β (MW/m ² k)	K (W/m K)					
	$l_c=3$ nm	% change	$l_c =5$ nm	% change	$l_c =8$ nm	% change
12	387.1909	0.31%	387.574	0.41%	387.934	0.50%
30	387.1919	0.31%	387.575	0.41%	387.935	0.50%
50	387.1929	0.31%	387.576	0.41%	387.936	0.50%
100	387.1939	0.31%	387.577	0.41%	387.937	0.50%
500	387.1949	0.31%	387.578	0.41%	387.938	0.50%
1000	387.1959	0.31%	387.579	0.41%	387.939	0.50%
2500	387.1969	0.31%	387.580	0.41%	387.940	0.50%
5000	387.2969	0.34%	387.680	0.44%	388.040	0.53%
10000	387.3969	0.36%	387.780	0.46%	388.140	0.55%

Figures 5.109 and 5.110 show the effect of thermal contact conductance on the thermal conductivity for Model “A” and Model “B”, respectively. It can be observed that as the length of carbon nanotubes increased the thermal conductivity also increased.

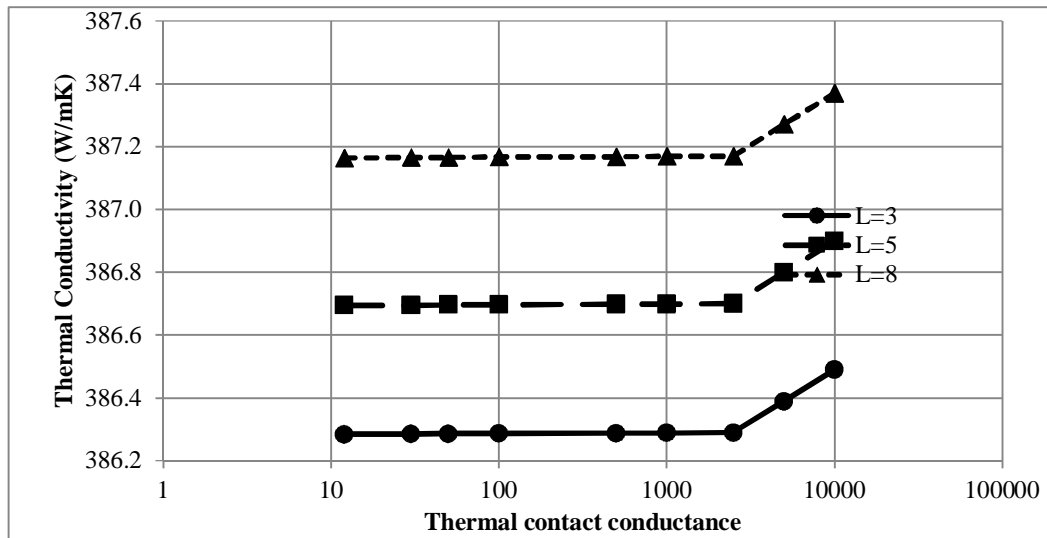


Figure 5.109: Effect of thermal contact conductance on thermal conductivity for chiral carbon nanotube (5, 10) reinforced copper metal matrix (Model “A”)

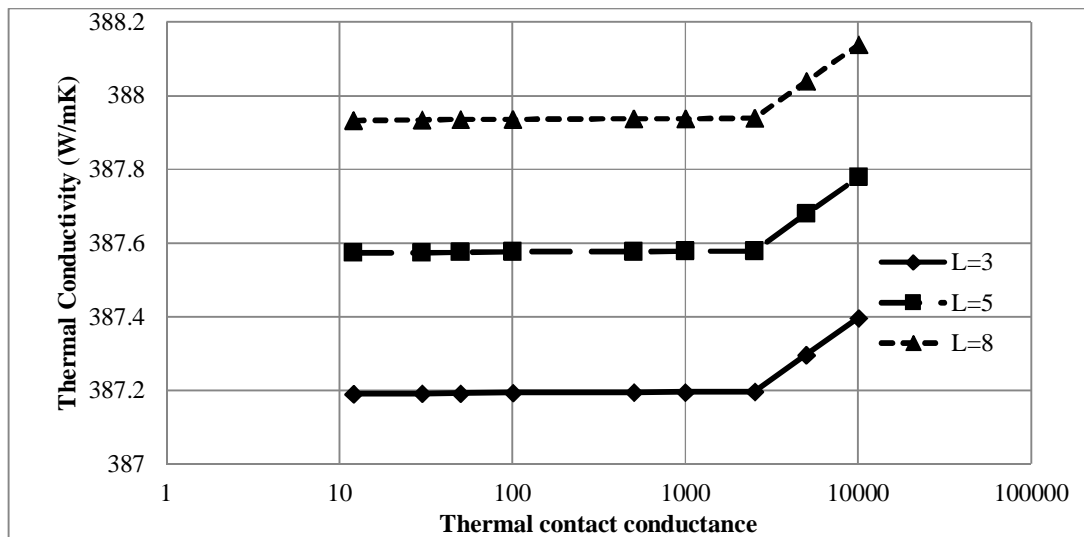


Figure 5.110: Effect of thermal contact conductance on thermal conductivity for chiral carbon nanotube (5, 10) reinforced copper metal matrix (Model “B”)

Figures 5.111, 5.112 and 5.113 present a comparison between different types of carbon nanotubes reinforced copper metal matrix at different lengths. The results calculated at 3% volume fraction show slight changing on the thermal conductivity when the thermal contact conductance increased from 12 MW/m² K to 10000 MW/m² K. The zigzag carbon nanotube (5, 0) shows a higher prediction than armchair and chiral type. It can be observed from the previous tables that the thermal conductivity increases by 0.57% at 12 MW/m² K and 0.62% at 10000 MW/m² K for Zigzag. However, for armchair carbon nanotubes (5, 5) the decrement varied as 34% to 0.40% while for chiral carbon nanotubes (5, 10) varied as 0.07% to 0.13% at the same length, respectively.

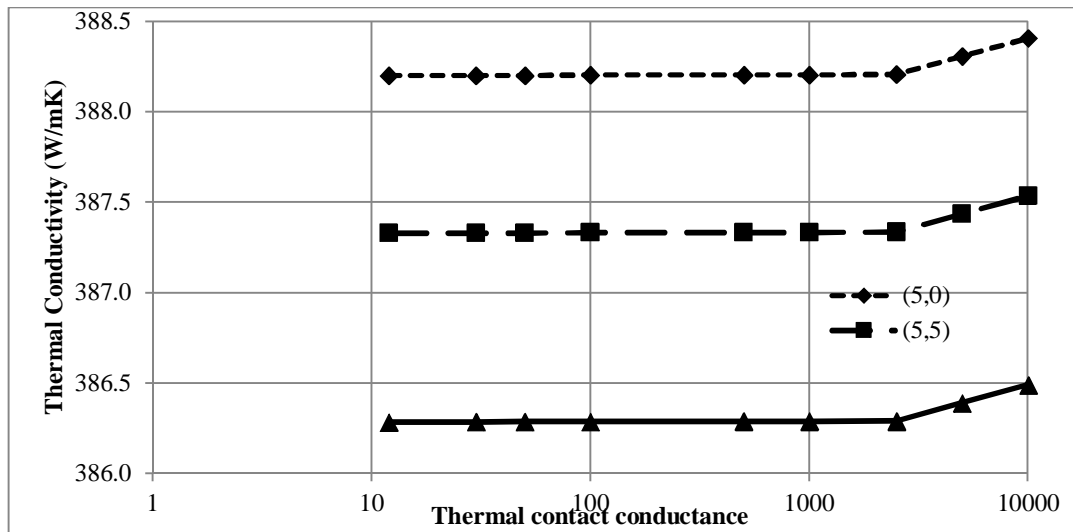


Figure 5.111: Effect of thermal contact on thermal conductivity for different chiral index carbon nanotube reinforced copper metal matrix ($l_c = 3$ nm)

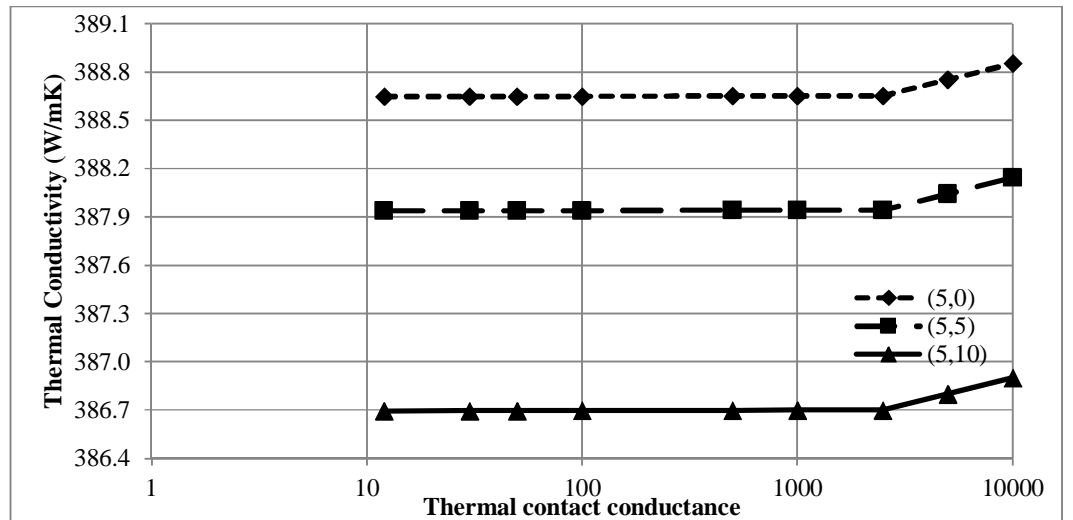


Figure 5.112: Effect of thermal contact on thermal conductivity for different chiral index carbon nanotube reinforced copper metal matrix ($l_c = 5$ nm)

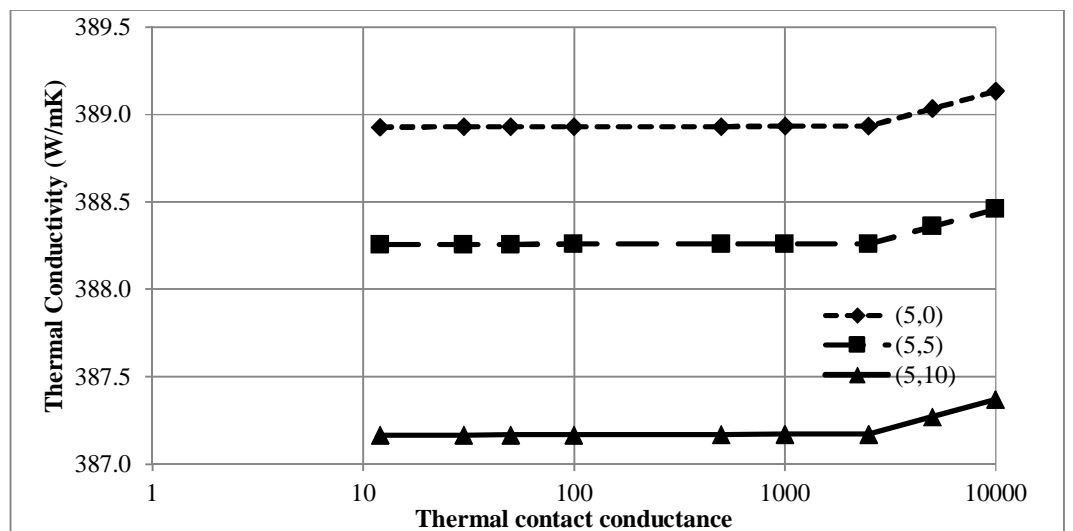


Figure 5.113: Effect of thermal contact on thermal conductivity for different chiral index carbon nanotube reinforced copper metal matrix ($l_c = 8$ nm)

However, for armchair (5, 5) carbon nanotubes reinforced aluminum metal matrixes at different lengths, Tables 5.35 (a) and (b) shows the variation of the effective thermal conductivity with change of the thermal contact conductance for Model “A” and “B”. It can be seen that the effective thermal conductivity is slightly increased with respect to the matrix thermal conductivity. For model “A”, at $l_c = 3$ nm and $\beta = 12$ MW/m²K, the thermal conductivity of the new composite was 202.0599W/m K which is about 0.95% decrement of the matrix thermal conductivity while at $\beta = 10000$ MW/m²K, the thermal conductivity of the new composite was 202.2659 W/m K which is about 0.85% decrement of the matrix thermal conductivity. Similarly, for model “B”, $l_c = 3$ nm and $\beta = 12$ MW/m²K, the thermal conductivity of the new composite was 204.419W/m K which is about 0.21% increment of the matrix thermal conductivity while at $\beta = 10000$ MW/m²K, the thermal conductivity of the new composite was 204.724 W/m K which is about 0.35% increment of the matrix thermal conductivity.

Table 5.35: Effect of thermal contact conductance on thermal conductivity for armchair carbon nanotube reinforced aluminum matrix at different length: (a) Model (A), and (b) Model (B)

(a) Model (A)

β (MW/m ² k)	K (W/m K)					
	$l_c=3$ nm	% change	$l_c =5$ nm	% change	$l_c =8$ nm	% change
12	202.0599	-0.95%	202.700	-0.64%	203.50	-0.24%
30	202.0609	-0.95%	202.701	-0.64%	203.50	-0.24%
50	202.0619	-0.95%	202.702	-0.64%	203.50	-0.24%
100	202.0629	-0.95%	202.702	-0.64%	203.50	-0.24%
500	202.0639	-0.95%	202.703	-0.64%	203.51	-0.24%
1000	202.0649	-0.95%	202.704	-0.64%	203.51	-0.24%
2500	202.0659	-0.95%	202.705	-0.63%	203.51	-0.24%
5000	202.1659	-0.90%	202.805	-0.59%	203.61	-0.19%
10000	202.2659	-0.85%	202.905	-0.54%	203.71	-0.14%

(b) Model (B)

β (MW/m ² k)	K (W/m K)					
	$l_c=3$ nm	% change	$l_c =5$ nm	% change	$l_c =8$ nm	% change
12	204.419	0.21%	205.281	0.63%	205.47	0.72%
30	204.420	0.21%	205.282	0.63%	205.47	0.72%
50	204.421	0.21%	205.283	0.63%	205.48	0.72%
100	204.422	0.21%	205.284	0.63%	205.48	0.72%
500	204.423	0.21%	205.285	0.63%	205.48	0.72%
1000	204.424	0.21%	205.286	0.63%	205.48	0.72%
2500	204.524	0.26%	205.287	0.63%	205.48	0.73%
5000	204.624	0.31%	205.387	0.68%	205.58	0.77%
10000	204.724	0.35%	205.487	0.73%	205.68	0.82%

Figures 5.114 and 5.115 show the effect of thermal contact conductance on the thermal conductivity for Model “A” and Model “B”, respectively. It can be observed that as the length of carbon nanotubes increased the thermal conductivity also increased.

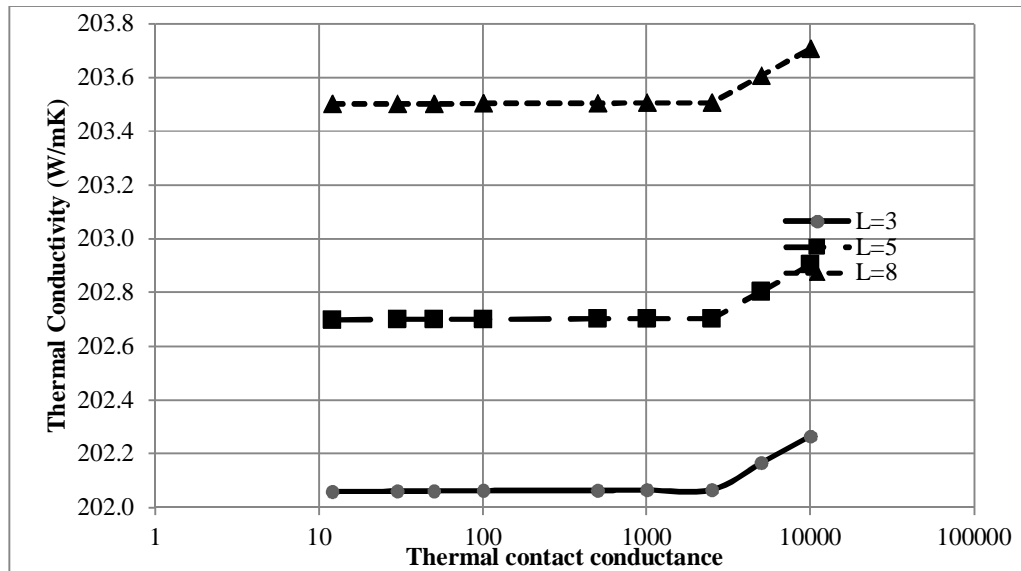


Figure 5.114: Effect of thermal contact conductance on thermal conductivity for armchair carbon nanotube (5, 5) reinforced aluminum metal matrix (Model “A”)

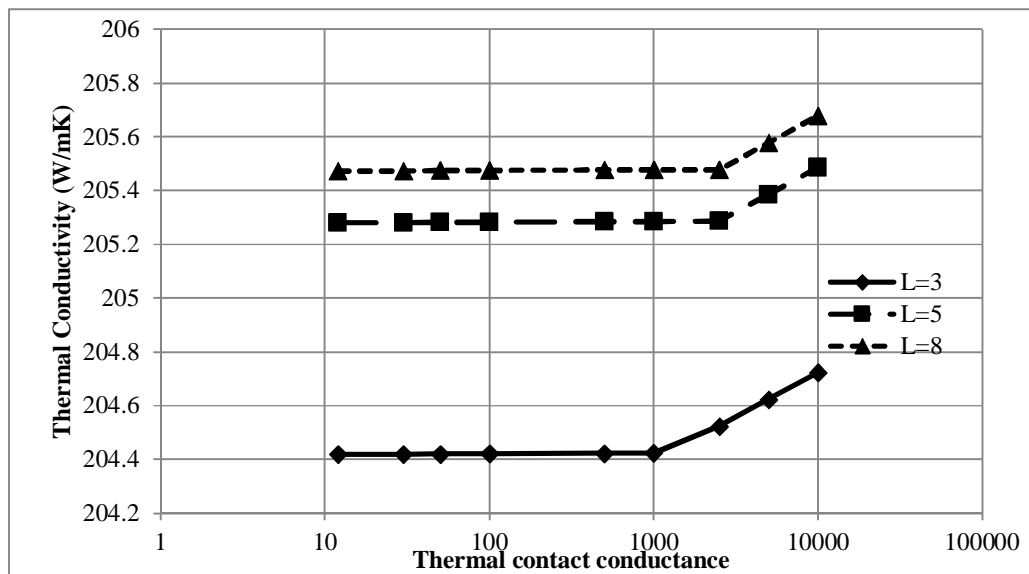


Figure 5.115: Effect of thermal contact conductance on thermal conductivity for armchair carbon nanotube (5, 5) reinforced aluminum metal matrix (Model “B”)

For zigzag (5, 0) carbon nanotubes reinforced Aluminum metal matrixes at different lengths, Tables 5.36 (a) and (b) shows the variation of the effective thermal conductivity with change of the thermal contact conductance for Model “A” and “B”. It can be seen that the effective thermal conductivity is slightly increased with respect to the matrix

thermal conductivity. For model “A”, at $l_c = 3$ nm and $\beta = 12$ MW/m²K, the thermal conductivity of the new composite was 202.606 W/m K which is about 0.68% decrement of the matrix thermal conductivity, while at $\beta = 10000$ MW/m²K, the thermal conductivity of the new composite was 202.812 W/m K which is about 0.58% decrement of the matrix thermal conductivity. Similarly, for model “B”, $L = 3$ nm and $\beta = 12$ MW/m²K, the thermal conductivity of the new composite was 205.374 W/m K which is about 0.67% increment of the matrix thermal conductivity while at $\beta = 10000$ MW/m²K, the thermal conductivity of the composite was 205.580 W/m K which is about 0.77% increment of the matrix thermal conductivity.

Table 5.36: Effect of thermal contact conductance on thermal conductivity for zigzag carbon nanotube reinforced aluminum matrix at different length: (a) Model (A), and (b) Model (B)

(a) Model (A)

β (MW/m ² k)	K (W/m K)					
	$l_c=3$ nm	% change	$l_c =5$ nm	% change	$l_c =8$ nm	% change
12	202.606	-0.68%	203.05	-0.47%	203.63	-0.18%
30	202.607	-0.68%	203.05	-0.47%	203.63	-0.18%
50	202.608	-0.68%	203.05	-0.47%	203.63	-0.18%
100	202.609	-0.68%	203.05	-0.46%	203.63	-0.18%
500	202.610	-0.68%	203.05	-0.46%	203.63	-0.18%
1000	202.611	-0.68%	203.05	-0.46%	203.64	-0.18%
2500	202.612	-0.68%	203.06	-0.46%	203.64	-0.18%
5000	202.712	-0.63%	203.16	-0.41%	203.74	-0.13%
10000	202.812	-0.58%	203.26	-0.37%	203.84	-0.08%

(b) Model (B)

β (MW/m ² k)	K (W/m K)					
	$l_c=3$ nm	% change	$l_c =5$ nm	% change	$l_c =8$ nm	% change
12	205.374	0.67%	206.268	1.11%	206.49	1.22%
30	205.375	0.67%	206.269	1.11%	206.49	1.22%
50	205.376	0.67%	206.270	1.11%	206.50	1.22%
100	205.377	0.67%	206.271	1.11%	206.50	1.22%
500	205.378	0.68%	206.272	1.11%	206.50	1.22%
1000	205.379	0.68%	206.273	1.11%	206.50	1.22%
2500	205.380	0.68%	206.274	1.11%	206.50	1.23%
5000	205.480	0.73%	206.374	1.16%	206.60	1.27%
10000	205.580	0.77%	206.474	1.21%	206.70	1.32%

Figures 5.116 and 5.117 show the effect of thermal contact conductance on the thermal conductivity for Model “A” and Model “B”, respectively. It can be observed that as the length of carbon nanotubes increased the thermal conductivity also increased.

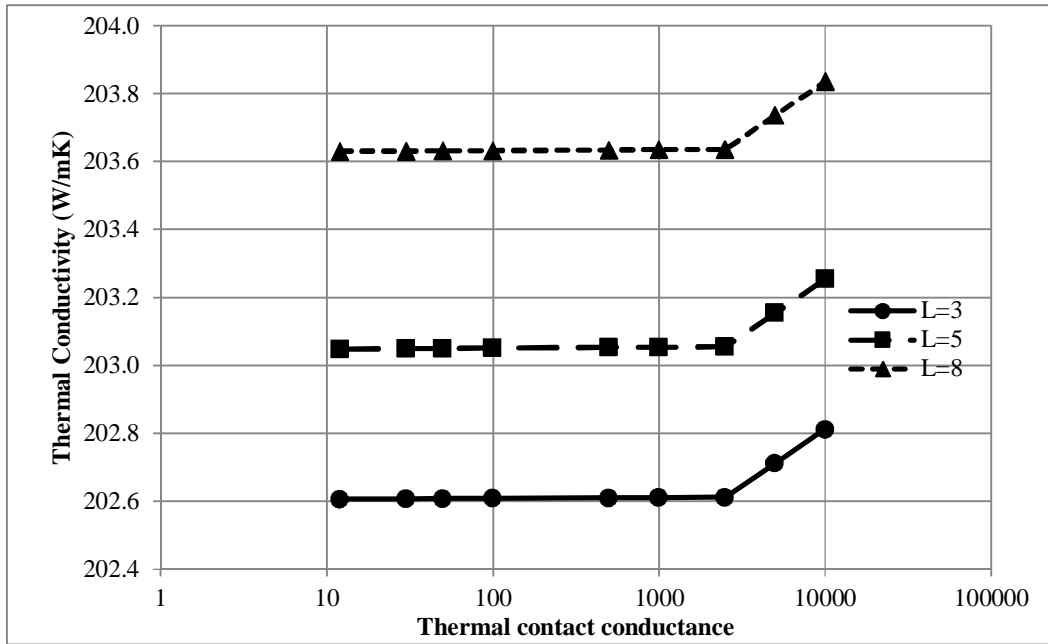


Figure 5.116: Effect of thermal contact conductance on thermal conductivity for zigzag carbon nanotube (5, 0) reinforced aluminum metal matrix (Model “A”)

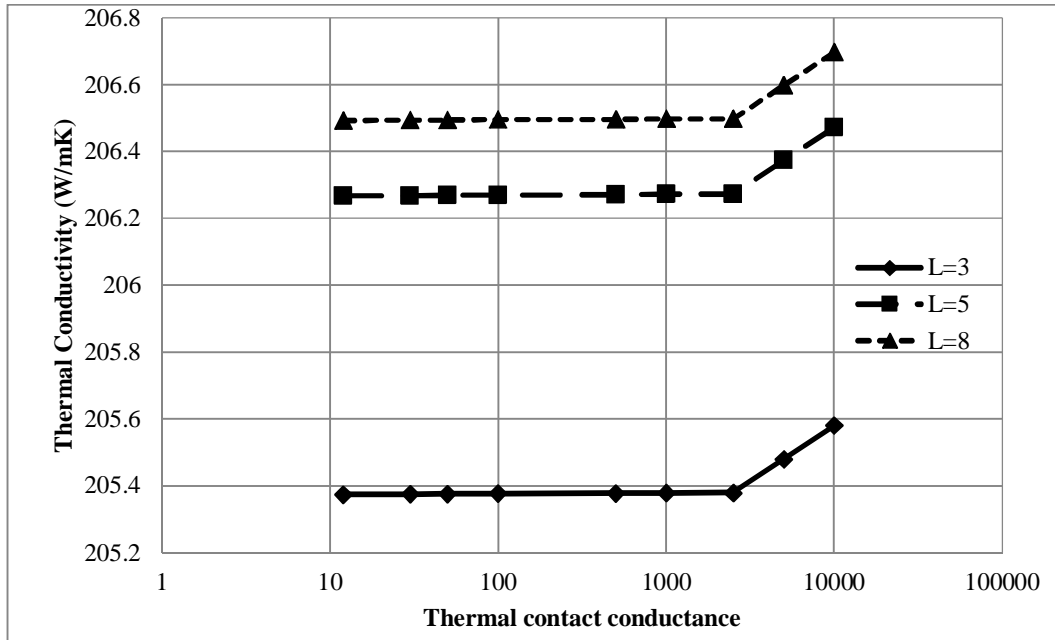


Figure 5.117: Effect of thermal contact conductance on thermal conductivity for zigzag carbon nanotube (5, 0) reinforced aluminum metal matrix (Model “B”)

However, For chiral (5, 10) carbon nanotubes reinforced aluminum metal matrixes at different lengths, Tables 5.37 (a) and (b) shows the variation of the effective thermal conductivity with change of the thermal contact conductance for model “A” and “B”. It can be seen that the effective thermal conductivity is slightly increased with respect to

the matrix thermal conductivity. For model “A”, at $l_c = 3$ nm and $\beta = 12$ MW/m²K, the thermal conductivity of the composite was 201.244 W/m K which is about 1.35% decrement of the matrix thermal conductivity while at $\beta = 10000$ MW/m²K, the thermal conductivity of the new composite was 201.450 W/m K which is about 1.25% decrement of the matrix thermal conductivity. Similarly, for model “B”, $l_c = 3$ nm and $\beta = 12$ MW/m²K, the thermal conductivity of the new composite was 203.354 W/m K which is about 0.32% decrement of the matrix thermal conductivity while at $\beta = 10000$ MW/m²K, the thermal conductivity of the composite was 203.560 W/m K which is about 0.22% decrement of the matrix thermal conductivity.

Table 5.37: Effect of thermal contact conductance on thermal conductivity for chiral carbon nanotube reinforced aluminum matrix at different length: (a) Model (A), and (b) Model (B)

(a) Model (A)

β (MW/m ² k)	K (W/m K)					
	$l_c=3$ nm	% change	$l_c =5$ nm	% change	$l_c =8$ nm	% change
12	201.244	-1.35%	202.198	-0.88%	203.318	-0.33%
30	201.245	-1.35%	202.199	-0.88%	203.319	-0.33%
50	201.246	-1.35%	202.200	-0.88%	203.320	-0.33%
100	201.247	-1.35%	202.201	-0.88%	203.321	-0.33%
500	201.248	-1.35%	202.202	-0.88%	203.322	-0.33%
1000	201.249	-1.35%	202.203	-0.88%	203.323	-0.33%
2500	201.250	-1.35%	202.204	-0.88%	203.324	-0.33%
5000	201.350	-1.30%	202.304	-0.31%	203.424	-0.28%
10000	201.450	-1.25%	202.404	-0.78%	203.524	-0.23%

(b) Model (B)

β (MW/m ² k)	K (W/m K)					
	$l_c=3$ nm	% change	$l_c =5$ nm	% change	$l_c =8$ nm	% change
12	203.354	-0.32%	204.430	0.21%	204.644	0.32%
30	203.355	-0.32%	204.431	0.21%	204.645	0.32%
50	203.356	-0.32%	204.432	0.21%	204.646	0.32%
100	203.357	-0.31%	204.433	0.21%	204.647	0.32%
500	203.358	-0.31%	204.434	0.21%	204.648	0.32%
1000	203.359	-0.31%	204.435	0.21%	204.649	0.32%
2500	203.360	-0.31%	204.436	0.21%	204.650	0.32%
5000	203.460	-0.26%	204.536	0.26%	204.750	0.37%
10000	203.560	-0.22%	204.636	0.31%	204.850	0.42%

Figures 5.118 and 5.119 show the effect of thermal contact conductance on the thermal conductivity for Model “A” and “B”, respectively. It can be observed that as the length of carbon nanotubes increased the thermal conductivity also increased.

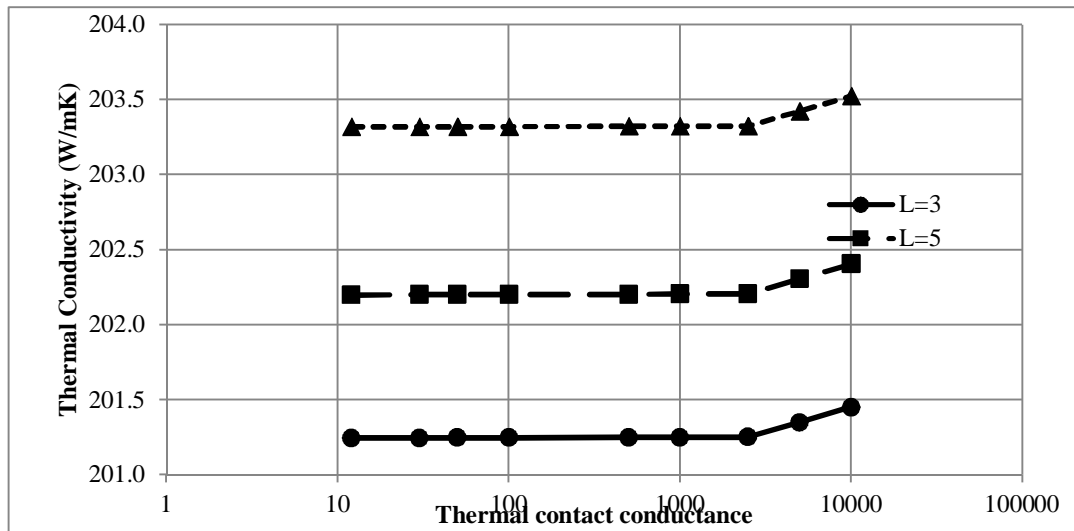


Figure 5.118: Effect of thermal contact conductance on thermal conductivity for chiral carbon nanotube (5, 10) reinforced aluminum metal matrix (Model “A”)

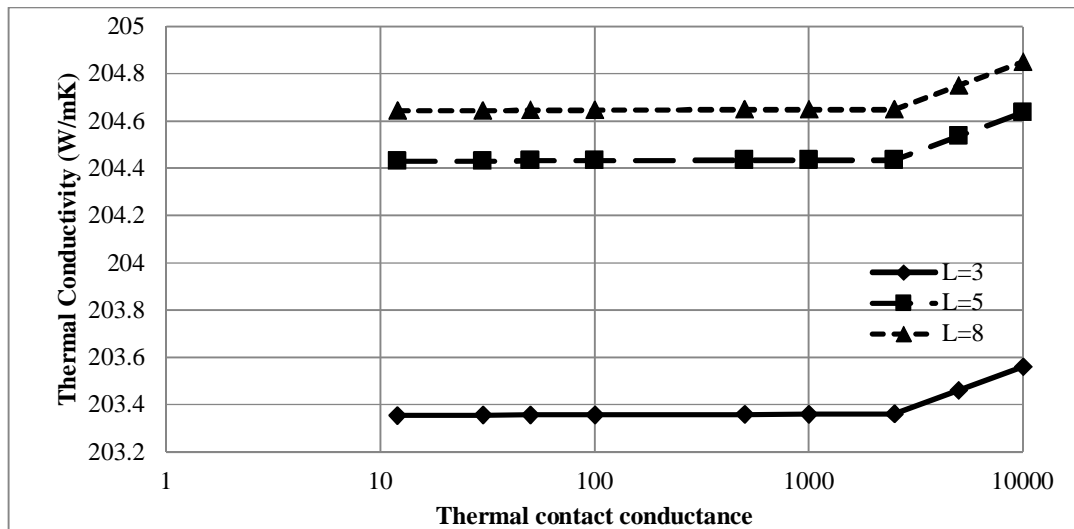


Figure 5.119: Effect of thermal contact conductance on thermal conductivity for chiral carbon nanotube (5, 10) reinforced aluminum metal matrix (Model “B”)

Figures 5.120, 5.121, and 5.122 present a comparison between different types of carbon nanotubes reinforced aluminum metal matrix at different lengths. The results calculated at 3% volume fraction show slight changing on the thermal conductivity when the thermal contact conductance increased from 12 MW/m² K to 10000 MW/m² K. The zigzag carbon nanotube (5, 0) shows a higher prediction than armchair (5, 5) and chiral (5, 10) type. It can be observed from the previous tables that the thermal conductivity increases by 0.67% at 12 MW/m² K and 0.77% at 10000 MW/m² K for Zigzag. However, for Armchair carbon nanotubes (5, 5) the decrement varied as 0.95% to 0.85% while for chiral carbon nanotubes (5, 10) varied as 0.32% to 0.22% at the same length respectively.

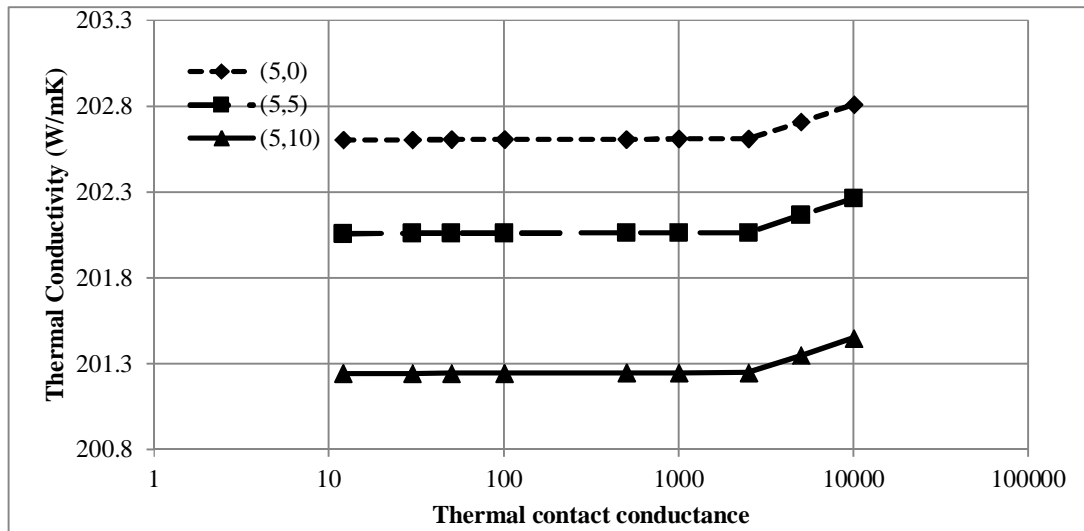


Figure 5.120: Effect of thermal contact on thermal conductivity for different chiral Index carbon nanotube reinforced aluminum metal matrix ($l_c = 3$ nm)

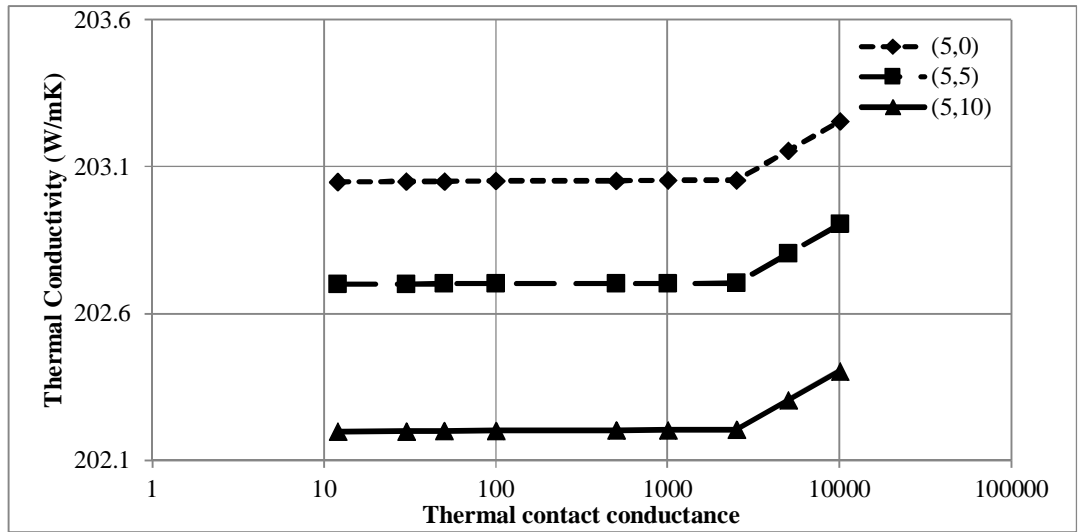


Figure 5.121: Effect of thermal contact on thermal conductivity for different chiral Index carbon nanotube reinforced aluminum metal matrix ($l_c = 5$ nm)

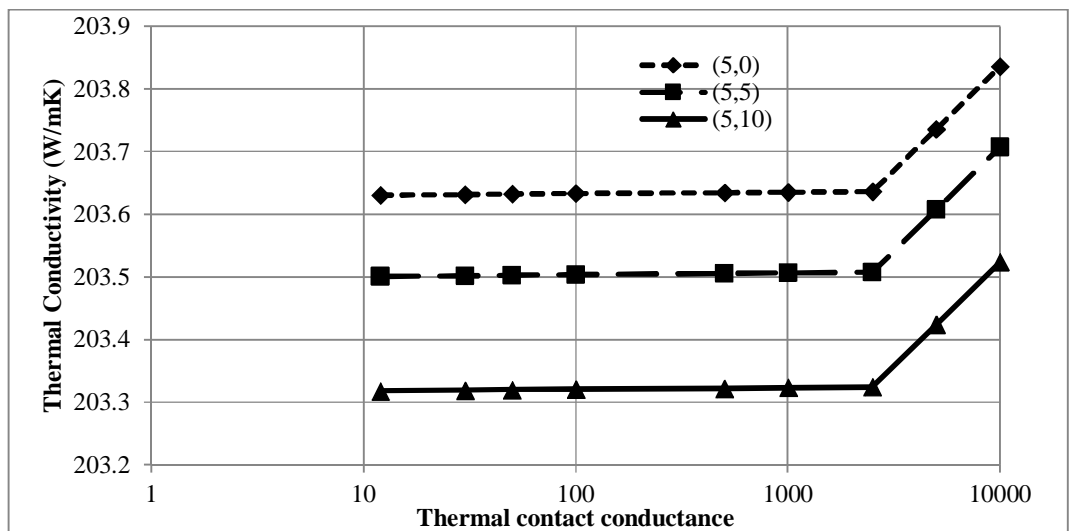


Figure 5.122: Effect of thermal contact on thermal conductivity for different chiral Index carbon nanotube reinforced aluminum metal matrix ($l_c = 8$ nm)

CHAPTER SIX

VALIDATIONS OF THE RESULTS

6.1 Overview

The validation is of particular importance, since it proves that the developed model can be effectively used for further simulation and prediction. To ensure the finite element model was sufficiently accurate, it was compared with existing theoretical results calculated by the MATLAB codes in terms of longitudinal Young's modulus, transverse Young's modulus and shear modulus for long and short fiber for the elastic properties of the new Nanocomposite and for the thermal conductivity of the thermal properties of the Nanocomposite.

6.2 Validation of Elastic Properties of Carbon Nanotubes Reinforced Metal Matrix Nanocomposite

The finite element results for elastic properties of carbon nanotubes reinforced metal matrixes Nanocomposite was determined by means of ANSYS-APDL macro and compared with the results obtained by MATLAB code based on rule of mixture theory.

6.2.1 Long Fiber Case

The finite element results show an acceptable agreement compared with the theoretical results. The deviation percentages were calculated for all cases and presented. It can be observed from the Figures 6.1, 6.2, and 6.3 that the elastic properties results of carbon nanotube reinforced iron matrix have an increasing trend with the increase of volume fractions of carbon nanotube, while Figure 6.4 shows constant trend for major Poisson's ratio because the value of both iron matrix and the carbon nanotube is the same. The results are in good agreement for the finite element results compared to those of rule of mixture. It can be observed that finite element

prediction shows higher value than theoretical results for carbon nanotube reinforced Iron matrix as presented in Table 6.1. the variation range is 0.5 to less than 2% for any of the elastic properties.

Table 6.1: Validation of elastic properties for carbon nanotube reinforced iron metal matrix

Vol. (%)	Longitudinal Young's Modulus (E_L)(GPa)		Transverse Young's Modulus (E_T) (GPa)		Shear Modulus (G) (GPa)		Percent Deviation (%)		
	Theoretical	FEA	Theoretical	FEA	Theoretical	FEA	E_L	E_T	G
3%	233.7	234.9	215.1	216.6	84.1	84.5	-0.5%	-0.7%	-0.5%
7%	265.3	268.1	222.3	225.5	87.1	87.9	-1.1%	-1.4%	-0.9%
11%	296.9	301.3	230.0	234.3	90.3	91.2	-1.5%	-1.9%	-1.0%

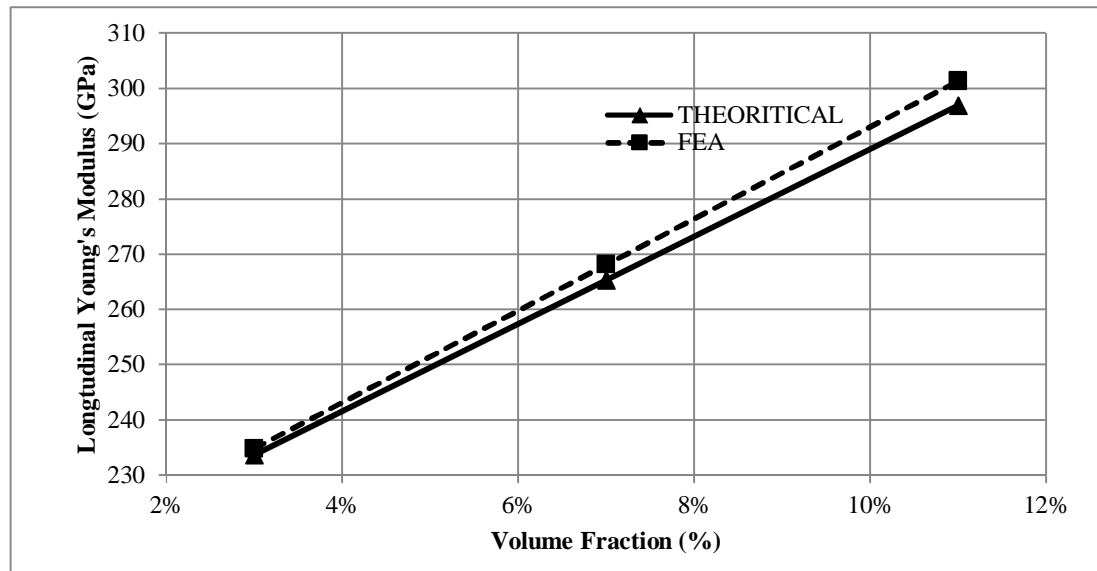


Figure 6.1: Longitudinal Young's modulus for carbon nanotube reinforced Iron metal matrix validation

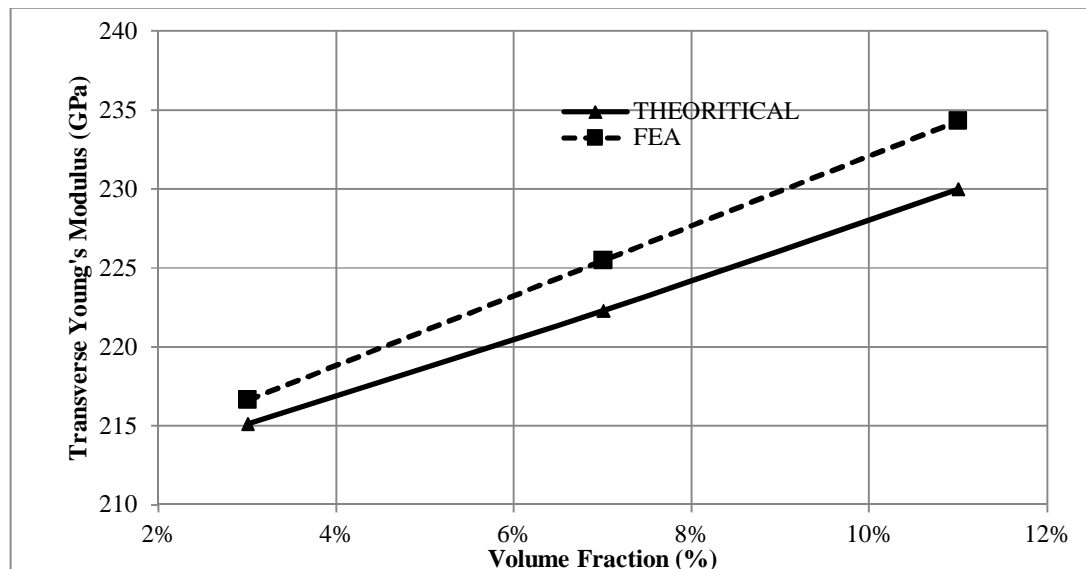


Figure 6.2: Transverse Young's modulus for carbon nanotube reinforced iron metal matrix validation

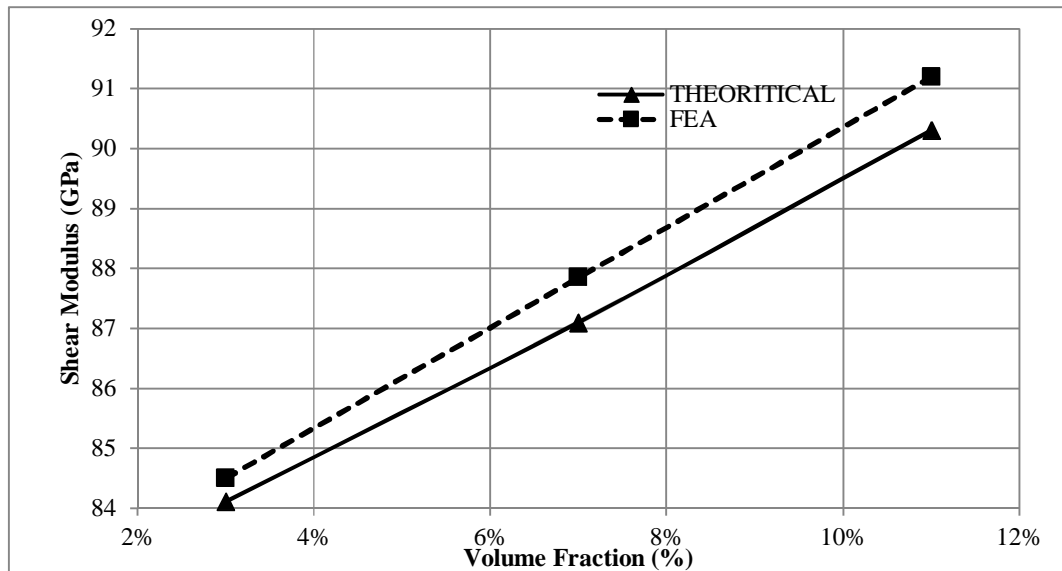


Figure 6.3: Shear modulus for carbon nanotube reinforced iron metal matrix validation

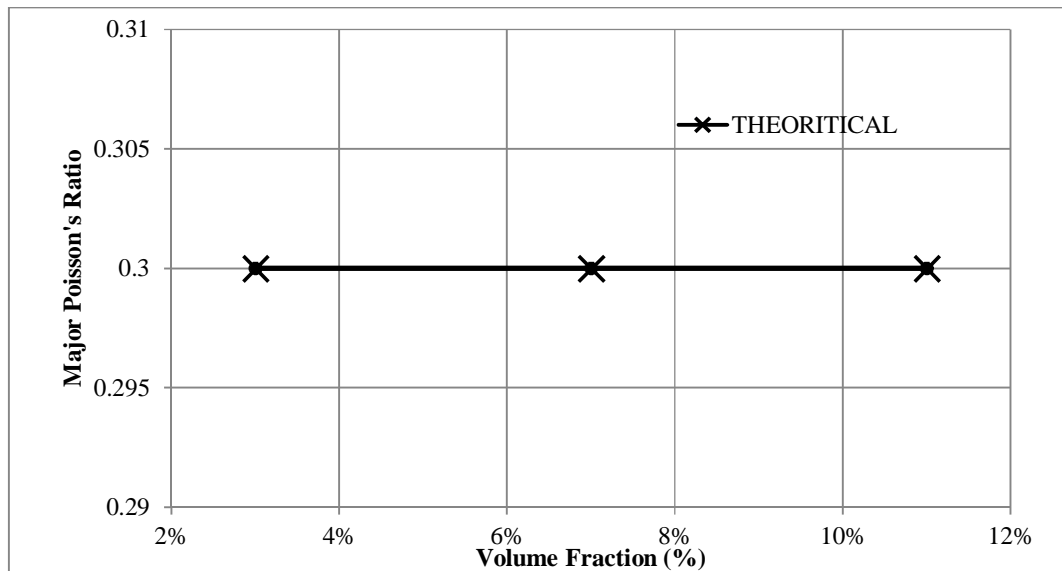


Figure 6.4: Major Poisson's ratio for carbon nanotube reinforced iron metal matrix validation

Similarly, for carbon nanotube reinforced copper matrix. It can be observed from the Figures 6.5, 6.6, and 6.7 that the elastic properties results of carbon nanotube reinforced copper matrix have an increasing trend with the increase in volume fraction of carbon nanotube, while Figure, 6.8 shows decreasing trend for major Poisson's ratio. The results are in good agreement for the finite element results compared to those of rule of mixture. It can be observed that finite element prediction shows higher value than theoretical results for carbon nanotube reinforced copper matrix as presented in Table 6.2.

Table 6.2: Validation of elastic properties for carbon nanotube reinforced copper metal matrix

Vol. (%)	Longitudinal Young's Modulus (E_L)(GPa)		Transverse Young's Modulus (E_T)(GPa)		Shear Modulus (G)(GPa)		Percent Deviation (%)		
	Theoretical	FEA	Theoretical	FEA	Theoretical	FEA	E_L	E_T	G
3%	156.1	157.7	133.5	136.2	49.3	50.3	-1.0%	-2.1%	-2%
7%	190.9	192.2	138.4	144.6	51.2	52.2	-0.7%	-4.4%	-2%
11%	225.7	227.8	143.8	152.9	53.30	54.3	-0.9%	-6.3%	-1.9%

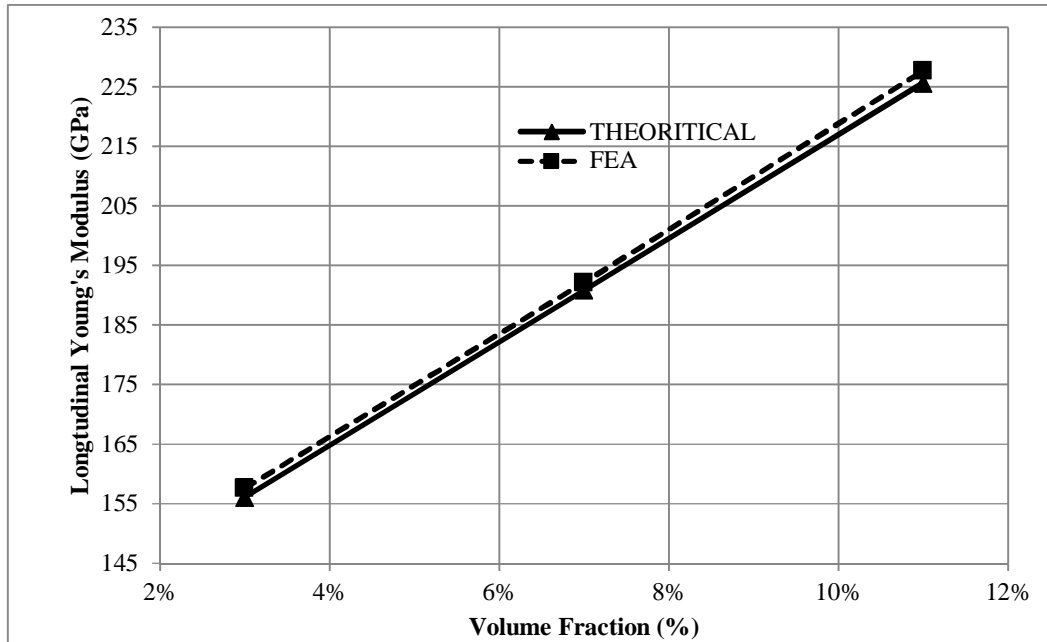


Figure 6.5: Longitudinal Young's modulus for carbon nanotube reinforced copper metal matrix validation

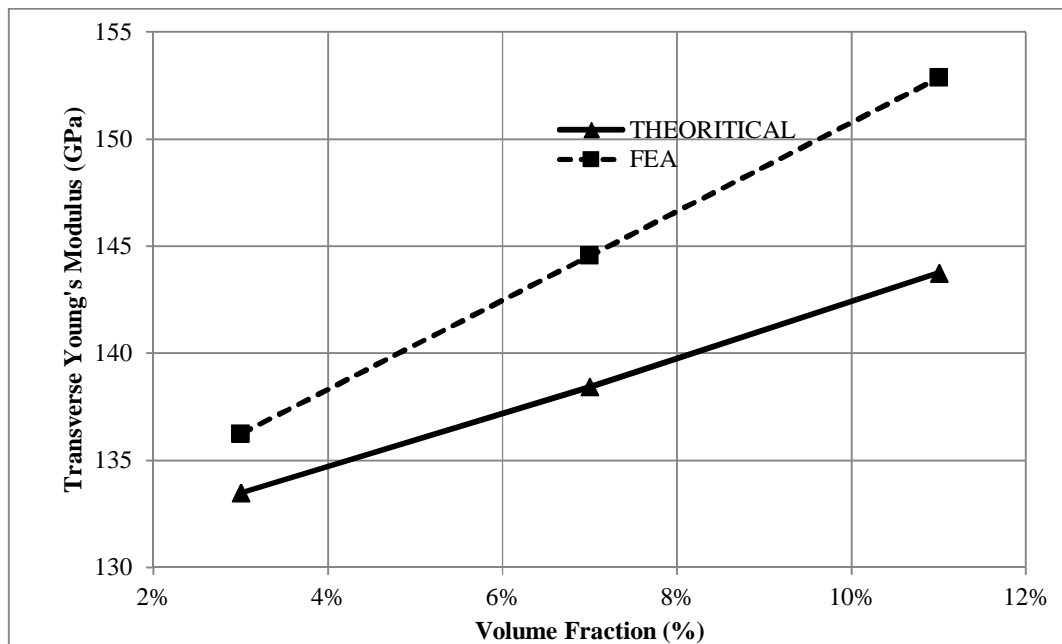


Figure 6.6: Transverse modulus for carbon nanotube reinforced copper metal matrix validation

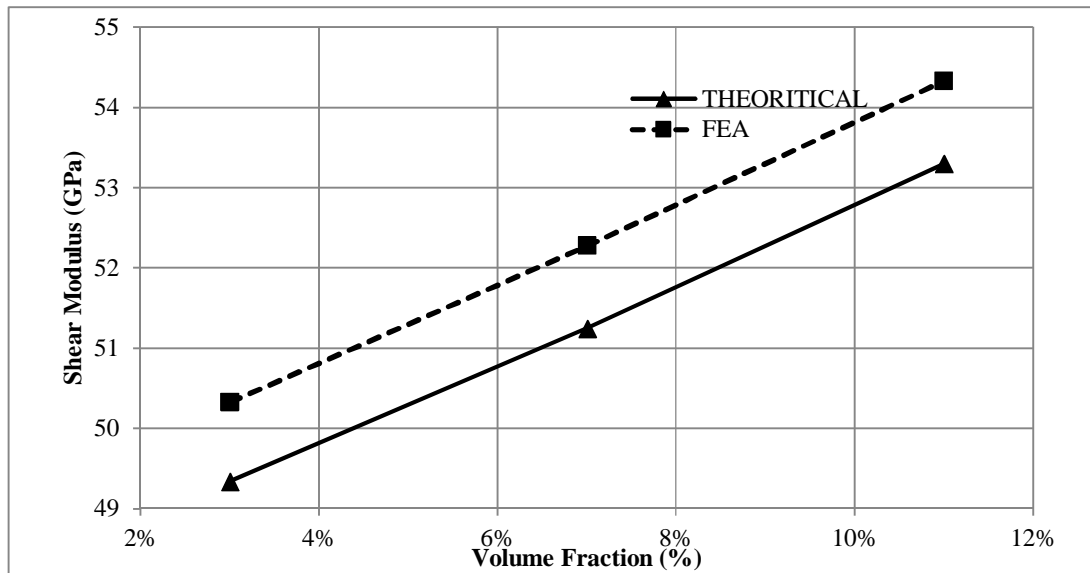


Figure 6.7: Shear modulus for carbon nanotube reinforced copper metal matrix validation

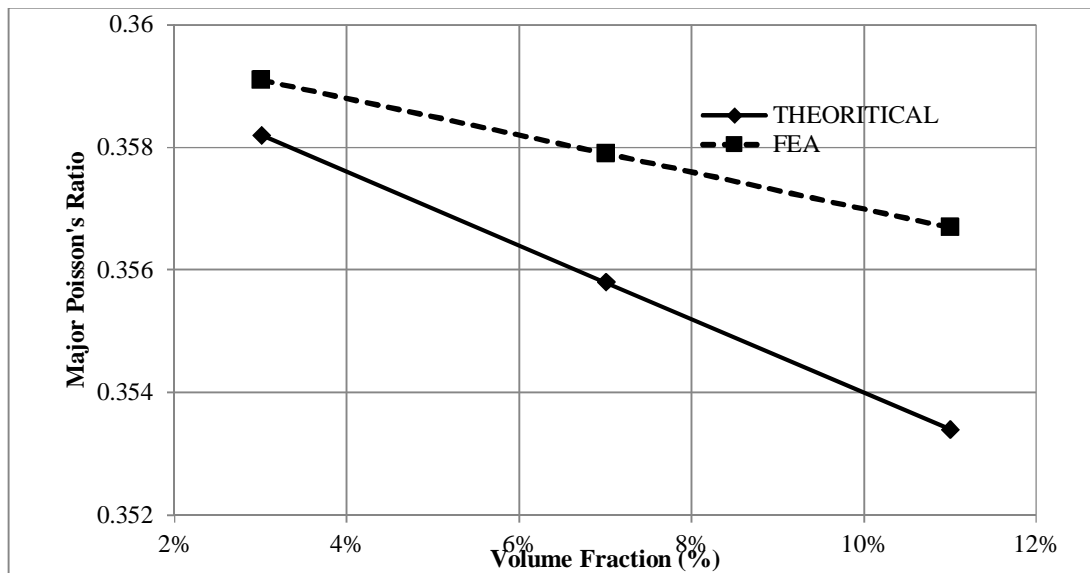


Figure 6.8: Major Poisson's ratio for carbon nanotube reinforced copper metal matrix validation

However, for carbon nanotube reinforced aluminum matrix; It can be observed from the Figures 6.9, 6.10, and 6.11 that the elastic properties results of carbon nanotube reinforced aluminum matrix have an increasing trend with the increase in volume fraction of carbon nanotube for different chiral indices while Figure, 6.12 shows decreasing trend for major Poisson's ratio. The results are in good agreement for the finite element results compared to those of rule of mixture. It can be observed that finite element prediction shows higher value than theoretical results for carbon nanotube reinforced aluminum matrix for transverse and shear modulus, while lower values than theoretical results for longitudinal modulus as presented in Table 6.3.

Table 6.3: Validation of elastic properties for carbon nanotube reinforced aluminum metal matrix

Vol. (%)	Longitudinal Young's Modulus (E_L)(GPa)		Transverse Young's Modulus (E_T)(GPa)		Shear Modulus (G)(GPa)		Percent Deviation (%)		
	Theoretical	FEA	Theoretical	FEA	Theoretical	FEA	E_L	E_T	G
3%	97.9	94.96	72.01	74.74	26.76	26.9	-3%	4%	1%
7%	135.1	114.91	74.87	77.54	27.85	28.4	-15%	4%	2%
11%	172.3	134.86	77.98	81.79	29.03	30.1	-22%	-%	4%

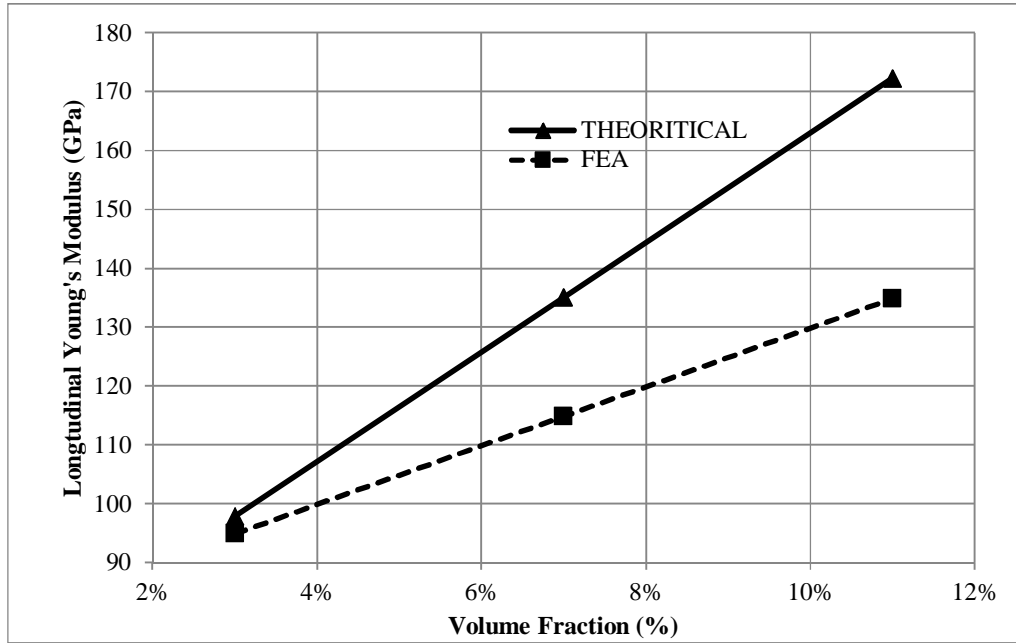


Figure 6.9: Longitudinal Young's modulus for carbon nanotube reinforced aluminum metal matrix validation

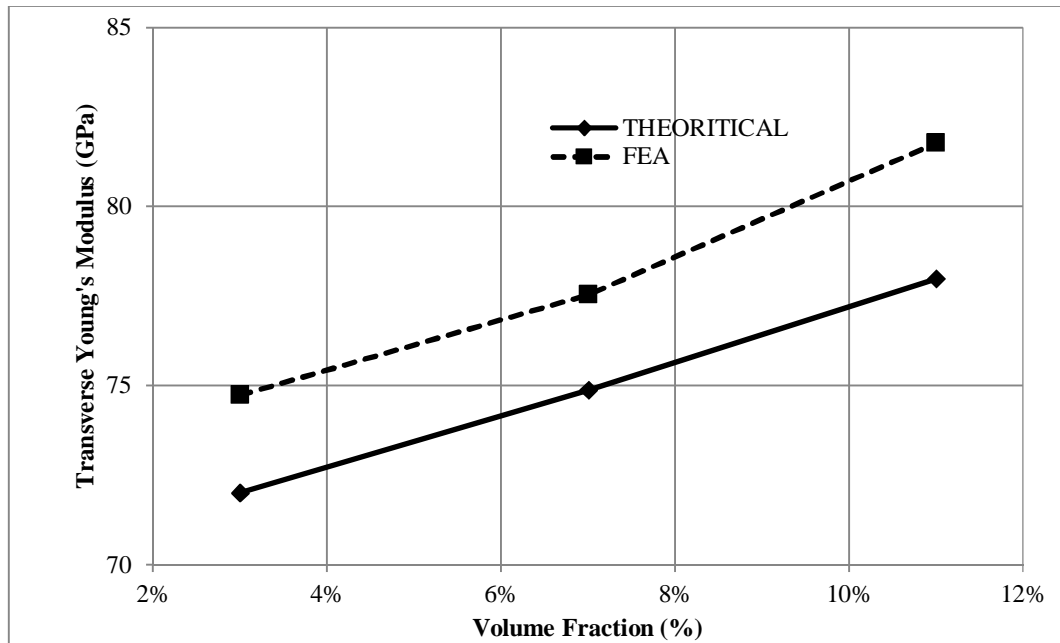


Figure 6.10: Transverse modulus for carbon nanotube reinforced aluminum metal matrix validation

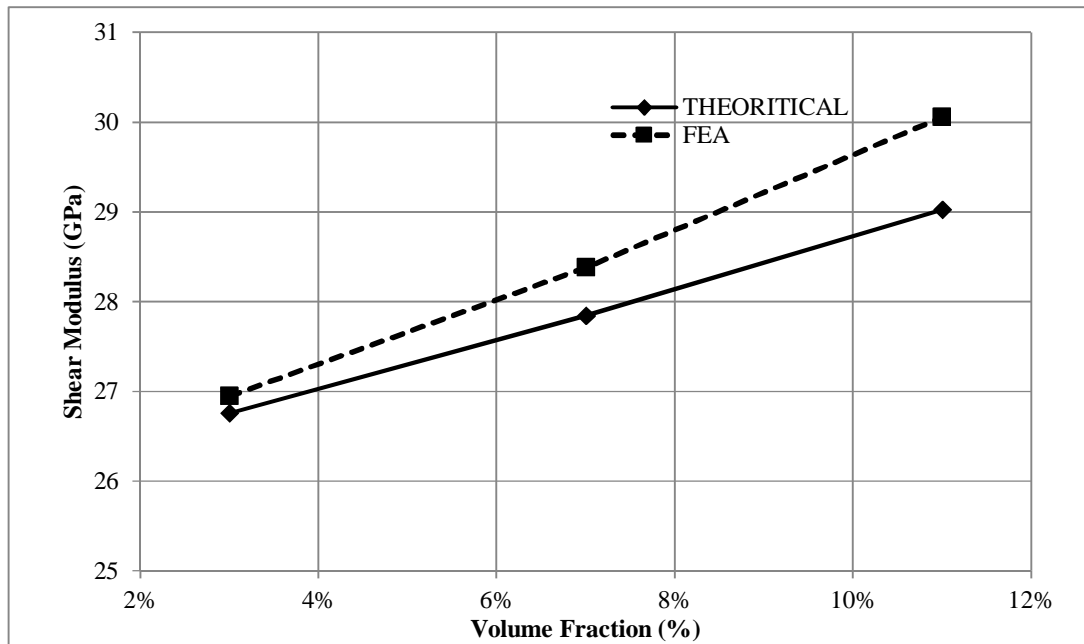


Figure 6.11: Shear modulus for carbon nanotube reinforced aluminum metal matrix validation

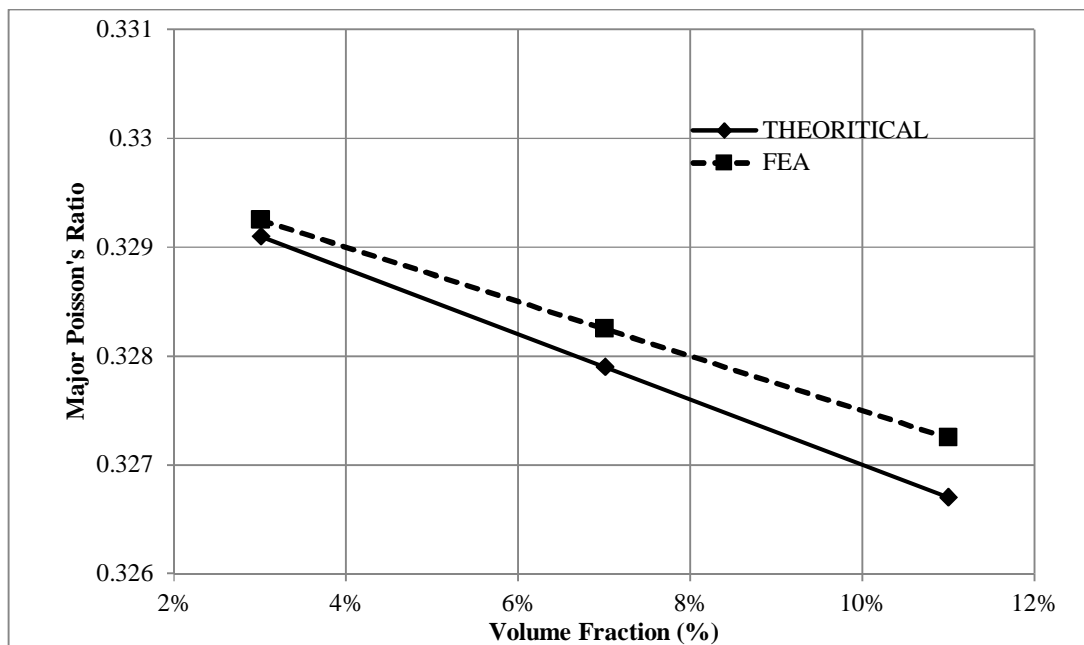


Figure 6.12: Major Poisson's ratio for carbon nanotube reinforced aluminum metal matrix validation

The results for longitudinal Young's modulus shows high deviation at volume fraction of 11% because the theoretical results corresponds to the rule of mixtures which the property of a composition can be calculated as the sum of its constituent material properties multiplied by the corresponding volume fractions.

6.2.2 Short Fiber Case

The finite element results show an acceptable agreement compared with the theoretical results. The deviation percentage were calculated for all cases and presented.

6.2.2.1 Longitudinal Young's Modulus

Longitudinal modulus of composite is the ratio of longitudinal stress to the longitudinal strain. It can be observed from the Figures 6.13, 6.14, 6.15 that the longitudinal modulus results of different chiral index of carbon nanotube treated as short fiber reinforced iron matrix have an increasing trend with the increase in volume fraction. The results are in good agreement for the finite element results compared to those of rule of mixture. It can be observed that finite element prediction shows lower values than theoretical results for different chiral index of carbon nanotube reinforced Iron matrix as presented in Table 6.4 (a), (b), and (c) respectively.

Table 6.4: Validation of longitudinal Young's Modulus for carbon nanotube (a) armchair, (b) zigzag, and (c) chiral treated as short fiber reinforced iron metal matrix

(a) Armchair

Vol. (%)	Longitudinal Young's Modulus (GPa)						Percent Deviation (%)		
	$l_c=3$		$l_c=5$		$l_c=8$		$l_c=3$	$l_c=5$	$l_c=8$
	Theoretical	FEA	Theoretical	FEA	Theoretical	FEA			
3%	227.3	225.7	229.2	226.6	230.6	227.9	-0.7%	-1.2%	-1.2%
7%	250.8	246.7	255.2	248.7	258.4	251.9	-1.7%	-2.6%	-2.6%
11%	274.9	267.7	281.7	270.8	286.5	275.8	-2.7%	-4.0%	-3.9%

(b) Zigzag

Vol. (%)	Longitudinal Young's Modulus (GPa)						Percent Deviation (%)		
	$l_c=3$		$l_c=5$		$l_c=8$		$l_c=3$	$l_c=5$	$l_c=8$
	Theoretical	FEA	Theoretical	FEA	Theoretical	FEA			
3%	229.4	228.5	230.8	229.6	231.8	230.8	-0.4%	-0.5%	-0.4%
7%	255.5	253.2	258.9	255.8	261.0	258.5	-0.9%	-1.2%	-1.0%
11%	282.1	277.9	287.2	282.0	290.5	286.3	-1.5%	-1.8%	-1.4%

(c) Chiral

Vol. (%)	Longitudinal Young's Modulus (GPa)						Percent Deviation (%)		
	$l_c=3$		$l_c=5$		$l_c=8$		$l_c=3$	$l_c=5$	$l_c=8$
	Theoretical	FEA	Theoretical	FEA	Theoretical	FEA			
3%	225.4	224.5	227.7	226.1	229.4	227.6	-0.4%	-0.7%	-0.8%
7%	246.5	243.8	251.6	247.5	255.6	251.1	-1.1%	-1.6%	-1.8%
11%	268.2	263.1	276.1	268.9	282.2	274.6	-1.9%	-2.6%	-2.7%

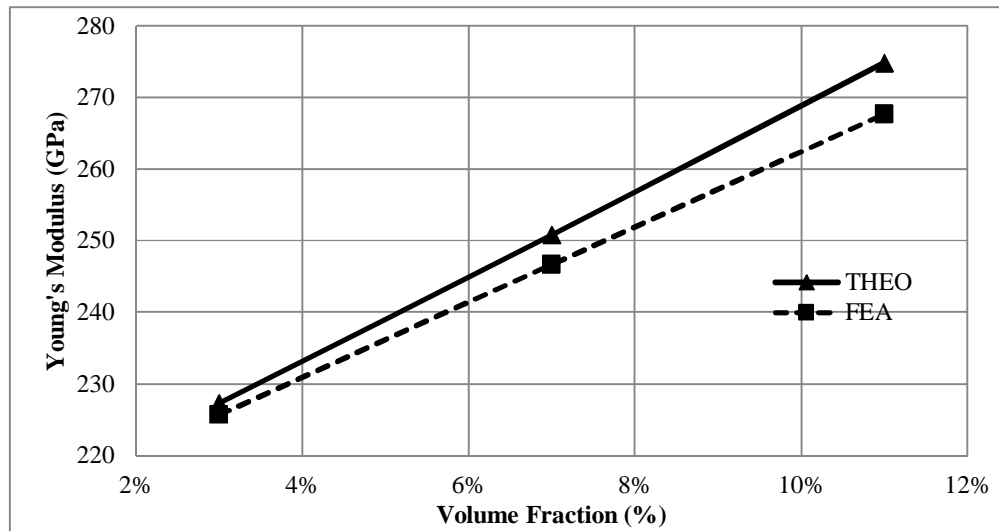


Figure 6.13: Validation of longitudinal Young's modulus for armchair (5, 5) carbon nanotubes reinforced iron metal matrix ($l_c=3\text{nm}$)

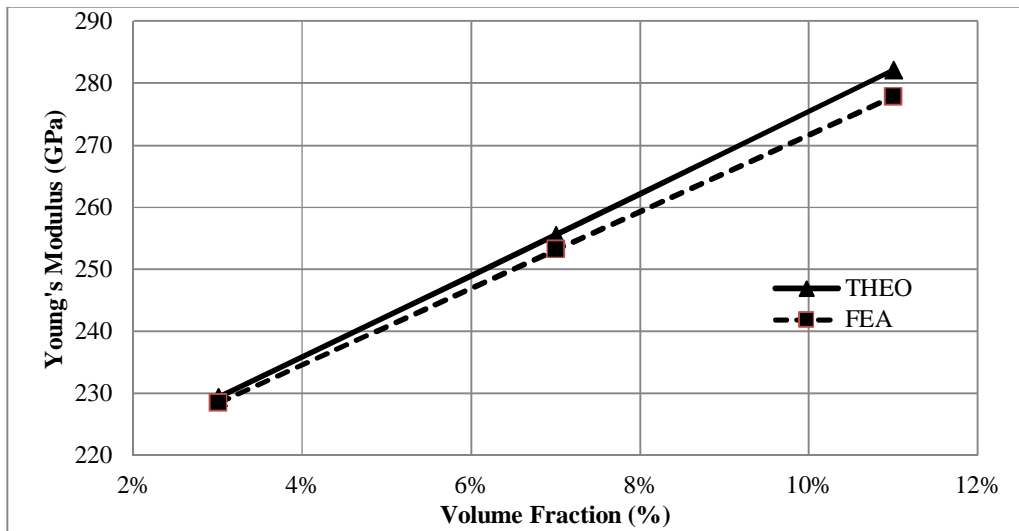


Figure 6.14: Validation of longitudinal Young's modulus for zigzag (5, 0) carbon nanotubes reinforced iron metal matrix ($l_c=3\text{nm}$)

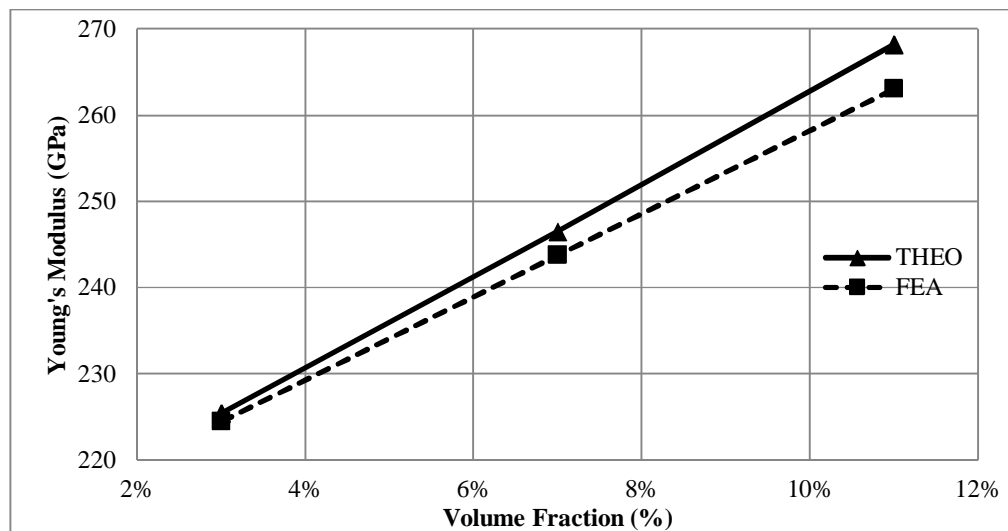


Figure 6.15: Validation of longitudinal Young's modulus for chiral (5, 10) carbon nanotubes reinforced iron metal matrix ($l_c=3\text{nm}$)

Similarly, the finite element results show an acceptable agreement compared with the theoretical results for carbon nanotubes treated as short fiber reinforced copper matrix. It can be observed from the Figures 6.16, 6.17, 6.18 that the longitudinal modulus results of different chiral indices of carbon nanotube treated as short fiber reinforced Copper matrix have an increasing trend with the increase in volume fraction. The results are in good agreement for the finite element results compared to those of rule of mixture. It can be observed that finite element prediction shows higher values than theoretical results for different chiral index of carbon nanotube reinforced copper matrix as presented in Table 6.5 (a), (b), and (c) respectively.

Table 6.5: Validation of longitudinal Young's modulus carbon nanotube (a) armchair, (b) zigzag, and (c) chiral treated as short fiber reinforced copper metal matrix

(a) Armchair

Vol. (%)	Longitudinal Young's Modulus (GPa)						Percent Deviation (%)		
	$l_c=3$		$l_c=5$		$l_c=8$		$l_c=3$	$l_c=5$	$l_c=8$
	Theoretical	FEA	Theoretical	FEA	Theoretical	FEA			
3%	145.7	146.5	148.5	149.1	150.7	151.1	0.5%	0.4%	0.3%
7%	167.3	168.4	173.7	174.6	178.6	179.3	0.7%	0.5%	0.4%
11%	189.6	190.4	199.4	200.1	207.0	207.5	0.4%	0.4%	0.2%

(b) Zigzag

Vol. (%)	Longitudinal Young's Modulus (GPa)						Percent Deviation (%)		
	$l_c=3$		$l_c=5$		$l_c=8$		$l_c=3$	$l_c=5$	$l_c=8$
	Theoretical	FEA	Theoretical	FEA	Theoretical	FEA			
3%	148.7	149.3	151.0	151.4	152.6	152.9	0.4%	0.3%	0.2%
7%	174.1	175.0	179.3	180.0	183.0	183.5	0.5%	0.4%	0.3%
11%	200.1	200.7	208.2	208.6	213.8	214.1	0.3%	0.2%	0.1%

(c) Chiral

Volume Fraction (%)	Longitudinal Young's Modulus (GPa)						Percent Deviation (%)		
	$l_c=3$		$l_c=5$		$l_c=8$		$l_c=3$	$l_c=5$	$l_c=8$
	Theoretical	FEA	Theoretical	FEA	Theoretical	FEA			
3%	143.3	144.1	146.2	146.9	148.7	149.3	0.6%	0.5%	0.4%
7%	161.8	162.9	168.4	169.5	174.2	175.1	0.7%	0.7%	0.5%
11%	181.0	181.8	191.4	192.1	200.3	200.9	0.4%	0.4%	0.3%

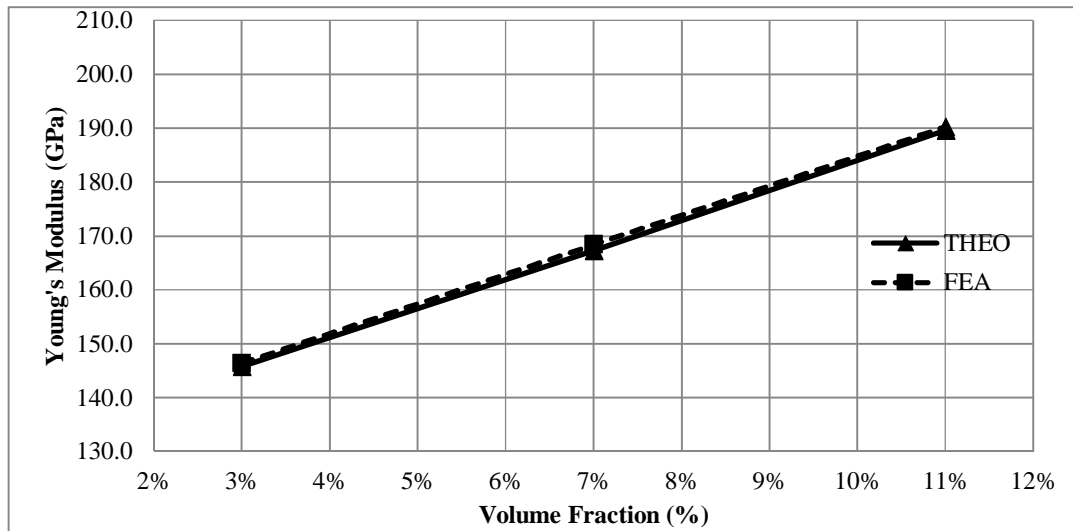


Figure 6.16: Validation of longitudinal Young's modulus for armchair (5, 5) carbon nanotubes reinforced copper metal matrix ($l_c=3\text{nm}$)

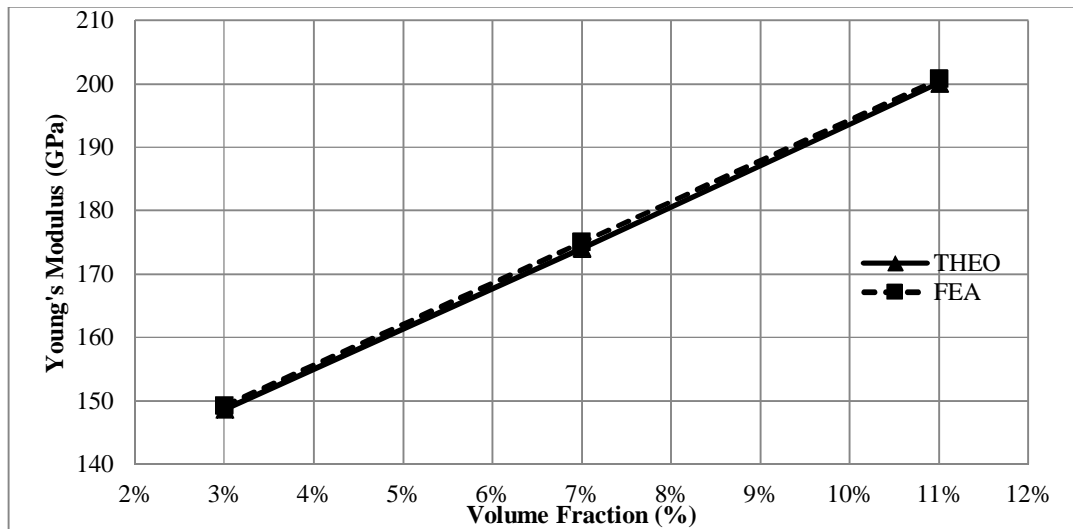


Figure 6.17: Validation of longitudinal Young's modulus for zigzag (5, 0) carbon nanotubes reinforced copper metal matrix ($l_c=3\text{nm}$)

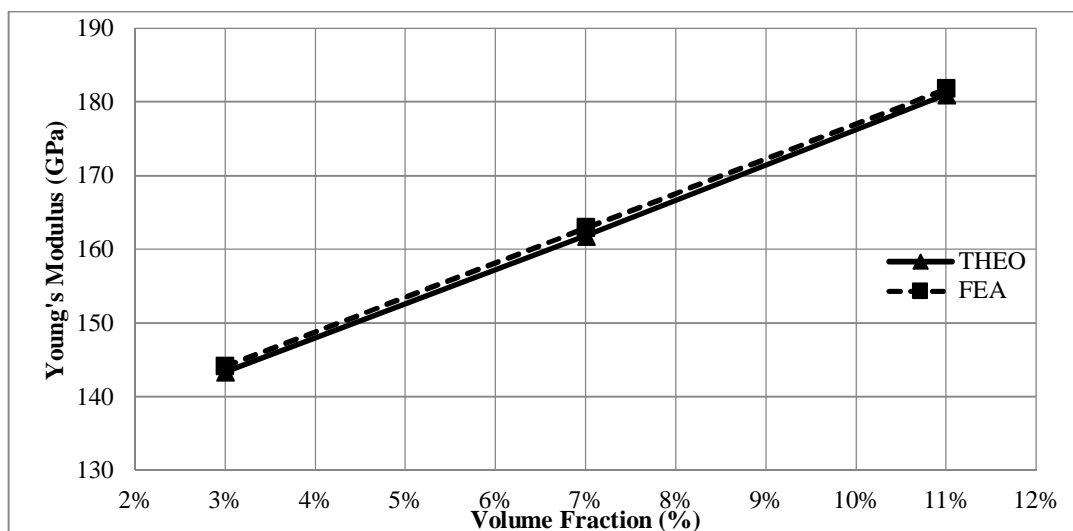


Figure 6.18: Validation of longitudinal Young's modulus for chiral (5, 10) carbon nanotubes reinforced copper metal matrix ($l_c=3\text{nm}$)

However, the finite element results show an acceptable agreement compared with the theoretical results for carbon nanotubes treated as short fiber reinforced aluminum matrix. It can be observed from the Figures 6.19, 6.20, 6.21 that the longitudinal modulus results of different chiral indices of carbon nanotube treated as short fiber reinforced aluminum matrix have an increasing trend with the increase in volume fraction. The results are in good agreement for the finite element results compared to those of rule of mixture. It can be observed that finite element prediction shows higher values than theoretical results for chiral carbon nanotube and lower values for armchair and zigzag carbon nanotube reinforced aluminum matrix as presented in Table 6.6 (a), (b), and (c) respectively.

Table 6.6: Validation of longitudinal Young's modulus for carbon nanotube (a) armchair, (b) zigzag, and (c) chiral treated as short fiber reinforced aluminum metal matrix

(a) Armchair

Volume Fraction (%)	Longitudinal Young's Modulus (GPa)						Percent Deviation (%)		
	$l_c=3$		$l_c=5$		$l_c=8$		$l_c=3$	$l_c=5$	$l_c=8$
	Theoretical	FEA	Theoretical	FEA	Theoretical	FEA			
3%	82.1	81.9	85.3	83.5	88.3	83.9	-0.2%	-2.2%	-5.2%
7%	98.9	98.1	106.5	101.6	113.3	102.5	-0.8%	-4.8%	-10.5%
11%	116.5	115.3	128.4	119.7	139.1	121.1	-1.0%	-7.3%	-14.9%

(b) Zigzag

Volume Fraction (%)	Longitudinal Young's Modulus (GPa)						Percent Deviation (%)		
	$l_c=3$		$l_c=5$		$l_c=8$		$l_c=3$	$l_c=5$	$l_c=8$
	Theoretical	FEA	Theoretical	FEA	Theoretical	FEA			
3%	85.59	83.5	88.8	84.1	91.3	84.5	-2.5%	-5.6%	-8.0%
7%	107.06	101.6	114.4	103.0	120.3	103.8	-5.4%	-11.1%	-15.9%
11%	129.33	119.7	140.8	121.9	149.8	123.2	-8.0%	-15.5%	-21.6%

(c) Chiral

Volume Fraction (%)	Longitudinal Young's Modulus (GPa)						Percent Deviation (%)		
	$l_c=3$		$l_c=5$		$l_c=8$		$l_c=3$	$l_c=5$	$l_c=8$
	Theoretical	FEA	Theoretical	FEA	Theoretical	FEA			
3%	79.6	82.4	82.6	83.0	83.5	85.6	3.4%	0.5%	2.5%
7%	93.1	98.9	100.1	100.2	101.4	107.2	5.9%	0.1%	5.4%
11%	107.3	115.4	117.5	118.5	119.4	129.5	7.0%	0.8%	7.8%

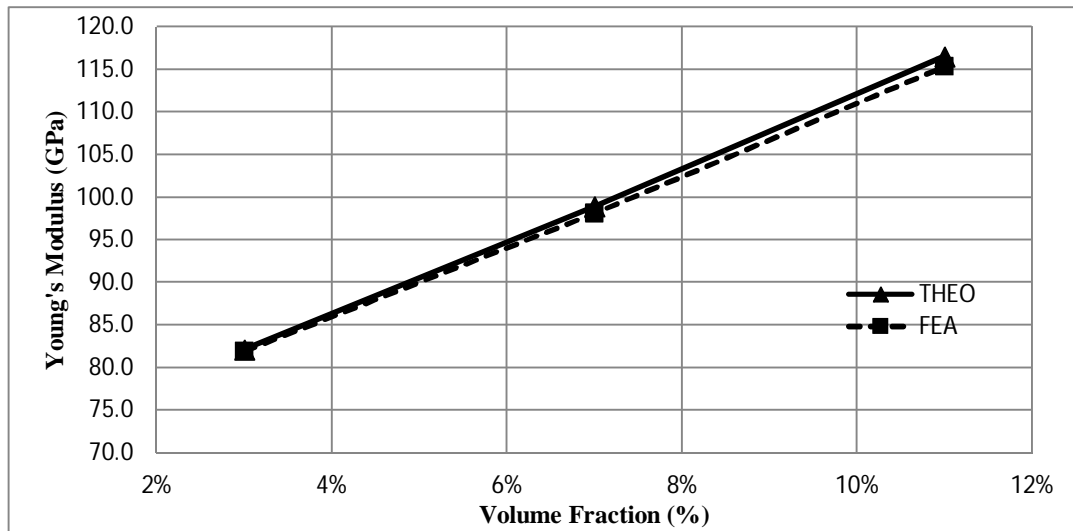


Figure 6.19: Validation of longitudinal Young's modulus for armchair (5, 5) carbon nanotubes reinforced aluminum metal matrix ($l_c=3\text{nm}$)

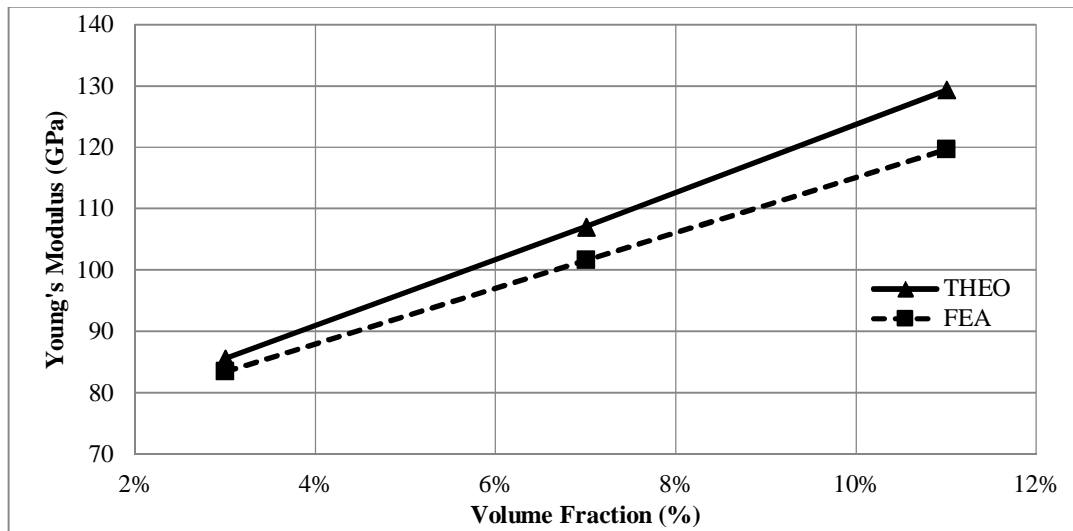


Figure 6.20: Validation of longitudinal Young's modulus for zigzag (5, 0) carbon nanotubes reinforced aluminum metal matrix ($l_c=3\text{nm}$)

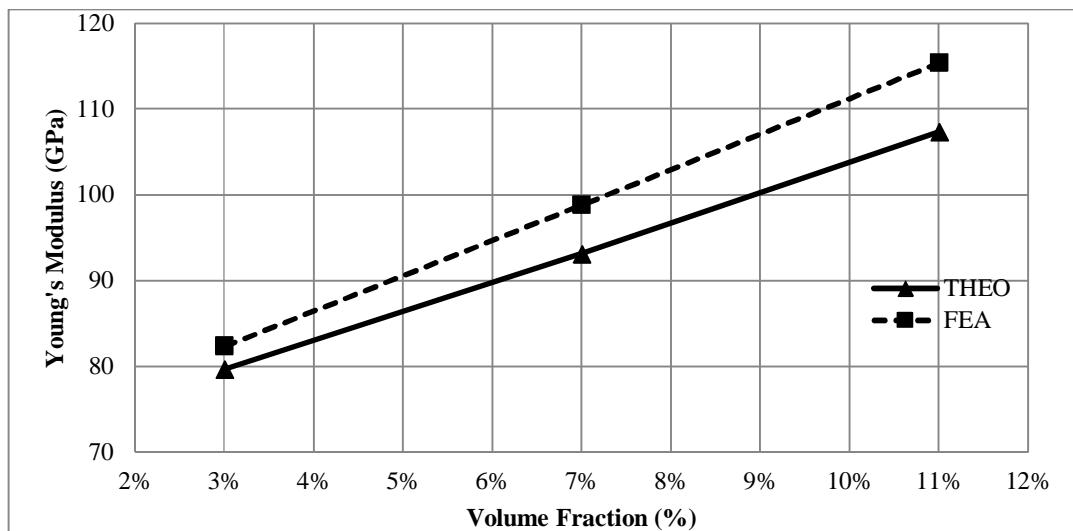


Figure 6.21: Validation of longitudinal Young's modulus for chiral (5, 10) carbon nanotubes reinforced aluminum metal matrix ($l_c=3\text{nm}$)

6.2.2.2 Transverse Modulus

Finite element results show an acceptable agreement with the theoretical results. The deviation percentage was calculated and presented. It can be observed from the Figure 6.22 that finite element results of armchair carbon nanotube treated as short fiber reinforced iron matrix shows higher values than theoretical results. It can be observed that, transverse modulus finite element prediction for copper and aluminum matrices show lower prediction as can be seen in Figures 6.23 and 6.24. The results are in good agreement compared to those of rule of mixture as presented in Tables 6.7 (a), (b), and (c), respectively. The results show increasing trend in linear manner while in reality it should be a nonlinear increase because the results are relatively close.

Table 6.7: Validation of Transverse modulus for armchair carbon nanotube reinforced (a) iron, (b) copper, and (c) aluminum metal matrix ($l_c=3$)

(a) Iron

Volume Fraction (%)	Transverse Modulus (GPa)		Percent Deviation (%)
	Theoretical	FEA	
3%	214.967	216.440	0.7%
7%	217.792	221.121	1.5%
11%	220.446	225.375	2.2%

(b) Copper

Volume Fraction (%)	Transverse Modulus (GPa)		Percent Deviation (%)
	Theoretical	FEA	
3%	138.2	135.5	-2.03%
7%	149.8	144.0	-4.01%
11%	162.1	154.4	-4.99%

(c) Aluminum

Volume Fraction (%)	Transverse Modulus (GPa)		Percent Deviation (%)
	Theoretical	FEA	
3%	75.3	72.9	-3.3%
7%	82.7	79.1	-4.5%
11%	90.7	87.1	-4.2%

6.2.2.3 Shear Modulus

Shear modulus of composite is the ratio of shear stress to the Shear strain. The finite element results show higher values compared to those of rule of mixture. It can be observed that deviation is high as presented in Table 6.8(a), (b), and (c), respectively, because of the theoretical prediction is very low since it depends on the fraction of shear modulus and volume fraction of matrix and reinforcement.

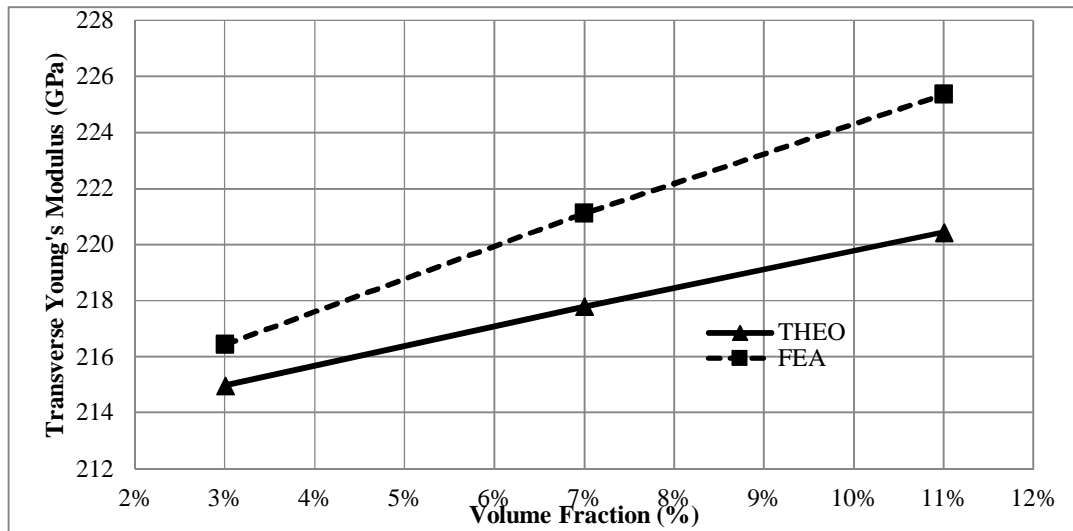


Figure 6.22: Validation of transverse modulus for carbon nanotubes treated as short fiber reinforced iron metal matrix

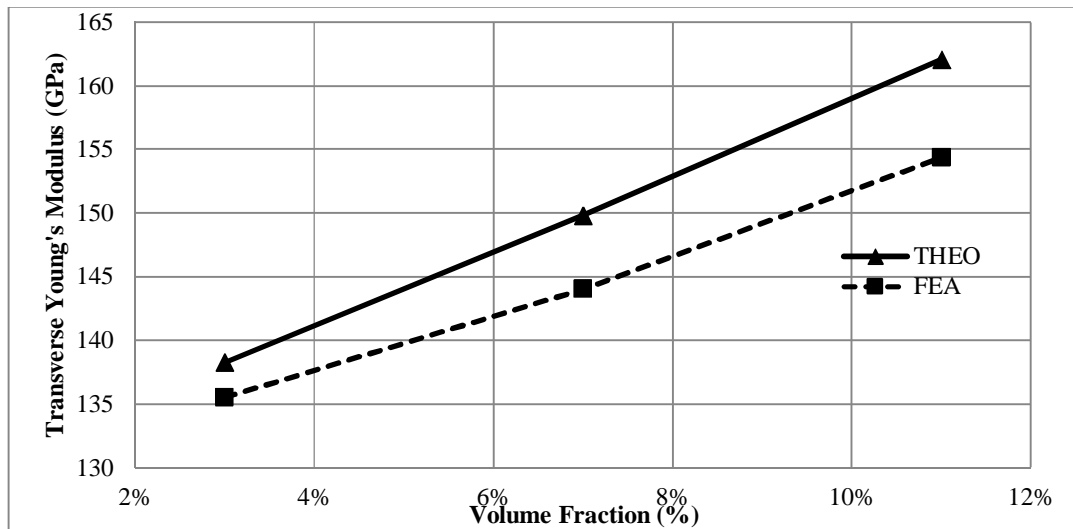


Figure 6.23: Validation of transverse modulus for carbon nanotubes treated as short fiber reinforced copper metal matrix

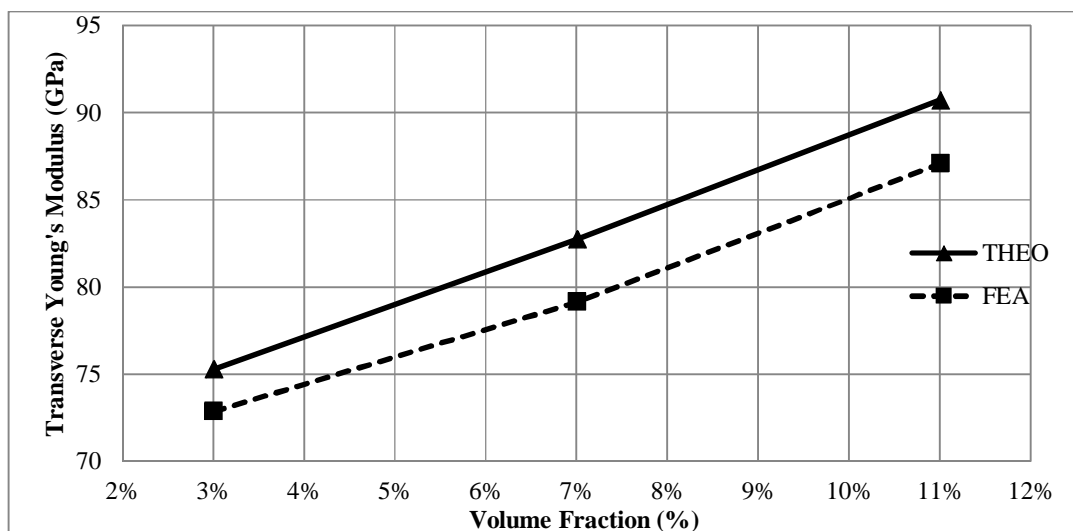


Figure 6.24: Validation of transverse modulus for carbon nanotubes treated as short fiber reinforced aluminum metal matrix

It can be observed from the Figure 6.25, 6.26, and 6.27 that the shear modulus results of carbon nanotube treated as short fiber reinforced Iron, Copper, and Aluminum matrixes have an increasing trend with the increase in volume fraction. The results show increasing trend in linear manner while in reality it should be a nonlinear increase because the results are relatively close.

Table 6.8: Validation of shear modulus for armchair carbon nanotube reinforced (a)iron, (b) copper, and (c) aluminum metal matrix (lc=3nm)

(a) Iron

Volume Fraction (%)	Shear Modulus (GPa)		Percent Deviation (%)
	Theoretical	FEA	
3%	49.4	82.8	40%
7%	51.6	83.8	38%
11%	54.0	84.7	36%

(b) Copper

Volume Fraction (%)	Shear Modulus (GPa)		Percent Deviation (%)
	Theoretical	FEA	
3%	27.3	48.6	43.8%
7%	28.7	50.9	43.5%
11%	30.2	53.8	43.9%

(c) Aluminum

Volume Fraction (%)	Shear Modulus (GPa)		Percent Deviation (%)
	Theoretical	FEA	
3%	14.2	26.1	46%
7%	15.0	26.9	44%
11%	15.9	27.7	43%

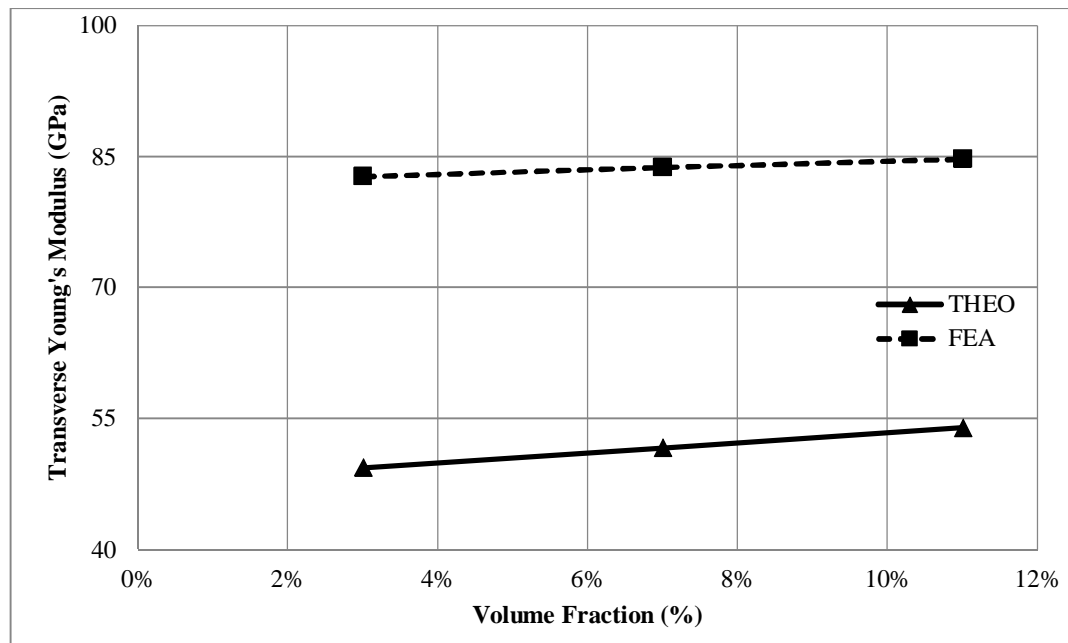


Figure 6.25: Validation of shear modulus for carbon nanotubes treated as short fiber reinforced iron metal matrix

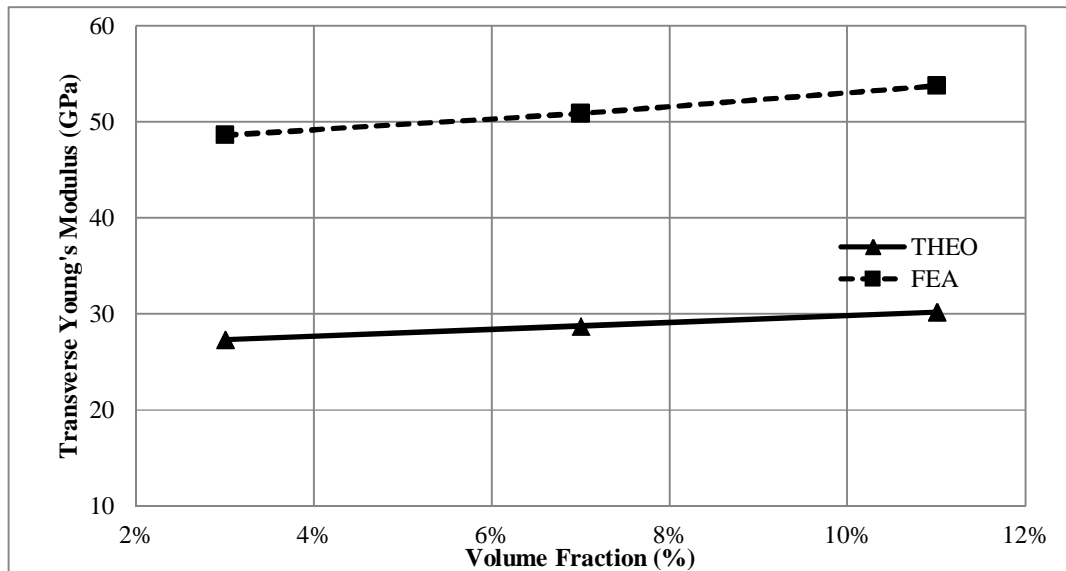


Figure 6.26: Validation of shear modulus for carbon nanotubes treated as short fiber reinforced copper metal matrix

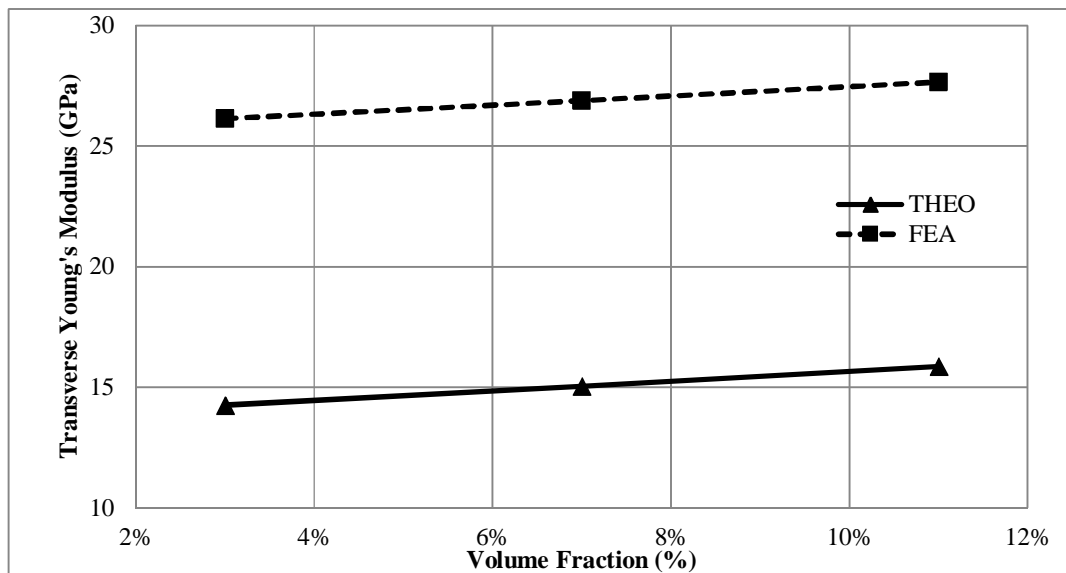


Figure 6.27: Validation of shear modulus for carbon nanotubes treated as short fiber reinforced aluminum metal matrix

6.3 Validation of thermal conductivity of carbon nanotubes reinforced metal matrix nanocomposite

The finite element results for thermal conductivity of carbon nanotubes reinforced metal matrixes Nanocomposite was determined by means of ANSYS-APDL macro and compared with the results obtained by MATLAB code based on rule of mixture theory. The results show an acceptable agreement and the deviation percentages are calculated for all cases.

6.3.1 Validation with existing theoretical models

Theoretical results obtained by using the MATLAB code are compared with some existing theoretical models. It can be seen that there are various factors which may contribute to lowering the effective thermal conductivity predicted by various theoretical models. The theoretical models are based on various assumptions and these assumptions also affect the effective conductivity obtained theoretically, experimentally and through computational methods. Figure 6.28, 6.29 and 6.30 show a comparison between the present model and these models for Aluminum, Copper and Iron metal matrixes Nanocomposite. The predicted results are thus in tune with these theoretical model findings [139]. This may be considered as an indirect verification of the accuracy of the code used and of the assumptions made. It may also be inferred that the predictions may be close to actual values of the effective longitudinal conductivity.

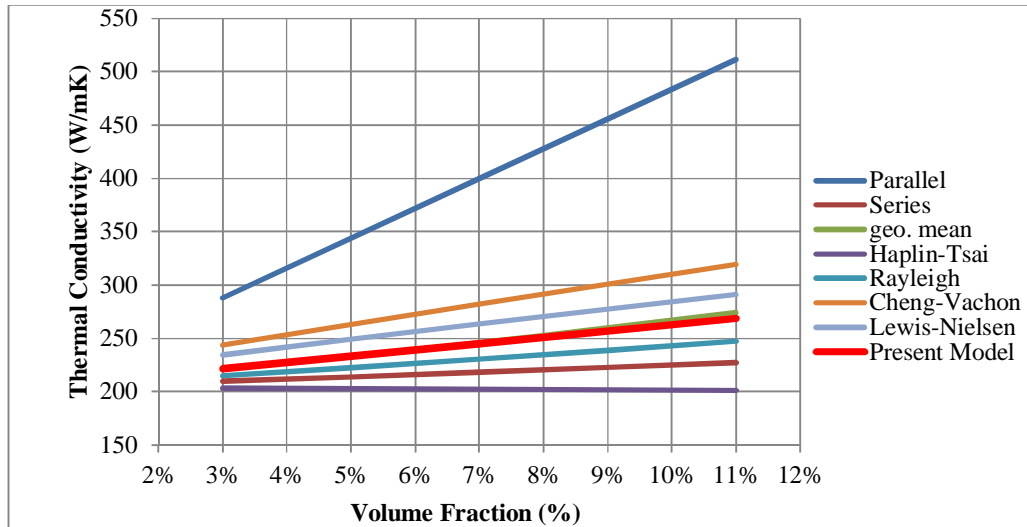


Figure 6.28: Comparison between the thermal conductivity models for carbon nanotube reinforced aluminum matrix

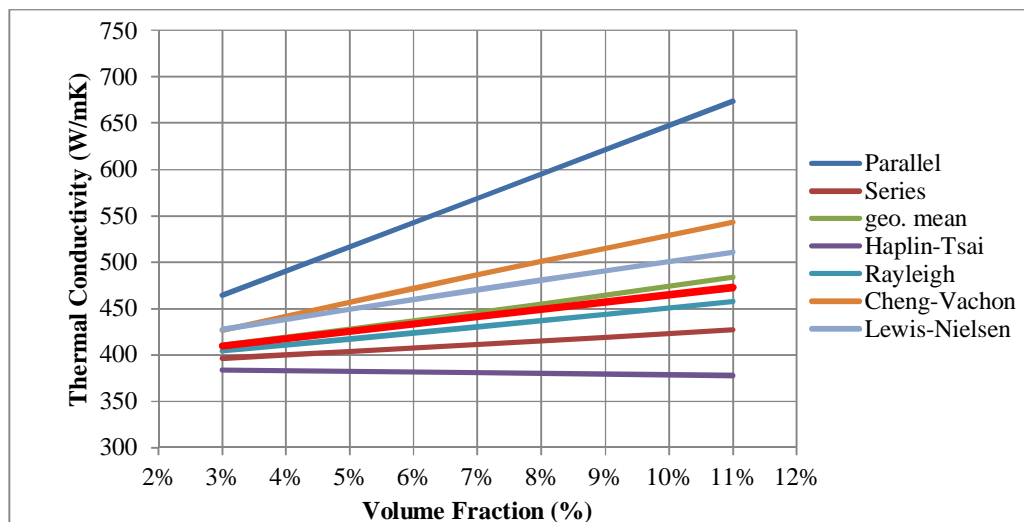


Figure 6.29: Comparison between the thermal conductivity models for carbon nanotube reinforced copper matrix

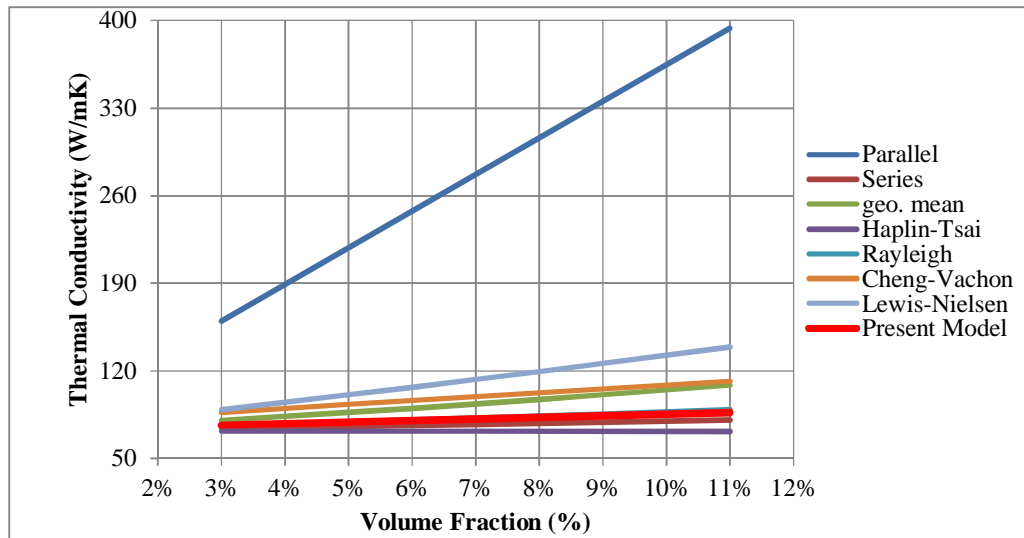


Figure 6.30: Comparison between the thermal conductivity models for carbon nanotube reinforced iron matrix

6.3.2 Validation of Thermal Conductivity of Carbon Nanotubes Reinforced Metal Matrix Nanocomposite

The finite element results for thermal conductivity of carbon nanotubes reinforced metal matrixes Nanocomposite was predicted by means of ANSYS-APDL macro and compared with the theoretical calculations made based on modified Bagchi and Nomura [87]. The results obtained were in agreeable range.

6.3.2.1 Long Fiber Case

The finite element results for model “A” and model “B” are in good and acceptable agreement compared to the theoretical results. It can be observed from the Figures 6.31, 6.32, 6.33 that the thermal conductivity results of armchair, zigzag, and chiral carbon nanotube treated as long fiber reinforced iron matrix have an increasing linearly with the increase in volume fraction of carbon nanotube. Finite element predictions for the two models show higher values than theoretical results. The deviation percentage were calculated for all cases and presented in Tables 6.9 (a), (b), and (c).

Table 6.9: Validation of thermal conductivity for (a) armchair (b) zigzag, and (c) chiral carbon nanotube treated as long fiber reinforced iron, metal matrix

(a) armchair

Vol. (%)	Theoretical (W/m K)	Finite Element (W/m K)		Deviation (%)	
		Model A	Model B	Model A	Model B
3%	76.5	78.2	79.0	2.2%	3.2%
7%	81.6	85.5	87.3	4.8%	7.0%
11%	86.7	92.8	95.6	7.1%	10.4%

(b) Zigzag

Vol. (%)	Theoretical (W/m K)	Finite Element (W/m K)		Deviation (%)	
		Model A	Model B	Model A	Model B
3%	77.6	78.6	79.2	1.3%	2.1%
7%	84.0	86.5	87.8	2.9%	4.5%
11%	90.5	94.3	96.4	4.2%	6.5%

(c) Chiral

Vol. (%)	Theoretical (W/m K)	Finite Element (W/m K)		Deviation (%)	
		Model A	Model B	Model A	Model B
3%	75.8	77.9	78.5	2.7%	3.6%
7%	80.0	84.8	86.3	6.0%	7.9%
11%	84.1	91.7	94.0	9.0%	11.8%

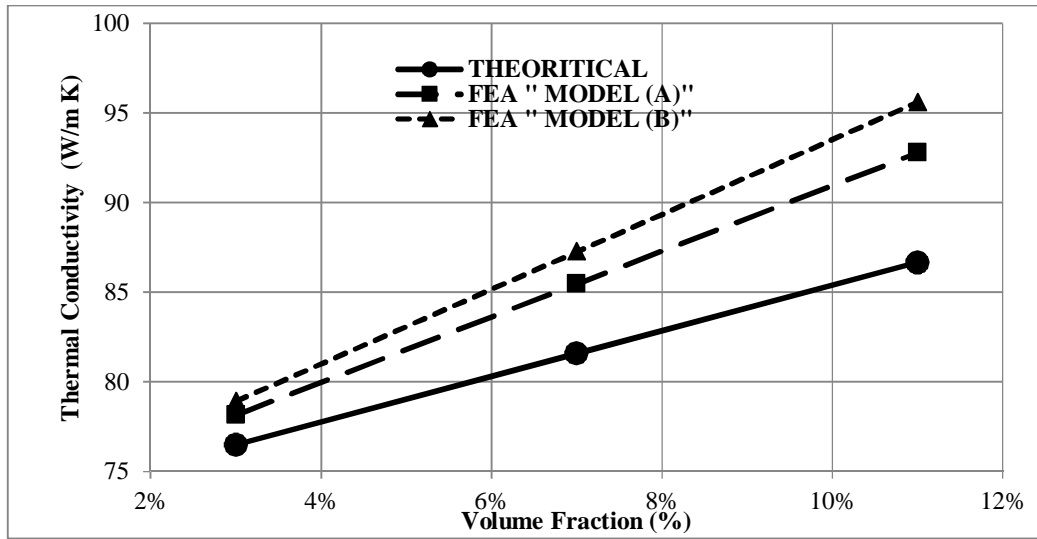


Figure 6.31: Validation of thermal conductivity of armchair carbon nanotube treated as long fiber reinforced iron metal matrix

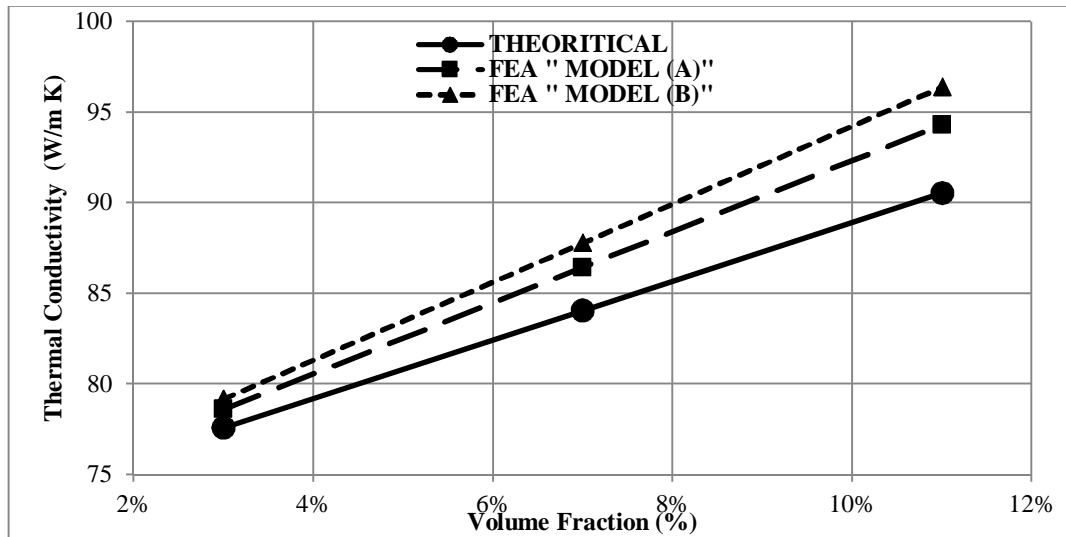


Figure 6.32: Validation of thermal conductivity of zigzag carbon nanotube treated as long fiber reinforced iron metal matrix

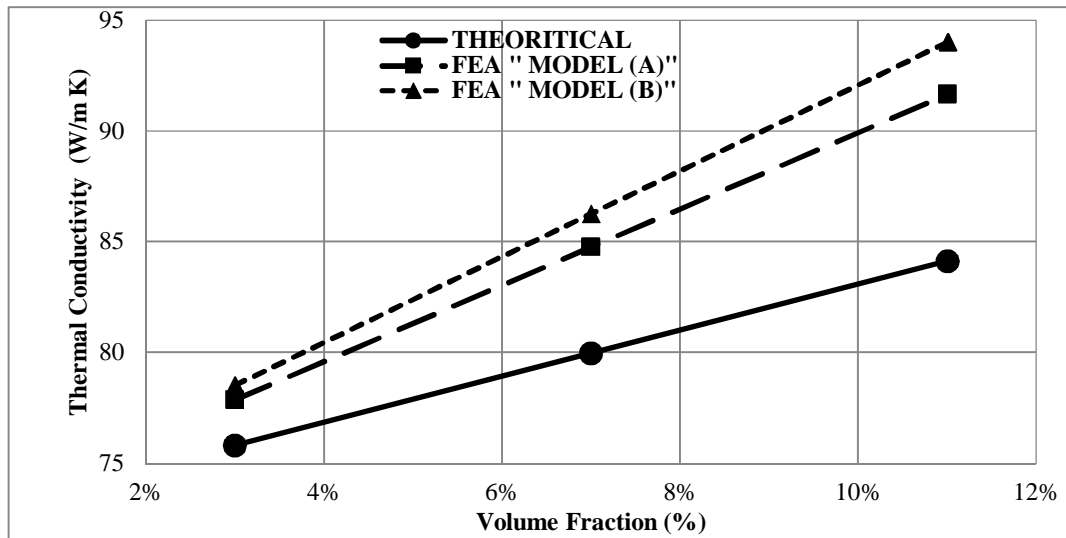


Figure 6.33: Validation of thermal conductivity of chiral carbon nanotube treated as long fiber reinforced iron metal matrix

Similarly, for carbon nanotube reinforced copper matrix. It can be observed from the Figures 6.34, 6.35, and 6.36 that the thermal conductivity results of armchair, zigzag, and chiral carbon nanotube treated as long fiber reinforced copper matrix have a linear increasing trend with the increase in volume fraction of carbon nanotube. Finite element predictions for the two models show higher value than theoretical results. The deviation percentage were calculated for all cases and presented in Tables 6.10 (a), (b), and (c).

Table 6.10: Validation of thermal conductivity for (a) armchair (b) zigzag, and (c) chiral carbon nanotube treated as long fiber reinforced copper metal matrix

(a) Armchair

Vol. (%)	Theoretical (W/m K)	Finite Element (W/m K)		Deviation (%)	
		Model A	Model B	Model A	Model B
3%	409.6	411.2	413.9	0.4%	1.0%
7%	441.2	444.8	451.1	0.8%	2.3%
11%	472.7	478.4	488.3	1.2%	3.3%

(b) Zigzag

Vol. (%)	Theoretical (W/m K)	Finite Element (W/m K)		Deviation (%)	
		Model A	Model B	Model A	Model B
3%	412.4	414.6	415.3	0.5%	0.7%
7%	447.6	452.8	454.3	1.2%	1.5%
11%	482.8	490.9	493.3	1.7%	2.2%

(c) Chiral

Vol. (%)	Theoretical (W/m K)	Finite Element (W/m K)		Deviation (%)	
		Model A	Model B	Model A	Model B
3%	404.7	410.6	412.4	1.4%	1.9%
7%	429.7	443.3	447.5	3.2%	4.2%
11%	454.6	476.1	482.7	4.7%	6.2%

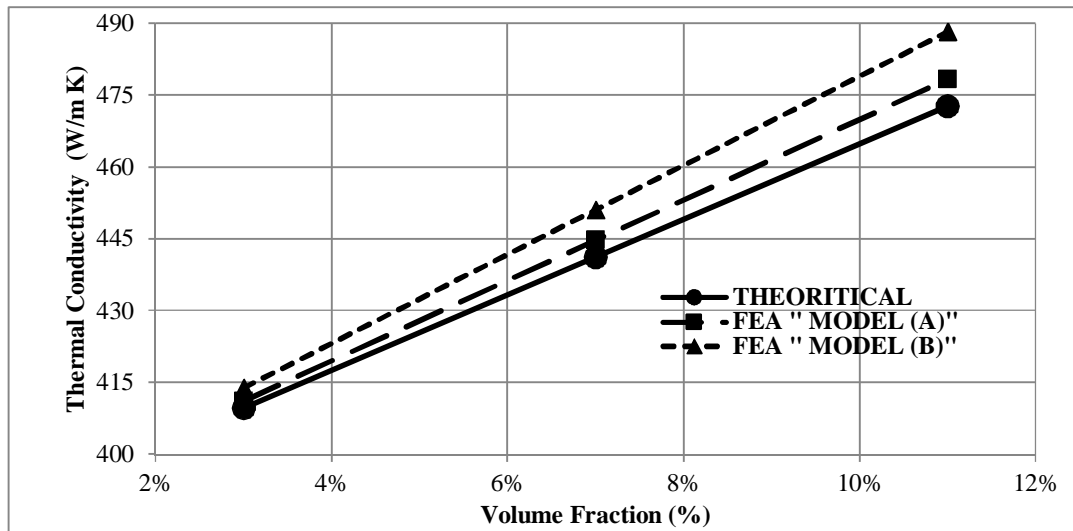


Figure 6.34: Validation of thermal conductivity of armchair carbon nanotube treated as long fiber reinforced copper metal matrix

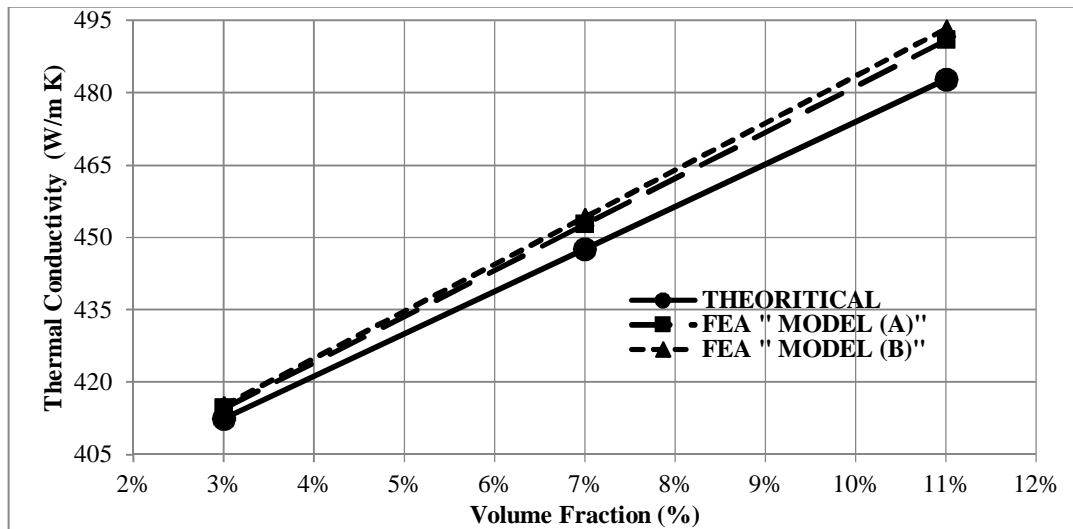


Figure 6.35: Validation of thermal conductivity of zigzag carbon nanotube treated as long fiber reinforced copper metal matrix

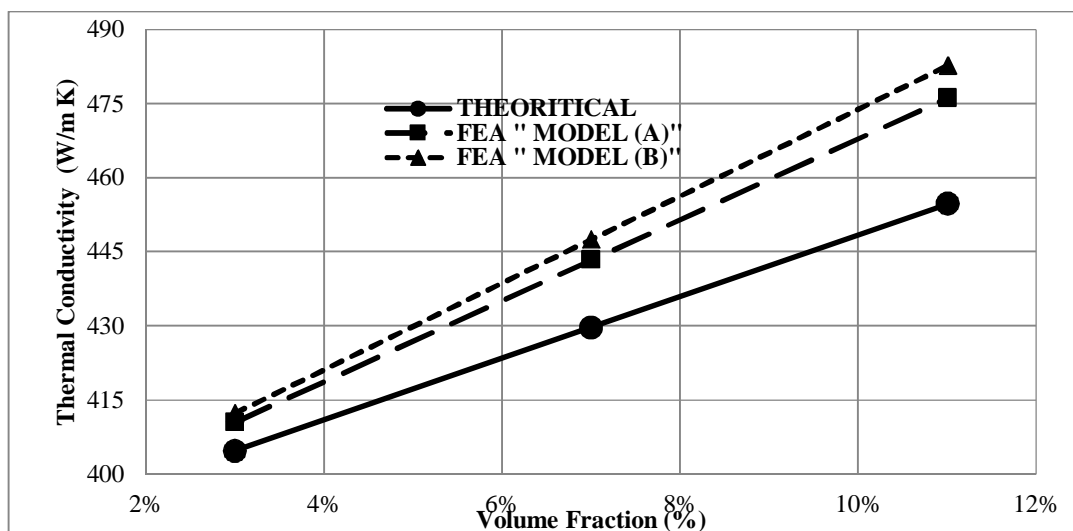


Figure 6.36: Validation of thermal conductivity of chiral carbon nanotube treated as long fiber reinforced copper metal matrix

However, for carbon nanotube reinforced aluminum matrix; It can be observed from the Figures 6.37, 6.38 and 6.39 that the thermal conductivity results of Armchair, Zigzag, and Chiral carbon nanotube treated as long fiber reinforced aluminum matrix have a linear increasing trend with the increase in volume fraction of carbon nanotube. Finite element predictions for the two models show higher value than theoretical results. The deviation percentage were calculated for all cases and presented in Tables 6.11 (a), b), and (c).

Table 6.11: Validation of thermal conductivity for (a) armchair (b) zigzag, and (c) chiral carbon nanotube treated as long fiber reinforced aluminum metal matrix

(a) Armchair

Vol. (%)	Theoretical (W/m K)	Finite Element (W/m K)		Deviation (%)	
		Model A	Model B	Model A	Model B
3%	221.6	223.3	224.4	0.7%	1.3%
7%	245.1	248.9	251.7	1.6%	2.7%
11%	268.6	274.7	278.9	2.3%	3.9%

(b) Zigzag

Vol. (%)	Theoretical (W/m K)	Finite Element (W/m K)		Deviation (%)	
		Model A	Model B	Model A	Model B
3%	223.6	224.6	225.6	0.4%	0.9%
7%	249.8	252.1	254.3	0.9%	1.8%
11%	275.9	279.5	283.1	1.3%	2.6%

(c) Chiral

Vol. (%)	Theoretical (W/m K)	Finite Element (W/m K)		Deviation (%)	
		Model A	Model B	Model A	Model B
3%	219.7	222.2	224.0	1.1%	2.0%
7%	240.7	246.5	250.7	2.4%	4.2%
11%	261.6	270.7	277.4	3.5%	6.0%

6.3.2.2 Short Fiber Case

(a) Effect of Volume Fraction

The finite element results for model “A” and model “B” are in good and acceptable agreement compared to the theoretical results. It can be observed from the Figures 6.40, 6.41, 6.42 at carbon nanotube length of 3 nm that the thermal conductivity results of Armchair, Zigzag, and Chiral carbon nanotube treated as short fiber reinforced iron matrix have linear increasing trend with the increase in volume fraction of carbon nanotube.

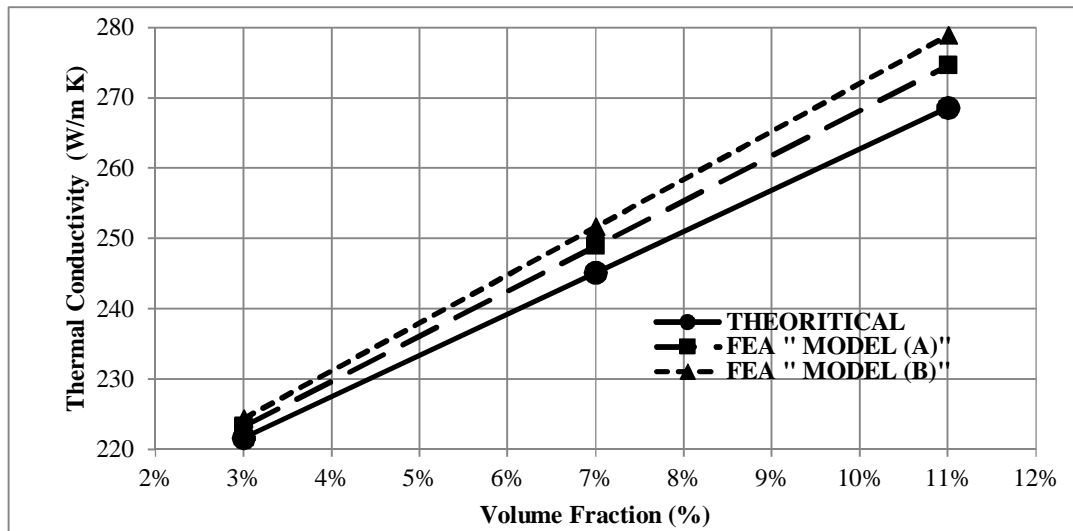


Figure 6.37: Validation of thermal conductivity of armchair carbon nanotube treated as long fiber reinforced aluminum metal matrix

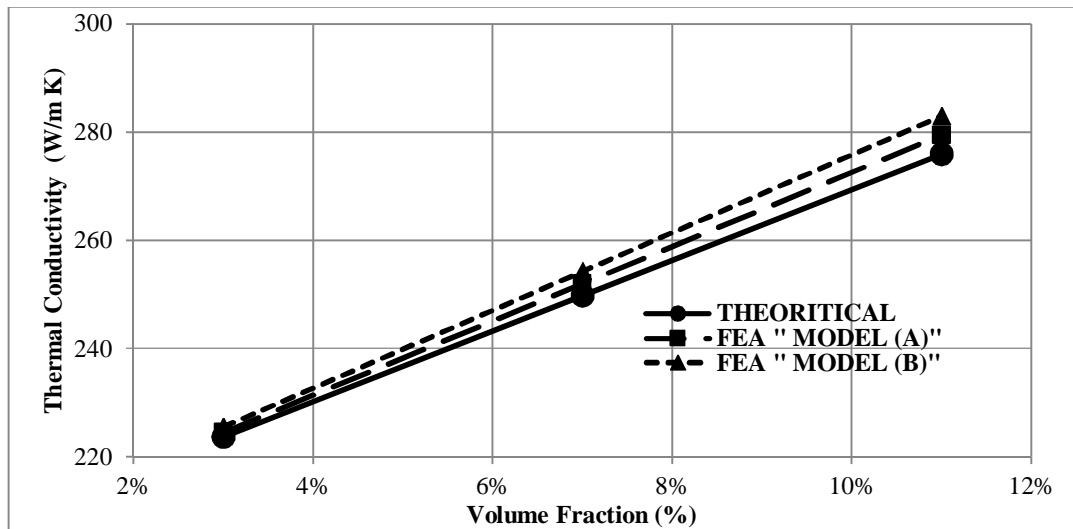


Figure 6.38: Validation of thermal conductivity of zigzag carbon nanotube treated as long fiber reinforced aluminum metal matrix

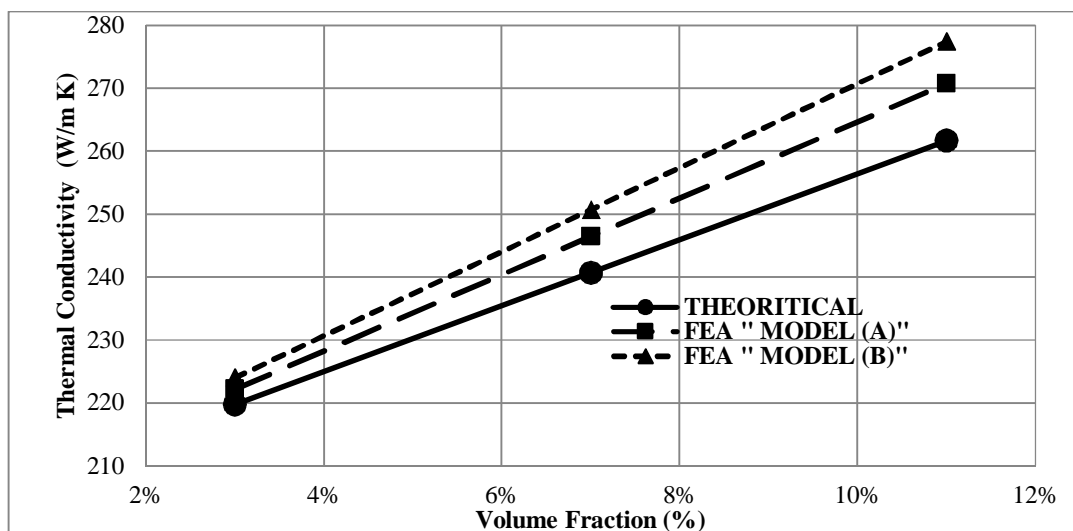


Figure 6.39: Validation of thermal conductivity of chiral carbon nanotube treated as long fiber reinforced aluminum metal matrix

Finite element predictions for the two models show lower prediction values than theoretical results. The deviation percentage were calculated for all cases and presented in Tables 6.12 (a), (b), and (c).

Table 6.12: Validation of thermal conductivity for (a) armchair (b) zigzag, and (c) chiral carbon nanotube reinforced iron metal matrix at $l_c=3\text{nm}$

(a) Armchair

Vol. (%)	Theoretical (W/m K)	Finite Element (W/m K)		Deviation (%)	
		Model A	Model B	Model A	Model B
3%	76.5	73.8	74.2	-3.6%	-3.1%
7%	81.6	75.2	76.1	-7.8%	-6.7%
11%	86.7	76.6	78.0	-11.6%	-10.0%

(b) Zigzag

Vol. (%)	Theoretical (W/m K)	Finite Element (W/m K)		Deviation (%)	
		Model A	Model B	Model A	Model B
3%	77.6	74.1	74.4	-4.4%	-4.1%
7%	84.0	76.1	76.6	-9.5%	-8.8%
11%	90.5	78.0	78.9	-13.9%	-12.8%

(c) Chiral

Vol. (%)	Theoretical (W/m K)	Finite Element (W/m K)		Deviation (%)	
		Model A	Model B	Model A	Model B
3%	75.8	73.6	74.0	-2.9%	-2.4%
7%	80.0	74.9	75.7	-6.4%	-5.4%
11%	84.1	76.1	77.4	-9.5%	-8.0%

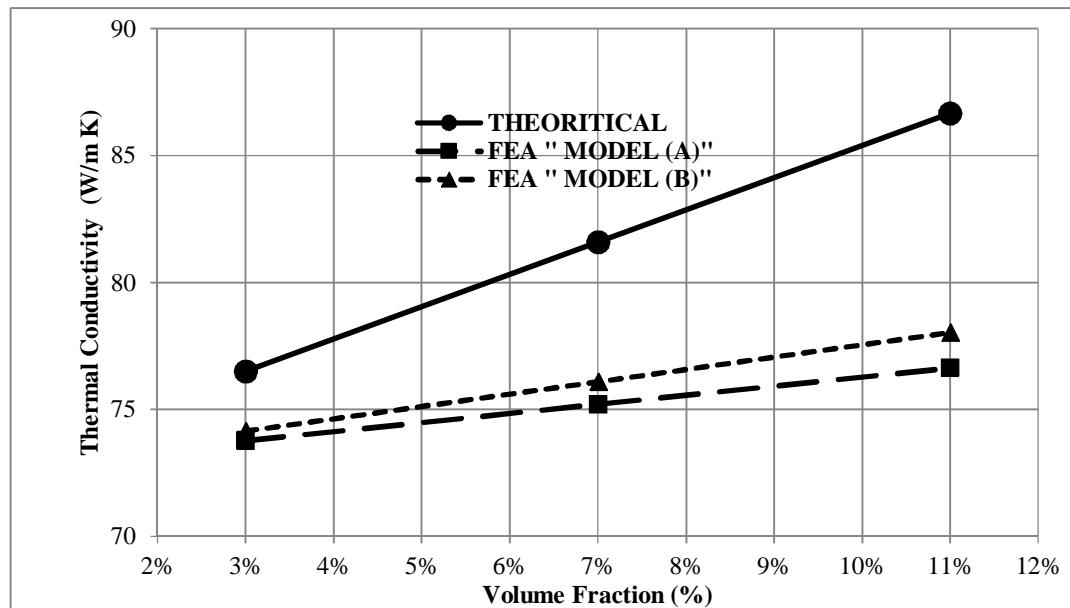


Figure 6.40: Validation of thermal conductivity for armchair (5, 5) carbon nanotubes (as short fiber " $l_c=3$ ") reinforced iron metal matrix

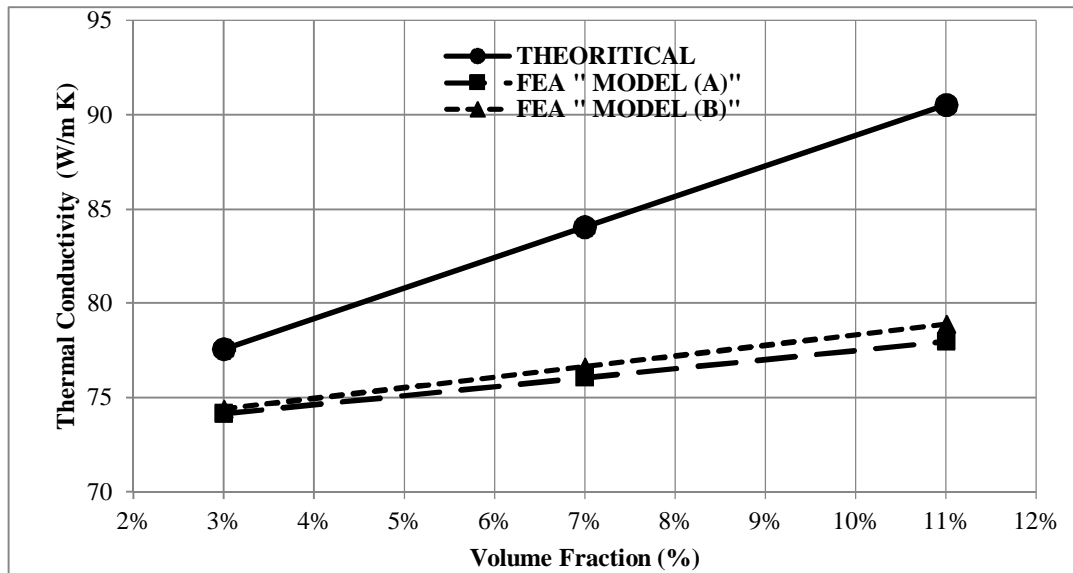


Figure 6.41: Validation of thermal conductivity for zigzag (5, 0) carbon nanotubes (as short fiber " $l_c=3$ ") reinforced iron metal matrix

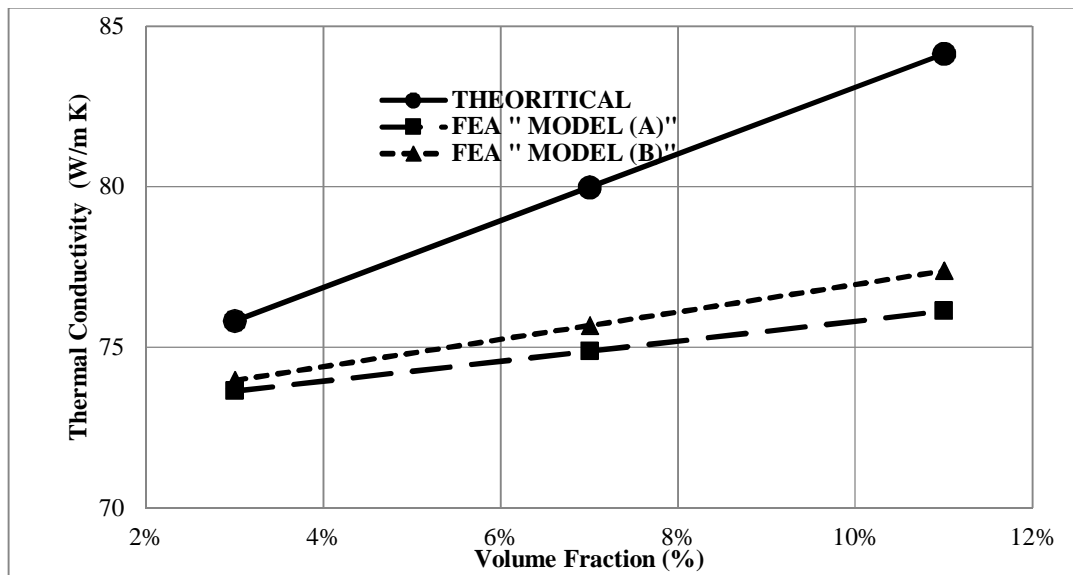


Figure 6.42: Validation of thermal conductivity for chiral (5, 10) carbon nanotubes (as short fiber " $l_c=3$ ") reinforced iron metal matrix

Similarly, the finite element results of model "A" and model "B" for carbon nanotube reinforced copper matrix are in good and acceptable agreement compared to the theoretical results. It can be observed from the Figures 6.43, 6.44, 6.45 at carbon nanotube length of 3 nm that the thermal conductivity results of armchair, zigzag, and chiral carbon nanotube treated as short fiber reinforced copper matrix have an increasing trend with the increase in volume fraction of carbon nanotube. Finite element predictions for the two models show lower prediction values than theoretical results. The deviation percentage were calculated for all cases and presented in Tables 6.13 (a), (b), and (c).

Table 6.13: Validation of thermal conductivity for (a) armchair (b) zigzag, and (c) chiral carbon nanotube reinforced copper metal matrix at $l_c=3nm$

(a) Armchair

Vol. (%)	Theoretical (W/m K)	Finite Element (W/m K)		Deviation (%)	
		Model A	Model B	Model A	Model B
3%	409.6	396.4	398.2	-3.2%	-2.8%
7%	441.2	410.3	414.4	-7.0%	-6.1%
11%	472.7	424.2	430.7	-10.2%	-8.9%

(b) Zigzag

Vol. (%)	Theoretical (W/m K)	Finite Element (W/m K)		Deviation (%)	
		Model A	Model B	Model A	Model B
3%	412.4	399.4	400.9	-3.1%	-2.8%
7%	447.6	417.4	420.7	-6.8%	-6.0%
11%	482.8	435.3	440.6	-9.8%	-8.7%

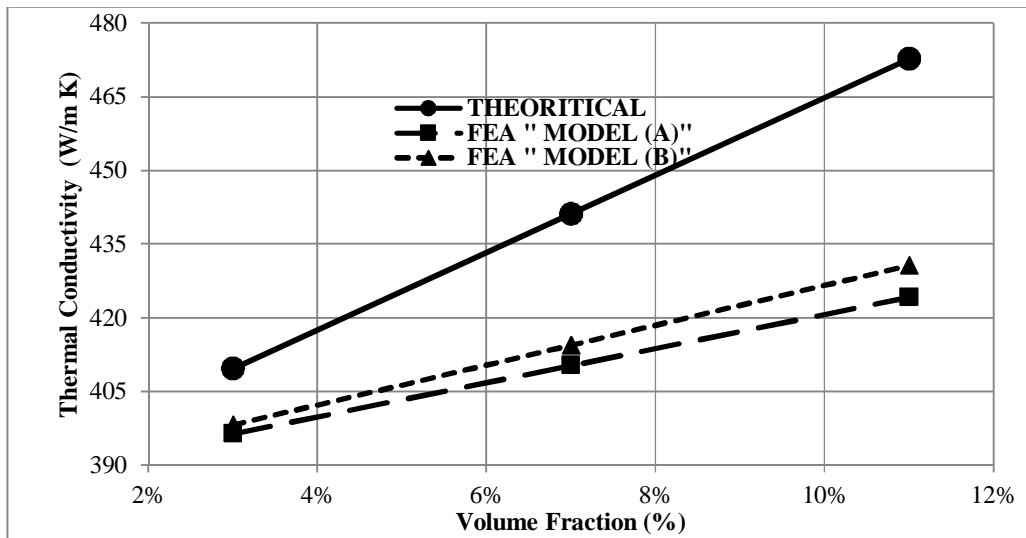


Figure 6.43: validation of thermal conductivity for armchair (5, 5) carbon nanotubes (as short fiber " $l_c=3$ ") reinforced copper metal matrix

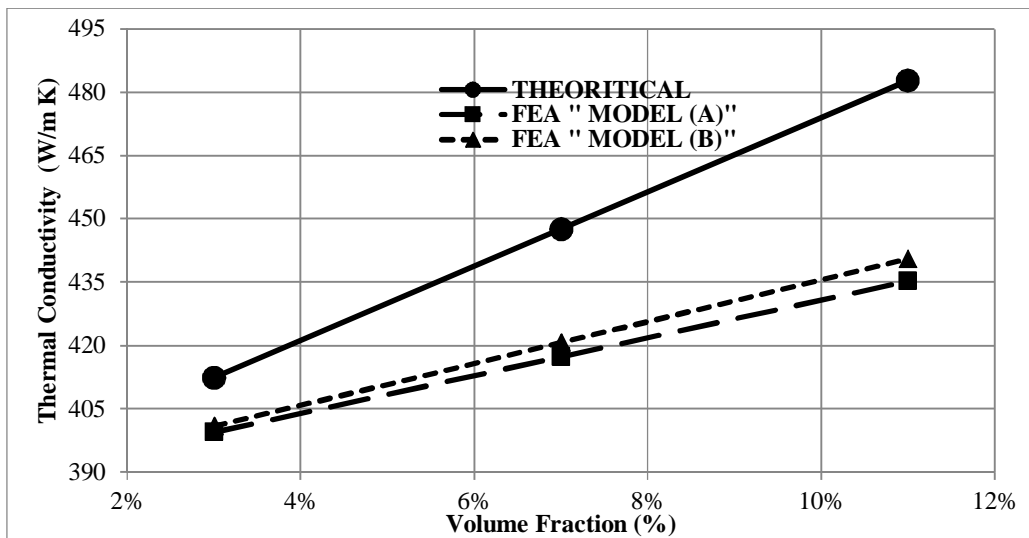


Figure 6.44: Validation of thermal conductivity for zigzag (5, 0) carbon nanotubes (as short fiber " $l_c=3$ ") reinforced copper metal matrix

(c) Chiral

Vol. (%)	Theoretical (W/m K)	Finite Element (W/m K)		Deviation (%)	
		Model A	Model B	Model A	Model B
3%	404.7	395.6	396.3	-2.2%	-2.1%
7%	429.7	408.5	410.0	-4.9%	-4.6%
11%	454.6	421.3	423.7	-7.3%	-6.8%

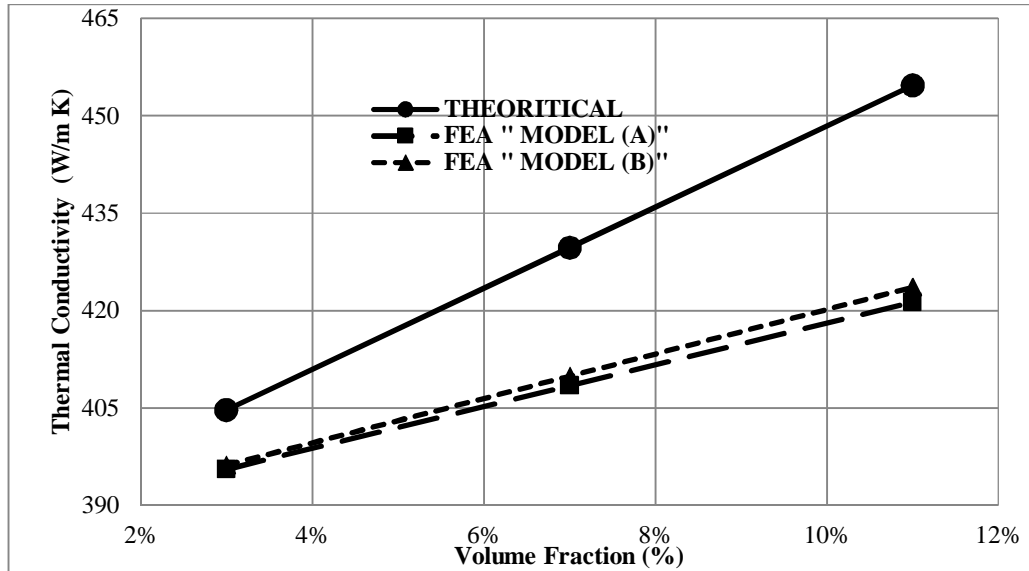


Figure 6.45: Validation of thermal conductivity for chiral (5, 10) carbon nanotubes (as short fiber " $l_c=3$ ") reinforced copper metal matrix

However, the finite element results of model "A" and model "B" for carbon nanotube reinforced aluminum matrix are in good and acceptable agreement compared to the theoretical results. It can be observed from the Figures 6.46, 6.47, 6.48 at carbon nanotube length of 3 nm that the thermal conductivity results of armchair, zigzag, and chiral carbon nanotube treated as short fiber reinforced aluminum matrix have linear increasing trend with the increase in volume fraction of carbon nanotube. Finite element predictions for the two models show lower prediction values than theoretical results. The deviation percentage were calculated for all cases and presented in Tables 6.14 (a), (b), and (c), respectively.

Table 6.14: Validation of thermal conductivity for (a) armchair (b) zigzag, and (c) chiral carbon nanotube reinforced aluminum metal matrix at $l_c=3$ nm

(a) Armchair

Vol. (%)	Theoretical (W/m K)	Finite Element (W/m K)		Deviation (%)	
		Model A	Model B	Model A	Model B
3%	221.6	214.1	216.6	-3.4%	-2.3%
7%	245.1	227.5	233.3	-7.2%	-4.8%
11%	268.6	240.9	250.0	-10.3%	-6.9%

(b) Zigzag

Vol. (%)	Theoretical (W/m K)	Finite Element (W/m K)		Deviation (%)	
		Model A	Model B	Model A	Model B
3%	223.6	215.9	219.2	-3.4%	-2.0%
7%	249.8	231.9	239.4	-7.2%	-4.1%
11%	275.9	247.8	259.7	-10.2%	-5.9%

(c) Chiral

Vol. (%)	Theoretical (W/m K)	Finite Element (W/m K)		Deviation (%)	
		Model A	Model B	Model A	Model B
3%	219.7	210.9	214.3	-4.0%	-2.5%
7%	240.7	220.2	228.0	-8.5%	-5.3%
11%	261.6	229.4	241.7	-12.3%	-7.6%

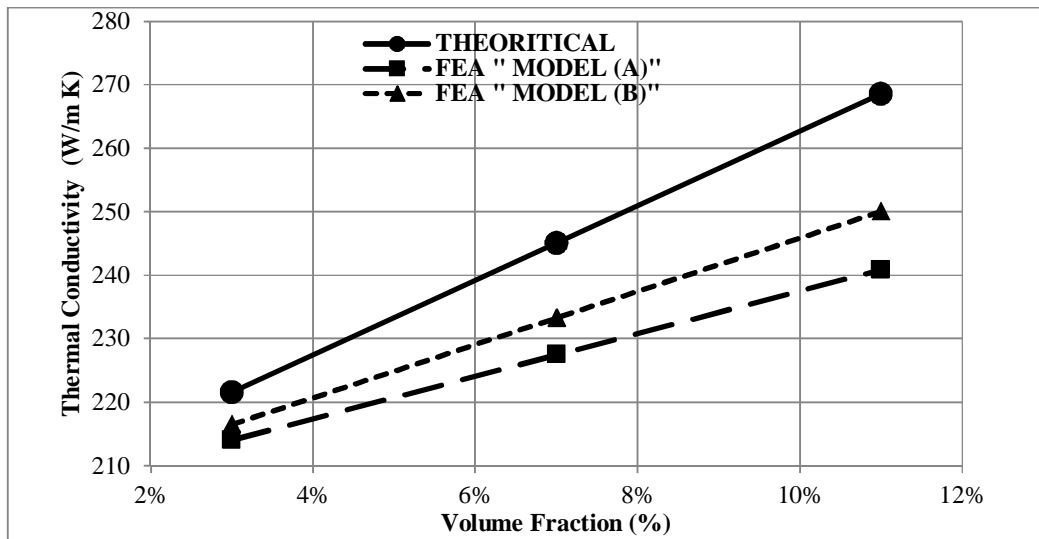


Figure 6.46: Validation of thermal conductivity for armchair (5, 5) carbon nanotubes (as short fiber " $l_c=3$ ") reinforced aluminum metal matrix

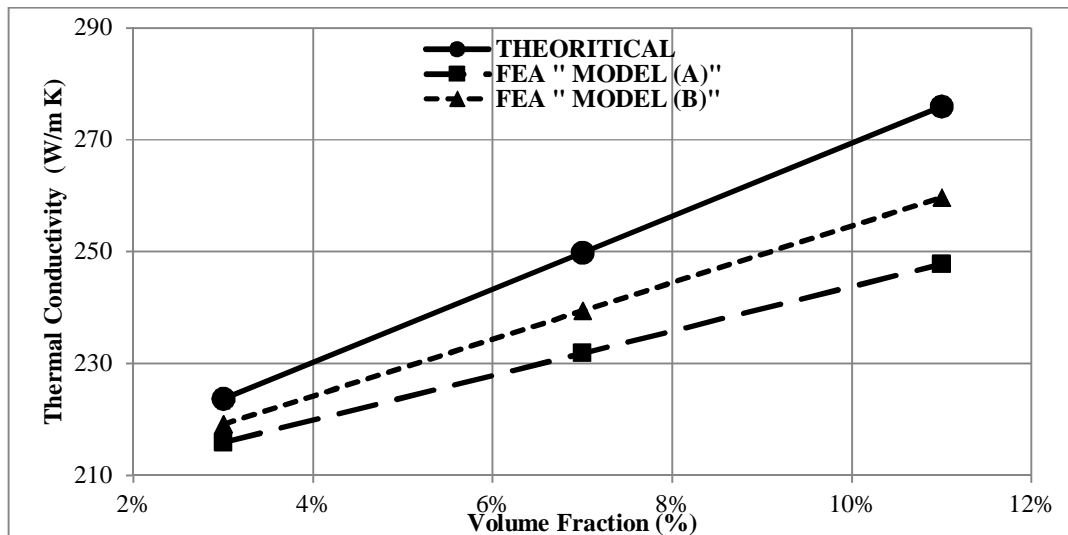


Figure 6.47: Validation of thermal conductivity for zigzag (5, 0) carbon nanotubes (as short fiber " $l_c=3$ ") reinforced aluminum metal matrix

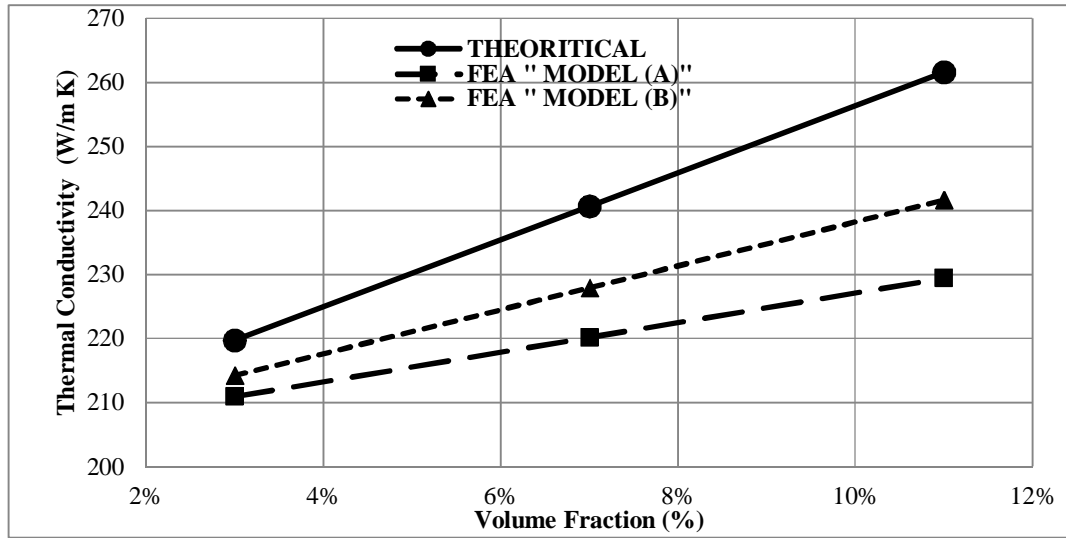


Figure 6.48: Validation of thermal conductivity for chiral (5, 10) carbon nanotubes (as short fiber " $l_c=3$ ") reinforced aluminum metal matrix

(b) Effect of Length

The finite element results of model "A" and model "B" for carbon nanotube reinforced Iron matrix are in good and acceptable agreement compared to the theoretical results. It can be observed from the Figures 6.49, 6.50, 6.51 at different carbon nanotube length and 3% volume fraction that the thermal conductivity results of armchair, zigzag, and chiral carbon nanotube treated as short fiber reinforced iron matrix have linear increasing trend with the increase in length of carbon nanotube. Finite element predictions for the two models show higher prediction values than theoretical results. The deviation percentage were calculated for all cases and presented in Tables 6.15 (a), (b), and (c), respectively

Table 6.15: Validation of thermal conductivity for (a) armchair (b) zigzag, and (c) chiral carbon nanotube reinforced iron metal matrix at different lengths

(a) Armchair

length (nm)	Theoretical (W/m K)	Finite Element (W/m K)		Deviation (%)	
		Model A	Model B	Model A	Model B
3	73.8	74.4	74.958	0.7%	1.5%
5	74.4	74.9	75.456	0.6%	1.4%
8	75.2	75.8	76.352	0.7%	1.5%

(b) Zigzag

length (nm)	Theoretical (W/m K)	Finite Element (W/m K)		Deviation (%)	
		Model A	Model B	Model A	Model B
3	74.7	75.1	75.4	0.6%	1.0%
5	75.5	75.8	76.2	0.4%	0.9%
8	76.6	77.0	77.4	0.5%	1.1%

(c) Chiral

length (nm)	Theoretical (W/m K)	Finite Element (W/m K)		Deviation (%)	
		Model A	Model B	Model A	Model B
3	72.9	73.6	74.0	1.0%	1.4%
5	73.6	74.2	74.5	0.9%	1.3%
8	74.2	74.9	75.2	0.9%	1.3%

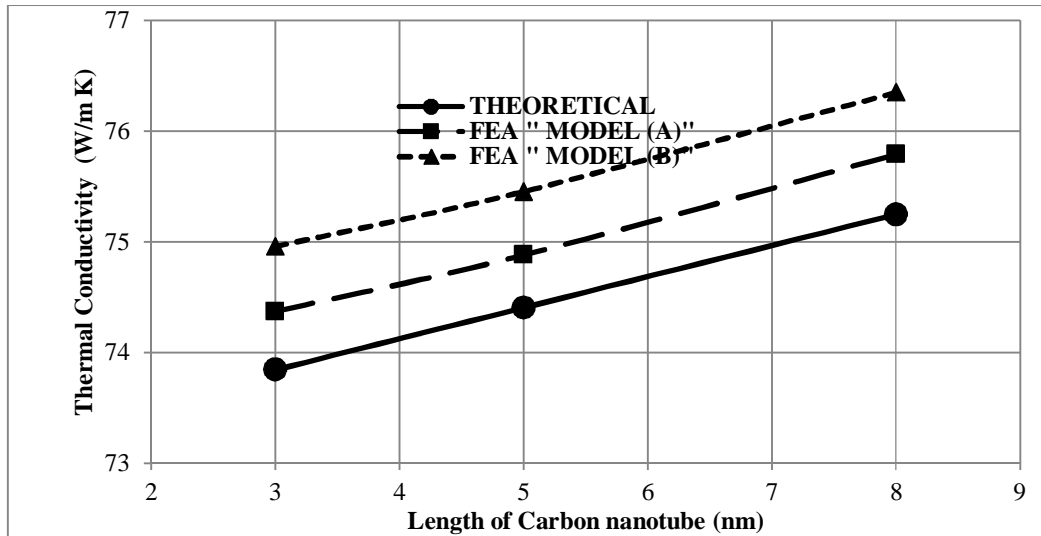


Figure 6.49: Validation of thermal conductivity for armchair (5, 5) carbon nanotubes (as short fiber) reinforced iron metal matrix at different lengths

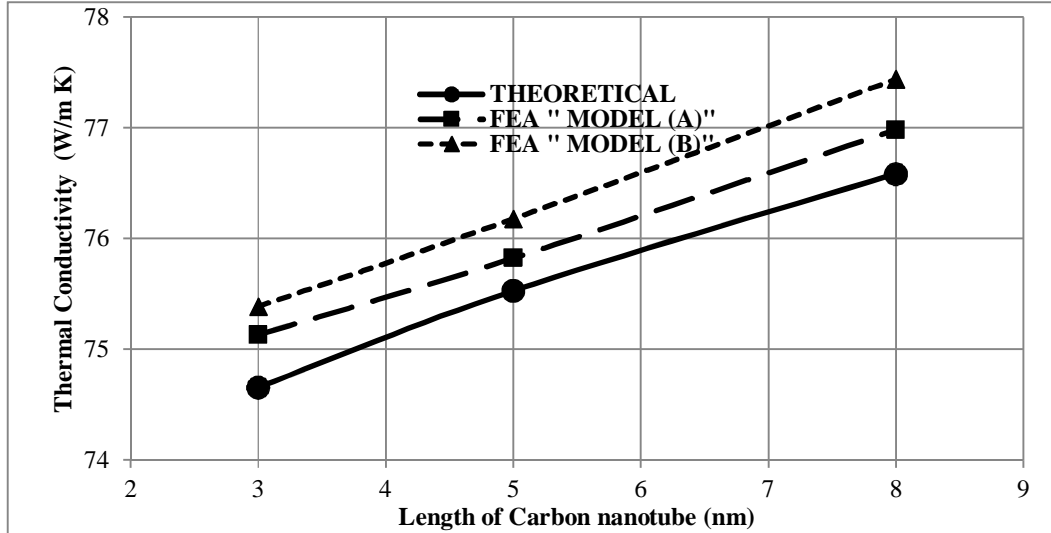


Figure 6.50: Validation of thermal conductivity for zigzag (5, 0) carbon nanotubes (as short fiber) reinforced iron metal matrix at different lengths

Similarly, the finite element results of model "A" and model "B" for carbon nanotube reinforced copper matrix are in good and acceptable agreement compared to the theoretical results. It can be observed from the Figures 6.52, 6.53, 6.54 at different carbon nanotube length and 3% volume fraction that the thermal conductivity results of

armchair, zigzag, and chiral carbon nanotube treated as short fiber reinforced Copper matrix have linear increasing trend with the increase in length of carbon nanotube. Finite element predictions for the two models show higher prediction values than theoretical results. The deviation percentage were calculated for all cases and presented in Tables 6.16 (a), (b), and (c), respectively.

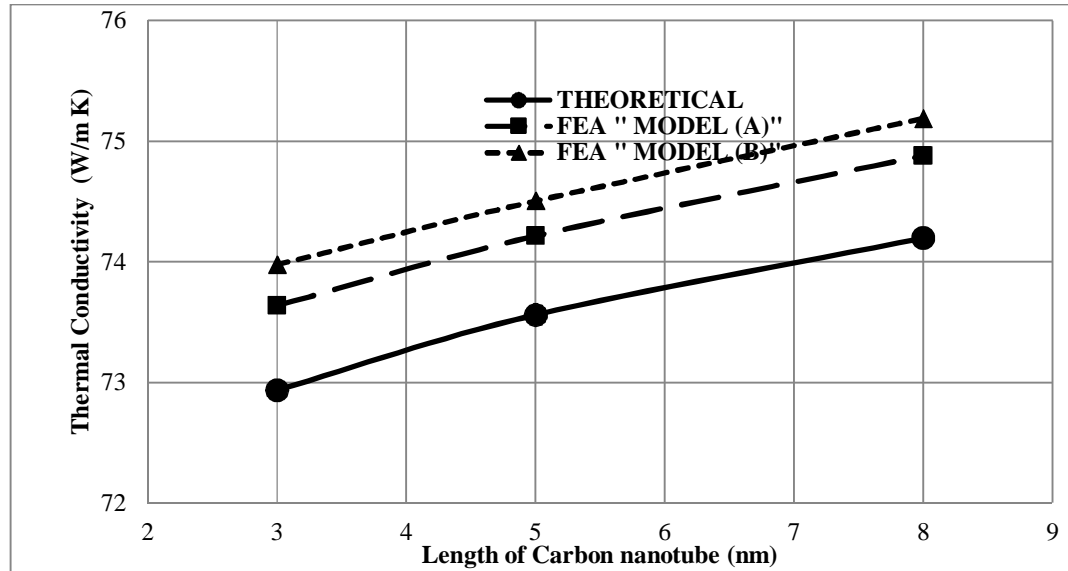


Figure 6.51: Validation of thermal conductivity for chiral (5, 10) carbon nanotubes (as short fiber) reinforced iron metal matrix at different lengths

Table 6.16: Validation of thermal conductivity for (a) armchair (b) zigzag, and (c) chiral carbon nanotube reinforced copper metal matrix at different lengths

(a) Armchair

length (nm)	Theoretical (W/m K)	Finite Element (W/m K)		Deviation (%)	
		Model A	Model B	Model A	Model B
3	393.1	396.4	398.192	0.8%	1.3%
5	397.8	399.8	402.494	0.5%	1.2%
8	404.9	405.5	408.032	0.1%	0.8%

(b) Zigzag

length (nm)	Theoretical (W/m K)	Finite Element (W/m K)		Deviation (%)	
		Model A	Model B	Model A	Model B
3	394.6	397.4	399.9	0.7%	1.3%
5	400.3	401.2	403.5	0.2%	0.8%
8	408.9	409.5	409.6	0.1%	0.2%

(c) Chiral

length (nm)	Theoretical (W/m K)	Finite Element (W/m K)		Deviation (%)	
		Model A	Model B	Model A	Model B
3	391.6	393.6	395.3	0.5%	0.9%
5	395.4	396.3	397.6	0.2%	0.6%
8	401.0	402.9	403.5	0.5%	-0.6%

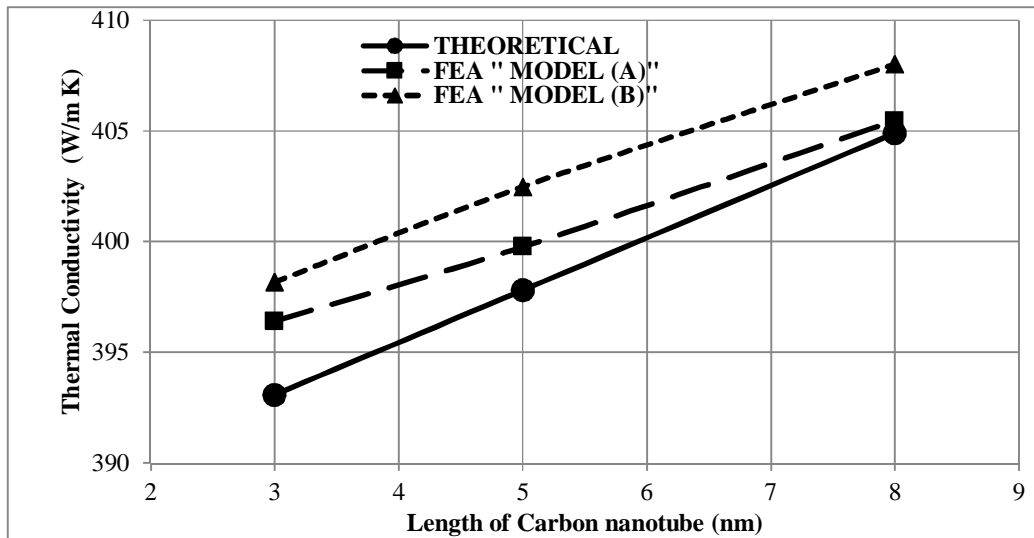


Figure 6.52: Validation of thermal conductivity for armchair (5, 5) carbon nanotubes (as short fiber) reinforced copper metal matrix at different lengths

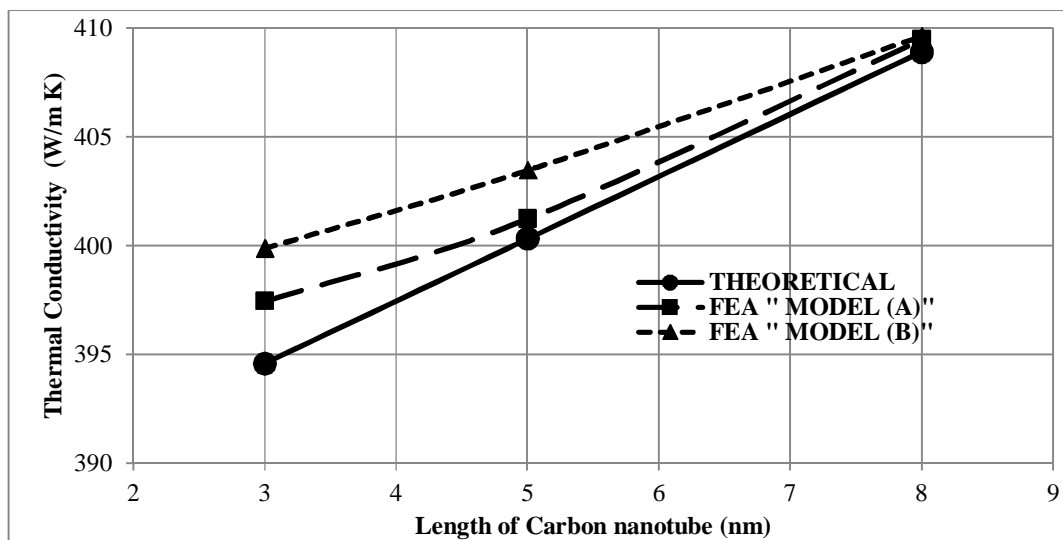


Figure 6.53: Validation of thermal conductivity for zigzag (5, 0) carbon nanotubes (as short fiber) reinforced copper metal matrix at different lengths

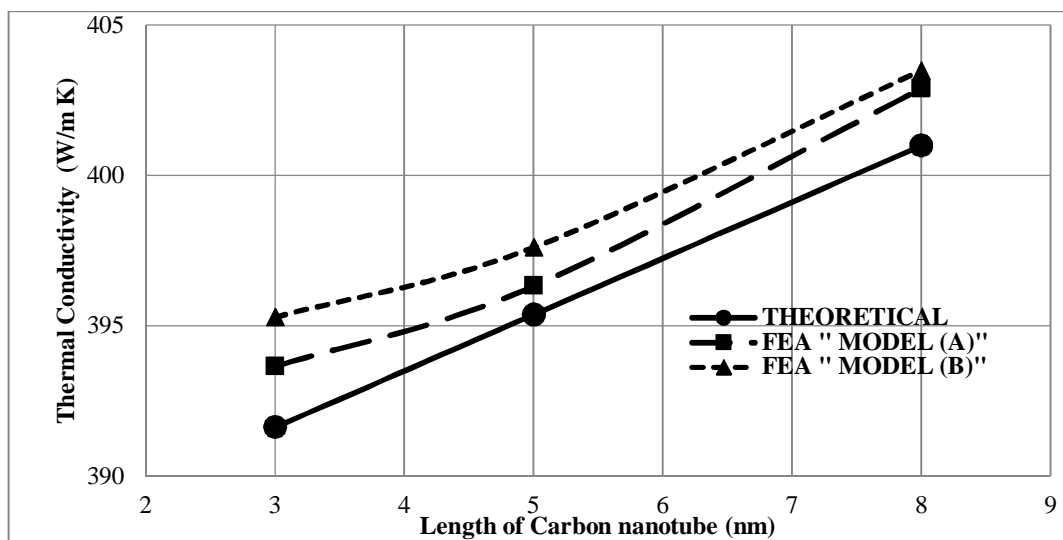


Figure 6.54: Validation of thermal conductivity for chiral (5, 10) carbon nanotubes (as short fiber) reinforced copper metal matrix at different lengths

However, the finite element results of model “A” and model “B” for carbon nanotube reinforced aluminum matrix are in good and acceptable agreement compared to the theoretical results. It can be observed from the Figures 6.55, 6.56, 6.57 at different carbon nanotube length and 3% volume fraction that the thermal conductivity results of armchair, zigzag, and chiral carbon nanotube treated as short fiber reinforced aluminum matrix have linear increasing trend with the increase in length of carbon nanotube. Finite element predictions for the two models show higher prediction values than theoretical results because the complex geometrical shape and arrangement of carbon nanotubes not taken in consideration for theoretical estimation of the effective thermal conductivity of the carbon nanotubes reinforced composite. The deviation percentage were calculated for all cases and presented in Tables 6.17 (a), (b), and (c).

Table 6.17: Validation of thermal conductivity for a) armchair (b) zigzag, and (c) chiral carbon nanotube reinforced aluminum metal matrix at different lengths

(a) Armchair

length (nm)	Theoretical (W/m K)	Finite Element (W/m K)		Deviation (%)	
		Model A	Model B	Model A	Model B
3	209.3	214.1	216.558	2.3%	3.5%
5	212.8	216.3	217.956	1.6%	2.4%
8	218.1	218.9	221.052	0.4%	1.4%

(b) Zigzag

length (nm)	Theoretical (W/m K)	Finite Element (W/m K)		Deviation (%)	
		Model A	Model B	Model A	Model B
3	209.9	215.9	219.2	2.9%	4.4%
5	213.8	217.4	220.3	1.7%	3.0%
8	219.7	220.6	221.9	0.4%	1.0%

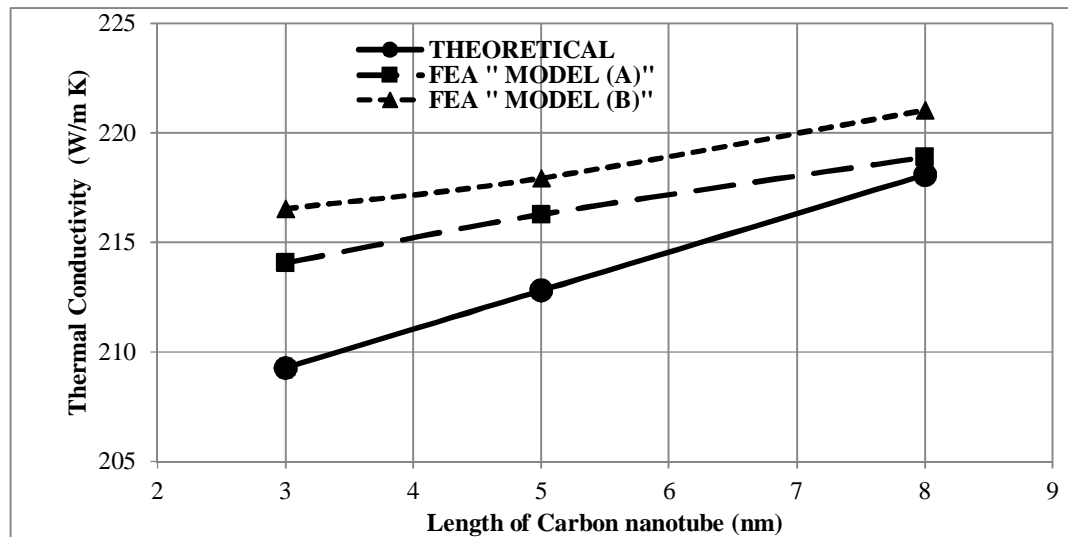


Figure 6.55: Validation of thermal conductivity for armchair (5, 5) carbon nanotubes (as short fiber) reinforced aluminum metal matrix at different lengths

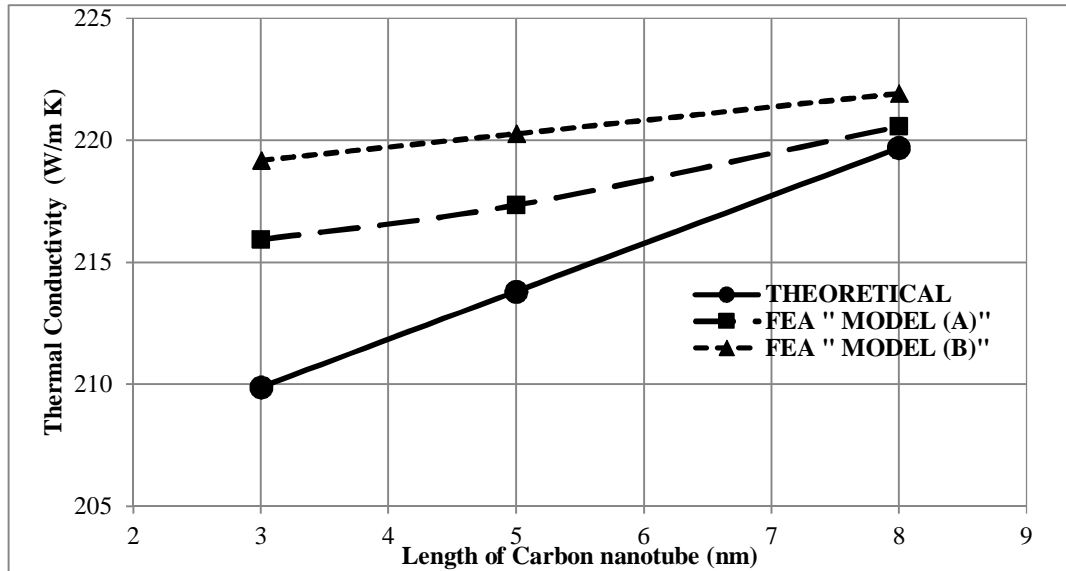


Figure 6.56: Validation of thermal conductivity for zigzag (5, 0) carbon nanotubes (as short fiber) reinforced aluminum metal matrix at different lengths

(c) Chiral

length (nm)	Theoretical (W/m K)	Finite Element (W/m K)		Deviation (%)	
		Model A	Model B	Model A	Model B
3	208.7	210.9	213.7	1.1%	2.4%
5	211.9	213.6	215.6	0.8%	1.8%
8	216.6	217.8	218.6	0.6%	0.9%

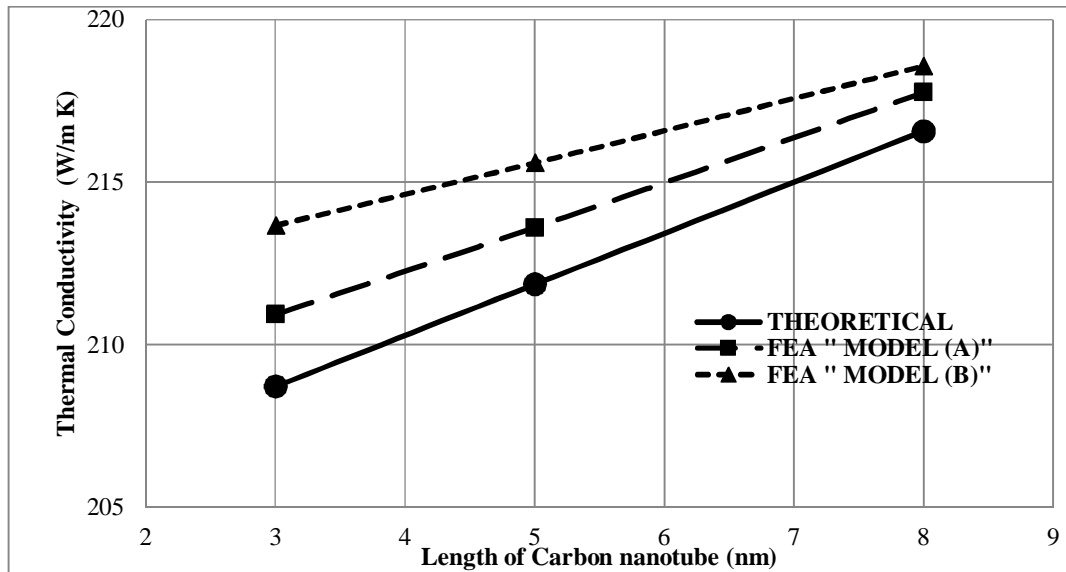


Figure 6.57: Validation of thermal conductivity for chiral (5, 10) carbon nanotubes (as short fiber) reinforced aluminum metal matrix at different lengths

(c) Effect of Diameter

The finite element results of model “A” and model “B” for carbon nanotube reinforced iron matrix are in good and acceptable agreement compared to the theoretical results. It can be observed from the Figures 6.58, 6.59, and 6.60 at different carbon

nanotube diameters, different lengths, and 3% volume fraction that the thermal conductivity results of armchair, zigzag, and chiral carbon nanotube treated as short fiber reinforced iron matrix have a decreasing trend with the increase in diameter of carbon nanotube. Finite element predictions for model “B” show higher prediction values than theoretical results while the finite element results for Model “A” shows a lower prediction than theoretical results because the complex geometrical shape and arrangement of carbon nanotubes not taken in consideration for theoretical estimation of the effective thermal conductivity of the carbon nanotubes reinforced composite. The deviation percentage were calculated for all cases and presented in Tables 6.18 (a) at $l_c=3$ nm, (b) at $l_c=5$ nm, (c) at $l_c=8$ nm, respectively.

Table 6.18: Validation of thermal conductivity for carbon nanotube reinforced iron metal matrix at different diameters and (a) at $l_c=3$ nm, (b) at $l_c=5$ nm, (c) at $l_c=8$ nm,

(a) at $l_c=3$ nm

Diameter (nm)	Theoretical (W/m K)	Finite Element (W/m K)		Deviation (%)	
		Model A	Model B	Model A	Model B
0.561	74.2	74.1	74.392	-0.1%	0.3%
0.848	73.8	73.8	74.158	-0.1%	0.4%
1.206	73.6	73.5	73.978	-0.1%	0.5%

(b) at $l_c=5$ nm

Diameter (nm)	Theoretical (W/m K)	Finite Element (W/m K)		Deviation (%)	
		Model A	Model B	Model A	Model B
0.561	75.1	74.9	75.3	-0.3%	0.3%
0.848	74.6	74.5	74.9	-0.2%	0.3%
1.206	74.3	74.0	74.5	-0.3%	0.3%

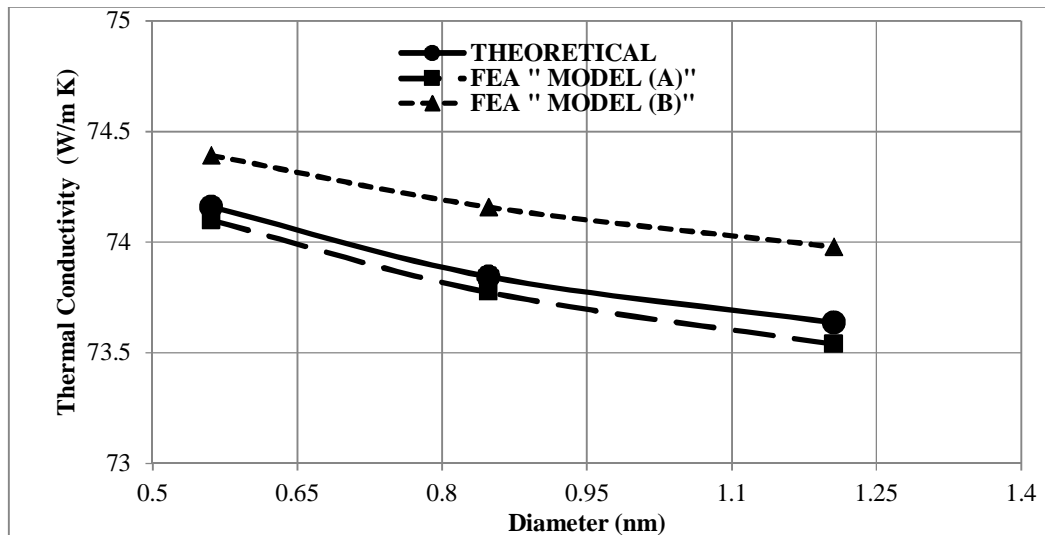


Figure 6.58: Validation of thermal conductivity for carbon nanotubes (as Short Fiber) reinforced iron metal matrix at different diameters and at $l_c= 3$ nm

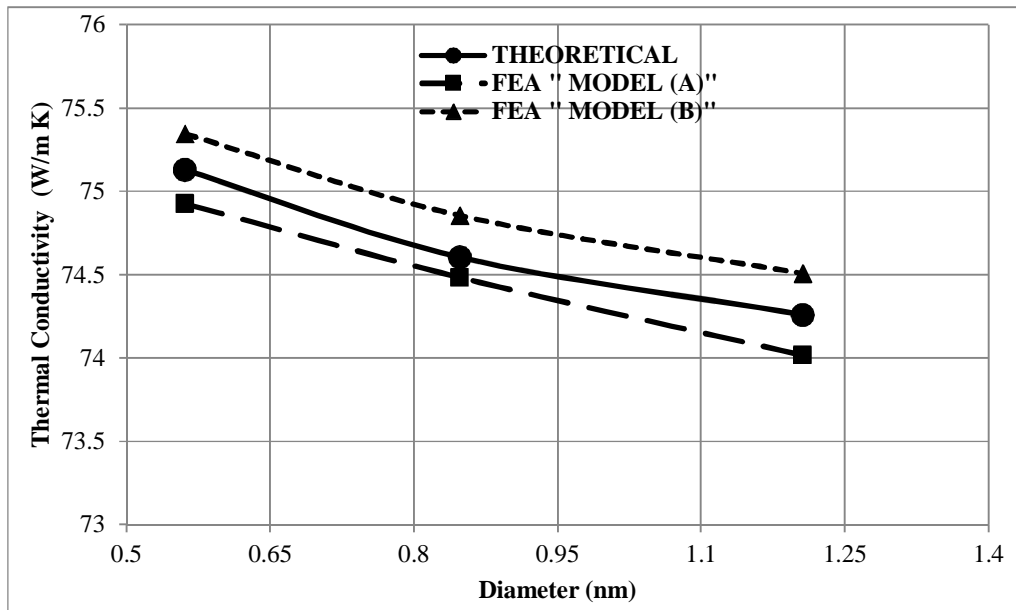


Figure 6.59: Validation of thermal conductivity for carbon nanotubes (as Short Fiber) reinforced iron metal matrix at different diameters and at $l_c= 5\text{nm}$

(c) at $l_c=8 \text{ nm}$

Diameter (nm)	Theoretical (W/m K)	Finite Element (W/m K)		Deviation (%)	
		Model A	Model B	Model A	Model B
0.561	76.6	76.3	76.8	-0.4%	0.3%
0.848	75.7	75.3	76.0	-0.6%	0.3%
1.206	75.0	74.5	75.2	-0.6%	0.3%

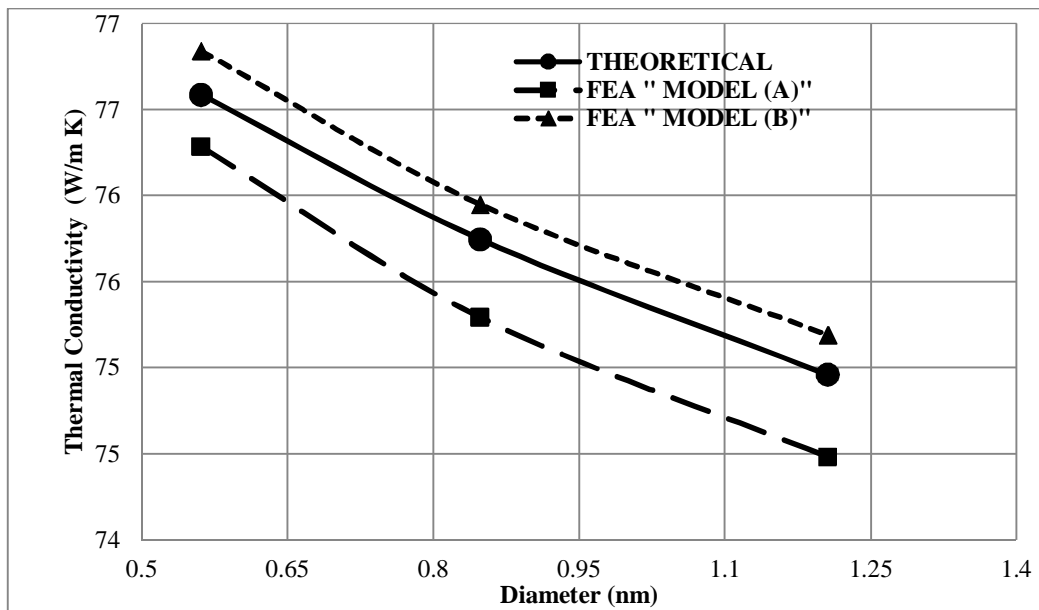


Figure 6.60: Validation of thermal conductivity for carbon nanotubes (as Short Fiber) reinforced iron metal matrix at different diameters and at $l_c= 8\text{nm}$

Similarly, the finite element results of model “A” and model “B” for carbon nanotube reinforced copper matrix are in good and acceptable agreement compared to the theoretical results. It can be observed from the Figures 6.61, 6.62, and 6.63 at different carbon nanotube diameters, different lengths, and 3% volume fraction that the thermal conductivity results of armchair, zigzag, and chiral carbon nanotube treated as short fiber reinforced copper matrix have a decreasing trend with the increase in diameter of carbon nanotube. Finite element predictions for the two models show higher prediction values than theoretical results because the complex geometrical shape and arrangement of carbon nanotubes are not taken in consideration for theoretical estimation of the effective thermal conductivity of the carbon nanotubes reinforced composite. The deviation percentage were calculated for all cases and presented in Tables 6.19(a) at $l_c=3$ nm, (b) at $l_c=5$ nm, (c) at $l_c=8$ nm, respectively.

Table 6.19: Validation of thermal conductivity for armchair carbon nanotube reinforced copper metal matrix at different diameters (a) at $l_c=3$ nm, (b) at $l_c=5$ nm, (c) at $l_c=8$ nm,

(a) at $l_c=3$ nm

Diameter (nm)	Theoretical (W/m K)	Finite Element (W/m K)		Deviation (%)	
		Model A	Model B	Model A	Model B
0.561	394.6	399.4	400.892	1.2%	1.6%
0.848	393.1	396.4	398.192	0.8%	1.3%
1.206	391.6	395.6	396.278	1.0%	1.2%

(b) at $l_c=5$ nm

Diameter (nm)	Theoretical (W/m K)	Finite Element (W/m K)		Deviation (%)	
		Model A	Model B	Model A	Model B
0.561	399.9	401.3	403.5	0.4%	0.9%
0.848	397.8	399.8	401.5	0.5%	0.9%
1.206	395.4	396.3	397.6	0.2%	0.6%

(c) at $l_c=8$ nm

Diameter (nm)	Theoretical (W/m K)	Finite Element (W/m K)		Deviation (%)	
		Model A	Model B	Model A	Model B
0.561	406.5	408.9	409.6	0.6%	-0.8%
0.848	403.5	404.9	407.0	0.3%	-0.9%
1.206	398.9	401.1	402.5	0.6%	-0.9%

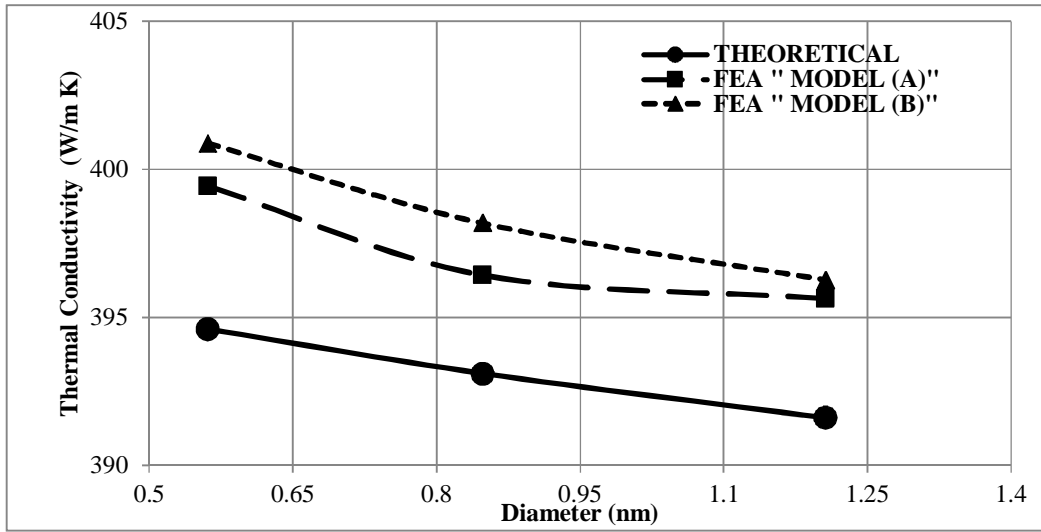


Figure 6.61: Validation of thermal conductivity carbon nanotubes (as Short Fiber) reinforced Copper metal matrix at different diameters and at $l_c = 3\text{nm}$

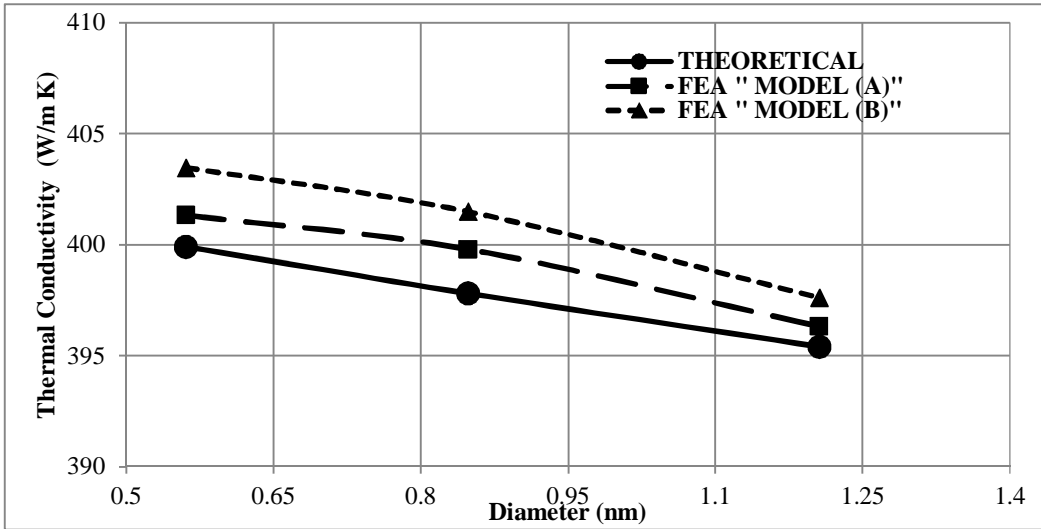


Figure 6.62: Validation of thermal conductivity for carbon nanotubes (as Short Fiber) reinforced Copper metal matrix at different diameters and at $l_c = 5\text{nm}$

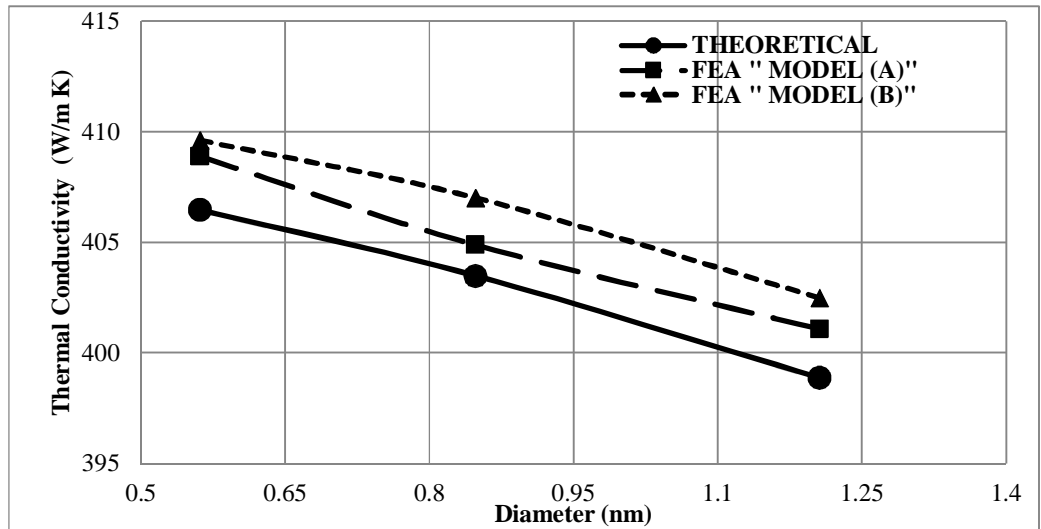


Figure 6.63: Validation of thermal conductivity for carbon nanotubes (as Short Fiber) reinforced Copper metal matrix at different diameters and at $l_c = 8\text{nm}$

However, the finite element results of model “A” and model “B” for carbon nanotube reinforced aluminum matrix are in good and acceptable agreement compared to the theoretical results. It can be observed from the Figures 6.64, 6.65, and 6.66 at different carbon nanotube diameters, different lengths, and 3% volume fraction that the thermal conductivity results of armchair, zigzag, and chiral carbon nanotube treated as short fiber reinforced aluminum matrix have a decreasing trend with the increase in diameter of carbon nanotube. Finite element predictions for the two models show higher prediction values than theoretical results because the complex geometrical shape and arrangement of carbon nanotubes are not taken in consideration for theoretical estimation of the effective thermal conductivity of the carbon nanotubes reinforced composite. The deviation percentage were calculated for all cases and presented in Tables 6.20(a) at $l_c=3$ nm, (b) at $l_c=5$ nm, (c) at $l_c=8$ nm, respectively.

Table 6.20: Validation of thermal conductivity for armchair carbon nanotube reinforced aluminum metal matrix at different diameters and (a) at $l_c=3$ nm, (b) at $l_c=5$ nm, (c) at $l_c=8$ nm,

(a) at $l_c=3$ nm

Diameter (nm)	Theoretical (W/m K)	Finite Element (W/m K)		Deviation (%)	
		Model A	Model B	Model A	Model B
0.561	209.9	215.9	219.192	2.9%	4.4%
0.848	209.3	214.1	216.558	2.3%	3.5%
1.206	208.7	210.9	214.278	1.1%	2.7%

(b) at $l_c=5$ nm

Diameter (nm)	Theoretical (W/m K)	Finite Element (W/m K)		Deviation (%)	
		Model A	Model B	Model A	Model B
0.561	213.8	217.4	220.3	1.7%	3.0%
0.848	212.8	216.3	218.0	1.6%	2.4%
1.206	211.9	214.3	215.6	1.1%	1.7%

(c) at $l_c=8$ nm

Diameter (nm)	Theoretical (W/m K)	Finite Element (W/m K)		Deviation (%)	
		Model A	Model B	Model A	Model B
0.561	219.5	219.9	220.9	0.2%	0.7%
0.848	218.1	218.7	220.0	0.3%	0.8%
1.206	216.6	216.8	217.6	0.1%	0.5%

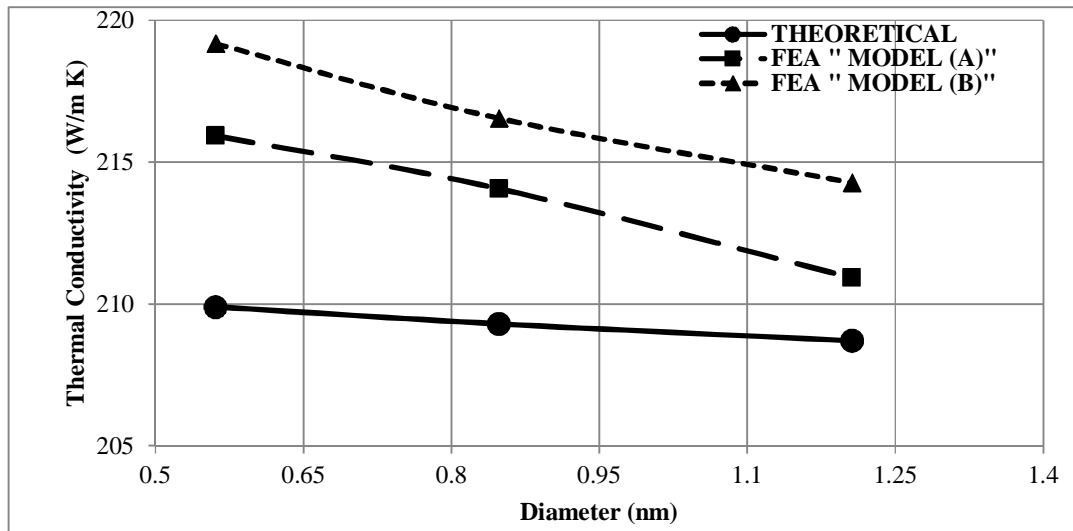


Figure 6.64: Validation of thermal conductivity carbon nanotubes (as Short Fiber) reinforced Aluminum metal matrix at different diameters and at $l_c = 3\text{nm}$

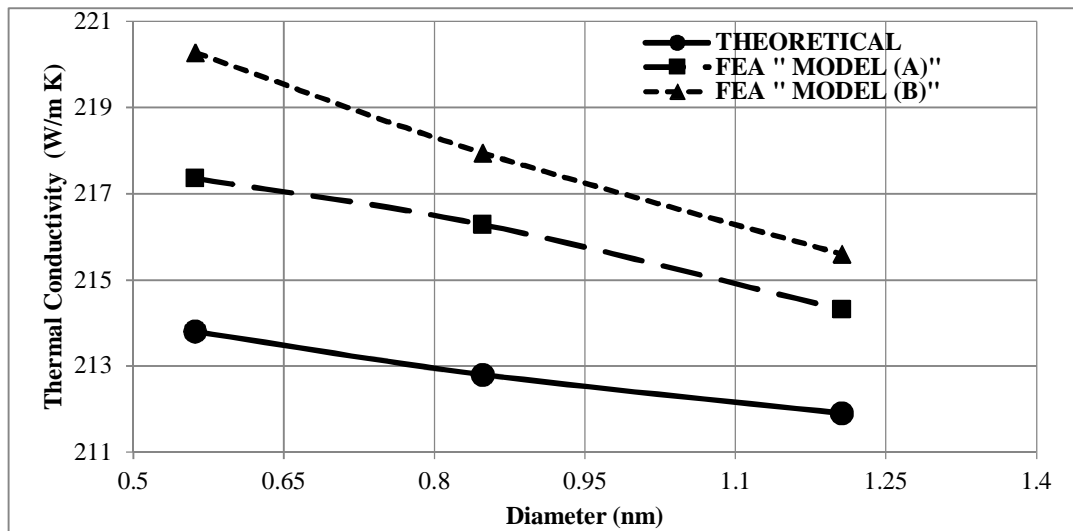


Figure 6.65: Validation of thermal conductivity carbon nanotubes (as Short Fiber) reinforced Aluminum metal matrix at different diameters and at $l_c = 5\text{nm}$

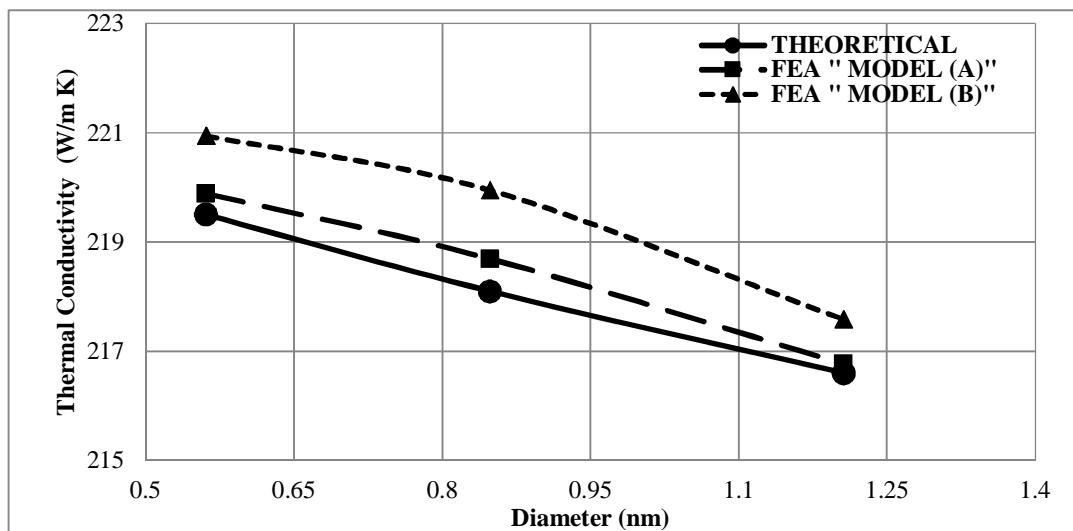


Figure 6.66: Validation of thermal conductivity carbon nanotubes (as Short Fiber) reinforced Aluminum metal matrix at different diameters and at $l_c = 8\text{nm}$

6.3.2.3 Validation of thermal contact conductance for carbon nanotubes reinforced metal matrix nanocomposite

The finite element results of model “A” and model “B” for carbon nanotube reinforced Iron matrix are in good and acceptable agreement compared to the theoretical results. It can be observed from the Figures 6.67, 6.68, and 6.69 at 3% volume fraction that the thermal conductivity results of armchair, zigzag, and chiral carbon nanotube treated as short fiber reinforced iron matrix show insensitive increase with the increase in thermal contact conductance. Finite element predictions for the two models show lower prediction values than theoretical results. The deviation percentage were calculated for all cases and presented in Tables 6.21 (a), (b), and (c), respectively.

Table 6.21: Validation of thermal contact conductance for (a) armchair (5, 5), (b) zigzag (5, 0), (c) chiral (5, 10) carbon nanotube reinforced iron metal matrix

(a) Armchair

β (MW/m ² K)	Theoretical (W/m K)	Finite Element (W/m K)		Deviation (%)	
		Model A	Model B	Model A	Model B
12	73.101	72.009	72.960	-1.5%	-0.2%
30	73.102	72.010	72.961	-1.5%	-0.2%
50	73.103	72.011	72.962	-1.5%	-0.2%
100	73.107	72.012	72.963	-1.5%	-0.2%
500	73.133	72.013	72.964	-1.5%	-0.2%
1000	73.166	72.014	72.965	-1.6%	-0.3%
2500	73.266	72.015	73.065	-1.7%	-0.3%
5000	73.431	72.115	73.165	-1.8%	-0.4%
10000	73.762	72.215	73.265	-2.1%	-0.7%

(b) Zigzag

β (MW/m ² K)	Theoretical (W/m K)	Finite Element (W/m K)		Deviation (%)	
		Model A	Model B	Model A	Model B
12	73.301	72.203	72.329	-1.5%	-1.3%
30	73.301	72.204	72.330	-1.5%	-1.3%
50	73.302	72.205	72.331	-1.5%	-1.3%
100	73.305	72.206	72.332	-1.5%	-1.3%
500	73.323	72.207	72.333	-1.5%	-1.3%
1000	73.346	72.208	72.334	-1.6%	-1.4%
2500	73.415	72.209	72.335	-1.6%	-1.5%
5000	73.530	72.309	72.435	-1.7%	-1.5%
10000	73.760	72.409	72.535	-1.8%	-1.7%

(c) Chiral

β (MW/m ² K)	Theoretical (W/m K)	Finite Element (W/m K)		Deviation (%)	
		Model A	Model B	Model A	Model B
12	73.001	71.718	72.574	-1.8%	-0.6%
30	73.002	71.719	72.575	-1.8%	-0.6%
50	73.003	71.720	72.576	-1.8%	-0.6%
100	73.007	71.721	72.577	-1.8%	-0.6%
500	73.033	71.722	72.578	-1.8%	-0.6%
1000	73.066	71.723	72.579	-1.8%	-0.7%
2500	73.166	71.724	72.580	-2.0%	-0.8%
5000	73.331	71.824	72.680	-2.1%	-0.9%
10000	73.662	71.924	72.780	-2.4%	-1.2%

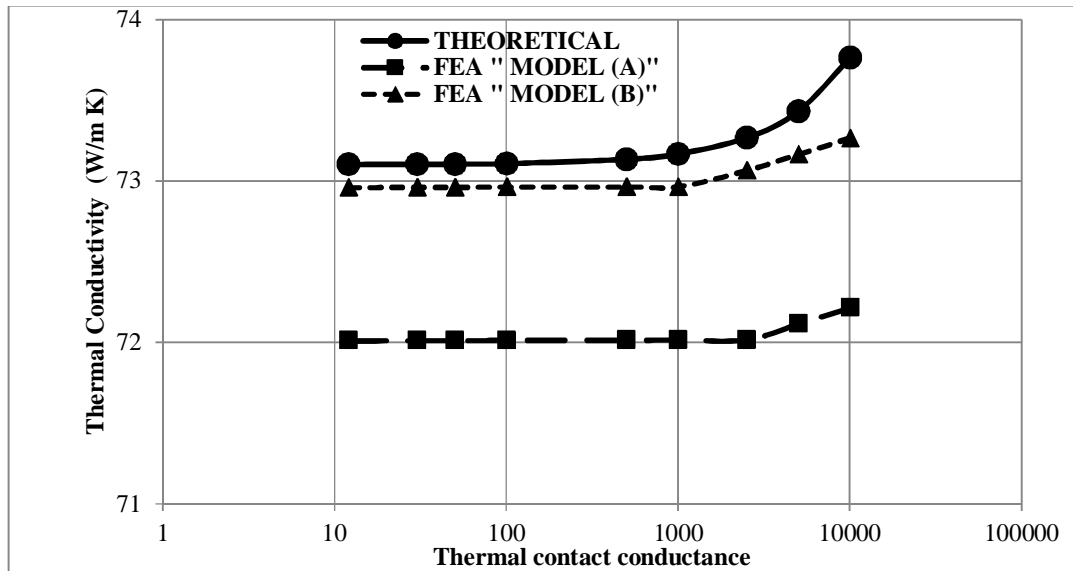


Figure 6.67: Validation of thermal contact conductance for armchair (5, 5) carbon nanotubes (as Short Fiber) reinforced Iron metal matrix

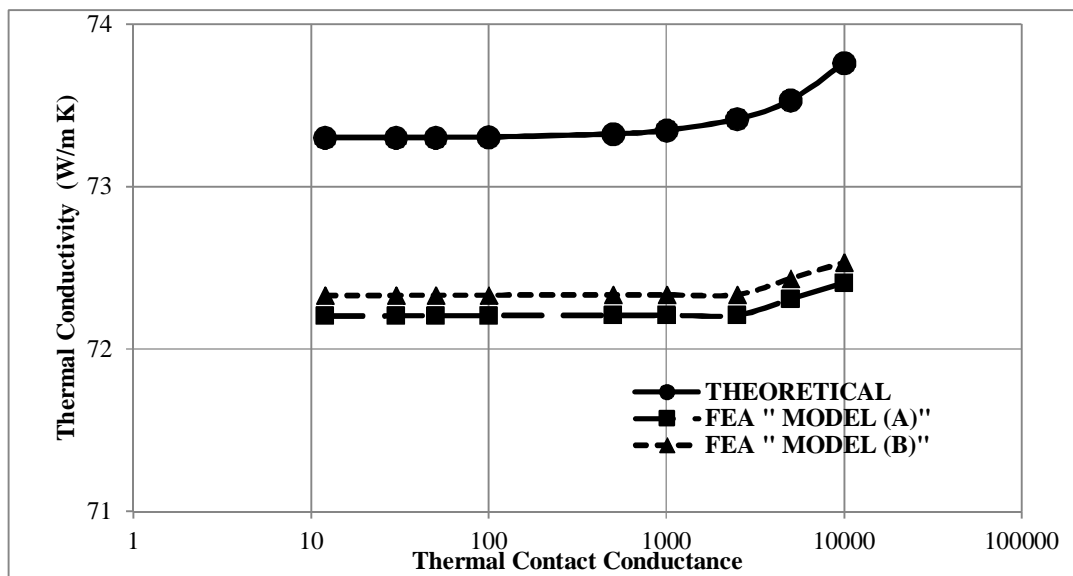


Figure 6.68: Validation of thermal contact conductance for zigzag (5, 0) for carbon nanotubes (as Short Fiber) reinforced Iron metal matrix

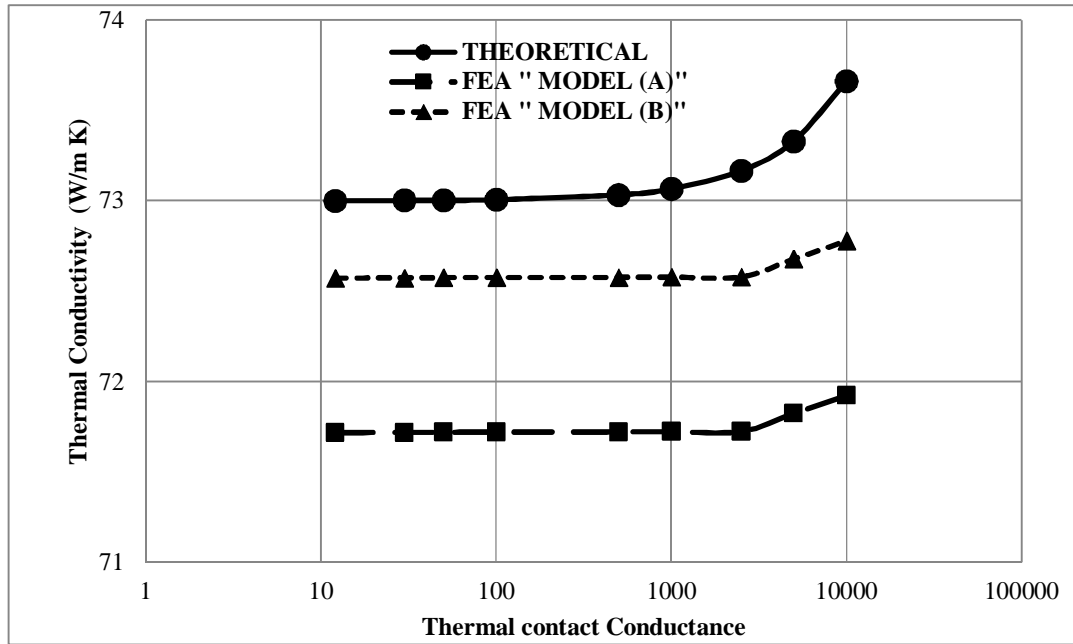


Figure 6.69: Validation of thermal contact conductance for chiral (5, 10) carbon nanotubes (as Short Fiber) reinforced iron metal

Similarly, the finite element results of model “A” and model “B” for carbon nanotube reinforced copper matrix are in good and acceptable agreement compared to the theoretical results. It can be observed from the Figures 6.70, 6.71, and 6.72 at 3% volume fraction that the thermal conductivity results of armchair, zigzag, and chiral carbon nanotube treated as short fiber reinforced copper matrix show insensitive with the increase in thermal contact conductance. Finite element predictions for the two models show higher prediction values than theoretical results. The deviation percentage were calculated for all cases and presented in Tables 6.22(a), (b), and (c), respectively.

Table 6.22: Validation of thermal contact conductance for (a) armchair (5, 5), (b) zigzag (5, 0), (c) chiral (5, 10) carbon nanotube reinforced copper metal

(a) Armchair

β (MW/m ² K)	Theoretical (W/m K)	Finite Element (W/m K)		Deviation (%)	
		Model A	Model B	Model A	Model B
12	387.101	387.329	388.165	0.1%	0.3%
30	387.102	387.330	388.166	0.1%	0.3%
50	387.103	387.331	388.167	0.1%	0.3%
100	387.107	387.332	388.168	0.1%	0.3%
500	387.133	387.333	388.169	0.1%	0.3%
1000	387.166	387.334	388.170	0.0%	0.3%
2500	387.266	387.335	388.270	0.0%	0.3%
5000	387.431	387.535	388.370	0.0%	0.2%
10000	387.762	387.935	388.470	0.0%	0.2%

(b) Zigzag

β (MW/m ² K)	Theoretical (W/m K)	Finite Element (W/m K)		Deviation (%)	
		Model A	Model B	Model A	Model B
12	387.301	388.200	388.725	0.2%	0.4%
30	387.301	388.201	388.726	0.2%	0.4%
50	387.302	388.202	388.727	0.2%	0.4%
100	387.305	388.203	388.728	0.2%	0.4%
500	387.323	388.204	388.729	0.2%	0.4%
1000	387.346	388.205	388.730	0.2%	0.4%
2500	387.415	388.206	388.731	0.2%	0.3%
5000	387.530	388.306	388.831	0.2%	0.3%
10000	387.760	388.406	388.931	0.2%	0.3%

(c) Chiral

β (MW/m ² K)	Theoretical (W/m K)	Finite Element (W/m K)		Deviation (%)	
		Model A	Model B	Model A	Model B
12	386.910	386.284	387.191	-0.2%	0.1%
30	386.911	386.285	387.192	-0.2%	0.1%
50	386.912	386.286	387.193	-0.2%	0.1%
100	386.913	386.287	387.194	-0.2%	0.1%
500	386.917	386.288	387.195	-0.2%	0.1%
1000	386.943	386.289	387.196	-0.2%	0.1%
2500	386.976	386.290	387.197	-0.2%	0.1%
5000	387.076	386.390	387.297	-0.2%	0.1%
10000	387.241	386.490	387.397	-0.2%	0.0%

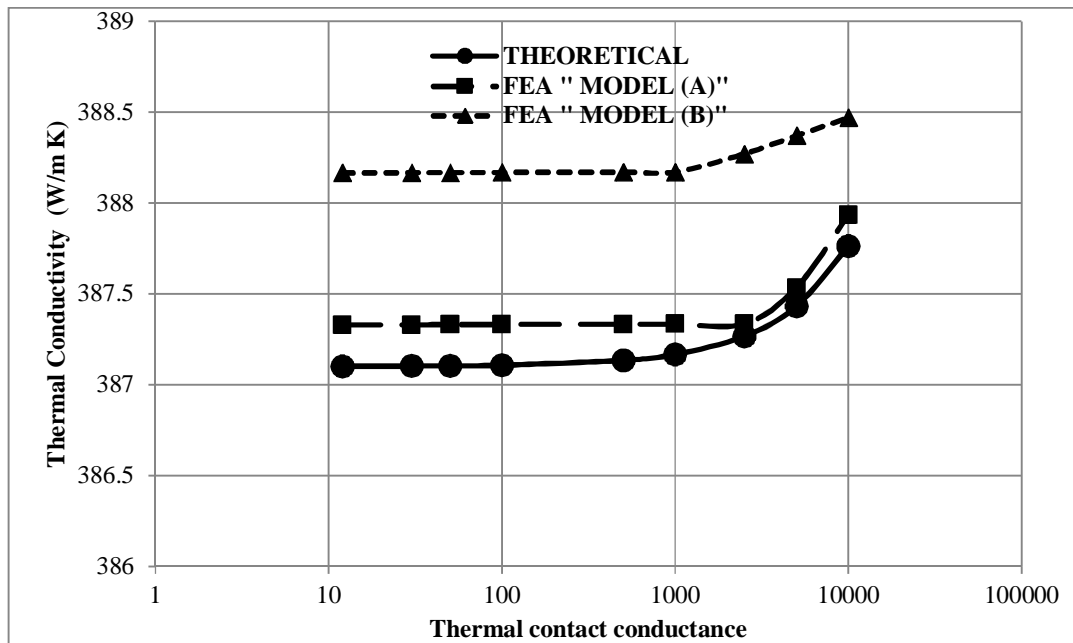


Figure 6.70: Validation of thermal contact conductance for armchair (5, 5) carbon nanotubes (as Short Fiber) reinforced Copper metal matrix

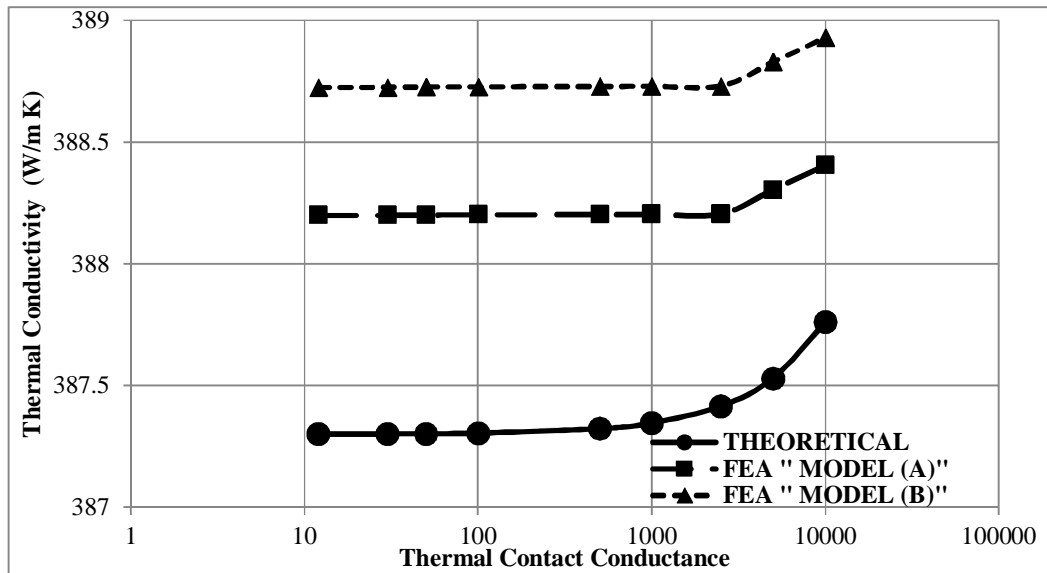


Figure 6.71: Validation of thermal contact conductance for zigzag (5, 0) for carbon nanotubes (as short fiber) reinforced copper metal matrix

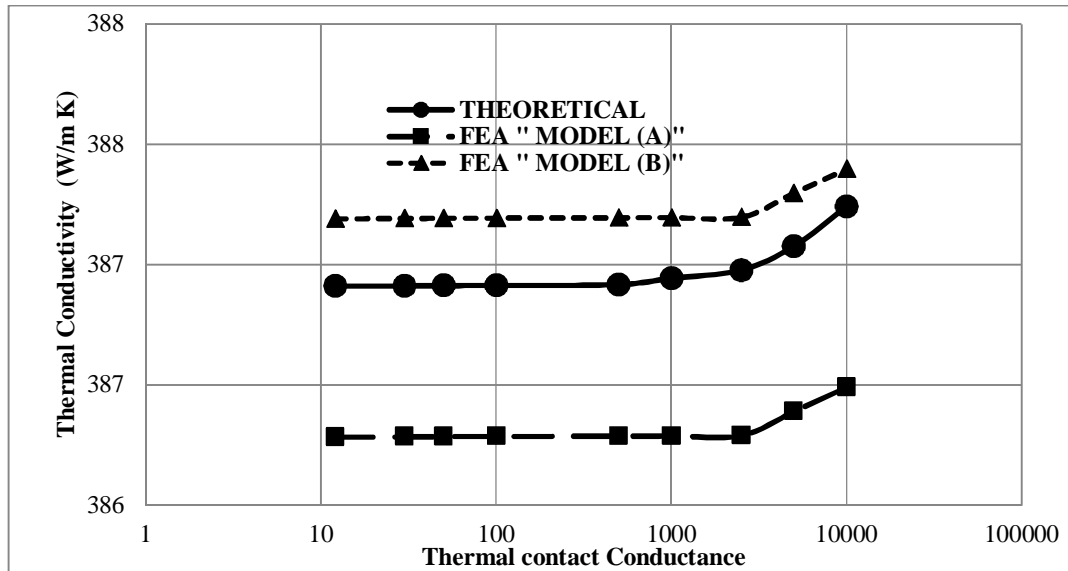


Figure 6.72: Validation of thermal contact conductance for chiral (5, 10) carbon nanotubes (as Short Fiber) reinforced copper metal matrix

However, the finite element results of model “a” and model “b” for carbon nanotube reinforced aluminum matrix are in good and acceptable agreement compared to the theoretical results. It can be observed from the figures 6.73, 6.74, and 6.75 at 3% volume fraction that the thermal conductivity results of armchair, zigzag, and chiral carbon nanotube treated as short fiber reinforced aluminum matrix show insensitive with the increase in thermal contact conductance. Finite element predictions for the two models show lower prediction values than theoretical results. The deviation percentage were calculated for all cases and presented in tables 6.23(a), (b), and (c), respectively.

Table 6.23: validation of thermal contact conductance for (a) armchair (5, 5), (b) zigzag (5, 0), (c) chiral (5, 10) carbon nanotube reinforced aluminum metal matrix

(a) Armchair

β (mw/m ² k)	Theoretical (w/m k)	Finite element (w/m k)		Deviation (%)	
		Model A	Model B	Model A	Model B
12	205.101	202.060	204.419	-1.5%	-0.3%
30	205.102	202.061	204.420	-1.5%	-0.3%
50	205.103	202.062	204.421	-1.5%	-0.3%
100	205.107	202.063	204.422	-1.5%	-0.3%
500	205.133	202.064	204.423	-1.5%	-0.3%
1000	205.166	202.065	204.424	-1.5%	-0.4%
2500	205.266	202.066	204.524	-1.6%	-0.4%
5000	205.431	202.166	204.624	-1.6%	-0.4%
10000	205.762	202.266	204.724	-1.7%	-0.5%

(b) Zigzag

β (mw/m ² k)	Theoretical (w/m k)	Finite element (w/m k)		Deviation (%)	
		Model A	Model B	Model A	Model B
12	205.301	202.606	204.374	-1.3%	-0.5%
30	205.301	202.607	204.375	-1.3%	-0.5%
50	205.302	202.608	204.376	-1.3%	-0.5%
100	205.305	202.609	204.377	-1.3%	-0.5%
500	205.323	202.610	204.378	-1.3%	-0.5%
1000	205.346	202.611	204.379	-1.3%	-0.5%
2500	205.415	202.612	204.380	-1.4%	-0.5%
5000	205.530	202.712	204.480	-1.4%	-0.5%
10000	205.760	202.812	204.580	-1.4%	-0.6%

(c) Chiral

β (mw/m ² k)	Theoretical (w/m k)	Finite element (w/m k)		Deviation (%)	
		Model A	Model B	Model A	Model B
12	205.001	201.244	203.354	-1.8%	-0.8%
30	205.002	201.245	203.355	-1.8%	-0.8%
50	205.003	201.246	203.356	-1.8%	-0.8%
100	205.007	201.247	203.357	-1.8%	-0.8%
500	205.033	201.248	203.358	-1.8%	-0.8%
1000	205.066	201.249	203.359	-1.9%	-0.8%
2500	205.166	201.250	203.360	-1.9%	-0.9%
5000	205.331	201.350	203.460	-1.9%	-0.9%
10000	205.662	201.450	203.560	-2.0%	-1.0%

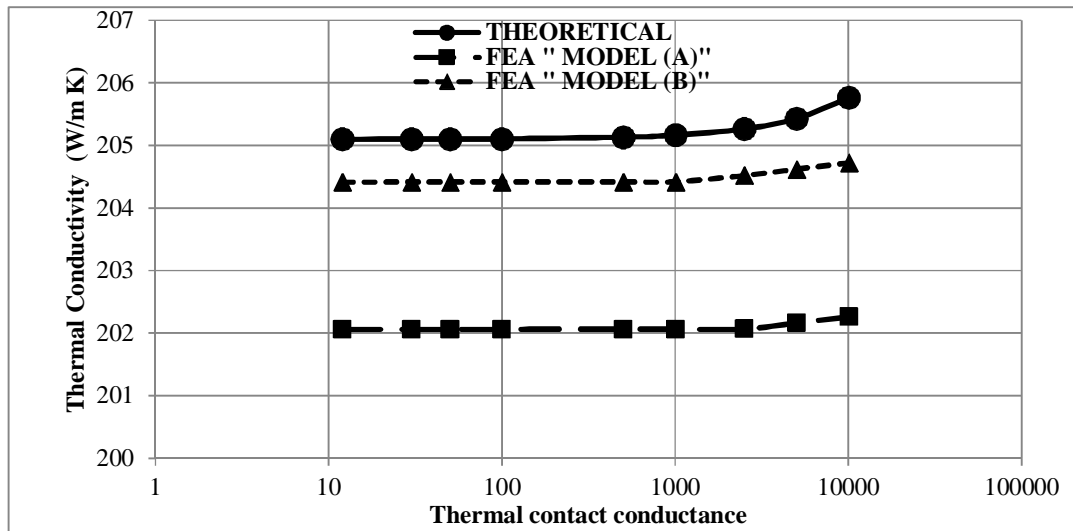


Figure 6.73: Validation of thermal contact conductance for armchair (5, 5) carbon nanotubes (as short fiber) reinforced aluminum metal matrix

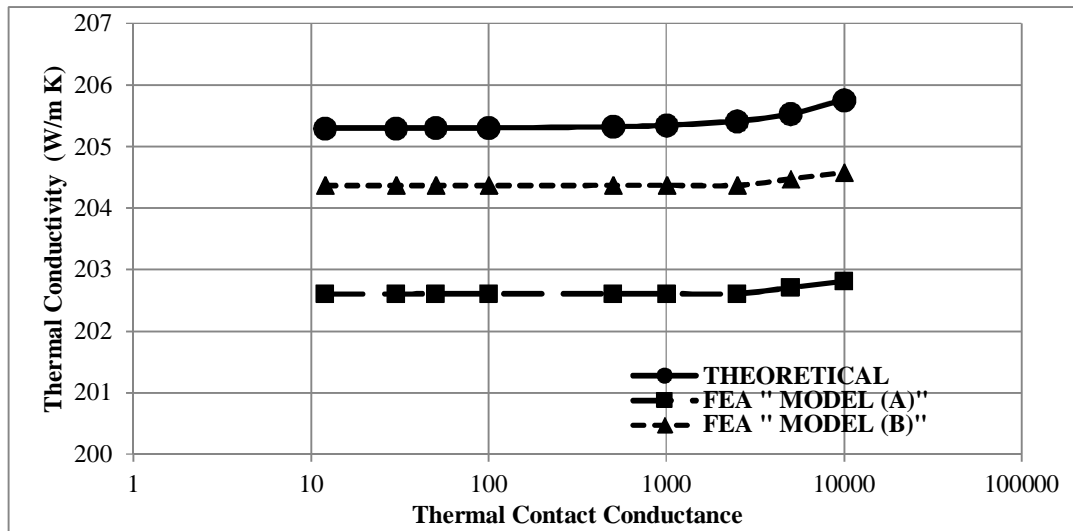


Figure 6.74: Validation of thermal contact conductance for zigzag (5, 0) carbon nanotubes (as short fiber) reinforced aluminum metal matrix

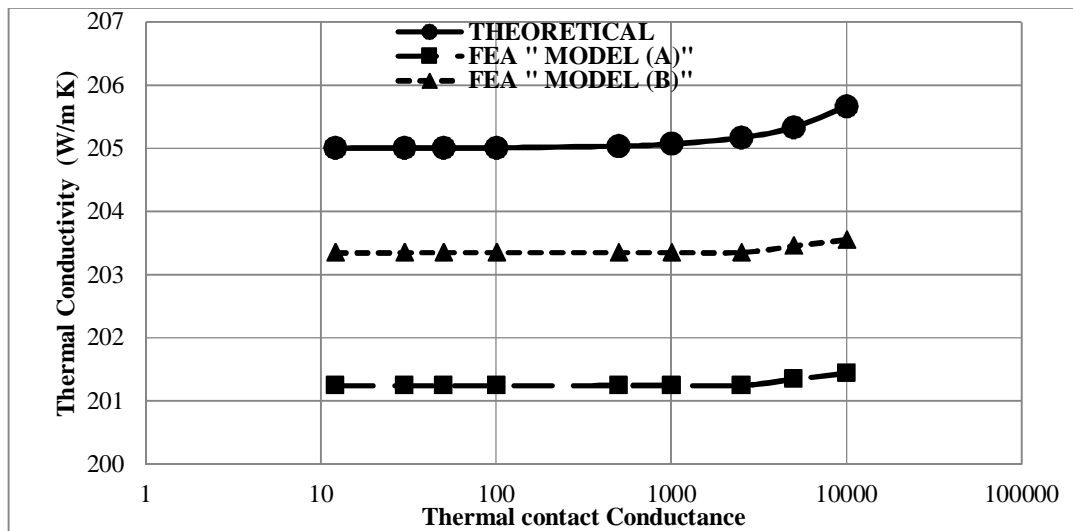


Figure 6.75: Validation of thermal contact conductance for chiral (5, 10) carbon nanotubes (as Short Fiber) reinforced aluminum metal matrix

CHAPTER SEVEN

CONCLUSIONS AND RECOMMENDATIONS

7.1 Conclusions

In terms of calculating the mechanical and thermal properties, this research provides an important database of three basic and major metals in industry: Iron, copper and aluminum, during reinforcing them in various forms of carbon nanotubes. It also provides a computerized tool to calculate the characteristic of any metal in general, and to make a simulation model in the virtual media by using “ANSYS” software. It facilitates, for researchers in this field, to predict the different results of their research before going into practical experiments which are of high cost and consuming of a lot of time.

The analysis was carried out with different representative volume element which was modeled for studying specific geometric and material properties. The results obtained were in agreeable range of the theoretical predictions. Following are brief summary and conclusion of individual analysis mentioned above. The following conclusions can be drawn from the obtained results for elastic and thermal properties of carbon nanotubes reinforced metal matrix composites:

1. An ANSYS-APDL macro developed to evaluate the effective elastic properties Nanocomposite and the results were compared with existing theoretical results calculated by the MATLAB codes based on rule of mixture theory in terms of longitudinal Young's modulus, transverse Young's modulus, shear modulus, and Poisson's ratio for long and short fiber cases for the elastic properties of the new Nanocomposite.
2. Two cases were considered: one case deals with continuous Carbon nanotubes and the second case deals with short Carbon nanotubes reinforcements at three kind of metal matrixes.

3. The predicted results for longitudinal Young's modulus show that the finite element prediction has higher value than theoretical results for carbon nanotube treated as long fiber reinforced iron, copper matrixes, and lower value for aluminum matrix. However, the finite element results show lower values than theoretical results for iron and aluminum matrix while it show higher values than the theoretical results for copper when the carbon nanotubes treated as short fiber.
4. The predicted results for transverse Young's modulus show that the finite element results have higher values than theoretical results for carbon nanotube treated as long fiber reinforced iron, copper, and aluminum matrix. However, the finite element results show higher values than theoretical results for iron matrix while show lower values than the theoretical results for copper and aluminum when the carbon nanotubes treated as short fiber.
5. Shear modulus prediction results show that the finite element results have higher values than theoretical results for carbon nanotube treated as long fiber reinforced iron, copper, and aluminum matrix. However, the finite element results show higher values than theoretical results for iron, copper and aluminum when the carbon nanotubes treated as short fiber.
6. Short fiber reinforced composites can offer some of the property advantages that continuous fiber reinforced composites contain, along with an economical flow processing that favors large-scale production. The elastic properties in short and long fiber generally sensitive with volume fraction.
7. The analysis of the representative volume elements with constant diameter revealed that the effective thermal conductivity of a Nanocomposite increases with the increase of carbon nanotubes length.
8. The finite element analysis of representative volume elements, which were modeled with carbon nanotubes, having fixed length and varying diameters showed that the effective thermal conductivity decreases with increase in diameter of the carbon nanotubes.
9. The representative of the finite element analysis on volume elements which has carbon nanotubes with geometric parameters fixed i.e. length, diameter and volume fraction of carbon nanotubes, showed that the effective thermal conductivity is insensitive with change in interface resistance and the composite kept constant with different thermal contact resistance. This is an alignment with the theoretical predictions.

10. The finite element analysis of the representative volume elements with same carbon nanotubes and varying volume fractions showed that the effective thermal conductivity varies linearly as predicted with the theoretical model. One of the reasons for getting linear relationship of effective conductivity with the volume fraction is the assumption made during mathematical and finite element modeling of the Nanocomposite that there is no interaction between the neighboring carbon nanotubes.
11. It was found that the interfacial resistance is not the single most important factor affecting heat flow in carbon nanotube reinforced metal matrix Nanocomposite.

7.2 Recommendations

A wide range of topics can be considered for further research is listed below:

1. The effective mechanical properties of carbon nanotubes with defects. The effect of such defects can be studied by the current ANSYS-APDL macro with certain modification. Factors such as fraction and distribution of the defects can be investigated.
2. Carbon nanotube bundles behavior can be investigated also by the current ANSYS-APDL macro. Because the interaction among nanotubes in a bundle is van der Waals force, which can be modeled by the same approach. The buckling behavior of the carbon nanotubes bundles can be predicted.
3. The effect of interface layer on the elastic properties of carbon nanotubes reinforced metal matrix Nanocomposite
4. Developing models which address random dispersions of the carbon nanotubes, effective thermal conductivities of non-aligned inclusions and influence of thermal properties in transverse directions.

REFERENCES

- 1 Baughman, R.H., Zakhidov, A.A., and Heer, W.A.d.: 'Carbon Nanotubes-the Route Toward Applications ', *Science*, 2002, 297, (5582), pp. 787-792
- 2 Jain, K.K.: 'The Role of Nanobiotechnology in Drug Discovery', *Drug Discovery Today*, 2005, 10, (21), pp. 1435-1442
- 3 Watlington, K.: 'Emerging Nanotechnologies for Site Remediation and Wastewater Treatment', National Technical Information Service, 2005, pp. 50
- 4 Coleman, J.N., Khan, U., Blau, W.J., and Gun'ko, Y.K.: 'Small but strong: A review of the mechanical properties of carbon nanotube-polymer composites ', *Carbon*, 2006, 44, (9), pp. 1624-1652.
- 5 Ajayan, P.M., and Ebbesen, T.W.: 'Nanometre-Size Tubes of Carbon ', *Reports on Progress in Physics*, 1997, 60, (10), pp. 1025-1062
- 6 Bhushan, B.: 'Handbook of Nanotechnology' (Springer, 2010, 3rd edn.)
- 7 Dresselhaus, M.S., Dresselhaus, G., and Saito, R.: 'Physics of Carbon Nanotubes', *Carbon*, 1995, 33, (7), pp. 883-891
- 8 Rafiei, S.: 'Foundations of Nanotechnology: Mechanics of Carbon Nanotubes' (Apple Academic Press, Inc, 2015.)
- 9 Crainic, N., and Marques, A.T.: 'Nanocomposites: a State-of-the-Art Review', *Key Engineering Materials*, 2002, 230-232, pp. 656-659
- 10 Carreño-Morelli, E., Yang, J., Schaller, R., and Bonjour, C.: 'Carbon nanotube reinforced metal matrix composites'. *Proc. European Conference on Powder Metallurgy Valencia, Spain, October 20-22 2003*
- 11 Durand, L.P.: 'Composite Materials Research Progress' (Nova Science Publishers, Inc., 2008)
- 12 Borst, R.d., and Sadowski, T.: 'Lecture Notes on Composite Materials ' (Springer Science + Business Media B.V., 2008)
- 13 Yang, J., and Schaller, R.: 'Mechanical spectroscopy of Mg reinforced with Al₂O₃ short fibers and C nanotubes', *Materials Science and Engineering A*, 2004, 370, (1-2), pp. 512-515
- 14 Davim, J.P.: 'Metal Matrix Composites: Materials, Manufacturing and Engineering' (Degruyter, 2014)
- 15 Evans, A., Marchi, C.S., and A. Mortensen: 'Metal Matrix Composites in Industry, An Introduction and a Survey' (Kluwer Academic Publishers, 2003)
- 16 Ajayan, P.M., Schadler, L.S., and Braun, P.V.: 'Nanocomposite Science and Technology' (WILEY-VCH Verlag GmbH Co. , 2003)
- 17 Manias, E.: 'Nanocomposites: Stiffer by design', *Nature Materials*, 2007, 6, pp. 9-11
- 18 Küçükıldırım, B.O., and Ayşegül Akdoğan Eker: 'Mechanical Behavior of Industrial Grade MWCNT and Glass Fiber Reinforced Polyester Hybrid Nanocomposites', *International Journal of Arts and Sciences*, 2010, 3, (9), pp. 252-257
- 19 Thostenson, E.T., Ren, Z., and Chou, T.-W.: 'Advances in the science and technology next term of carbon nanotubes and their previous term composites:next term a review', *Composites Science and Technology*, 2001, 61, (13), pp. 1899-1912

- 20 Mamedov, A.A., Kotov, N.A., Prato, M., Guldi, D.M., Wicksted, J.P., and Hirsch, A.: 'Molecular Design of Strong Single-Wall Carbon Nanotube/Polyelectrolyte Multilayer Composites', *Nature Materials*, 2002, 1, (3), pp. 190-194
- 21 Sinnott, S.B., and Andrews, R.: 'Carbon nanotubes: synthesis, properties, and applications', *Critical Reviews in Solid State and Materials Sciences*, 2001, 26, (3), pp. 145-249
- 22 Chen, X., Xia, J., Peng, J., Li, W., and Xie, S.: 'Carbon-nanotube metal-matrix composites prepared by electroless plating ', *Composites Science and Technology*, 2000, 60, (3), pp. 301-306
- 23 Agarwal, A., Bakshi, S.R., and Lahiri, D.: 'Carbon Nanotubes Reinforced Metal Matrix Composites' (CRC Press, Taylor & Francis Group, 2011)
- 24 Jorio, A., Dresselhaus, G., and Dresselhaus, M.S.: 'Carbon Nanotubes: Advanced Topics in the Synthesis, Structure, Properties and Applications' (Springer Science+Business Media, 2008)
- 25 Tang, Z., and Sheng, P.: 'Nanoscale Phenomena: Basic Science to Device Applications' (Springer, 2008)
- 26 Chuang, T.-J., Anderson, P.M., Wu, M.-K., and Hsieh, S.: 'Nanomechanics of Materials and Structures' (Springer, 2006)
- 27 Dresselhaus, M.S., Dresselhaus, G., Charlier, J.C., and Hernandez, E.: 'Electronic, thermal and mechanical properties of carbon nanotubes', *Philosophical Transactions The Royal Society A*, 2004, 362, pp. 2065-2098
- 28 Gunes, I.S., and Jana, S.C.: 'Shape Memory Polymers and Their Nanocomposites: A Review of Science and Technology of New Multifunctional Materials ', *Journal of Nanoscience and Nanotechnology*, 2008, 8, (4), pp. 1616-1637
- 29 Hussain, F., Hojjati, M., Okamoto, M., and Gorgan, R.E.: 'Polymer-Matrix Nanocomposites, Processing, Manufacturing, and Application: An Overview', *Journal of Composite Materials*, 2006, 40, (17), pp. 1511-1575
- 30 Peigney, A.: 'Composite materials: Tougher ceramics with nanotubes', *Nature Materials*, 2003, 2, (1), pp. 15-16
- 31 BREUER, O., and SUNDARARAJ, U.: 'Big Returns From Small Fibers: A Review of Polymer/Carbon Nanotube Composites', *Polymer Composites*, 2004, 25, (6), pp. 630-645
- 32 Esawi, A.M.K., and Farag, M.M.: 'Carbon nanotube reinforced composites: Potential and current challenges ', *Materials & Design*, 2007, 28, (9), pp. 2394-2401
- 33 Cho, J., Boccaccini, A.R., and Shaffer, M.S.P.: 'Ceramic matrix composites containing carbon nanotubes', *Journal of Materials Science*, 2009, 44, pp. 1934-1951
- 34 Tjong, S.C.: 'Carbon Nanotube Reinforced Composites :Metal and Ceramic Matrices' (Wiley-VCH Verlag GmbH & Co., Weinheim, 2009)
- 35 Iijima, S.: 'Helical Microtubules of Graphitic Carbon', *Nature* 1991, 354, pp. 56-58
- 36 Cadek, M., Coleman, J.N., Barron, V., Hedicke, K., and W. J. Blau: 'Morphological and Mechanical Properties of Carbon-Nanotube-Reinforced Semicrystalline and Amorphous Polymer Composites', *Applied Physics Letters*, 2002, 81, (5123)
- 37 Qian, D., Dickey, E.C., Andrews, R., and Rantell, T.: 'Load transfer and deformation mechanisms in carbon nanotube-polystyrene composites', *Applied Physics Letters*, 2000, 76, (20), pp. 2868-1870
- 38 Kroto, H.W., Heath, J.R., O'Brien, S.C., Curl, R.F., and Smalley, R.E.: 'C60: Buckminsterfullerene', *Nature*, 1985, 318, (6042), pp. 162-163
- 39 Iijima, S., and Ichihashi, T.: 'Single-Shell Carbon Nanotubes of 1-Nm Diameter', *Nature*, 1993, 363, pp. 603-605

- 40 Dresselhaus, M.S., Dresselhaus, G., Saito, R., and Jorio, A.: ‘Raman spectroscopy of carbon nanotubes’, in Editor : ‘Book Raman spectroscopy of carbon nanotubes’ (2005, edn.), pp. 47-99
- 41 Lau, A.K.-T., and Hui, D.: ‘The revolutionary creation of new advanced materials-carbon nanotube composites ’, *Composites Part B: Engineering*, 2002, 33, (4), pp. 263-277
- 42 Qian, D., Wagner, G.J., Liu, W.K., Yu, M.-F., and Ruoff, R.S.: ‘Mechanics of Carbon Nanotubes’, *Applied Mechanics Reviews*, 2002, 55, (6), pp. 495-533
- 43 Hata, K., Futaba, D.N., Mizuno, K., Namai, T., Yumura, M., and S. Iijima: ‘Water-Assisted Highly Efficient Synthesis of Impurity-Free Single-Walled Carbon Nanotubes’, *Science*, 2004, 306, (5700), pp. 1362–1364
- 44 Huang, J., Kim, D.H., Seelaboyina, R., Rao, B.K., Wang, D., Park, M., and W. Choi: ‘Catalysts Effect on Single-Walled Carbon Nanotube Branching’, *Diamond and Related Materials*, 2007, 16, (8), pp. 1524 – 1529,
- 45 M.Odegard, G., S.Gates, T., M.Nicholson, L., and E.Wise, K.: ‘Equivalent Continuum Modeling of Nano-Structured Materials’, *Composite Science and Technology*, 2002, 62, (14), pp. 1869-1880
- 46 Broza, G.: ‘Synthesis, Properties, Functionalization and Applications of Carbon Nanotubes: A State of the Art Review’, *Chemistry & Chemical Technology*, 2010, 4, (1), pp. 35-45
- 47 William A. Goddard, I., Brenner, D.W., Lyshevski, S.E., and Iafrate, G.J.: ‘Handbook of Nanoscience, Engineering, and Technology’ (CRC Press is an imprint of Taylor & Francis Group, 2007, 2nd edition edn.)
- 48 Meyyappan, M.: ‘Carbon nanotubes science and applications’ (CRC Press: Boca Raton, 2005)
- 49 Andrews, R., Jacques, D., Qian, D., and Dickey, E.C.: ‘Purification and Structural Annealing of Multiwalled Carbon Nanotubes at Graphitization Temperatures’, *Carbon*, 2001, 39, (11), pp. 1681–1687
- 50 Sattler, K.D.: ‘Handbook of Nanophysics : Nanotubes and Nanowires’ (CRC Press is an imprint of Taylor & Francis Group,, 2011)
- 51 Kainer, K.U.: ‘Metal Matrix Composites: Custom-made Materials for Automotive and Aerospace Engineering’ (Wiley-VCH Verlag GmbH & Co. KGaA, 2006)
- 52 Bakshi, S.R., Lahiri, D., and Agarwal, A.: ‘Carbon Nanotube Reinforced Metal Matrix Composites – a review’, *International Materials Reviews*, 2010, 55, (1), pp. 41-64
- 53 Kuzumaki, T., Miyazawa, K., Ichinose, H., and Ito, K.: ‘Processing of Carbon Nanotube Reinforced Aluminum Composite’, *Journal Materials Research* 1998, 13, (9), pp. 2445-2449
- 54 Xu, C.L., Wei, B.Q., Ma, R.Z., Liang, J., Ma, X.K., and Wu, D.H.: ‘Fabrication of aluminum–carbon nanotube composites and their electrical properties ’, *Carbon*, 1999, 37, (5), pp. 855-858
- 55 Zhong, R., Cong, H., and Hou, P.: ‘Fabrication of nano-Al based composites reinforced by single-walled carbon nanotubes ’, *Carbon*, 2003, 41, (4), pp. 848-851
- 56 George, R., Kashyap, K.T., Rahul, R., and Yamdagni, S.: ‘Strengthening in carbon nanotube/aluminium (CNT/Al) composites’, *Scripta materialia*, 2005, 53, (10), pp. 1159-1163
- 57 Esawi, A.M.K., and Borady, M.A.E.: ‘Carbon nanotube-reinforced aluminium strips’, *Composites Science and Technology*, 2008, 68, pp. 486–492
- 58 Laha, T., and Agarwal, A.: ‘Effect of Sintering on Thermally Sprayed Carbon Nanotube Reinforced Aluminum Nanocomposite’, *Materials Science and Engineering A* 2008, 480, pp. 323-332

- 59 Dong, S.R., Tu, J.P., and Zhang, X.B.: 'An investigation of the sliding wear behavior of Cu-matrix composite reinforced by carbon nanotubes', *Materials Science and Engineering: A*, 2001, 313, (1-1), pp. 83-87
- 60 Shurong, D., and Xiaobin, Z.: 'Mechanical Properties of Cu-Based Composites Reinforced by Carbon Nanotubes', *Transactions of Nonferrous Metals Society in China* 1999, 9, (3), pp. 457-461
- 61 Kim, K.T., Cha, S.I., Hong, S.H., and Hong, S.H.: 'Microstructures and Tensile Behavior of Carbon Nanotubes Reinforced Cu Matrix Nanocomposites', *Materials Science and Engineering A*, 2006, 430, pp. 27-33
- 62 Daoush, W.M.: 'Processing and Characterization of CNT/Cu Nanocomposites by Powder Technology', *Powder Metallurgy and Metal Ceramics*, 2008, 47, pp. 38-45
- 63 Daoush, W.M., Lim, B.K., Mo, C.B., Nam, D.H., and Hong, S.H.: 'Electrical and Mechanical Properties of Carbon Nanotube Reinforced Copper Nanocomposites Fabricated by Electroless Deposition Process', *Materials Science and Engineering A*, 2009, 513-514, pp. 247-253
- 64 Chen, X., Zhang, G., Chen, C., Zhou, L., Li, S., and Li, X.: 'Carbon Nanotube Composite Deposits with High Hardness and High Wear Resistance (pages 514-518)', *Advanced Engineering Materials*, 2003, 5, (7), pp. 514-518
- 65 Jiang-ping, T., Li-ping, Z., Wei-xiang, C., Xin-bing, Z., Fu, L., and Xiao-bin, Z.: 'Preparation of Ni-CNT Composite Coatings on Aluminum Substrate and its Friction and Wear Behavior', *Transactions of the Nonferrous Metals Society of China* 2004, 14, (5), pp. 880-884
- 66 Chen, W.X., Tu, J.P., Wang, L.Y., Gan, H.Y., Xu, Z.D., and Zhang, X.B.: 'Tribological application of carbon nanotubes in a metal-based composite coating and composites', *Carbon*, 2003, 41, (2), pp. 215-222
- 67 Kuzumaki, T., Ujiie, O., Ichinose, H., and Ito, K.: 'Mechanical Characteristics and Preparation of Carbon Nanotube Fiber-Reinforced Ti Composite', *Advanced Engineering Materials* 2000, 2, (7), pp. 416-418
- 68 Carreño-Morelli, E., Yang, J., Couteau, E., Hernadi, K., Seo, J.W., Bonjour, C., Forró, L., and Schaller, R.: 'Carbon Nanotube/Magnesium Composites', *Physica Status Solidi (a)*, 2004, 201, (8), pp. R53-R55
- 69 Contescu, C.I., and Putyera, K.: 'Dekker Encyclopedia of Nanoscience and Nanotechnology' (CRC Press 2009, 2nd edn.)
- 70 Mallick, P.K.: 'Fiber Reinforced Composites: Materials, Manufacturing, and Design' (CRC Press is an imprint of Taylor & Francis Group, 2007, 3rd edn.)
- 71 Agarwal, B.D., Broutman, L.J., and Chandrashekhara, K.: 'Analysis and Performance of Fiber Composites' (John Wiley & Sons., 2006, 3rd edn.)
- 72 Daniel, I.M., and Ishai, O.: 'Engineering Mechanics of Composite Materials' (Oxford University Press, 1994)
- 73 Elhajjar, R., Saponara, V.L., and Muliana, A.: 'Smart Composites Mechanics and Design' (CRC Press. Taylor & Francis Group, 2014)
- 74 Vasiliev, V.V., and Morozov, E.V.: 'Mechanics and Analysis of Composite Materials' (Elsevier Science Ltd., 2001)
- 75 Kaw, A.K.: 'Mechanics of Composite Materials' (CRC Press is an imprint of Taylor & Francis Group, LLC, 2006, 2nd edn.)
- 76 Donaldson, S.L., and Miracle, D.B.: 'ASM Handbook Composites' (ASM International, 2001)
- 77 Cristescu, N.D., Craciun, E.-M., and Soós, E.: 'Mechanics of Elastic Composites' (Chapman & Hall/CRC, 2004)
- 78 Jones, R.M.: 'Mechanics of Composite Materials' (Taylor & Francis, Philadelphia, 1999, 2nd edn.)
- 79 Barbero, E.J.: 'Introduction to Composite Materials Design' (CRC Press. Taylor & Francis Group, 2011, 2nd edn.)

- 80 Ebrahimi, F.: 'Finite Element Analysis– Applications in Mechanical Engineering'
(InTech, 2012)
- 81 Barbero, E.J.: 'Finite Element Analysis of Composite Materials Using ANSYS'
(CRC Press, 2013)
- 82 Cazacu, O.: 'Mechanics of Heterogeneous Materials from Microstructure to
Macro-scale Properties' (ISTE Ltd and Wiley, 2008)
- 83 Kollar, L.P., and Springer, G.S.: 'Mechanics of Composite Structure' (Cambridge
University Press, 2003)
- 84 Haghi, A.K., Oluwafemi, O.S., Maria, H.J., and Jose, J.P.: 'Composites and
Nanocomposites' (Apple Academic Press, Inc., 2013)
- 85 Hong, S.H., Seo, J., and Moon, K.: 'Advanced Materials, Mechanical and
Structural Engineering' (Taylor & Francis Group, 2016)
- 86 J. Hone, M. Whitney, and Zettl, A.: 'Thermal Conductivity of Single-Walled
Carbon Nanotubes', *Synthetic Metals*, 1999, 103, (1-3), pp. 2498–2499
- 87 Bagchi, A., and Nomura, S.: 'On the Effective Thermal Conductivity of Carbon
Nanotube Reinforced Polymer Composites', *Composites Science and
Technology*, 2006, 66, pp. 1703–1712
- 88 Nicolais, L., Borzacchiello, A., and Lee, S.M.: 'Wiley Encyclopedia of
Composites', in Editor (Ed.)^(Eds.): 'Book Wiley Encyclopedia of Composites'
(John Wiley & Sons, Inc., 2012, 2nd edn.), pp. 3444
- 89 Nan, C.-W., Shi, Z., and Lin, Y.: 'A simple model for thermal conductivity of
carbon nanotube-based- composite', *Chemical Physics Letters*, 2003, 375, pp.
666-669
- 90 G.M.Odegard, T.S.Gates, and K.E.Wise: 'Constitutive Modeling of Nanotube-
Reinforced Polymer Composites', *American Institute of Aeronautics and
Astronautics*, 2002, pp. 1427
- 91 Raabe, D.: 'Computational Materials Science: The Simulation of Materials
Microstructures and Properties' (Wiley-VCH, 1998)
- 92 Lee, J.G.: 'Computational Materials Science: An Introduction' (CRC Press.
Taylor & Francis Group, 2012)
- 93 Aboudi, J.: 'Micromechanical Analysis of Thermo-Inelastic Multiphase Short-
Fiber Composites', *Composites Engineering*, 1995, 5, (7), pp. 839–850
- 94 Valavala, P.K., and Odegard, G.M.: 'Modeling Techniques for Determination of
Mechanical Properties of Polymer Nanocomposites', *Reviews on Advanced
Materials Science* 2005, 9, (1), pp. 34-44
- 95 Treacy, M.M.J., Ebbesen, T.W., and Gibson, J.M.: 'Exceptionally High Young's
Modulus Observed for Individual Carbon Nanotubes', *Nature*, 1996, 381, pp. 678-
680
- 96 L.Jin, C.Bower, and O.Zhou: 'Alignment of Carbon Nanotubes in a Polymer
Matrix by Mechanical Stretching', *Applied Physics Letters*, 1998, 73, pp. 1197-
1199
- 97 C.Bower, R.Rosen, L.Jin, J.Han, and O.Zhou: 'Deformation of Carbon Nanotubes
in Nano-Tube Composites', *Applied Physics Letters*, 1999, 74, pp. 3317-3319
- 98 P.M.Ajayan, L.S.Schadler, S.C.Giannaris, and A.Rubio: 'Single-Walled
Carbontube Polymer Composites:Strength and Weakness', *Advanced Materials*,
2000, 12, pp. 750-753
- 99 Lu, J.P.: 'Elastic Properties of Single and Multilayered Carbon Nanotubes',
Journal of the Physics and Chemistry of Solids, 1997, 58, pp. 1649-1652
- 100 Griebel, M., and Hamaekers, J.: 'Molecular Dynamics Simulations of The Elastic
Modulii of Polymer-Carbon Nanotube Composites', *Computer Methods in
Applied Mechanics and Engineering*, 2004, 193, pp. 1773-1788
- 101 Parrinello, M., and Rahman, A.: 'Crystal Structure and Pair Potentials: A
Molecular Dynamics Study', *Physical Review Letters*, 1980, 45, (14), pp. 1196-
1199

- 102 S.J.V.Frankland, V.M.Harik, G.M.Odegard, D.W.Brenne, r., and T.S.Gates: 'The Stress-Strain Behavior of Polymer-Nanotube Composites from Molecular Dynamics Simulations', *Composites Science and Technology*, 2003, 63, pp. 1655-1661
- 103 G.M.Odegard, T.S.Gates, K.E.Wise, C.Park, and E.J.Siochic: 'Constitutive Modeling of Nanotube-Reinforced Polymer Composites', *Composite Science and Technology*, 2003, 63, pp. 1671-1687
- 104 Fisher, F.T., Bradshaw, R.D., and Brinson, L.C.: 'Fiber Waviness in Nanotube-Reinforced Polymer Composites-I: Modulus Predictions Using Effective Nanotube Properties,' *Composite Science and Technology*, 2003, 63, pp. 1689-1703
- 105 Chen, X.L., and Liu, Y.J.: 'Square Representative Volume Elements for Evaluation the Effective Material Properties of Carbon Nanotube-Based Composites', *Computational Material Science*, 2004, 29, pp. 1-11
- 106 Liu, Y.J., and Chen, X.L.: 'Evaluations of the Effective Material Properties of Carbon Nanotube-Based Composites Using a Nanoscale Representative Volume Element', *Mechanics of Materials* 2003, 35, pp. 69-81
- 107 BAL, S., and SAMAL, S.S.: 'Carbon nanotube reinforced polymer composites—A state of the art', *Bulletin of Materials Science*, 2007, 30, (4), pp. 379-386
- 108 Li, S., and Gao, X.-L.: 'Handbook of Micromechanics and Nanomechanics' (CRC Press. Taylor & Francis Group, 2013)
- 109 Kane, D., Micolich, A., and Roger, P.: 'Nanomaterials Science and Applications' (Taylor & Francis Group, LLC, 2016)
- 110 Musa, S.M.: 'Computational Finite Element Methods in Nanotechnology' (CRC Press, 2013)
- 111 Kaveh, A.: 'Computational Structural Analysis and Finite Element Methods' (Springler, 2014)
- 112 Fan, C.-W., Huang, J.-H., Hwu, C., and Liu, Y.-Y.: 'Mechanical Properties of Single-walled Carbon Nanotubes - A Finite Element Approach', *Advanced Materials Research*, 2008, 33-37, pp. 937-942
- 113 Kalamkarov, A.L., Georgiades, A.V., Rokkam, S.K., Veedu, V.P., and Ghasemi-Nejhad, M.N.: 'Analytical and Numerical Techniques to Predict Carbon Nanotubes Properties', *International Journal of Solids and Structures*, 2006, 43, pp. 6832-6854
- 114 Ávila, A.F., and Lacerda, G.S.R.: 'Molecular Mechanics Applied to Single-Walled Carbon Nanotubes', *Materials Research*, 2008, 11, (3), pp. 325-333
- 115 Hu, N.: 'Composites and Their Properties' (InTech, 2012)
- 116 Islam, M.S., and Szpunar, J.: 'Effects of Orientation of Carbon Nanotubes on CNT Bundle Based Silk Composite Using Finite Element Method', *Modeling and Numerical Simulation of Material Science*, 2013, (3), pp. 33-38
- 117 Rémond, Y., Ahzi, S., Baniassadi, M., and Garmestani, H.: 'Applied RVE Reconstruction and Homogenization of Heterogeneous Materials' (John Wiley & Sons, Inc. and ISTE Ltd 2016)
- 118 Liu, Y.J., and Chen, X.L.: 'Continuum Models of Carbon Nanotube-Based Composites Using the Boundary Element Method', *Electronic Journal of Boundary Elements*, 2003, 1, (2), pp. 316-335
- 119 Islam, M.S., Riktan, F.O., Chowdhury, S.C., Chowdhury, M.M.R., and Ahmed, S.: 'Evaluation of Tensile Modulus of Carbon Nanotube Bundle Based Composite with Interface Using Finite Element Method'. Proc. 2011 COMSOL Conference, Bangalore2011
- 120 Husain, M., and Khan, Z.H.: 'Advanced Nanomaterials' (Springer 2016)
- 121 Freitag, M., Tsang, J.C., Kirtley, J., Carlsen, A., Chen, J., Troeman, A., Hilgenkamp, H., and Avouris, P.: 'Electrically Excited, Localized Infrared

- Emission From Single Carbon Nanotubes', *Nano Letters*, 2006, 6, (7), pp. 1425–1433
- 122 Glushanin, S., Topolov, V.Y., and Krivoruchko, A.V.: 'Features of piezoelectric properties of 0-3 PbTiO₃-type ceramic/polymer composites', *Materials Chemistry and Physics*, 2006, 97, (2-3), pp. 357-364
 - 123 Moisala, A., Li, Q., Kinloch, I.A., and Windle, A.H.: 'Thermal and electrical conductivity of single and multi-walled carbon nanotube-epoxy composites', *Composites Science and Technology*, 2006, 66, (10), pp. 1285-1288
 - 124 Baker, A.J.: 'Finite Elements Computational Engineering Sciences' (John Wiley & Sons, Ltd, 2012)
 - 125 Tserpes, K.I., and Papanikos, P.: 'Finite element modeling of single-walled carbon nanotubes', *Composites Part B: Engineering*, 2005, 36, pp. 468-477
 - 126 Lee, H.-H.: 'Finite Element Simulations with ANSYS Workbench 14' (SDC Publications, 2012)
 - 127 Lawrence, K.: 'ANSYS Tutorial Release 14' (SDC Publications, 2012)
 - 128 Schröder, J., and Wriggers, P.: 'Advanced Finite Element Technologies' (Springler, 2016)
 - 129 Moaveni, S.: 'Finite Element Analysis Theory and Application with ANSYS' (Prentice Hall, 2007, 3rd edn.)
 - 130 Madenci, E., and Guven, I.: 'The Finite Element Method and Applications in Engineering Using ANSYS' (Springer International Publishing, 2015)
 - 131 Alawadhi, E.M.: 'Finite Element Simulations Using ANSYS' (CRC Press 2010)
 - 132 Chen, X., and Liu, Y.: 'Finite Element Modeling and Simulation with ANSYS Workbench' (CRC Press 2015)
 - 133 Rangel, J.H., Brostow, W., and Castlano, V.M.: 'Mechanical modeling of single-walled carbon nanotube using finite element approach', *Polimery*, 2013, 58, (4), pp. 276-281
 - 134 Miller, E.: 'Introduction to the ANSYS Parametric Design Language (APDL)' (PADT, Inc, 2016, 2nd edn.)
 - 135 Cook, R.D., Malkus, D.S., Plesha, M.E., and Witt, R.J.: 'Concepts and applications of finite element analysis' (John Willy & sons, INC, 2002, Fourth edn.)
 - 136 Li, S.: 'General Unit Cell for Micromechanical Analyses of Unidirectional Composites,' *Composites Part A*, 2000, 3, (6), pp. 815-816
 - 137 Kim, B.R., and Lee, H.K.: 'An RVE-Based Micromechanical Analysis of Fiber-Reinforced Composites Considering Fiber Size Dependence', *Composite Structures*, 2009, 90, (4), pp. 418-427
 - 138 ANSYS: 'Documentation for Release 15.0' (SAS IP, Inc, 2013)
 - 139 Zimmer, M., Fan, X., Bao, J., Liang, R., Wang, B., Zhang, C., and Brooks, J.: 'Through-Thickness Thermal Conductivity Prediction Study on Nanocomposites and Multiscale Composites', *Materials Sciences and Applications*, 2012, 3, pp. 131-138

BIODATA OF THE AUTHOR

The author was born on 7th July 1966 in Rafah city, Gaza Strip, Palestine. He finished his higher secondary education at Al-Hadi Arafa secondary school in Libya. In 1991, author completed his Bachelor of Science degree in Mechanical Engineering from Garyounis University in Libya. He received his Master's degree in Mechanical Engineering from University Putra Malaysia at Serdang, Malaysia in 2007. The author enrolled in Sudan University of Science and Technology, College of Graduate Studies as a Ph.D Candidate in Faculty of Engineering, Mechanical Engineering School. His research interests are in the field of composite materials, Nanocomposite, and finite element analysis.

LIST OF PUBLICATIONS

1. Carbon Nanotubes and Their Composites: A Review. Sudan Engineering Society Journal, vol. 58, no. 1, March 2012.
2. Carbon Nanotubes: Challenges and Opportunities. Proceedings of International Conference on Computing, Electrical and Electronic Engineering (ICCEEE 2013), 26-28 August 2013, Khartoum, Sudan
3. Determination of Elastic Properties of Carbon Nanotubes Treated as Long Fiber for Reinforcing Iron Matrix”, 1st Conference of Industrial Technology (CIT2017) 17-18 May 2017, Misrata, Libya